ADVANCES IN GEOLOGY OF UNCONVENTIONAL HYDROCARBON RESOURCES

EDITED BY: Dawei Lv, Jon Jincai Zhang and Dongdong Wang
PUBLISHED IN: Frontiers in Earth Science

frontiers Research Topics

ISSN 1664-8714
ISBN 978-2-88976-085-5
DOI 10.3389/978-2-88976-085-5

About Frontiers

Frontiers is more than just an open-access publisher of scholarly articles: it is a pioneering approach to the world of academia, radically improving the way scholarly research is managed. The grand vision of Frontiers is a world where all people have an equal opportunity to seek, share and generate knowledge. Frontiers provides immediate and permanent online open access to all its publications, but this alone is not enough to realize our grand goals.

Frontiers Journal Series

The Frontiers Journal Series is a multi-tier and interdisciplinary set of open-access, online journals, promising a paradigm shift from the current review, selection and dissemination processes in academic publishing. All Frontiers journals are driven by researchers for researchers; therefore, they constitute a service to the scholarly community. At the same time, the Frontiers Journal Series operates on a revolutionary invention, the tiered publishing system, initially addressing specific communities of scholars, and gradually climbing up to broader public understanding, thus serving the interests of the lay society, too.

Dedication to Quality

Each Frontiers article is a landmark of the highest quality, thanks to genuinely collaborative interactions between authors and review editors, who include some of the world's best academicians. Research must be certified by peers before entering a stream of knowledge that may eventually reach the public - and shape society; therefore, Frontiers only applies the most rigorous and unbiased reviews.
Frontiers revolutionizes research publishing by freely delivering the most outstanding research, evaluated with no bias from both the academic and social point of view. By applying the most advanced information technologies, Frontiers is catapulting scholarly publishing into a new generation.

What are Frontiers Research Topics?

Frontiers Research Topics are very popular trademarks of the Frontiers Journals Series: they are collections of at least ten articles, all centered on a particular subject. With their unique mix of varied contributions from Original Research to Review Articles, Frontiers Research Topics unify the most influential researchers, the latest key findings and historical advances in a hot research area! Find out more on how to host your own Frontiers Research Topic or contribute to one as an author by contacting the Frontiers Editorial Office: frontiersin.org/about/contact

ADVANCES IN GEOLOGY OF UNCONVENTIONAL HYDROCARBON RESOURCES

Topic Editors:
Dawei Lv, Shandong University of Science and Technology, China
Jon Jincai Zhang, Sinopec Tech Houston Center (STHC), United States
Dongdong Wang, Shandong University of Science and Technology, China

Citation: Lv, D., Zhang, J. J., Wang, D. eds. (2022). Advances in Geology of Unconventional Hydrocarbon Resources. Lausanne: Frontiers Media SA. doi: 10.3389/978-2-88976-085-5

Table of Contents

frontiers | Frontiers in Earth Science

EDITORIAL
published: 13 April 2022
doi: 10.3389/feart.2022.846863

Editorial: Advances in Geology of Unconventional Hydrocarbon Resources

Dawei Lv[1]*, *Jon Jincai Zhang*[2]* *Dongdong Wang*[1]

[1]College of Earth Science and Engineering, Shandong University of Science and Technology, Qingdao, China, [2]Sinopec Tech Houston Center, Houston, TX, United States

Keywords: geology, unconventional hydrocarbon resources, shale gas, shale oil, exploration and production

Editorial on the Research Topic

Advances in Geology of Unconventional Hydrocarbon Resources

For deepening our understanding on geological theory of unconventional oil and gas, we initiated this research topic and have gathered contributions from scientists working in diverse geoscience disciplines who have common interests in unconventional resources. In total, 16 papers have been included. The main topics include the following aspects: 1) shale gas in the Wufeng and Longmaxi formations, in the Marcellus formation, and shale gas exploration potential in southwestern Shandong Province of China; 2) shale oil in the Ordos Basin, in the Bohai Bay Basin, and in the Junggar Basin; 3) tight sandstone reservoirs and hydrocarbon reservoirs in volcanic rocks. These papers are briefly introduced in the following sections, and for more details readers can access each full paper from the links shown in this paper.

SHALE GAS

The Fuling shale gas play was the first commercial, and remains the largest, shale gas field in China, producing more than 400×10^8 m^3 of shale gas since its discovery in 2012. The major shale gas formations are the Wufeng and Longmaxi formations (Zheng et al., 2020); prolific because they are marine sediments with overpressures (Zhang, 2019). Herein are presented several papers. Wang et al. studied the accumulation mechanisms of normal-pressured fractured shale gas in the Wufeng–Longmaxi Formation in southeastern Chongqing. They found that the reason resulting in normal-pressure accumulation in this region was the intense tectonic activity. These tectonic movements could have potentially improved permeability of the shales. Wang et al. investigated shale gas exploration and development of the Longmaxi formation in the Sichuan Basin. They found that the diagenetic evolution is an important controlling factor on shale gas reservoirs. Sun et al. found that the shallow Longmaxi shale reservoir in Guizhou Province is dominated by adsorbed gas. The adsorbed gas occurs mostly in the organic matter nanopores.

Shale gas was also discovered in very old formations. Zhou et al. studied shale gas potential in the lower Cambrian Qiongzhusi shale formation in the Sichuan Basin. They concluded that the thick shale in the Deyang-Anyue rift would be the focus of shale gas exploration in the Qiongzhusi Formation.

Currently, although most shale gas plays are located in southern China, there is also shale gas exploration potential in northern China. For example, Li et al. discussed shale gas exploration in southwestern Shandong Province. Zhang et al. studied gas and oil potentials of the Lishui Sag in the

Edited by:
David R. Lentz,
University of New Brunswick
Fredericton, Canada

Reviewed by:
Dave Keighley,
University of New Brunswick
Fredericton, Canada

****Correspondence:***
Jon Jincai Zhang
zhangjon@gmail.com
Dawei Lv
lvdawei95@163.com

Specialty section:
This article was submitted to Economic Geology, a section of the journal Frontiers in Earth Science

Received: *31 December 2021*
Accepted: *21 March 2022*
Published: *13 April 2022*

Citation:
Lv D, Zhang JJ and Wang D (2022) Editorial: Advances in Geology of Unconventional Hydrocarbon Resources. Front. Earth Sci. 10:846863. doi: 10.3389/feart.2022.846863

eastern China Sea Shelf Basin through modelling hydrocarbon generation of deeply buried type III kerogen.

To produce shale gas and other unconventional resources, hydraulic fracturing operations are needed, Ferguson et al. discussed effects of carbonate minerals on shale and hydraulic fracturing fluid reactions that can potentially impact porosity and microfracture integrity in the Marcellus formation in the United States.

SHALE OIL

Shale oil has been explored extensively in China. For example, Sinopec recently announced a discovery of shale oil with a predicted reserve of 458 million tonnes in the Jiyang Depression of the Bohai Bay Basin in November of 2021. The terrestrial sedimentation of the source rocks and tight shales affect shale oil abundance and its flowing ability. Zhang et al. studied sedimentary facies and evolution characteristics in the Nanpu area in the Bohai Bay Basin. Xu et al. presented a case study of the Shahejie Formation in the Dongying Sag of the Jiyang Depression in the Bohai Bay Basin to evaluate the movable shale oil resource. Furthermore, hydrocarbon reservoirs in volcanic rocks were discussed in the Laizhouwan Sag of the Bohai Bay Basin Xie et al.

Using experimental methods, Luo et al. evaluated the mobility of shale oil in the Junggar Basin. The Lucaogou Formation in the Jimsar Sag of the Junggar Basin is a typical lacustrine-deposited shale oil, and it was the first large-scale shale oil field in China. Zhao et al. discussed the total scanning fluorescence applications in shale oil in the same basin. Hou et al. presented a case study on the Chang 7 Member in the Ordos Basin for quantitative measurement of retained oil in organic-rich shale cores.

REFERENCES

Zhang, J. (2019). *Applied Petroleum Geomechanics*. 1st edition. USA: Gulf Professional Publisher of Elsevier, 515.

Zheng, H., Zhang, J., and Qi, Y. (2020). Geology and Geomechanics of Hydraulic Fracturing in the Marcellus Shale Gas Play and Their Potential Applications to the Fuling Shale Gas Development. *Energ. Geosci.* 1, 36–46. doi:10.1016/j.engeos.2020.05.002

Conflict of Interest: The authors declare that the research was conducted in the absence of any commercial or financial relationships that could be construed as a potential conflict of interest.

TIGHT RESERVOIRS

In tight reservoirs, rock matrices have very low permeability; therefore, rock properties and natural fractures are key factors to control reservoir profitability. Wang et al. presented on the sedimentological influence on physical properties of a tight sandstone reservoir in the Cretaceous Nenjiang Formation in the southern Songliao Basin. A case study conducted by Zeng et al. in the Ordos Basin tight sandstone reservoir proves that wells drilled in the zone of faults have a higher oil production.

A tight sandstone reservoir in the Tarim Basin was discussed by Li et al. They conducted a quantitative evaluation of tight sandstone reservoir based on diagenetic facies in the Kepingtage Formation. This study identifies a favourable area for hydrocarbon exploration and development.

SUMMARY

In summary, the papers in this collection present an overview of research and case studies on unconventional hydrocarbon resources from a range of perspectives. We hope the articles in this research topic can provide insight and enhance our understanding in unconventional hydrocarbon resources, particularly unconventional oil and gas research and exploration in China.

AUTHOR CONTRIBUTIONS

All authors listed have contributed to the research topic and this editorial article substantially and intellectually. All agreed to the publication.

frontiers in Earth Science

ORIGINAL RESEARCH
published: 29 January 2021
doi: 10.3389/feart.2020.609834

Modeling Hydrocarbon Generation of Deeply Buried Type III Kerogen: A Study on Gas and Oil Potential of Lishui Sag, East China Sea Shelf Basin

Jinliang Zhang[1], *Yang Li*[1]*, *Jinshui Liu*[2], *Xue Yan*[1], *Lianjie Li*[1] *and Wenlong Shen*[2]

[1]Faculty of Geographical Science, Beijing Normal University, Beijing, China, [2]CNOOC China Ltd., Shanghai, China

The hydrocarbon generation model and hydrocarbon potential are investigated in the Lishui Sag, based on gold-tube pyrolysis experiments of deeply buried type III kerogen. From this, we discuss the classification of kerogen types of source rocks with mixed organic matter sources. The hydrocarbon generated from the source rocks of the Lingfeng Formation and Yueguifeng Formation is dominated by natural gases with little oil in the West subsag, and the hydrocarbon generation model of the Lingfeng Formation is similar to that of Yueguifeng Formation, but the gas potential of Lingfeng Formation is higher than that of Yueguifeng Formation. The hydrocarbon potential of the Yueguifeng Formation in the East subsag is much higher than the West subsag, and it has considerable oil potential. Macerals diversity of source rocks is responsible for the difference of hydrocarbon generation characteristics for type III kerogen in the Lishui Sag. It is not rigorous to evaluate the hydrocarbon potential of kerogen only based on pyrolysis parameters. Application of kerogen type index (KTI) can improve the accuracy of the classification of kerogen types with mixed organic matter sources. According to the classical kerogen classification template, the selected samples belong to type III kerogen. In this article, the selected samples were further subdivided into type III and type II/III based on the KTI value. Type III kerogen ($0.5 \leq KTI < 1.5$) mainly produces gas, and type II/III kerogen ($1.5 \leq KTI < 5$) mainly produces gas, but its oil potential is higher than that of type III.

Keywords: source rock, gold tube pyrolysis, kerogen, modeling hydrocarbon generation, hydrocarbon potential

OPEN ACCESS

Edited by:
Dawei Lv,
Shandong University of Science and Technology, China

Reviewed by:
Dong Wu,
Chengdu University of Technology, China
Wang Yougong,
Northeast Petroleum University, China

***Correspondence:**
Yang Li
lyugly@163.com

Specialty section:
This article was submitted to Sedimentology, Stratigraphy and Diagenesis, a section of the journal Frontiers in Earth Science

Received: *24 September 2020*
Accepted: *22 December 2020*
Published: *29 January 2021*

Citation:
Zhang J, Li Y, Liu J, Yan X, Li L and Shen W (2021) Modeling Hydrocarbon Generation of Deeply Buried Type III Kerogen: A Study on Gas and Oil Potential of Lishui Sag, East China Sea Shelf Basin. Front. Earth Sci. 8:609834. doi: 10.3389/feart.2020.609834

INTRODUCTION

Comprehensive evaluation of source rocks is the basis of oil and gas potential of a sedimentary basin, and hydrocarbon generation simulation of source rocks becomes an important part of oil and gas exploration. The hydrocarbon generation model of source rocks is closely related to the types of kerogen, and the chart based on rock pyrolysis parameters proposed by Tissot and Welte is usually used to divide the types of kerogen (Tissot and Welte, 1984). The term kerogen represents the organic constituent of the sedimentary rocks that is neither soluble in aqueous alkaline solvents nor in the common organic solvents (Tissot and Welte, 1984). Kerogen is widely accepted as the source material of hydrocarbon and the hydrocarbon generation model of kerogen proposed by Tissot points out that type I kerogen is mainly deposited in lake environment and mainly generates oil; type II kerogen is deposited in marine environment with oil and gas dipping properties; and type III kerogen is a kind of gas dipping organic matter deposited in continental environment. However, with the development of

oil and gas exploration to deep and unconventional fields and the deepening of kerogen hydrocarbon generation simulation research, the Tissot model shows some limitations (Li et al., 2018; Agrawal and Sharma, 2020). The discovery of type III kerogen in delta plain deposits, which is dominated by oil generation, also indicates that the type of kerogen cannot determine the type of hydrocarbon generation (Agrawal and Sharma, 2020). Based on the hydrocarbon generation simulation experiments, the diversity of kerogen types is the main reason for the difference of hydrocarbon generation modes of source rocks (Tissot, 1984; Dembicki, 2009). Even then, due to the different sedimentary environment, source and evolution of organic matter of source rocks in different basins, the same type of kerogen has its own hydrocarbon generation characteristics (Horsfield, 1989; Liu et al., 2012). Therefore, in order to judge the hydrocarbon generation potential of a basin, it is not enough to just know the organic matter types of the source rocks. In recent years, most of the hydrocarbon generation and expulsion simulation experiments for source rocks in various basins have focused on the hydrocarbon generation characteristics of coal, type I and type II kerogen, and crude oil cracking, while there is little relevant research on hydrocarbon generation and expulsion simulation of type III kerogen (Jasper et al., 2009; Tian et al., 2009; Tian et al., 2012; Wang et al., 2014; Hill et al., 2003). Meanwhile, more and more hydrocarbon generating sags with type III kerogen as the main organic matter type have been found such as Xihu Sag and Lishui Sag in the East China Sea Shelf basin (ECSSB) (Su et al., 2013; Cheng et al., 2019; Li et al., 2019).

The Lishui Sag has a low degree of exploration and is located at the gateway of developing oil and gas resources in the ECSSB (Chen et al., 2008; Su et al., 2014; Li et al., 2016; Zhang et al., 2019; Liu et al., 2020; Sun et al., 2020). Up to now, one oil-gas field and six oil-bearing structures have been discovered, indicating that it has certain exploration potential. However, only fluorescence and gas logging anomalies have been obtained in five wells (Zhang et al., 2015; Li et al., 2020). It is considered that the insufficient hydrocarbon supply capacity of local subsags is one of the main failure reasons. Therefore, it is necessary to re-evaluate the hydrocarbon generation potential of source rocks in each subsag (Shen et al., 2019). The Lishui Sag is a typical hydrocarbon bearing depression with type III kerogen as the main kerogen type of source rocks, which is representative in the ECSSB (Li et al., 2019). Therefore, the study of hydrocarbon generation and hydrocarbon potential of type III kerogen in Lishui Sag has significance to the evaluation of oil and gas potential of other sags in the basin. In this research, the model of hydrocarbon generation of type III kerogen in mature stage under deep buried conditions is studied by gold tube pyrolysis experiments. The reasons for the difference of hydrocarbon generation characteristics are discussed. In addition, the hydrocarbon generation potential of source rocks in different layers of the Lishui Sag is evaluated.

GEOLOGICAL BACKGROUND

The Lishui Sag is located in the southwest of Taibei basin in the ECSSB and adjacent to Jiaojiang sag in the north. It is a Cenozoic single fault half graben depression formed on the basement of Mesozoic residual basin. The Lishui Sag is divided into two subsags, the East subsag and the West subsag, with an area of 1.46×10^4 km^2 (**Figure 1A**). The area of East subsag is about 4.8×10^3 km^2, and the maximum deposit thickness is more than 7.5 km; the area of West subsag is about 9.8×10^3 km^2, and the maximum deposit thickness is 12 km. The faults in Lishui Sag are mainly NNE-NE trending. From west to east, the faults can be divided into four structural zones: western slope structural zone, central inversion structural zone, Lingfeng ridge, and Eastern step-fault zone (**Figure 1B**; Ge et al., 2007). In Lishui Sag, oil and gas are mainly discovered in the Paleocene. The main source rocks are the mudstones in lower Paleocene Yueguifeng (E_1y) Formation and overlying Lingfeng (E_1l) Formation. The Mingyuefeng Formation (E_1m) is the main reservoir (**Figure 1C**; Li et al., 2019). The main source rocks in Lishui Sag are deeply buried (more than 3 km) and have reached mature stage. Some source rocks in the E_1y formation buried more than 4 km deep have reached the over mature stage. The kerogen types of source rocks in Lishui Sag are relatively simple. According to the classical classification chart of kerogen types, more than 86% of the source rocks are type III, which provides a good sample condition for exploring the hydrocarbon generation characteristics of typical type III kerogen in this article (Chen et al., 2008; Su et al., 2014; Li et al., 2019).

MATERIALS AND METHODS

Samples Selection and Preparation

As mentioned above, the hydrocarbon generation characteristics of source rocks are greatly affected by organic matter type, sedimentary environment, and maturity, so the above factors should be fully considered when selecting samples. In view of the limited number of wells in the Lishui Sag, and the burial depth of source rock, the well location with good oil and gas displaying the source rock of E_1y formation should be selected as the sampling well. Secondly, considering the influence of heterogeneity of source rock at the same layer, single subsag should not be selected for sampling well. At the same time, due to the differences in sedimentary environment, the source rocks of the E_1y and E_1l formations should be sampled. The samples selected in this experiment are mudstones of the E_1l formation and E_1y formation in LD well in the West subsag, and the organic matter type is typical type III kerogen, which is representative in the whole area. Meanwhile, mudstones of the E_1y formation in W1 well of the East subsag are selected for comparative study (**Figure 2**). Due to the burial depth, the three mudstone samples have reached the mature stage. In order to avoid the influence of maturity in the same layer, the vitrinite reflectance (Ro) of the samples from the E_1y formation has little difference. The source rocks in the Lishui Sag are mainly type III kerogen and are mostly gray or gray-black mudstone, and their TOC is relatively low. Therefore, in order to ensure the validity and accuracy of the experimental results, the kerogen was selected instead of source rock for hydrocarbon generation simulation experiment. The preparation process of kerogen is as follows: Soxhlet extracting

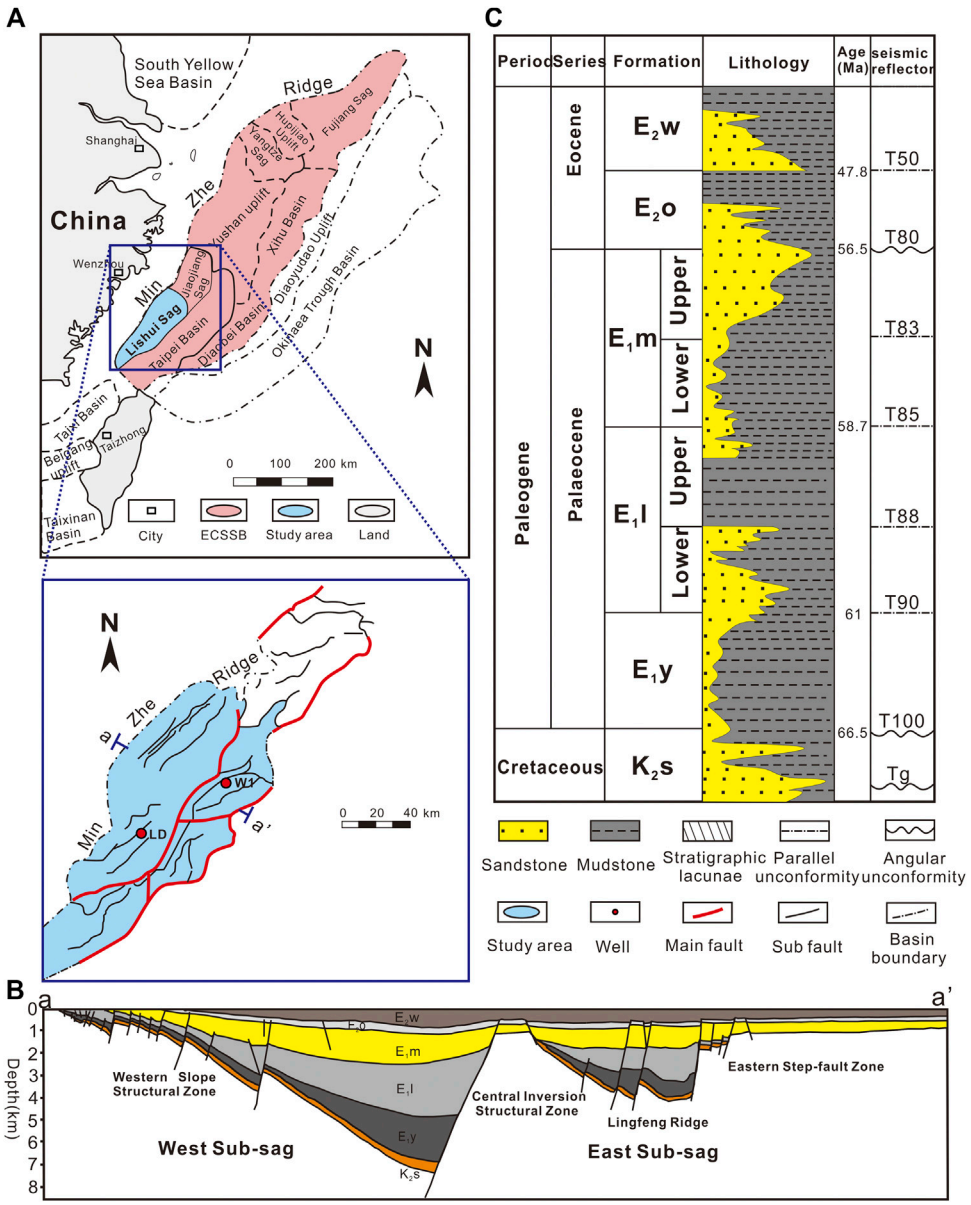

FIGURE 1 | Geographical location **(A),** structural features **(B),** and stratigraphic column **(C)** of the Lishui Sag.

mudstone powder (0.5 kg) for 72 h; adding dilute hydrochloric acid with a mass fraction of 20% to the extracted sample, and heating the sample in a water bath at 80°C for 4 h; after no bubbles are generated, the supernatant is decanted by centrifugation; adding hydrofluoric acid and repeating the above steps; adding distilled water several times to remove inorganic salt, and finally drying in an oven at 80°C to obtain the separated kerogen. The basic information of samples is shown in **Table 1**.

Experimental Process and Conditions

At present, simulation experiments of hydrocarbon generation of source rocks can be divided into open systems, semiopen systems, and closed systems (Behar et al., 1995; Tang et al., 1996; Dieckmann et al., 1998; Dieckmann et al., 2000; Zhang et al., 2008; Bayon et al., 2011; Wang et al., 2011; Hartwig et al., 2012.; Xu et al., 2020). Previous experiments show that the products of simulation experiments of hydrocarbon generation in closed system are closer to the hydrocarbon generating components of source rocks under geological conditions (Zhang et al., 2008). In this study, the gold tube pyrolysis experiment was carried out in a closed system and the experimental process and conditions are as follows: the kerogen sample was sealed into gold tube with inner diameter of 3 and 40 mm in length under the protection of argon and placed in an autoclave with a pressure of 50 MPa (Tang et al., 1996; Ruble et al., 2001; Hill et al., 2007; Zhang et al., 2008). Each sample was divided into two groups (12 in each group) and

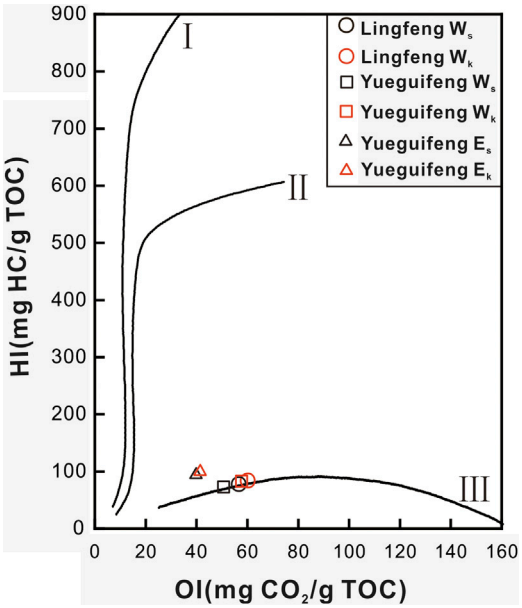

FIGURE 2 | Kerogen type classification of the selected samples. Note: W_s, source rock in the West subsag; W_k, corresponding kerogen in the West subsag; E_s, source rock in the East subsag; E_k, corresponding kerogen in the East subsag.

heated from room temperature to the required temperature at the heating rate of 2°C/h and 20°C/h, respectively, and the temperature interval was 24°C. Because water participates in the maturation process and expulsion of hydrocarbon in source rocks under geological conditions (Seewald, 2003; Lewan and Roy, 2011), and it has an important impact on the thermal stability of source rocks (Ruble et al., 2003), in our gold tube pyrolysis experiment a fixed amount of distilled water (about 15% of the sample weight) is added to each sample. After the thermal simulation experiment, qualitative and quantitative analysis of gases (including nonhydrocarbon gas) and carbon isotope analysis of hydrocarbon gas (C_1-C_3) and CO_2 were carried out. The light component (C_6-C_{14}) of thermal simulation oil was qualitatively and quantitatively analyzed by gas chromatography, and the heavy component (C_{14}^+) of thermal simulation oil was analyzed by organic extraction and weighing. The whole components of thermal simulation oil were analyzed by Gas Chromatography-Mass Spectrometry (GC-MS), and the yield and kinetic parameters of hydrocarbon generation were calculated. At the end of the experiment, the kinetic parameters of hydrocarbon generation, thermal simulation gas production, and isotope data of each component of each sample can be obtained.

RESULTS

Hydrocarbon Generation Model

Because the selected samples have entered the mature stage, the starting temperature for the simulation experiment of hydrocarbon generation in gold tube is 350°C, which is used to simulate the present maturity and the hydrocarbon generation characteristics. In this experiment, a four-component model is adopted. C_1 represents methane, C_2-C_5 represents heavy hydrocarbon gases, C_6-C_{14} represents light oil components, and C_{14}^+ represents heavy oil components, where C_1-C_5 represents natural gas components and C_6^+ represents oil components. According to the simulation results, it can be seen that, under different heating rates, the simulated temperatures at which hydrocarbon generation products begin to generate and decrease are slightly different (**Figure 3**).

As shown in **Table 2**, under a heating rate of 20°C/h, the methane yield of Lingfeng Formation in the West subsag increases rapidly at 432°C (*Ro* = 1.19), and the maximum methane yield reaches 91.97 mg/g TOC when the temperature reaches 599.8°C (*Ro* = 3.87). The yield of heavy hydrocarbon gases increases at 408°C (*Ro* = 0.96). When the temperature reaches 481.7°C (*Ro* = 1.19), the yield of heavy hydrocarbon gases reaches the maximum value of 8.48 mg/g TOC. With the increase of temperature, the yield of heavy hydrocarbon gases begins to decrease, and the methane yield increases sharply. When the temperature reaches 551.8°C (*Ro* = 3.06), the yield of heavy hydrocarbon gases is close to zero, and methane is the main hydrocarbon generating gas. The maximum yields of heavy oil and light oil components are 8.15 mg/g TOC and 14.36 mg/g TOC, respectively, at 456.5°C (*Ro* = 1.50). The yield of heavy oil components is close to zero when the temperature is higher than 551.8°C (*Ro* = 3.06), and the yield of light oil components is close to zero when the temperature is higher than 575.8°C (*Ro* = 3.50). At this time, the main hydrocarbon generation product is methane (**Figure 3A**). Under a heating rate of 2°C/h, the methane yield of the Lingfeng Formation in the West subsag increases rapidly at 384°C (*Ro* = 1.08) and reaches 96.3 mg/g TOC when the temperature reaches 578°C (*Ro* = 4.22). With the increase of temperature, the yield tends to be stable. When the temperature reaches 442°C (*Ro* = 1.85), the yield of heavy hydrocarbon gases reaches the maximum value of 9.06 mg/g TOC. With the increase of temperature, the yield of heavy hydrocarbon gases begins to decrease. When the temperature reaches 540°C (*Ro* = 3.67), the yield of heavy hydrocarbon gases is close to zero. The maximum yields of heavy oil and light oil

TABLE 1 | Basic information of the selected samples.

Sample	Well	Depth (m)	Formation	TOC (%)	Ro (%)	HI (mg/g)	OI (mg/g)
Source rock	LD	3334.00	E_1l	1.84	0.82	83.70	58.70
Kerogen	LD	3334.00	E_1l	9.33		89.92	61.31
Source rock	LD	3759.50	E_1y	2.96	0.94	79.05	52.70
Kerogen	LD	3759.50	E_1y	13.13		88.12	59.86
Source rock	W1	3813.00	E_1y	2.49	0.95	103.61	41.37
Kerogen	W1	3813.00	E_1y	27.66		108.03	43.24

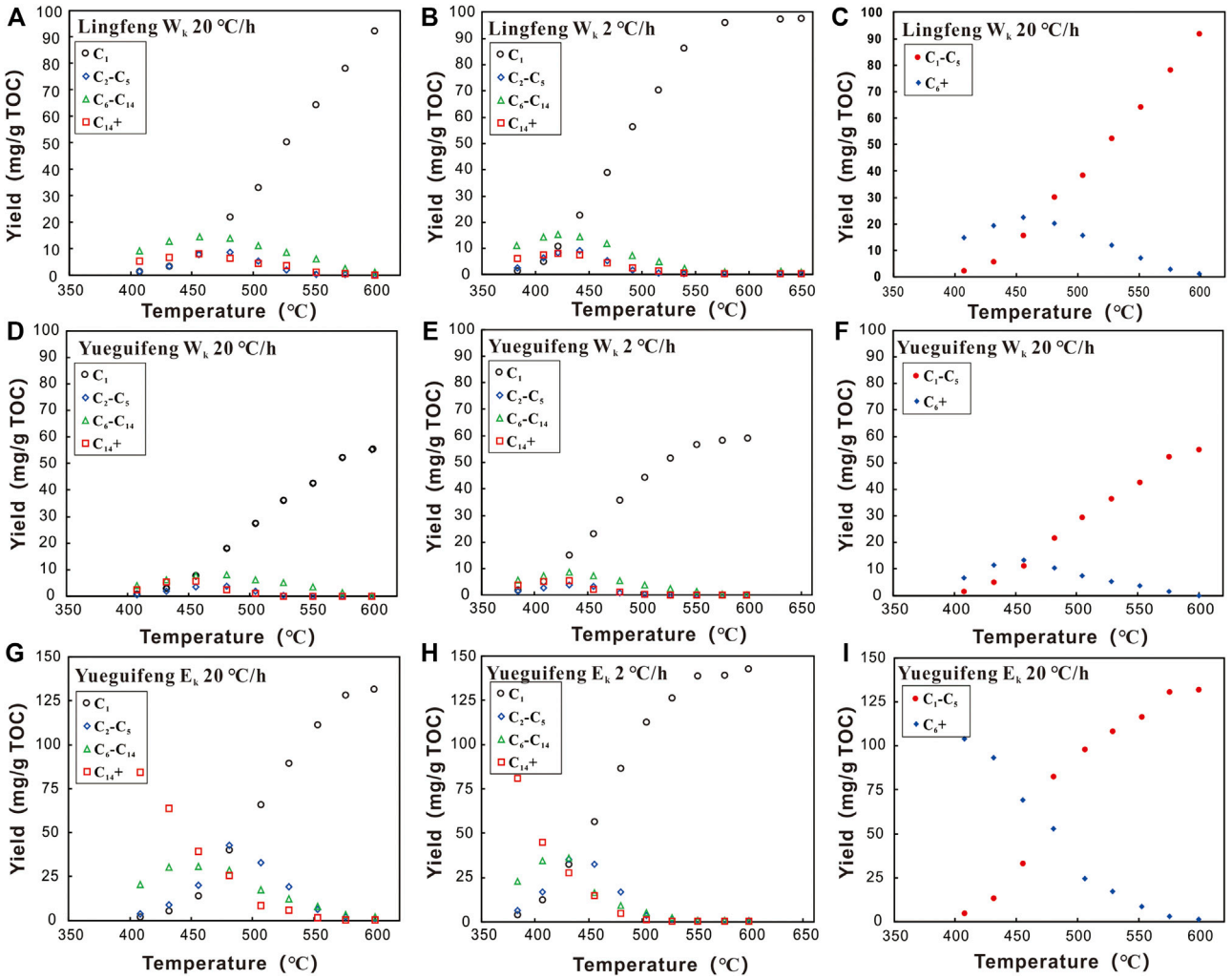

FIGURE 3 | Hydrocarbon generation characteristics of kerogen in source rocks of Lishui Sag under two heating rates.

components are 7.93 mg/g TOC and 14.90 mg/g TOC, respectively, at 422°C (*Ro* = 1.55). When the temperature is higher than 516°C (*Ro* = 3.22), the yield of heavy oil components is close to zero, and the yield of light oil components is close to zero when the temperature is higher than 540°C (*Ro* = 3.67) (**Figure 3B**). If the hydrocarbon generating components are divided into natural gas and oil components, the sample of Lingfeng Formation in the West subsag generates oil slightly earlier than gas under the heating rate of 20°C/h and reaches the maximum yield at 456.5°C (*Ro* = 1.50) and then starts cracking to form natural gas. When the temperature reaches 599.8°C (*Ro* = 3.87), the maximum yield of natural gas is achieved (**Figure 3C**).

Under a heating rate of 20°C/h, the methane yield of Yueguifeng Formation in West subsag begins to increase rapidly at 432°C (*Ro* = 1.19). When the temperature reaches 599.8°C (*Ro* = 3.87), the maximum methane yield reaches 55.13 mg/g TOC. When the temperature reaches 481.7°C (*Ro* = 1.84), the yield of heavy hydrocarbon gases reaches the maximum value of 3.77 mg/g TOC. With the increase of temperature, the yield of heavy hydrocarbon gases begins to decrease. When the temperature reaches 528.1°C (*Ro* = 2.62), the yield of heavy hydrocarbon gases is close to zero. The maximum yield of heavy oil and light oil components are 2.36 mg/g Toc and 8.07 mg/g TOC at 481.7°C (*Ro* = 1.84) (**Figure 3D**). Under the heating rate of 2°C/h, the methane yield of Yueguifeng Formation in the West subsag begins to increase rapidly at 408.3°C (*Ro* = 1.36), and the maximum methane yield reaches 58.89 mg/g TOC when the temperature reaches 599.1°C (*Ro* = 4.45). When the temperature is 432.6°C (*Ro* = 1.69), the heavy hydrocarbon gases yield reaches the maximum value of 3.97 mg/g TOC. With temperature continuous increase to 551.9°C (*Ro* = 3.86), the heavy hydrocarbon gases yield is close to zero. The maximum yield of heavy oil components is 5.48 mg/g TOC at 432.6°C (*Ro* = 1.69), and the maximum yield of light oil components is 8.61 mg/g TOC at 432.6°C (*Ro* = 1.69). The yield of light oil components is higher than that of heavy oil components (**Figure 3E**). The time of oil

TABLE 2 | Yield and carbon isotope data of different compositions by gold tube hydrocarbon generation simulation experiment.

ID	Temperature °C	Heating rate °C/h	easyRo %	C_1 mg/g TOC	C_1-C_5 mg/g TOC	C_2-C_5 mg/g TOC	C_6-C_{14} mg/g TOC	C_{14+} mg/g TOC	C_{6+} mg/g TOC
WL-1	408.00	20	0.96	0.92	2.22	1.30	9.22	5.36	14.68
WL-2	432.00	20	1.19	2.61	5.80	3.19	12.65	6.75	19.29
WL-3	456.50	20	1.50	7.90	15.73	7.83	14.36	8.15	22.51
WL-4	481.70	20	1.84	21.79	30.27	8.48	13.93	6.32	20.26
WL-5	504.70	20	2.23	33.00	38.30	5.30	11.15	4.39	15.54
WL-6	528.10	20	2.62	50.27	52.23	1.96	8.57	3.43	12.11
WL-7	551.80	20	3.06	63.93	64.22	0.29	6.00	1.18	7.18
WL-8	575.80	20	3.50	78.05	78.19	0.15	2.36	0.43	2.79
WL-9	599.80	20	3.87	91.97	91.97	0.00	1.18	0.00	1.18
WL-10	384.00	2	1.08	1.69	3.93	2.24	10.93	6.00	16.93
WL-11	408.00	2	1.35	4.83	11.14	6.30	14.47	7.29	21.76
WL-12	422.00	2	1.55	10.51	18.62	8.11	14.90	7.93	22.83
WL-13	442.00	2	1.85	22.56	31.62	9.06	14.15	7.18	21.33
WL-14	468.00	2	2.30	38.60	43.75	5.15	11.58	4.39	15.97
WL-15	492.00	2	2.76	56.02	57.55	1.52	7.07	2.47	9.54
WL-16	516.00	2	3.22	70.37	70.81	0.44	4.82	1.29	6.11
WL-17	540.00	2	3.67	86.10	86.25	0.15	2.25	0.32	2.57
WL-18	578.00	2	4.22	96.16	96.30	0.15	0.64	0.11	0.75
WL-19	630.00	2	4.66	97.10	97.10	0.00	0.00	0.00	0.00
WL-20	650.00	2	4.90	97.32	97.32	0.00	0.00	0.00	0.00
WY-1	408.00	20	0.96	0.93	1.60	0.67	4.19	2.44	6.63
WY-2	432.00	20	1.19	3.11	5.01	1.91	6.25	5.33	11.58
WY-3	456.50	20	1.50	7.69	11.24	3.55	7.84	5.56	13.40
WY-4	481.70	20	1.84	18.00	21.76	3.77	8.07	2.36	10.43
WY-5	504.70	20	2.23	27.37	29.39	2.01	6.32	1.14	7.46
WY-6	528.10	20	2.62	35.99	36.40	0.41	5.10	0.15	5.26
WY-7	551.80	20	3.06	42.59	42.59	0.00	3.66	0.00	3.66
WY-8	575.80	20	3.50	52.24	52.39	0.00	1.37	0.00	1.37
WY-9	599.80	20	3.87	55.13	55.13	0.00	0.00	0.00	0.00
WY-10	384.40	2	1.08	1.96	3.41	1.44	5.71	3.88	9.60
WY-11	408.30	2	1.36	4.91	7.69	2.78	7.46	5.33	12.95
WY-12	432.60	2	1.69	15.11	19.07	3.97	8.61	5.48	14.09
WY-13	455.30	2	2.05	23.18	26.38	3.20	7.39	2.28	9.67
WY-14	479.60	2	2.52	35.77	36.81	1.03	5.48	1.29	6.78
WY-15	503.10	2	2.99	44.33	44.75	0.41	3.88	0.30	4.19
WY-16	527.10	2	3.42	51.64	51.85	0.21	2.44	0.15	2.59
WY-17	551.90	2	3.86	56.82	56.93	0.10	1.52	0.08	1.60
WY-18	576.00	2	4.19	58.40	58.40	0.00	0.38	0.00	0.38
WY-19	599.10	2	4.45	58.89	58.89	0.00	0.00	0.00	0.00
EY-1	408.10	20	0.96	1.71	4.96	3.26	19.96	83.91	103.87
EY-2	432.00	20	1.19	5.10	13.38	8.28	29.86	63.52	93.38

(Continued on following page)

TABLE 2 | (*Continued*) Yield and carbon isotope data of different compositions by gold tube hydrocarbon generation simulation experiment.

ID	Temperature °C	Heating rate °C/h	easyRo %	C_1 mg/g TOC	C_1-C_5 mg/g TOC	C_2-C_5 mg/g TOC	C_6-C_{14} mg/g TOC	C_{14+} mg/g TOC	C_{6+} mg/g TOC
EY-3	456.00	20	1.47	13.59	33.25	19.66	30.30	38.79	69.09
EY-4	481.20	20	1.81	39.76	82.29	42.53	28.02	24.98	53.00
EY-5	506.60	20	2.19	65.67	97.98	32.31	16.85	7.88	24.73
EY-6	529.50	20	2.54	89.28	108.19	18.91	11.97	5.35	17.28
EY-7	553.00	20	2.99	110.35	116.16	5.81	7.45	1.19	8.64
EY-8	576.00	20	3.32	128.65	130.42	1.77	3.04	0.00	3.04
EY-9	600.00	20	3.87	130.98	131.72	0.74	1.41	0.00	1.41
EY-10	384.20	2	1.08	3.75	9.93	6.18	22.23	80.73	102.96
EY-11	407.40	2	1.38	11.91	28.38	16.47	34.16	44.61	78.78
EY-12	431.90	2	1.69	32.15	67.04	34.89	35.76	27.33	63.09
EY-13	456.00	2	2.09	55.91	87.91	31.99	15.98	14.24	30.26
EY-14	480.70	2	2.52	86.28	102.50	16.23	8.97	4.30	13.27
EY-15	504.50	2	2.99	112.03	115.34	3.31	4.66	0.90	5.57
EY-16	528.50	2	3.49	125.83	126.86	1.03	1.99	0.00	1.99
EY-17	552.40	2	3.89	138.31	138.85	0.54	0.51	0.00	0.51
EY-18	577.50	2	4.19	138.85	139.34	0.49	0.36	0.00	0.36
EY-19	600.00	2	4.45	142.27	142.56	0.29	0.14	0.00	0.14

and gas generation of Yueguifeng Formation in the West subsag is similar. Under a heating rate of 20°C/h and the temperature of 432°C (*Ro* = 1.69), the oil reaches the maximum yield and then begins to crack to form natural gas. When the temperature reaches 599.8°C (*Ro* = 3.87), the maximum yield of natural gas is achieved (**Figure 3F**).

Under a heating rate of 20°C/h, the methane yield of Yueguifeng Formation in the East subsag begins to increase rapidly at 432°C (*Ro* = 1.19), and the maximum methane yield reaches 130.98 mg/g TOC when the temperature reaches 600°C (*Ro* = 3.87). When the temperature reaches 481.2°C (*Ro* = 1.81), the yield of heavy hydrocarbon gases reaches the maximum value of 42.53 mg/g TOC. With the increase of temperature, the yield of heavy hydrocarbon gases begins to decrease. When the temperature reaches 600°C (*Ro* = 3.87), the yield of heavy hydrocarbon gases is close to zero. The maximum yield of heavy hydrocarbon gases is 83.91 mg/g TOC at 408.1°C (*Ro* = 0.96). With the increase of simulation temperature, the yield of heavy hydrocarbon gases decreases gradually. The maximum yield of light oil reaches 30.30 mg/g TOC at 456°C (*Ro* = 1.47) and then decreases with the increase of simulated temperature (**Figure 3G**). Under the heating rate of 2°C/h, the methane yield of Yueguifeng Formation in East subsag begins to increase rapidly at 407.4°C (*Ro* = 1.38), and the maximum methane yield reaches 142.27 mg/g TOC when the temperature reaches 600°C (*Ro* = 4.45). When the temperature is 431.9°C (*Ro* = 1.69), the yield of heavy hydrocarbon gases reaches the maximum value of 34.89 mg/g TOC, and the yield of heavy hydrocarbon gases gradually decreases with the increase of temperature. The maximum yield of heavy oil components is 80.73 mg/g TOC at 384.2°C (*Ro* = 1.08), and the maximum yield of light oil components is 35.76 mg/g TOC at 431.9°C (*Ro* = 1.69) (**Figure 3H**). The sample of Yueguifeng Formation in the East subsag generates oil earlier than gas. Under the heating rate of 20°C/h and temperature of 408.1°C (*Ro* = 0.96), the sample begins to crack to form natural gas. When the temperature reaches 600°C (*Ro* = 3.87), the natural gas yield reaches the maximum (**Figure 3I**).

Kinetic Characteristics of Hydrocarbon Generation

In our gold tube pyrolysis experiment, the hydrocarbon gas yields provide the necessary data for calculating the gas generation kinetics parameters. It is widely accepted that the hydrocarbon generation process of sedimentary organic matter follows the principle of parallel first-order reaction kinetics (Tissot and Welte, 1984; Cramer et al., 2001; Cramer, 2004; Tian et al., 2009; Kotarba and Lewan, 2013; Wang et al., 2014; Wang et al., 2018). Based on this principle, using pyrolysis data and the Lawrence Livermore National Lab Kinetics software, a series of specific kinetic parameters (such as activation energy and frequency factor) are calculated for total hydrocarbon generation (**Table 3**).

As mentioned above, the source rocks in Lishui Sag are dominated by gas generation, so we focus on the kinetic parameters of natural gas. At different heating rates, the experimental yield of natural gas is in good agreement with the simulation results, which ensures the accuracy of the calculation of kinetic parameters of hydrocarbon generation (**Figures 4A,C,E**). The activation energy range of natural gas in Lingfeng Formation of the West subsag is 45–65 kcal/mol, the main activation energy is 53 kcal/mol, the average activation energy is 58.37 kcal/mol, and the frequency factor is 9.8×10^{11} s^{-1} (**Figures 4A,B**). The activation energy range of natural gas of Yueguifeng Formation in the West subsag is 47–68 kcal/mol, the main activation energy value is 60 kcal/mol, the average activation energy is 57.11 kcal/mol with frequency factor of 1.2×10^{12} s^{-1} (**Figures 4C,D**). The natural gas activation energy of Yueguifeng Formation in the East subsag is 46–64 kcal/mol, the main activation energy is 60 kcal/mol, the average activation energy is 53.31 kcal/mol, and the frequency

TABLE 3 | Data of kinetic parameters of hydrocarbon generation from source rocks in the Lishui Sag.

	Lingfeng formation in the west subsag						Yueguifeng formation in the west subsag						Yueguifeng formation in the east sub sag			
Components	C_1	C_2-C_5	C_1-C_5	C_6-C_{14}	C_{14+}	C_{6+}	C_1	C_2-C_5	C_1-C_5	C_6-C_{14}	C_{14+}	C_{6+}	C_1	C_2-C_5	C_1-C_5	C_6-C_{14}
A (S^{-1})	8.5×10^{11}	4.49×10^{13}	9.8×10^{11}	5.03×10^{13}	2.1×10^{13}	4.79×10^{13}	2.2×10^{12}	3.2×10^{13}	1.2×10^{12}	8.8×10^{12}	4.56×10^{13}	8.8×10^{12}	8.9×10^{12}	1.2×10^{13}	6.5×10^{11}	1.5×10^{15}
E (kcal/mol)	**Frequency distribution (%)**						**Frequency distribution (%)**						**Frequency distribution (%)**			
41	0	0	0	0	0	0	0	0	0	4.99	0	3.42	0	0	0	0
42	0	0	0	0	28.69	0	0	0	0	0	0.34	0	0	0	0	0
43	0	0	0	0	1.27	11.52	0	0	0	0	0	0	0	0.02	0	0
44	0	0	0	0	0	0	0.01	0	0	0	0.22	0.28	0	0	0	0
45	0	0	0.11	0	0	0	0	0	0	0.42	0	1.25	0	0.21	0	0
46	0.04	0	0.53	0.11	2.47	2.63	0	0	0	0	0	0	0	0	0.44	0
47	0.21	0	0	0	8.32	0	0	0.17	0.64	0	3.29	0	0.51	0	0	0
48	0	0	0.25	1.84	0	0	0.25	0	0.6	0	0	0	0.09	1.64	0	0
49	0	0	0	0	3.36	6.11	0.63	0	0	8.88	0	8.06	0	3.46	0	0
50	0	0.91	0	0	4.13	7.64	0	0	0	0	0	0	0	0	0	0
51	0	0	0	0	3.73	3.67	0	0.26	0	37.6	0	10.13	0	0	0	25.03
52	2.05	4.41	2.58	3.41	0	19.3	0	0	5.25	0	0	62.53	0	0	27.17	2.09
53	15.81	0	19.32	8.51	13.59	1.7	1.71	20.76	22.44	15.98	0	0	25.15	62.85	13.03	0
54	0	0	0	8.44	4.17	4.57	23.66	0	0	14.93	73.61	0	0	20.9	0	0
55	0	0	0	25.97	13.82	30.36	0	0	0	0	0	11.04	3.16	0	13.94	0
56	27.45	62.35	14.26	0	2.4	0	0	62.1	26.29	14.81	14.49	3.3	25.1	9.46	9.83	12.01
57	0	0	11.78	0	14.07	10.35	30.34	4.02	4.12	1.37	6.73	0	0	1.45	0.71	0
58	0	20.27	0	43.19	0	2.14	2.97	10.27	0	1.03	0	0	20.53	0	11.73	0
59	10.96	11.01	0	0	0	0	0	0	0	0	1.33	0	0	0	0	0
60	21.62	0	26.27	0	0	0	0	2.42	30.87	0	0	0	10.64	0	19.43	52.32
61	0	0	4.96	4.2	0	0	31.14	0	0	0	0	0	8.68	0	0	0
62	0	0.49	0	4.33	0	0	0	0	0.78	0	0	0	0	0	0	0
63	0	0.55	0	0	0	0	0	0	0	0	0	0	0	0	0	3.11
64	11.72	0	5.85	0	0	0	0.86	0	7.57	0	0	0	6.15	0	3.73	5.44
65	10.13	0	14.08	0	0	0	6.44	0	0	0	0	0	0	0	0	0
66	0	0	0	0	0	0	0	0	0	0	0	0	0	0	0	0
67	0	0	0	0	0	0	0	0	0	0	0	0	0	0	0	0
68	0	0	0	0	0	0	2.01	0	1.43	0	0	0	0	0	0	0
69	0	0	0	0	0	0	0	0	0	0	0	0	2.18	0	0	0.57

factor is 6.5×10^{11} s^{-1} (**Figures 4E,F**). The frequency factor (A) refers to the factor of the total number of effective collisions of activated molecules, and the larger the value is, the easier the chemical reaction will be (Galwey and Brown, 2002; He et al., 2020).

DISCUSSION

Difference Analysis of Hydrocarbon Generation Characteristics

Under different heating rates, the maximum yield of hydrocarbon generation products of the selected samples in Lishui Sag is stable (**Figure 3**), indicating that, in geological history, the hydrocarbon generation potential of source rocks depends on the composition and structure of kerogen and has little to do with sedimentation rate and geothermal gradient. The oil components yield of the Yueguifeng and Lingfeng Formations in the West subsag is low, and, with the increase of simulation temperature, the maximum yield almost simultaneously begins to decrease, indicating that the source rocks of the West subsag are typical gas-prone source rocks. According to the principle of conservation of mass, the methane generated by the source rocks of the West subsag should be mainly generated by direct cracking of kerogen, and the proportion of methane converted from oil components is relatively small. Although the degree of thermal evolution of the source rock in Yueguifeng Formation is relatively high, the distribution characteristics of its oil yield first increased and then decreased, which indicates the source rocks of Yueguifeng Formation are still in the main hydrocarbon generation period. The maximum yield of natural gas of Lingfeng Formation in the West subsag is higher than that of Yueguifeng Formation, which indicates that the gas generation potential of Lingfeng formation source rock is higher than that of Yueguifeng Formation. The hydrocarbon generation characteristics of the Yueguifeng Formation source rocks in the East subsag are quite different from those in the West subsag. Firstly, the yield of source rock of Yueguifeng Formation in the East subsag is much higher than that in the West subsag. It is worth noting that the sample of Yueguifeng Formation in the East subsag has relative high oil potential. The simulation results show that, at the temperature which is equivalent to the current maturity, the oil component has reached the maximum yield. Due to its high thermal evolution, it may be in the stage of oil generation peak or after the oil generation peak. At the heating rate of 20°C/h, when the simulated temperature is lower than 456°C (*Ro* = 1.47), the yield of heavy oil components decreases, while the yield of light oil components increases, and the yield of overall oil component also decreases. It shows that, with the increase of simulation temperature, heavy oil components will crack to form light oil components and natural gas (**Figures 3G,I**). In the case of similar thermal evolution degree, the hydrocarbon generation potential of Yueguifeng Formation in the East subsag is much higher than that in the West subsag, which may be related to the composition of organic matter.

In this study, the distribution characteristics of activation energy of methane and oil components are selected to analyze the difference of hydrocarbon generation kinetics of source rocks in the Lishui Sag. The range of activation energy for methane of the Lingfeng Formation in the West subsag is 46–65 kcal/mol, and the main activation energy value is 56 kcal/mol. The range of

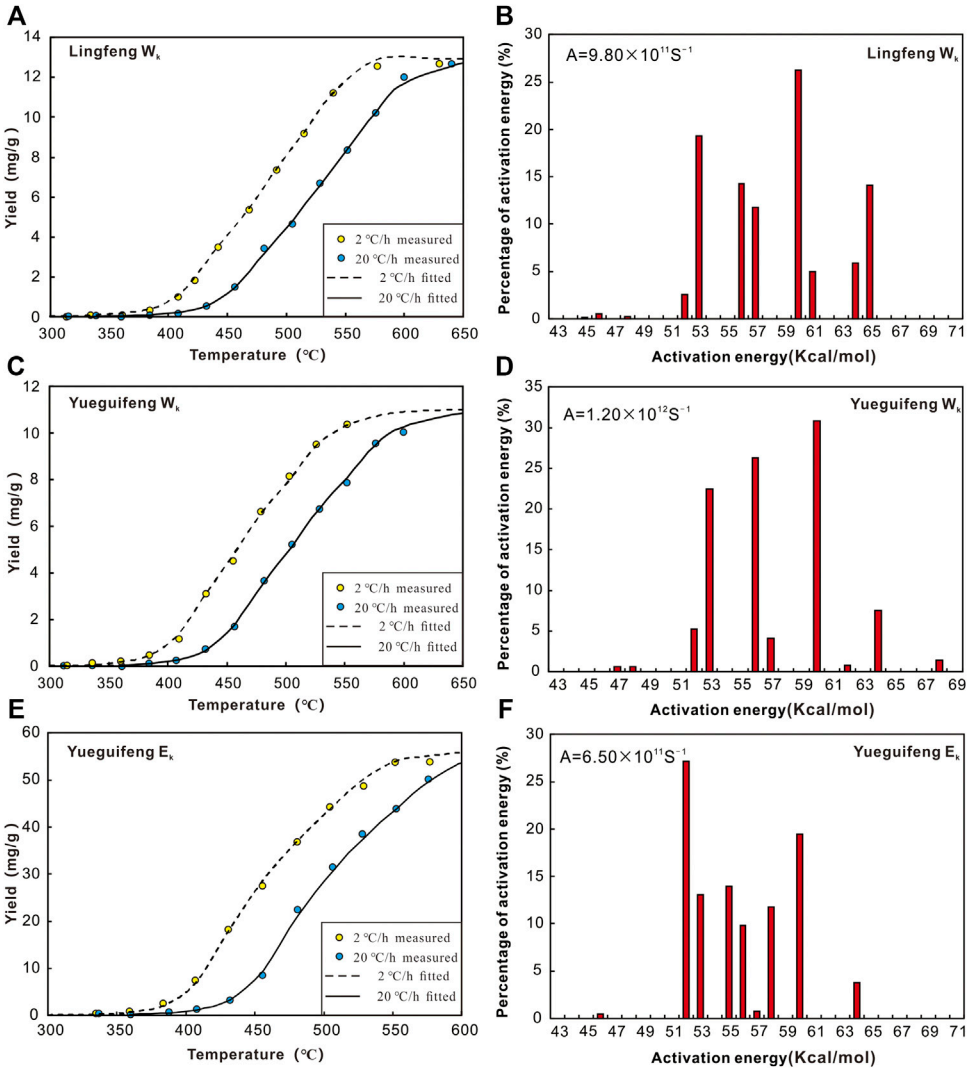

FIGURE 4 | Fitting results of natural gas yield and distribution of activation energy for hydrocarbon generation of the source rocks in the Lishui Sag. A = frequency factor.

activation energy for methane of the Yueguifeng Formation in the West subsag is 44–68 kcal/mol, and the main activation energy value is 61 kcal/mol. The activation energy range of methane for the sample of the Yueguifeng Formation in the East subsag is 47–69 kcal/mol, and the main activation energy value is 53 kcal/mol (**Figure 5A**). According to the distribution of activation energy for methane, when the average activation energy difference is small, the distribution range of methane activation energy of Lingfeng Formation in the West subsag is the narrowest, which indicates that it is easier to generate methane. On the whole, there is little difference in the kinetic characteristics of methane generation in Lishui Sag. The range of activation energy for oil components in Lingfeng Formation of the West subsag is 43–58 kcal/mol, and the main activation energy value is 55 kcal/mol. The range of activation energy for oil components in Yueguifeng Formation in the West subsag is 41–56 kcal/mol, and the main activation energy value is 52 kcal/mol. And the range of activation energy for oil components in Yueguifeng Formation in the East subsag is 31–47 kcal/mol with a main activation energy value of 41 kcal/mol (**Figure 5B**). Obviously, the hydrocarbon generation kinetic characteristics of the samples of Lingfeng and Yueguifeng Formations in the West subsag are similar, while the samples of Yueguifeng Formation in the East subsag show its particularity with lower distribution range and average activation energy, and its oil generating capacity and potential are much higher than those of source rocks in the West subsag.

Macerals of Kerogen Control the Model of Hydrocarbon Generation

Li et al. (2019) indicate that the mudstone of Yueguifeng Formation shows high maturity and the advantage of aquatic organic matter input. The organic matter input heterogeneity of Lingfeng Formation mudstone is high, aquatic input is dominant

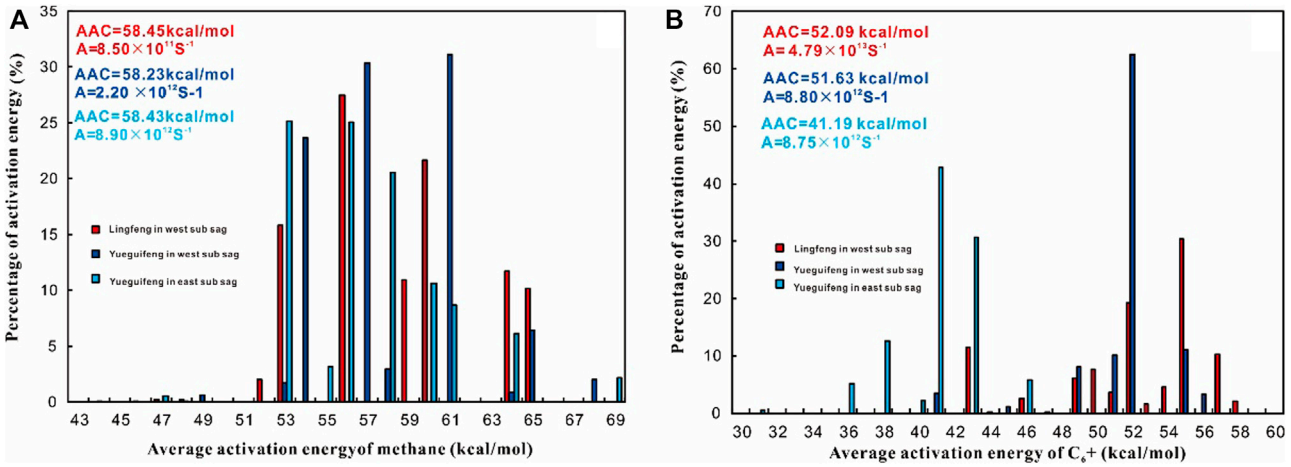

FIGURE 5 | Distribution of activation energy for hydrocarbon generation of methane and oil components AAC: average activation energy.

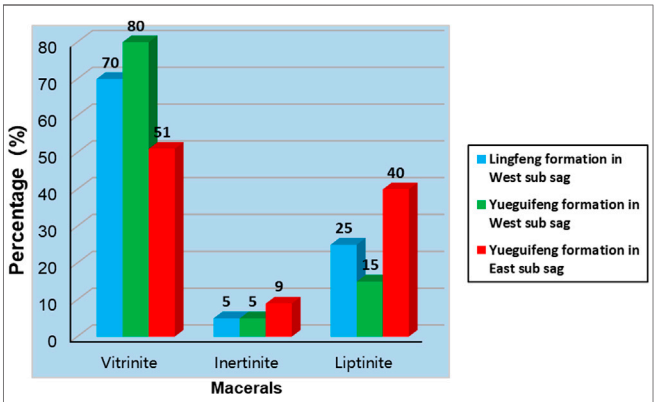

FIGURE 6 | Maceral composition of selected samples in the Lishui Sag.

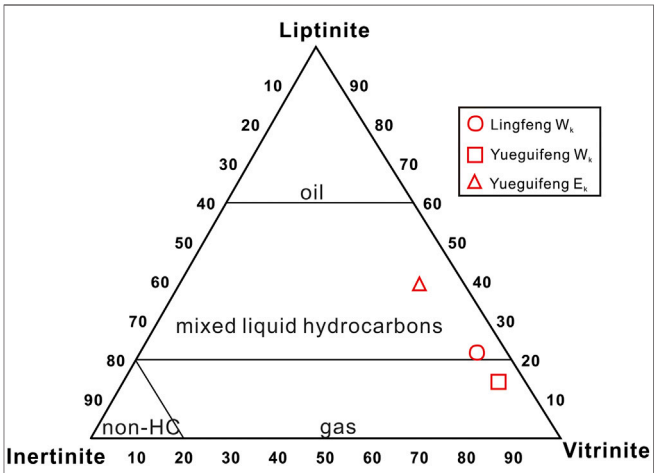

FIGURE 7 | Ternary plots of the maceral composition, showing anticipated hydrocarbon phase of the selected samples in the Lishui Sag (modified after Tissot and Welte, 1984).

in the lower part, and terrigenous input is dominant in the upper part. The mudstone of Yueguifeng Formation was deposited in saline lake with high clay content and relatively high salinity, while the mudstone of Lingfeng Formation was deposited in the transitional sedimentary environment. Generally, the source rocks in Lishui Sag show the characteristics of mixed organic matter input and the evolution process of sedimentary environment from continental facies to marine facies. The instability of organic matter input and the transitional sedimentary environment may be the main reasons for the dominance of type III kerogen of source rocks in Lishui Sag. As mentioned above, although the kerogen types of the source rocks in Lishui Sag are consistent in terms of pyrolysis parameters, their hydrocarbon generation characteristics are quite different. Therefore, it is not rigorous to judge the hydrocarbon generation potential of source rocks only from the types of kerogen derived from pyrolysis parameters. In this study, the maceral analysis of the selected samples was carried out in order to analyze the causes of the differences in hydrocarbon generation characteristics of the source rocks in Lishui Sag.

As shown in **Figure 6**, the maceral composition of source rocks in the West subsag and the East subsag is dominated by vitrinite. The vitrinite content of Lingfeng Formation and Yueguifeng Formation in the West subsag is dominant (≥70%), while the vitrinite content of Yueguifeng Formation in the East subsag is much lower than that in the West subsag. The content of liptinite in source rocks of Yueguifeng Formation in the East subsag is second only to vitrinite and much higher than that in the West subsag. There is a consensus that vitrinite is the main gas dipping macerals, and liptinite is the main oil dipping macerals (Tissot and Welte, 1984; Peters et al., 2005; Hakimi and Ahmed, 2016). According to the maceral composition, the source rocks in Lishui Sag are dominated by gas generation, and the source rocks of Yueguifeng Formation in the East subsag also have certain oil generation potential (**Figure 7**).

Classification of Kerogen Types From Mixed Organic Matter Sources

Through the hydrocarbon generation simulation experiment and maceral analysis of source rocks in the Lishui Sag, a limitation in inference of the hydrocarbon generation potential of source rocks is highlighted when only based on the types of kerogen obtained by pyrolysis parameters, especially for the source rocks with mixed organic matter sources. According to the classification of kerogen types in source rocks, many schemes have been proposed (Tissot and Welte, 1984; Van Krevelen, 1993). The results of previous studies show that the combination of kerogen type index (KTI = S_2/S_3 = HI/OI) can more effectively distinguish the boundary of kerogen types, especially for the mixed region division of type II and type III kerogen (Huang et al., 1982; Huang et al., 1984; Peters et al., 2005). However, it should be noted that, due to the differences in the research objects of scholars, there is no consensus on the value limit of KTI in the classification of kerogen types. Peters et al. (2005) classified kerogen into five types according to pyrolysis parameters and S_2/S_3 values. The values of S_2/S_3 for different types of kerogen are type IV < 1, 1 ≤ type III < 5, 5 ≤ type II/III < 10, 10 ≤ type II < 15, type I ≥ 15 (Peters et al., 2005). According to the pyrolysis parameters of hydrogen index (HI), oxygen index (OI), and their ratios, Huang et al. (1982) established an X-type diagram for the classification of kerogen types and divided kerogen into five types. With the improvement of the data and the deepening of the research, the value limits of HI/OI are adjusted: type III_2 < 0.5, 0.5 ≤ type III_1 < 1.5, 1.5 ≤ type II < 15, 1.5 ≤ type I_2 < 40,type I_1 ≥ 40 (Huang et al., 1984). In this study, based on the hydrogen index, the types of kerogen should be typical type III, but its hydrocarbon generation characteristics are quite different. Therefore, the kerogen type should be redefined according to the hydrocarbon generation characteristics of the source rocks in Lishui Sag. Based on the hydrocarbon generation characteristics of the source rocks derived from mixed organic matter in the Lishui Sag, a new value limit of kerogen type index is proposed to classify kerogen types. Type IV kerogen (KTI < 0.5) has low hydrocarbon generation capacity, and "dead carbon" occurs when hydrogen index is lower than 50 mg/g; type III kerogen (0.5 ≤ KTI < 1.5) mainly produces gas, and, with the increase of KTI value, a small amount of liquid hydrocarbon may be produced; type II/III kerogen (1.5 ≤ KTI < 5) mainly produces gas, but its oil generation capacity is much higher than that of type III kerogen; type II kerogen (5 ≤ KTI < 15) and type I kerogen (KTI > 15) are mainly oil prone (**Figure 8**). According to the dynamic characteristics of the selected kerogen, the main activation energy for methane of type II/III kerogen is less than that of type III kerogen, and the range of activation energy is similar. However, the main activation energy for oil components of type II/III kerogen is significantly smaller than that in type III kerogen, and the range of activation energy is also smaller than that of type III kerogen (**Figure 5**). The above phenomena indicate that the kinetic characteristics of gas generation between type II/III kerogen and type III kerogen are similar, but type II/III kerogen is easier to generate oil.

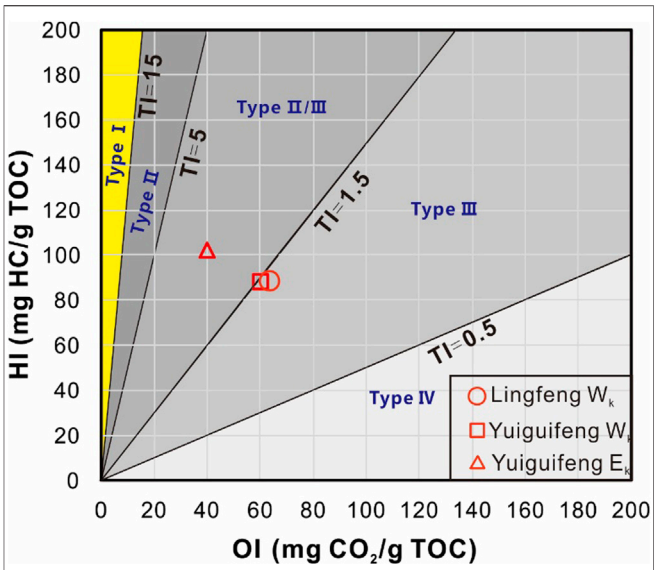

FIGURE 8 | Classification chart of kerogen types (modified after Van Krevelen, 1993; Peters et al., 2005).

CONCLUSION

According to the characteristics of pyrolysis hydrogen index and oxygen index, the kerogen type of source rocks in Lishui Sag is mainly type III kerogen. Due to deep burial, the source rocks in Lishui Sag are basically in mature stage. The simulation of hydrocarbon generation by gold tube pyrolysis experiment shows that the source rocks in Lishui Sag mainly generate natural gas, and the hydrocarbon generation characteristics of source rocks in different structural positions are quite different. The oil yield of type III kerogen in Lingfeng and Yueguifeng Formations in the West subsag is relatively low. The natural gas is dominantly methane, which is mainly produced by direct cracking of kerogen. Based on the maximum yield and kinetic characteristics of hydrocarbon generation, the hydrocarbon potential of Lingfeng Formation in the West subsag is higher than that in Yueguifeng Formation. The hydrocarbon potential of Yueguifeng Formation source rock in the East subsag is much higher than that in the West subsag, and it has considerable oil potential.

Maceral analysis shows that the content of liptinite of the Yueguifeng Formation in the East subsag is much higher than that of the West subsag, which may responsible for the difference of hydrocarbon generation characteristics. For source rocks with mixed sources of organic matter, it is not rigorous to judge the type of kerogen only by hydrogen index and oxygen index, and maceral analysis should be supplemented to comprehensively judge hydrocarbon potential. Comprehensive use of kerogen type index (KTI), pyrolysis hydrogen index, and oxygen index can improve the accuracy of kerogen type classification of source rocks with mixed organic matter sources. We subdivided the mainly gas producing kerogen with mixed organic matter source into type III and

type II/III. Type III kerogen (0.5 ≤ KTI < 1.5) mainly produces gas and, with the increase of KTI value, a small amount of liquid hydrocarbon may be produced. Type II/III kerogen (1.5 ≤ KTI <5) mainly produces gas, but its oil production capacity is much higher than that of type III kerogen.

In this study, the hydrocarbon generation model of type III kerogen with different maturity and structural position in Lishui Sag was investigated by the gold tube hydrocarbon generation simulation experiment in a closed system, and its hydrocarbon generation potential was evaluated, so as to provide theoretical basis for oil and gas exploration in Lishui Sag at the early stage of exploration. Based on the gold tube pyrolysis experiment, it is found that the hydrocarbon generation modes of type III kerogen divided by traditional pyrolysis parameters are quite different, which emphasizes the importance of maceral analysis in oil and gas potential evaluation. The next exploration direction of Lishui Sag should be in the East subsag, mainly for oil and gas, and the West subsag should be mainly for gas traps.

DATA AVAILABILITY STATEMENT

The original contributions presented in the study are included in the article/supplementary materials; further inquiries can be directed to the corresponding author.

AUTHOR CONTRIBUTIONS

JZ participated in conceptualization. YL carried out conceptualization, methodology, writing original draft, and validation and software. JL, LL, WS, and XY performed data curation and used software.

FUNDING

This article was supported by the Major National R&D Projects of China (No. 2016ZX05027–001-006).

REFERENCES

Agrawal, V., and Sharma, S. (2020). Are we modeling the properties of unconventional shales correctly. *Fuel* 267, 1–7. doi:10.1016/j.fuel.2020.117316

Bayon, R. L., Brey, G. P., Ernst, W. G., and Mählmann, R. F. (2011). Experimental kinetic study of organic matter maturation: time and pressure effects on vitrinite reflectance at 400°C. *Org. Geochem.* 42, 340–355. doi:10.1016/j.orggeochem.2011.01.011

Behar, F., Vandenbroucke, M., Teerman, S. C., Hatcher, P. G., Leblond, C., and Lerat, O. (1995). Experimental simulation of gas generation from coals and a marine kerogen. *Chem. Geol.* 126, 247–260. doi:10.1016/0009-2541(95)00121-2

Chen, J. P., Ge, H. P., Chen, X. D., Deng, C. P., and Liang, D. J. (2008). Classification and origin of natural gases from Lishui Sag, the east China Sea basin. *Sci. China Earth Sci.* 51, 122–130. doi:10.1007/s11430-008-5001-5

Cheng, X., Hou, D., Zhao, Z., Chen, X., and Diao, H. (2019). Sources of natural gases in the Xihu Sag, east China Sea basin: insights from stable carbon isotopes and confined system pyrolysis. *Energy Fuels* 33, 2166–2175. doi:10.1021/acs.energyfuels.9b00090

Cramer, B., Faber, E., Gerling, P., and Krooss, B. M. (2001). Reaction kinetics of stable carbon isotopes in natural gassinsights from dry, open system pyrolysis experiments. *Energy Fuels* 15, 517–532. doi:10.1021/ef000086h

Cramer, B. (2004). Methane generation from coal during open system pyrolysis investigated by isotope specific Gaussian distributed reaction kinetics. *Org. Geochem.* 35, 379–392. doi:10.1016/j.orggeochem.2004.01.004

Dembicki, H. (2009). Three common source rock evaluation errors made by geologists during prospect or play appraisals. *AAPG Bull.* 93, 341–356. doi:10.1306/10230808076

Dieckmann, V., Schenk, H. J., and Horsfield, B. (2000). Assessing the overlap of primary and secondary reactions by closed- versus open-system pyrolysis of marine kerogens. *J. Anal. Appl. Pyrol.* 56, 33–46. doi:10.1016/S0165-2370(00)00083-8

Dieckmann, V., Schenk, H. J., Horsfield, B., and Welte, D. H. (1998). Kinetics of petroleum generation and cracking by programmed-temperature closed-system pyrolysis of Toarcian Shales. *Fuel* 77, 23–31. doi:10.1016/S0016-2361(97)00165-8

Galwey, A. K., and Brown, M. E. (2002). Application of the Arrhenius equation to solid state kinetics: can this be justified?. *Thermochim. Acta.* 386 (1), 91–98. doi:10.1016/S0040-6031(01)00769-9

Ge, H., Chen, J., Chen, X., Deng, C. P., and Liang, D. (2007). Discussion on the type and origin of natural gas in Lishui Sag of the East China Sea basin. *Sci. China Earth Sci.* 51, 104–110. doi:10.1007/s11430-008-5001-5

Hakimi, M. H., and Ahmed, A. F. (2016). Petroleum source rock characterisation and hydrocarbon generation modeling of the Cretaceous sediments in the Jiza sub-basin, eastern Yemen. *Mar. Petrol. Geol.* 75, 356–373. doi:10.1016/j.marpetgeo.2016.04.008

Hartwig, A., Primio, R. D., Anka, Z., and Horsfield, B. (2012). Source rock characteristics and compositional kinetic models of Cretaceous organic rich black shales offshore southwestern Africa. *Org. Geochem.* 51, 17–34. doi:10.1016/j.orggeochem.2012.07.008

He, L., Ma, Y., Yue, C. T., Wu, J., and Li, S. (2020). Kinetic modeling of Kukersite oil shale pyrolysis with thermal bitumen as an intermediate. *Fuel* 279, 118371. doi:10.1016/j.fuel.2020.118371

Hill, R. J., Tang, Y. C., and Kaplan, I. R. (2003). Insights into oil cracking based on laboratory experiments. *Org. Geochem.* 34, 1651–1672. doi:10.1016/S0146-6380(03)00173-6

Hill, R. J., Zhang, E., Katz, B. J., and Tang, Y. (2007). Modeling of gas generation from the Barnett Shale, Fort Worth Basin, Texas. *AAPG (Am. Assoc. Pet. Geol.) Bull.* 91, 501–521. doi:10.1306/12060606063

Horsfield, B. (1989). Practical criteria for classifying kerogens: some observations from pyrolysis-gas chromatography. *Geochem. Cosmochim. Acta.* 53, 891–901. doi:10.1016/0016-7037(89)90033-1

Huang, D., and Li, J. (1982). Diagram of kerogen classification and the characters of kerogen of standard humic type. *Geochimica* 1, 21–30 [in Chinese]. doi:10.19700/j.0379-1726.1982.01.003

Huang, D., Li, J., and Zhang, D. (1984). Kerogen types and study on effectiveness, limitation and interrelation of their identification parameters. *Acta Sedimentol. Sin.* 3, 18–33+135 [in Chinese]. doi:10.14027/j.cnki.cjxb.1984.03.002

Jasper, K., Krooss, B. M., Flajs, G., Hartkopf-Fröder, C., and Littke, R. (2009). Characteristics of type III kerogen in coal-bearing strata from the Pennsylvanian (Upper Carboniferous) in the Ruhr Basin, Western Germany: comparison of coals, dispersed organic matter, kerogen concentrates and coal–mineral mixtures. *Int. J. Coal Geol.* 80, 1–19. doi:10.1016/j.coal.2009.07.003

Kotarba, M. J., and Lewan, M. D. (2013). Sources of natural gases in Middle Cambrian reservoirs in Polish and Lithuanian Baltic Basin as determined by stable isotopes and hydrous pyrolysis of Lower Palaeozoic source rocks. *Chem. Geol.* 345, 62–76. doi:10.1016/j.chemgeo.2013.02.023

Lewan, M. D., and Roy, S. (2011). Role of water in hydrocarbon generation from Type-I kerogen in Mahogany oil shale of the Green River Formation. *Org. Geochem.* 42, 31–41. doi:10.1016/j.orggeochem.2010.10.004

Li, D. Y., Jiang, X. D., Xu, F., Liu, J., and Hou, G. (2016). Geochemistry of the Paleocene in Lishui Sag, East China Sea Shelf basin: implications for tectonic background and provenance. *Acta Geol. Sin.-Engl. Ed.* 90, 166–181. doi:10.1111/1755-6724.12649

Li, J., Ma, W., Wang, Y., Wang, D., Xie, Z., Li, Z., et al. (2018). Modeling of the whole hydrocarbon-generating process of sapropelic source rock. *Petrol. Explor. Dev.* 45, 445–454. doi:10.1016/S1876-3804(18)30051-X

Li, N., Zhang, J., Shen, W., Liu, Y., Liu, H., Wang, J., et al. (2020). Recovery of the erosion thickness and characterization of the paleogeomorphology in the southern Lishui Sag, East China Sea Shelf basin. *J. Ocean Univ. China* 19, 320–330. doi:10.1007/s11802-020-3957-8

Li, Y., Zhang, J., Liu, Y., Shen, W., Chang, X., Sun, Z., et al. (2019). Organic geochemistry, distribution and hydrocarbon potential of source rocks in the Paleocene, Lishui sag, East China Sea Shelf basin. *Mar. Petrol. Geol.* 107, 382–396. doi:10.1016/j.marpetgeo.2019.05.025

Liu, L., Li, Y., Dong, H., and Sun, Z. (2020). Diagenesis and reservoir quality of Paleocene tight sandstones, Lishui Sag, East China Sea Shelf basin. *J. Petrol. Sci. Eng.* 195, 107615. doi:10.1016/j.petrol.2020.107615

Liu, W. H., Wang, J., TengerQin, J. Z., and Zheng, L. J. (2012). Stable carbon isotopes of gaseous alkanes as genetic indicators inferred from laboratory pyrolysis experiments of various marine hydrocarbon source materials from southern China. *Sci. China Earth Sci.* 55, 966–974. doi:10.1007/s11430-012-4392-5

Peters, K. E., Walters, C. C., and Moldowan, J. M. (2005). *The biomarker guide: biomarkers and isotopes in petroleum exploration and earth history*. 2nd Edn. Cambridge, United Kingdom: Cambridge University Press, 75–76

Ruble, T. E., Lewan, M. D., and Philp, R. P. (2001). New insights on the green river petroleum system in the uinta basin from hydrous pyrolysis experiments. *AAPG (Am. Assoc. Pet. Geol.) Bull.* 85, 1333–1371. doi:10.1306/8626CAB9-173B-11D7-8645000102C1865D

Ruble, T. E., Lewan, M. D., and Philp, R. P. (2003). New insights on the Green River petroleum system in the Uinta basin from hydrous-pyrolysis experiments: reply. *AAPG (Am. Assoc. Pet. Geol.) Bull.* 87, 1535–1541. doi:10.1306/0423030137r

Seewald, J. S. (2003). Organic-inorganic interactions in petroleum-producing sedimentary basins. *Nature* 426, 327–333. doi:10.1038/nature02132

Shen, W., Qi, B., and Xu, G. (2019). The seismic inversion based organic matter abundance predictionmethod for source rocks and its application in Lishui Sag. *China Offshore Oil Gas.* 31, 68–74 [in Chinese]. doi:10.11935/j.issn.1673-1506.2019.03.008

Su, A., Chen, H. H., Cao, L. S., Lei, M., Wang, C., Liu, Y., et al. (2014). Genesis, source and charging of oil and gas in Lishui sag, East China Sea basin. *Petrol. Explor. Dev.* 41, 574–584. doi:10.1016/S1876-3804(14)60068-9

Su, A., Chen, H. H., Wang, C. W., Li, P., Zhang, H., Xiong, W., et al. (2013). Genesis and maturity identification of oil and gas in the Xihu sag, East China Sea basin. *Petrol. Explor. Dev.* 40, 558–565. doi:10.1016/S1876-3804(13)60073-7

Sun, Z., Zhang, J., Liu, Y., Shen, W., Li, Y., and Li, L. (2020). Sedimentological signatures and identification of Paleocene sedimentary facies in the Lishui Sag, East China Sea Shelf basin. *Can. J. Earth Sci.* 57, 377–395. doi:10.1139/cjes-2019-0022

Tang, Y., Jenden, P. D., Nigrini, A., and Teerman, S. C. (1996). Modeling early methane generation in coal. *Energy Fuels* 10, 659–671. doi:10.1021/ef950153l

Tian, H., Xiao, X., Wilkins, R. W., and Tang, Y. (2012). An experimental comparison of gas generation from three oil fractions: implications for the chemical and stable carbon isotopic signatures of oil cracking gas. *Org. Geochem.* 46, 96–112. doi:10.1016/j.orggeochem.2012.01.013

Tian, H., Xiao, X., Yang, L., Xiao, Z., Guo, L., Shen, J., et al. (2009). Pyrolysis of oil at high temperatures: gas potentials, chemical and carbon isotopic signatures. *Chin. Sci. Bull.* 54, 1217–1224. doi:10.1007/s11434-008-0590-0

Tissot, B. P. (1984). Recent advances in petroleum geochemistry applied to hydrocarbon exploration. *AAPG Bull.* 68, 546–563. doi:10.1306/AD461336-16F7-11D7-8645000102C1865D

Tissot, B. P., and Welte, D. H. (1984). *Petroleum formation and occurrence*. New York, NY: Springer-Verlag

Van Krevelen, D. W. (1993). *Coal: typology, physics, chemistry, constitution*. Amsterdam, Netherlands: Elsevier, 979

Wang, M., Lu, S. F., and Xue, H. T. (2011). Kinetic simulation of hydrocarbon generation from lacustrine type I kerogen from the Songliao Basin: model comparison and geological application. *Mar. Petrol. Geol.* 28, 1714–1726. doi:10.1016/j.marpetgeo.2011.07.004

Wang, Q., Zou, H., Hao, F., Zhu, Y., Zhou, X., Wang, Y., et al. (2014). Modeling hydrocarbon generation from the Paleogene source rocks in Liaodong Bay, Bohai Sea: a study on gas potential of oil-prone source rocks. *Org. Geochem.* 76, 204–219. doi:10.1016/j.orggeochem.2014.08.007

Wang, Y., Zou, Y., Zhan, Z., Lin, X.-H., and Liang, T. (2018). Origin of natural gas in the Turpan-Hami Basin, NW China: evidence from pyrolytic simulation experiment. *Int. J. Coal Geol.* 195, 238–249. doi:10.1016/j.coal.2018.06.007

Xu, C., Ye, J., Liu, J., Caoa, Q., Sheng, Y., and Yu, H. (2020). Simulation of hydrocarbon generation and expulsion for the dark mudstone with type-III kerogen of Pinghu Formation in Xihu Sag, East China Sea Basin under near geological conditions. *Oil Gas Geol.* 41, 359–366 [in Chinese]. doi:10.11743/ogg20200212

Zhang, E., Hill, R. J., Katz, B. J., and Tang, Y. (2008). Modeling of gas generation from the Cameo coal zone in the Piceance Basin, Colorado. *American AAPG Bulletin* 92, 1077–1106. doi:10.1306/04020806015

Zhang, J., Guo, J., Liu, J., and Shen, W. (2019). 3D-Basin modelling of the Lishui Sag: research of hydrocarbon potential, petroleum generation and migration. *Energies* 12 (4), 650. doi:10.3390/en12040650

Zhang, M., Zhang, J. L., Xu, F., Li, J., Liu, J., Hou, G., et al. (2015). Paleocene sequence stratigraphy and depositional systems in the Lishui Sag, East China Sea Shelf Basin. *Mar. Petrol. Geol.* 59, 390–405. doi:10.1016/j.marpetgeo.2014.09.015

Conflict of Interest: Authors JL and WS are employed by CNOOC China Ltd.

The remaining authors declare that the research was conducted in the absence of any commercial or financial relationships that could be construed as a potential conflict of interest.

frontiers in Earth Science

ORIGINAL RESEARCH
published: 02 February 2021
doi: 10.3389/feart.2020.597535

Quantitative Evaluation of Tight Sandstone Reservoir Based on Diagenetic Facies—A Case of Lower Silurian Kepingtage Formation in Shuntuoguole Low Uplift, Tarim Basin, China

Bin Li[1,2], *Hanbing Zhang*[3]*, *Qingsong Xia*[1,2], *Jun Peng*[1,2] *and Qiang Guo*[1]

[1]School of Geoscience and Technology, Southwest Petroleum University, Chengdu Sichuan, China, [2]State Key Laboratory of Oil and Gas Reservoir Geology and Exploration, Southwest Petroleum University, Chengdu, China, [3]PetroChina Zhejiang Oilfield Company, Hangzhou, China

The tight sandstone reservoirs of the Lower Silurian Kepingtage Formation are important exploratory targets for tight gas resources in the Shuntuoguole Low Uplift of Tarim Basin. How to evaluate tight sandstone reservoir is an urgent problem to be solved. In this study, we investigated the effects of diagenesis on the heterogeneity of tight sandstone deposits in similar sedimentary facies and established the relationship between the diagenetic facies and reservoir quality. Cores of the tight sandstone reservoirs of Lower Silurian Kepingtage Formation in Shuntuoguole Low Uplift are studied with thin section observation, SEM, XRD, and mercury injection. Quantification of diagenesis influencing porosity suggests that sandstone densification is mainly controlled by compaction, cementation, and hydrocarbon charging (bitumen charging), and the reservoir properties are effectively improved by dissolution, based on which 6 types of diagenetic facies are classified. Interpretation of the log data from individual wells with "K nearest neighbor" algorithm concludes that top and base of the upper member of Kepingtage Formation are believed to have favorably diagenetic reservoirs mainly falling in Type V; favorably diagenetic facies develop best in the lower member of Kepingtage Formation predominated by Types V and VI which mainly distribute in its top. Composite analysis of diagenetic facies, sedimentary facies, and porosity distribution shows that the favorable area of further exploration and development is east of Well SH903 and north of Well SH10. The quantitative identification of diagenetic facies based on logging information can provide reasonable results for the evolution of the tight sandstone reservoirs for a similar area in the Tarim Basin.

Keywords: tight sandstone, diagenesis, quantitative evaluation, Kepingtage formation, Tarim basin

OPEN ACCESS

Edited by:
Dongdong Wang,
Shandong University of Science and Technology, China

Reviewed by:
Bing Tian,
Inner Mongolia University of Science and Technology, China
Renchao Yang,
Shandong University of Science and Technology, China

***Correspondence:**
Hanbing Zhang
zhanghb_swpu@163.com

Specialty section:
This article was submitted to Sedimentology, Stratigraphy and Diagenesis, a section of the journal Frontiers in Earth Science

Received: *21 August 2020*
Accepted: *06 November 2020*
Published: *02 February 2021*

Citation:
Li B, Zhang H, Xia Q, Peng J and Guo Q (2021) Quantitative Evaluation of Tight Sandstone Reservoir Based on Diagenetic Facies—A Case of Lower Silurian Kepingtage Formation in Shuntuoguole Low Uplift, Tarim Basin, China. Front. Earth Sci. 8:597535. doi: 10.3389/feart.2020.597535

INTRODUCTION

The evaluation and prediction of the tight sandstone reservoirs have been hotspots for the petroleum industry (Guo et al., 2019; Ren et al., 2019; Xiao et al., 2019; Li et al., 2020). The actual exploration effect of the traditional method for the evaluation of tight sandstone reservoirs is poor, which is mainly because the fact that the reservoir physical parameters can not reflect the strong heterogeneity of tight sandstone reservoir (Nian et al., 2016; Zhu et al., 2016; Zhou et al., 2019; Qiao et al., 2020). Continuous researches on diagenesis have made significant achievements in which multi-technological quantitative evaluation is used (Hao et al., 2010; Guo et al., 2018; Qin et al., 2018; Xi et al., 2019). Rapid quantitative evaluation of diagenesis based on diagenetic facies study is the most widely used now and will be the major methodology (Jiang et al., 2014; Zhu et al., 2016; Cui Y et al., 2017). Diagenetic facies including mineral constituents, cement, fabric, pores, and fractures, which reflects the current mineral composition and fabric features and is the genetic mark representing reservoir nature, type, and quality, is the result of sediments which underwent diagenesis and a period of diagenetic evolution (Zou et al., 2008; Li et al., 2019; Li et al., 2020). Diagenetic facies study focusing on the effects of diagenesis process on reservoir properties and pore configuration (Ochoa, 2010; Cui et al., 2017; Lai et al., 2018) is to effectively help hydrocarbon exploration and development by determining the spatial distribution of high-quality reservoir to provide reliable evidence for reservoir prediction (Maast et al., 2011; Meng et al., 2015; Li et al., 2019).

The previous study of diagenetic facies mainly relied on relative core analysis, especially on data of thin section, SEM, and cathode luminescence reflecting microscopic features (Lai et al., 2013; Qin et al., 2018). Limitation of core data results in the inability to show the vertical variation of the diagenetic facies whereas log data continuously record all the physical properties of the penetrated layers (Aysen et al., 2011; Cui et al., 2017; Lai et al., 2019; Zhou et al., 2019). Thus, core-based diagenetic facies identification combined with related well log responses to different diagenetic facies leads to the identification of vertically continuous diagenetic facies in individual wells, so that diagenesis can be evaluated quantitatively and rapidly.

Lower Silurian Kepingtage Formation in Shuntuoguole low uplift is typical tight sandstone with very high heterogeneity (Zhao et al., 2015; Yin et al., 2017; Wang et al., 2020). In relatively stable tectonic settings, sedimentation is the basis of reservoir development while diagenesis which plays a vital role in the intensification of sandstones determines the reservoir quality and distribution. Therefore, systematical quantitative studies of diagenesis and diagenetic facies result in the identification of the high-quality reservoir distribution pattern and are of great significance to the prediction of Silurian tight reservoirs in the study area.

GEOLOGIC SETTING

Located in the Xinjiang Uygur Autonomous Region, northwest of China, Tarim Basin is a large composite sedimentary basin developed on the Presinian metabase. Shuntuoguole low uplift, lying in the north of central uplift zone of Tarim Basin with Awati Sag to the west, Manjiaer Sag to the east, Tabei Uplift to the north, and Tazhong Uplift to the south, is a "saddle" hinge structure between two positive south-north structural belts and two negative east-west structural belts, which is wide in the northern and narrow in the southern (Xiong et al., 2013). It is a sub-low-uplift on the northern slope of central Tarim Basin (**Figure 1A**). The Paleozoic, Mesozoic, and Cenozoic strata are completely distributed, and the Ordovician, Silurian, Devonian, and Jurassic Cretaceous are missing in some parts, so the overall tectonic activity is relatively stable (Li et al., 2012). The Silurian in the study area is mainly a set of clastic rocks of shoreside-shallow shelf facies, lithologically composed of gray-green argillaceous siltstone, gray mudstone, and purple-red siltstone (Zhao et al., 2015). The Silurian is composed of the Kepingtage Formation, the Tataaiertage Formation, and the Imutantawu Formation. The research horizon is the Kepingtage Formation mainly divided into a lower member (S_1k^1), middle member (S_1k^2), and upper member (S_1k^3). The lower member (S_1k^1) is composed of Barrier bar and Shoreface interbedded deposits, and sandstone reservoir developed (Sun et al., 2013). The upper member (S_1k^3) developed the delta front environment, mainly developing underwater distributary channels, mouth bar, and underwater distributary interchannel microfacies (Zeng et al., 2018; Yin et al., 2017). Gray mudstone developed in the middle member (S_1k^2) and upper part of upper member (S_1k^3), constitutes a good cap layer in the region, thus forming several sets of favorable reservoir-cap assemblages in the study area (**Figure 1B**). They are the major exploration targets for Paleozoic clastic rock hydrocarbon exploration in the Shuntuoguole region (Xiong et al., 2013; Cai et al., 2014; Peng et al., 2018; Wang et al., 2020).

SAMPLES AND METHODS

This study takes 300 cores (sampling from 5,164–5,712 m) from 8 wells in the low uplift in Shuntuoguole. 308 thin sections with each one having 200 points are made for a series of tests, including petrology, petrophysical property, porous structure, and diagenesis. Polarizing microscope (LV100POL) is used to observe the mineral composition, shape, texture, optical feature, and type and size of the pores. Microscopic shape and texture are observed for 55 samples using a Scanning electronic microscope (XL30). Clay mineralogical content is analyzed for 53 samples through X-ray diffraction (D/max2,500 PC). Physical properties and pore configuration of the sandstone are analyzed for 122 samples using mercury intrusion porosimeter (AutoPore9500). The original porosity of the sandstone is restored through particle size analyzer (SFY-D Acoustic Screener and CG-1 Centrifugal Settling Particle Size Distribution Analyzer).

RESULTS

Reservoir Lithologies

Kepingtage Formation mainly consists of fine sandstone (grain sizes ranging from 0.09 to 0.25 mm) which contains litharenite

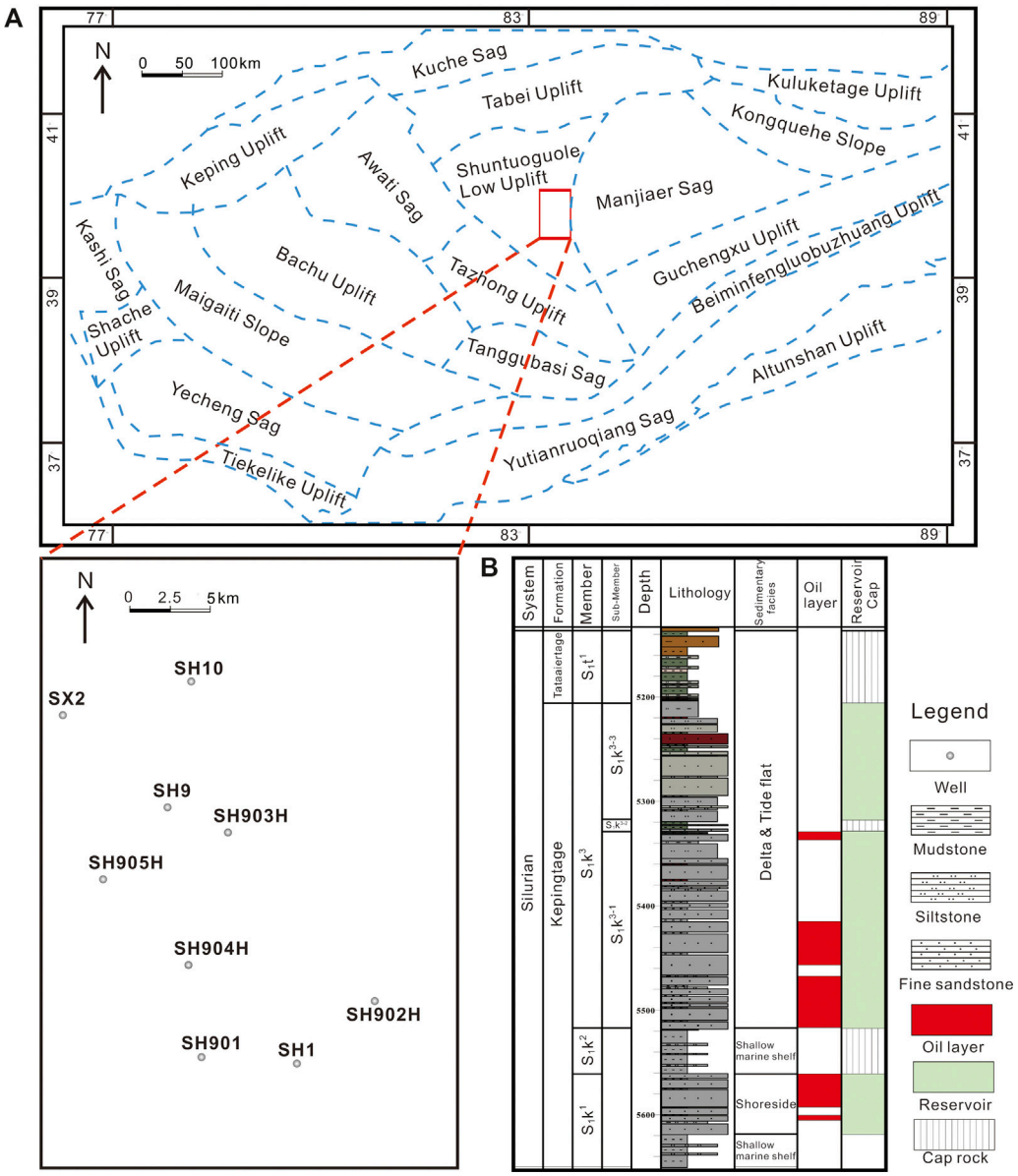

FIGURE 1 | Structural location and well location distribution in the study area. **(A)** Location of Shuntuoguole low uplift and surrounding structural features. **(B)** Lithological profile and reservoir-caprock assemblage of Kepingtage Formation (S_1k^1, totally 90 ~ 150m thick shoreside (non-barrier coast)-shallow marine shelf facies deposit that is different from common high-energy shoreside due to low-energy water body, mainly consists of fine-grain sandstone with medium-grain sandstone and siltstone in the upper part and mudstone in the lower part. S_1k^2, 43 ~ 59m thick, deposited in the shallow marine shelf. S_1k^3, 287 ~ 342m thick, depositing in delta (tidal action) depositional system, mainly consists of silt-fine sandstone interbedded with silty mudstones, with a 15 ~ 30m mudstone in its middle part. The three sandstone members, S_1k^{3-3}, S_1k^{3-1}, and S_1k^1, containing reservoirs with abundant oil and gas, form several favorable reservoir-cap assemblages in combination with S_1k^{3-2}, S_1k^2, and S_1t^1).

(61.86%), sublitharenite (17.63%), and feldspathic litharenite (11.22%) (**Figure 2**).

The clastic constituents predominantly comprise quartz (62.0%) that mainly contain single-crystal quartz with some chert. They comprise less feldspar (7.0%), which is commonly sericitized, and K-spar content is higher than plagioclase. The proportion of debris in the rock fragments which primarily consist of metamorphic rock debris and sedimentary rock debris. Besides, heavy minerals like zircon, tourmaline, garnet, apatite, and pyrite can be seen despite their very low content. Grains sorting is good and poorly rounded.

The cement account for 66.7% of interstitial materials, and the first biggest proportion is calcareous cement (45.7%) with calcite that is inhomogeneous as the main composition. The second is siliceous cement (16.7%) which is dominated by quartz overgrowth and intergranular authigenic quartz. There is very little clay (0.4%) which is mainly illite-smectite hybrid, illite, and

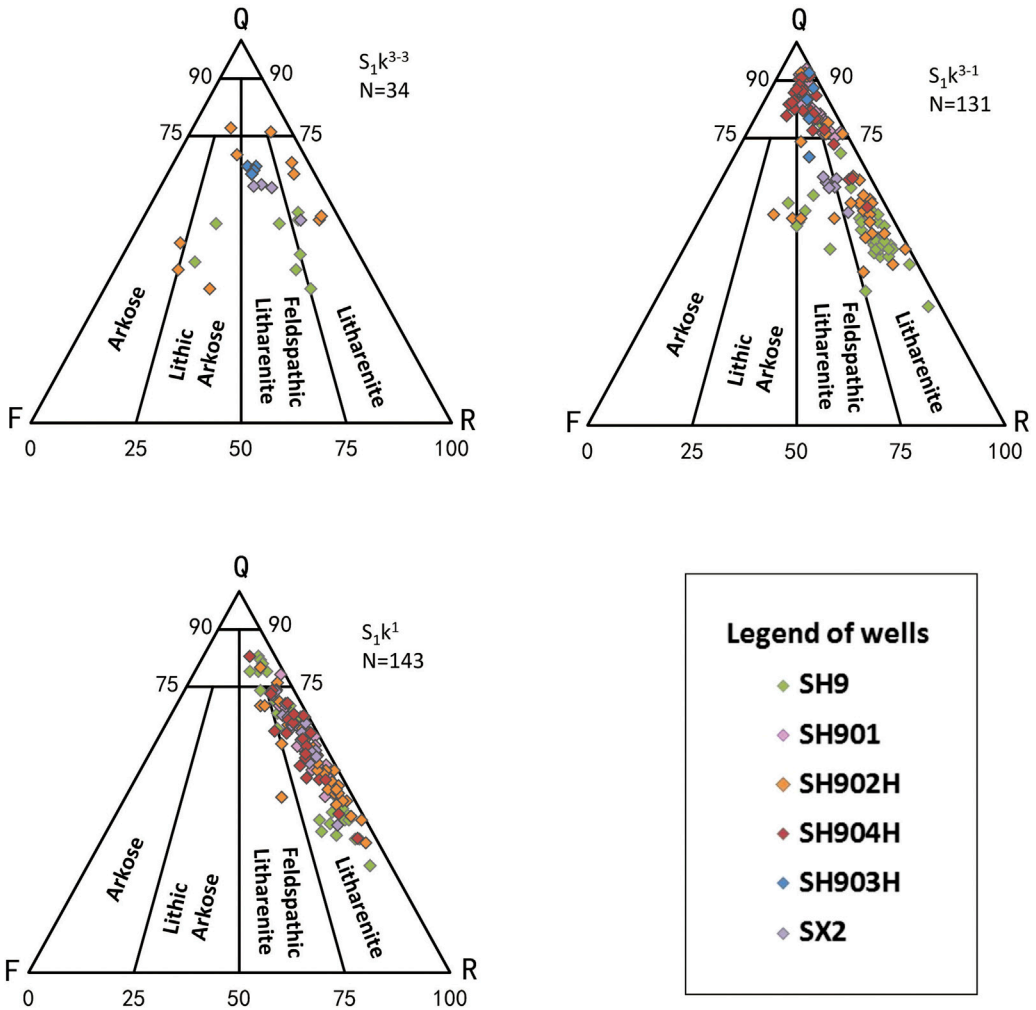

FIGURE 2 | Composition determined from thin-section analysis (a. S_1k^{3-3}. **B**. S_1k^{3-1}. **C**. S_1k^1.). (Q—Quartz + Chert; F—Feldspar; R—Rock fragments) (ternary diagram from Zhao and Zhu, 2006).

chlorite. Moreover, argillaceous matrix (27%) and slight bitumen (6.3%) are also seen in the interstitial materials.

Reservoir Properties

Kepingtage Formation sandstone mainly contains secondary dissolved pores, primary intergranular pores, microfractures, and composition matrix pores. The secondary dissolved pores, accounting for about 52.3% of plane porosity, include intergranular dissolved pores that are the most dominant, intragranular dissolved pores, intercrystal pores, and moldic pores (**Figure 3A**). Primary intergranular pores (Figure 3b) take 39.2% while microfractures that are commonly filled by bitumen or argillaceous material only take about 2.2% of the plane porosity. For the three sandstone members, S_1k^{3-3} is dominated by primary intergranular pores, whereas S_1k^{3-1} and S_1k^1 dominantly contain secondary intergranular pores (**Figure 4**).

Core-based data from 1,400 samples show that Kepingtage Formation has generally poor physical properties. Porosity ranges from 0.5% to 16.4% and averages 7.0%, while air permeability, which is mainly 0.1–1 mD, ranges from 0.01 to 15.4 mD and averages 0.54 mD (**Figure 5**). Physical properties of the three sandstone members worsen increasingly with deeper burial: S_1k^{3-3} porosity is 9.1% with an air permeability of 1.34 mD; S_1k^{3-1} porosity is 7.50% with an air permeability of 0.57mD; S_1k^1 porosity is 6.1% with an air permeability of 0.32 mD.

Diagenesis

Kepingtage Formation underwent compaction, cementation, dissolution, metasomasis, hydrocarbon charging, and structural fracturing. It is the reworking of the multiple diageneses that leads to the property variations of different sandstone zones (Carvalho et al., 2014; Zhao et al., 2015; Peng, et al., 2018; Zeng et al., 2018).

Compaction which worked throughout the burial history of the sandstone reservoir (Zhou et al., 2008) reduced the primary pores sharply at the early stage of diagenesis (Paxton et al., 2002). Kepingtage Formation experienced strong compaction which mainly accounts for the reduction of the Petrophysical

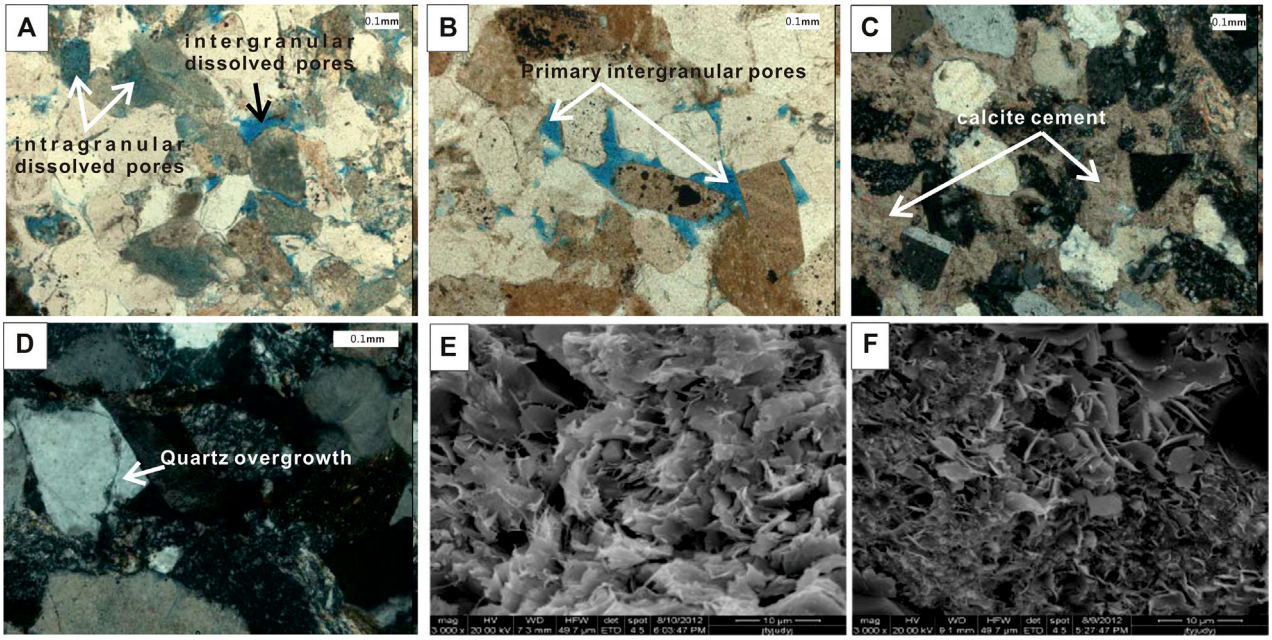

FIGURE 3 | Microphotographs of Kepingtage Formation reservoir rocks **(A)** Intergranular dissolved pores and intragranular dissolved pores, fine to medium grained litharenite, Well Sh904H, 5576.58m, 10 × 10, (-) **(B)** Residual primary intergranular pores and intergranular dissolved pores, fine-medium grained quartz litharenite, Well Sh901, 5503.62m, 10 × 10, (-) **(C)** Intergrowth calcite cement, fine to medium grained litharenite, Well Sh904H, 5584.40m, 10 × 10, (+) **(D)** Quartz overgrowth, fine to medium grained litharenite, Well Sh904H, 5511.08m, 10 × 20, (+) **(E)** Particle surface with filamentous and laminated illite-smectite mixed layer, fine-medium grained quartz litharenite, Well Sh904H, 5367.66m, SEM, 300×. **(F)** Particle surface with laminated chlorite, fine to medium grained litharenite, Well SX2, 5678.26m, SEM 3000×.

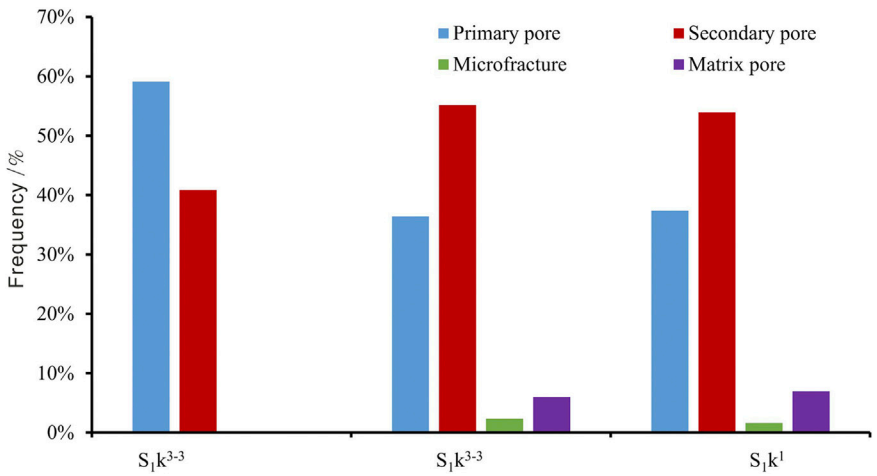

FIGURE 4 | Pore type distribution in different sandstone members of Kepingtage Formation.

property. Deep burial and high content of rock fragments which caused Kepingtage Formation to undergo strong compaction are the predominant causes of reduced porosity. Mechanical compaction was dominant and pressolution functioned little. Microscope-based analysis of compaction finds 1) that intergranular contact changes from point contact to line contact, even to concave-convex contact (**Figure 3b**), 2) that plastic grains like mica and soft debris became deformed and even fractured, and 3) that rigid grains such as quartz and feldspar misplaced or broken under compression.

Cementation is common in Kepingtage Formation, including calcareous cementation, siliceous cementation, and clay cementation. Cement generally reduces the porosity due to their filling up the pore space, but they can also resist

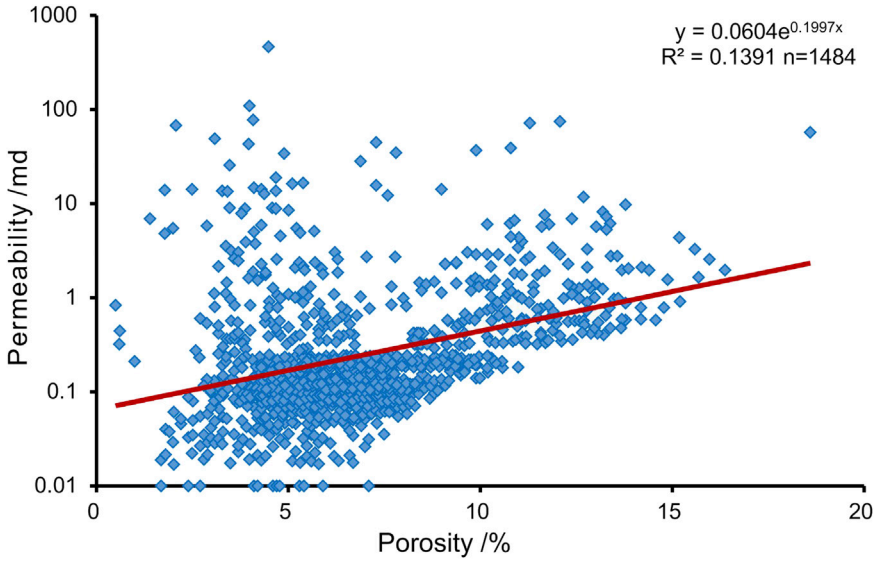

FIGURE 5 | Cross plot of porosity and permeability of Kepingtage Formation.

compaction by enhancing the frame strength (Zaid, 2013; Yuan et al., 2015; Peng, 2018).

(1) Calcareous cementation. Calcareous cement primarily consists of calcite. Microscope-based observation and thermometry of primary inclusion captured by the calcite-cement show that early- and late-stage calcite cementations occurred. The early-stage cement has intergrowth texture with alternation of rock fragments of which quartz has no overgrowth at their edges (**Figure 3C**). The homogenization temperature of the inclusion ranges from 80°C to 100°C. The late-stage calcite cement is commonly clot-shaped or granular with quartz overgrowth. The homogenization temperature of the inclusion ranges from 140 to 150°C.
(2) Siliceous cementation. In sandstones with intense calcareous cementation, siliceous cement, developing to a relatively low degree, have quartz overgrowth around the surface in an ear-like or irregular ring-like shape, with the enlarged edge of 0.01–0.08 mm thick (**Figure 3D**).
(3) Clay cementation. Clay cement that mainly contains illite, illite-smectite mixed layer, and chlorite, with very little kaolinite and chlorite-smectite mixed layer. SEM-based observation shows that illite occurs in sheet-like and cellular shapes on the clay particle surface, or extends outward in filament shape along the surface. The illite-smectite mixed layer resembles the irregular sheet of illite in morphology (**Figure 3E**) while chlorite whose individual morphology resembles niddles commonly coats the particle (**Figure 3F**).

Dissolution plays a vital role in the improvement of the physical properties of the reservoir. According to the SEM observation, dissolution occurs at the feldspar particle edge or cleavage where soluble compositions are dissolved, and residual part is sieve-like or wreckage-like with intergranular pores and intragranular pores (**Figure 3A**); feldspar is entirely eroded where mold pores are formed.

Metasomatism indicates rock fragments were alternated with calcite, and with feldspar and quartz, or with pyrite, and the alternated fragment particle has sawtooth-like or embayed edges (**Figure 3C**).

Hydrocarbon charging slows down the cementation rate and accelerates dissolution (Li et al., 2003; Molenaar et al., 2008; Guo et al., 2018; Wang et al., 2020), but residual bitumen filling the pores reduces porosity. Two stages of bitumen charging are identified. Residual bitumen during the first charging stage filled the primary intergranular pores along the eroded edge of the grains (**Figure 6A**), and the oil inclusion displays light gray-yellow or light yellow fluorescence (**Figure 6B**). Residual bitumen during the second charging filled the space beyond the quartz overgrowth edge (**Figure 6C**) and the dissolved pores of calcite cement, and the oil inclusion displays light bluish-green, light green, or green fluorescence (**Figure 6D**).

QUANTITATIVE EVALUATION OF DIAGENESIS

Diagenesis and Porosity

Diagenesis controls the pore evolution of the sandstone reservoir (Pan et al., 2011; Zhao, 2015; Peng, 2018; Li et al., 2019; Xiao et al., 2019). Based on the above diagenesis study, a quantitative evaluate method of the effect of diagenetic events on sandstone porosity was performed using a screen test of particle size and thin section identification. First of all, the relationship between unconsolidated sandstone porosity and sorting coefficient under Earth surface condition (Beard and Weyl, 1973) is used to calculate initial porosity:

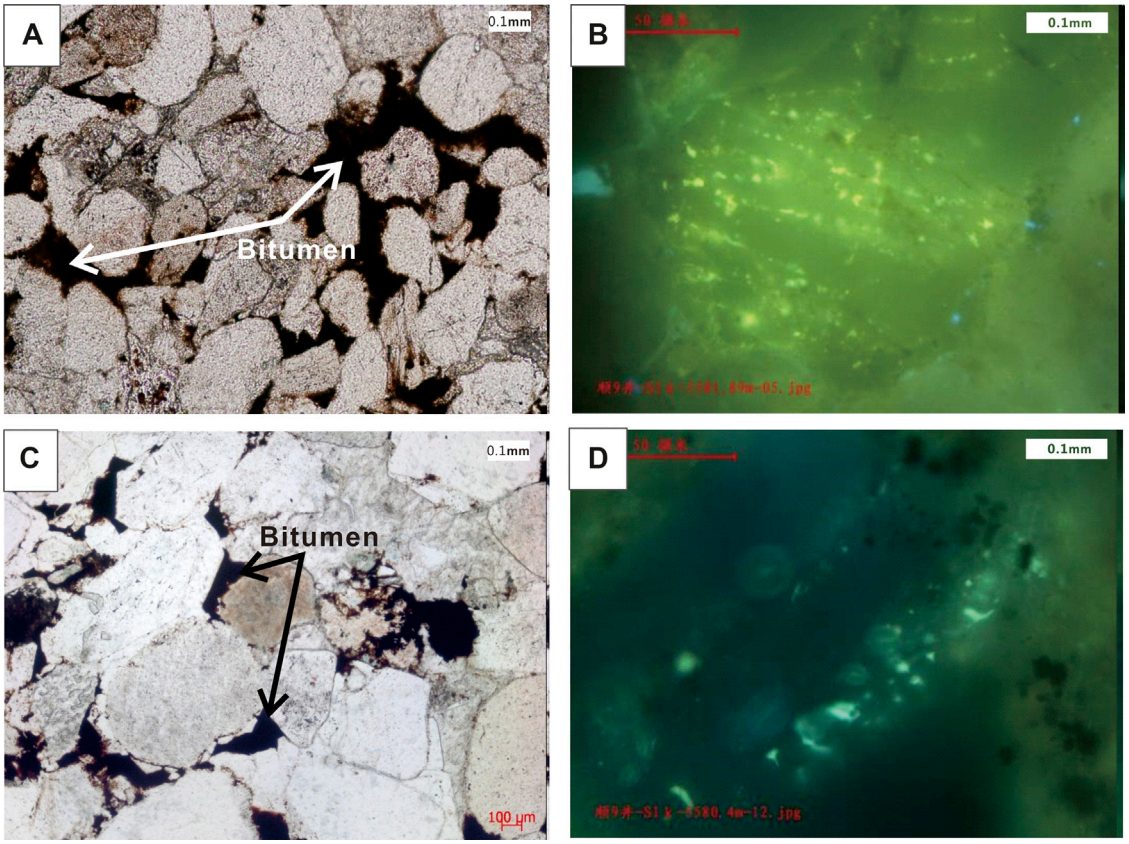

FIGURE 6 | Microphotography of reservoir bitumen and fluorescent photography of inclusion **(A)** Bitumen filling along the corroded edge of the grains, Well Sh9, 5335.79m, 10 × 10 (-) **(B)** The hydrocarbon inclusions developed in quartz grains with a beaded distribution in the cracks, displaying yellow fluorescence, fine grayish sandstone with oily spots, Well Sh9, 5581.89m. **(C)** Bitumen filling into the dissolved pores of calcite cement later than quartz overgrowth, Well Sh9, 5476.48m, 10 × 10 (-). **(D)** The hydrocarbon inclusions develop in quartz grain cracks, which are scattered and uneven in size, displaying bluish-green fluorescence, fine grayish sandstone with oily spots, Well Sh9, 5580.4m.

$$\text{Initial porosity} = 20.91 + 22.90/S_O \quad (1)$$

where P_o is the Trask sorting coefficient.

And then the contents of different cement, different pore types, and bitumen are calculated. Effects of different diagenetic events on porosity are calculated quantitatively using the relationship between the plane porosity and measured porosity (**Table 1**):

$$\text{Compaction} - \text{Reduced porosity} - \text{initial porosity} - (\text{total cementcontent} + \text{bitumen content} + \text{primary intergranular pore volume} \times \text{measured porosity}/\text{plane porosity}) \quad (2)$$

$$\text{Cementation} - \text{Reduced porosity} = \text{cement content} \quad (3)$$

$$\text{Bitumen} - \text{charging} - \text{reduced porosity} = \text{bitumen content} \quad (4)$$

$$\text{Dissolution} - \text{enhanced porosity} = \text{dissolved pore volume} \times \text{measured porosity}/\text{plane porosity} \quad (5)$$

The quantitative calculation shows that the Kepingtage Formation is densified due to compaction, cementation, and hydrocarbon charging (bitumen filling) whereas its reservoir porosity is enhanced due to dissolution. Comparison of the evolution of the three sandstone members of Kepingtage Formation suggests that compaction influenced S_1K^1 most due to its biggest burial depth and its highest content of plastic grains of rock fragments. The physical properties of S_1K^{3-3} are best because of secondary pores generated from relatively good dissolution though a lot of pore space was filled by calcareous cement and sandstone porosity was affected by cementation. None of the three sandstone members of Kepingtage Formation has been influenced significantly by clay cementation. Besides, bitumen filling has also reduced porosity, which is the most obvious in the S_1K^{3-1} sandstone reservoir.

Classification and Characteristics of Diagenetic Facies

Since there has been no unified scenario for classification and naming of diagenetic facies so far (Zou et al., 2008; Cui et al., 2017; Lai et al., 2018; Li et al., 2019), this study proposes "cause (type and intensity of diagenesis) + effect (influence on the reservoir)" scenario on the basis of practicability and quantification. Based on the characteristics and differences

TABLE 1 | Relationship between diagenesis and porosity of Kepingtage Formation.

Sub-member	Well	P_i (%)	Compaction	Cementation				Hydro-Carbon charging	Dissolution				Current porosity (%)	Number of data gathering point
			RP due to compaction (%)	RP due to carbonate cementation (%)	RP due to siliceous cementation (%)	RP due to clay cementation (%)	Total RP due to cementation (%)	RP due to bitumen filling (%)	IP due to feldspar dissolution (%)	IP due to rock fragment dissolution (%)	IP due to quartz dissolution (%)	Total IP due to dissolution (%)		
S_1K^{3-3}	SH9	36.18	19.74	5.63	1.40	0.13	7.16	1.95	2.12	0.76	0.15	3.03	10.36	8
	SH902H	38.53	23.53	8.10	1.45	0.00	9.55	2.10	3.40	1.21	0.24	4.85	8.20	10
	SX2	37.63	16.68	11.50	2.30	0.00	13.80	3.75	4.38	1.56	0.31	6.25	9.65	4
Average		37.45	19.98	8.41	1.72	0.04	10.17	2.60	3.30	1.18	0.24	4.72	9.42	
S_1K^{3-1}	SH9	37.04	21.19	9	0.58	0.18	9.76	3.52	3.47	1.73	0.58	5.78	8.35	40
	SH902H	37.27	24.13	5.55	1.56	0.47	7.58	3.61	2.53	1.27	0.42	4.22	6.17	33
	SH904H	34.54	18.98	4.1	2.05	1.07	7.22	4.26	0.53	0.26	0.09	0.88	4.96	28
Average		36.28	21.43	6.22	1.40	0.57	8.19	3.80	2.18	1.09	0.36	3.63	6.49	
S_1K^{1}	SH9	34.15	24.22	4.18	1.24	0.08	5.50	0.75	1.46	1.12	0.08	2.66	6.34	31
	SH901	31.18	21.87	3.31	2.31	0.66	6.28	0.86	1.66	1.27	0.09	3.02	5.19	19
	SH902H	36.18	28.04	1.54	3.55	0.02	5.11	1.62	2.23	1.71	0.12	4.06	5.47	39
	SH904H	33.03	22.11	5.15	2.00	0.67	7.82	1.55	2.07	1.58	0.11	3.76	5.31	22
Average		33.64	24.06	3.55	2.28	0.36	6.18	1.20	1.86	1.42	0.10	3.38	5.58	

RP, reduced porosity; IP, Incremental porosity.

TABLE 2 | Diagenetic facies types and characteristics of kepingtage formation.

DF	Types of sand-stone	CC (%)	CR	CCC (%)	BC (%)	PIPV (%)	SDV (%)	Por (%)	Perm (mD)	DP (MPa)
I	Litharenite, sublitharenite	60.3–100, 75.2	Line, and line-concave/convex	0–8, 1.82	0.5–5, 2.65	0–3.1, 1.08	0–5.4, 2.49	2.5–5.4, 4.38	0.01–3.4, 0.34	0.2–3, 1.54
II	Litharenite, sublitharenite	3.8–61.4, 30.9	Point-line	9–38, 19.14	1–6, 3.67	0–2.9, 0.98	0–4.5, 1.71	1.7–5.4, 3.44	0.01–0.88, 0.17	0.46–3.97, 1.35
III	Sublitharenite	41.0–77.3, 61.7	Point-line	0–7, 2.53	7–17, 10.9	0.51–3.77, 2.51	0–1.53, 0.52	0.6–7, 4.49	0.06–0.55, 0.34	—
IV	Quartzarenite, sublitharenite	17.0–69.1, 51.7	Point, and point-line	0–5, 2.51	0–4, 0.52	4.97–12.13, 7.29	0–3, 1.16	5.8–13.4, 8.65	0.1–6.02, 0.93	0.15–2.58, 0.91
V	Litharenite	30.9–82.2, 58.7	Point-line, and line	0–9, 2.55	0.2–5, 1.6	1.11–8.56, 3.75	2.13–7.3, 3.88	5.5–13.7, 7.66	0.03–5.59, 0.47	0.15–2.09, 1.03
VI	Litharenite	22.1–71.9, 59.5	Point-line, and line	0–9, 2.67	0	0–4.32, 1.2	5.52–13.26, 7.74	6.1–15.6. 9.35	0.02–6.54, 0.75	0.1–2.96, 1.1

of diagenetic facies, this scenario classifies Kepingtage Formation sandstones into 6 types of diagenetic facies with parameters like compaction coefficient, calcareous cement content, bitumen content, primary intergranular pore volume, and secondary pore volume (from thin section analysis), and measured physical properties, and pore texture (from mercury intrusion): tight facies from strong compaction (Type I), tight facies from calcareous cementation (Type II), tight facies from bitumen filling (Type III), porosity preservation facies from weak diagenesis (Type IV), porosity enhancement facies from medium dissolution (Type V), and porosity generation facies from strong dissolution (Type VI). According to the clastic rock reservoir evaluation criteria of the Kepingtage Formation (Cai et al., 2014),Types I, II, and III are unfavorable diagenetic facies while Types IV, V, and VI are favorable. The characteristics of each diagenetic facies are shown in **Table 2**.

Automatic Identification of Diagenetic Facies

The effective identification of diagenetic facies is a difficult problem in reservoir evaluation. Due to the limitation of the core data, it is a common method to characterize sandstone reservoir by logging curve (Zhou et al., 2008; Hao et al., 2010; Qiao et al., 2020; Zhu et al., 2020). Scholars adopt different methods, including multi-parameter comprehensive identification (Paxton et al., 2002; Jiang et al., 2014; Lai et al., 2019; Li et al., 2019), optimization of Logging Mathematical Model for Identification (Cui et al., 2017; Qin et al., 2018; Guo et al., 2019). The well logs including GR that reflects the lithology and sedimentary environment of sandstone, AC, DEN and CNL that directly indicate porosity differences, and the resistivity logs like RILM and RILD are used to characterize the distribution of diagenetic facies continuously and quantitatively. Picking different logs for specific diagenetic facies as sampled data, this study actualizes the automatic identification of the vertical diagenetic facies using "K nearest neighbor (KNN)" discriminance (He et al., 2014; Lai et al., 2019; Zhou et al., 2019).

The KNN algorithm is to express n term well log value in the training sample set of different diagenetic facies samples as n-dimension characteristic vector, and then to calculate similarity between n-dimension vector point that is formed by well log data to be classified and each n-dimension sector in training sample set. If the very point and the majority of K samples of the nearest neighbor belong to the same diagenetic facies type, the sample belongs to the same type accordingly. In this way, obvious overlap of the well logs for different diagenetic facies types can be solved easily (**Table 3**).

The Algorithm goes as follows

(1) A training sample set is generated based on the known diagenetic facies classification.
(2) Similarity between the unknown sample and each sample in the training sample set is calculated using the following equation:

$$S\left(d_i, d_j\right) = \frac{\sum_{k=1}^{M} S_{ik} \times S_{jk}}{\sqrt{\sum_{k=1}^{M} S_{ik}^2} \sqrt{\sum_{k=1}^{M} S_{jk}^2}} \tag{6}$$

where d_i is the vector derived from well log value of the unknown sample; d_j is the characteristic vector of well log response for the j-th training sample; M is the number of dimensions of the characteristic vector; S_{ik} and S_{jk} are the k-th dimension of correspondent vectors, respectively.

(3) Weight for each category of the unknown sample in the known categorized sample set is calculated with the following equation:

$$p\left(\overline{x}, C_j\right) = \sum_{d_1 \epsilon D} S\left(\overline{x}, \overline{d_i}\right) y\left(\overline{d_i}, C_j\right) \tag{7}$$

where $\overline{x}$ is the characteristic vector of the unknown sample; $S(\overline{x}, \overline{d_i})$ is the similarity; $y(\overline{d_i}, C_j)$ is the category property function. If $\overline{d_i}$ belongs to Category C_j, the value of the function is 1, otherwise, the value is 0.

(4) The Unknown sample is categorized into the known category with the biggest weight.

The diagenetic facies of individual wells in the study area is identified with the above algorithm on Matlab software platform (**Figure 7**). To verify the accuracy of the identification result, this study correlates the log-based identified facies with core-based ones. The correlation shows that matching rate is up to 78.6%, and the favorable diagenetic facies corresponds well to the show of oil and gas from the mud log data (**Figure 7**), suggesting the prediction of the diagenetic facies of the non-coring intervals with the above method is reliable. The logging information of tight sandstone can effectively reflect the lithologic and property changes of reservoir, and can be used as a reliable basis for diagenetic facies identification.

Distribution Regularity of Diagenetic Facies

The spatial distribution of different types of diagenetic facies is a key problem in the evaluation of the tight sandstone reservoirs. Traditional diagenetic facies prediction is based on reservoir parameters such as thickness, porosity, and permeability (Zou et al., 2008; Hao et al., 2010; Lai et al., 2013; Guo et al., 2019; Li et al., 2020; Qiao et al., 2020). However, there is a problem of low accuracy under the influence of reservoir heterogeneity. Identification of diagenetic facies logging effectively solves the problem of fewer sample points (He et al., 2014; Cui et al., 2017; Lai et al., 2019). At the same time, the prediction of reservoir main control factors is used for reference and has high accuracy and good practical effect.

The vertical distribution pattern was discussed by calculating proportions of different diagenetic facies in each sandstone member of the Kepingtage Formation (**Figure 8**). Unfavorable

TABLE 3 | Bore log responses for samples of different diagenetic facies.

Diagenetic facies	DEN (g cm^{-3})	CNL (%)	AC (μm m^{-1})	GR (API)	RILM (Ω·m)	RILD (Ω·m)
I	1.99–2.61	6.38–36.03	60.46–107.98	37.48–114.16	3.98–54.89	4.13–41.91
II	2.03–2.62	6.57–38.26	60.96–91.88	53.70–99.21	3.91–24.70	4.29–32.05
III	2.40–2.58	8.29–16.81	62.69–73.32	60.96–76.28	5.58–10.04	6.03–9.31
IV	2.13–2.59	6.45–23.87	62.80–88.91	43.98–90.42	4.50–11.54	4.00–13.55
V	2.12–2.62	8.11–21.52	60.73–93.89	54.48–116.01	3.93–13.62	3.24–18.14
VI	1.99–2.62	8.55–22.50	62.88–96.72	54.49–108.46	4.19–51.04	3.45–21.37

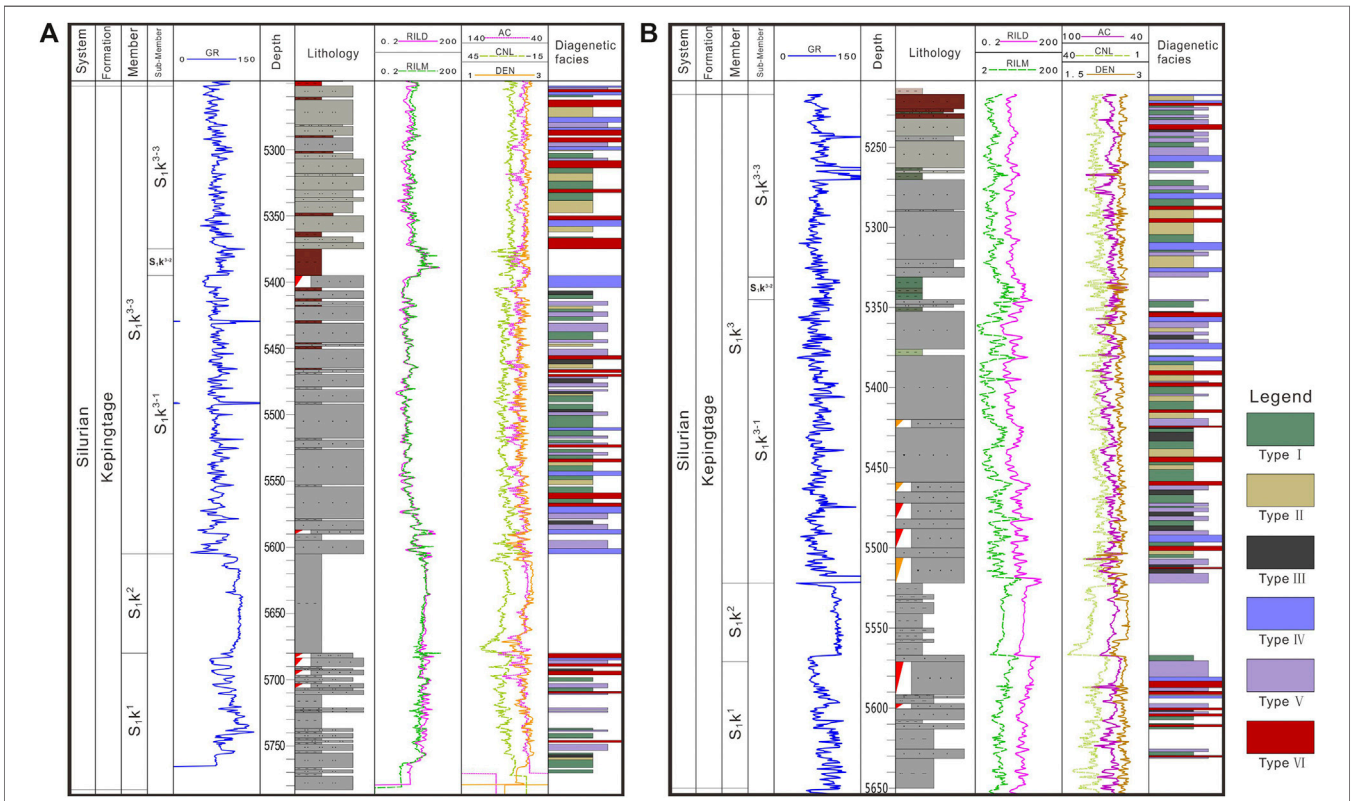

FIGURE 7 | The identification result of diagenetic facies of Kepingtage Formation (A. Well SH903H. **B**. Well SH10.) (The first fifth tracks display system, formation, member, sub-member, and gamma curve respectively. Depth and lithology are shown in the sixth and seventh track. The eighth and ninth tracks display the key logs involved in diagenetic facies calculation. The last track exhibits the results of the diagenetic facies identification.).

diagenetic facies occupies 50% of S_1k^{3-3}, of which Type I takes up 26.9%, Type II 21.6%, and Type III a smaller proportion. All the three types of favorable diagenetic facies develop in this zone, primarily Type V (25.1%), secondarily Type IV (15.9%), and then Type VI. The favorable diagenetic facies predominantly occur in the top and bottom sandstone zones although mud log does not show oil and gas.

The 60% diagenetic facies of S_1k^{3-1} is unfavorable, where Types I, II, and III develop well of which Type III occupies the biggest proportion (13.2%). Favorable diagenetic facies, which do not develop regularly, are mainly Type V and Type VI, and then Type IV. Evidence of oil and gas is commonly discovered in the bottom sandbody.

Favorable diagenetic facies develop best in S_1k^1, occupying over 75% of which Types V and VI are predominant. They primarily occur in the top part with a great quantity of evidence of oil and gas. Unfavorable diagenetic facies are mainly Type I (22.2%) while the other two are seldom seen. The above analysis is consistent with the result of the quantitative calculation of pore evolution.

Due to the lack of effective prediction methods, the study of diagenetic facies distribution is less (Hao et al., 2010; Pan et al., 2011; Cai et al., 2014; Li et al., 2019). Most scholars believe that sedimentary differentiation, which results in the spatial distribution variation in debris mineral composition, interstitial material content, granule size, and pore fluid property, provides different prerequisites for the later diagenesis, so the diagenetic facies distribution is

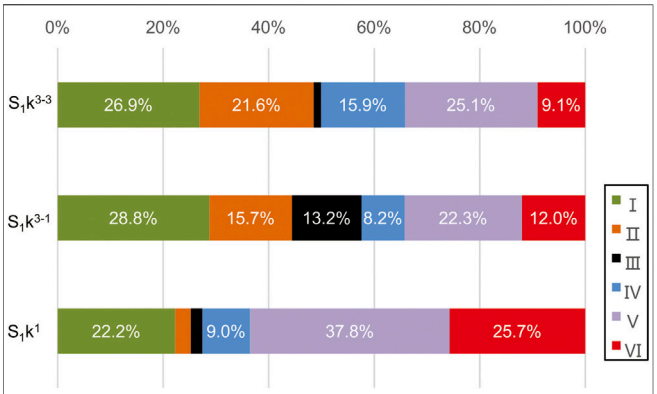

FIGURE 8 | Distribution of Diagenetic Facies Types for sandstone members of Kepingtage Formation. (The three rows respectively represent the diagenetic facies prediction results of the three sandstone members of the Kepingtage Formation. Different colors represent the percentage ratios of different diagenetic facies. The order from left to right is the type I to type VI, as shown in the legend.)

significantly controlled by sedimentary facies (Zhang et al., 2011; Zeng et al., 2018; Qiao et al., 2020). In this study, the face-controlling method is used to study the favorable diagenetic facies distribution. Analysis of diagenetic facies and sedimentary facies of core samples combined shows that underwater distributary channels and mouth bar sand bodies primarily develop in S_1k^{3-3} and S_1k^{3-1}. All types of diagenetic facies occur in the major part of the channel and its peripheries. The sandbody in the main part of the channel is thick and rich in quartz. The mid-part of the sandbody is favorable for primary intergranular pore preservation and the development of Type IV diagenetic facies whereas the upper and lower parts predominantly contain Types V and VI diagenetic facies. On the channel peripheries where the sandbodies are thinner with lower quartz content and stronger calcareous cementation, Type I and Type II diagenetic facies predominantly occur. In the mouth bar where the sandbody rich in quartz is well rounded and well-graded, types of favorable diagenetic facies occur. The Shoreface barrier bars has a high content of quartz and high sorting degree which make it easier for acid fluid to enter commonly occur in S_1k^1, and mainly develop Type V and Type VI diagenetic facies.

The purpose of diagenetic facies evaluation is to predict the range of favorable diagenetic facies distribution. This study evaluates the favorable diagenetic facies in the upper and lower members of Kepingtage Formation, identifies their distribution pattern, and draws a diagenetic facies distribution map (**Figure 9**) based on the lateral distribution pattern of the sedimentary facies in combination with porosity contours.

According to the diagenetic facies map, Type I facies occurs in S_1k^3 extensively. Type II facies occur in the peripheries of the underwater distributary channel and eastern fluvial channel (inferred) where Well SH903H is located. Type III facies

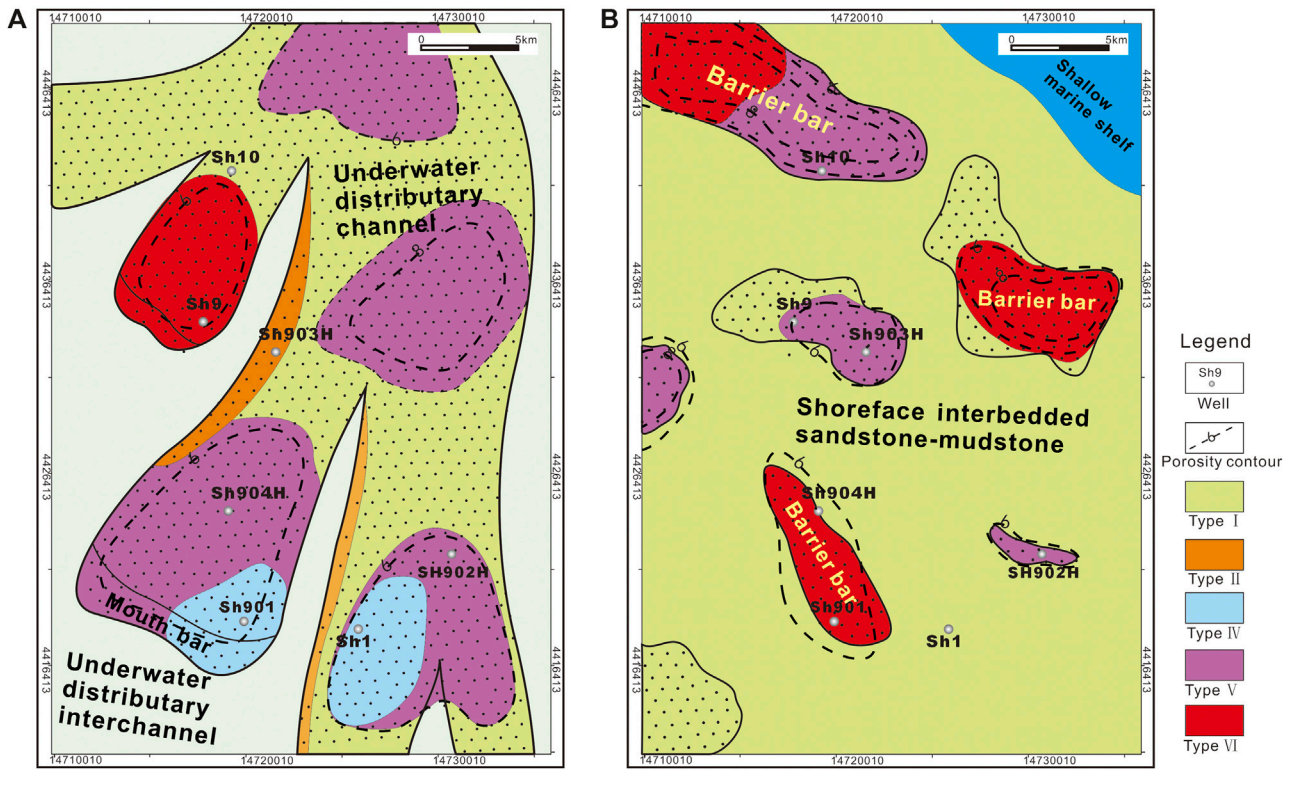

FIGURE 9 | Distribution of diagenetic facies in Kepingtage Formation (a. S_1k^3. **B**. S_1k^1.). (Diagenetic facies boundaries are dotted lines representing the approximate range of distribution, and distribution is based on dominant diagenetic facies in single Well identification and the distribution refers to the sedimentary microfacies. Plane map of sedimentary microfacies are modified after Sun et al., 2013. Porosity contour is mapped according to the plane map of seismic porosity).

typically occurs in Wells SH1 and SH901 area while Type V facies distributes in the area where Wells SH902H and SH904H lie. Porosity distribution shows that the area to the northeast of Well SH903H is the areas with high porosity values, which lie in the fluvial channel fairway. They are supposed to be the Type V facies distribution areas where both primary intergranular pores and secondary dissolved pores develop. Type VI diagenetic facies mainly distributes in the Well SH9 area.

Favorable Type V and Type VI diagenetic facies commonly occur in barrier bar sandbodies within S_1k^1. Type V facies distribute in Wells SH10, SH902H, and SH903H areas. It is inferred that the area of high porosity value to the west of Well SH903H contains Type V facies. Type VI facies dominantly distributes where Wells SH904H and SH901 are located because this area is a fracture-developed belt which is favorable for fluid dissolution. The northwest and east parts of the study area which are also fracture-developed have high porosity values and, therefore, are thought to have Type VI diagenetic facies dominantly. Type I diagenetic facies occurs extensively in the areas with alternating beds of sandstone and mudstone. Analysis of the lateral distribution of diagenetic facies comes to the conclusion that favorable diagenetic facies develop extensively to the east of Well SH903H and to the north of Well SH10, which are supposed to be the targets of future exploration and development.

CONCLUSIONS

(1) The quantitative evaluation of porosity in the Kepingtag Formation diagenetic event supposed that the tightness of sandstone results from compaction, cementation, and hydrocarbon charging (bitumen filling) whereas the improvement of the reservoir properties is controlled by dissolution.

(2) 6 types of diagenetic facies of Kepingtage sandstone are identified based on this study proposes "cause (type and intensity of diagenesis) + effect (influence on the reservoir)" scenario: tight facies from strong compaction (Type I), tight facies from carbonate cementation (Type II), tight facies from bitumen filling (Type III), porosity preservation facies from weak diagenesis (Type IV), porosity enhancement from medium dissolution (Type V), and porosity generation facies from strong dissolution (Type VI), of which Types I, II, and III are unfavorable whereas Types IV, V, and VI are favorable for effective reservoir development.

(3) The results of the quantitative evaluation of diagenetic facies show that the distribution of diagenetic facies is mainly controlled by sedimentary microfacies, and the favorable diagenetic facies are mainly developed in the middle of underwater distribution channel and barrier bar thick sandbodies. Favorable diagenetic facies are best developed in S_1k^1 sandstone, of which Type V and Type VI, occurring primarily in its top, are dominant. The analysis of the lateral distribution of diagenetic facies in combination with the sedimentary facies and porosity concludes that the areas to the east of Well Sh903H and the north of Well SH10 are favorable for the future exploration and development.

(4) A method for the quantitative identification of diagenetic facies was established, and the well logging parameters reflecting the tight sandstone rocks, sedimentary environment, and physical characteristics were selected for setting the similarity with the corresponding sample. The study adopted "KNN" discriminance to identify the vertical diagenetic facies, and the accuracy reached 78.6%. It shows that the logging information of tight sandstone can effectively reflect the lithology and physical property changes of the rock. Therefore, the quantitative identification of diagenetic facies based on logging parameters can provide reasonable results for the evolution of the tight sandstone reservoirs.

DATA AVAILABILITY STATEMENT

The original contributions presented in the study are included in the article/Supplementary Material, further inquiries can be directed to the corresponding author.

AUTHOR CONTRIBUTIONS

All authors listed have made a substantial, direct, and intellectual contribution to the work and approved it for publication.

FUNDING

This study originated from the state key scientific project "Enrichment regularity and exploration direction of clastic rock series of giant-medium oil-gas field in Tarim Basin (No. 2011ZX05002-003) supported by SINOPEC Exploration and Production Research Institute of Northwest Oilfield Branch Company to whom we are very grateful.

REFERENCES

Aysen, O., Cumella, S. P., Milliken, K. L., and Laubach, S. E. (2011). Prediction of lithofacies and reservoir quality using well logs, late cretaceous Williams Fork Formation, Mamm Creek field, Piceance Basin, Colorado. *AAPG (Am. Assoc. Pet. Geol.) Bull.* 95 (10), 1699–1723. doi:10.1306/01191109143

Beard, D. C., and Weyl, P. K. (1973). Influence of texture on porosity and permeability of unconsolidated sand. *AAPG (Am. Assoc. Pet. Geol.) Bull.* 57 (2), 349–369. doi:10.1306/819a4272-16c5-11d7-8645000102c1865d

Cai, Y., Li, Y., Ge, S., Ding, Y., and Xu, W. (2014). Reservoir evaluation of lower member of Kepingtage formation in Shuntuoguole region, Tazhong. *Special Oil Gas Reservoirs.* 21 (4), 39–46 (in Chinese with English Abstract).

Carvalho, A. S. G., Dani, N., De Ros, L. F., and Zambonato, E. E. (2014). The impact of early diagenesis on the reservoir quality of pre-salt (Aptian) sandstones in the Espirito Santo Basin, Eastern Brazil. *J. Petrol. Geol.* 37 (2), 127–141. doi:10.1111/jpg.12574

Cui, Y., Wang, G., Jones, S. J., Zhou, Z., Ran, Y., Lai, J., et al. (2017). Prediction of diagenetic facies using well logs–a case study from the upper Triassic Yanchang Formation, Ordos Basin, China. *Mar. Petrol. Geol.* 81, 50–65. doi:10.1016/j.marpetgeo.2017.01.001

Guo, R., Xie, Q., Qu, X., Chu, M., Li, S., Ma, D., et al. (2019). Fractal characteristics of pore-throat structure and permeability estimation of tight sandstone reservoirs: a case study of Chang 7 of the Upper Triassic Yanchang Formation in Longdong area, Ordos Basin, China. *J. Petrol. Sci. Eng.* 184, 1–14. doi:10.1016/j.petrol.2019.106555

Guo, S., Lyu, X., and Zhang, Y. (2018). Relationship between tight sandstone reservoir formation and hydrocarbon charging: a case study of a Jurassic reservoir in the eastern Kuqa Depression, Tarim Basin, NW China. *J. Nat. Gas Sci. Eng.* 52, 304–316. doi:10.1016/j.jngse.2018.01.031

Hao, G. L., Shan, X. L., Liu, W. Z., and Wang, Q. B. (2010). Quantitative research of diagenesis: its effect on pore evolution of the Fuyu oil reservoir in the north Qijia region. *Min. Sci. Technol.* 20 (5), 770–777. doi:10.1016/s1674-5264(09)60279-9

He, H. J., Bi, J. X., Zeng, D. Q., et al. (2014). Fracture identification in conventional log through KNN classification algorithm based on slope of logging curve: a case study of reef flat facies reservoir in Puguang Gas field. *Sino-Global Energy.* 19 (1), 70–74 (in Chinese with English Abstract).

Jiang, Y. Q., Wang, M., and Diao, Y. X. (2014). Quantitative evaluation and prediction of diagenesis facies with low porosity and permeability sandstone in central Sichuan: a case study of 2nd member of Xujiahe Formation in Suining-Pengxi area. *Chin. Geol.* 41 (2), 437–449 (in Chinese with English Abstract).

Lai, J., Fan, X., Pang, X., Zhang, X., Xiao, C., Zhao, X., et al. (2019). Correlating diagenetic facies with well logs (conventional and image) in sandstones: the Eocene–Oligocene Suweiyi Formation in Dina 2 Gasfield, Kuqa depression of China. *J. Petrol. Sci. Eng.* 174, 617–636. doi:10.1016/j.petrol.2018.11.061

Lai, J., Wang, G., Wang, S., Cao, J., Li, M., Pang, X., et al. (2018). Review of diagenetic facies in tight sandstones: diagenesis, diagenetic minerals, and prediction via well logs. *Earth Sci. Rev.* 185, 234–258. doi:10.1016/j.earscirev.2018.06.009

Lai, J., Wang, G. W., Wang, S. N., et al. (2013). Research status and advances in the diagenetic facies of clastic reservoirs. *Adv. Earth Sci.* 28 (1), 39–50 (in Chinese with English Abstract).

Li, C. S., Yang, H., Liu, J., Rui, Z., Cai, Z., and Zhu, Y. (2012). Distribution and erosion of the Paleozoic tectonic unconformities in the Tarim Basin, Northwest China: significance for the evolution of paleo-uplifts and tectonic geography during deformation. *J. Asian Earth Sci.* 46, 1–19. doi:10.1016/j.jseaes.2011.10.004

Li, M., Guo, Y., Li, Z., and Wang, H. (2020). The diagenetic controls of the reservoir heterogeneity in the tight sand gas reservoirs of the Zizhou Area in China's east Ordos Basin: implications for reservoir quality predictions. *Mar. Petrol. Geol.* 112, 104088. doi:10.1016/j.marpetgeo.2019.104088

Li, Y., Chang, X., Yin, W., Wang, G., Zhang, J., Shi, B., et al. (2019). Quantitative identification of diagenetic facies and controls on reservoir quality for tight sandstones: a case study of the Triassic Chang 9 oil layer, Zhenjing area, Ordos Basin. *Mar. Petrol. Geol.* 102, 680–694. doi:10.1016/j.marpetgeo.2019.01.025

Li, Y. X., Liu, H. J., Yuan, D. S., et al. (2003). Effect of oil charging on resevoir's diagenetic mineral evolution. *Oil Gas Geol.* 24 (3), 274–280 (in Chinese with English Abstract).

Maast, T. E., Jahren, J., and Bjørlykke, K. (2011). Diagenetic controls on reservoir quality in middle to upper Jurassic sandstones in the south Viking Graben, North sea. *AAPG (Am. Assoc. Pet. Geol.) Bull.* 95 (11), 1883–1905. doi:10.1306/03071110122

Meng, Y. L., Wu, L., and Sun, H. B. (2015). Dynamics of diagenesis and prediction of diagenetic facies under abnormally low pressure in the Southern Liaohe West Sag. *Earth Sci. Front.* 22 (1), 206–214 (in Chinese with English Abstract).

Molenaar, N., Cyziene, J., Sliaupa, S., and Craven, J. (2008). Lack of inhibiting effect of oil emplacement on quartz cementation: evidence from Cambrian reservoir sandstones, Paleozoic Baltic Basin. *Geol. Soc. Am. Bull.* 120 (9), 1280–1295. doi:10.1130/b25979.1

Nian, T., Wang, G., Xiao, C., Zhou, L., Sun, Y., and Song, H. (2016). Determination of in-situ stress orientation and subsurface fracture analysis from image-core integration: an example from ultra-deep tight sandstone (BSJQK Formation) in the Kelasu Belt, Tarim Basin. *J. Petrol. Sci. Eng.* 147, 495–503. doi:10.1016/j.petrol.2016.09.020

Ochoa, R. I. (2010). Porosity characterization and diagenetic facies analysis of the Cambrian Mount Simon Sandstone: Implications for a regional carbon dioxide sequestration reservoir. Dissertation. West Lafayette: Purdue University.

Pan, G. F., Liu, Z., Zhao, S., et al. (2011). Quantitative simulation of sandstone porosity evolution: a case from Yanchang Formation of the Zhenjing area, Ordos Basin. *Acta Pet. Sin.* 41 (11), 249–256 (in Chinese with English Abstract).

Paxton, S. T., Szabo, J. O., Ajdukiewicz, J. M., et al. (2002). Construction of an intergranular volume compaction curve for evaluating and predicting compaction and porosity loss in rigid-grain sandstone reservoirs. *AAPG (Am. Assoc. Pet. Geol.) Bull.* 86 (12), 2047–2067.

Peng, J., Han, H., Xia, Q., and Li, B. (2018). Fractal characterization and genetic mechanism of micro-pore structure in deeply buried tight sandstone reservoirs: a case study of Kalpintag Formation in Shuntuoguole area, Tarim Basin. *Acta Pet. Sin.* 39 (07), 775–791 (in Chinese).

Qiao, J., Zeng, J., Jiang, S., and Wang, Y. (2020). Impacts of sedimentology and diagenesis on pore structure and reservoir quality in tight oil sandstone reservoirs: Implications for macroscopic and microscopic heterogeneities. *Mar. Petrol. Geol.* 111, 279–300. doi:10.1016/j.marpetgeo.2019.08.008

Qin, R., Pan, H., Zhao, P., Deng, C., Peng, L., Liu, Y., et al. (2018). Petrophysical parameters prediction and uncertainty analysis in tight sandstone reservoirs using Bayesian inversion method. *J. Nat. Gas Sci. Eng.* 55, 431–443. doi:10.1016/j.jngse.2018.04.031

Ren, D., Zhou, D., Liu, D., Dong, F., Ma, S., and Huang, H. (2019). Formation mechanism of the upper triassic Yanchang formation tight sandstone reservoir in Ordos Basin—take Chang 6 reservoir in Jiyuan oil field as an example. *J. Petrol. Sci. Eng.* 178, 497–505. doi:10.1016/j.petrol.2019.03.021

Sun, N. Q., Yun, L., Pu, R. H., et al. (2013). The microfacies and reservoir distribution of the lower member of Kepingtage Formation in Shun 9 well area in Tarim Basin. *J. Jilin Univ. (Earth Sci. Ed.).* 43 (6), 1716–1725 (in Chinese with English Abstract).

Wang, Q., Huang, H., Chen, H., and Zhao, Y. (2020). Secondary alteration of ancient Shuntuoguole oil reservoirs, Tarim Basin, NW China. *Mar. Petrol. Geol.* 111, 202–218. doi:10.1016/j.marpetgeo.2019.08.013

Xi, K., Cao, Y., Liu, K., Jahren, J., Zhu, R., Yuan, G., et al. (2019). Authigenic minerals related to wettability and their impacts on oil accumulation in tight sandstone reservoirs: an example from the Lower Cretaceous Quantou Formation in the southern Songliao Basin, China. *J. Asian Earth Sci.* 178, 173–192. doi:10.1016/j.jseaes.2018.04.025

Xiao, Z, Ding, W, Hao, S, Taleghani, A D, Wang, X, Zhou, X, et al. (2019). Quantitative analysis of tight sandstone reservoir heterogeneity based on rescaled range analysis and empirical mode decomposition: a case study of the Chang 7 reservoir in the Dingbian oilfield. *J. Petrol. Sci. Eng.* 182, 106326. doi:10.1016/j.petrol.2019.106326

Xiong, W. L., Chen, H. H., Yun, L., et al. (2013). Hydrocarbon charging history for Silurian reservoirs of Shuntuoguole block in the north slope of Tazhong uplift, Tarim Basin: constraints from fluid inclusion of Well Shun9. *Acta Pet. Sin.* 34 (2), 239–246 (in Chinese with English Abstract).

Yin, S., Ding, W, Zhou, W, Shan, Y, Xie, R, Guo, C, et al. (2017). *In situ* stress field evaluation of deep marine tight sandstone oil reservoir: a case study of Silurian strata in northern Tazhong area, Tarim Basin, NW China. *Mar. Petrol. Geol.* 80, 49–69. doi:10.1016/j.marpetgeo.2016.11.021

Yuan, G. H., Cao, Y. C., Jia, Z. Z., et al. (2015). Research progress on anomalously high porosity zones in deeply buried clastic reservoirs in petroliferous basin. *Nat. Gas Geosci.* 26 (1), 28–42 (in Chinese with English Abstract).

Zaid, S. M. (2013). Provenance, diagenesis, tectonic setting and reservoir quality of the sandstones of the Kareem Formation, Gulf of Suez, Egypt. *J. Afr. Earth Sci.* 85 (2), 31–52. doi:10.1016/j.jafrearsci.2013.04.010

Zeng, Q., Zhang, X., Zhang, R., Zhao, J., Hou, G., and Ji, Y. (2018). Characteristics of tidal action sedimentary system and distribution of favorable sand bodies of Silurian in Tazhong area, Tarim basin, NW China. *Quat. Int.* 468, 62–71. doi:10.1016/j.quaint.2017.02.016

Zhang, X. X., Zou, C. N., Zhu, R. K., et al. (2011). Reservoir diagenetic facies of the upper triassic Xujiahe Formation in the central Sichuan Basin. *Acta Pet. Sin.* 32 (2), 257–264 (in Chinese with English Abstract).

Zhao, C. L., and Zhu, X. M. (2006). *Sedimentary petrology*. 3rd Edition. Beijing: Petroleum Industry Press (in Chinese).

Zhao, S., Zhang, S, and Wan, Y (2015). Feldspar dissolution and its effect on reservoir in Kepingtage Formation, Shuntuoguole low uplift, central Trim Basin. *Petrol. Geol. Exp.* 37 (03), 293–299 (in Chinese).

Zhou, H. Y., Hu, J. Y., Zheng, J. Z., et al. (2008). Diagenesis and pore evolution of reservoirs in south Turgai Basin. *Acta Petrol. Mineral.* 27 (6), 547–558 (in Chinese with English Abstract).

Zhou, X., Zhang, C., Zhang, Z., Zhang, R., Zhu, L., and Zhang, C. (2019). A saturation evaluation method in tight gas sandstones based on diagenetic facies. *Mar. Petrol. Geol.* 107, 310–325. doi:10.1016/j.marpetgeo.2019.05.022

Zhu, P., Dong, Y., Chen, M., Li, Z., Han, B., Wang, J., et al. (2020). Quantitative evaluation of pore structure from mineralogical and diagenetic information extracted from well logs in tight sandstone reservoirs. *J. Nat. Gas Sci. Eng.* 80, 103376. doi:10.1016/j.jngse.2020.103376

Zhu, R., Wu, S., Su, L., Cui, J., Mao, Z., and Zhang, X. (2016). Problems and future works of porous texture characterization of tight reservoirs in China. *Acta Pet. Sin.* 37 (11), 1323–1336 (in Chinese).

Zou, C. N., Tao, S. Z., Zhou, H., Zhang, X. X., He, D. B., Zhou, C. M., et al. (2008). Genesis classification and evaluation method of diagenetic facies. *Petrol. Explor. Dev.* 35 (5), 526–540. doi:10.1016/s1876-3804(09)60086-0

Conflict of Interest: Author ZH was employed by PetroChina Zhejiang Oilfield Company.

The remaining authors declare that the research was conducted in the absence of any commercial or financial relationships that could be construed as a potential conflict of interest.

frontiers in Earth Science

ORIGINAL RESEARCH
published: 24 February 2021
doi: 10.3389/feart.2021.606701

Sedimentological Influence on Physical Properties of a Tight Sandstone Reservoir: The Cretaceous Nenjiang Formation, Southern Songliao Basin, Northeast China

Jinkai Wang[1,2], Jialin Fu[1], Jieming Wang[3], Kai Zhao[3], Jinliang Zhang[4] and Jifu Liu[4]*

[1]College of Earth Science and Engineering, Shandong University of Science and Technology, Qingdao, China, [2]Laboratory for Marine Mineral Resources, Qingdao National Laboratory for Marine Science and Technology, Qingdao, China, [3]Research Institute of Petroleum Exploration and Development, Beijing, China, [4]College of Resources Science and Technology, Beijing Normal University, Beijing, China

OPEN ACCESS

Edited by:
Jon Jincai Zhang,
Sinopec Tech Houston Center (STHC), United States

Reviewed by:
Chao Liang,
China University of Petroleum (Huadong), China
Deyong Li,
Ocean University of China, China
David Mark Hodgson,
University of Leeds, United Kingdom

****Correspondence:***
Jinkai Wang
wangjk@sdust.edu.cn

Specialty section:
This article was submitted to Sedimentology, Stratigraphy and Diagenesis, a section of the journal Frontiers in Earth Science

Received: *15 September 2020*
Accepted: *06 January 2021*
Published: *24 February 2021*

Citation:
Wang J, Fu J, Wang J, Zhao K, Zhang J and Liu J (2021) Sedimentological Influence on Physical Properties of a Tight Sandstone Reservoir: The Cretaceous Nenjiang Formation, Southern Songliao Basin, Northeast China. Front. Earth Sci. 9:606701. doi: 10.3389/feart.2021.606701

Abstract: The Nenjiang Formation, south of Songliao Basin, has many hydrocarbon bearing units, but currently the understanding of the distribution of viable reservoir sandstones is too limited to support a development strategy. Therefore, a detailed study on the sedimentary microfacies and reservoir properties has been completed in order to reduce uncertainty and improve subsurface predictions. Nine lithofacies and five lithofacies associations were identified supporting the development of a sedimentary model of a river-dominated delta front setting, which could be divided into four sedimentary environments: subaqueous distributary channel-fill, mouth bar, sand sheet, and interdistributary bay. The distribution sandbodies extend to the south in a tongue-like form, and they thin and pinch out. Finally, the influence of sedimentary process on properties was assessed by establishing the correlation between microfacies and reservoir physical parameters, such as porosity, permeability, pore radius, throat radius, and clay minerals. It is revealed that the correspondence between reservoir physical properties and microfacies types is strong; the physical properties of the subaqueous distributary channel and mouth bar are the best.

Keywords: southern Songliao basin, sedimentary characteristics, diagenesis, rock facies, lithofacies

INTRODUCTION

Lithofacies are identified by mineral composition, structure, color, and sedimentary structure of rocks, which is directly related to the sedimentary environment and facies of silicic clastic rocks. Early lithofacies type analysis and application were based on fluvial facies sandbodies (Miall, 1985). The changes of lithofacies characteristics reflect the changes of various conditions during the formation of sandbodies of different scales, such as hydrodynamic conditions, sediment transport mode, and the degree of external interference (Qi et al., 2009; Wu D. et al., 2019). The combination of these single lithofacies forms lithofacies associations, which is the result of multistage sedimentation and superposition (Eyles et al., 2010; Ding et al., 2014). Lithofacies associations and the arrangement of architectural elements can be used to interpret the climatic and environmental conditions during deposition and the paleohydrodynamic conditions (Jin et al., 2019).

According to the literature, many researchers have carried out conventional, but not detailed, sedimentary facies research in the Songliao Basin. These studies were usually at a large scale and the fourth member of the Cretaceous Nenjiang Formation was presumed to be a single prograding sequence (Liu et al., 1993; Sun et al., 2006). Most authors interpreted that tectonic movement controls the sedimentary facies types in the southern Songliao Basin (Li et al., 2009; Huang et al., 2013; Wang J. et al., 2014); the sedimentary facies types of the Nenjiang Formation in the Songliao Basin are gravity flows, alluvial fans, deltas, and rivers (Zhang et al., 2014; Li et al., 2015; Lv et al., 2016; Wang D.-d. et al., 2016). In this sedimentary period, there are two main river deltas, one comes from the northeast, which plays an important role in the sedimentary process of the first member of the Nenjiang Formation, the other comes from the east (Liu et al., 2016; Wang W. et al., 2016). Other interpret that the Nenjiang Formation in the Songliao Basin is a mud-prone delta with poor continuity, which has minor sand components and a lower angle, compared with the traditional delta. In addition to delta sedimentary environments, other sedimentary environments of the Nenjiang Formation include deep and shallow lakes (Gao and Wang, 2010; Wang L. et al., 2014) and even deep-water turbidite fans (Pan et al., 2017; Wang et al., 2018). Recently, some researchers established a new ultrafine-grained sedimentary model in the Songliao Basin: the channel fan, which includes straight and sinuous channels extending from north to south. This system is dominated by fine sediment and contains a large amount of sandstone, fluvial sedimentary structure, and internal erosion surfaces. In addition, the system also contains abundant terrestrial organic debris, showing bedload and suspended load transport (Tong et al., 2018; Mo et al., 2019). A series of diagenetic processes will occur after sediment deposition, which will directly affect the size and sorting of reservoir pores (Guo and Mao, 2019). Compaction and cementation greatly reduce the porosity of the reservoir, and at the same time the pore throats are blocked and the rock permeability is also greatly reduced, which is the main factor behind the formation of tight reservoir (Shi et al., 2015; Yang et al., 2017). However, in the middle and late diagenesis, some organic acid solutions will dissolve mineral particles and cements in pores, thus expanding the pores of rocks and improving its permeability. The main minerals of dissolution are potash feldspar and calcite (Wang et al., 2020). However, the location and degree of dissolution are quite different, which will lead to a different degree of dissolution of rock particles and cements, resulting in less strength in the correlation between porosity and permeability, and being prone to high porosity, low permeability, or high permeability and low porosity (Wang et al., 2018).

Many research results have made the structural evolution characteristics and sedimentary environment of Changling fault depression in the south of Songliao Basin clear, which provide a wealth of sources for this study (Meng et al., 2016; Xu et al., 2019; Cai et al., 2020). However, the characterization of sedimentary facies and evaluation of the fourth member of Nenjiang Formation in the south of Songliao Basin are not sufficient and need detailed research (Li et al., 2017; Zhang and Wang, 2019). Here, we refine the characterization of microfacies in the areas with high well density to establish corresponding lithofacies models (either single or composite lithofacies model) and investigate the influence of sedimentation and diagenesis on reservoir physical properties. Through the study of fine reservoir description, we establish a new integrated sedimentary model and lithofacies model, discuss the factors controlling the sandstone physical properties, and play a positive guiding role in the effective development of this reservoir.

GEOLOGICAL SETTING

General Situation of the Study Area

Songliao Basin is the largest inland sedimentary basin fill of Mesozoic Cenozoic in eastern China, which is divided into two parts, the south and the north, with Songhua River as the boundary. The southern Songliao Basin comprises four first-order structural units: western slope, central depression, southeast uplift, and southwest uplift, among which the central depression and southeast uplift are important geological units for hydrocarbon exploration (**Figures 1A,B**) (Li et al., 2007; Zhang and Huang, 2010). The study area (H168 block) is located in Qian'an County, in Songyuan City of the Jilin province northeast of China, and its regional tectonic location is in the south of the Changling depression of the southern Songliao Basin. The structural characteristics of the Changling sag are relatively gentle. Its tectonic evolution has gone through three stages: early fault subsidence, middle subsidence, and tectonic quiescence. It mainly includes the Qian'an subsag and Heidimiao subsag, and the Hei168 block is located in the Heidimiao subsag, its east part is Huazijing terrace, and its northwest part is Daan-Honggang terrace. At present, 122 horizontal wells have been drilled and 117 wells have been put into production in the study area, which is a typical thin-layer reservoir developed by horizontal wells (**Figures 1C,D**).

Stratigraphic and Tectonic Evolution in the Study Area

Overall, the Songliao Basin experienced warm, humid climate during the Cretaceous period (Liu et al., 2003). The tectonic process includes three stages: early fault depression, middle depression, and late shrinkage. During the basin expansion stage (the early fault depression and middle depression stages), the Denglouku Formation, Quantou Formation, Qingshankou Formation, and Yaojia Formation were successively deposited in the study area. In the low subsidence stage (the late shrinkage stage) of the basin evolution, deltaic and lacustrine strata are Nenjiang Formation (**Figure 2A**), Sifangtai Formation, and Mingshui Formation. The Yanshan V episode tectonic movement in the late Mingshui Formation resulted in strong inversion and uplift, forming the present structural form. The period of the Nenjiang Formation is the last stage (Li et al., 2018). The Nenjiang Formation comprises a large delta that built out into a lacustrine water body during the second flooding period

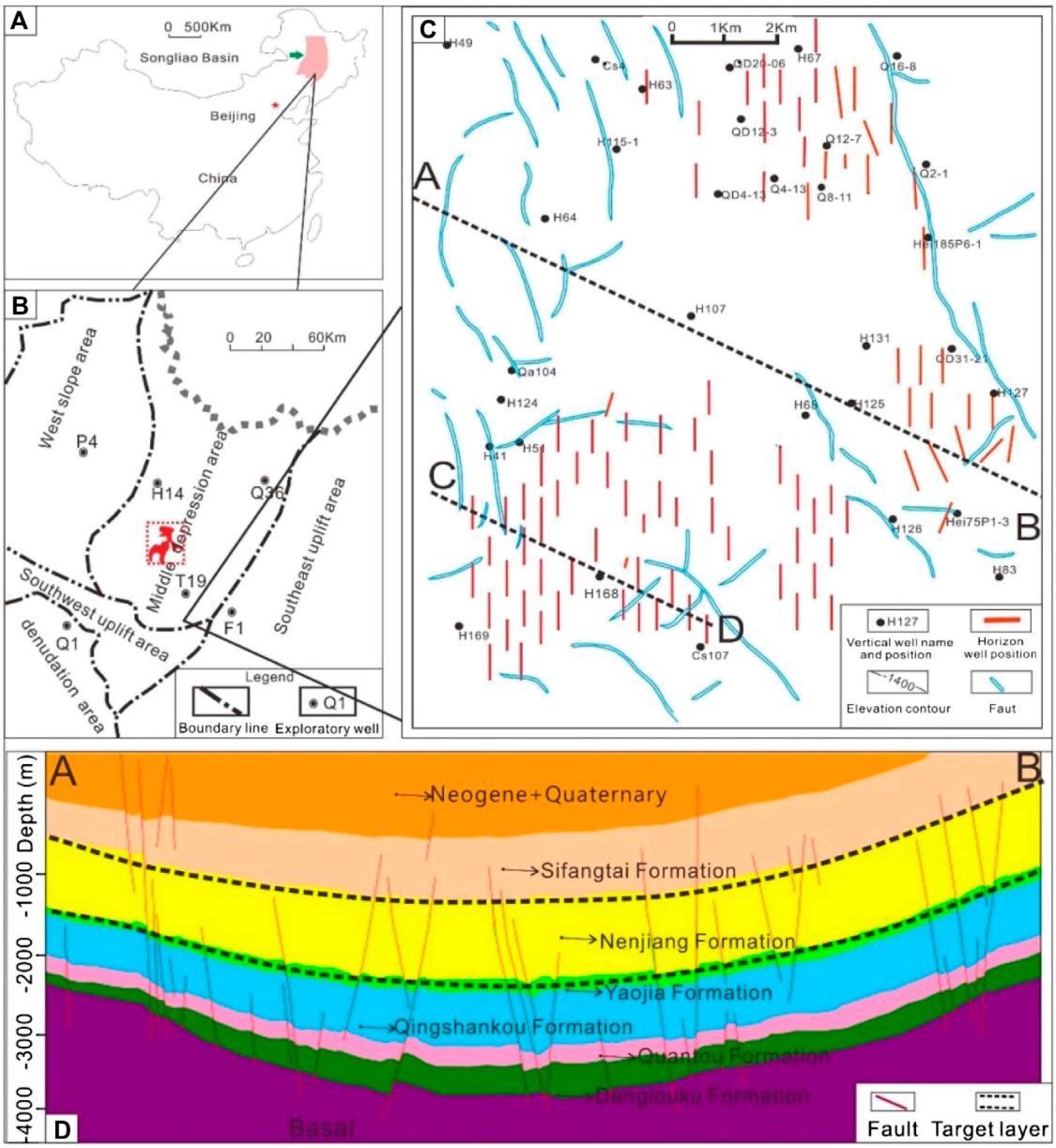

FIGURE 1 | Location map of the study area. **(A)** Location of Songlike Basin; **(B)** location of Changling Depression in southern Songlike basin; **(C)** location and well location map of the study area; **(D)** stratigraphic profile of the study area.

(Feng and Zhang, 2012; Huang et al., 2013). The relative lake level decreased continuously during the Nenjiang Formation period except for a short rise in the middle of the fourth member, and the main sedimentary types are semideep lake, delta, and shallow lake (**Figure 2B**).

METHODOLOGY

In this study, we obtained 35 rock samples of 4 cored wells (HN-20-1, HH75-X-4, QE37-14, and HF-5-2) at different depths. Using these rock samples, a large number of micro characterization experiments have been carried out by means of optical or electronic microscope, such as thin section analysis, scanning electron microscope, and X-ray diffraction analysis experiment. On the basis of these experimental results, the micro components, pore structure, and diagenesis of reservoir sandstone have been characterized in detail, and the single and combined lithofacies models are established. Then, the characteristics of rock lithology, sandstone type, grain size, and sorting are studied in detail, the plan form and vertical distribution of microfacies are characterized, and the

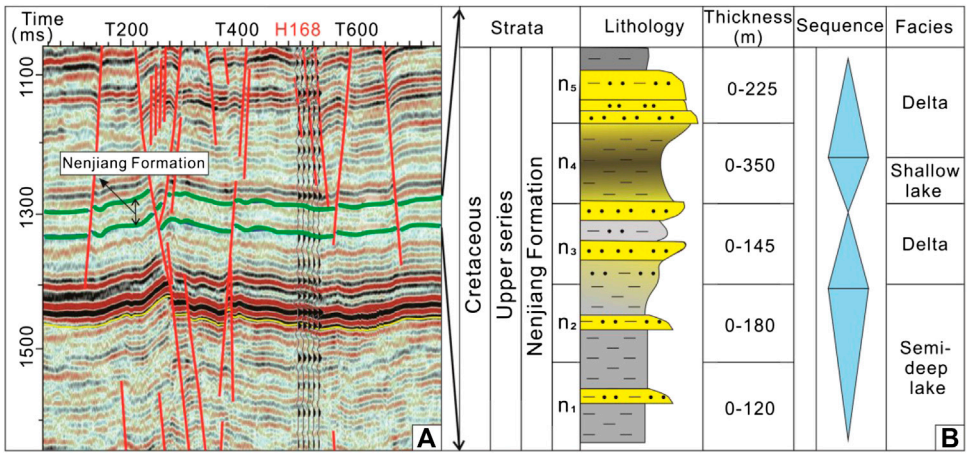

FIGURE 2 | Formation evolution information: **(A)** seismic interpretation profile and **(B)** lithologic profile.

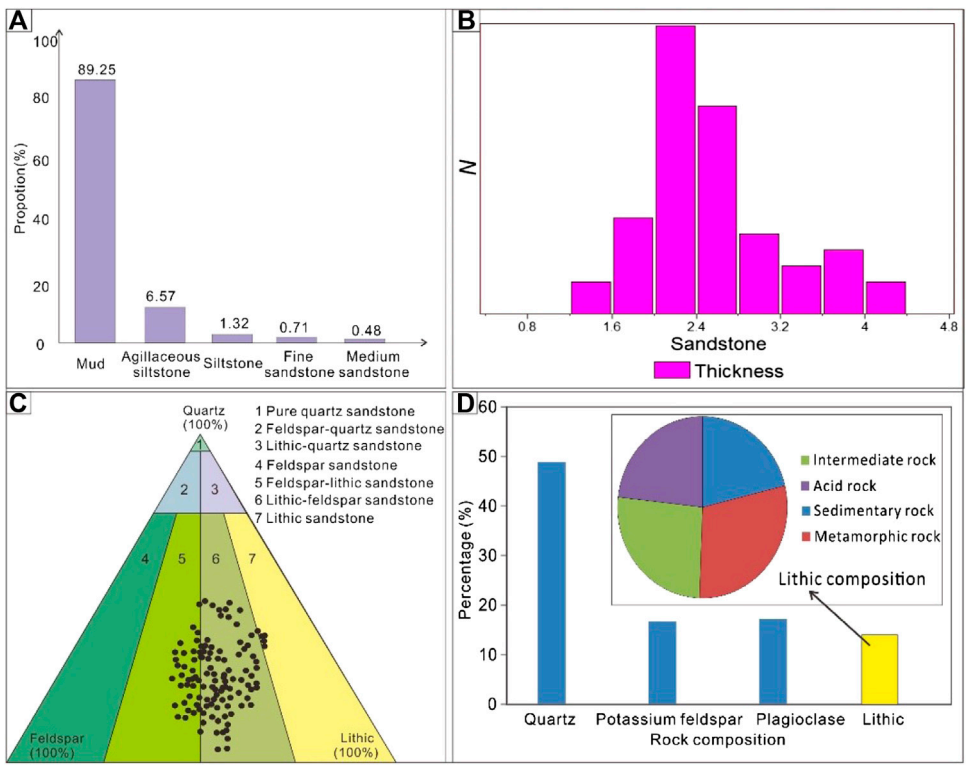

FIGURE 3 | Rock types, thickness, and major compositions: **(A)** lithology statistical chart; **(B)** sandstone thickness statistics; **(C)** lithologic classification of sandstone; **(D)** sandstone components and its lithic types.

sedimentary model is established. Finally, the sandstone diagenesis in the study area is characterized by using the micro pore structure experimental parameters, and the variation law of reservoir pore and throat, as well as their internal filler type, is clarified.

SEDIMENTARY CHARACTERISTICS

Lithologic Characteristics

The lithology of the fourth member of the Nenjiang Formation is mainly mudstone, whose content is as high as 90% (**Figure 3A**).

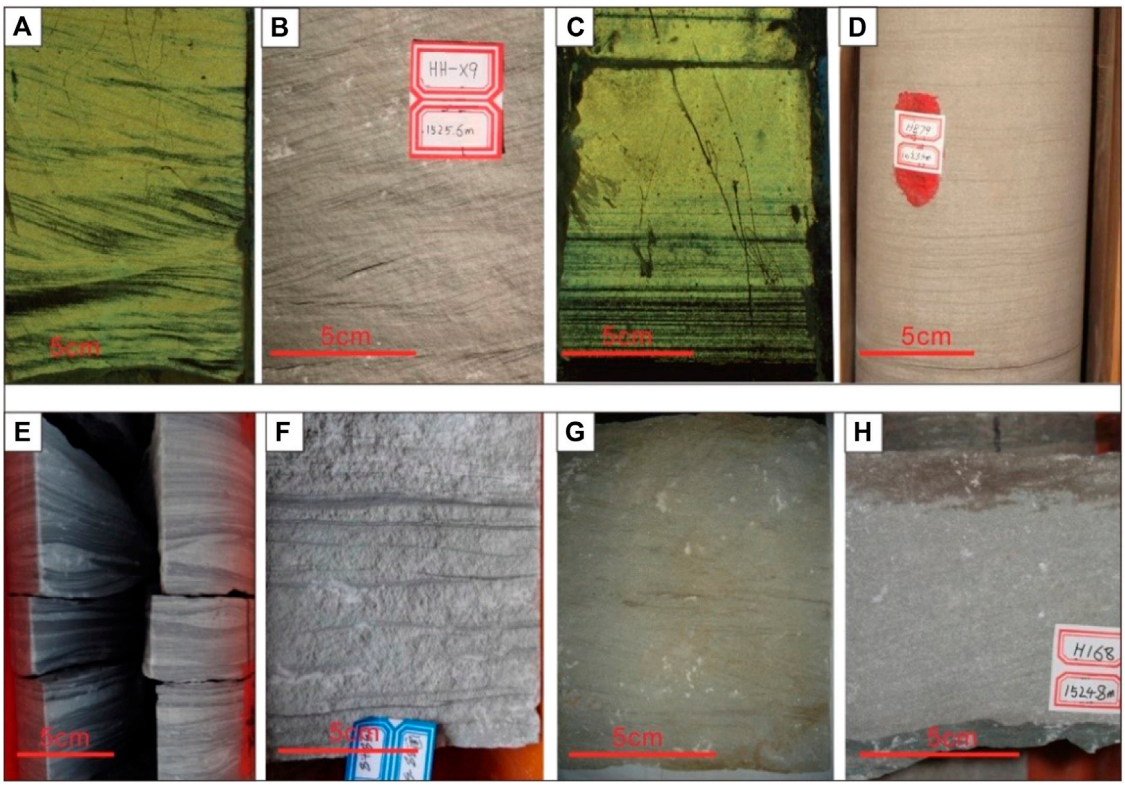

FIGURE 4 | Sedimentary structure of the study area: **(A)** HH75-X-4, 1446.5m, ripple cross lamination; **(B)** HH-9X, 1525.6m, ripple cross lamination; **(C)** HH75-X-4, 1456.8m, parallel bedding; **(D)** HH79, 1523.5m, parallel bedding; **(E)** HH-X9, 1520.4m, wavy bedding; **(F)** HE-88–2, 1584.8m, flaser bedding; **G**: QE37–14, 1505.3m, trough cross bedding; **(H)** H168, 1524.8m, cross bedding.

The lithology of sandstone is mainly gray medium- and fine-grained sandstone, siltstone, and argillaceous siltstone, showing normal and inverse grading. The thickness range of a single sand body is 1–5 m, with an average of 2.2 m (**Figure 3B**). According to Folk's three terminal sandstone classification method (Folk, 1968), the relative content of quartz, feldspar, and rock debris shows that the main types of sandstone are lithic feldspar sandstone (**Figure 3C**), of which the average content of quartz is 32%; feldspar content is 31% (potash feldspar), and lithics is 37%, which includes igneous rocks, metamorphic rocks, and mica debris. All these suggest that the sediment source area is far away from the provenance area and belongs to the terminal position of the river (Wu J. et al., 2019), and the source area lithology is complex, mainly metamorphic rock and intermediate magmatic rock (**Figure 3D**).

Sedimentary Structure

Through core observation, it can be found that the sedimentary structures shown in the rocks in the study area mainly include cross bedding, parallel bedding, wavy bedding, and sand ripple bedding, which are consistent with an interpretation of the sedimentary environment of river-dominated delta front (**Figure 4**).

The sedimentary structures show weak hydrodynamic characteristics. The strong scour structures at the bottom of the subaqueous distributary channel are rare; therefore, the trough cross bedding in the core is not obvious. The main sedimentary structure includes planer cross bedding, parallel bedding, ripple lamination, and other sedimentary structures. The single sand body of the mouth bar is relatively thick, mainly composed of fine sand and silty sand; the sedimentary structures include current sand ripple bedding, parallel bedding, low angle cross bedding, and wave formed sand ripple bedding. The sand sheet is well sorted and is mostly fine sandstone and siltstone. There is no large-scale cross bedding. Parallel bedding and low angle cross bedding are mainly developed. There are also sand ripple bedding and wavy bedding. The biogenetic structure is not developed.

The grain size parameters of sandstone in the study area were obtained by using the casting slice observation method. The grain size of the reservoir rock in the study area is generally small, and the cumulative curve of grain size probability is mostly two-stage (composed of jump population and suspension population). The particle size of the sediment is small, but the distribution range is large. The cut-off point between the saltating population and the suspended population is between 2.5Φ and 4.0Φ. The suspended population content is mostly between 10 and 40%, and the jumping population content is generally more than 60% (**Figures 5A–C**). In the C-M diagram, the sample points are concentrated in the QR segment and a few in the RS segment. The QR segment is parallel to the baseline of C = M, which represents

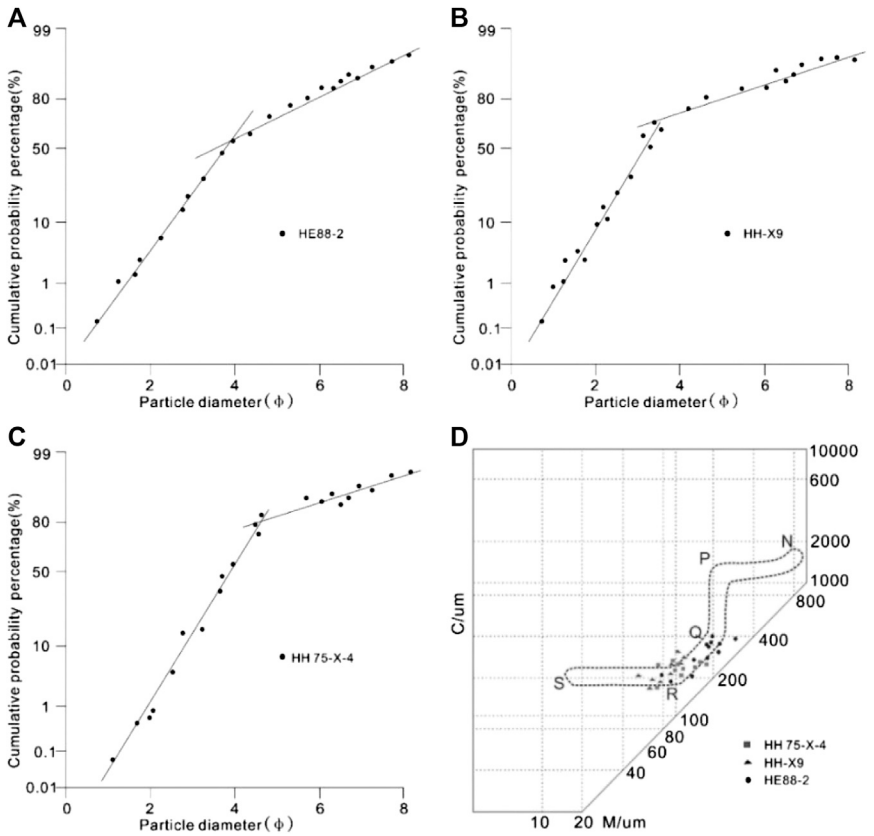

FIGURE 5 | Grain size cumulative probability curve and C-M diagram of sandstone: **(A–C)** cumulative curve of grain size probability and **(D)** the C-M diagram of different samples of three core wells.

the deposition mechanism of gradual suspension. In the fluid, the particle size of suspended materials gradually becomes finer from the base to the top, which is often caused by the development of turbulence, and its C and M increase in proportion. RS section is a uniform suspension, which is a complete suspension with no change of particle size and density with depth, reflecting a weak and calm sedimentary environment (**Figures 5D**).

Lithofacies Characteristics

The grain size range of sediments is relatively small, the types of sedimentary rocks are relatively unified, and the sedimentary sequences formed are relatively similar. It is difficult to distinguish their microfacies types from rock types alone and to understand the relationship between different microfacies types. Therefore, this study identifies sedimentary microfacies based on the combination of lithofacies characteristics. On the basis of identified lithofacies types, a model of single lithofacies and composite lithofacies is established.

(1) Single Lithofacies

Nine lithofacies types were identified in the delta facies according to the characteristics of rock fabric, bedding, and grain order of the study area (Cheng et al., 2017; Kallepalli and Richardson, 2017); the morphology and characteristics of each lithofacies are shown in **Figure 6**.

These lithofacies include (1) the massive fine sandstone facies (FIM), which was formed under rapid deposition; (2) trough cross bedding sandstone facies (FIT), which was formed by migration of 3D dune-scale bedforms at the base of subaqueous distributary channel; (3) oblique bedding fine sandstone facies (FIO), which was usually formed in the deposition environment of mouth bar or sand sheet; (4) low-angle cross-bedding fine sandstone facies (FIL), which was usually formed by deposition in subaqueous distributary channels with weak current action; (5) inverse graded sandstone facies (SI), which was usually formed by waxing hyperpycnal flows that deposit on the mouth bar; (6) ripple cross lamination fine sandstone facies (PR), which was formed in a relatively quiet water environment and mainly composed of argillaceous siltstone; (7) ripple cross lamination and lenticular bedding siltstone facies (SiC), which was usually formed by the interdistributary bay setting; (8) ripple cross lamination siltstone facies (SiR), which was formed in the front of the river controlled delta with weak hydrodynamic force (Gugliotta et al., 2015; Xu et al., 2020); and (9) the horizontal bedding mudstone facies (MH), which was formed by suspension deposition in the interdistributary bay-fill.

Lithofacies symbol		Lithofacies model	Sedimentary structure	Corresponding core		Sedimentary facies of cored section
				Photo	well & MD	
FIM	Fine sand facies		Massive bedding		HB56 1408.6m	Subaqueous distributary channel
FIT	Fine sand facies		Trough cross-bedding		HH9 1522.4m	Subaqueous distributary channel
FIO	Fine sand facies		Oblique bedding		HB79 1527.1m	Mouth bar
FIL	Fine sand facies		Oblique bedding		HB79 1526.2m	Sand sheet
SI	Inverse grading sand facies		Graded bedding		HB168 1556.7m	Mouth bar
PR	Argillaceous siltstone facies		Ripple bedding		HH9 1524.7m	Inter distributary bay-fill
SiC	Siltstone facies		Ripple bedding Lenticular bedding		HB79 1521.2m	Inter distributary bay-fill Sand sheet
SiR	Siltstone facies		Ripple bedding		HB88-2 1584.8m	Inter-distributary bay-fill Sand sheet
MH	Mudstone facies withthin thin silt layer		Horizontal bedding		HB178 1654.6m	Inter-distributary bay-fill

FIGURE 6 | Nine single lithofacies types and their corresponding relations with sedimentary structures and facies.

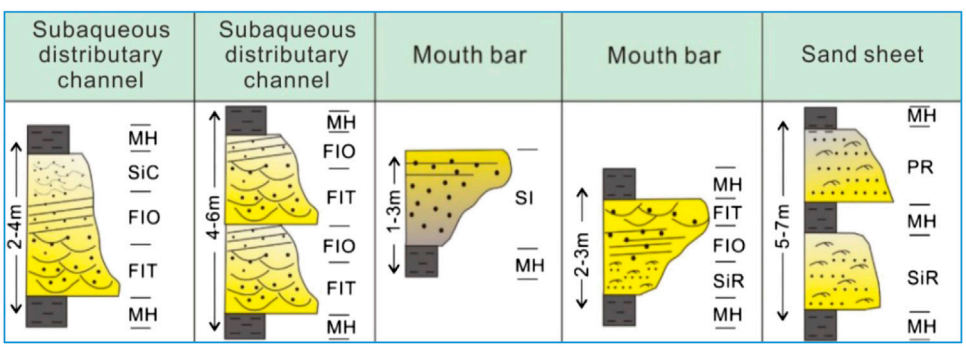

FIGURE 7 | Five combined lithofacies types of delta front facies in the study area (different single lithofacies are superimposed vertically according to certain rules).

TABLE 1 | Corresponding relationship between sedimentary microfacies and logging curves.

Microfacies types	Logging response characteristics	Logging curve shape SP GR	Well name	Sand body shape	Lithologic characteristics
Subaqueous distributary channel	Smooth box or bell-shaped characteristics	fx1	Hb178	Fx10	Fine sandstone equal grain size good properties
	Dentate box or bell-shaped characteristics	fx2	QD20-06	fx11	Fine sandstone muddy strips in the middle
	Low amplitude bell-shaped characteristics	fx3	Q4-13	fx12	Siltstone with higher clay content
Mouth bar	Smooth funnel-shaped characteristics	fx4	H115-1	fx13	Fine sandstone and siltstone good properties
	Medium or small funnel-shaped characteristics	fx5	QD31-21	fx14	Siltstone and argillaceous siltstone
Sand sheet	Medium or big finger-shaped characteristics	fx6	H83	fx15	Siltstone thin sand body
	Medium finger-shaped characteristics	fx7	H64	fx16	Siltstone and argillaceous siltstone thin sand body
Interdistributary bay-fill	Small finger-shaped characteristics	fx8	Q16-8	fx17	Argillaceous siltstone and silty mudstone
	Unobvious low-amplitude protrusion	fx9	HH79-8	fx18	Silty mudstone

(2) Lithofacies Combinations

Lithofacies were combined to form five lithofacies association identified according to observation and description of core. These are (1) MH-SiC-TIO-FIT–MH; (2) MH-FIO-FIT-FIO-FIT-MH; (3) SI-MH; (4) MH-FIT-FIO-SiC-MH; and (5) MH-PR-MH-SiC-MH. These lithofacies combination types coincide with sedimentary environments (**Figure 7**). The MH-SiC-TIO-FIT-MH type represents the single distributary channel deposition model, the MH-FIO-FIT-FIO-FIT-MH type is the main combination of lithofacies which is usually related to the vertical superposition of multiple channels, the SI-MH type and the MH-FIT-FIO-SiC-MH type are interpreted to represent mouth bar, and the MH-PR-MH-SiR-MH is related to splay in interdistributary bay-fills.

Sedimentary Facies and Microfacies Characteristics

Based on the analysis of lithological characteristics, sedimentary structure, and other sedimentary facies markers, combined with the sedimentary background and environment of the fourth member of the Nenjiang Formation of the Songliao Basin, the types of sedimentary facies are determined as a transgressive delta. By analyzing the lithology, rock color, lithofacies type, and other facies indicators, it can be concluded that the study area is located in the delta front. The delta front can be divided into four different parts in the study area: subaqueous distributary channel-fill, mouth bar, sand sheet, and interdistributary bay-fill. The log response characteristics, curve shape, sand body shape, and lithology of each sedimentary microfacies sand body are very different, which are their main distinguishing features (**Table 1**).

(1) Subaqueous Distributary Channel-Fill

The distributary channel is the subaqueous extension part of the onshore branch channel. In the process of extension, the channel widens, and the bifurcation increases, the flow velocity decreases, and the deposition rate increases. The lithology is mainly grayish white fine to medium sandstone, with trough cross bedding, parallel bedding, and small trough cross bedding which can be seen from the bottom to the top; SP log curve is box shaped; sand body vertically presents a positive rhythm of coarse and fine from the bottom to the top. The subaqueous distributary channel-fill thickness in the study area is generally 2–4 m. The base of these sand bodies is an erosional overlain by trough cross bedding and muddy gravel. The middle is oblique bedded sandstone and the upper is laminated sandstone. The top is sand ripple bedding with an increased mud content (**Figure 8A**).

(2) Mouth Bar

The mouth bar formed after the branch channel entered the lake where the distributive channel bifurcates. Most of the mouth bar in the study area coarsens upward, increasing sand content and better sorting. SP log curve of the mouth bar sand body is funnel-shaped with abrupt change at the top and gradual change at the base. The mouth bar of the study area is mainly composed of fine sand and silty sandstone; its thickness is generally more than 2.5 m. The base of the sand body has more gradual contact with the underlying rock layer and the top contact is abrupt with the overlying mudstone layer. The bedding structures include small cross bedding, parallel bedding, and low angle oblique bedding (**Figure 8B**).

(3) Sand Sheet

The sand sheet is distributed in the front and flank of the mouth bar. It is characterized by a wide distribution area, but the particle size becomes smaller and the sandbodies become thinner. It is mostly distributed in the front of the delta front, where the hydrodynamic conditions are weak. The shape of SP log curve is usually finger- and cone-like, and the amplitude is generally high and medium. The sand sheet sandstone is well sorted; its lithology is mostly argillaceous siltstone and siltstone, with a thickness of 1–2 m. Small cross bedding, parallel bedding, and flow sand ripple bedding are usually found in the sand sheet, in addition to some biogenic structures (**Figure 8C**).

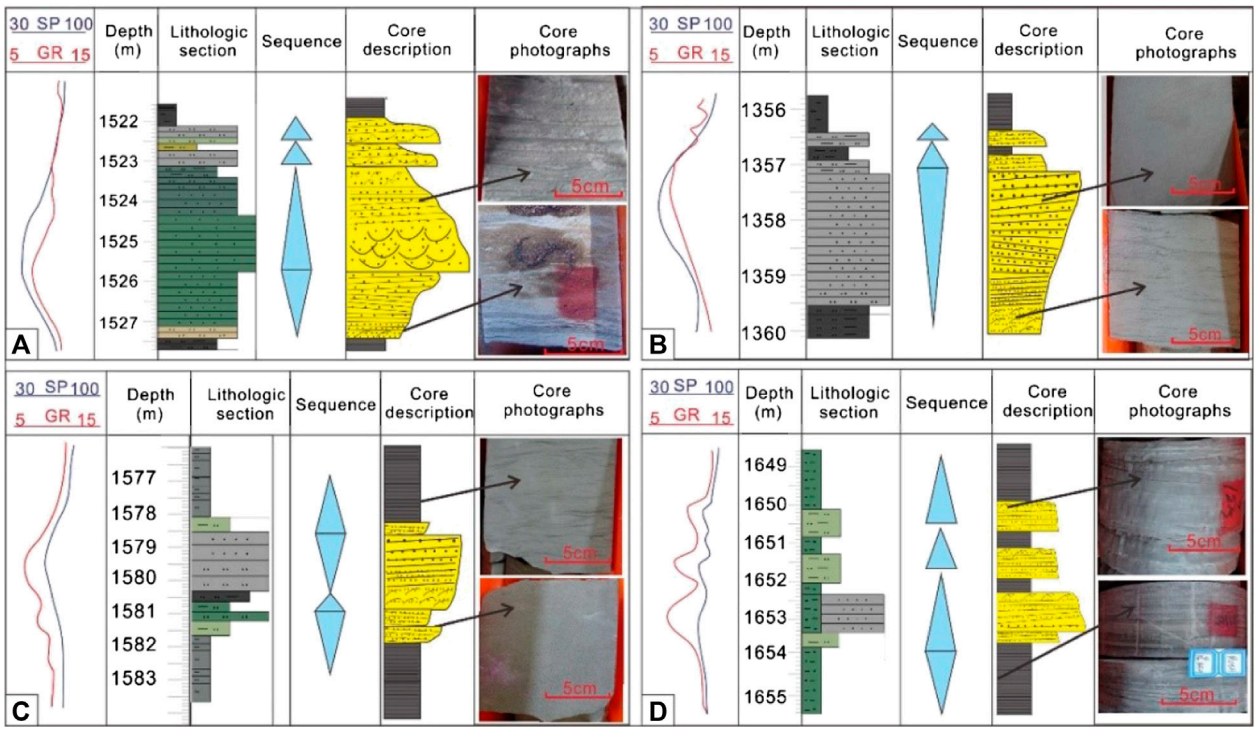

FIGURE 8 | Characteristics of the microfacies: **(A)** characteristics of subaqueous distributary channel and mouth bar, HB79; **(B)** characteristics of mouth bar, HB56; **(C)** characteristics of sand sheet, HH9; **(D)** characteristics of interdistributary bay-fill, HB178.

(4) Interdistributary Bay-Fill

Because of the river overflow and the change of water depth, an interdistributary bay forms. Longitudinally, it is usually composed of multiple sand bodies. There are mudstone interbeds in the middle of the sand bodies, and the thickness is uneven. In terms of internal structure, there are obvious interbeds between each single sand body and other sand bodies in the sequence. Log curves are similar through the sand bodies but have correlated peaks, which are generally tooth-shaped, conical, or elliptical, with moderate or low amplitudes, at the mudstone interbeds (**Figure 8D**).

DISCUSSION

Distribution of Sedimentary Microfacies

According to the distribution law of sedimentary microfacies, the Sanzhao and Gulong depressions in the northern part of the study area are the main source areas. The progradational delta distributed sediment southward along the long axis of the basin. The delta front facies sand bodies extend to the inner part of the study area, forming a reservoir mainly composed of sheet sand. The catchment area of Songliao Basin is in the south, basinward of the delta front subfacies, and the sedimentary microfacies are dominated by the sand sheet. Most of the thin layers in the fourth member of Nenjiang Formation are poor in physical properties, and there is no effective oil-bearing layer (**Figure 9B**). The $k_2n_4^6$ sandbody thickness is 3–5 m, and the two microfacies, distributary channel-fill and mouth bar, account for a relatively high proportion. Therefore, its sand body has good physical properties, which is the main oil-bearing layer in the fourth member of Nenjiang Formation and the target member of our study (**Figure 9C**).

Analysis of previous research results shows that the sediments of the study area are derived from the northeast (Jia et al., 2007; Huang et al., 2013; Bao and Niu 2017). Affected by this, the thickness of sandstone in the northeast is larger than that in the southwest. The thickness of sand body decreases gradually from southwest to northeast until it pinches out. However, there is no boundary of sandstone disappearance in the study area. The distribution area of sandstone here is very large, and its thickness is between 1 and 4 m, with an average thickness of 3.5 m.

Sedimentary Model

According to the structural evolution characteristics of Songliao Basin and the sedimentary facies, a sedimentary model of river delta in the study area is established (**Figure 10**).

The sedimentary model is derived from the interrelationship between the sedimentary environment, sedimentation, and the results (sedimentary facies). The sedimentary model not only shows the most typical characteristics of sedimentary facies, but also shows the formation mechanism and process of sedimentary facies (Ye, 2005; Feng and Zhang, 2012; Gao et al., 2017). The sedimentary system of Songliao Basin was dominated by a process of progradation; during the first member and the

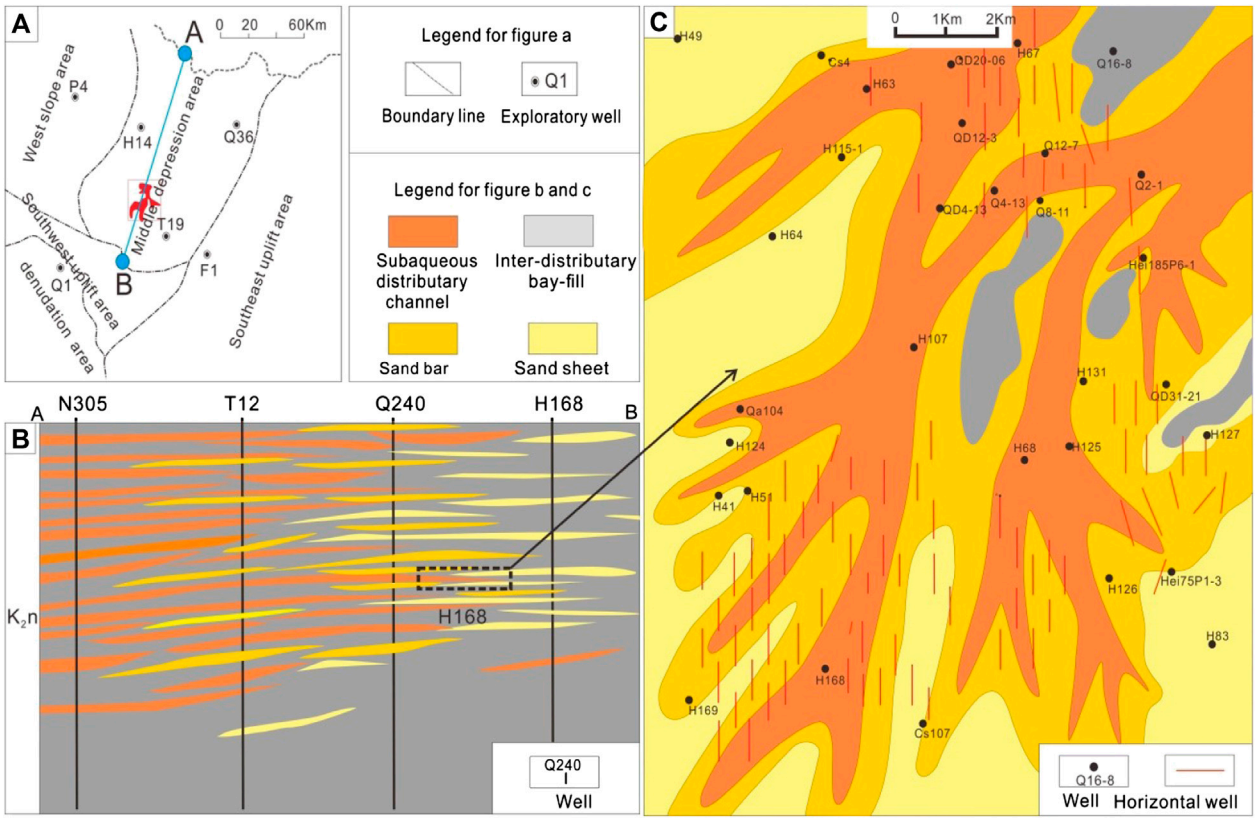

FIGURE 9 | Distribution map of sedimentary microfacies of the layer K2n46: **(A)** location of the southern Songlike Basin; **(B)** lithological profile of connecting wells, planar graph of the sedimentary microfacies.

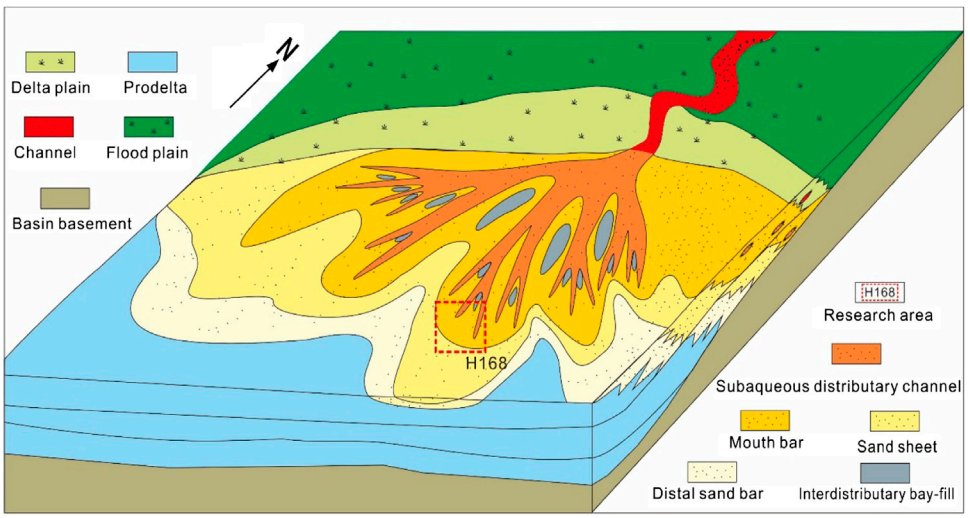

FIGURE 10 | Sedimentary model of river delta (the study area is located in the delta front area).

second member of Nenjiang Formation, the relative lake level rose and the water body deepened continuously. From the late stage of the second member of the Nenjiang Formation, the relative lake level began to decrease until the third member ended. In the early stage of the fourth member of Nenjiang Formation, the basement tectonic activity in the southern Songliao Basin

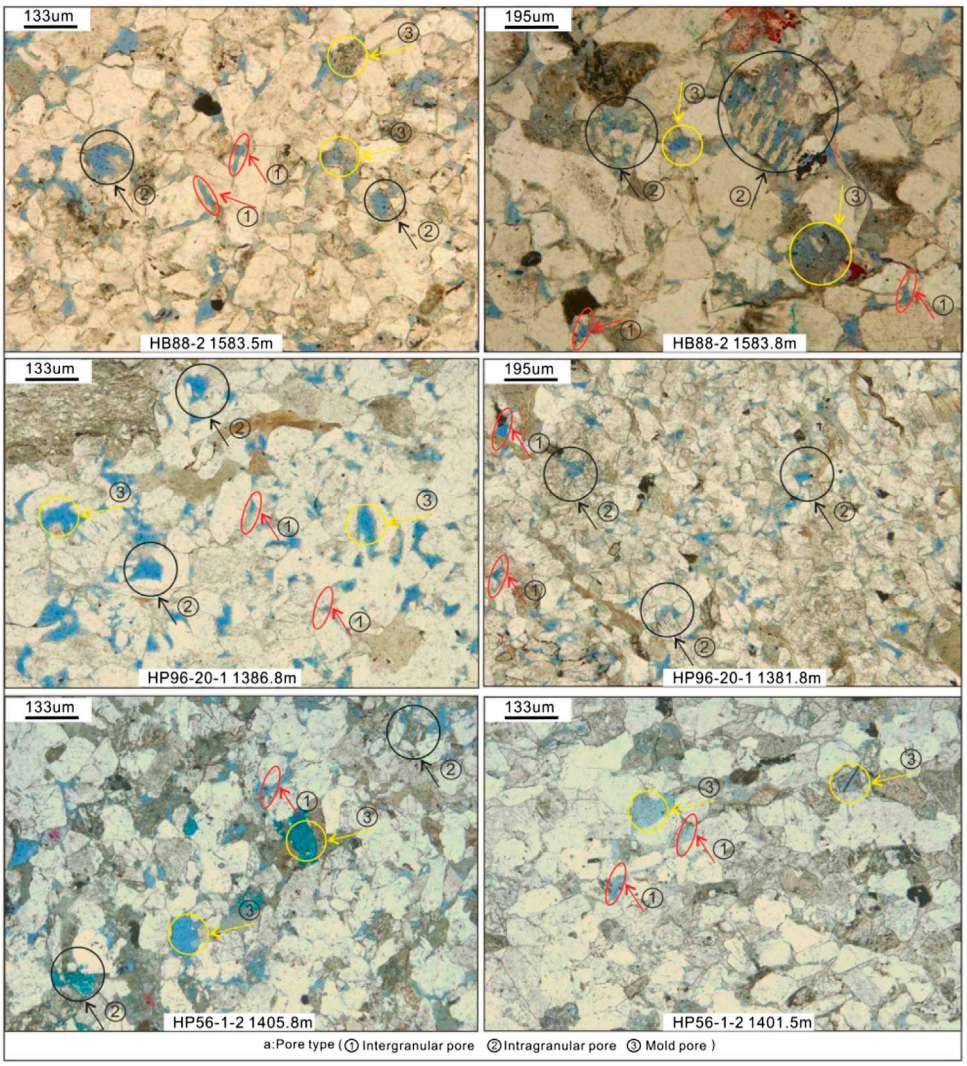

FIGURE 11 | The different pore types of the sandstone (① intergranular pores; ② dissolution pore of feldspar; and ③ mold pore of the debris dissolution).

gradually weakened, which entered the active period of depression. At the end of the fourth member of Nenjiang Formation, the relative lake-level fallen and the delta continued to prograde southward, forming the deposition dominated by mouth bar and sand sheet. The fifth member of Nenjiang Formation is a period of continuous rising of relative lake level.

Analysis of the Influence Degree of Sedimentation on Reservoir Properties

(1) Because the target area is located at the end of the delta front, distal to the source area, the deposits are predominantly fine-grained, and mudstone accounts for a relatively high proportion, sandstone are very fine grained, and the deposits are well sorted. Under the influence of these conditions, the pores of sandstone are relatively small, and the smaller intergranular pores are dominant (46%). In addition, due to the influence of parent rock lithology in the source area, the content of feldspar and lithics in sandstone is higher, which increases the probability of particle dissolution. Therefore, the content of dissolution pores and mold pores related to dissolution is 29 and 17% respectively. Dissolution depends largely on the cement in the pores, and the content of early carbonate cement in the pores of the rock is very high, with an average of 18%, which is easily dissoluted by the organic acid. But the clay mineral content is low (15%) mainly composed of illite/montmorillonite (I/M) mixed layer, which has little effect on the physical properties of the reservoir and only plays a role of interstitial filling, respectively. In addition, other types of pores in the rock are relatively small (**Figure 11**).

The probability distribution of sandstone pore and throat radius is obtained by using the constant velocity mercury injection experiment. The correlation between these data and

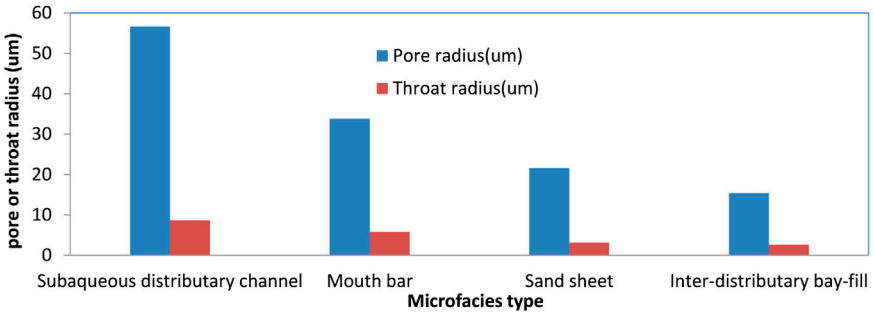

FIGURE 12 | Statistical chart of relationship between sandstone pore and throat size and microfacies.

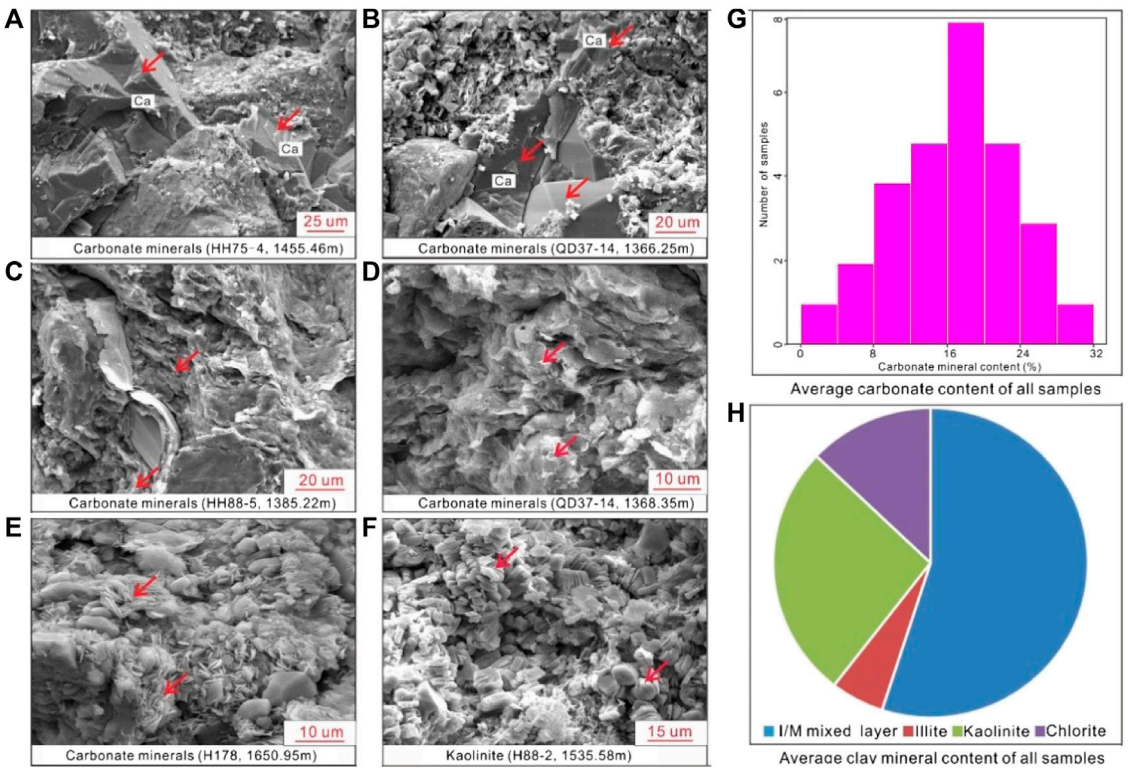

FIGURE 13 | Pore characteristics of sandstone: **(A–F)** pore structure and mineral characteristics observed by SEM; **(G, H)** content of different cementation minerals.

sedimentary microfacies shows that the physical conditions of distributary channel sandbodies are the best, which have good storage and seepage performance. The average of pore radius is 56.6 um, and the average of throat radius is 8.6 um. The physical conditions of the mouth bar sandbodies are the second, the average of pore radius is 33.8 um, and the throat radius is 5.7 um. The physical properties of the sand sheet body at the delta front are very poor, with an average pore radius of 21.5 um and an average throat radius of 3.1 um. The physical properties of the interdistributary sandbodies are the worst, with an average pore radius of 15.3 um and an average throat radius of 2.5 um, almost without storage and seepage performance. This shows that the size and distribution of pores and throats are greatly influenced by sedimentary microfacies (**Figure 12**).

(2) Due to the influence of sedimentary environment, the sandstone in the study area has finer grain size, more argillaceous sediments, and high clay mineral content. The sandstone interstitial material includes mud, carbonate, and clay minerals; the mud is mostly recrystallized and locally distributed in a muddy strip (Zhang et al., 2018; Li et al., 2019; Zhang et al., 2020). Carbonate cementation (calcite and dolomite) is an important cementation, which is one of the main factors to destroy the reservoir conditions in the study

area. According to the precipitation sequence and composition changes, they can be divided into early and late stages.

The carbonate minerals in the study area are mainly early cements, which are mainly formed in the late stage of early diagenesis. The crystal morphology of calcite is generally poor, while that of dolomite is better (**Figures 13A,B**). The results of whole rock X-ray diffraction show that the mineral content of carbonate rock is between 5 and 25%, with an average of 18% (**Figure 13G**). The early carbonate cement fills the primary pores, reduces the porosity and permeability of rocks, and destroys the reservoir performance. The clay mineral content in the fourth member of Nenjiang Formation is relatively high, and clay cementation is also the most important cementation in the study area. Clay cements include the I/M mixed layer (**Figure 13C**), illite (**Figure 13D**), chlorite (**Figure 13E**), and kaolinite (**Figure 13F**) of which the content of the I/M mixed layer is the highest, reaching 55% (**Figure 13H**). This shows that the hydrodynamic conditions are weak, but later diagenesis is strong.

(3) Different microfacies lead to different types of sandbodies, which leads to great differences in porosity and permeability of rocks, so the distribution range of sandstone porosity and permeability of each microfacies can directly reflect the matching relationship between different sedimentary microfacies and reservoir physical properties. For the reservoir in the study area, the physical properties of the subaqueous distributary channel-fill and mouth bar are the best, with an average porosity of more than 13% and a permeability of more than 17×10^{-3} μm^2; the sand body of the sand sheet is the second, with a porosity of 10.48% and a permeability of 9.36×10^{-3} μm^2; the sandstone physical properties of the interdistributary bay-fill are the worst, with an average porosity of only 8.33% and a permeability of only 3.55×10^{-3} μm^2. The correspondence between the physical properties of the reservoir and the types of sedimentary microfacies is very good, which reflects the control of the depositional processes and detrital mineralogy on the reservoir performance, as have been interpreted from deep-water settings (Porten et al., 2016).

CONCLUSION

(1) The sandstone content of the K_2n_4 strata in southern Songliao Basin is merely 10%, which indicates long transport distance for the sediments. The sedimentary facies support interpretation of a river-dominated delta front which includes four microfacies: subaqueous distributary channel, mouth bar, sand sheet, and interdistributary bay-fill. The lake basin in the study area was gradually shrinking during the deposition period of Nenjiang Formation, and the river delta continued to prograde southward, which causes the sand body to become tongue-like and gradually thinned to the south.

(2) There are 9 single lithofacies types and five lithofacies associations in the target layer of the study area. The single lithofacies mainly consist of SIT, SR and PR, and the main combination of lithofacies is MH-FIT-FIO-FIT-FIO-MH, which show the vertical superposition of positive rhythm channel sand bodies. This is consistent with the characteristics of microfacies in the study area.

(3) Influenced by sedimentary environment and distance from source area, the grain size of sediment is very fine, which determines that the primary porosity and permeability of sandstone are low. In addition, the compaction and cementation in the diagenesis stage are strong, which reduces reservoir pore space. Therefore, the pores of the sandstone are mainly formed by lithic and feldspar dissolution in the study area. Dissolution depends largely on the cement in the pores, and the content of early carbonate cement in the pores of the rock is very high, with an average of 18%, but the clay mineral content of is low (15%) which is mainly composed of illite/montmorillonite- (I/M-) mixed layer. The absolute content of clay mineral has little effect on the physical properties of the reservoir and only plays a role of interstitial filling.

DATA AVAILABILITY STATEMENT

The original contributions presented in the study are included in the article/Supplementary Material; further inquiries can be directed to the corresponding author.

AUTHOR CONTRIBUTIONS

JW was mainly responsible for the conception of the article. He put forward a good idea and completed the research content related to sedimentary facies in the article. KZ was in charge of sedimentary facies research and carried out rock analysis experiments. JZ gave some good ideas to the lithofacies model establishing. Xie has been engaged in the research on the reservoir property influence factors.

FUNDING

Projects ZR2020MD035 was supported by the Natural Science Foundation of Shandong Province. Projects 51504143 and 51674156 were supported by the National Natural Science Foundation of China.

ACKNOWLEDGMENTS

The authors would like to thank workers from the Jilin oilfield for supplying the research data.

REFERENCES

Bao, Y., and Niu, F. (2017). Constraining sedimentary structure using frequency - dependent p wave particle motion: a case study of the Songlike Basin in NE China. *J. Geophys. Res. Solid Earth* 122 (11), 9083–9094. doi:10.1002/2017JB014721

Cai, J., Xu, K., Zhu, Y., Hu, F., and Li, L. (2020). Prediction and analysis of net ecosystem carbon exchange based on gradient boosting regression and random forest. *Appl. Energy* 262, 114566. doi:10.1016/j.apenergy.2020.114566

Cheng, T., Kang, H., Du, X., Li, Q., Bai, B., and Jia, H. (2017). Non-marine sequence stratigraphic characteristics of Nanjing Formation, northern Songlike basin. *Fault-Block Oil Gas Field* 24 (4), 481–485.

Ding, F., Zhang, J., Xie, J., Li, C., Shi, C., Zhang, P., et al. (2014). Fine description of structure and sedimentary microfacies of Li32 block of Lijin oilfield, Dongying depression, China. *Arab. J. Geosci.* 7 (5), 1693–1704. doi:10.1007/s12517-013-0972-8

Eyles, N., Eyle, s. C., and Miall, A. D. (2010). Lithofacies types and vertical profile models; an alternative approach to the description and environmental interpretation of glacial diamict and diamictite sequences. *Sedimentology* 33 (1), 151. doi:10.1111/j.1365-3091.1983.tb00679.x

Feng, Z., and Zhang, S. (2012). Depositional evolution and accumulation response of Yautia-Nanjing Formation in Songlike basin. *Earth Sci. Front.* 19 (1), 78–87.

Folk, R. (1968). *Petrology of sedimentary rocks*. Austin: Hemphill Publishing Company.

Gao, Y., Qu, X., Jiang, L., Wang, S., and Wang, P. (2017). Lithology and stratigraphic interfaces prediction of the continental scientific drilling project of cretaceous Songlike basin. *Earth Sci. Front* 24 (1), 242–256.

Gao, Y., and Wang, P. (2010). Sedimentary facies and cyclostratigraphy of the Cretaceous first member of Nanjing Formation in the Southeast uplift zone, Songlike Basin and its correlation with the CCSD-SK-I. *Acta Petrol. Sin.* 26 (1), 99–108.

Gugliotta, M., Flint, S., Hodgson, D., and Veiga, G. (2015). Stratigraphic record of river-dominated crevasse subdeltas with tidal influence (lajas formation, Argentina). *J. Sediment. Res.* 85 (3), 265–284. 10.2110/jsr.2015.19

Guo, S., and Mao, W. (2019). Division of diagenesis and pore evolution of a permian shanxi shale in the ordos basin, China. *J. Petrol. Sci. Eng.* 182, 106351. doi:10.1016/j.petrol.2019.106351

Huang, W., Zhang, S., Zhang, C., and Wei, W. (2013). Sequence configuration and sedimentary evolution of Nanjing formation in the Songlike Basin. *Acta Sedimentol. Sin.* 31 (5), 920–927.

Jia, J., Wang, P., Shao, R., Cheng, R., Zhang, B., Hou, J., et al. (2007). Stratigraphical sequence and regional correlation of yingcheng Formation in the southeast of Songlike basin. *J. Jilin Univ.* 37 (6), 1110–1123.

Jin, J., Liu, D., Ji, Y., Yang, Z., Gao, C., Wang, J., et al. (2019). Research on lithofacies types, cause mechanisms and distribution of a gravel braided-river alluvial fan: a case study of the modern Poplar river alluvial fan, northwestern Junggar Basin. *Acta Sedimentol. Sin.* 37 (2), 254–267.

Kallepalli, A., and Richardson, M. (2017). Digital shoreline analysis system-based change detection along the highly eroding Krishna–Godavari delta front. *J. Appl. Remote Sens.* 11 (3), 36018–36011. doi:10.1117/1.JRS.11.036018

Li, G., Wan, X., Batten, D., Bengtsond, P., Xi, D., and Wang, P. (2009). Spinicaudatans from the upper cretaceous Nanjing Formation of the Songlike basin, northeast China: taxonomy and biostratigraphy. *Cretac. Res.* 30 (3), 687–698. doi:10.1016/j.cretres.2008.12.008

Li, J., Liu, S., Zhang, J., Fan, Z., Sun, Z., Zhang, M., et al. (2015). Architecture and facies model in a non-marine to shallow-marine setting with continuous base-level rise: an example from the cretaceous Denglouku Formation in the Changling depression, Songlike Basin, China. *Mar. Petrol. Geol.* 68, 381–393. doi:10.1016/j.marpetgeo.2015.09.002

Li, S., Li, H., Xu, W., and Dong, Z. (2007). Sequence architectures and sedimentary features of lower cretaceous in the southern Songlike Basin. *Nat. Gas. Ind.* 27 (4), 36–39.

Li, X., Zhang, J., Liu, L., Fan, Z., and Meng, N. (2018). Reservoir architecture and fracture characterization of low-permeability sandstone reservoir: a case study of Biandong oilfield, Jinhu depression, northern Jiangsu Basin, China. *Arab. J. Geosci.* 11 (14), 380. doi:10.1007/s12517-018-3682-4

Li, Y., Chang, X., Yin, W., and Wang, G. (2019). Quantitative identification of diagenetic facies and controls on reservoir quality for tight sandstones: a case study of the Triassic Chang 9 oil layer, Zhenjing area, Ordos Basin. *Mar. Petrol. Geol.* 102, 680–694. doi:10.1016/j.marpetgeo.2019.01.025

Li, Z., Lu, S., Li, J., Xiao, D., Chen, H., and Li, Y. (2017). Sedimentary characteristics and evolution of member 1 of Yautia Formation of cretaceous in zhaoyuan-taipingchuan area of Songlike basin. *J. Petrol. Sci. Eng.* 148, 52–63. doi:10.1016/j.petrol.2016.09.038

Liu, H., Miao, H., Chen, W., Li, L., and Bai, L. (2003). Resource potential in the shallow middle part of Songlike Basin. *China Pet. Explor.* 8 (3), 13–17.

Liu, L., Zhang, J., Wang, R., Wang, J., Yu, J., Sun, Z., et al. (2016). Facies architectural analysis and three-dimensional modeling of Wen79 fault block, Wellie oilfield, Donghu depression, China. *Arab. J. Geosci.* 9 (18), 714. doi:10.1007/s12517-016-2749-3

Liu, Z., Wang, D., Liu, L., Liu, W., Wang, P., Du, X., et al. (1993). Sedimentary characteristics of the cretaceous in the Songlike basin. *Acta Geologica Sin.* 6 (2), 167–180.

Lv, Da., Wang, D., Li, Z., Liu, H., and Li, Y. (2016). Depositional environment, sequence stratigraphy and sedimentary mineralization mechanism in the coal bed- and oil shale-bearing succession: a case from the Paleogene Huangshan Basin of China. *J. Petrol. Sci. Eng.* 148, 32–51. doi:10.1016/J.PETROL.2016.09.028

Meng, Q., Zhang, S., Sun, G., Fu, X., Wang, C., and Shang, Y. (2016). A seismic geomorphology study of the fluvial and lacustrine-delta facies of the Cretaceous Quantou-Nanjing Formations in Songlike Basin, China. *Mar. Petrol. Geol.* 78, 836–847. doi:10.1016/j.marpetgeo.2016.01.017

Miall, A. (1985). Architectural-element analysis: a new method of facies analysis applied to fluvial deposits. *Earth Sci. Rev.* 22 (4), 261–308. doi:10.1016/0012-8252(85)90001-7

Mo, W., Wu, C., Su, N., Zhang, S., and Wang, M. (2019). Seismic imaging of the sedimentary system of the upper 3 cretaceous Nanjing Formation in northern Songlike basin. *J. Earth Sci.* 30 (4), 1–11. doi:10.1007/s12583-017-0970-y

Pan, S., Liu, H., Carlos, Z., Liu, C., Liang, S., Zhang, Q., et al. (2017). Sublacustrine hyperpycnal channel-fan system in a large depression basin: a case study of Nen 1 Member, Cretaceous Nanjing Formation in the Songlike Basin, NE China. *Petrol. Explor. Dev.* 44 (6), 911–922.

Porten, K., Kane, I., Warcho, M., and Southern, S. (2016). A sedimentological process-based approach to depositional reservoir quality of deep-marine sandstones: an example from the springar formation, northwestern vring basin, Norwegian sea [J]. *J. Sediment. Res.* 86 (11), 1269–1286.

Qi, Y., Zhang, Z., Zhou, M., and Zheng, W. (2009). Lithofacies and sedimentary facies from middle Triassic fluvial deposits of Youfangzhuang Formation, Jiyuan area, western Henan. *Acta Sedimentol. Sin.* 27 (2), 254–264.

Shi, L., Jin, Z., Yan, W., Zhu, X., Xu, X., and Peng, B. (2015). Influences of overpressure on reservoir compaction and cementation: a case from northwestern subsag, Bozhong sag, Bohai Bay Basin, East China. *Petrol. Explor. Dev.* 42 (3), 339–347. doi:10.1016/S1876-3804(15)30024-0

Sun, Y., Zhong, J., Jiang, Z., Yu, W., Cao, Y., and Rao, M. (2006). Study of sequence stratigraphy of depression period in southern Songlike Basin. *J. China Univ. Petrol.* 30 (5), 1–7.

Tong, X., Hu, J., Xi, D., and Zhu, M. (2018). Depositional environment of the Late Santonin lacustrine source rocks in the Songlike Basin (NE China): implications from organic geochemical analyses. *Org. Geochem.* 124, 215–227.

Wang, D.-d., Shao, L.-y., Li, Z.-x., Li, M.-p., Lv, D., and Liu, H. (2016). The hydrocarbon generation characteristics, reservoir performance and preservation conditions of continental coal measures shale gas. *J. Petrol. Sci. Eng.* 145, 609–628. doi:10.1016/j.petrol.2016.06.031

Wang, J., Fu, J., Xie, J., and Wang, J. (2020). Quantitative characterisations of gas loss and numerical simulations of underground gas storage based on gas displacement experiments performed with systems of small-core devices connected in series. *J. Nat. Gas Sci. Eng.* 81, 103495. doi:10.1016/j.jngse.2020.103495

Wang, J., Zhang, J., and Xie, J. (2018). Analysis of the factors that influence diagenesis in the terminal fan reservoir of fuyu oil layer in the southern Songlike basin, northeast China. *Open Geosci.* 10 (1), 866–881. doi:10.1515/geo-2018-0068

Wang, J., Zhang, J., and Xie, J. (2014). Initial gas full-component simulation experiment of Ban-876 underground gas storage. *J. Nat. Gas Sci. Eng.* 18, 131–136. doi:10.1016/j.jngse.2014.02.006

Wang, L., Wu, C., Mo, W., and Zhang, S. (2014). Sedimentary characteristics and identification of muddy deltaic in Nanjing Formation of Songlike basin. *Acta Sci. Nauralium Univ. Pekin.* 50 (3), 497–506.

Wang, W., Min, W., Lu, S., Chen, S., Zheng, M., and Wu, X. (2016). Basin modelling of gas migration and accumulation in volcanic reservoirs in the Xujiaweizi fault-depression, Songlike Basin. *Arabian J. Geosci.* 9 (2), 166. doi:10.1007/s12517-015-2072-4

Wu, D., Li, H., Jiang, L., Hu, S., Wang, Y., Zhang, Y., et al. (2019). Diagenesis and reservoir quality in tight gas bearing sandstones of a tidally influenced fan delta deposit: the Oligocene Zhuhai Formation, western Pearl River Mouth Basin, South China Sea. *Mar. Petrol. Geol.* 107, 278–300. doi:10.1016/j.marpetgeo.2019.05.028

Wu, J., Liang, C., Hu, Z., Yang, R., Xie, J., Wang, R., et al. .(2019). Sedimentation mechanisms and enrichment of organic matter in the ordovician wufeng formation-silurian longmaxi Formation in the sichuan basin. *Mar. Petrol. Geol.* 101, 556–565. doi:10.1016/j.marpetgeo.2018.11.025

Xu, G., Liu, J., Gugliotta, M., Saito, Y., Chen, L., Zhang, X., et al. (2020). Link between East Asian summer monsoon and sedimentation in river-mouth sandbars since the early Holocene preserved in the Yangtze River subaqueous delta front. *Quat. Res.* 95, 84–96. doi:10.1017/qua.2020.1

Xu, J., Liu, Z., Bechtel, A., and Sachsenhofer, R. (2019). Organic matter accumulation in the upper cretaceous Qingshankou and Nanjing formations, Songlike basin (NE China): implications from high-resolution geochemical analysis. *Mar. Petrol. Geol.* 102, 187–201.

Yang, Y., Qiu, L., Cao, Y., and Cheng, C. (2017). Reservoir quality and diagenesis of the permian lucaogou formation tight carbonates in jimsar sag, junggar basin, west China. *J. Earth Sci.* 28 (6), 1032–1046. doi:10.1007/s12583-016-0931-6

Ye, D. (2005). Lower cretaceous sequence stratigraphic framework and hydrocarbon accumulation in the southeast rise, Songlike Basin, China. *Chin. J. Geol.* 40 (2), 227–236.

Zhang, C., Zhang, S., Wei, W., Wu, C., Liang, J., Niu, W., et al. (2014). Sedimentary filling and sequence structure dominated by T-R cycles of the Nanjing Formation in the Songlike Basin. *Sci. China Earth Sci.* 57 (2), 278–296.

Zhang, M., and Wang, Y. (2019). Paleoseismic event recorded in the upper cretaceous Nanjing Formation in southeastern area of the Songlike basin (NE China). *Aust. J. Earth Sci.* 66 (1), 95–110. doi:10.1080/08120099.2018.1499550

Zhang, P., Zhang, J., Wang, J., Li, M., Liang, J., and Wang, Y. (2018). Flow units classification for geostatistical three-dimensional modeling of a non-marine sandstone reservoir: a case study from the Paleocene funing formation of the Gaoji oilfield, East China. *Open Geosci.* 10 (1), 113–120. doi:10.1515/geo-2018-0009

Zhang, X., and Huang, Y. (2010). Sedimentary evolution characteristics of the Nanjing formation in the southern Songlike Basin. *J. Yangtze Univ.* 7 (1), 165–167.

Zhang, X., Pang, X., Jin, Z., et al. (2020). Depositional model for mixed carbonate-clastic sediments in the middle cambrian lower zhangxia formation, xiaweidian, north China. *Adv. Geo-Energy Res.* 4 (1), 29–42. doi:10.26804/ager.2020.01.04

Conflict of Interest: The authors declare that the research was conducted in the absence of any commercial or financial relationships that could be construed as a potential conflict of interest.

The reviewer DL declared a past coauthorship with one of the authors, JW, and the handling editor. The reviewer CL declared a past coauthorship with one other author, JX, and the handling editor.

frontiers in Earth Science

ORIGINAL RESEARCH
published: 31 March 2021
doi: 10.3389/feart.2021.654136

Occurrence of Irreducible Water and Its Influences on Gas-Bearing Property of Gas Shales From Shallow Longmaxi Formation in the Xishui Area, Guizhou, Southern China

Jian Sun[1,2], Xianming Xiao[1], Qiang Wei[3], Peng Cheng[2] and Hui Tian[2]*

[1] School of Energy Resources, China University of Geosciences (Beijing), Beijing, China, [2] State Key Laboratory of Organic Geochemistry, Guangzhou Institute of Geochemistry, Chinese Academy of Sciences, Guangzhou, China, [3] School of Earth Sciences, East China University of Technology, Nanchang, China

Systematic studies are quite rare on the gas-bearing property and its controlling factors of the shallow Longmaxi shale outside the Sichuan Basin. In a previous study, the gas in place contents of a suit of Longmaxi shale samples with a depth range of 362–394 m from the well XK2, which was drilled in the Xishui area, Guizhou, southern China, were reported. In the present study, the pore structure parameters and irreducible water occurrence characteristics of those samples, and their influences on the gas-bearing property were further investigated. The results show that, compared to the dry sample, the non-micropore specific surface areas and micropore volumes of the moist sample are significantly reduced by an average value of 61 and 30%, respectively, and that the water averagely occupies 82 and 41% of the inorganic and organic non-micropore specific surface areas, respectively, and 44 and 18% of the inorganic and organic micropore volumes, respectively. The shallow shale reservoir is dominated by adsorbed gas. It accounts for 66–93% of the total gas. The water significantly decreases the adsorption capacity of the inorganic matte (mainly clay minerals) pores, but has a limited influence on that of the organic matter pores. The adsorbed gas occurs mostly in the organic matter nanopores, and even if the shales were highly saturated with the water, they can still store a certain amount of the adsorbed gas. These results are to provide some guides for the evaluation and exploration of the shallow Longmaxi shale located in the strongly tectonic transformation areas of southern China.

Keywords: Longmaxi formation, shallow shale, irreducible water, pore structure, gas-bearing property, adsorbed gas

OPEN ACCESS

Edited by:
Dawei Lv,
Shandong University of Science and Technology, China

Reviewed by:
Qingyong Luo,
China University of Petroleum, China
Xianfeng Tan,
Chongqing University of Science and Technology, China

****Correspondence:***
Xianming Xiao
xmxiao@cugb.edu.cn

Specialty section:
This article was submitted to Economic Geology, a section of the journal Frontiers in Earth Science

Received: *15 January 2021*
Accepted: *08 March 2021*
Published: *31 March 2021*

Citation:
Sun J, Xiao XM, Wei Q, Cheng P and Tian H (2021) Occurrence of Irreducible Water and Its Influences on Gas-Bearing Property of Gas Shales From Shallow Longmaxi Formation in the Xishui Area, Guizhou, Southern China. Front. Earth Sci. 9:654136. doi: 10.3389/feart.2021.654136

Abbreviations: ρ_b, density of free gas; ρ_{sample}, apparent density of the shale; BET, Brunauer-Emmett-Teller; BJH, Barrett-Joyner-Halenda; DA, Dubinin-Astakhov; DFT, Density Functional Theory; GBP, gas-bearing property; GIP, gas in place; IM, inorganic matter; M, average molar mass; OM, organic matter; P/P_0, relative pressure; PSD, pore-size distribution; Q_{ads}, adsorbed gas content; Q_{free}, free gas content; Q_{total}, total gas content; R^2, correlation coefficient; S_{BET}, specific surface area; S_{BET-IM}, BET surface area of inorganic matter; S_{BET-OM}, BET surface area of organic matter; S_W, water saturation; TOC, total organic carbon; V_{mic}, micropore volume; V_{mic-IM}, inorganic matter micropore volume; V_{mic-OM}, organic matter micropore volume.

INTRODUCTION

Shale gas, mainly stored as free and adsorbed states, is a typical unconventional natural gas (Jarvie et al., 2007; Bustin et al., 2008; Ross and Bustin, 2009). For different shale reservoirs, not only do their gas contents vary greatly, but the percentages of the adsorbed and free gasses can differ widely. For examples, the percentages of adsorbed gas in the Barnett and Lewis shales (United States) are approximately 20% and in a range of 60–85%, respectively (Curtis, 2002), and the free gas percentage of Longmaxi shale samples from the Jiaoshiba Block in the Sichuan Basin, varies from 60 to 75% (Dong et al., 2014). The gas-bearing property (GBP) and gas in place (GIP) content of shales are not only related to their geological conditions (temperature and pressure), but also restricted by their geochemical properties. For a specific gas shale, the free gas content is mainly related to its porosity, gas saturation, and geological temperature and pressure (Bustin et al., 2008; Gasparik et al., 2012; Pan and Connell, 2015; Ye et al., 2016; Zhang Y. S. et al., 2020), but the controlling mechanism of the adsorbed gas is more complex. Except for the factors mentioned above, the adsorbed gas content is also correlated with its pore type, property and structure, which are comprehensively controlled by the organic matter content and type, mineral composition, and thermal maturity (Yang and Aplin, 1998; Dewhurst et al., 1999; Chalmers and Bustin, 2007, 2008; Ross and Bustin, 2007; Curtis et al., 2010, 2011; Song et al., 2013; Zhang et al., 2013; Shan et al., 2017; Chen et al., 2018; Hou et al., 2018; Li et al., 2018; Bhowrnik and Dutta, 2019; Klewiah et al., 2019; Wang and Guo, 2019; Gou et al., 2020; Zhang Y. F. et al., 2020). High-pressure adsorption experiments based on dry samples are generally carried out to evaluate the adsorption capacity of the targeted shales. The achieved results show that, for high and over mature shales, nanopores are extremely developed in their OM (organic matter), and the TOC (total organic carbon) content presents an obvious positive linear relation to the adsorption capacity (Chalmers and Bustin, 2008; Ross and Bustin, 2009; Gasparik et al., 2012, 2014; Tan et al., 2014; Pan et al., 2016; Tian et al., 2016; Fu, 2017; Wang and Guo, 2019), with a R^2 (correlation coefficient) of 0.67–0.99 (Pan et al., 2016; Fu, 2017). Moreover, clay minerals can also have some gas adsorption capacities to methane (Aringhieri, 2004; Sondergeld et al., 2010; Curtis et al., 2011; Ji et al., 2012; Gasparik et al., 2014; Chen et al., 2016). According to the methane adsorption experiments carried out by Ji et al. (2012), kaolinite, chlorite, and illite could adsorb methane with an amount up to 2.5, 2.3, and 1.8 m^3/t, respectively.

Shale reservoirs always have some water in their pore system (Li et al., 2016a; Hu et al., 2018). Recently, quite a few papers have been related to the occurrence characteristics and mechanism of the pore water in gas shales and its influences on their adsorption capacities (Chalmers and Bustin, 2008; Ross and Bustin, 2009; Gasparik et al., 2014; Chen et al., 2016; Li et al., 2016b; Liu et al., 2018; Bai et al., 2020; Wang et al., 2020). The results imply that water can coexist in non-micropores and micropores in absorbed and condensed states, respectively (Newsham et al., 2003; Charriere and Philippe, 2010), and distributes in both OM and IM (inorganic matter) pores (Cheng et al., 2017, 2018), which significantly reduces the methane adsorption capacity (Ross and Bustin, 2009; Gasparik et al., 2014). Nevertheless, those findings are mainly obtained from the laboratory data, with determination results calculated from relevant theoretical models for samples with different water saturations derived from equilibrium water adsorption experiments (Chareonsuppanimit et al., 2012; Gasparik et al., 2012, 2014; Ji et al., 2012; Zhang et al., 2012; Yaguzhinsky et al., 2013), lacking the constraint and validation of data from geological gas shales (Li et al., 2016b).

After the commercial development of the Longmaxi shale gas in the Sichuan Basin, southern China (Li and Zhang, 2015; Guo, 2016), the exploration of shallow marine shale gas outside the Sichuan Basin has made significant progresses. For instance, the GIP content of the Longmaxi shale in the Zhaotong Block, Yunnan Province can reach 3.81 m^3/t, with an initial gas production of 0.39–1.12 $\times$ 10^4 m^3/d although its burial depth is less than 1,000 m (Tian, 2018; Yang, 2018; Liang et al., 2020). The shallow marine shale gas in southern China is expected to become a new exploration field (Li, 2018; Liang et al., 2020).

The shallow Longmaxi shale in northern Guizhou develops widely, and is expected to have a huge amount of shale gas resources (Liang et al., 2008; Li et al., 2012; Hu et al., 2014). Sun et al. (2020) reported the data of geochemistry and GIP contents of a suit of Longmaxi shale samples taken from the well XK2 in this area, and revealed that the shallow Longmaxi shale really contains a high content of shale gas. On the basis of the previous work, the pore structures of those shale samples under the moist and dry conditions were analyzed, respectively, the pore water occurrence characteristics in nanopores were investigated, and the influences of them on the GBP were discussed.

MATERIALS AND METHODS

Samples

There are totally sixteen Longmaxi shale samples investigated in this study, which were collected from the well XK2 in northern Guizhou, southern China (**Figure 1**). The collection and preparation methods of those samples, and their geochemical characteristics, pore water contents and total porosity were reported by Sun et al. (2020) and are briefly summarized here. The 16 shale core samples (with a depth interval of 362–394 m) were collected at an interval of about 2 m. Each sample was quickly divided into two parts. One part was immediately conducted on the GIP content test, and the other part was sealed in plastic bags and sent to the laboratory for the analysis of the pore water content, TOC content, mineral composition, total porosity (Sun et al., 2020). The pore water content of the studied shale samples was measured by the oven-drying and weight-loss method, each sample was drilled from its middle to obtain a small cylinder sample (15 mm in diameter and 20 mm in length). The shale TOC content was measured by a LECO CS-230 carbon-sulfur analyzer, the samples were crushed into powders of 80 mesh sizes. X-ray diffraction (XRD) analysis of the sample powders (200 mesh) was carried out using a Bruker D8 Advance X-ray diffractometer. The total porosity was determined by the differences between the shale skeletal density

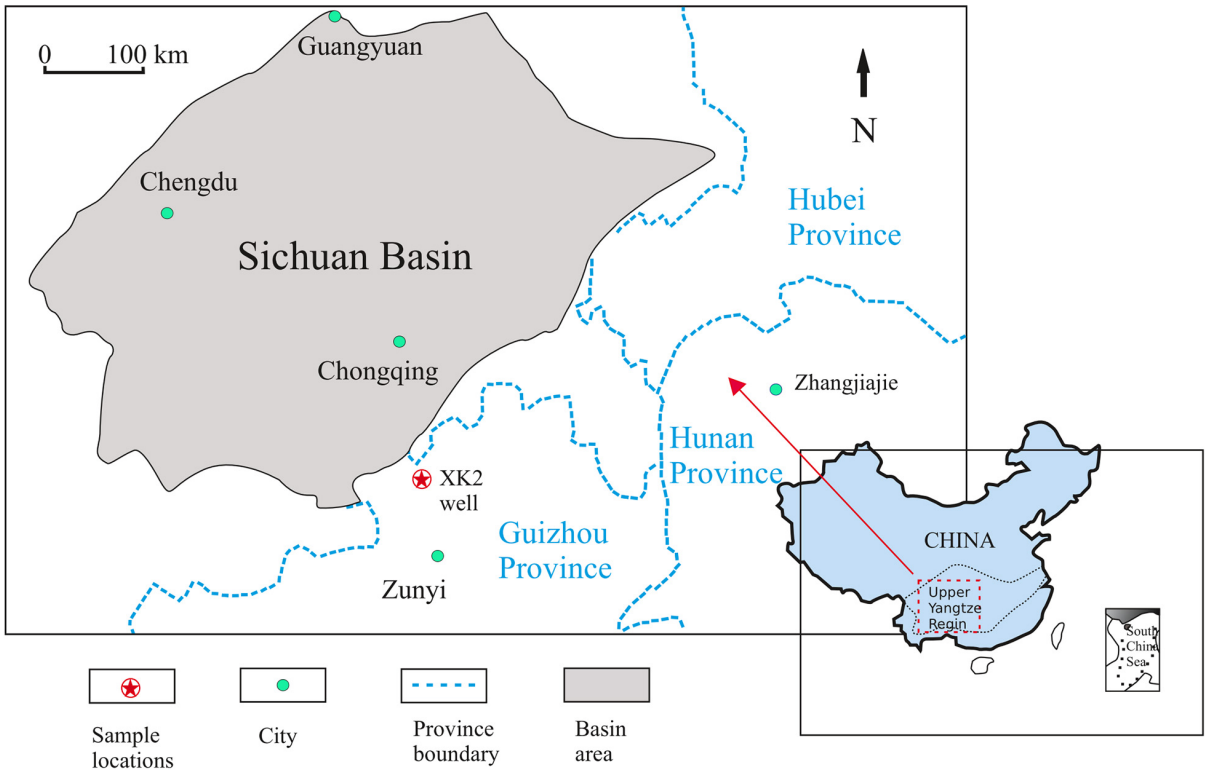

FIGURE 1 | Map showing the location of the well XK2 [modified from Cheng et al. (2018)].

and the apparent density, the two densities were measured with a helium pycnometer (Ultrapyc 1200e) and a hydrometer (DAHO-120M), respectively.

The samples have the TOC, clay mineral, quartz, and carbonate mineral contents of 1.50–8.04%, 20.70–57.00%, 25.00–60.00%, and 4.80–15.80%, respectively, with the porosity of 3.03–5.50% (**Table 1**). The measured pore water content of those samples is between 5.01 and 12.38 mg/g (**Table 1**). It was deemed to be the connate irreducible water content by Sun et al. (2020). This is because the samples were taken from a gas-bearing shale stratum with an ultra-low water saturation, and the gas in the shales prevented the inflow of outside water during the drilling and sampling processes. Therefore, it should be kept in mind that the pore water content of the studied samples can be basically representative for that in their reservoir conditions.

Low Pressure N_2 and CO_2 Adsorption Experiments

The non-micropore (mesopore + macropore) and micropore structures of the moist and dry shale samples were tested using low-pressure N_2 and CO_2 adsorption experiments, respectively, by a Micromeritics ASAP 2020 apparatus. The main experimental methods are summarized below. The samples were crushed into 20–40 meshes (380–830 μm), and each sample was prepared into two parts. One part retained the irreducible water (i.e., the moist sample), and the other part was dried in a vacuum oven for 12 h at a temperature of 110℃ to remove the water and/or volatile substances (i.e., the dry sample). For the dry sample, loaded approximately 1 g into sample tube for further degassing under the high vacuum conditions (<10 mmHg) at 110°C for 12 h in degassing station of the apparatus, and then it was moved to the analysis station for the adsorption experiment. The moist sample was directly placed in the analysis station for the freezing, degassing and adsorption experiments. The samples were tested at a P/P_0 (the relative pressure) of 0.005–0.995 and a liquid nitrogen temperature of 77.35 K for the N_2 adsorption, and at a P/P_0 of 1×10^{-5}–0.03 and a temperature of 273.15 K (ice-water mixture environment) for the CO_2 adsorption. For the N_2 adsorption, the adsorption and desorption isotherms were tested to analyze the type of hysteresis. According to the N_2 adsorption isotherms, the modified BET (Brunauer-Emmett-Teller) equation was utilized to determine the non-micropore specific surface area (Brunauer et al., 1938; Gregg and Sing, 1982; Tian et al., 2015), and the BJH (Barrett-Joyner-Halenda) model was adopted to determine the non-micropore pore-size distribution (PSD) (Barrett et al., 1951; Tian et al., 2013; Pan et al., 2015) for the dry and moist samples. The micropore volume was determined by DA (Dubinin-Astakhov) equation (Dubinin, 1989; Clarkson and Bustin, 1999; Ross and Bustin, 2009; Cheng et al., 2017), and the DFT (Density Functional Theory) was utilized calculating the micropore PSD on the basis of the CO_2 adsorption data from the both sample sets (Mastalerz et al., 2013; Lin et al., 2014).

TABLE 1 | Data of geochemistry, mineral composition, and pore water content of the studied shale samples.

Sample ID	Depth (m)	TOC (%)	Pore water (mg/g)	Apparent density (g/cm^3)	Porosity (%)	Mineral composition (%)				
						Quartz	Feldspar	Total clays	Total carbonates	Pyrite
JX-1	362.61	1.50	8.02	2.64	3.03	30.60	16.00	47.00	4.80	1.60
JX-2	366.90	2.37	10.96	2.63	3.42	27.40	12.20	51.60	7.60	1.40
JX-3	370.04	2.72	12.38	2.60	3.96	25.00	8.50	57.00	7.30	2.00
JX-4	375.06	4.38	8.60	2.51	4.10	33.80	7.30	46.10	10.90	2.00
JX-5	376.78	4.15	8.24	2.50	4.39	36.30	9.90	39.20	12.00	2.50
JX-6	377.51	3.78	8.46	2.50	4.20	35.00	12.20	38.80	11.70	2.40
JX-7	381.70	3.73	5.01	2.50	3.84	53.90	5.60	25.20	13.10	2.30
JX-8	383.56	3.61	6.20	2.50	4.20	45.50	10.20	31.80	10.10	2.50
JX-9	385.26	4.48	5.44	2.48	3.63	56.30	6.60	20.70	14.00	2.30
JX-10	387.52	4.25	5.21	2.51	3.59	57.70	6.20	21.00	10.50	4.70
JX-11	388.89	4.97	6.50	2.47	4.15	50.10	7.80	28.60	10.60	2.80
JX-12	390.48	5.48	5.44	2.49	4.42	52.50	7.60	26.60	8.00	5.30
JX-13	391.92	7.07	5.56	2.39	4.63	60.00	8.70	23.10	6.40	1.90
JX-14	392.36	8.04	6.17	2.43	5.41	41.40	8.40	36.70	12.10	1.50
JX-15	393.03	6.47	6.85	2.41	4.96	53.90	4.50	22.30	15.80	3.50
JX-16	394.01	7.81	10.36	2.43	5.50	34.10	10.40	40.20	15.50	2.90

Data are cited from Sun et al. (2020).

Calculation of Water Saturation

According to the pore water content, porosity and apparent density data of the shale samples from the well XK2 (**Table 1**), their water saturation (S_W, %) can be determined by Eq. 1:

$$S_W = \frac{C_{IW}\ \rho_{sample}}{10\ \Phi\ \rho_w} \quad (1)$$

where C_{IW} is the pore water content (mg/g); Φ is the porosity (%); ρ_{sample} is the apparent density (g/cm^3); ρ_w is the pore water density (g/cm^3), and it is supposed that its density is 1 g/cm^3 for all samples.

Calculation of the Shale Free and Adsorbed Gas Contents

According to the shale gas composition from the well XK2 reported by Sun et al. (2020), the shale gas from the XK2 well shale samples consists of CH_4, C_2H_6, and CO_2 with an average content of 93.99, 1.21, and 4.80%, respectively, while other gasses, such as C_3, N_2 and so on were not detected due to their negligible contents. Thus, the average molar mass (M) of the shale gas was calculated using Eq. 2. The free gas density (ρ_b) was obtained by a PVTsim software. Combined with the porosity, water saturation and apparent density data, the free gas content (Q_{free}) was determined using Eq. 3. The adsorbed gas content (Q_{ads}) was obtained by the difference between the total gas content (Q_{total}) (i.e., the GIP content) and the Q_{free} (Eq. 4). These equations are as follows:

$$M = aM_1 + bM_2 + cM_3 \quad (2)$$

$$Q_{free} = \frac{22400\Phi\ (1 - S_w)\ \rho_b}{M\rho_{sample}} \quad (3)$$

$$Q_{ads} = Q_{total} - Q_{free} \quad (4)$$

where M is the average molar mass of the shale gas (g/mol); Q_{free}, Q_{ads}, and Q_{total} are the free, adsorbed, and total gas contents, respectively (m^3/t); M_1, M_2, and M_3 are the molar mass of CH_4, C_2H_6 and CO_2, respectively (g/mol); a, b, and c are the volume percentages of CH_4, C_2H_6, and CO_2, respectively (%); ρ_b is the free gas density (g/ml), and it can be determined using a PVTsim software based on the reservoir temperature, pressure, and gas composition data.

RESULTS AND DISCUSSION

Pore Structures of the Moist and Dry Samples

Low Pressure N_2 Adsorption and Pore Distribution

Figure 2 displays the isotherms of N_2 adsorption and desorption of the dry and moist samples. It should be noted that the N_2 adsorption and desorption of the studied 16 shale samples are mainly controlled by their TOC contents, the selected 8 samples in **Figure 2** form a TOC gradient, and can reflect the characteristics of the whole sample set (same in **Figures 3–5** below). **Figure 2** indicates that the adsorption quantity of the moist sample is definitely less than that of its corresponding dry sample. Furthermore, the isotherm shapes of the dry and moist samples are significantly different. For the dry sample, the isotherm of N_2 adsorption is very close to the type II isotherm according to the IUPAC (International Union of Pure and Applied Chemistry) (Brunauer et al., 1940; Sing et al., 1985; Rouquerol et al., 1994). It shows a distinct hysteresis loop, without plateau at the p/p_0 approximately 1, and a notable adsorption quantity, besides, can be seen at the lowest p/p_0 (<0.01), implying that the mesopore, macropore, and micropore are well developed in the dry sample (Sing et al., 1985).

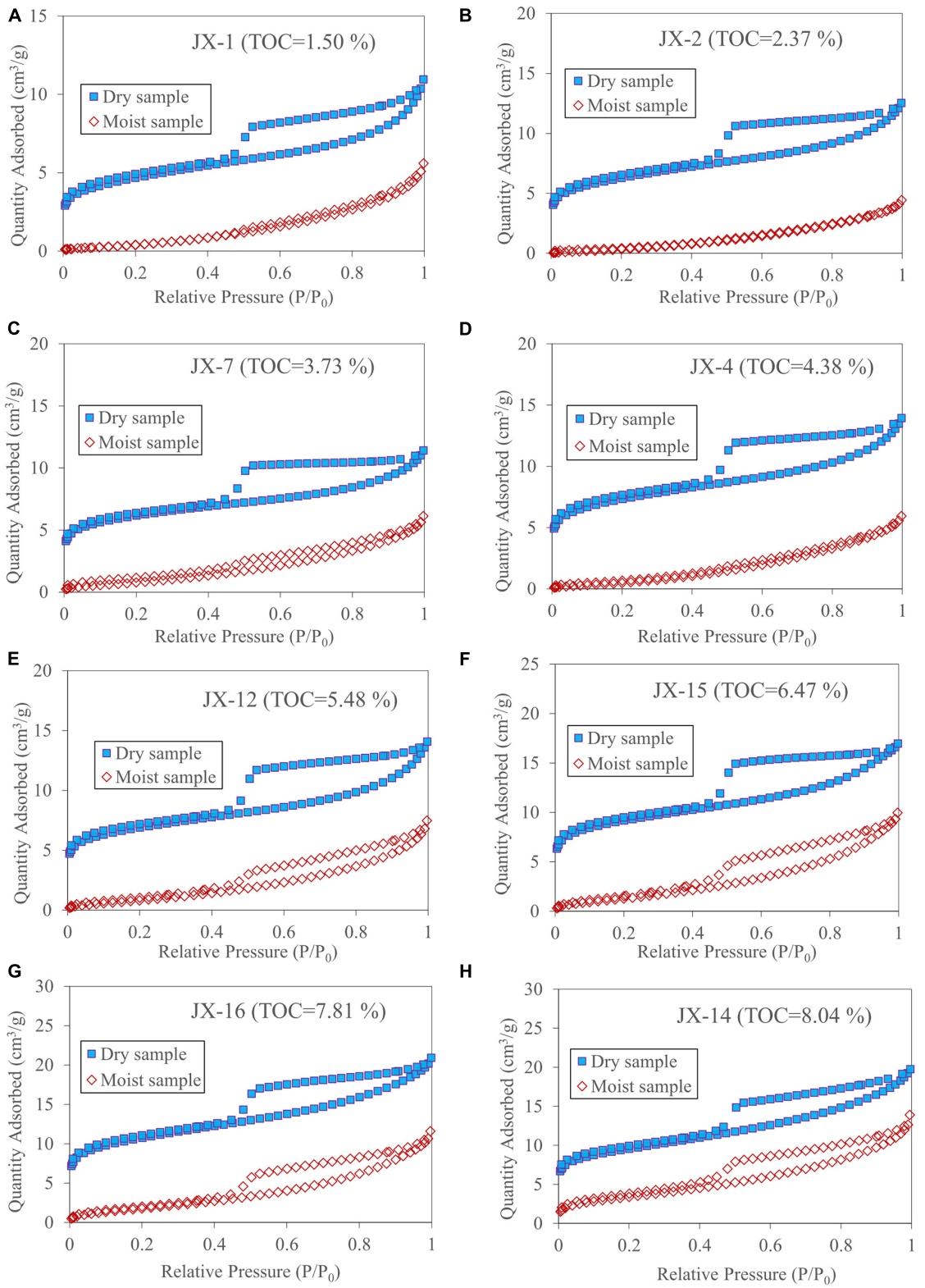

FIGURE 2 | Plots displaying a comparison of the low-pressure N_2 adsorption and desorption isotherms of the selected 8 pairs (moist and dry) shale samples with different TOC contents **(A–H)**. The difference between the moist and dry samples indicates that water influences the N_2 adsorption capacity and pore structure. Besides, the N_2 adsorption quantities of different samples are likely related to their TOC contents, which will be discussed in see section "Controlling Factors of the Shale Pore Structure."

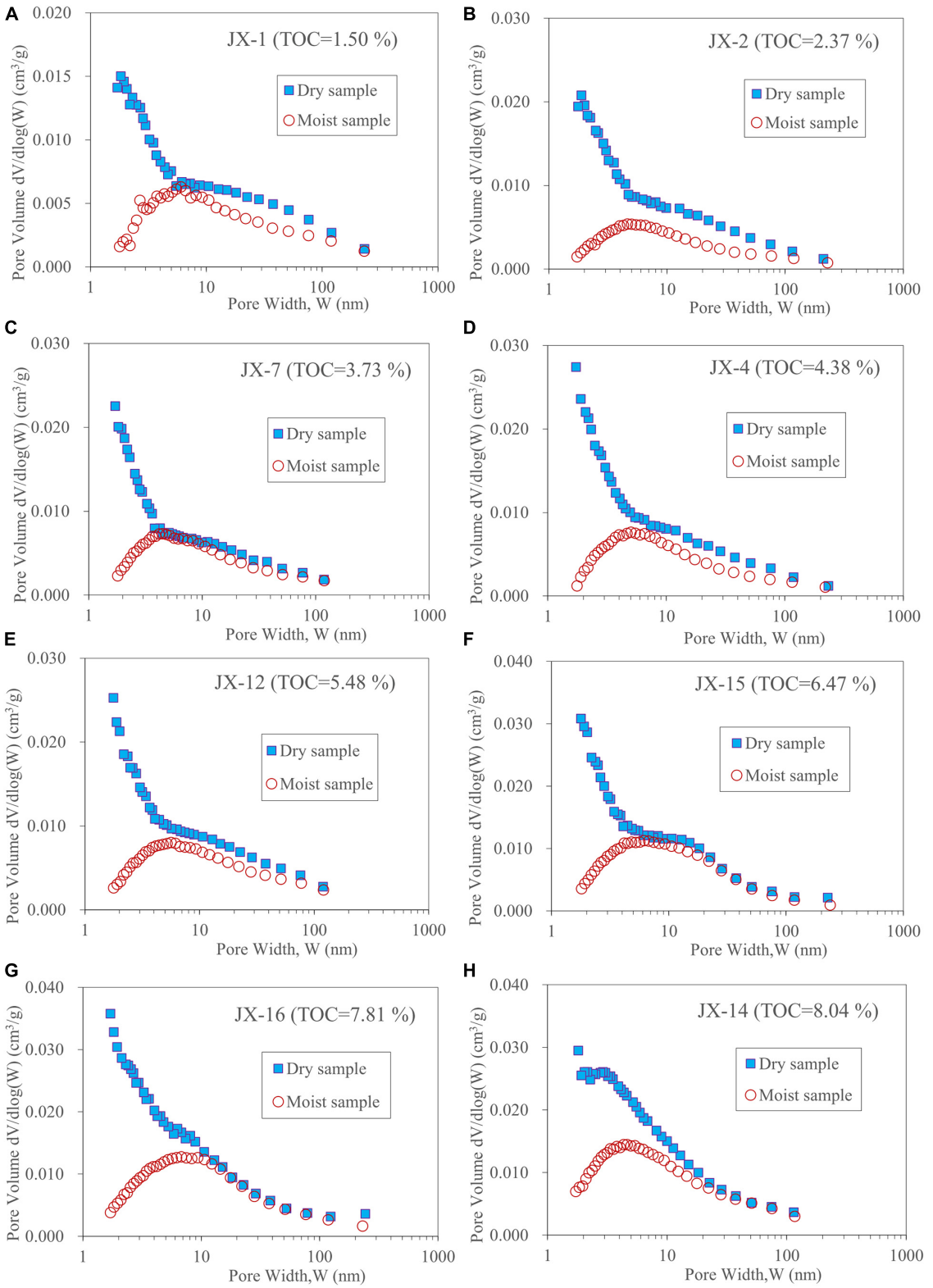

FIGURE 3 | Plots showing the BJH pore-size distributions of the selected 8 pairs (dry and moist) samples based on the N_2 adsorption analysis **(A–H)**. The dry and moist samples have different PSD shapes. Note that water in sample JX-2 **(B)** occupies a broader pore size range compared with other samples shown in **A,C–H**, up to 110 nm, may be due to, in part, its greater pore water content (**Table 2**).

Meanwhile, the shape of hysteretic loop for the dry sample is typically Type B, indicating the fracture-type pore is dominant (Brunauer et al., 1940; De, 1958). However, the hysteresis loop of the moist sample is less developed than that of the dry sample, especially the samples with low TOC contents (such as samples JX-1, JX-2, and JX-4 concomitantly with a higher water content), their hysteresis loops are not notable. It can be seen from the above results that not only the irreducible water in the shales takes up some pore spaces, but it also changes the pore structure characteristics to some extent, especially for the low TOC samples.

The BET surface area (S_{BET}), representative for non-micropores, of the dry sample is 6.16–14.83 m^2/g and averages 10.17 m^2/g. The S_{BET} of the moist sample is obviously lower than that of its corresponding dry sample, and has a range of 2.15–6.66 m^2/g (the average value is about 4.00 m^2/g) (**Table 1**). Compared with the dry sample, the S_{BET} of the moist sample is reduced averagely by 61%.

Figure 3 presents the BJH pore-size distributions (PSD) for the moist and dry samples. For the dry sample, the PSD tends to decrease with increasing pore size, the non-micropores are mainly distributed in the pores <10 nm, and meanwhile, an overall increase in PSD value was observed with increasing TOC. However, for the moist sample, the PSD shows a unimodal peak, and the main peak appears in the pore range of 4–7 nm (**Figure 3**). Compared with the dry sample, the PSD of the moist sample decreases notably in the pores <10 nm. The difference between the dry and moist samples is not significant for the pores >10 nm, indicating the water is mostly distributed in the pores <10 nm. It should be noted that, compared with samples JX1 and JX7, the adsorption quantity and PSD value of sample JX2 are slightly higher under the dry condition and lower under the moist condition, which is likely attributed to its greater clay mineral content (51.60%) (**Table 2**).

TABLE 2 | Data of total S_{BET} and V_{mic}, and calculated organic and inorganic S_{BET} and V_{mic} of the studied samples under dry and moist conditions.

Sample ID	Pore structure parameter	Moist sample	Dry sample	Moist sample		Dry sample	
		Total pore		OM pore	IM pore	OM pore	IM pore
JX-1	BET surface area (m^2/g)	2.15	6.16	1.01	1.14	1.71	4.45
JX-2		2.58	7.94	1.59	0.99	2.70	5.24
JX-3		3.13	8.91	1.83	1.30	3.10	5.81
JX-4		3.53	10.01	2.95	0.58	4.99	5.03
JX-5		3.42	9.79	2.79	0.63	4.73	5.07
JX-6		2.97	9.77	2.54	0.43	4.30	5.47
JX-7		2.93	8.53	2.51	0.42	4.25	4.29
JX-8		3.41	9.07	2.43	0.98	4.11	4.96
JX-9		4.05	9.94	3.01	1.04	5.10	4.83
JX-10		3.50	9.16	2.86	0.64	4.84	4.32
JX-11		4.52	10.26	3.34	1.17	5.66	4.60
JX-12		4.37	9.50	3.69	0.69	6.24	3.26
JX-13		5.01	12.85	4.76	0.26	8.05	4.80
JX-14		6.66	14.04	5.41	1.25	9.16	4.88
JX-15		5.21	11.96	4.35	0.86	7.37	4.59
JX-16		6.53	14.83	5.25	1.28	8.89	5.93
JX-1	Micropore volume (cm^3/g)	0.0039	0.0060	0.0014	0.0026	0.0017	0.0043
JX-2		0.0046	0.0070	0.0021	0.0025	0.0026	0.0044
JX-3		0.0056	0.0076	0.0024	0.0031	0.0030	0.0046
JX-4		0.0065	0.0100	0.0039	0.0026	0.0048	0.0052
JX-5		0.0060	0.0100	0.0037	0.0022	0.0046	0.0055
JX-6		0.0062	0.0092	0.0034	0.0028	0.0042	0.0051
JX-7		0.0064	0.0089	0.0034	0.0031	0.0041	0.0048
JX-8		0.0059	0.0090	0.0032	0.0026	0.0040	0.0050
JX-9		0.0069	0.0095	0.0040	0.0029	0.0049	0.0046
JX-10		0.0065	0.0093	0.0038	0.0026	0.0047	0.0046
JX-11		0.0067	0.0103	0.0045	0.0022	0.0055	0.0048
JX-12		0.0083	0.0112	0.0049	0.0034	0.0060	0.0052
JX-13		0.0083	0.0117	0.0064	0.0019	0.0078	0.0039
JX-14		0.0094	0.0131	0.0072	0.0022	0.0088	0.0042
JX-15		0.0088	0.0125	0.0058	0.0030	0.0071	0.0053
JX-16		0.0099	0.0131	0.0070	0.0028	0.0086	0.0045

Low Pressure CO_2 Adsorption and Pore Distribution

Figure 4 shows the CO_2 adsorption isotherms of the dry and moist samples. The shape of the adsorption isotherms of the dry sample exhibits Type I, which likes that of the moist sample, suggesting both the dry and moist samples present abundant micropores. Furthermore, the CO_2 adsorption quantities of the moist sample are slightly less than those of the corresponding dry sample. Combined with **Figures 2**, **3**, it can be considered that the influence from the irreducible water on micropores is relatively less than that on non-micropores.

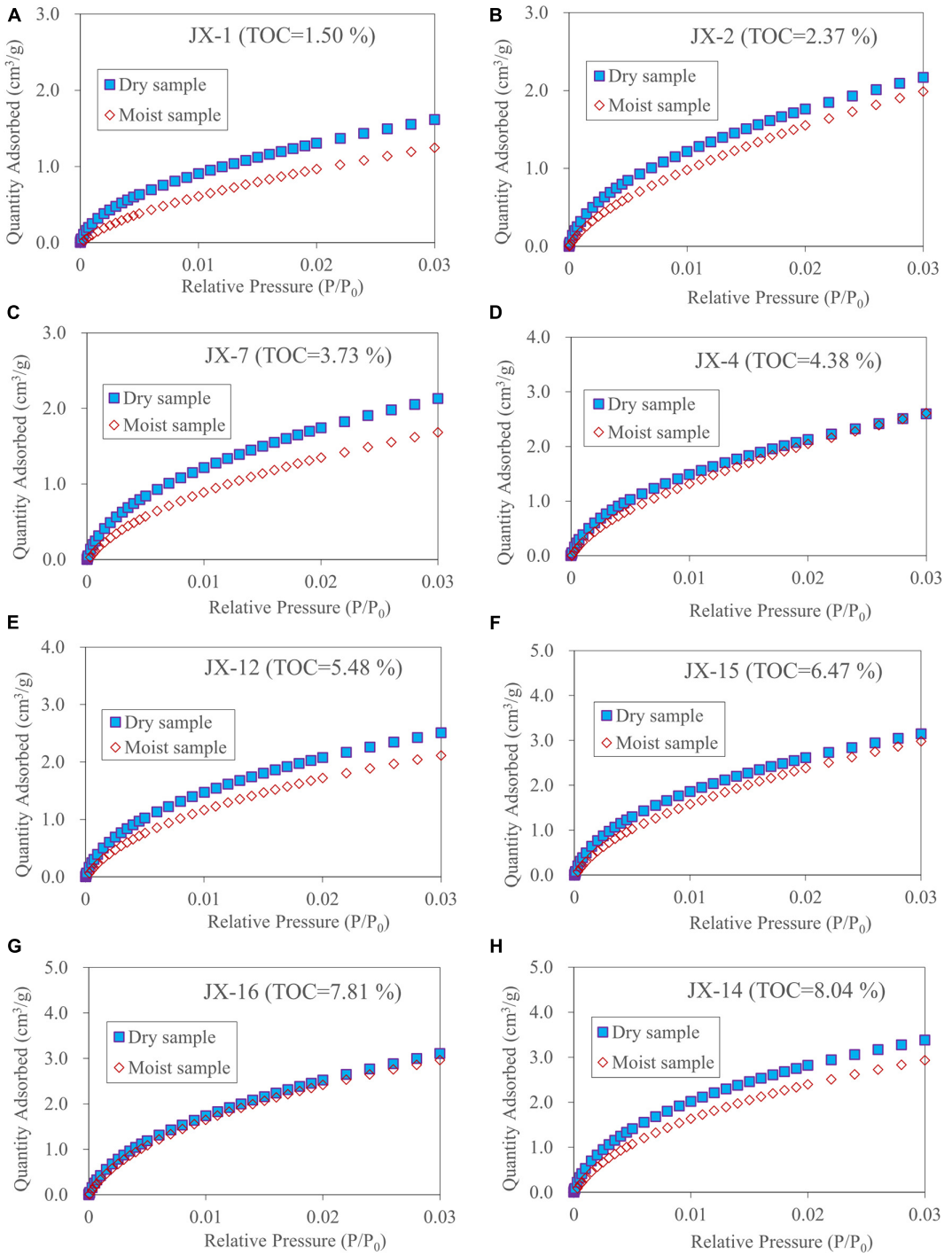

FIGURE 4 | Plots showing the low-pressure CO_2 adsorption isotherms of the selected 8 pairs (dry and moist) samples **(A–H)**. The adsorption isotherm shape and adsorption quantity of the moist sample are close to those of the corresponding dry sample, implying a small effect of irreducible water on micropores.

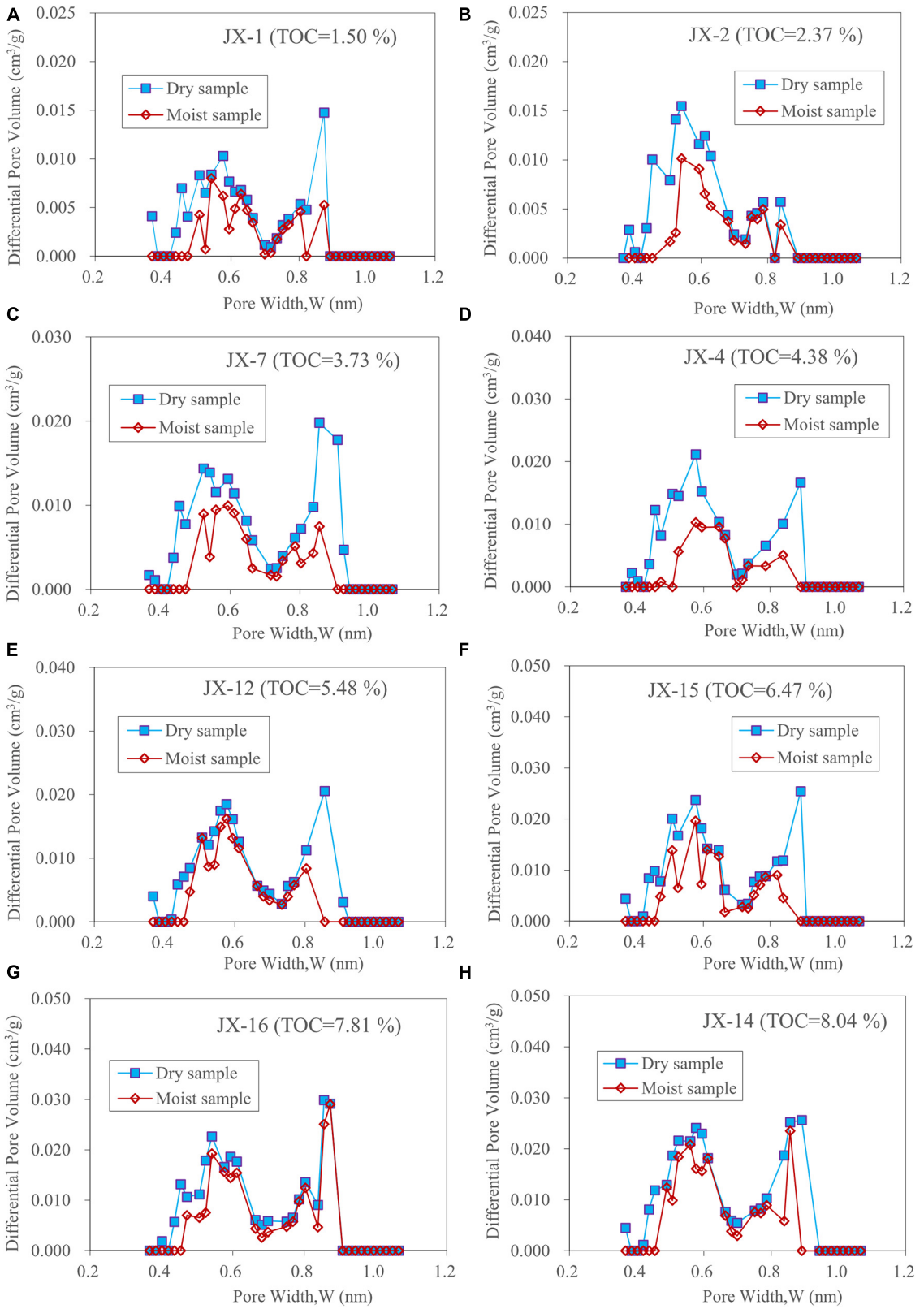

FIGURE 5 | Plots showing the pore-size distribution of the selected 8 pairs (dry and moist) samples based on the CO_2 adsorption analysis **(A–H)**. There is no distinct difference between the dry and moist samples.

The micropore volume (V_{mic}) of the dry sample is 0.0060–0.0131 cm^3/g (an average of 0.0099 cm^3/g), while the moist sample has a V_{mic} of 0.0039–0.0099 cm^3/g (an average of 0.0069 cm^3/g) (**Table 1**). Compared to the dry sample, the V_{mic} of the moist sample cut down about 30% on average, much less than the reduction extent of the S_{BET} (61% on average).

The micropore PSDs of the moist and dry samples were presented in **Figure 5**. It is clear that the dry sample displays a similar PSD to that of the moist sample, and both of them show bimodal characteristics. The main peaks of the PSD values of the dry sample occur at approximately 0.52–0.58 nm and 0.84–0.89 nm, respectively, and those of the moist sample occur at 0.54–0.59 nm and 0.79–0.87 nm, respectively. Moreover, the PSD value of the moist sample differs little from that of the corresponding dry sample, further illustrating that the influence of the irreducible water on micropores is less than that on non-micropores. It should be pointed out that the maximum equilibrium pressure (P/P_0) of the CO_2 adsorption experiment in the present study was about 0.03 (1 bar), which is significant lower than the CO_2 saturation pressure at 273 K (34.5 bar), hence the effective micropore range characterized by our CO_2 adsorption experiment is only 0.36–0.93 nm, while the larger micropores (0.93–2.00 nm) were not detected.

Controlling Factors of the Shale Pore Structure

Figure 6 displays the relationships of TOC and clay mineral contents with the S_{BET} (**Figures 6A,B**) and V_{mic} (**Figures 6C,D**). To avoid the impact of clay minerals on the pore structure parameters being masked by TOC, the S_{BET}, and V_{mic} were normalized to per unit TOC (1%), so they can directly reflect the contribution of clay minerals to the S_{BET} and V_{mic}. For the dry sample, the S_{BET} is positively linearly correlated with TOC, having a correlation coefficient(R^2)of 0.92 (**Figure 6A**), and a linear relationship also exists between the S_{BET} and the clay mineral (R^2 = 0.47) (**Figure 6B**). These results imply the S_{BET} of the dry sample is controlled by both TOC and clay minerals, and the former is the main controlling factor, which is because the clay minerals in the studied samples consist of chlorite and illite (Sun et al., 2020) with low specific surface areas (Gasparik et al., 2012; Ji et al., 2012; Liu et al., 2018).

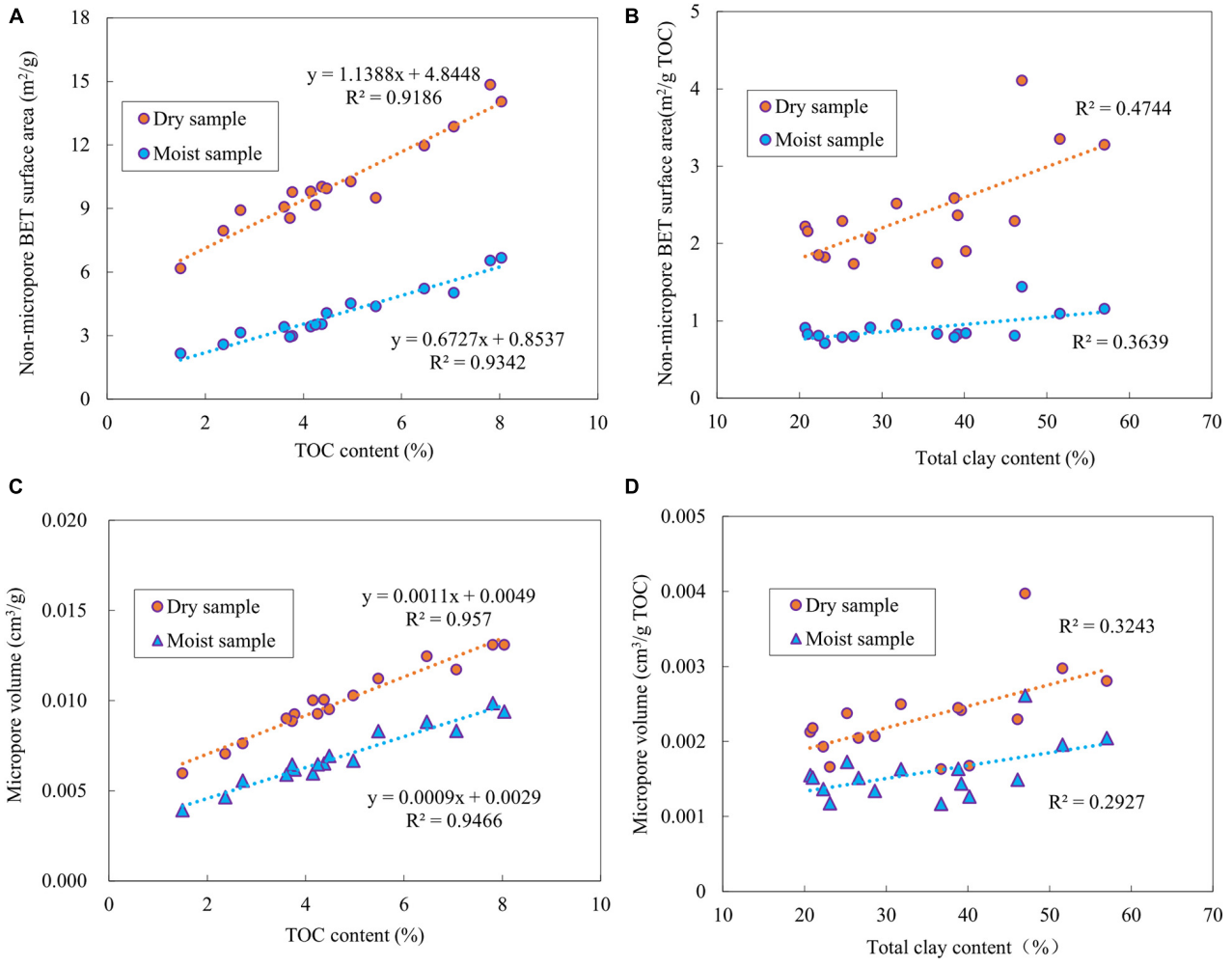

FIGURE 6 | The correlations of S_{BET} **(A,B)** and V_{mic} **(C,D)** with TOC and clay minerals.

For the moist sample, the S_{BET} still has an obvious positive linear correlation with TOC (R^2 = 0.93) (**Figure 6A**), however, its correlation with clay minerals decreases (the R^2 reduces from 0.47 to 0.36) (**Figure 6B**). Therefore, a conclusion can be made that the irreducible water shows a more obvious influence on the non-micropores of clay minerals compared with that of organic matter.

The V_{mic} of the dry sample shows a notable positive linear correlation with TOC (R^2 = 0.96) (**Figure 6C**), and a weak positive linear correlation with clay minerals (R^2 = 0.32) (**Figure 6D**). For the moist sample, the V_{mic} is still apparently correlated to TOC (R^2 = 0.95) (**Figure 6C**), while the weak linear relationship seems exist between the V_{mic} and clay minerals, but having a lower R^2 value (0.29) compared to

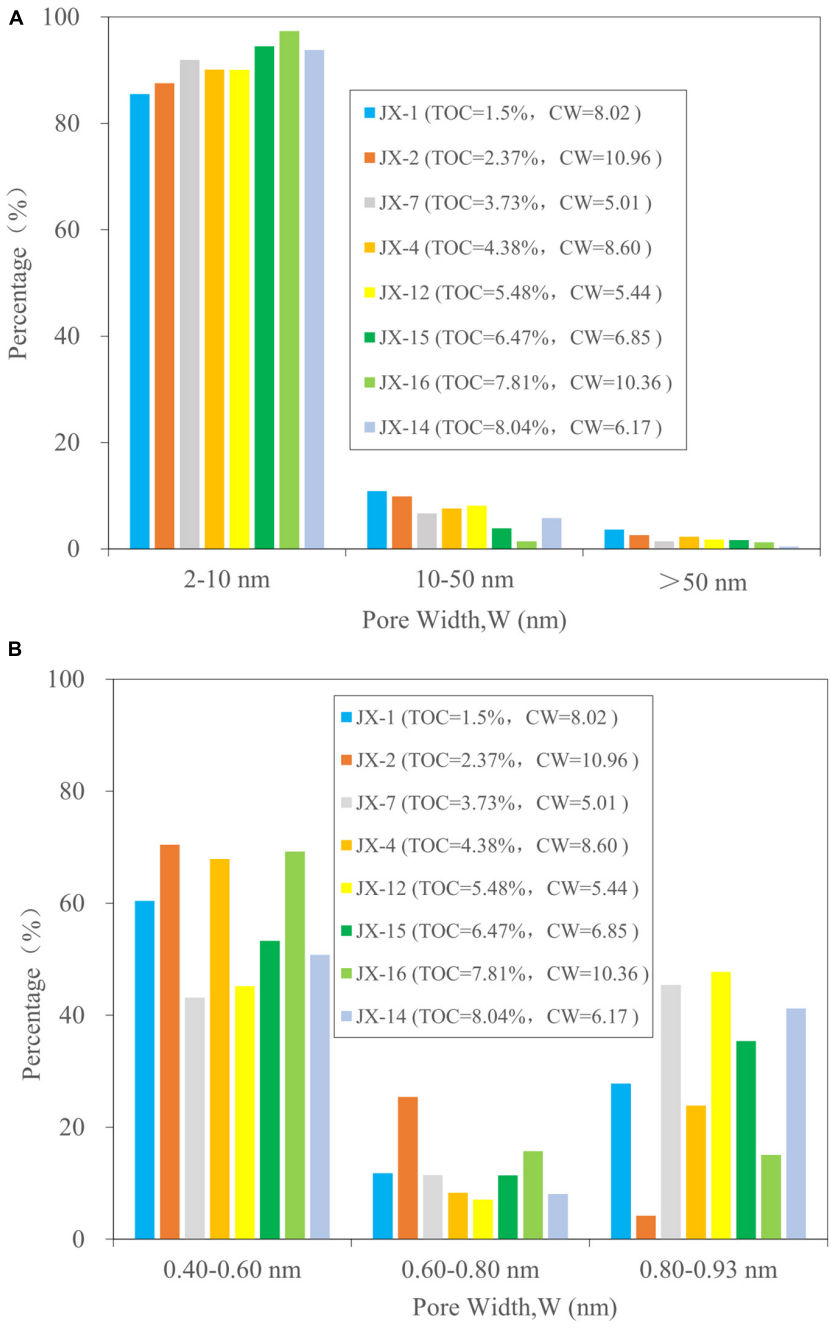

FIGURE 7 | Percentages occupied by irreducible water in the non-micropores **(A)** and micropores **(B)** for the selected 8 samples. It should be pointed out that pores smaller than 0.40 nm were not counted since the diameter of H_2O molecules is approximately 0.40 nm, and the percentages occupied by water in the pores of 0.93–2.00 nm were not observed since the effective micropore range is only 0.36–0.93 nm in the present study.

the dry sample (**Figure 6D**). Combined with **Figure 6B**, it is clear that the effect of the irreducible water on micropores is less significant than that on non-micropores. This is because clay minerals have a greater contribution to mesopores and macropores than that to the micropores (Chalmers and Bustin, 2008; Bakshi et al., 2017, 2018).

Occurrence of Irreducible Water in Shale Nanopores

Occurrence of Pore Water in Different Size Nanopores

Occurrence of the irreducible water in different size nanopores can be reflected by their volumes occupied by the water in different pore sizes relative to the total pore volume occupied by the water. For a specific shale sample, these volumes occupied by the water can be largely calculated by the difference between its dry and moist conditions. As seen from the results of the representative samples in **Figure 7**, in the range of non-micropores, the percentages occupied by the water decrease with increasing pore size. The water occurs mainly in the pores of 2–10 nm, and the occupation percentage varies from 85.50 to 97.34%. This is followed by the pores of 10–50 nm, with an occupation percentage range of 1.44–10.88%, while the percentage occupied by the water in macropores (>50 nm) is the lowest, which is 0.42–3.62% (**Figure 7A**). In the micropore range, the water occurs mostly in the pores of 0.40–0.60 nm and 0.80–0.93 nm, with average percentages of 57.54 and 30.07%, respectively. The occupied volume in pores between 0.60 and 0.80 nm is the least, with an average percentage of about 12.39% (**Figure 7B**). According to the above results, the irreducible water distributes mainly in mesopores of <10 nm and micropores of 0.40–0.60 nm and 0.80–0.93 nm.

Occurrence of Irreducible Water in OM and IM Nanopores

It is conventionally believed that inorganic matter (such as clay minerals) pores are hydrophilic and the organic pores are hydrophobic. However, a few recent papers document that water occurs widely in organic pores especially in high and over mature shales (Cheng et al., 2017, 2018). There

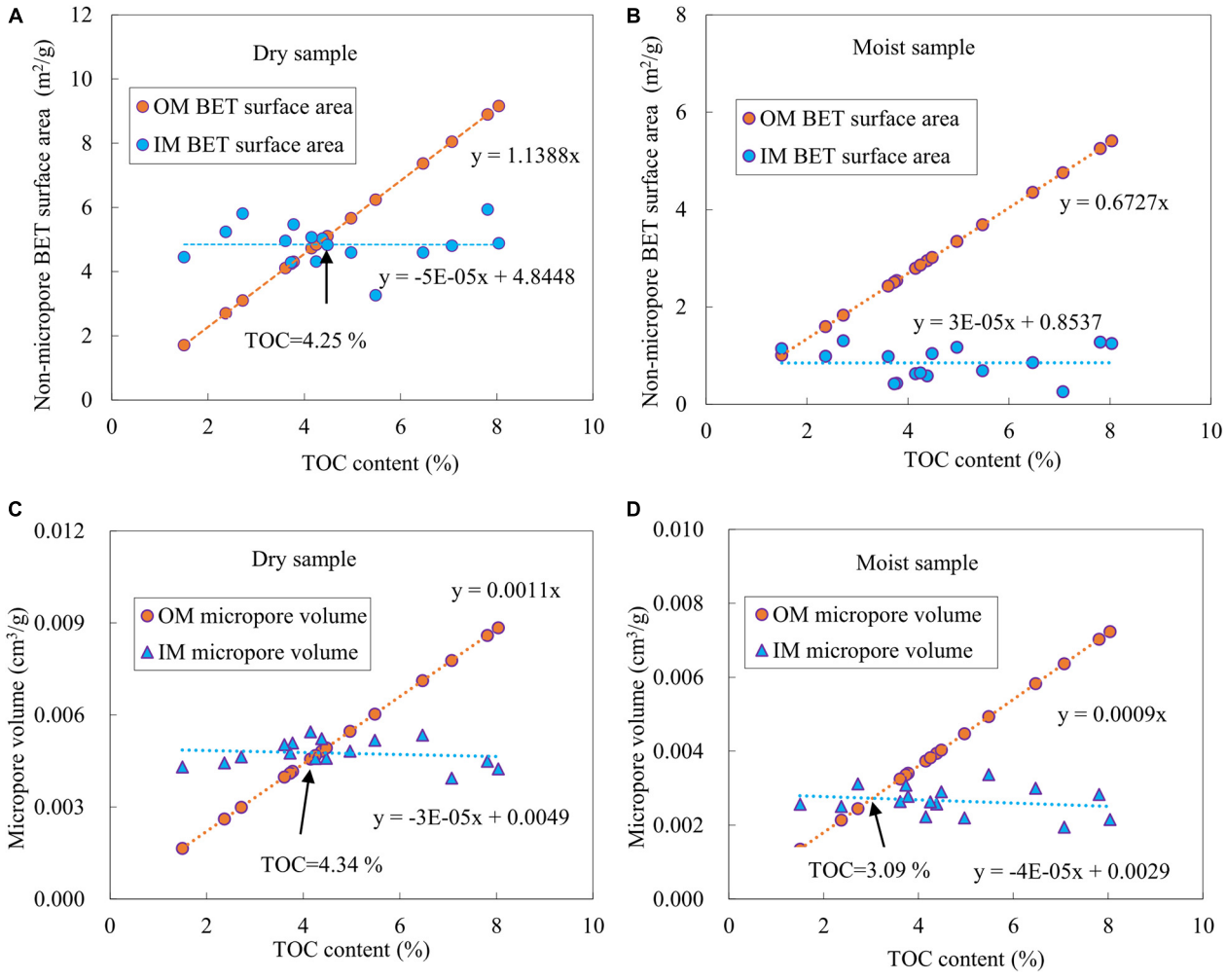

FIGURE 8 | The relationships of TOC with S_{BET-OM}, S_{BET-IM} **(A,B)**, and V_{mic-OM}, V_{mic-IM} **(C,D)** for the dry and moist samples. See details in text.

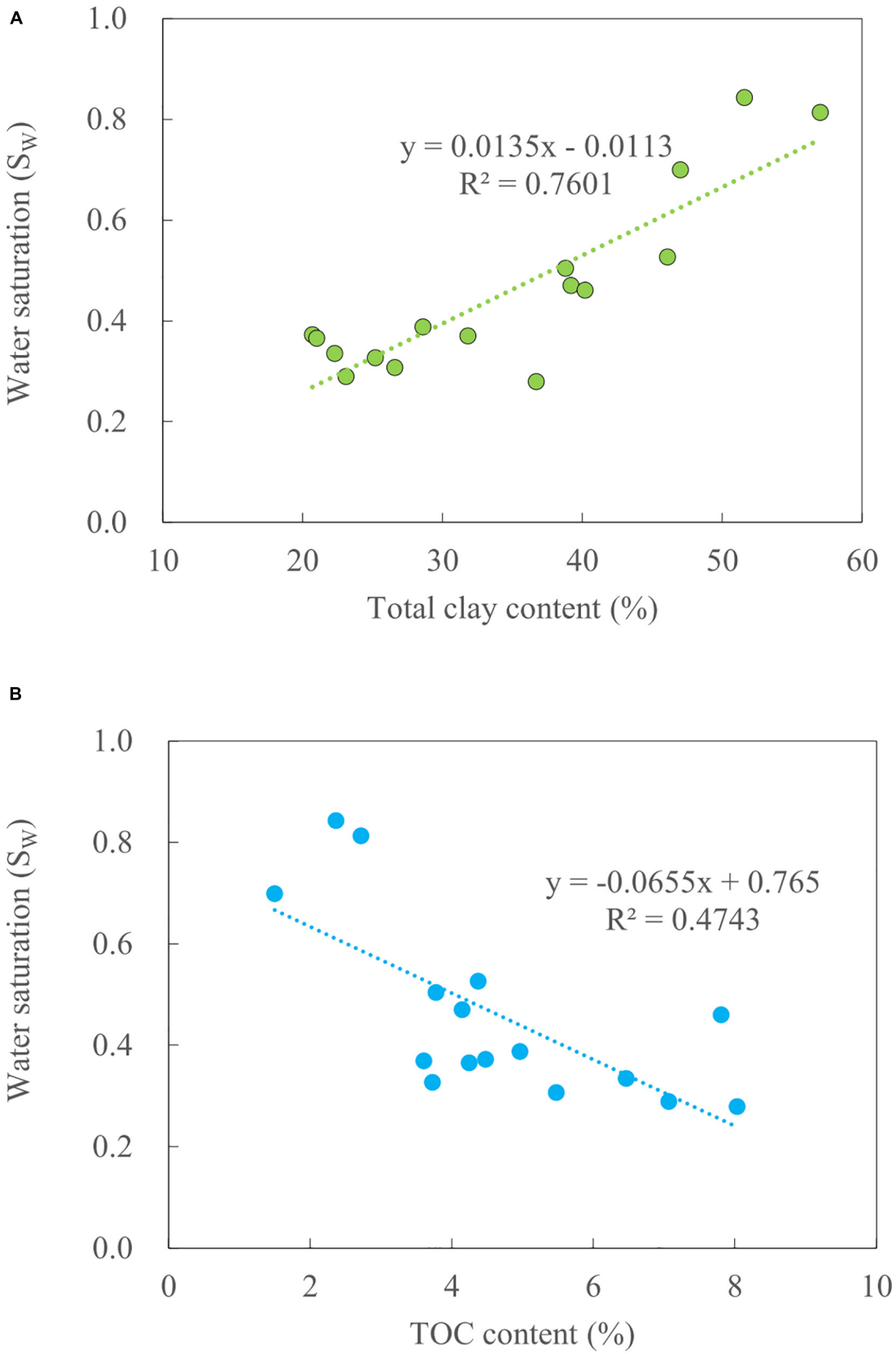

FIGURE 9 | Relationships of S_W with total clay mineral **(A)** and TOC contents **(B)**. See details in text.

are mainly two understandings on the mechanism of the hydrophilicity of organic pore. One is that some organic pore surfaces contain hydrophilic adsorption sites, such as oxygen-containing groups (Bahadur et al., 2017), water molecules can be adsorbed to the organic pore surfaces by forming hydrogen bonds with oxygen-containing groups. Moreover, even if the organic pore contains no containing-oxygen groups, it is inherently hydrophilic (Kozbial et al., 2014; Wei and Jia, 2015). Therefore, water can occupy both in shale inorganic and organic pores.

It is difficult to determine the OM and IM pores of shale samples precisely (Löhr et al., 2015). The means based on the linear positive relationship between TOC and total porosity for a set of shale samples is commonly adopted at present. According to this method, the OM porosity of a shale sample is the product of its TOC and the regressed line slope, and the difference between its total porosity and OM porosity is considered to be the IM porosity (Zhang et al., 2012; Tian et al., 2013, 2015; Hu et al., 2017; Sun et al., 2020). In the present study, the S_{BET} and V_{mic} of both the moist and dry samples exhibit strong positive linear correlations with TOC (R^2 values of 0.91–0.95) (**Figures 6A,C**). Therefore, the above linear regression method can be also applied to estimate the OM and IM pore structure parameters (S_{BET} and V_{mic}) of the studied samples, as reported by Cheng et al. (2018). The OM S_{BET} of a shale sample is the product of its TOC and the regressed line slope (**Figure 6A**), and the difference between its total S_{BET} and OM S_{BET} is considered to be the IM S_{BET}; the estimation of OM, IM V_{mic} is based on the same method.

The determined results indicate that the S_{BET-OM} (BET surface area of OM) and S_{BET-IM} (BET surface area of IM) values of the dry sample are 1.71–9.16 and 3.26–5.93 m^2/g, respectively (**Table 1**), and that the S_{BET-OM} is greater than the S_{BET-IM} for the samples with TOC contents >4.25% (**Figure 8A**). However, for the moist sample, the S_{BET-OM} and S_{BET-IM} values are 1.01–5.41 and 0.26–1.30 m^2/g, respectively (**Table 1**), and the S_{BET-OM} is greater than the S_{BET-IM} for all studied samples (**Figure 8B**).

The V_{mic-OM} (OM micropore volume) and V_{mic-IM} (IM micropore volume) values of the dry sample are 0.0017–0.0088 and 0.0039–0.0055 cm^3/g, respectively, and those of the moist sample are 0.0014–0.0072 and 0.0019–0.0034 cm^3/g, respectively (**Table 1**). Moreover, the V_{mic-OM} is greater than the V_{mic-IM} for the dry samples with TOC contents >4.34% (**Figure 8C**) and for the moist samples with TOC contents >3.09% (**Figure 8D**).

It was supposed that the difference of pore structure parameters between the moist and dry samples could present the space taken by the irreducible water. A further calculation based on the data in **Table 1** reports that the water occupies 82% of the S_{BET-IM} and 41% of the S_{BET-OM}, and 44% of the V_{mic-IM} and 18% of the V_{mic-OM} for the studied shale samples. Therefore, it is believed the irreducible water occurs preferentially in the IM pores, occupying a greater part of their non-micropore surface areas, and near a half of their micropore volumes, but its influence on the OM pores is limited, and most of the OM pores can still provide spaces for the storage of shale gas.

Gas-Bearing Property and Its Controlling Factors

Control of TOC on Gas-Bearing Property

The water saturation (S_W) of the studied shale samples varies greatly, ranging from 27.71 to 84.28%, with an average of 45.83% (**Table 3**). It is close to that of the Longmaxi shales from the wells Shao101 and YQ1 (>60%) outside the Sichuan Basin (Liu and Wang, 2013; Fang et al., 2014), and greater than that of the Longmaxi shales in the Sichuan Basin (10–45%) (Liu and Wang, 2013; Fang et al., 2014; Wei and Wei, 2014) and the gas shales in North America (10–35%) (Boyer et al., 2006; Bowker, 2007;

TABLE 3 | Calculated data of water saturation, and absorbed and free gas contents of the studied shale samples.

Sample ID	Depth (m)	TOC (%)	Water Saturation (%)	Gas content (m^3/t)			Percentage of adsorbed gas (%)	Percentage of free gas (%)
				Free gas	Adsorbed gas	Total gas [a]		
JX-1	362.61	1.50	69.88	0.13	0.75	0.88	85.63	14.37
JX-2	366.90	2.37	84.28	0.08	1.09	1.17	93.45	6.55
JX-3	370.04	2.72	81.28	0.11	1.10	1.21	91.22	8.78
JX-4	375.06	4.38	52.65	0.29	1.15	1.44	79.72	20.28
JX-5	376.78	4.15	46.92	0.35	1.26	1.61	78.12	21.88
JX-6	377.51	3.78	50.36	0.32	0.78	1.10	71.20	28.80
JX-7	381.70	3.73	32.62	0.40	0.77	1.17	66.06	33.94
JX-8	383.56	3.61	36.90	0.41	0.93	1.34	69.45	30.55
JX-9	385.26	4.48	37.17	0.36	0.90	1.26	71.72	28.28
JX-10	387.52	4.25	36.43	0.35	0.93	1.28	72.31	27.69
JX-11	388.89	4.97	38.69	0.40	0.88	1.28	68.56	31.44
JX-12	390.48	5.48	30.65	0.48	1.91	2.39	79.78	20.22
JX-13	391.92	7.07	28.70	0.54	1.52	2.06	73.75	26.25
JX-14	392.36	8.04	27.71	0.63	2.09	2.72	76.76	23.24
JX-15	393.03	6.47	33.28	0.54	2.17	2.71	80.10	19.90
JX-16	394.01	7.81	45.77	0.48	2.56	3.04	84.12	15.88

[a]: *Data cited from Sun et al. (2020).*

Cipolla et al., 2010; Wang, 2012). As illustrated in **Figure 9**, the S_W is positively related to the total clay minerals (R^2 = 0.76, **Figure 9A**), but presents a negative linear relationship to some extent with TOC (R^2 = 0.47, **Figure 9B**). This implies the irreducible water not only mostly occurs, but also has a greater saturation in the pores of clay minerals.

The calculated free gas (Q_{free}) and adsorbed gas (Q_{ads}) of the studied samples are presented in **Table 3**. The Q_{free} is 0.08–0.63 m^3/t and averages 0.37 m^3/t, while the Q_{ads} is 0.75–2.56 m^3/t and averages 1.30 m^3/t, accounting for 66.06–93.45% of the total gas (77.62% on average). Pan et al. (2016) reported a GIP model based on a Longmaxi shale (TOC = 3.98%) from the Pengshui Block, South China. According to their GIP model, at the depth of 400 m, the Q_{ads} is about 88% of the GIP content without taking into account the influence of the pore water. For the well XK2 in the present study, the adsorbed gas percentage of the shale samples with TOC≈4% is in the range of 70–80%, indicating the irreducible water should reduce the Q_{ads} to some extent.

Figure 10 presents the positive linear relationships of TOC with the Q_{free} and Q_{ads} for the studied samples, with R^2 values of 0.67 and 0.80, respectively. The correlation coefficient between the TOC and Q_{ads} is significantly lower than that between the TOC and methane adsorption capacity reported by Pan et al. (2016) on the basis of dry Longmaxi samples (R^2 : 0.96–0.97), and similar to that proposed by Chalmers and Bustin (2008) based on the moisture-equilibrated shale samples (R^2 = 0.67). Therefore, compared with the dry shale samples, not only the actual adsorption capacity of the moist sample is reduced, but its correlation with TOC is also decreased, and the high-pressure CH_4 adsorption experiment results conducted on dry shale samples can not be directly applied to the geological adsorption gas evaluation.

Based on the linear regression equations presented in **Figure 10**, the Q_{ads} and Q_{free} in OM and IM pores for the studied samples were also estimated by a similar method discussed in section "Occurrence of Irreducible Water in OM and IM

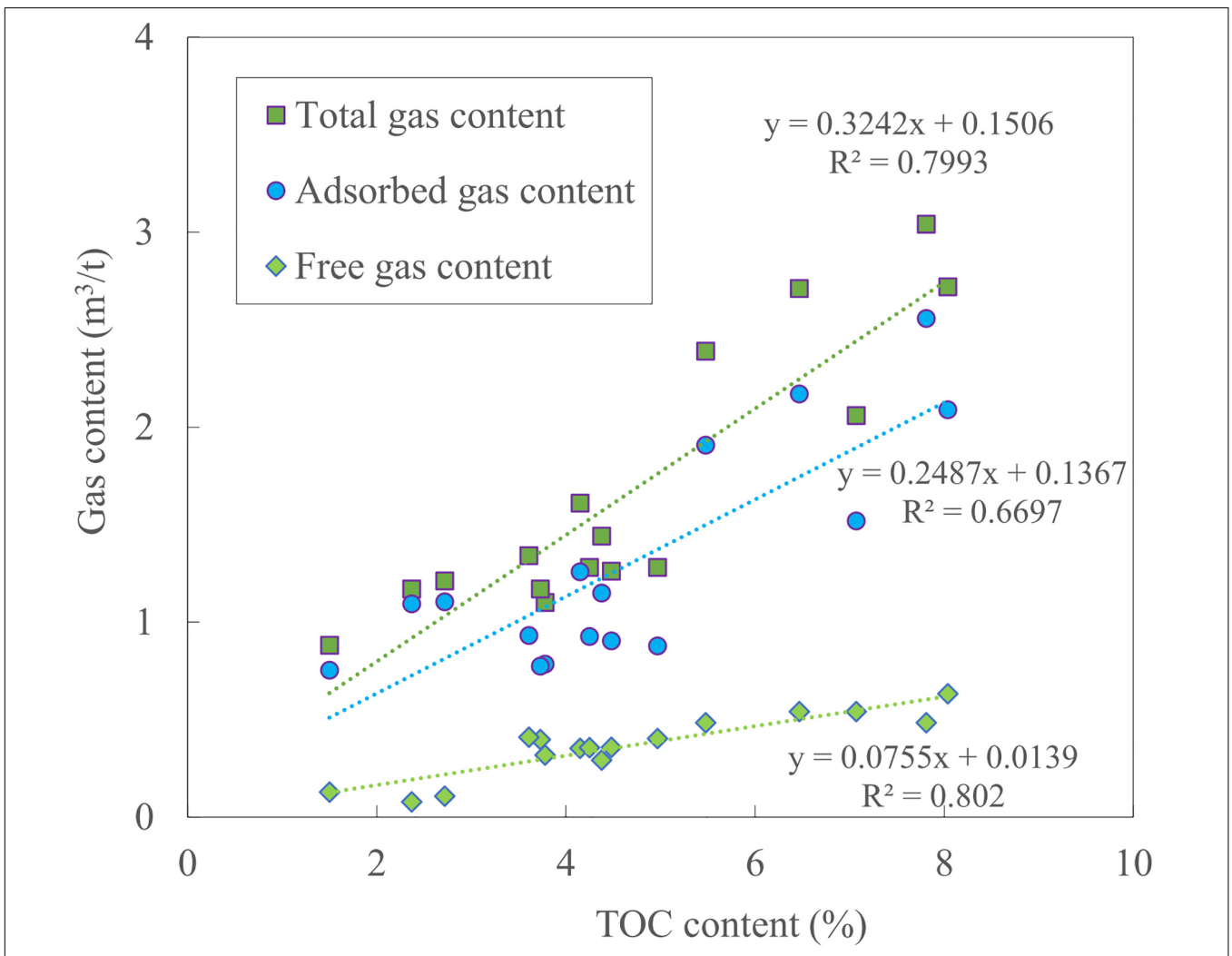

FIGURE 10 | Correlations of TOC with free, adsorbed, and total gasses for the studied shale samples. Their positive correlations indicate that TOC directly controls the gas-bearing property, so the adsorbed and free gas contents in the OM and IM pores could be determined from their linear regression equations.

Nanopores". The calculated Q_{ads} and Q_{free} in OM pores are 1.16 and 0.35 m^3/t on averages, respectively, accounting for 89% of the total absorbed gas and 95% of the total free gas, and those in IM pores are 0.14 and 0.02 m^3/t on averages, respectively, accounting for 11% of the total absorbed gas and 5% of the total free gas. From those results, a conclusion could be draw that the shale gas stored mostly in OM pores, and IM pores contain a little gas due to the effect of irreducible water.

Relationship Between Irreducible Water and Gas-Bearing Property

Figure 11 presents the relationships of the GBP (presented by Q_{total}, Q_{ads}, and Q_{free}) with the water content (**Figures 11A,B**) and water saturation (S_W) (**Figures 11C,D**). The Q_{ads} shows a rapid drop and then a slow decrease (**Figure 11A**) with increasing the water content. Since the shale gas of the studied samples is mostly in the adsorbed state, the trend of the Q_{total} follows that of the Q_{ads} (**Figure 11B**). In **Figure 11A**, the data of Lower Cretaceous shales from British Columbia, Canada reported by Ross and Bustin (2009) were included, and the two sets of data seem keeping the same trend with increasing water content.

The relationships of the S_W with the Q_{total}, Q_{ads}, and Q_{free} follow similar trends as described above. As the S_W is less than 40%, the Q_{ads} and Q_{tota} decrease rapidly with increasing S_W (**Figures 11C,D**), but these trends tend to slow with further increasing S_W (**Figures 11C,D**). This result is in agreement with that of the Longmaxi shale in the Weiyuan-Changning Block, Sichuan Basin reported by Hu et al. (2018). They revealed that the Q_{ads} declined significantly in the S_W range of <30%, while it decreased slowly when the S_W increased from 30 to 50%.

The influences of the irreducible water on the GBP can be explained by its occurrence characteristics in different nanopores. According to our results, the irreducible water occurs mostly in non-micropores, especially the non-micropores of clay minerals, with a great reduction of their non-micropore surface areas. Although OM pores also contain a small amount of irreducible water, the reductions of their non-micropore surface areas and micropore volumes are limited due to their hydrophobic nature. Therefore, the irreducible water mainly affects the adsorption capacity of IM pores, and OM pores contribute mostly to the shale adsorption capacity. In conditions of low S_W, the water preferentially occupies the pores in clay minerals, significantly decreases their adsorption capacities, causing the adsorbed gas decrease rapidly with increasing the water content or S_W. With the further increase of S_W, the reduction of adsorption capacity is still mainly from clay minerals even when the S_W reaches a high level, while the OM pores still have a certain adsorption capacity. This is why the absorbed gas content decreases slowly

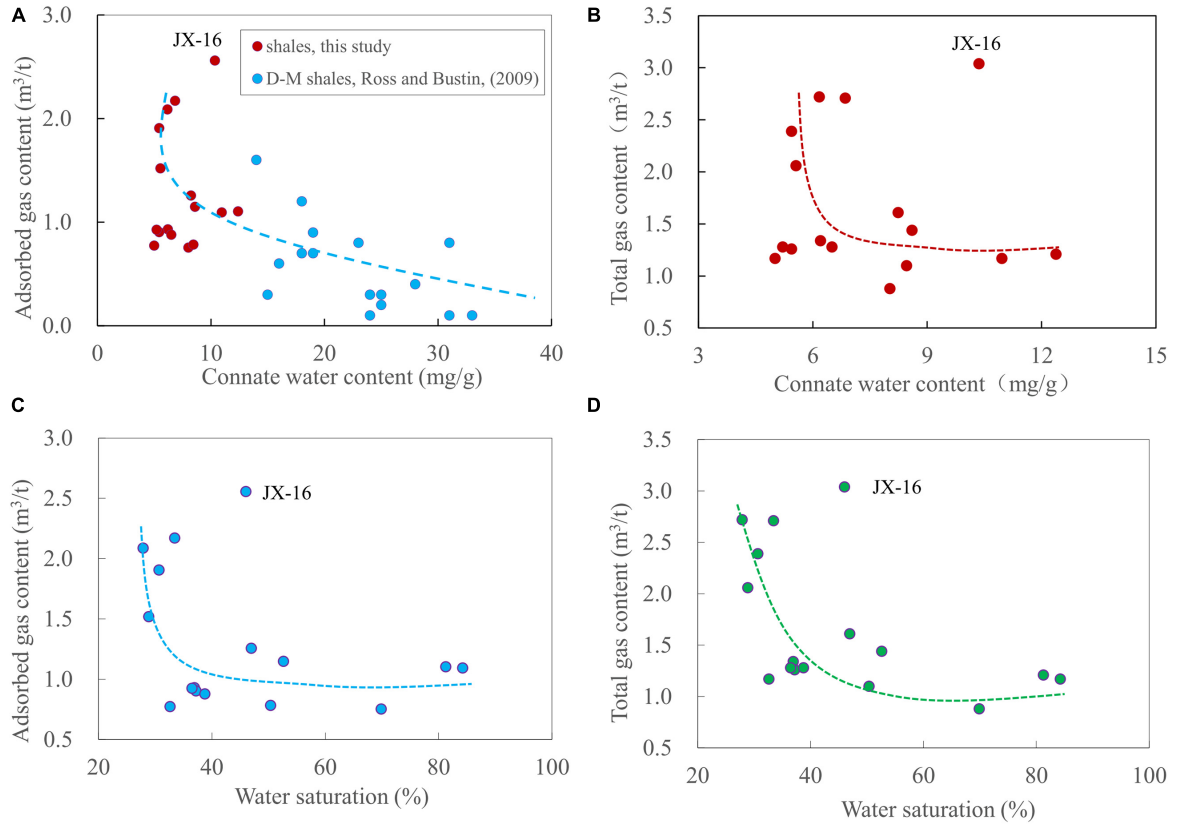

FIGURE 11 | Plots showing the relationships of irreducible water contents with the Q_{ads} **(A)** and Q_{total} **(B)**, and the correlations of the S_W with the Q_{ads} **(C)** and Q_{total} **(D)**. The D-M shale data were measured at 30°C (Ross and Bustin, 2009). It should be noted that, since the sample JX-16 is away from the trend of the regression line, the regression line have not included the data of this sample.

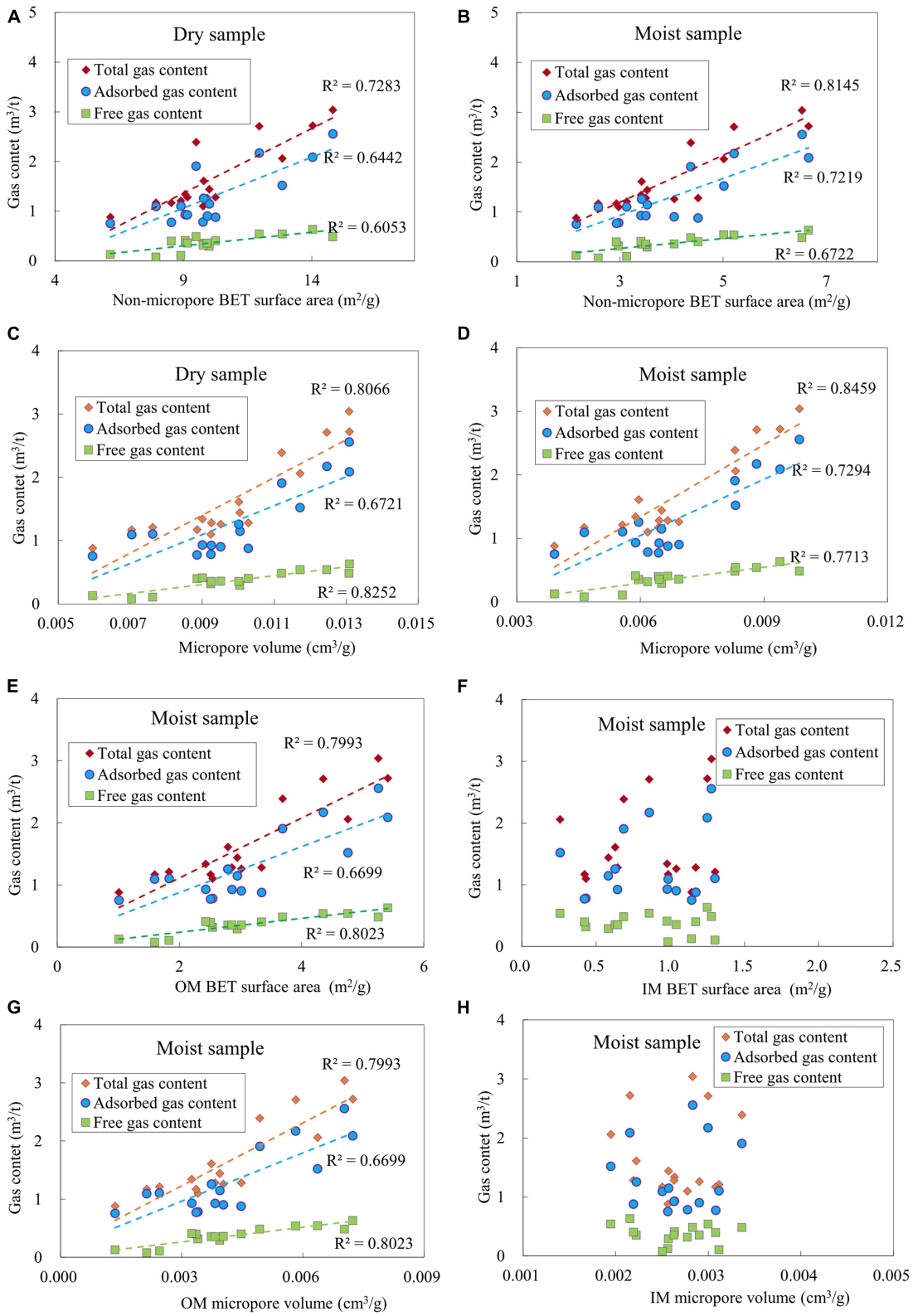

FIGURE 12 | Plots showing the correlations of the contents of absorbed, free and total gasses with the BET surface areas **(A,B)** and micropore volumes **(C,D)** for the studied shale samples, and the relationships of the contents of absorbed, free and total gasses with the OM, IM BET surface areas **(E,F)** and OM, IM micropore volumes **(G,H)** for the moist shale samples. **(A–D)** their correlations of the moist sample are obviously better than those of the dry sample; **(E–H)** the gas-bearing property shows positively relationships with the OM pore structure parameters, while displays no correlations with the IM pore structure parameters.

with further increasing water content or S_W as it exceeds a certain amount.

Figures 12A–D displays the correlations between the pore structure parameters (S_{BET} and V_{mic}) and GBP (Q_{total}, Q_{ads}, and Q_{free}) for both the moist and dry samples. It is clear that their correlations are better for the moist sample than those for the dry sample. **Figures 12E–H** further represents the relationships of the Q_{total}, Q_{ads}, and Q_{free} with either OM or IM pore structure parameters for the moist sample. They display obvious positive linear correlations with the OM pores, but reveal unclear correlations with the IM pores. Chalmers and Bustin (2008) made an explanation for a high CH_4 adsorption capacity of the moisture-equilibrated shale samples. They claimed gas and water took different sorption sites in shales. The present study results further demonstrate that the OM pores provide the most sorption sites for shale gas and control the Q_{ads}, affecting the GBP.

CONCLUSION

The pore structure, irreducible water occurrence characteristics, gas-bearing property, and their relationships of the shallow Longmaxi shales from the well XK2 were investigated, and the main conclusions are as follows:

- The micropore, mesopore, and macropore of the dry and moist samples are all well developed. Compared with the dry sample, the non-micropore BET surface area and micropore volume of the moist sample are reduced by 61 and 30% on averages, respectively.
- The irreducible water occurs mainly in IM pores, especially smaller mesopores (2–10 nm). The water occupies averagely 82 and 41% of the inorganic and organic non-micropore BET surface areas, respectively, and 44 and 18% of the inorganic and organic micropore volumes, respectively.
- The irreducible water significantly reduces the adsorbed gas content in IM pores, but its influence on OM pores is limited, and the OM pores store approximately 89% of the adsorbed gas and 95% of the free gas.

DATA AVAILABILITY STATEMENT

The original contributions presented in the study are included in the article/supplementary material, further inquiries can be directed to the corresponding author.

AUTHOR CONTRIBUTIONS

JS conducted the experimental work, analyzed the data, and wrote the manuscript. XMX designed the study and reviewed the manuscript. QW conducted the experimental work. PC analyzed the data. HT reviewed the manuscript. All authors contributed to the article and approved the submitted version.

FUNDING

This study was jointly supported by the National Natural Science Foundation of China (U1810201, U19B6003-03, 4203000087, and 41925014), and Natural Science Foundation of Guangdong Province (2016A030310119).

ACKNOWLEDGMENTS

Dr. Li Guanfang from Institute of Geology and Geophysics, Chinese Academy of Sciences, is thanked for helping us to collect the shale samples.

REFERENCES

Aringhieri, R. (2004). Nanoporosity characteristics of some natural clay minerals and soils. *Clay. Miner.* 52, 700–704. doi: 10.1346/CCMN.2004.0520604

Bahadur, J., Contescu, C. I., Rai, D. K., Gallego, N. C., and Melnichenko, Y. B. (2017). Clustering of water molecules in ultra-microporous carbon: in-situ small-angle neutron scattering. *Carbon* 111, 681–688. doi: 10.1016/j.carbon.2016.10.040

Bai, J. J., Kang, Y. L., Chen, M. J., Chen, Z. X., You, L. J., Li, X. C., et al. (2020). Impact of surface chemistry and pore structure on water vapor adsorption behavior in gas shale. *Chem. Eng. J.* 402:126238. doi: 10.1016/j.cej.2020.126238

Bakshi, T., Prusty, B. K., Pathak, K., Nayak, B. R., Mani, D., and Pal, S. K. (2017). Source rock characteristics and pore characterization of Indian shale. *J. Nat. Gas Sci. Eng.* 45, 761–770. doi: 10.1016/j.jngse.2017.06.010

Bakshi, T., Prusty, B. K., Pathak, K., and Pal, S. K. (2018). Pore characteristics of Damodar valley shale and their effect on gas storage potential. *J. Nat. Gas Sci. Eng.* 162, 725–735. doi: 10.1016/j.petrol.2017.10.091

Barrett, E. P., Joyner, L. G., and Halenda, P. P. (1951). The determination of pore volume and area distribution in porous substances. I: computations from nitrogen isotherms. *J. Am. Chem. Soc.* 73, 373–380. doi: 10.1021/ja01145a126

Bhowrnik, S., and Dutta, P. (2019). A study on the effect of gas shale composition and pore structure on methane sorption. *J. Nat. Gas Sci. Eng.* 62, 144–156. doi: 10.1016/j.jngse.2018.12.009

Bowker, K. A. (2007). Barnett shale gas production, fort worth basin: issues and discussion. *AAPG Bull.* 91, 523–533. doi: 10.1306/06190606018

Boyer, C., Kieschnick, J., Suarez, R. R., Lewis, R. E., and Waters, G. (2006). Producing gas from its source. *Oilfield Rev.* 18, 36–49.

Brunauer, S., Deming, L. S., Deming, W. E., and Teller, E. (1938). Adsorption of gases inmultimolecular layers. *J. Am. Chem. Soc.* 60, 309–319.

Brunauer, S., Deming, L. S., Deming, W. E., and Teller, E. (1940). On a theory of the van der waals adsorption of gases. *J. Am. Chem. Soc.* 62, 1723–1732. doi: 10.1021/ja01864a025

Bustin, R. M., Bustin, A., Chalmers, D. R. G., Murthy, V., Laxmi, C., and Cui, X. (2008). *Shale Gas Opportunities and Challenges*. San Antonio, TX: AAPG Annual Convention.

Chalmers, G. R. L., and Bustin, R. M. (2007). The organic matter distribution and methane capacity of the lower cretaceous strata of Northeastern British Columbia. *Int. J. Coal Geol.* 70, 223–239. doi: 10.1016/j.coal.2006.05.001

Chalmers, G. R. L., and Bustin, R. M. (2008). Lower Cretaceous gas shales in northeastern British Columbia, part I: geological controls on methane adsorption capacity. *Bull. Can. Pet. Geol.* 56, 1–21. doi: 10.2113/gscpgbull.56.1.1

Chareonsuppanimit, P., Mohammad, S. A., Robinson, R. L., and Gasem, K. A. M. (2012). High-pressure adsorption of gases on shales: measurements and modeling. *Int. J. Coal Geol.* 95, 34–46. doi: 10.1016/j.coal.2012.02.005

Charriere, D., and Philippe, B. P. (2010). Water sorption on coals. *J. Colloid. Interface. Sci.* 344, 460–467. doi: 10.1016/j.jcis.2009.11.064

Chen, S. B., Han, Y. F., Fu, C. Q., Zhang, H., Zhu, Y. M., and Zuo, Z. X. (2016). Micro and nano-size pores of clay minerals in shale reservoirs: implication for

the accumulation of shale gas. *Sedim. Geol.* 342, 180–190. doi: 10.1016/j.sedgeo.2016.06.022

Chen, S. B., Zuo, Z. X., Moore, T. A., Han, Y. F., and Uwamahoro, C. (2018). Nanoscale pore changes in a marine shale: a case study using pyrolysis experiments and nitrogen adsorption. *Energy Fuels* 32, 9020–9032. doi: 10.1021/acs.energyfuels.8b01405

Cheng, P., Tian, H., Xiao, X. M., Gai, H. F., Li, T. F., and Wang, X. (2017). Water distribution in overmature organic-rich shales: Implications from water adsorption experiments. *Energy Fuels* 31, 13120–13132. doi: 10.1021/acs.energyfuels.7b01531

Cheng, P., Xiao, X. M., Tian, H., and Wang, X. (2018). Water content and equilibrium saturation and their influencing factors of the lower paleozoic overmature organic-rich shales in the upper yangtze region of Southern China. *Energy Fuels* 32, 11452–11466. doi: 10.1021/acs.energyfuels.8b03011

Cipolla, C. L., Lolon, E. P., Erdle, J. C., and Rubin, B. (2010). Reservoir Modeling in Shale-Gas Reservoirs. *Paper Presented at the SPE Eastern Regional Meeting*. SPE-125530-MS, Charleston, WV, doi: 10.2118/125530-MS

Clarkson, C. R., and Bustin, R. M. (1999). The effect of pore structure and gaspressure upon the transport properties of coal: a laboratory andmodeling study 1: isotherms and pore volume distributions. *Fuel* 78, 1333–1344. doi: 10.1016/S0016-2361(99)00056-3

Curtis, J. B. (2002). Fractured shale-gas systems. *AAPG Bull.* 86, 1921–1938. doi: 10.1306/61EEDDBE-173E-11D7-8645000102C1865D

Curtis, M. E., Ambrose, R. J., Sondergeld, C. H., and Rai, C. S. (2010). "Structural characterization of gas shales on the micro-and nano-scales," in *Proceedings of the Canadian Unconventional Resources and International Petroleum Conference*, Calgary, ALB, 19–21. doi: 10.2118/137693-MS

Curtis, M. E., Ambrose, R. J., Sondergeld, C. H., and Rai, C. S. (2011). "Transmission and scanning electron microscopy investigation of pore connectivity of gas shales on the nanoscale," in *Proceedings of the North American Unconventional Gas Conference and Exhibition*, Woodlands, TX, 14–16. doi: 10.2118/144391-MS

De, B. J. H. (1958). "The shape of capillaries," in *The Structure and Properties of Porous Materials*, eds D. H. Evertt and F. S. Stone (London: Butterworths), 68–94.

Dewhurst, D. N., Aplin, A. C., and Sarda, J. P. (1999). Influence of clay fractionon pore-scale properties and hydraulic conductivity of experimentally compacted mudstones. *J. Geophys. Res. Atmos.* 104, 29261–29274. doi: 10.1029/1999JB900276

Dong, D. Z., Gao, S. K., Huang, J. L., Guan, Q. Z., Wang, S. F., and Wang, Y. M. (2014). A discussion on the shale gas exploration and development prospect in the Sichuan Basin. *Nat. Gas. Ind.* 34, 1–15. doi: 10.1016/j.ngib.2015.02.002

Dubinin, M. M. (1989). Fundamentals of the theory of adsorption inmicropores of carbon adsorbents: characteristics of their adsorption properties and microporous structures. *Carbon* 27, 457–467. doi: 10.1016/0008-6223(89)90078-X

Fang, Z. H., Huang, Z. L., Wang, Q. Z., Zheng, D. W., and Liu, H. L. (2014). Cause and significance of the ultra-low water saturation in gas-enriched shale reservoir. *Nat. Gas. Geosci.* 25, 471–476. doi: 10.11764/j.issn.1672-1926.2014.03.0471

Fu, C. Q. (2017). Study on shale reservoir characteristics and shale gas enrichment of Wufeng Formation and Longmaxi Formation in southeast Chongqing. *Chin. Uni. Min. Technol.* ***Q,

Gasparik, M., Bertier, P., Gensterblum, Y., Ghanizadeh, A., Krooss, B. M., and Littke, R. (2014). Geological controls on the methane storage capacity in organic-rich shales. *Int. J. Coal. Geol.* 123, 34–51. doi: 10.1016/j.coal.2013.06.010

Gasparik, M., Ghanizadeh, A., Bertier, P., Gensterblum, Y., Bouw, S., and Krooss, B. M. (2012). High-pressure methane sorption isotherms of black shales from The Netherlands. *Energy Fuel* 26, 4995–5004. doi: 10.1021/ef300405g

Gou, Q. Y., Xu, S., Hao, F., Zhang, B. Q., Shu, Z. G., Yang, F., et al. (2020). Quantitative calculated shale gas contents with different lithofacies: a case study of Fuling gas shale, Sichuan Basin, China. *J. Nat. Gas Sci. Eng.* 76:103222. doi: 10.1016/j.jngse.2020.103222

Gregg, S. J., and Sing, K. S. W. (1982). *Adsorption, Surface Area and Porosity*, 2nd Edn. New York, NY: Academic Press, 312. doi: 10.1524/zpch.1969.63.1_4.220

Guo, T. L. (2016). Discovery and characteristics of the fuling shale gas field and its enlightenment and thinking. *Earth Sci. Front.* 23, 29–43.

Hou, H. H., Shao, L. Y., Li, Y. H., Li, Z., Zhang, W. L., and Wen, H. J. (2018). The pore structure and fractal characteristics of shales with low thermal maturity from the Yuqia Coalfield, northern Qaidam Basin, North Western China. *Front. Earth Sci.* 12:148–159. doi: 10.1007/s11707-016-0617-y

Hu, C. L., Zhang, Y. F., Wang, Z. F., Li, J. J., and Zhang, H. B. (2014). Shale features and exploration prospect of shale gas in longmaxi formation in Northern Guizhou. *Special Oil Gas Reserv.* 21, 44–47.

Hu, H. Y., Hao, F., Lin, J. F., Lu, Y. C., Ma, Y. Q., and Li, Q. (2017). Organic matter-hosted pore system in theWufeng-Longmaxi (O_3w-S_1l) shale, Jiaoshiba area, Eastern Sichuan Basin, China. *Int. J. Coal. Geol.* 173, 40–50. doi: 10.1016/j.coal.2017.02.004

Hu, Z. M., Duan, X. G., He, Y. B., Wu, J. F., Chang, J., Liu, L., et al. (2018). Influence of reservoir primary water on shale gas occurrence and flow capacity. *Nat. Gas. Ind.* 38, 44–51.

Jarvie, D. M., Hill, R. J., Ruble, T. E., and Pollastro, R. M. (2007). Unconventional shale-gas systems: the Mississippian Barnett shale of north-central texas as one model for thermogenic shale-gas assessment. *AAPG Bull.* 91, 475–499. doi: 10.1306/12190606068

Ji, L. M., Zhang, T. W., Milliken, K. L., Qu, J. L., and Zhang, X. L. (2012). Experimental investigation of main controls to methane adsorption in clay-rich rocks. *Appl. Geochem.* 27, 2533–2545. doi: 10.1016/j.apgeochem.2012.08.027

Klewiah, I., Berawala, D. S., Walker, H. C. A., Andersen, P. O., and Nadeau, P. H. (2019). Review of experimental sorption studies of CO_2 and CH_4 in shales. *J. Nat. Gas Sci. Eng.* 73:103045. doi: 10.1016/j.jngse.2019.103045

Kozbial, A., Li, Z. T., Sun, J. N., Gong, X., Zhou, F., Wang, Y. J., et al. (2014). Understanding the intrinsic water wettability of graphite. *Carbon* 74, 218–225. doi: 10.1016/j.carbon.2014.03.025

Li, H. X., and Zhang, Y. W. (2015). Global shale gas exploration and development today and China's shale gas development strategy. *Sino Glob. Energy* 20, 22–29.

Li, J., Li, X. F., Wang, X. Z., Li, Y. Y., Shi, J. T., Feng, D., et al. (2016a). A quantitative model to determine water-saturation distribution characteristics inside shale inorganic pores. *Acta. Pet. Sin.* 37, 903–913. doi: 10.7623/syxb201607009

Li, J., Li, X. F., Wang, X. Z., Li, Y. Y., Wu, K. L., Shi, J. T., et al. (2016b). Water distribution characteristic and effect on methane adsorption capacity in shale clay. *Int. J. Coal. Geol.* 159, 135–154. doi: 10.1016/j.coal.2016.03.012

Li, J. L., Xie, R. Y., You, J. J., and Wang, L. F. (2012). Reservoir forming condition and exploration prospect of shale-gas in Guizhou qianbei area. *China Min. Mag.* 21, 55–59.

Li, Q. W., Pang, X. Q., Tang, L., Chen, G., Shao, X. H., Jia, N., et al. (2018). Occurrence features and gas content analysis of marine and continental shales: a comparative study of Longmaxi Formation and Yanchang Formation. *J. Nat. Gas Sci. Eng.* 56, 504–522. doi: 10.1016/j.jngse.2018.06.019

Li, S. (2018). "Evaluation of shallow shale gas potential in T Structure of Zhaotong demonstration area. Natural gas professional committee of the China petroleum society," in *Proceedings of the 2018 National Natural Gas Academic Annual Conference (03 Unconventional Gas Reservoirs)*, 153–159. doi: 10.26914/c.cnkihy.2018.002595

Liang, D. G., Guo, T. L., Chen, J. P., Bian, L. Z., and Zhao, Z. (2008). Some progresses on studies of hydrocarbon generation and accumulation in marine sedimentary regions, Southern China (Part 1): distribution of four suits of regional marine source rocks. *Mar. Ori. Pet. Geol.* 13, 1–16.

Liang, X., Xu, Z. Y., Zhang, Z., Wang, W. X., Zhang, J. H., Lu, H. L., et al. (2020). Breakthrough of shallow shale gas exploration in Taiyang anticline area and its significance for resource development in Zhaotong, Yunnan province, China. *Pet. Exp. Dev* 47, 1–18.

Lin, W., Mastalerz, M., Schimmelmann, A., and Chen, Y. Y. (2014). Influence of soxhlet-extractable bitumen and oil on porosity in thermally maturing organic-rich shales. *Int. J. Coal. Geol.* 132, 38–50. doi: 10.1016/j.coal.2014.08.003

Liu, H. L., and Wang, H. Y. (2013). Ultra-low water saturation characteristics and thei dentification of over pressured play fairways of marine shales in South China. *Nat. Gas. Ind.* 33, 140–144. doi: 10.3787/j.issn.1000-0976.2013.07.025

Liu, X., Zhang, J. C., Liu, Y., Huang, H., and Liu, Z. Y. (2018). Main factors controlling the wettability of gas shales: a case study of over-mature marine shale in the Longmaxi Formation. *J. Nat. Gas Sci. Eng.* 56, 18–28. doi: 10.1016/j.jngse.2018.05.017

Löhr, S. C., Baruch, E. T., Hall, P. A., and Kennedy, M. J. (2015). Is organic pore development in gas shales influenced by the primary porosity and structure of

thermally immature organic matter? *Org. Geochem.* 87, 119–132. doi: 10.1016/j.orggeochem.2015.07.010

Mastalerz, M., Schimmelmann, A., Drobniak, A., and Chen, Y. Y. (2013). Porosity of devonian and mississippian New Albany Shale across a maturation gradient: insights from organic petrology, gas adsorption, and mercury intrusion. *AAPG Bull.* 97, 1621–1643. doi: 10.1306/04011312194

Newsham, K. E., Rushing, J. A., and Lasswell, P. M. (2003). Use of vapor desorption data to characterize high vapillary pressures in a basin-centered gas accumulation with ultra-low connate water saturations. *Paper Presented at the SPE Annual Technical Conference and Exhibition.* SPE-84596-MS, Denver, CO, 1–9. doi: 10.2118/84596-MS

Pan, L., Xiao, X. M., Tian, H., Zhou, Q., Chen, L., Li, T. F., et al. (2015). A preliminary study on the characterization and controlling factors of porosity and pore structure of the Permian shales in Lower Yangtze region, Eastern China. *Int. J. Coal Geol.* 146, 68–78. doi: 10.1016/j.coal.2015.05.005

Pan, L., Xiao, X., Tian, H., Zhou, Q., and Cheng, P. (2016). Geological models of gas in place of the Longmaxi shale in Southeast Chongqing, South China. *Mar. Pet. Geol.* 73, 433–444. doi: 10.1016/j.marpetgeo.2016.03.018

Pan, Z. J., and Connell, L. D. (2015). Reservoir simulation of free and adsorbed gas production from shale. *Nat. Gas Sci. Eng.* 22, 359–370. doi: 10.1016/j.jngse.2014.12.013

Ross, D. J. K., and Bustin, R. M. (2007). Shale gas potential of the Lower Jurassic Gordondale Member, northeastern British Columbia, Canada. *Bull. Can. Petrol. Geol.* 55, 51–75. doi: 10.2113/gscpgbull.55.1.51

Ross, D. J. K., and Bustin, R. M. (2009). The importance of shale composition and pore structure upon gas storage potential of shale gas reservoirs. *Mar. Pet. Geol.* 26, 916–927. doi: 10.1016/j.marpetgeo.2008.06.004

Rouquerol, J., Avnir, D., Fairbridge, C. W., Everett, D. H., Haynes, J. H., Pernicone, N., et al. (1994). Recommendations for the characterization of porous solids. *Pure Appl. Chem.* 66, 1739–1758. doi: 10.1351/pac199466081739

Shan, C. A., Zhang, T. S., Wei, Y., and Zhao, Z. (2017). Shale gas reservoir characteristics of Ordovician-Silurian formations in the central Yangtze area, China. *Front. Earth Sci.* 11:184–201. doi: 10.1007/s11707-016-0565-4

Sing, K. S. W., Everett, D. H., Haul, R. A. W., Moscou, L., Pierotti, R. A., Rouquerol, J., et al. (1985). Reporting physisorption data for gas/sold systems with special reference to the determination of surface area and porosity. *Pure. Appl. Chem.* 57, 603–619. doi: 10.1351/pac198557040603

Sondergeld, C. H., Ambrose, R. J., Rai, C. S., and Moncrieff, J. (2010). "Micro-structural studies of gas shales," in *Proceedings of the SPE Unconventional Gas Conference*, Pittsburgh, PA, 23–25. doi: 10.2523/131771-MS

Song, X., Wang, S. B., Cao, T. T., and Song, Z. G. (2013). The methane adsorption features of Cambrian shales in the Yangtze Platform. *Acta Geol. Sin* 87, 1041–1048.

Sun, J., Xiao, X. M., Wei, Q., Cheng, P., Tian, H., and Wu, Y. W. (2020). Gas in place and its controlling factors of the shallow Longmaxi shale in the Xishui area. Guizhou, China. *J. Nat. Gas. Sci. Eng.* 77:103272. doi: 10.1016/j.jngse.2020.103272

Tan, J. Q., Weniger, P., Krooss, B., Merkel, A., Horsfield, B., Zhang, J., et al. (2014). Shale gas potential of the major marine shale formations in the Upper Yangtze Platform, South China, Part II: methane sorption capacity. *Fuel* 129, 204–218. doi: 10.1016/j.fuel.2014.03.064

Tian, H., Li, T. F., Zhang, T. W., and Xiao, X. M. (2016). Characterization of methane adsorption on overmature Lower Silurian—Upper Ordovician shales in Sichuan Basin, southwest China: experimental results and geological implications. *Int. J. Coal. Geol.* 156, 36–49. doi: 10.1016/j.coal.2016.01.013

Tian, G. (2018). Zhejiang Oilfield of Petrochina Company has achieved breakthrough in shallow shale gas field. *Nat. Gas. Ind.* 38:40.

Tian, H., Pan, L., Xiao, X. M., Wilkins, R. W. T., Meng, Z. P., and Huang, B. J. (2013). A preliminary study on thepore characterization of Lower Silurian black shales in the Chuandong Thrust Fold Belt, southwestern China using low pressure N_2 adsorption and FE-SEM methods. *Mar. Petrol. Geol.* 48, 8–19. doi: 10.1016/j.marpetgeo.2013.07.008

Tian, H., Pan, L., Zhang, T. W., Xiao, X. M., Meng, Z. P., and Huang, B. J. (2015). Pore characterization of organic-rich lower Cambrian shales in Qiannan depression of Guizhou province, southwestern China. *Mar. Petrol. Geol.* 62, 28–43. doi: 10.1016/j.marpetgeo.2015.01.004

Wang, F. (2012). "Unique shale properties and their impacts on fluid flow-"Advances in shale"," in *Oral Presentation at State Key Laboratory of Org Geochem* (Guangzhou: Chinese Academy of Sciences).

Wang, F. T., and Guo, S. B. (2019). Shale gas content evolution in the Ordos Basin. *Int. J. Coal. Geol.* 211:103231. doi: 10.1016/j.coal.2019.103231

Wang, L., Wang, D. B., Cai, C. H., Li, N., Zhang, L., and Yang, M. L. (2020). Effect of water occupancy on the excess adsorption of methane in montmorillonites. *J. Nat. Gas. Sci. Eng.* 80:103393. doi: 10.1016/j.jngse.2020.103393

Wei, Y. Y., and Jia, C. Q. (2015). Intrinsic wettability of graphitic carbon. *Carbon* 87, 10–17. doi: 10.1016/j.carbon.2015.02.019

Wei, Z. H., and Wei, X. F. (2014). Comparison of gas-bearing property between different pore types of shale: a case from the Upper Ordovician Wufeng and Longmaxi formation in the Jiaoshiba area, Sichuan Basin. *Nat. Gas Ind.* 34, 37–41. doi: 10.3787/j.issn.1000-0976.2014.06.006

Yaguzhinsky, L. S., Motovilov, K. A., Volkov, E. M., Hu, Z. M., Liu, H. L., and Yu, R. Z. (2013). Impact of temperature on the isothermal adsorption/desorption characteristics of shale gas. *Pet. Explor. Dev.* 40, 514–519.

Yang, B. H. (2018). Zhejiang oilfield: towards to the shallow shale gas development. *Petrol. Knowl.* 22.

Yang, Y., and Aplin, A. C. (1998). Influence of lithology and compaction onthe pore size distribution and modelled permeability of some mudstones from the Norwegian margin. *Mar. Petrol. Geol.* 15, 163–175. doi: 10.1016/S0264-8172(98)00008-7

Ye, Z. H., Chen, D., Pan, Z. J., Zhang, G. Q., Xia, Y., and Ding, X. (2016). An improved Langmuir model for evaluating methane adsorption capacity in shale under various pressures and temperatures. *J. Nat. Gas. Sci. Eng.* 31, 658–680. doi: 10.1016/j.jngse.2016.03.070

Zhang, H., Zhu, Y. M., Xia, X. H., Lin, H., and Chen, J. (2013). Comparison and explanation of the absorptivity of organic matters and clay minerals in shales. *J. Chin. Coal. Soc.* 38, 812–816.

Zhang, T. W., Ellis, G. S., Ruppel, S. C., Milliken, K., and Yang, R. S. (2012). Effect of organic-matter type and thermal maturity on methane adsorption in shale-gas systems. *Org. Geochem.* 47, 120–131. doi: 10.1016/j.orggeochem.2012.03.012

Zhang, Y. F., Yu, B. S., Pan, Z. J., Hou, C. H., Zuo, Q. W., and Sun, M. D. (2020). Effect of thermal maturity on shale pore structure: a combined study using extracted organic matter and bulk shale from Sichuan Basin, China. *J. Nat. Gas Sci. Eng.* 74:103089. doi: 10.1016/j.jngse.2019.103089

Zhang, Y. S., Lv, D. W., Wang, Y., Liu, H. Y., Song, G. Z., Gao, J., et al. (2020). Geological characteristics and abnormal pore pressure prediction in shale oil formations of the Dongying depression, China. *Energy Sci. Eng.* 8, 1962–1979. doi: 10.1002/ese3.641

Conflict of Interest: The authors declare that the research was conducted in the absence of any commercial or financial relationships that could be construed as a potential conflict of interest.

frontiers in Earth Science

ORIGINAL RESEARCH
published: 06 April 2021
doi: 10.3389/feart.2021.663574

Experimental Methods for the Quantitative Assessment of the Volume Fraction of Movable Shale Oil: A Case Study in the Jimsar Sag, Junggar Basin, China

Xia Luo, Zhongying Zhao*, Lianhua Hou*, Senhu Lin, Feifei Sun, Lijun Zhang and Yan Zhang*

Research Institute of Petroleum Exploration and Development, PetroChina, Beijing, China

OPEN ACCESS

Edited by:
Dongdong Wang, Shandong University of Science and Technology, China

Reviewed by:
Weilong Peng, SINOPEC Petroleum Exploration and Production Research Institute, China
Binfeng Cao, Institute of Geology and Geophysics (CAS), China

***Correspondence:**
Xia Luo
luoxia69@petrochina.com.cn
Zhongying Zhao
zhaozhongying@petrochina.com.cn
Lianhua Hou
houlh@petrochina.com.cn

Specialty section:
This article was submitted to Economic Geology, a section of the journal Frontiers in Earth Science

Received: *03 February 2021*
Accepted: *12 March 2021*
Published: *06 April 2021*

Citation:
Luo X, Zhao Z, Hou L, Lin S, Sun F, Zhang L and Zhang Y (2021) Experimental Methods for the Quantitative Assessment of the Volume Fraction of Movable Shale Oil: A Case Study in the Jimsar Sag, Junggar Basin, China. Front. Earth Sci. 9:663574. doi: 10.3389/feart.2021.663574

Deep insights into the movability of the retained shale oil are of great significance to shale oil. Rock and crude oil samples were collected from well J174 in the Jimsar Sag, Junggar Basin. Rock samples were subjected to different extraction followed by analysis of the component in the extracts, and measurement of porosity in conjunction with nuclear magnetic resonance and high-pressure mercury injection analysis. The results of these analyses were used to establish an experimental method for quantitative assessment of movable shale oil. The extract content of the component varied among different extraction and between mud shale and non-mud shale samples. The saturated hydrocarbon in the extracts of the mud shale was similar to those of the non-mud shale after extraction with $CHCl_3$ alone or after sequential extraction with $nC_6 + CHCl_3$. The aromatic hydrocarbon in the extract were significantly lower for the mud shale than for the non-mud shale after extraction with nC_6, but the opposite was observed after sequential extraction with $nC_6 + CHCl_3$. The contents of the non-hydrocarbon in the extract were significantly lower for the mud shale than for the non-mud shale after extraction with nC_6, but the opposite was observed after extraction with $CHCl_3$ or $nC_6 + CHCl_3$. The contents of the asphaltene in the extract were not significantly different for the mud shale and non-mud shale after extraction with nC_6, but the contents were higher for the mud shale than for the non-mud shale after extraction with $nC_6 + CHCl_3$ or $CHCl_3$. The viscosity of the crude oil was negatively correlated with the saturated hydrocarbon, was positively correlated with the aromatic hydrocarbon and non-hydrocarbon, and was not correlated with the asphaltene. For the mud shale and non-mud shale, their porosity after extraction with nC_6 or $CHCl_3$ was higher than their original porosity. Moreover, their porosity after extraction with $CHCl_3$ was higher than after extraction with nC_6. The movable oil was significantly correlated with the lithology, with sandstone allowing for a higher fluid movability than mud shale and dolomite allowing for a higher fluid movability than siliceous rocks.

Keywords: shale oil, volume fraction of movable oil, retained oil, sequential extraction, Jimsar Sag

INTRODUCTION

Shale oil has drawn a great deal of attention in terms of the global exploration and production of unconventional oil and gas (Goodarzi, 2020; Kim and Shin, 2020; Solarin, 2020; Kara and Isik, 2021). China's terrestrial shale oil has a huge resource potential, and breakthroughs have been achieved in the Permian Lucaogou Formation in the Jimsar Sag, Junggar Basin, as well as in the Chang 7 Member in the Ordos Basin (Hou et al., 2020a,b, 2021; Hu et al., 2020; Ma et al., 2020; Zhao et al., 2020). However, the shale oil is only in its initial stage and is under geological conditions that are dramatically different from those of the marine shale oil in North America. Chinese shale oil is mainly distributed in Mesozoic-Cenozoic shale strata, where the lacustrine mud shale is characterized by a low thermal maturity, with *Ro* values primarily ranging from 0.5 to 1.2%. The high stratigraphic heterogeneity, high oil density, and low oil fluidity pose significant challenges in the exploration and production of such shale oil. Therefore, it is extremely important to obtain a comprehensive, in-depth understanding of the movability of the retained oil in shale (Liu et al., 2012; Tao et al., 2012; Li et al., 2015; Xie et al., 2015). In this study, core samples of different lithologies were collected from the different strata in well J174 in the Jimsar Sag, Junggar Basin, and then, the samples were subjected to different extraction treatments with n-hexane (nC_6) and chloroform ($CHCl_3$), followed by porosity measurements to explore how the extract composition of the component and the rock porosity vary with the extraction treatments and rock types. Moreover, the volume fraction of the movable oil in the different lithologies was addressed from different aspects via nuclear magnetic resonance (NMR) analysis and high-pressure mercury injection analysis of representative rock samples.

SAMPLES AND METHODS

Rock and crude oil samples were collected from well J174 in the Jimsar Sag, Junggar Basin. The main crude oil production depths in well J174 are 3246–3285 m, at which the main lithology is characterized by the frequent interbedding of dolomitic siltstone with thin dolomitic shale. The rock samples were divided into mud shale samples and non-mud shale samples. The mud shale samples were mainly siliceous and dolomitic, while the non-mud shale samples were mainly muddy siltstone, dolomitic siltstone, and dolomite.

Rock cores were obtained through drilling, while the other samples were broken (120 mesh) for basic geological analysis (**Appendix Table A1**). The cores were separately subjected to single-solvent extraction with nC_6, single-solvent extraction with $CHCl_3$, and sequential extraction with nC_6 + $CHCl_3$. The porosity and permeability were measured by the helium method (Burnham, 2017; Gao and Li, 2018; Dong and Harris, 2020). The extraction steps were completed in the North China Oilfield Research Institute of the China National Petroleum Corporation (CNPC), while the rock porosity and permeability were determined in the Key Laboratory of Natural Gas Formation and Development of CNPC. The powdered samples were divided into two parts. (1) One part was extracted using only $CHCl_3$, and the extract was subjected to component-group isolation and quantification. (2) The other part was extracted using nC_6 and $CHCl_3$ in sequence, followed by component-group isolation and quantification for each solvent extract. All of the extraction experiments were conducted at Yangtze University. Representative lithological samples were selected for thermal dissolution followed by NMR and high-pressure mercury injection analysis in the Key Laboratory of Natural Gas Formation and Development of CNPC.

RESULTS AND DISCUSSION

Different Extraction Treatments

The powdered samples were either first extracted using nC_6 and then $CHCl_3$ or using only $CHCl_3$. The contents of the saturated hydrocarbon, the aromatic hydrocarbon, the asphaltene, and the non-hydrocarbon in each extract were determined. The experimental results are presented in **Appendix Table A2**. The cores were extracted using only nC_6 or only $CHCl_3$, followed by porosity and permeability measurements. The experimental results are also presented in **Appendix Table A2**. Five samples (#3, #9, #15, #16, and #22) were selected for NMR analysis,

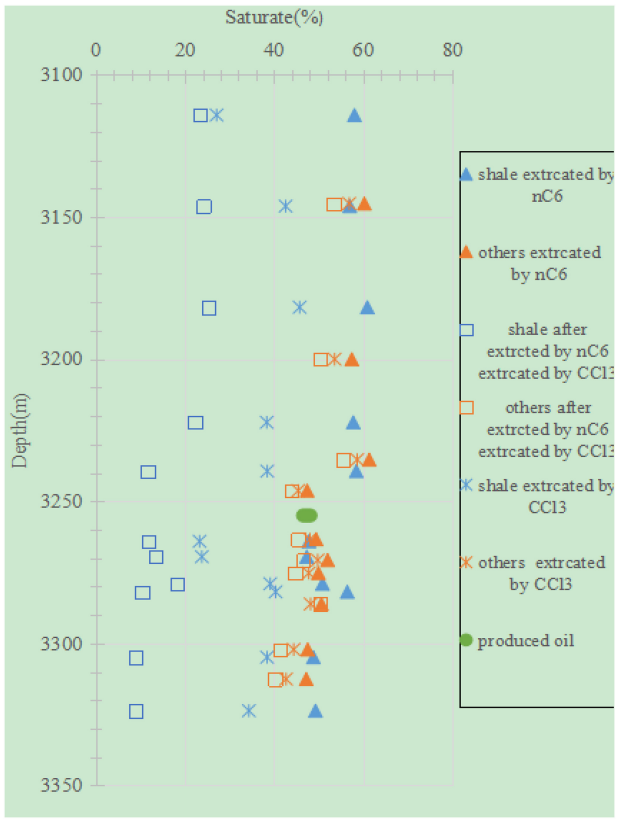

FIGURE 1 | Depth profile of the extract contents of the saturated hydrocarbon from the mud shale versus the non-mud shale after the different extraction treatments.

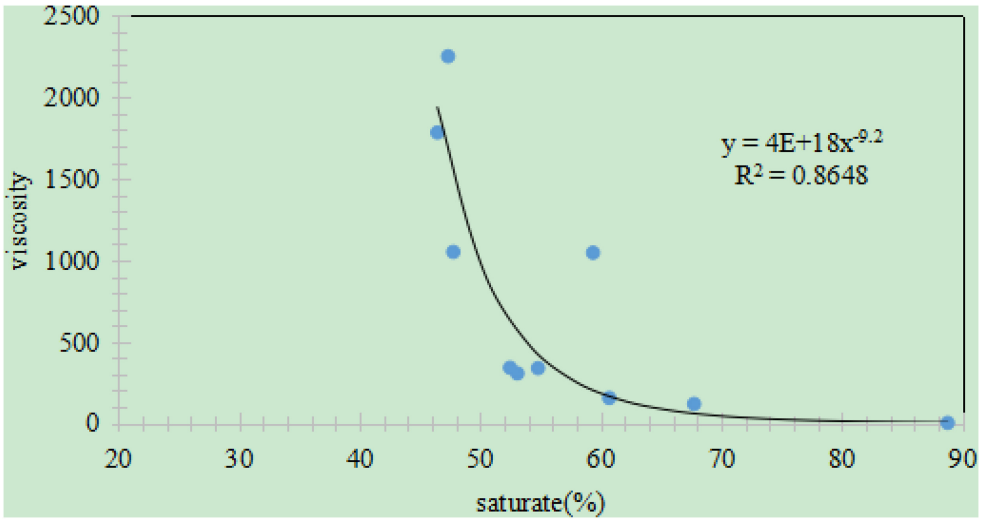

FIGURE 2 | Relationship between the content of the saturated hydrocarbon and the viscosity (20°C) for the crude oil extracted from the Jimsar Sag.

of which four (#3, #9, #15, and #22) were also subjected to high-pressure mercury injection analysis. The experimental results are presented in **Appendix Tables A3**, **A4**, respectively.

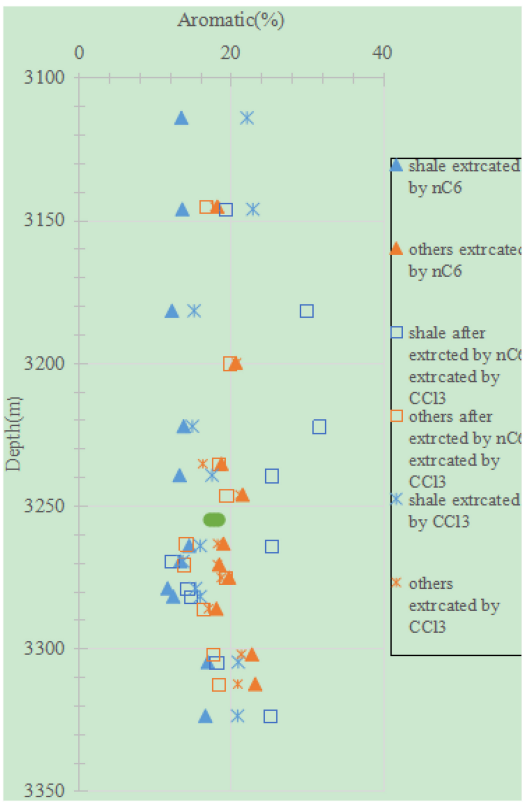

FIGURE 3 | Depth profile of the extract contents of the aromatic hydrocarbon from the mud shale versus the non-mud shale after different extraction treatments.

Extract Contents of the Component After Extraction

Saturated Hydrocarbon

The extract contents (as a percentage of the total extracted components; the same hereafter) of the saturated hydrocarbon were similar for the mud shale samples and the non-mud shale samples after extraction with nC_6. The extract contents of the saturated hydrocarbon from the samples of the oil-producing strata were similar to those of the crude oil samples (**Figure 1**). However, there was a significant difference in the extract contents of the saturated hydrocarbon for the two rock types after sequential extraction with nC_6 and $CHCl_3$. The mud shale samples had significantly smaller contents than the non-mud shale samples (**Figure 1**). For the oil-producing strata, the extract contents of the saturated hydrocarbon for the non-mud shale samples after sequential extraction with nC_6 + $CHCl_3$ were similar to those of the saturated hydrocarbon in crude oil samples, but the extract contents from the mud shale samples were significantly lower than those of the crude oil samples. The extract contents of the saturated hydrocarbon from the mud shale samples were lower than those from the non-mud shale samples after extraction with $CHCl_3$, which is similar to the case of the sequential extraction with nC_6 + $CHCl_3$. In other words, the mud shale was similar to the non-mud shale in terms of the extract contents of the saturated hydrocarbon after single-solvent extraction with $CHCl_3$ or after sequential extraction with nC_6 + $CHCl_3$. For the non-mud shale samples of the oil-producing strata, the extract contents of the saturated hydrocarbon were similar to those of the crude oil samples (**Figure 1**). However, the extract contents of the saturated hydrocarbon from the mud shale samples decreased in the order of single-solvent extraction with nC_6, single-solvent extraction with $CHCl_3$, and sequential extraction with nC_6 and $CHCl_3$. That is, the extract content gradually shifts toward the left along the abscissa in **Figure 1** when samples from the same sampling depth

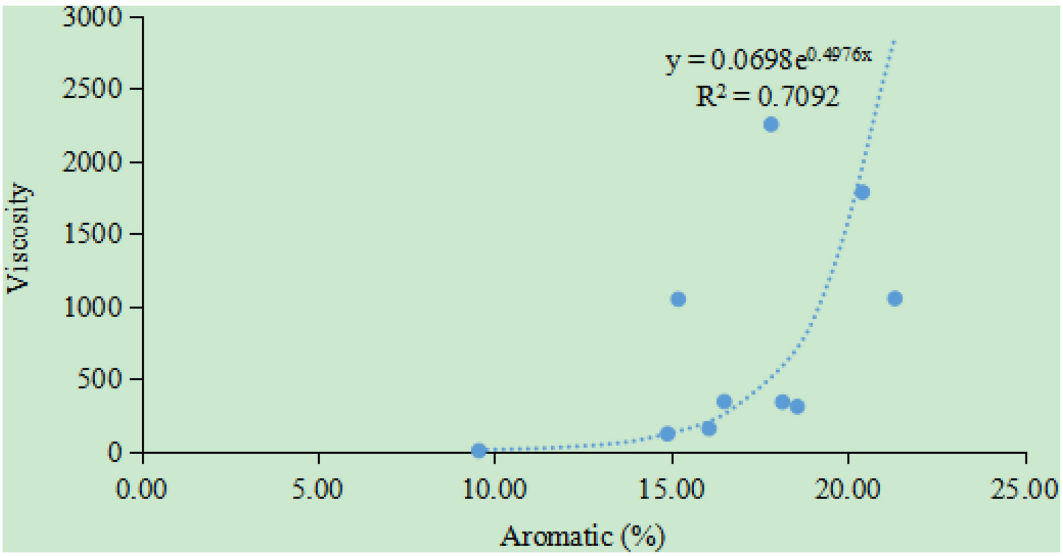

FIGURE 4 | Relationship between the content of the aromatic hydrocarbon and the viscosity (20°C) for crude oil extracted from the Jimsar Sag (the crude oil data were provided by the Xinjiang Oilfield Company of CNPC).

were separately subjected to the above-mentioned extraction treatments. This indicates that the extract contents of the saturated hydrocarbon from the mud shale samples are greatly dependent on the polarity of the organic solvent, with a higher polarity leading to a weaker extraction and thus a lower extract content. However, this pattern was not obvious for the non-mud shale samples.

Moreover, the higher the saturated hydrocarbon content, the lower the viscosity is (**Figure 2**), exhibiting an obvious negative correlation with a correlation coefficient R^2 of 0.86. Studies have shown that for crude oil, the higher the content of the saturated hydrocarbon, the lower the viscosity, and the easier it is to extract it from underground reservoirs (Boak and Kleinberg, 2020; Zhang et al., 2021).

Aromatic Hydrocarbon

The extract contents of the aromatic hydrocarbon from the mud shale samples after extraction with nC_6 were significantly lower than those from the non-mud shale samples (**Figure 3**). Moreover, the extract contents from the non-mud shale samples of the oil-producing strata were similar to those of the crude oil samples, but the extract contents from the mud shale samples from the same strata were obviously higher. However, the opposite patterns were observed for the case of the sequential extraction with nC_6 + $CHCl_3$. (1) The extract contents of the aromatic hydrocarbon from the mud shale samples after sequential extraction with nC_6 + $CHCl_3$ were significantly higher than those of from the non-mud shale samples (**Figure 3**). (2) For the oil-producing strata, the extract contents from the non-mud shale samples were lower than those of the crude oil samples, but the extract contents from the mud shale samples were significantly higher. For extraction with $CHCl_3$, the extract contents of the aromatic hydrocarbon from the mud shale samples versus the non-mud shale samples did not exhibit a clear trend, which is consistent with the results of other

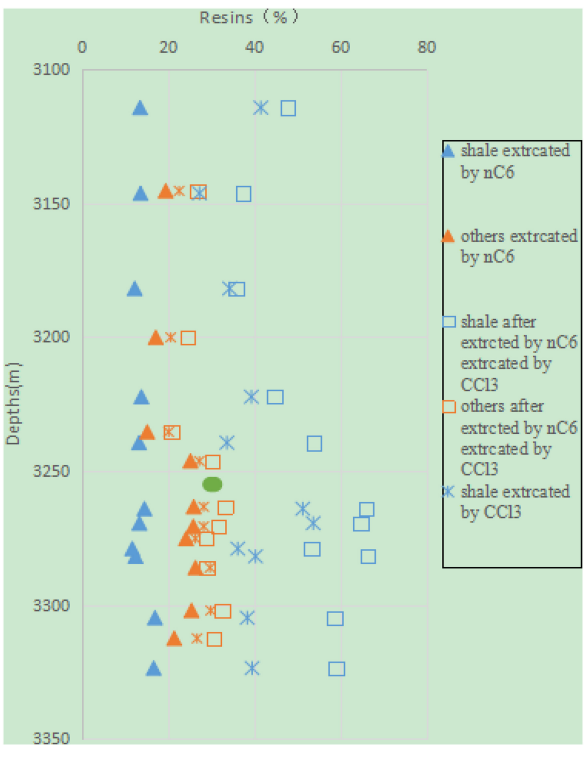

FIGURE 5 | Depth profile of the extract contents of the non-hydrocarbon from the mud shale versus the non-mud shale after different extraction treatments.

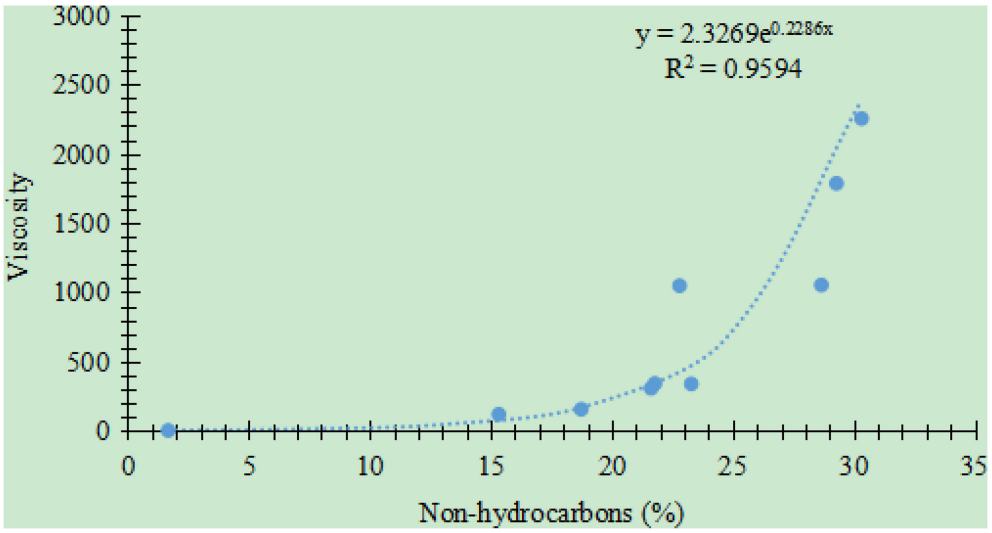

FIGURE 6 | Relationship between the content of the non-hydrocarbon and the viscosity (20°C) for crude oil extracted from the Jimsar Sag (the crude oil data were provided by the Xinjiang Oilfield Company of CNPC).

studies (Chishti and Williams, 1999; Jefimova et al., 2014; Fang et al., 2019).

For the mud shale, the extract contents of the aromatic hydrocarbon decreased in the order of $nC_6 + CHCl_3$, $CHCl_3$, and nC_6. This indicates that the aromatic hydrocarbon in the shale oil can be extracted by chloroform and n-hexane. For the non-mud shale, the extract contents obtained using the three extraction treatments did not vary significantly.

Moreover, the higher the aromatic content, the higher the viscosity of the crude oil, exhibiting an obvious positive correlation with an R^2 of 0.71 (**Figure 4**). For the crude oil, the higher the content of the aromatic hydrocarbon, the heavier the oil (i.e., the higher the viscosity), and the harder it is to extract it from underground reservoirs (Chen et al., 2010; Yu et al., 2018; Aily et al., 2019).

Non-hydrocarbon

For the non-hydrocarbon, its extract contents after extraction with nC_6 were significantly lower for the mud shale samples than for the non-mud shale samples (**Figure 5**). But the opposite was observed for the case of sequential extraction with $nC_6 + CHCl_3$. The extract contents of the non-hydrocarbon from the mud shale samples were higher than those from the non-mud shale samples. This pattern was also similarly observed for the case of extraction with $CHCl_3$. As is shown above, the extract contents of the non-hydrocarbon after extraction with $CHCl_3$ or $nC_6 + CHCl_3$ were higher for the mud shale samples than for the non-mud shale samples.

For a given sample, the extract contents decreased in the order of $nC_6 + CHCl_3$, $CHCl_3$, and nC_6. This suggests that the more polar the solvent, the higher the content of the extracted non-hydrocarbon.

Moreover, the higher the non-hydrocarbon content, the higher the viscosity of the crude oil, exhibiting an obvious positive correlation with an R^2 of 0.96 (**Figure 6**). This suggests that for crude oil, the higher the non-hydrocarbon content, the heavier the oil (i.e., the higher

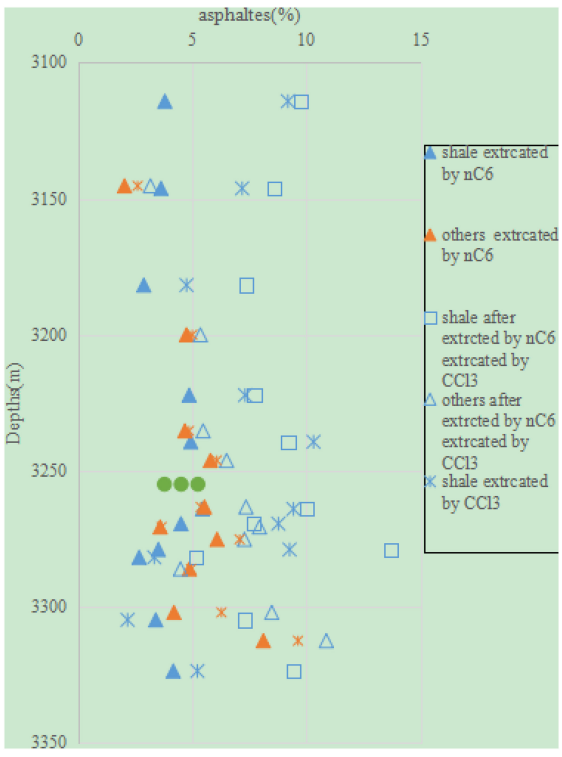

FIGURE 7 | Depth profile of the extract contents of the asphaltene from the mud shale versus the non-mud shale samples after different extraction treatments.

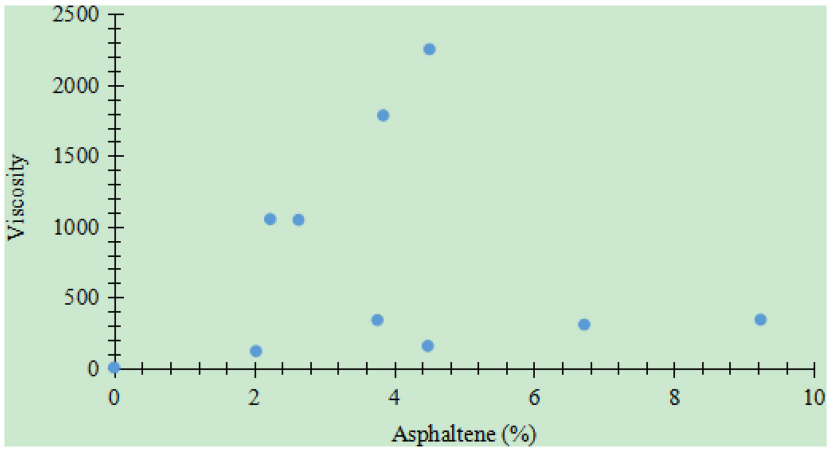

FIGURE 8 | Relationship between the content of the asphaltene and the viscosity (20°C) for crude oil extracted from the Jimsar Sag (the crude oil data were provided by the Xinjiang Oilfield Company of CNPC).

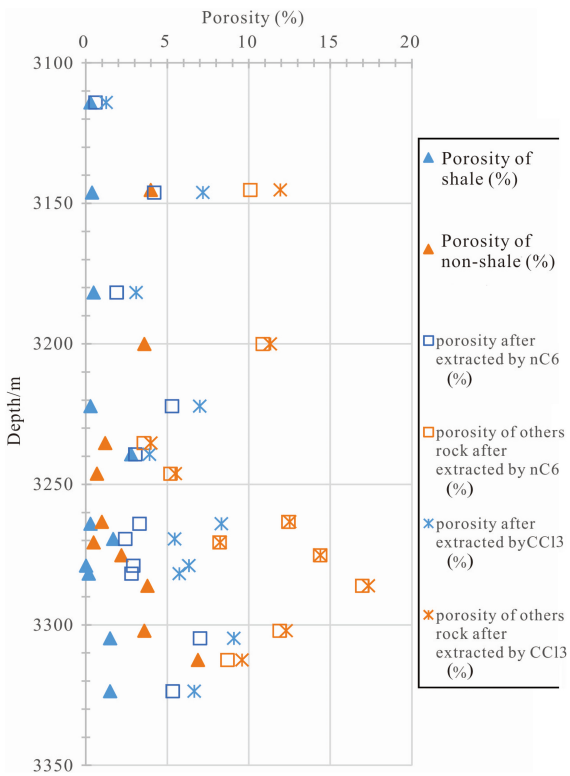

FIGURE 9 | Porosity of the mud shale samples versus the non-mud shale after extraction with nC_6 alone or with $CHCl_3$ alone.

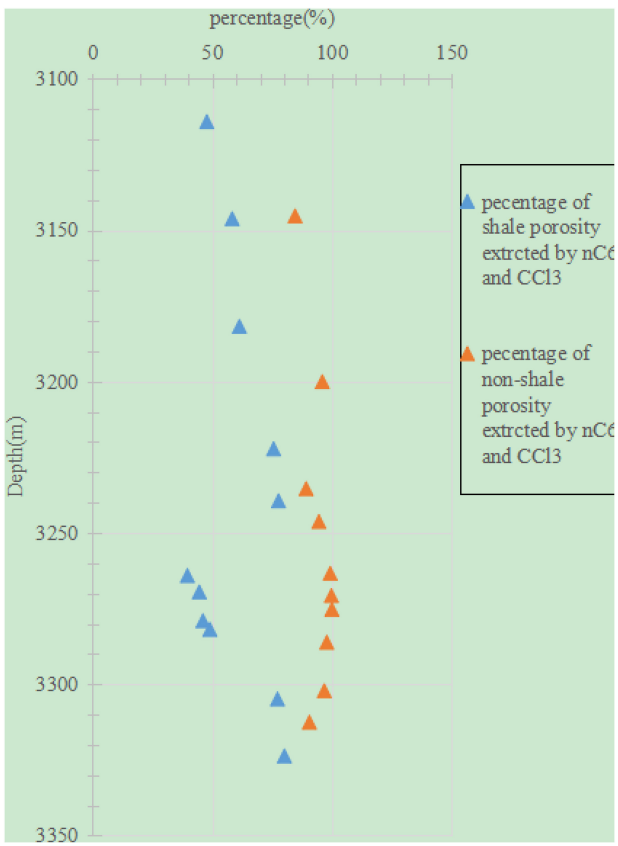

FIGURE 10 | Porosity of the mud shale samples versus the non-mud shale after sequential extraction with nC_6 + $CHCl_3$.

the viscosity), and the harder it is to extract in from underground reservoirs.

Asphaltene

For extraction with nC_6, the extract contents of the asphaltene from the mud shale samples versus the non-mud shale samples do not exhibit a clear trend. For extraction with nC_6 + $CHCl_3$, the extract contents were significantly higher for the mud shale samples than for the non-mud shale samples. For extraction with

$CHCl_3$, the extract contents were generally higher for the mud shale samples than for the non-mud shale samples (**Figure 7**).

For the mud shale samples, the extract contents of the asphaltene decreased in the order of $nC_6 + CHCl_3$, $CHCl_3$, and nC_6. This suggests that the higher the polarity of the organic solvent ($nC_6 + CHCl_3$), the higher the content of the extracted asphaltene. The lower the polarity of the organic solvent (nC_6), the smaller the content of the extracted asphaltene is. This pattern was also observed for the non-mud shale samples.

Moreover, there was no obvious correlation between the viscosity of the crude oil and the content of the asphaltene (**Figure 8**). The content of the asphaltene did not affect the viscosity of the crude oil.

Porosity After the Different Extraction Treatments

The original porosity of the non-mud shale samples were generally slightly higher than those of the mud shale samples. After single-solvent extraction with nC_6 or $CHCl_3$, the porosity of the non-mud shale was still higher than those of the mud shale (**Figure 9**). For the mud shale and non-mud shale samples, the porosity after extraction with nC_6 or $CHCl_3$ was higher than the original porosity. In particular, the porosity after extraction with $CHCl_3$ were higher than those after extraction with nC_6, and both values were higher than the original porosity. This shows that extraction with organic solvents increases the porosity of mud shale and non-mud shale. The higher the polarity, the larger the increase is. After sequential extraction with $nC_6 + CHCl_3$, the increase was more obvious for the non-mud shale samples than for the mud shale samples (**Figure 10**).

CONCLUSION

In this study, an experimental method for quantitative assessment of movable shale oil was established. The results revealed that the extract contents of the four components vary among the different extraction treatments and different lithology. The mud shale and non-mud shale exhibited similar extract contents of the saturated hydrocarbon after single-solvent extraction with $CHCl_3$ or sequential extraction with $nC_6 + CHCl_3$. For the aromatic hydrocarbon, the mud shale exhibited lower extract content than the non-mud shale after extraction with nC_6, but they exhibited higher extract content after extraction with $nC_6 + CHCl_3$. However, for extraction with $CHCl_3$, the extract contents of the aromatic hydrocarbon from the mud shale versus non-mud shale did not exhibit a clear trend. For the non-hydrocarbon, the mud shale exhibited lower extract content than the non-mud shale after single-solvent extraction with nC_6, but they exhibited higher extract content after single-solvent extraction with $CHCl_3$ or sequential extraction with $nC_6 + CHCl_3$. For the asphaltene, its content in the nC_6 extract did not exhibit a clear trend between the mud shale and the non-mud shale. In contrast, its extract content was higher for the mud shale than for the non-mud shale after extraction with $nC_6 + CHCl_3$ or with $CHCl_3$ alone. The viscosity of the crude oil exhibits a negative correlation with the saturated hydrocarbon, positive correlations with the aromatic hydrocarbon and the non-hydrocarbon, and no correlation with the asphaltene. The porosity after single-solvent extraction with nC_6 or $CHCl_3$ was higher than their original porosity. In particular, the porosity after extraction with $CHCl_3$ was higher than that after extraction with nC_6. There was correlation between the movable shale oil and lithology, with sandstone allowing for a higher fluid movability than mud shale and dolomite allowing for a higher fluid movability than siliceous rocks.

DATA AVAILABILITY STATEMENT

The original contributions presented in the study are included in the article/supplementary material, further inquiries can be directed to the corresponding author/s.

AUTHOR CONTRIBUTIONS

XL: conceptualization, methodology, investigation, and writing. ZZ: formal analysis, resources, data curation, and writing. LH: software, validation, project administration, and methodology. SL: software, project administration, and data validation. FS: data validation and analysis and software. LZ: data interpretation, draft, and approval. YZ: drawing of figures, data analysis, and references. All authors contributed to the article and approved the submitted version.

FUNDING

This study was funded by the PetroChina Co., Ltd. (Grant No. 2015D-4810-02; 2018ycq03). The funder was not involved in the study design, collection, analysis, interpretation of data, the writing of this article or the decision to submit it for publication.

ACKNOWLEDGMENTS

We sincerely thank Garcia for his continuous care and help. We also thank Wilson for reviewing our article. We benefit from Allen for providing polishing and editing services to our manuscript.

REFERENCES

Aily, M. E., Mansour, E. M., Desouky, S. M., and Helmi, M. E. (2019). Modeling viscosity of moderate and light dead oils in the presence of complex aromatic structure. *J. Pet. Sci. Eng.* 173, 426–433. doi: 10.1016/j.petrol.2018.10.024

Boak, J., and Kleinberg, R. (2020). *Future Energy*, 3rd Edn, Amsterdam: Elsevier Press.

Burnham, A. K. (2017). Porosity and permeability of Green River oil shale and their changes during retorting. *Fuel* 203, 208–213. doi: 10.1016/j.fuel.2017.04.119

Chen, Y. L., He, J., Wang, Y. P., and Li, P. (2010). GC-MS used in study on the mechanism of the viscosity reduction of heavy oil through aquathermolysis catalyzed by aromatic sulfonic $H_3PMo_{12}O_{40}$. *Energy* 35, 3454–3460. doi: 10.1016/j.energy.2010.04.041

Chishti, H. M., and Williams, P. T. (1999). Aromatic and hetero-aromatic compositional changes during catalytic hydrotreatment of shale oil. *Fuel* 78, 1805–1815. doi: 10.1016/s0016-2361(99)00089-7

Dong, T., and Harris, N. B. (2020). The effect of thermal maturity on porosity development in the Upper devonian –lower Mississippian Woodford Shale, Permian Basin, US: insights into the role of silica nanospheres and microcrystalline quartz on porosity preservation. *Intern. J. Coal Geol.* 217:103346. doi: 10.1016/j.coal.2019.103346

Fang, R. H., Littke, R., Zieger, L., Baniaasad, A., Li, M. J., and Schwarzbauer, J. (2019). Changes of composition and content of Tricyclic Terpane, Hopane, Sterane, and aromatic biomarkers throughout the oil window: a detailed study on maturity parameters of Lower Toarcian Posidonia Shale of the Hils Syncline, NW Germany. *Organ. Geochem.* 138:103928. doi: 10.1016/j.orggeochem.2019.103928

Gao, J., and Li, Z. X. (2018). Water saturation-driven evolution of helium permeability in Carboniferous shale from Qaidam Basin, China: an experimental study. *Mar. Petrol. Geol.* 96, 371–390. doi: 10.1016/j.marpetgeo.2018.05.028

Goodarzi, F. (2020). Comparison of the geochemistry of lacustrine oil shales of Mississippian age from Nova Scotia and New Brunswick, Canada. *Intern. J. Coal Geol.* 220:103398. doi: 10.1016/j.coal.2020.103398

Hou, L. H., Luo, X., Han, W. X., Lin, S. H., Pang, Z. L., and Liu, J. Z. (2020a). Geochemical evaluation of the hydrocarbon potential of shale oil and its correlation with different minerals-a case study of the TYP shale in the Songliao Basin, China. *Energy Fuels* 34, 11998–12009. doi: 10.1021/acs.energyfuels.0c01285

Hou, L. H., Ma, W. J., Luo, X., and Liu, J. Z. (2020b). Characteristics and quantitative models for hydrocarbon generation-retention-production of shale under ICP conditions: example from the Chang 7 member in the Ordos Basin. *Fuel* 279:118497. doi: 10.1016/j.fuel.2020.118497

Hou, L. H., Ma, W. J., Luo, X., Liu, J. Z., Lin, S. H., and Zhao, Z. Y. (2021). Hydrocarbon generation-retention-expulsion mechanism and shale oil producibility of the Permian lucaogou shale in the Junggar Basin as simulated by semi-open pyrolysis experiments. *Mar. Petrol. Geol.* 125:104880. doi: 10.1016/j.marpetgeo.2020.104880

Hu, S. Y., Zhao, W. Z., Hou, L. H., Yang, Z., Zhu, R. K., Wu, S. T., et al. (2020). Development potential and technical strategy of continental shale oil in China. *Pet. Explor. Dev.* 47, 877–887. doi: 10.1016/s1876-3804(20)60103-3

Jefimova, J., Irha, N., Reinik, J., Kirso, U., and Steinnes, E. (2014). Leaching of polycyclic aromatic hydrocarbons from oil shale processing waste deposit: a long-term field study. *Sci. Total Environ.* 481, 605–610. doi: 10.1016/j.scitotenv.2014.02.105

Kara, B., and Isik, V. (2021). Reservoir characteristics and unconventional oil potential of Silurian aged Dadaş shale in southeast Turkey. *J. Pet. Sci. Eng.* 200:108365. doi: 10.1016/j.petrol.2021.108365

Kim, M., and Shin, H. (2020). Numerical simulation of undulating shale breaking with steam-assisted gravity drainage (UB-SAGD) for the oil sands reservoir with a shale barrier. *J. Pet. Sci. Eng.* 195:107604. doi: 10.1016/j.petrol.2020.107604

Li, W. H., Lu, S. F., Xue, H. T., Zhang, P. F., and Hu, Y. (2015). Oil content in argillaceous dolomite from the Jianghan Basin, China: application of new grading evaluation criteria to study shale oil potential. *Fuel* 143, 424–429. doi: 10.1016/j.fuel.2014.11.080

Liu, B., Lv, Y. F., Zhao, R., Tu, X. X., Guo, X. B., and Shen, Y. (2012). Formation overpressure and shale oil enrichment in the shale system of Lucaogou formation, Malang Sag, Santanghu Basin, NW China. *Pet. Explor. Dev.* 39, 744–750. doi: 10.1016/s1876-3804(12)60099-8

Ma, W. J., Hou, L. H., Luo, X., Tao, S. Z., Guan, P., Liu, J. Z., et al. (2020). Role of bitumen and NSOs during the decomposition process of a lacustrine Type-II kerogen in semi-open pyrolysis system. *Fuel* 259:116211. doi: 10.1016/j.fuel.2019.116211

Solarin, S. A. (2020). The effects of shale oil production, capital and labour on economic growth in the United States: a maximum likelihood analysis of the resource curse hypothesis. *Resour. Policy* 68:101799. doi: 10.1016/j.resourpol.2020.101799

Tao, S., Wang, Y. B., Tang, D. Z., Wu, D. M., Xu, H., and He, W. (2012). Organic petrology of Fukang Permian Lucaogou formation oil Shales at the northern foot of Bogda Mountain, Junggar Basin, China. *Intern. J. Coal Geol.* 99, 27–34. doi: 10.1016/j.coal.2012.05.001

Xie, X. M., Borjigin, T., Zhang, Q. Z., Zhang, Z. R., Qin, J. Z., Bian, L. Z., et al. (2015). Intact microbial fossils in the Permian Lucaogou Formation oil shale, Junggar Basin, NW China. *Intern. J. Coal Geol.* 146, 166–178. doi: 10.1016/j.coal.2015.05.011

Yu, Z. S., Dai, M. Q., Huang, M. M., Fang, S. W., Xu, J. C., Lin, Y., et al. (2018). Catalytic characteristics of the fast pyrolysis of microalgae over oil shale: analytical Py-GC/MS study. *Renew. Energy* 125, 465–471. doi: 10.1016/j.renene.2018.02.136

Zhang, L. Y., Wu, K. L., Chen, Z. X., Li, J., Yu, X. R., Hui, G., et al. (2021). The increased viscosity effect for fracturing fluid imbibition in shale. *Chem. Eng. Sci.* 232:116352. doi: 10.1016/j.ces.2020.116352

Zhao, W. Z., Zhu, R. K., Hu, S. Y., Hou, L. H., and Wu, S. T. (2020). Accumulation contribution differences between lacustrine organic-rich shales and mudstones and their significance in shale oil evaluation. *Pet. Explor. Dev.* 47, 1160–1171. doi: 10.1016/s1876-3804(20)60126-x
doi: 10.1016/j.petrol.2020.107926

Conflict of Interest: All authors are affiliated with the company PetroChina Co., Ltd.

APPENDIX

TABLE A1 | Basic geochemical information for the samples.

Samples	Depth (m)	Lithology	Type	Initial				Extracted after trichloromethane				Minerals (%)						
				TOC (%)	S_1 (mg/g)	S_2 (mg/g)	Tmax (°C)	TOC (%)	S_1 (mg/g)	S_2 (mg/g)	Tmax (°C)	Quartz	Potash feldspar	Plagioclase	Calcite	Dolomite	Pyrite	Clay
#1	3114.17	Silty mudstone	Shale	7.93	0.57	48.71	445	7.50	0.30	21.57	439	40.2	0	42.1	0	3.1	0	14.6
#2	3145.29	Dolomite	Non-shale	0.94	6.18	6.49	435	0.08	0.05	1.04	437	11	0	22.5	0	66.5	0	0
#3	3146.2	Silt-bearing mudstone	Shale	5.34	0.31	27.88	441	4.89	0.15	25.99	441	27.5	13.4	23.2	6.6	15.1	0	14.2
#4	3181.77	Dolomitic mudstone	Shale	6.12	1.07	43.61	444	5.65	0.20	40.76	440	30.1	0	36.4	0	22.2	0	11.3
#5	3200.04	Lime siltstone	Non-shale	1.15	5.63	5.28	433	0.20	0.12	1.16	435	25.9	6.4	41.2	15.9	10.6	0	0
#6	3222.24	Lime mudstone	Shale	3.87	2.78	26.25	437	3.39	0.26	22.28	437	29.3	2.6	29.1	0	34.6	0	4.4
#7	3235.38	Dolomitic siltstone	Non-shale	1.72	5.28	8.10	437	0.77	0.11	4.47	442	34.8	3.4	25.2	0	36.6	0	0
#8	3239.41	Dolomitic mudstone	Shale	2.54	3.22	9.77	437	1.46	0.08	4.01	444	20.4	6.9	28.5	0.0	36.3	0.0	7.9
#9	3246.26	Muddy siltstone	Non-shale	0.23	0.93	0.85	437	0.24	0.09	0.55	439	29.6	11.8	42.6	12	4	0	0
#10	3263.36	Dolomitic siltstone	Non-shale	3.34	28.42	22.98	430	0.75	0.12	1.93	435	27.7	0	26.9	0	45.3	0	0
#11	3264.09	Dolomitic mudstone	Shale	2.87	0.58	12.83	439	2.27	0.04	12.26	439	34.4	0	37.1	0	21.1	0	7.4
#12	3269.5	Dolomitic mudstone	Shale	8.76	0.76	66.73	440	7.32	0.05	55.80	443	23.3	0.9	28.8	0.8	31.5	5.2	9.5
#13	3270.7	Dolomitic siltstone	Non-shale	2.48	24.88	23.42	437	0.60	0.09	2.07	437	22	1.4	27.3	0.2	44.4	0	4.7
#14	3275.25	Dolomitic siltstone	Non-shale	2.06	30.74	27.71	435	0.27	0.08	1.11	437	24.3	0	50.3	0	25.3	0	0
#15	3279.01	Dolomitic mudstone	Shale	8.10	2.77	94.24	441	7.99	0.21	58.84	444	25.9	0	18.5	6.6	49	0	0
#16	3281.87	Dolomitic mudstone	Shale	11.01	0.97	88.36	446	9.96	0.40	59.73	443	11.2	0.7	16.9	0.0	66.0	0.0	5.2
#17	3286.14	Dolomitic siltstone	Non-shale	3.73	37.33	24.95	435	0.20	0.07	1.31	434	24.5	8.6	42.8	0	24.1	0	0
#18	3302.13	Dolomitic siltstone	Non-shale	2.13	19.05	17.28	435	0.12	0.11	0.88	437	27	0	38.4	0	34.6	0	0
#19	3304.86	Dolomitic mudstone	Shale	5.65	10.55	31.40	440	3.64	0.18	11.61	440	22.1	2	18.9	0	56.9	0	0
#20	3312.54	Lime siltstone	Non-shale	1.69	16.23	12.86	430	0.08	0.10	0.79	433	13.1	5.2	49	19.9	12.7	0	0
#21	3323.67	Dolomitic mudstone	Shale	5.91	3.80	34.33	4380	4.45	0.20	28.45	436	21.3	0	16.2	12.9	49.6	0	0

TABLE A2 | Analysis results of the extracts after different extraction treatments.

Samples	nC_6				$nC_6 + CHCl_3$				$CHCl_3$				nC_6		$CHCl_3$	
	Saturated	Aromatic	Resin	Asphaltene	Saturated	Aromatic	Resin	Asphaltene	Saturated	Aromatic	Resin	Asphaltene	K (mD)	Φ (%)	K (mD)	Φ (%)
#1	58.05	23.65	13.51	3.79	23.24	19.24	47.79	9.73	27.10	22.14	41.58	9.19	0.0043	0.60	0.0077	1.26
#2	60.27	18.23	19.47	2.02	53.35	16.67	26.82	3.16	56.88	17.93	22.59	2.60	0.0085	10.10	0.0151	11.94
#3	57.00	25.75	13.63	3.63	24.09	29.89	37.42	8.60	42.59	22.91	27.31	7.18	0.0058	4.20	0.0067	7.20
#4	60.95	23.91	12.27	2.87	25.25	31.61	35.77	7.37	45.75	15.18	34.33	4.74	0.0085	1.90	0.0120	3.10
#5	57.46	20.65	17.16	4.74	50.37	19.85	24.43	5.35	53.60	20.76	20.65	5.00	0.0120	10.87	0.0180	11.33
#6	57.78	23.55	13.81	4.86	22.17	25.34	44.78	7.71	38.36	14.95	39.38	7.31	0.0042	5.29	0.0067	7.00
#7	61.38	18.77	15.18	4.67	55.49	18.31	20.73	5.47	58.67	16.32	20.16	4.85	0.0055	3.57	0.0141	4.00
#8	58.47	23.33	13.27	4.93	11.58	25.34	53.88	9.20	38.46	17.54	33.69	10.31	0.0006	3.05	0.0037	3.93
#9	47.43	21.56	25.22	5.79	43.82	19.36	30.32	6.50	45.43	21.22	27.28	6.07	0.0010	5.20	0.0044	5.50
#10	48.98	34.32	12.33	4.37	13.32	28.20	52.25	6.23	33.98	19.65	38.17	5.60	0.0280	1.79	0.0830	3.08
#11	49.45	19.04	25.98	5.53	45.38	14.04	33.23	7.35	48.06	18.28	28.29	5.37	0.0018	12.43	0.0069	12.52
#12	47.82	32.22	14.53	5.44	11.82	12.21	65.98	9.99	23.27	15.99	51.31	9.43	0.0005	3.30	0.0034	8.32
#13	47.35	34.78	13.37	4.50	13.32	14.25	64.77	7.66	23.78	13.70	53.75	8.77	0.0006	2.43	0.0034	5.46
#14	52.03	18.50	25.88	3.59	46.55	13.82	31.69	7.94	49.80	18.26	28.29	3.65	0.0012	8.22	0.0023	8.24
#15	49.96	19.77	24.19	6.08	44.67	19.33	28.72	7.28	47.79	18.78	26.36	7.07	0.0081	14.39	0.0085	14.40
#16	50.88	33.92	11.70	3.51	18.28	14.70	53.31	13.71	39.13	15.39	36.22	9.26	0.0039	2.92	0.0067	6.33
#17	56.44	28.44	12.44	2.67	10.34	18.10	66.38	5.17	40.35	15.99	40.33	3.33	0.0007	2.82	0.0017	5.74
#18	50.63	18.12	26.38	4.87	50.25	16.33	28.94	4.48	48.20	17.09	29.76	4.94	0.0191	16.97	0.0370	17.35
#19	47.55	22.79	25.47	4.19	41.33	17.63	32.56	8.48	44.41	21.39	29.92	6.27	0.0046	11.91	0.0069	12.30
#20	48.84	30.79	16.98	3.40	8.85	25.17	58.69	7.29	38.43	20.99	38.42	2.16	0.0029	7.02	0.0049	9.09
#21	47.23	23.22	21.44	8.11	40.22	18.35	30.56	10.87	42.69	20.93	26.75	9.63	0.0021	8.69	0.0024	9.60

TABLE A3 | NMR analysis results.

No.	Lithology	0.05–0.1 μm	0.1–0.5 μm	0.5–1.0 μm	>1.0 μm	>0.05 μm
#3	Silt-bearing mudstone	2.99	3.12	1.58	0.57	8.26
#9	Muddy siltstone	5.34	5.50	3.02	1.52	15.37
#15	Dolomitic mudstone	4.20	26.08	22.47	15.75	68.50
#16	Dolomitic mudstone	5.81	7.61	10.96	26.70	51.09
#22	Dolomitic mudstone	3.00	5.49	3.65	9.87	22.02

TABLE A4 | High-pressure mercury injection results.

Samples	Lithology	>0.0037 μm	>0.018 μm	>0.048 μm	0.0037–0.018 μm	0.018–0.048 μm	0.048–0.133 μm	0.133–0.735 μm	0.735–0.942 μm	>0.942 μm
#3	Silt-bearing mudstone	60.69	9.629	4.282	51.061	5.347	3.223	1.059	0	0
#9	Muddy siltstone	80.74	67.27	49.71	13.47	17.56	33.64	16.055	0.015	0
#15	Dolomitic mudstone	81.91	80.84	77.04	1.07	3.8	37.75	39.29	13.437	9.88
#22	Dolomitic mudstone	85.75	14.81	3.358	70.94	11.452	3.358			

frontiers in Earth Science

ORIGINAL RESEARCH
published: 16 April 2021
doi: 10.3389/feart.2021.662586

Quantitative Measurement of Retained Oil in Organic-Rich Shale—A Case Study on the Chang 7 Member in the Ordos Basin, China

Lianhua Hou[1], Xia Luo[1], Senhu Lin[1], Zhongying Zhao[1] and Yong Li[2]*

[1] Research Institute of Petroleum Exploration & Development, PetroChina, Beijing, China, [2] State Key Laboratory of Organic Geochemistry, Guangzhou Institute of Geochemistry, Chinese Academy of Sciences, Guangzhou, China

This study proposes a method to calculate the retained oil content (W_O) in cores collected by a sealed tool from organic-rich shale with thermal maturity around%Ro = 0.8 in the Ordos Basin, China. Approaches such as soaking cores at low temperature, multiple extractions, multiple pyrolysis, and multiple chromatographic analyses were conducted and then the relationships between total retained oil content and mineral compositions were analyzed. The total retained oil content measured by the method proposed in this paper is 60–260% higher than that measured by a conventional pyrolysis method and 34–69% higher than the sum (W_O) of two extractions with dichloromethane (W_{O3}) and chloroform (W_{O4}). After extractions with dichloromethane and chloroform (W_{O5}), the oil retained in the organic-rich shale was 4.7–11.6%, which has not been extracted. Positive correlations exist between W_O (i.e., W_{O3} + W_{O4}) and total organic carbon (TOC) and S_1 (absorbed hydrocarbon by rock pyrolysis), and W_O has the highest correlation coefficient with the former. The method can provide important guidance for the objective analysis of retained oil in organic-rich shale, and it is reliable for the evaluation of shale oil reserves.

Keywords: organic-rich shale, retained oil, oil content calculation, pyrolysis, sealed coring

OPEN ACCESS

Edited by:
Dongdong Wang, Shandong University of Science and Technology, China

Reviewed by:
Wenxue Han, Shandong University of Science and Technology, China
Weijiao Ma, China University of Petroleum (Huadong), China

****Correspondence:***
Lianhua Hou
houlh@petrochina.com.cn

Specialty section:
This article was submitted to Economic Geology, a section of the journal Frontiers in Earth Science

Received: *01 February 2021*
Accepted: *25 February 2021*
Published: *16 April 2021*

Citation:
Hou L, Luo X, Lin S, Zhao Z and Li Y (2021) Quantitative Measurement of Retained Oil in Organic-Rich Shale—A Case Study on the Chang 7 Member in the Ordos Basin, China. Front. Earth Sci. 9:662586. doi: 10.3389/feart.2021.662586

INTRODUCTION

Since the groundbreaking progress made by the United States on shale oil in Bakken reserves in the 1950s, technology related to shale oil in the US has been developing rapidly and achieved its profitability in 2018 (Soeder, 2018; Hackley et al., 2020; Solarin et al., 2020; Ulrich-Schad et al., 2020). Drawing lessons from the experience of the USA's shale oil development, China began to explore the technology and practice on shale oil exploration and development and made a step forward on fields including geological theory, exploration and development technology, and experimental techniques (Hou et al., 2020; Hou et al., 2021a; Kang et al., 2020; Ma et al., 2020a; Ma et al., 2020b; Zhao et al., 2020a; Zhu et al., 2021). However, more researches are needed to tackle problems related to the quantitative evaluation of the total retained oil content, the occurrence mechanism of shale oil, and pores and fluid flowing mechanism in shale formation. Among these topics, objective quantitative evaluation on the retained oil content of organic-rich shale has always been the focus of ongoing researches (Jarvie, 2012; Chen and Jiang, 2016; Abrams et al., 2017; Jiang et al., 2017; Li M. W. et al., 2019).

There are two methods commonly used to measure the total retained oil in organic-rich shale: one is conventional chloroform bitumen "A" and the other is rock pyrolysis (Stroup, 1987; Johannes et al., 2007; Han et al., 2015; Nady and Hammad, 2015; Li J. B. et al., 2019). Because light hydrocarbon is easily lost, part of the hydrocarbons in S_1 is regarded as residual hydrocarbon. Besides, conventional chloroform bitumen "A" can hardly reveal whether the shale oil is free or absorbed. The other method is modified pyrolysis (Zink et al., 2016; Chen et al., 2017; Li et al., 2018; Li M. W. et al., 2019; Ma et al., 2019; Hou et al., 2021b). In conventional source rock pyrolysis, S_1 represents the residual hydrocarbon in rock, which is the oil that has already existed, and S_2 represents the hydrocarbon potential in kerogen. In shale oil evaluation, since S_1 has compositions similar to shale oil, they can be easily extracted by dichloromethane with weak polarity. Therefore, they are treated as free shale oil. However, S_1 does not represent all free shale oil and S_2 does not completely show the hydrocarbon potential in kerogen (Chen et al., 2018; Li et al., 2018; Li M. W. et al., 2019; Ma et al., 2019; Hou et al., 2020). S_2 contains small amounts of free oil and absorbed oil, so the pyrolysis method cannot estimate the content of absorbed shale oil.

The modified method requires instantly freezing cores by liquid nitrogen in the field (at −50°C) and then crushing them in a closed system (190°C). Pyrolysis analysis immediately follows. A light hydrocarbon restoring coefficient is estimated by forward modeling, and correction to the historical data of the shale with medium–high maturity is conducted. Absorbed oil can be separated from the already generated hydrocarbon oil by changing the heating rate. But this method still shows limitations in the following aspects: firstly, online analysis cannot be achieved as crushed samples enter the pyrolysis apparatus, resulting in a partial loss of light hydrocarbon. Secondly, the assumption that kerogen generates hydrocarbon at above 300°C lacks a reliable scientific proof. Besides, since there are only a few samples (in total 100 mg), a big error may exist. For shale with abundant organic matter [total organic carbon (TOC) as high as 20–30% and hydrocarbon potential up to 100 mg/g rock], the error is noticeably high (the maximum S_2 of a standard sample in China is 16.98 mg/g rock).

SAMPLES AND METHODS

Eleven samples from Well L85 drilled in the Chang 7 member in the Ordos Basin were collected (see basic geochemical information listed in **Table 1**). After taken into a sealed tool, the cores were wiped with cotton to remove the sealing fluid on their surface within 1.5 h so that they will not be eroded by the sealing fluid. Then, the cores are weighed and put into containers filled with dichloromethane solution. The cores should be completely submerged into the solution by at least 2 cm below. Finally, the containers (i.e., sealed bottles) containing the dichloromethane solution and cores were put into a freezer where the temperature remained below 20°C to prevent the dichloromethane solution from evaporating (the boiling point of dichloromethane is 39.5°C). After all these were done, the samples were moved from the field to the laboratory.

After immersing the cores for 10–30 days, 5 ml of methylbenzene was added to the bottle as the standard sample. The solution was placed into a crusher and then the crusher put into liquid nitrogen. The core sample was crushed into particles of 0.18 mm. The crushed sample and the dichloromethane were moved into a bottle and sealed with a cap, and then chromatographic analysis was immediately started (the above procedure is denoted as step 1). After being immersed for 10–30 days, the core sample was separated from the solution. The solution was measured and then 1 ml solution was taken and put into two flasks (labeled A and B) marked with internal rulers. Quantitative analysis of total hydrocarbon gas chromatography in a flask (A#) was conducted (the above procedure is denoted as step 2). Into another flask (B#), after full evaporation, solvent was add to 1 ml and then chromatographic analysis was conducted (the above procedure is denoted as step 3). The rest of solution was weighed after full evaporation. The rest of the crushed sample was placed into the dichloromethane solution after weighing and extraction. Of the solution, 1 ml was taken after the isochoric process and put into two flasks (labeled C and D) with internal rulers. Quantitative analysis of total hydrocarbon gas chromatography in a flask (C#) was conducted (the above procedure is denoted as step 4). Another flask (D#), after full evaporation, is added with solvent to 1 ml and then chromatographic analysis was started (the above procedure is denoted as step 5). The remaining solution was weighed after full evaporation. A certain amount of the sample powder was take after drying, weighed, and the pyrolysis analysis conducted (the above procedure is denoted as REP 1; the results are listed in **Table 2**). The remaining sample powder was placed into a chloroform solution after weighing and extraction. The solution was completely evaporated and weighed. Again, a certain amount of dried sample was weighed and rock pyrolysis was conducted (the above procedure is denoted as REP 2). The experiments above were conducted at the National Key Laboratory of Enhanced Oil Recovery, Research Institute of Petroleum Exploration & Development, PetroChina.

RESULTS AND DISCUSSION

Chromatographic Analysis

Figures 1–5 show the chromatographic analysis of the core samples that went through the above steps 1–5. Taking sample 6 as an example, the calculation process is given in **Appendix Table A1**. The samples have been completely immersed in dichloromethane solution for 10–30 days before being crushed in liquid nitrogen, and then followed by immediate gas chromatography analysis (**Figure 1**). The light components remain intact, and a complete series of light hydrocarbons, namely, nC$_5$, nC$_6$, nC$_7$, nC$_8$, and nC$_9$, can be detected. The peak area of nC$_7$ is the largest, and nC$_9$ is the main peak. The powder was separated from the solution after the sample was crushed and immersed for 10–30 days. After the isochoric process, 1 ml of the solution was added into flasks A and B with internal rulers.

TABLE 1 | Basic geochemical data of the experiment samples.

Sample no.	Depth (m)	TOC (%)	Quartz (%)	Potash feldspar (%)	Plagioclase (%)	Calcite (%)	Dolomite (%)	Siderite (%)	Pyrite (%)	Clay (%)
1	1,576.86	6.34	23.4	1.0	7.9	0.0	12.1	0.0	12.4	43.2
2	1,579.86	32.842	21.6	5.7	4.6	0.0	2.4	0.0	35.9	29.8
3	1,580.34	6.63	20.0	3.4	5.1	3.3	7.5	12.1	9.7	38.9
4	1,581.07	20.87	16.7	4.3	7.1	0.0	7.1	0.0	36.3	28.5
5	1,581.91	25.77	29.9	1.8	1.8	0.0	1.6	0.0	31.3	33.6
6	1,583.47	37.86	23.6	2.5	1.0	0.0	5.7	0.0	32.8	34.4
7	1,584.91	18.6	30.9	6.0	3.3	4.2	3.6	0.0	42.0	10.0
8	1,586.23	18.83	37.8	2.5	6.1	0.0	0.9	0.0	40.6	12.1
9	1,589.85	13.09	29.9	1.5	6.2	0.8	1.9	0	15.5	44.4
10	1,591.89	12.83	25.4	1.5	5.8	0.4	1.0	0.0	10.1	22.0
11	1,592.25	18.67	26.1	3.1	4.0	4.9	6.4	0.0	35.7	19.8

TOC, total organic carbon.

TABLE 2 | Pyrolysis results of samples after various treatments.

sample no.	depth (m)	s_{01} (mg/g)	s_{02} (mg/g)	t_{max0} (°C)	s_{11} (mg/g)	s_{12} (mg/g)	t_{max1} (°C)	s_{21} (mg/g)	s_{22} (mg/g)	t_{max2} (°C)
1	1,576.86	3.75	15.66	440	0.24	12.80	439	0.17	10.23	441
2	1,579.86	7.39	149.38	439	0.74	137.96	437	0.60	129.70	436
3	1,580.34	5.39	30.77	443	0.19	13.83	441	0.15	13.47	444
4	1,581.07	10.05	87.20	442	0.86	82.84	442	0.55	79.71	441
5	1,581.91	8.19	105.41	438	1.06	95.40	436	0.67	91.93	439
6	1,583.47	13.33	150.92	440	0.77	137.57	440	0.66	132.20	442
7	1,584.91	9.89	70.54	441	1.50	57.73	439	0.61	51.34	442
8	1,586.23	5.25	79.98	441	0.89	61.14	442	0.57	57.64	442
9	1,589.85	4.07	95.89	440	0.93	87.99	439	0.68	82.75	440
10	1,591.89	4.21	70.88	441	0.69	64.29	437	0.61	60.06	436
11	1,592.25	5.51	64.86	439	0.49	55.61	439	0.38	46.47	436

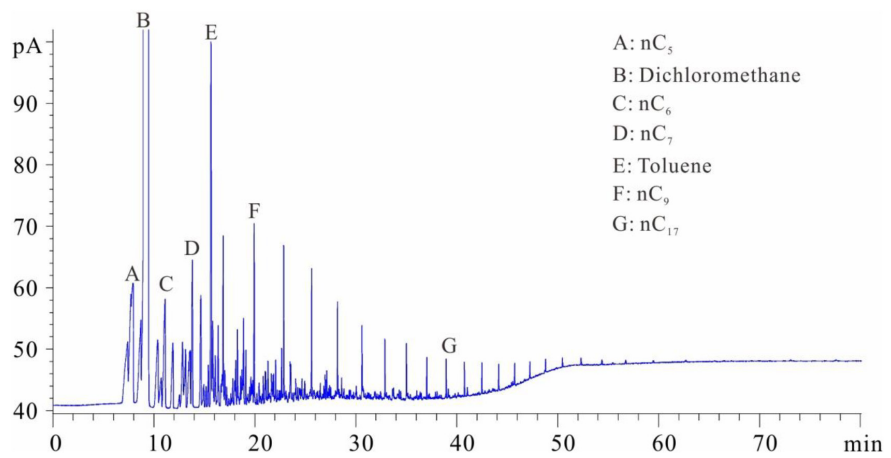

FIGURE 1 | Chromatogram of samples that were soaked first and then crushed (chromatogram after step 1).

Quantitative analysis of total hydrocarbon gas chromatography was directly conducted for flask A (see the result in **Figure 2**). Light hydrocarbons are lost as the immersion time increases (**Figure 2**). Among them, all of C_5 is lost, and the losses of nC_6 and nC_7 are 52.58 and 26.64%, respectively. C_8 and later hydrocarbons gradually increase, and W_{O1} is calculated to be 0.032 kg/t rock. In **Figure 2**, toluene and D-C_{24} standard samples are used for compound calibration. The results show that the error of the two types of standard samples for normal alkanes is 13.55%, and the calibration value of D-C_{24} is slightly higher, indicating that these two standard samples can be used. Solvent was added into flask B to 1 ml after fully evaporating and then chromatographic analysis proceeded (see the result in **Figure 3**). After the rock soaking solution volatilized completely at room

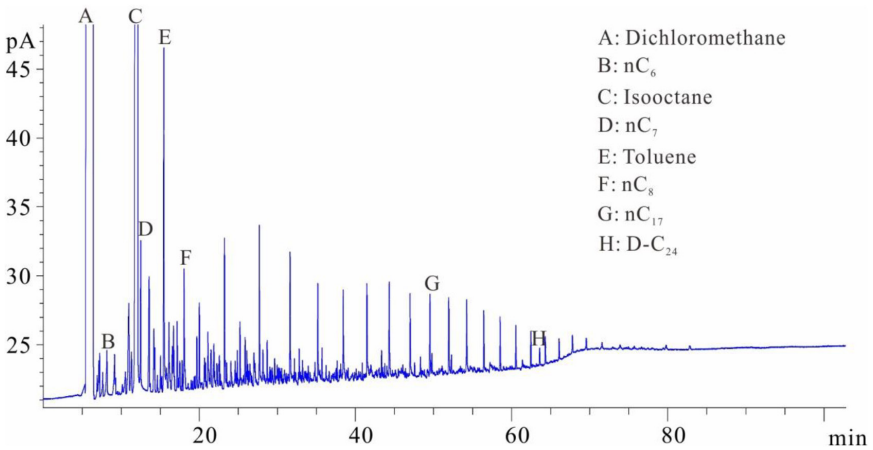

FIGURE 2 | Chromatogram of samples that were crushed first and then soaked (chromatogram after step 2).

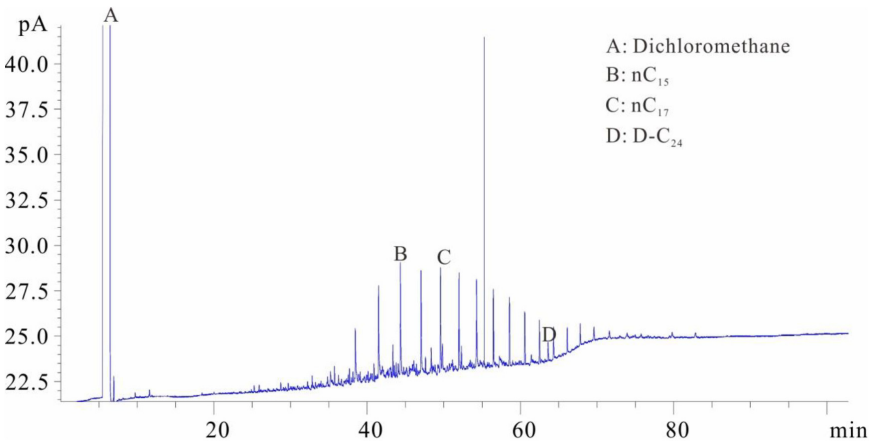

FIGURE 3 | Chromatogram of samples that were soaked first and then evaporated (chromatogram after step 3).

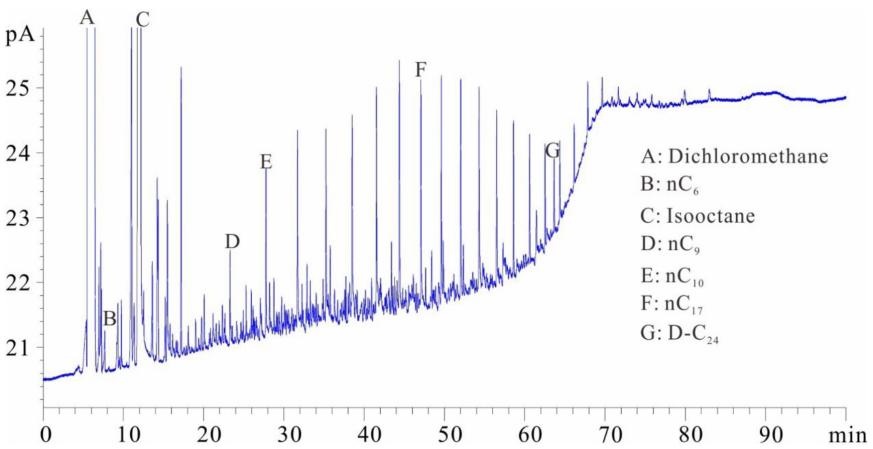

FIGURE 4 | Chromatogram of samples after dichloromethane extractions (chromatogram after step 4).

temperature, the hydrocarbons before nC_{13} are almost lost. The results show that the losses of nC_{13}, nC_{14}, and nC_{15} are 46.76, 14.57, and 0.43%, respectively. The two calculation results of nC_{16}–nC_{25} are within + 10%. Light hydrocarbons before C_{14} were quantitatively analyzed by chromatography. The pre-C_{14} hydrocarbons precipitated by sample soaking are 1.91 kg/t rock, accounting for 32.51% of the total hydrocarbons.

The samples were placed into the dichloromethane solution for extraction after separating the solution from the crushed sample. One milliliter of the extracted solution was collected and placed into flasks C and D with internal rulers after the isochoric process. Quantitative analysis of total hydrocarbon gas chromatography was directly conducted in flask C (similar to flask A) (see the result in **Figure 4**). The shales were soaked in dichloromethane and then extracted. The extraction product is divided into two parts: one part is that of hydrocarbons after C_{10} and the other part is of the isomeric hydrocarbons of C_6–C_7 (**Figure 4**). The molecular radius of this part of the hydrocarbons is small. The hydrocarbons in this part are stored in the shale nanopores and cannot be completely precipitated

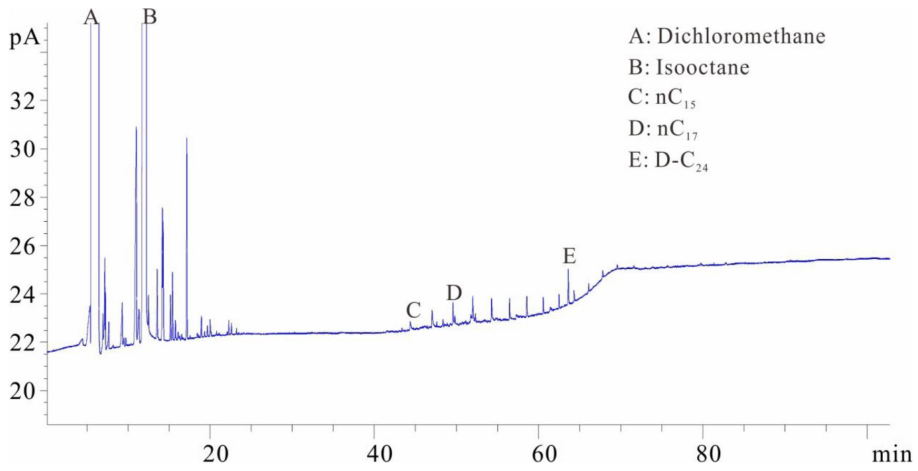

FIGURE 5 | Chromatogram of samples after chloroform extractions (chromatogram after step 5).

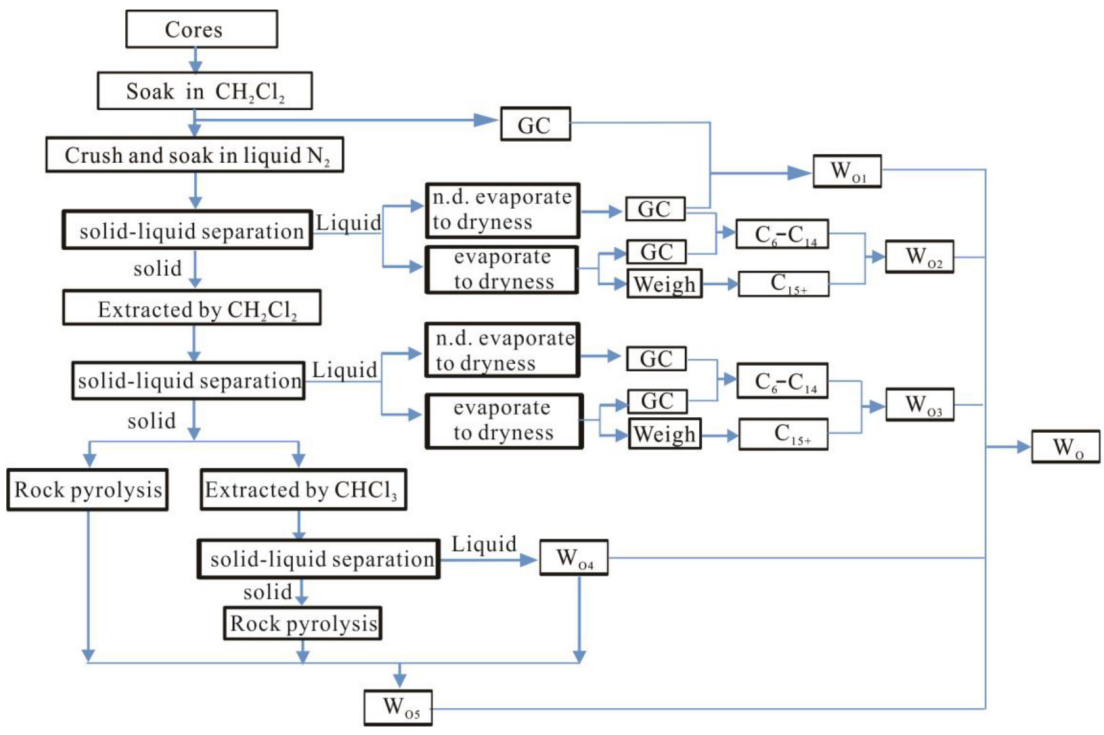

FIGURE 6 | Measuring procedures of the retained oil content in organic-rich shale.

by the dichloromethane. One milliliter solvent was added into flask D after fully evaporating and chromatographic analysis was conducted (similar to flask B) (**Figure 5**). The D volumetric flask is not easy to volatilize completely during the experiment, so the storage time is very long. Due to the long storage time, the normal alkanes before nC_{17} have all been lost. However, the C_6–C_7 isomeric alkanes in **Figure 4** are not significantly reduced in **Figure 5**. It is speculated that these C_6–C_7 isomeric alkanes may coexist with resins and asphaltenes and are extremely difficult to volatilize.

Pyrolysis Analysis

After drying the rock samples, pyrolysis analysis was immediately conducted. The results are denoted as S_{01}, S_{02}, and T_{max0} (**Table 2**). Pyrolysis analysis was conducted for the second time after the samples were extracted by dichloromethane and dried by fully evaporating (after REP 1) (Jiang et al., 2017; Li et al., 2018; Li M. W. et al., 2019; Li J. B. et al., 2019). The results are denoted as S_{11}, S_{12}, and T_{max1} (**Table 2**). After weighing, the remaining sample powder was placed in chloroform solution for extraction. Then, after chloroform evaporated, the samples were weighed and dried (after REP 2). Finally, pyrolysis experiment was done for the third time (Sun et al., 2019; Hou et al., 2020). The results are denoted as S_{21}, S_{22}, and T_{max2} (**Table 2**).

Calculations of Retained Oil Content in Organic-Rich Shale

We conducted sealed coring to organic shale that has a maturity level of%Ro = 0.8 in the Ordos Basin to calculate the total retained oil content. The core sample went through procedures including low-temperature soaking, multiple extractions, multiple pyrolysis, and multiple chromatographic analyses (refer to Section "Samples and Methods" for detailed experiment procedures). This study developed an integrated approach to measuring the total retained oil content in organic-rich shale (Chen and Jiang, 2016; Chen et al., 2018; Li et al., 2018; Li M. W. et al., 2019; Ma et al., 2019; Hou et al., 2020). The workflow is shown as follows (**Figure 6**).

The detailed calculation process is as follows:

$$W_{O1} = S_{T1} - S_{T2} \quad (1)$$

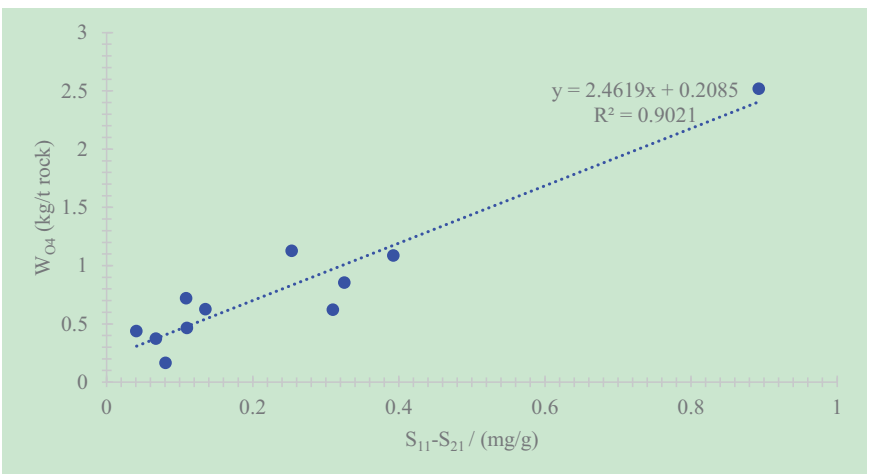

FIGURE 7 | Diagram between W_{O4} and S_{11}–S_{21}.

TABLE 3 | Calculation of oil content in organic-rich shale.

Sample no.	Depth (m)	W_{O1} (kg/t rock)	W_{O2} (kg/t rock)	W_{O3} (kg/t rock)	W_{O4} (kg/t rock)	W_{O5} (kg/t rock)	W_O (kg/t rock)
1	1576.86	0.015	1.587	3.530	0.372	0.607	6.111
2	1579.86	0.005	6.369	11.984	0.625	1.997	20.980
3	1580.34	0.089	3.557	8.861	0.438	0.632	13.577
4	1581.07	0.059	5.390	9.979	0.620	1.666	17.714
5	1581.91	0.006	4.361	15.882	1.086	2.059	23.394
6	1583.47	0.003	5.876	19.139	0.719	2.357	28.094
7	1584.91	0.092	3.458	8.631	2.518	1.925	16.624
8	1586.23	0.088	4.183	12.093	0.854	1.704	18.922
9	1589.85	0.015	2.354	7.487	1.126	0.593	11.575
10	1591.53	0.022	2.493	7.058	0.165	0.575	10.313
11	1592.25	0.009	4.502	7.861	0.464	1.236	14.072

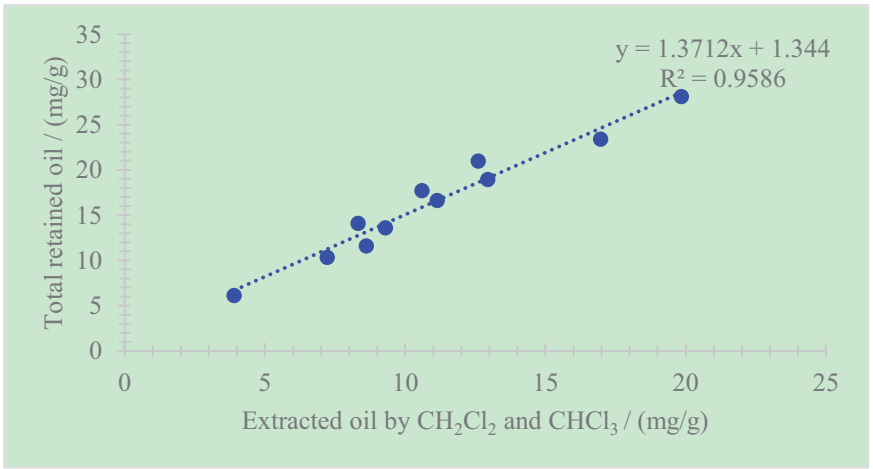

FIGURE 8 | Relationship between the total retained oil content and the extracted sum of dichloromethane and chloroform.

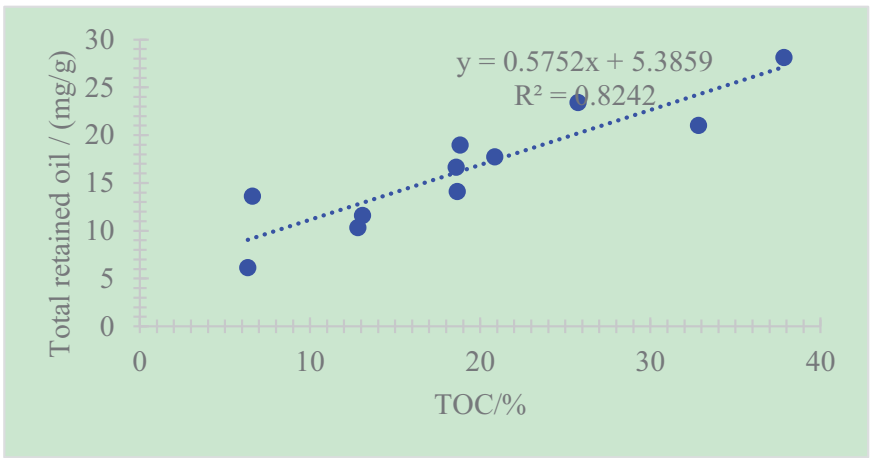

FIGURE 9 | Relationship between the total retained oil content and TOC.

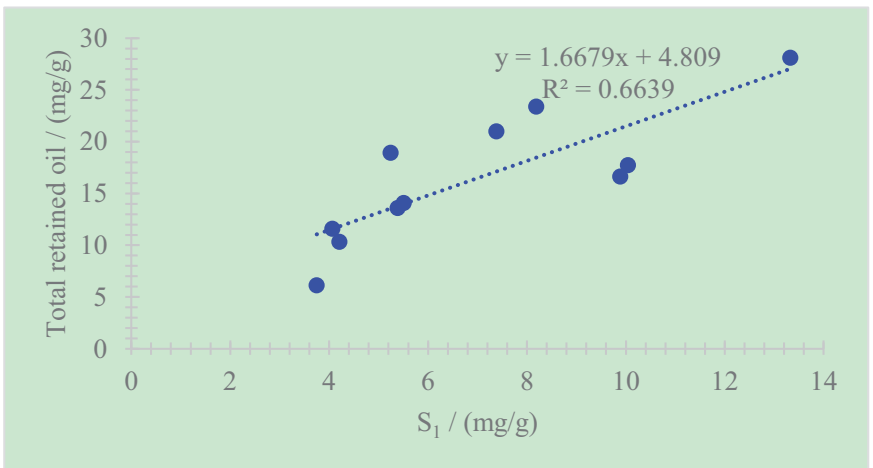

FIGURE 10 | Relationship between the total retained oil content and S_1.

W_{O1} refers to the difference (C_5–C_7) between the core samples after step 2 and after step 1 (in flask A#).

$$W_{O2} = S_{T3} - S_{T2} + W_{V1} \quad (2)$$

W_{O2} refers to the difference (C_6–C_{14}) between the core samples after step 3 (flask B#) and after step 2 (flask A#), plus the weight W_{V1} of the evaporated solution remaining after step 2. S_{T3} - S_{T2} refers to the light hydrocarbon in the sample.

$$W_{O3} = S_{T5} - S_{T4} + W_{V2} \quad (3)$$

W_{O3} represents the difference (C_6–C_{14}) between the core samples after step 5 (D#) and after step 4 (C#), plus the weight W_{V2} of the evaporated solution remaining after step 5. S_{T5} - S_{T4} refers to the light hydrocarbon in the sample.

The solution, after extracted by chloroform, filtered, and evaporated completely, is weighed to be W_{O4}. The hydrocarbons retained in the shale after chloroform extraction is defined as W_{O5}, and this part of hydrocarbons can be calculated from **Figure 7**. After the shale is extracted by dichloromethane and chloroform, the difference of the two pyrolysis S_1 values and the amount of chloroform extraction show a positive relationship. Therefore, pyrolysis analysis of the rock after chloroform extraction can infer the retained hydrocarbon content in the rock according to the S_1 content.

Therefore, the calculated oil content in shale should include five parts (**Table 3**), namely:

$$W_O = W_{O1} + W_{O2} + W_{O3} + W_{O4} + W_{O5} \quad (4)$$

The retained oil W_{O4} in organic-rich shale after extracted by dichloromethane and chloroform accounts for 4.65–11.58%. In other words, there is 4.65–11.58% of retained oil that can hardly be soluble in organic solvent in organic-rich shale, and this part of retained oil can hardly be extracted.

Correlation Analysis of Geochemical Parameters

The total retained oil content shows good correlations with the extracted sum of dichloromethane and chloroform, whose correlation coefficient is $R^2 = 0.96$ (**Figure 8**). This phenomenon illustrates that the primary components in the total retained oil are mainly soluble organic matter that can be extracted by dichloromethane and chloroform. In other words, the retained oil in organic-rich shale can be extracted using some techniques.

A positive correlation between the total retained oil content and TOC exists, with $R^2 = 0.82$ (**Figure 9**). This phenomenon demonstrates that the increase in TOC may cause more shale oil remaining in rock, namely, retained oil (Hou et al., 2020; Shao et al., 2020; Zhao et al., 2020b). To explore shale oil, shale with a higher TOC is the target.

A positive correlation exists between the total retained oil content and S_1 (Chen et al., 2017; Chen et al., 2018; Li et al., 2018; Li M. W. et al., 2019; Ma et al., 2019). The correlation coefficient is $R^2 = 0.66$ (**Figure 10**). The relatively weak correlation also shows that the retained oil in shale cannot be calculated objectively only by the method of conventional rock pyrolysis.

CONCLUSION

This study took sealed cores of organic-rich shale in the Ordos Basin and measured the total retained oil (W_O) *via* approaches including low-temperature soaking, multiple extractions, multiple pyrolysis, and multiple chromatographic analyses. The W_O value obtained from the new method is 60–260% higher than that obtained from conventional pyrolysis and 34–69% higher than the sum of the extractions by dichloromethane (W_{O3}) and chloroform (W_{O4}). Even after extraction by dichloromethane and chloroform, there remains 4.7–11.6% hydrocarbon retained in the organic-rich shale (W_{O5}). The total retained oil content (W_O) in the organic-rich shale exhibits a positive relationship with the sum of the extractions using dichloromethane and chloroform (W_{O3} + W_{O4}), with R^2 reaching 0.96. This indicates that the primary composition in the total retained oil is soluble organic matter and is extractable *via* dichloromethane and chloroform. Positive correlations can also be observed between W_O and TOC, and S_1 through coefficients of 0.82 and 0.66, respectively.

DATA AVAILABILITY STATEMENT

The original contributions presented in the study are included in the article/supplementary material, further inquiries can be directed to the corresponding author/s.

AUTHOR CONTRIBUTIONS

LH: conceptualization, methodology, investigation, and writing – original draft. XL: data curation, writing – review and editing. SL: formal analysis, resources. ZZ: software, validation, and project administration. YL: funding acquisition. All authors contributed to the article and approved the submitted version.

FUNDING

This study was funded by PetroChina Co., Ltd. (grant nos. 2015D-4810-02 and 2018ycq03), the Research on Exploration and Development Technology of Unconventional Oil and Gas Resources (2012A-4802-02), and the Formation Mechanism and Enrichment Regularity of Terrestrial Tight Oil (Shale Oil) in China (2014CB239000).

ACKNOWLEDGMENTS

We express our genuine appreciation to Professor Jones and Harris for their constructive comments and revisions. We also thank Dr. Johnson for his language editing and polishing work.

REFERENCES

Abrams, M. A., Gong, C. Y., Garnier, C., and Sephton, M. A. (2017). A new thermal extraction protocol to evaluate liquid rich unconventional oil in place and in-situ fluid chemistry. *Mar. Pet. Geol.* 88, 659–675. doi: 10.1016/j.marpetgeo.2017.09.014

Chen, Z. H., Guo, Q. L., Jiang, C. Q., Liu, X. J., Reyes, J., Mort, A., et al. (2017). Source rock characteristics and Rock-Eval-based hydrocarbon generation kinetic models of the lacustrine chang-7 Shale of triassic Yanchang Formation, Ordos Basin, China. *Int. J. Coal Geol.* 182, 52–65. doi: 10.1016/j.coal.2017.08.017

Chen, Z. H., and Jiang, C. Q. (2016). A revised method for organic porosity estimation in shale reservoirs using rock-eval data: example from Duvernay Formation in the western Canada sedimentary basin. *AAPG Bull.* 100, 405–422. doi: 10.1306/08261514173

Chen, Z. H., Li, M. W., Ma, X. X., Cao, T. T., Liu, X. J., Li, Z. M., et al. (2018). Generation kinetics based method for correcting effects of migrated oil on rock-eval data – an example from the eocene Qianjiang Formation, Jianghan Basin, China. *Int. J. Coal Geol.* 195, 84–101. doi: 10.1016/j.coal.2018.05.010

Hackley, P. C., Dennen, K. O., Garza, D., Lohr, C. D., Valentine, B. J., Hatcherian, J. J., et al. (2020). Oil-source rock correlation studies in the unconventional Upper Cretaceous Tuscaloosa marine shale (TMS) petroleum system, Mississippi and Louisiana, USA. *J. Pet. Sci. Eng.* 190:107015. doi: 10.1016/j.petrol.2020.107015

Han, H., Zhong, N. N., Huang, C. X., and Zhang, W. (2015). Pyrolysis kinetics of oil shale from northeast China: implications from thermogravimetric and rock–eval experiments. *Fuel* 159, 776–783. doi: 10.1016/j.fuel.2015.07.052

Hou, L. H., Luo, X., Han, W. X., Lin, S. H., Pang, Z. L., and Liu, J. Z. (2020). Geochemical evaluation of the hydrocarbon potential of shale oil and its correlation with different minerals-a case study of the TYP shale in the Songliao Basin, China. *Energy Fuels* 34, 11998–12009. doi: 10.1021/acs.energyfuels.0c01285

Hou, L. H., Ma, W. J., Luo, X., Liu, J. Z., Lin, S. H., and Zhao, Z. Y. (2021a). Hydrocarbon generation-retention-expulsion mechanism and shale oil producibility of the Permian lucaogou shale in the Junggar Basin as simulated by semi-open pyrolysis experiments. *Mar. Pet. Geol.* 125:104880. doi: 10.1016/j.marpetgeo.2020.104880

Hou, L. H., Luo, X., Zhao, Z. Y., and Zhang, L. J. (2021b). Identification of oil produced from shale and tight reservoirs in the permian lucaogou shale sequence, Jimsar Sag, Junggar Basin, NW China. *ACS Omega* 6, 2127–2142. doi: 10.1021/acsomega.0c05224

Jarvie, D. M. (2012). "Shale resource systems for oil and gas: part 1- shale-gas resource systems," in *Shale Reservoirs Giant Resources for the 21st Century*, Vol. 97, ed. J. A. Breyer (Tulsa: AAPG Memoir), 69–87.

Jiang, C. Q., Chen, Z. H., Lavoie, D., Percival, J. B., and Kabanov, P. (2017). Mineral carbon MinC (%) from Rock-Eval analysis as a reliable and cost-effective measurement of carbonate contents in shale source and reservoir rocks. *Mar. Pet. Geol.* 83, 184–194. doi: 10.1016/j.marpetgeo.2017.03.017

Johannes, I., Kruusement, K., and Veski, R. (2007). Evaluation of oil potential and pyrolysis kinetics of renewable fuel and shale samples by Rock-Eval analyzer. *J. Anal. Appl. Pyrol.* 79, 183–190. doi: 10.1016/j.jaap.2006.12.001

Kang, Z. Q., Zhao, Y. S., and Yang, D. (2020). Review of oil shale in-situ conversion technology. *Appl. Energy* 269:115121. doi: 10.1016/j.apenergy.2020.115121

Li, M. W., Chen, Z. H., Cao, T. T., Ma, X. X., Liu, X. J., Li, Z. M., et al. (2018). Expelled oils and their impacts on Rock-Eval data interpretation, Eocene Qianjiang Formation in Jianghan Basin, China. *Int. J. Coal Geol.* 191, 37–48. doi: 10.1016/j.coal.2018.03.001

Li, M. W., Chen, Z. H., Ma, X. X., Cao, T. T., Qian, M. H., Jiang, Q. G., et al. (2019). Shale oil resource potential and oil mobility characteristics of the Eocene-Oligocene Shahejie Formation, Jiyang Super-Depression, Bohai Bay Basin of China. *Int. J. Coal Geol.* 204, 130–143. doi: 10.1016/j.coal.2019.01.013

Li, J. B., Wan, M., Chen, Z. H., Lu, S. F., Jiang, C. Q., Chen, G. H., et al. (2019). Evaluating the total oil yield using a single routine Rock-Eval experiment on as-received shales. *J. Anal. Appl. Pyrol.* 144:104707. doi: 10.1016/j.jaap.2019.104707

Ma, W. J., Hou, L. H., Luo, X., Liu, J. Z., Tao, S. Z., Guan, P., et al. (2020a). Generation and expulsion process of the chang 7 oil shale in the ordos basin based on temperature-based semi-open pyrolysis: implications for in-situ conversion process. *J. Pet. Sci. Eng.* 190:107035. doi: 10.1016/j.petrol.2020.107035

Ma, W. J., Hou, L. H., Luo, X., Tao, S. Z., Guan, P., Liu, J. Z., et al. (2020b). Role of bitumen and NSOs during the decomposition process of a lacustrine Type-II kerogen in semi-open pyrolysis system. *Fuel* 259:116211. doi: 10.1016/j.fuel.2019.116211

Ma, X. X., Li, M. W., Pang, X. Q., Wei, X. Y., Qian, M. H., Tao, G. L., et al. (2019). Paradox in bulk and molecular geochemical data and implications for hydrocarbon migration in the inter-salt lacustrine shale oil reservoir, Qianjiang Formation, Jianghan Basin, central China. *Int. J. Coal Geol.* 209, 72–88. doi: 10.1016/j.coal.2019.05.005

Nady, M. M. E., and Hammad, M. M. (2015). Organic richness, kerogen types and maturity in the shales of the Dakhla and Duwi formations in Abu Tartur area, Western Desert, Egypt: implication of rock–eval pyrolysis. *Egypt. J. Pet.* 24, 423–428. doi: 10.1016/j.ejpe.2015.10.003

Shao, D. Y., Zhang, T. W., Ko, L. T., Li, Y. F., Yan, J. P., Zhang, L. L., et al. (2020). Experimental investigation of oil generation, retention, and expulsion within Type II kerogen-dominated marine shales: insights from gold-tube nonhydrous pyrolysis of Barnett and Woodford Shales using miniature core plugs. *Int. J. Coal Geol.* 217:103337. doi: 10.1016/j.coal.2019.103337

Soeder, D. J. (2018). The successful development of gas and oil resources from shales in North America. *J. Pet. Sci. Eng.* 163, 399–420. doi: 10.1016/j.petrol.2017.12.084

Solarin, S. A., Gil-Alana, L. A., and Lafuente, C. (2020). An investigation of long range reliance on shale oil and shale gas production in the U.S. market. *Energy* 195:116933. doi: 10.1016/j.energy.2020.116933

Stroup, C. H. (1987). The effect of organic matter type and organic carbon content on Rock-Eval hydrogen index in oil shales and source rocks. *Org. Geochem.* 11, 351–369. doi: 10.1016/0146-6380(87)90068-4

Sun, J., Xiao, X. M., Cheng, P., and Tian, H. (2019). Formation and evolution of nanopores in shales and its impact on retained oil during oil generation and expulsion based on pyrolysis experiments. *J. Pet. Sci. Eng.* 176, 509–520. doi: 10.1016/j.petrol.2019.01.071

Ulrich-Schad, J. D., Larson, E. C., Fernando, F., and Abulbasher, A. (2020). The Goldilocks view: support and skepticism of the impacts and pace of unconventional oil and gas development in the bakken shale of the United States. *Energy Res. Soc. Sci.* 70:101799. doi: 10.1016/j.erss.2020.101799

Zhao, W. Z., Zhu, R. K., Hu, S. Y., Hou, L. H., and Wu, S. T. (2020a). Accumulation contribution differences between lacustrine organic-rich shales and mudstones and their significance in shale oil evaluation. *Pet. Explor. Dev.* 47, 1160–1171. doi: 10.1016/s1876-3804(20)60126-x

Zhao, X. Z., Zhou, L. H., Pu, X. G., Jin, F. M., Shi, Z. N., Han, W. Z., et al. (2020b). Formation conditions and enrichment model of retained petroleum in lacustrine shale: a case study of the Paleogene in Huanghua depression, Bohai Bay Basin, China. *Pet. Explor. Dev.* 47, 916–930. doi: 10.1016/s1876-3804(20)60106-9

Zhu, J. Y., Yi, L. P., Yang, Z. Z., and Li, X. G. (2021). Numerical simulation on the in situ upgrading of oil shale reservoir under microwave heating. *Fuel* 287:119533.

Zink, K. G., Scheeder, G., Stueck, H. L., Biermann, S., and Blumenberg, M. (2016). Total shale oil inventory from an extended rock-eval approach on non-extracted and extracted source rocks from Germany. *Int. J. Coal Geol.* 163, 186–194. doi: 10.1016/j.coal.2016.06.023

Conflict of Interest: LH, XL, SL, and ZZ are employed by PetroChina Co., Ltd. The authors declare that this study received funding from PetroChina Co., Ltd. The funder was not involved in the study design, collection, analysis, interpretation of data, the writing of this article, or the decision to submit it for publication.

The remaining author declares that the research was conducted in the absence of any commercial or financial relationships that could be construed as a potential conflict of interest.

APPENDIX

TABLE A1 | Typical chromatogram table of sample 6 and the calculation process.

Hydro carbons	Peak area					Calculation process							
	Step 1	Step 2	Step 3	Step 4	Step 5	Step 1 (mg)	Step 2: toluene SS (mg)	Step 2: (D-C24 SS (mg)	Step 3 (mg)	Step 4 (mg)	Step 5 (mg)	Step 2 - Step 1	Step 3 - Step 2
*n*C5	129.234					6.851							
*n*C6	104.583	7.323		1.636		5.544	2.631	3.044		0.741		-52.540	
*n*C7	142.175	15.388		1.844		7.537	5.529	6.396		0.836		-26.640	
Toluene	245.039	36.152		19.204		12.990	12.990	15.027		8.704		0.000	
*n*C8	81.334	23.456		1.656		4.312	8.428	9.750		0.750		95.472	
*n*C9	80.899	33.309		4.488		4.289	11.968	13.845		2.034		179.075	
*n*C10	60.581	40.674		8.974		3.212	14.615	16.907		4.068		355.075	
*n*C11	52.359	36.367		11.264		2.776	13.067	15.116		5.105		370.781	
*n*C12	36.814	26.661		10.615		1.952	9.580	11.082		4.811		390.870	
*n*C13	25.254	24.416	11.724	11.062		1.339	8.773	10.149	5.40	5.014		555.311	-46.767
*n*C14	22.129	24.507	18.885	12.329		1.173	8.806	10.187	8.70	5.588		650.639	-14.570
*n*C15	20.682	29.183	26.211	14.538		1.096	10.486	12.130	12.08	6.589		856.402	-0.428
*n*C16	18.202	22.812	21.728	13.022	0.015	0.965	8.197	9.482	10.01	5.902	0.018	749.468	5.594
*n*C17	13.572	22.674	21.333	13.304	2.304	0.719	8.147	9.425	9.83	6.030	2.767	1,032.367	4.305
*n*C18	12.874	21.677	20.607	12.443	3.802	0.682	7.789	9.010	9.50	5.640	4.566	1,041.270	5.390
*n*C19	10.535	21.434	20.233	15.074	3.634	0.558	7.702	8.909	9.32	6.832	4.36	1,279.023	4.650
*n*C20	9.359	16.853	16.331	9.943	3.737	0.496	6.056	7.005	7.53	4.507	4.488	1,120.536	7.428
*n*C21	6.793	16.126	15.045	9.457	3.229	0.360	5.794	6.703	6.93	4.286	3.878	1,509.044	3.430
*n*C22	5.757	13.167	12.343	8.366	3.258	0.305	4.731	5.473	5.69	3.792	3.913	1,450.221	3.924
*n*C23	4.752	10.261	9.259	6.302	2.372	0.252	3.687	4.265	4.27	2.856	2.849	1,363.579	0.036
D-C24		5.389	4.861	4.942	6.528		1.936	2.240	2.24	2.24	7.84		0.000
*n*C24	3.969	7.392	6.956	4.545	1.334	0.210	2.656	3.073	3.21	2.060	1.602	1,162.362	4.323
*n*C25	3.124	6.122	5.539	3.729	1.102	0.166	2.200	2.545	2.55	1.690	1.323	1,228.266	0.305
*n*C26	2.623	5.933	3.321	3.298		0.139	2.132	2.466	1.53	1.495	0	1,433.130	
*n*C27		3.72		1.885			1.337	1.546		0.854	0		
*n*C28		1.826		0.701			0.656	0.759		0.318	0		
Before *n*C8	1,334.078	185.257				70.722	66.566	77.004			0		
Before *n*C14	2,376.689	696.425	86.998	186.434		125.993	250.237	289.477	40.09	84.503	0		
Before toluene				52.553	43.952					23.820	24.696		

frontiers in Earth Science

ORIGINAL RESEARCH
published: 22 April 2021
doi: 10.3389/feart.2021.661581

The Effect of Diagenetic Evolution on Shale Gas Exploration and Development of the Longmaxi Formation Shale, Sichuan Basin, China

Jia Wang[1,2,3], Xianfeng Tan[3]*, Jingchun Tian[1], Long Luo[3], Xuanbo Gao[3], Chao Luo[4], Chunlin Zeng[5], Lei Zhang[3] and Weiwei Xue[6]*

[1] Institute of Sedimentary Geology, Chengdu University of Technology, Chengdu, China, [2] Shandong Provincial Key Laboratory of Depositional Mineralization & Sedimentary Mineral, Shandong University of Science and Technology, Qingdao, China, [3] Chongqing Key Laboratory of Complex Oil and Gas Exploration and Development, Chongqing University of Science and Technology, Chongqing, China, [4] Exploration and Development Research Institute of Southwest Oil and Gas Field Company, PetroChina, Chengdu, China, [5] Chongqing Institute of Geology and Mineral Resources, Chongqing, China, [6] School of Earth Science and Engineering, Nanjing University, Nanjing, China

OPEN ACCESS

Edited by:
Dawei Lv,
Shandong University of Science and Technology, China

Reviewed by:
Ruyue Wang,
SINOPEC Petroleum Exploration and Production Research Institute, China
Kaikai Li,
China University of Geosciences, China

***Correspondence:**
Jia Wang
wangjia@cqust.edu.cn.com
Xianfeng Tan
xianfengtan8299@163.com

Specialty section:
This article was submitted to Sedimentology, Stratigraphy and Diagenesis, a section of the journal Frontiers in Earth Science

Received: 02 February 2021
Accepted: 26 February 2021
Published: 22 April 2021

Citation:
Wang J, Tan X, Tian J, Luo L, Gao X, Luo C, Zeng C, Zhang L and Xue W (2021) The Effect of Diagenetic Evolution on Shale Gas Exploration and Development of the Longmaxi Formation Shale, Sichuan Basin, China. Front. Earth Sci. 9:661581. doi: 10.3389/feart.2021.661581

Diagenetic evolution is an important controlling factor of shale gas reservoirs. In this study, based on field outcrop and drilling core data, analytical techniques including X-ray diffraction (XRD), field emission scanning electron microscope combined with a focused ion beam (FIB-FESEM), and energy-dispersive spectroscopy (EDS) analyses were performed to determine the diagenetic evolution of the Longmaxi Formation shale and reveal the effect of diagenetic evolution on the shale gas exploration and development in the Sichuan Basin, Southwest China. The eodiagenesis phase was subdivided into two evolution stages, and the mesodiagenesis phase was subdivided into three evolution stages in the basin margin and center. Absorbed capacity and artificial fracturing effect of the Longmaxi Formation shale gas were related to mineral composition, which was influenced by sedimentary characteristics and diagenetic evolution. The diagenetic system in the basin margin was more open than that in the basin center due to a different burial history. The more open diagenetic system, with more micro-fractures and soluble constitute (e.g., feldspar), was in favor for the formation and preservation of secondary dissolved pores and organic pores in the basin margin. The relatively closed diagenetic system with stronger compaction resulted in deformation of pore space in the central basin.

Keywords: shale, diagenetic evolution, structural evolution, organic matter, Longmaxi Formation, Sichuan Basin

INTRODUCTION

Shale gas, which is a kind of "self-generation and self-accumulation" gas reservoir, is a major unconventional hydrocarbon resource (Jarvie et al., 2007; Zou et al., 2016). Reservoir quality is key to shale gas exploration and development (Wang et al., 2018; Wang R. Y. et al., 2019; Wang et al., 2020a; Jia et al., 2019; Wang X. et al., 2019), which is mainly influenced by sedimentary

characteristics (Lv et al., 2020), structural history, and diagenetic evolution (Bjørlykke, 2014). In fact, sedimentary characteristics and structural history generally influenced reservoir quality by controlling diagenetic evolution (Dickinson, 1993; Bjørlykke and Jahren, 2012). However, previous studies have mainly focused on the diagenetic systems of conventional reservoirs (Bjørlykke and Jahren, 2012; Luo et al., 2019) but rarely report the diagenetic system of argillaceous (Lv et al., 2019) and other unconventional rocks (Day-Stirrat et al., 2010).

The study of diagenetic systems originated in the 1970s and 1980s and mainly focused on the diagenetic relationship between diagenesis and the evolution products of organic matter in deep clastic rock (Curtis, 1978; Boles and Franks, 1979). Subsequently, models of organic–inorganic interactions (Surdam et al., 1984; Burtner and Warner, 1986; Surdam, 1989; Buhman, 1992; Bjørlykke, 1993; Li and Li, 1994; Schoenherr et al., 2007), regional diagenesis (Seiver, 1979; Li and Li, 1994), and basin geological systems (Allen and Allen, 1990; Dickinson, 1993; Li, 1995; Dickinson et al., 1997) were proposed and promoted. In the early 2000s, scholars began to study the diagenesis process in terms of basin dynamics and focused their attention on the relationships between microscopic diagenetic characteristics and basin evolution or thermal fluid activity (Li et al., 2003; Archer et al., 2004; Bjørlykke and Jahren, 2012; Meng et al., 2012; Lv et al., 2015; Lai et al., 2016; Yuan et al., 2017, 2019). Consequently, the diagenetic system became a multi-dimensional research field (Li et al., 2003; Archer et al., 2004; Bjørlykke, 2014; Yuan et al., 2015, 2017; Lv et al., 2015; Lai et al., 2015, 2017, 2018; Luo et al., 2019).

During the research processes of exploration and development of shale gas (Schmoker, 1993; Curtis, 2002; Law and Curtis, 2002; Jarvie et al., 2007; Zhang et al., 2008; Zou et al., 2016), many researchers found that argillaceous rocks were influenced by tectonic evolution, geochemistry of basinal fluids, and several other factors concerning the transformation of minerals and organic hydrocarbon generation during the burial process (Robert et al., 2009; Milliken et al., 2012; Wang et al., 2015, 2020b; Kong et al., 2015; Dong et al., 2015; Luan et al., 2016; Zhao et al., 2016). The physical characteristics of shale and the enrichment ability of shale gas are understood to be largely restricted by the aforementioned factors (Jarvie et al., 2007; Loucks et al., 2009). This study aims to recover the whole diagenetic evolution process of argillaceous rocks and to reveal the effects of diagenetic evolution on shale gas exploration and development by using the Longmaxi Formation, Southwestern China, as a case study.

GEOLOGICAL SETTING

The Sichuan Basin is a petroliferous basin in Southwestern China, which is bounded by the fault zone of Longmen Mountain to the west, the fault zone of the Micang and Daba mountains to the north, and the Hunan-Guizhou-Hubei fold belt to the southeast (He et al., 2000; Zhao et al., 2003; Li, 2013). The geomorphic features are characterized by the north to northeast trending mountain range, which alternates with the northeast trend of the small intermontane basin and surface structures (**Figure 1A**). The Lower Silurian Longmaxi Formation in the study area

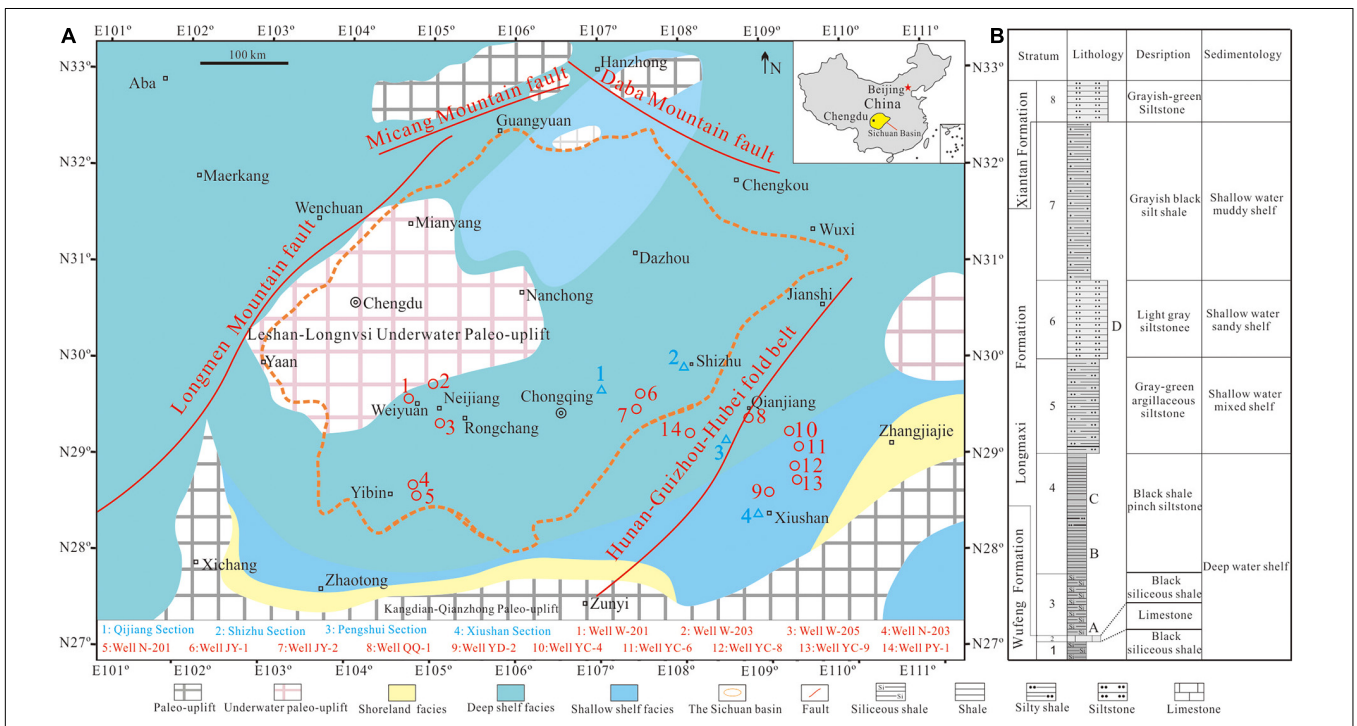

FIGURE 1 | A map **(A)** showing sedimentary characteristics and sampling locations of the Sichuan Basin (the inset map shows the basin location within China) (modified after Mou et al. (2011)). **(B)** The stratigraphic characteristics of the Longmaxi Formation in Xiushan section.

has a thickness of 60–120 m and was mainly deposited in a low-energy, anoxic marine shelf environment. The sedimentary paleogeography of the Longmaxi Formation shale was controlled by many uplifts such as the Kangdian-Qianzhong paleo-uplift and the Leshan-Longnvsi underwater paleo-uplift (**Figure 1A**; Liang et al., 2008; Wang et al., 2011; Wang J. et al., 2014). The lower part of the Longmaxi Formation consists of black siliceous shale, which was deposited in deep-water shelf facies (Mou et al., 2011). The middle part of the formation consists of black siliceous shale of deep-water shelf facies and black carbonaceous shale of shallow-water mixed shelf facies, whereas the upper part comprises silty mudstone or argillaceous siltstone of argillaceous shelf facies that deposited in a shallow, sandy continental shelf (Mou et al., 2011; **Figure 1B**).

SAMPLES AND METHODS

The Longmaxi Formation shale of five wells was analyzed in the central Sichuan Basin (**Figure 1A**). The Longmaxi Formation shale of nine wells and four field sections were studied in the basin margin (**Figure 1A**). The related data of seven wells (W-201, W-203, W-205, N-201, N203, JY-1, and JY-2) were collected from a previous research (**Figure 1A** and **Table 1**). In addition, 177 drilling cores (seven wells) and 111 field outcrop (four sections) samples of the Longmaxi Formation shale in the Sichuan Basin were collected in this study (**Figure 1A**). Large fragments from each sample were firstly removed for field emission scanning electron microscope combined with a focused ion beam (FIB-FESEM) analysis. All microscopic analyses were conducted at the State Key Laboratory of Oil and Gas Reservoir Geology and Exploitation, Chengdu University of Technology, China. A Quanta FEG 250 environmental FESEM was used with image magnifications of between 10 and 500,000. The samples were analyzed using a relatively low beam energy in a high-pressure (∼60 Pa) vacuum chamber environment, and the energy-dispersive spectroscopy (EDS) was performed on some important observation points of samples using the Oxford INCA X-Max20. Meanwhile, a gallium ion beam was then used to prepare planar cross sections for FESEM observation; four cross sections were prepared on shale samples; each planar cross-section prepared by FIB milling was typically 100 $\mu m^2 \times 100\ \mu m^2$ and 30–50 FESEM images. Finally, the three-dimensional imaging analysis of pores was realized by FIB-FESEM.

Some small samples were selected and dried at a low temperature before being ground into a 200 mesh. To remove carbonate rock before testing, 10% hydrochloric acid was subsequently added to each sample in a centrifuge tube and glass beaker. X-ray powder diffraction for all samples were obtained using a Bruker D8 ADVANCE at the State Key

TABLE 1 | Organic geochemial parameters of the Longmaxi Formation shale in the Sichuan Basin.

Region	Well/section	Number of samples	Rb (average, %)	Ro (average, %)	T_{max} (average,°C)	TOC (average, %)
Basin margin (Southeast Sichuan Basin)	QQ-1 well	19	3.50	2.56	489.70	2.64
	YQ-1 well	10	3.71	2.69	–	2.72
	PY-1 well	17	3.53	2.58	–	2.83
	Shizhu section	21	3.05	2.28	502.30	2.51
	Xiushan section	9	3.76	2.72	513.50	1.98
Basin center (Southwest Sichuan Basin)	W-201 well	43	2.77	2.11	–	1.89
	W-203 well	37	3.87	2.72	–	2.62

Rb, bitumen reflectance; Ro, vitrinite reflectance, according to the formula Ro = 0.618 × Rb + 0.4 (Jacob, 1985); T_{max} maximum pyrolysis peak temperature; TOC, total organic carbon. En dash indicates that the measurement is not available. The data of well W-201 and well W-203 are referenced from Wu (2018).

TABLE 2 | Mineral compositions of the organic-rich shale in the Sichuan Basin (XRD).

Location	Well/section (number of samples)	Quartz content (min–max/average, %)	Feldspar content (min–max/average, %)	Carbonate content (min–max/average, %)	Pyrite content (min–max/average, %)	Clay content (min–max/average, %)	Brittle content (min–max/average, %)
Basin margin (Southeast Sichuan Basin)	JY-1 well	18.4–70.6/44.4	3.2–15.0/8.3	0.0–31.5/9.7	0.0–4.8/0.5	16.6–62.8/40.9	37.2–83.4/59.1
	QQ-1 well (43)	32.0–70.0/45.9	3.0–20.0/12.6	0.0–12.0/6.4	0.0–8.0/2.3	16.0–58.0/35.2	40.0–81.0/64.9
	YD-2 well (13)	30.8–70.0/41.6	4.6–25.0/14.8	2.1–19.8/10.0	1.5–6.5/3.1	16.6–42.2/29.6	53.7–79.2/66.4
	YC-4 well (35)	27.4–49.2/35.8	6.9–19.3/12.3	2.8–24.6/8.9	2.2–5.3/4.1	17.0–50.9/38.2	49.2–77.9/61.1
	YC-6 well (23)	27.9–56.8/40.0	4.7–28.1/16.8	2.3–21.6/11.1	0.0–7.3/2.6	3.6–50.1/27.8	40.9–93.1/67.9
	YC-8 well (25)	25.7–52.2/40.8	1.7–28.7/16.9	0.2–23.5/9.4	0.0–7.0/2.5	7.1–58.2/29.3	39.5–90.7/67.1
	YC-9 well (38)	9.3–93.1/52.3	0.0–71.1/11.1	0.0–84.0/9.2	0.3–18.7/8.1	3.8–34.6/17.2	51.5–95.9/72.6
	Sections (111)	25.7–70.0/41.9	1.7–28.7/15.7	0.0–23.5/9.1	0.0–8.0/2.5	3.6.0–58.2/29.6	39.5–93.1/66.7
Basin center (Southwest Sichuan Basin)		25.3–65.3/50.0	0.0–9.1/3.4	7.9–19.9/13.3	0.0–2.2/0.6	26.5–53.4/29.7	43.4–73.5/66.7

The data of the Southeast Sichuan Basin are consist of sections of Shizhu, Pengshui, Xiushan, and Qijiang. The data of the Southwest Sichuan Basin are referenced from Wu (2018). The data of JY-1 well are referenced from Guo et al. (2014).

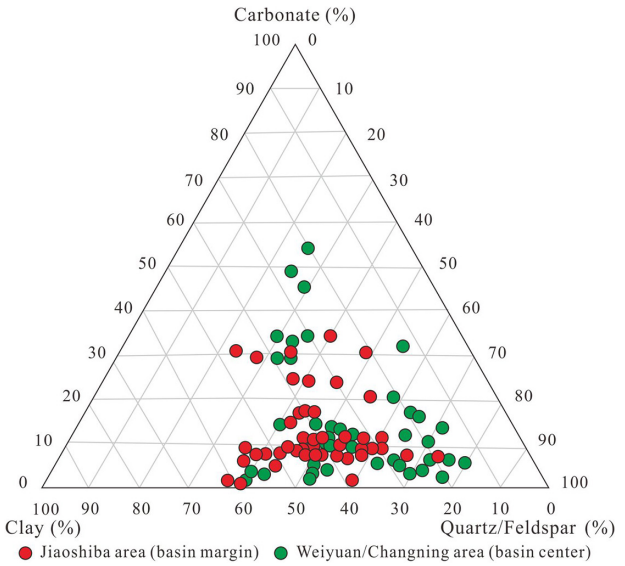

FIGURE 2 | A ternary diagram showing mineral compositions of shale samples in the Sichuan Basin (the data of Jiaoshiba area was referenced from Guo et al. (2014)).

Laboratory of Oil and Gas Reservoir Geology and Exploitation (Chengdu University of Technology, China) under 25°C and 50% humidity. Seventy-six samples (46 samples from wells and 30 samples from sections) were analyzed for total organic carbon (TOC) and bitumen reflectance (Rb), respectively, using a LECO CS230 carbon and a Leica MPV-III microphotometer under oil immersion, and the Rock-Eval parameters including volatile hydrocarbon content (S_1), remaining hydrocarbon generative potential (S_2), and temperature at maximum generation (T_{max}) values were determined using ROCK-EVAL 6 (RE6) at the Sichuan Coalfield Geology Bureau.

Density, porosity, and permeability data test of well YQ1 (10 samples) and QQ1 (43 samples) were analyzed in the Chongqing Key Laboratory of Complex Oil and Gas Exploration and Development using an automated permeameter-porosimeter (AP-608) and V-Sorb 2800TP. In addition, the diagenesis of the Longmaxi Formation black shale was determined by means of field outcrop and core observations.

RESULTS

Organic Geochemical Characteristics

Generally, TOC average values of the Longmaxi Formation shale are generally more than 2.0% (average, 1.89–2.83%) (**Table 1**). Typically, TOC values of shale in the lower part of the Longmaxi Formation are more than 3.0% (Wang et al., 2020b). The mean values of vitrinite reflectance (Ro) of each outcrop profile and well, which were calculated by bitumen reflectance (Rb) and Jacob's calculation formula ($Ro = 0.618 \times Rb + 0.4$), are generally greater than 2.5% (2.11–2.72%) in the basin margin and center (**Table 1**). T_{max} average values are greater than 480°C (489.70–513.50°C) in basin margin (**Table 1**). There is no obvious difference in TOC values between basin margin and center.

Mineralogy and Diagenesis Characteristics

Mineralogy

The Longmaxi Formation in the Sichuan Basin mainly consists of interbedded shale and argillaceous siltstone with unequal thicknesses. The average quartz contents of the shale vary from 35.8 to 52.3% in the Sichuan Basin margin, which were less than those (average, 50%) in the southwestern Sichuan Basin (basin center) (**Table 2** and **Figure 2**). The average carbonate mineral content of the Longmaxi Formation shale varies from 6.4 to 11.1% in the southeastern Sichuan Basin (basin margin), which were generally less than the average carbonate mineral content (average, 13.3%) in the southwestern Sichuan Basin (basin center) (**Table 2**). The carbonate mineral content of the Longmaxi Formation shale in the central basin (e.g., Weiyuan, Rongchang, and Zhaotong area) is more than 20% (Wang et al., 2020b). On the contrary, the average feldspar contents range from 8.3 to 16.9% in the basin margin and 3.4% in the basin center

TABLE 3 | Clay mineral compositions of the Longmaxi Formation shale in the Sichuan Basin (XRD).

Region	Wells	Number of samples	Clay mineral content (min–max/average, %)				Mixed layer ratio (min–max/average, S%)	
			Illite	Chlorite	Illite–smectite	Chlorite–smectite	Illite–smectite	Chlorite–smectite
Basin margin (Southeast Sichuan Basin)	YC-4	35	10–47/21.6	1–19/9.0	41–82/60.0	1–14/7.4	5–11/6.8	10–15/11.4
	YC-6	23	15–46/25.5	6–16/9.2	40–70/59.5	3–10/6.2	6–11/8.2	9–15/11.8
	YC-8	25	12–29/18.3	5–13/8.7	52–80/67.9	2–11/5.1	5–10/7.1	10–16/11.8
	YC-9	38	11–84/47.7	0–12/0.8	16–75/50.8	0–10/0.7	4–10/6.1	0–11/0.8
	QQ-1	43	40–53/45.8	6–18/10.9	33–49/43.3	0–8/0.5	5–10/8.2	1–14/7.9
	YD-2	13	38–62/52.3	2–10/6.8	32–60/40.9	0–8/0.5	8–10/9.1	1–10/5.6
Basin center (Southwest Sichuan Basin)	W-201	65	3–95/50.8	3–93/25.6	5–94/23.3	–	–	–
	W-205	17	22–70/45.8	0–10/10.6	0–57/33.0	-	–	–

The data of well W-201 and well W-205 are referenced from Wu (2018). En dash indicates that the measurement is not available.

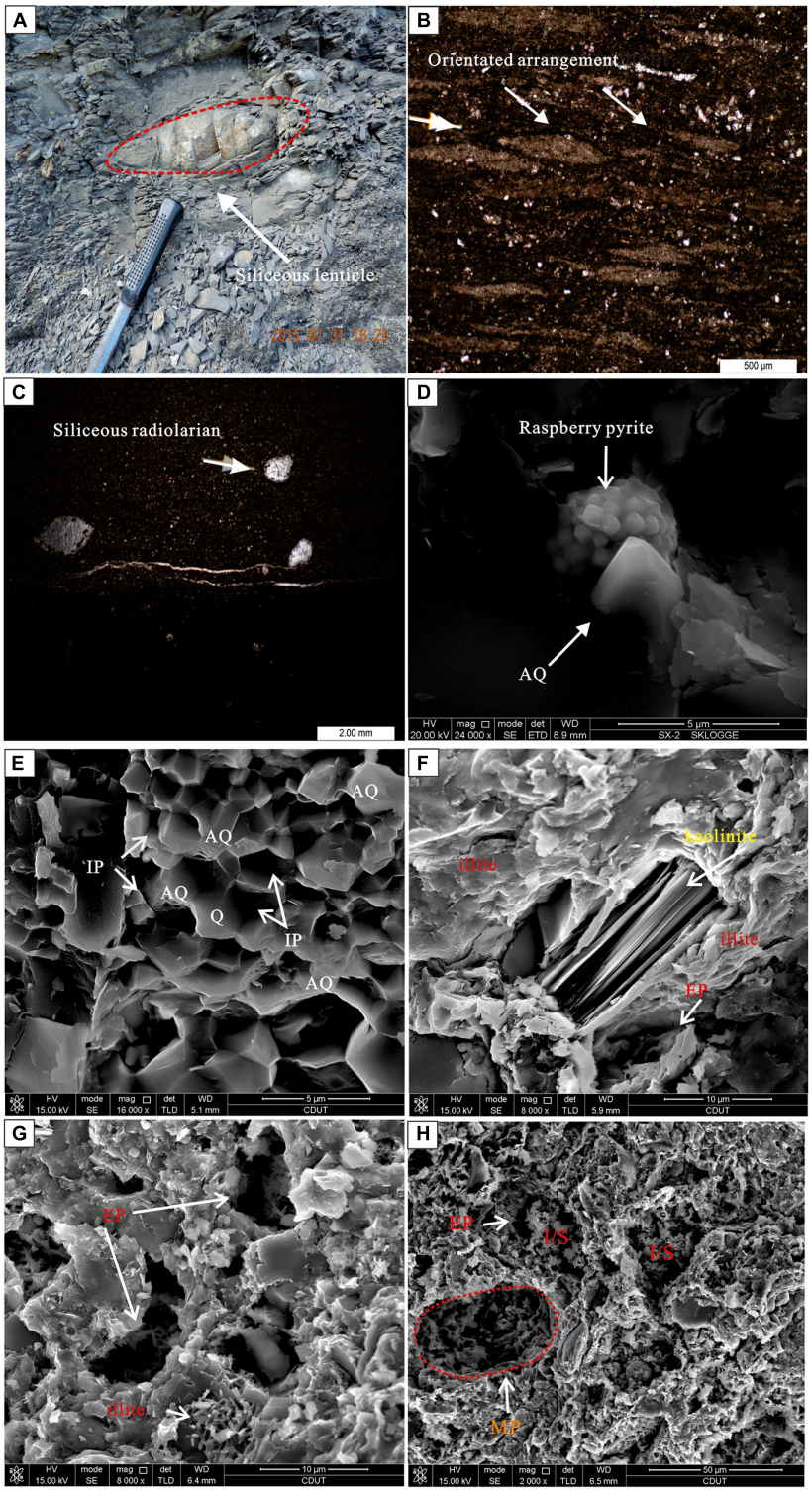

FIGURE 3 | Types and characteristics of pore spaces of the Longmaxi Formation shale in the Sichuan Basin [micrographs of thin sections and scanning electron microscope (SEM)]. **(A)** A photograph of the Longmaxi Formation Shale in the Xiushan field outcrop, showing the siliceous lenticle. **(B)** Micrographs of thin sections (MTS) showing the orientated arrangement of minerals, the Xiushan section, layer 3. **(C)** Micrographs of thin sections (MTS) showing the siliceous radiolarian, the Shizhu section, layer 4. **(D)** An SEM image showing strawberry pyrite and authigenic quartz (AQ), the Pengshui section, layer 2. **(E)** An SEM image showing inter-crystalline pores (IP) of authigenic quartz, the Shizhu section, layer 2. **(F)** An SEM image showing intergranular pores (EP) of clay minerals, the Xiushan section, layer 5. **(G)** An SEM image showing intergranular pores (EP) of illite, the Qijiang section, layer 6. **(H)** An SEM image showing intergranular pores (EP) and molded pores (MP) of illite–smectite mixed minerals, the Qijiang section, layer 5.

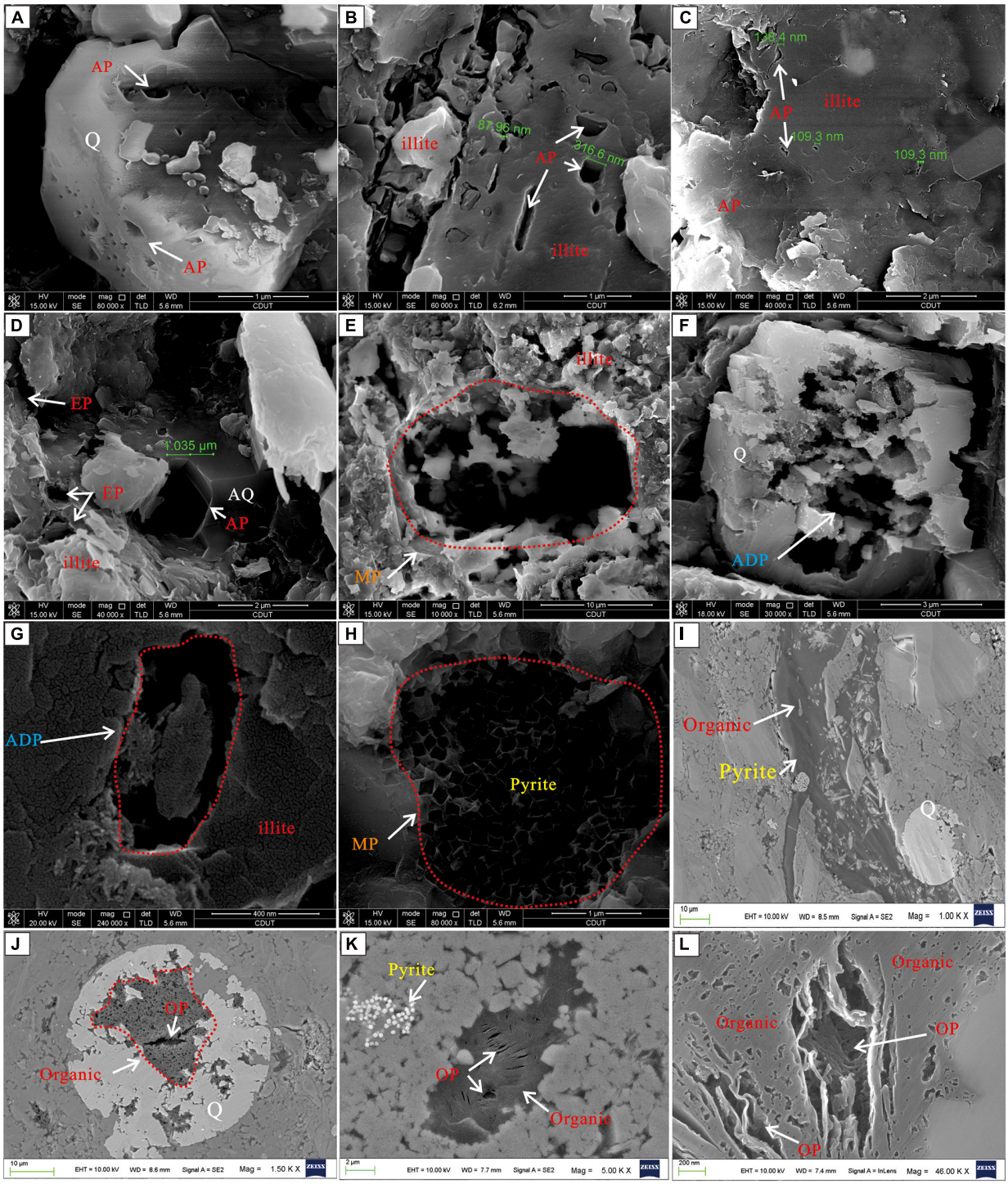

FIGURE 4 | Types and characteristics of pore spaces of the Longmaxi Formation shale in the Sichuan Basin [scanning electron microscope (SEM) and field emission scanning electron microscope (FESEM)]. **(A)** An SEM image showing intragranular pores (AP) of authigenic quartz (AQ), the Shizhu section, layer 4. **(B)** An SEM image showing intragranular pores (AP) of illite, the Xiushan section, layer 5. **(C)** An SEM image showing intragranular pores (AP) of illite, the Pengshui section, layer 4. **(D)** An SEM image showing intergranular pores (EP) of illite and intragranular pores (AP) of quartz, the Pengshui section, layer 7. **(E)** An SEM image showing intragranular dissolved pores (ADP) of quartz, the Xiushan section, layer 3. **(F)** Intragranular dissolved pores (ADP) of quartz, the Shizhu section, layer 4. **(G)** An SEM image showing intragranular dissolved pores (ADP), the Qijiang section, layer 7. **(H)** An SEM image showing molded pores (MP) of strawberry pyrite, the Pengshui section, layer 5. **(I)** An FESEM image showing organic matter and pyrite, well JY-2, 2,459.34 m. **(J)** An FESEM image showing organic micropore (OP), well JY-2, 2,459.36 m. **(K)** An FESEM image showing organic micropores (OPs) and pyrite, well W-201, 2,678.61 m. **(L)** An FESEM image showing organic micropores (OPs), well N-203, 2,325.64 m.

(**Table 2**). The average content of clay mineral in the basin margin (17.2–40.9%) is more than that in the basin center (average, 29.7%) (**Table 2**). The average contents of brittle mineral in the basin margin (59.1%–72.6%) are slightly more than those in the basin center (66.7%) (**Table 2** and **Figure 2**).

Diagenetic Characteristics

Clay mineral transformations

Clay minerals in the Longmaxi Formation shale mainly comprise illite, mixed illite–smectite, mixed chlorite–smectite, and chlorite (**Table 3**). The average illite content ranges from 18.3 to 52.3% in the basin margin, which is generally less (average, 45.8–50.8%) than that in the basin center (**Table 3**). The average chlorite content of the basin margin (0.8%–10.9%) is less than that in the basin center (10.6–25.6%) (**Table 3**). In contrast, the average mixed illite–smectite content in the basin margin (40.9–67.9%) is more than that in the basin center (average, 23.3–33.0%) (**Table 3**). The content of mixed chlorite–smectite in the basin margin ranges from 0.5 to 7.4% (**Table 3**). The smectite content of mixed illite–smectite ranges from 6.1 to 9.1 % in the basin margin (**Table 3**). The smectite contents within mixed chlorite–smectite vary from 0.8 to 11.8 % in the basin margin (**Table 3**).

Compaction

At outcrop, the shale samples are very tight and hard (**Figure 3A**). Clay minerals, organic matter, and mica in the shale were clearly aligned under the microscope (**Figure 3B**).

Silicification

The tight siliceous lenticle, whose diameters range from 0.1 to 0.5 m, was observed in the shale of the field outcrop (**Figure 3A**). Siliceous radiolarian shaped like ellipticity occurred as the result of biogenetic silicification (**Figure 3C**). Pore-filling authigenic quartz generally were observed under a scanning electron microscope (SEM) (**Figures 3D,E**).

Dissolution

The dissolution of the Longmaxi Formation shale generally occurred in soluble constituents, such as calcite, feldspar, and quartz, or at the edges of clay minerals and formed secondary pores or even molded pores (**Figures 4E,G,H**). Besides, some quartz grains were also dissolved by alkaline fluids (**Figure 4F**).

Pore Characteristics and Physical Property of the Reservoir

Pore spaces mainly consisted of inter-crystalline pores (**Figure 3E**), intergranular pores (**Figure 3F–H**), intragranular primary pores (**Figures 4A–D**), intragranular dissolved pores (**Figures 4E–G**), molded pores (**Figures 3H**, **4H**), organic pores (**Figures 4I–L**), and micro-fractures (**Figure 3F**). The intergranular pores, whose diameters range from 1 to 10 μm, were mainly developed in brittle minerals such as quartz and feldspar. In contrast, the intragranular pores were relatively less than intergranular pores in the brittle minerals. Dissolved pore spaces were widely developed on the surface of calcite and feldspar (diameters 0.1–10 μm). The diameters of organic matter pores range from 50 to 800 nm, which were distinguishable under FESEM (**Figures 4I–L**). Organic pores were extensively prevalent

TABLE 4 | Density, porosity, permeability, and specific surface area of the Longmaxi Formation shale in different wells.

Sample number	Well depth (m)	Density (g/cm^3)	Porosity (%)	Permeability (× 10^{-3}μm^2)	Specific surface (m^2/g)
YQI-01	1,136.91	2.69	1.64	0.0001	1.63
YQI-02	1,141.20	2.69	1.58	0.0005	1.43
YQI-03	1,145.55	2.66	1.78	0.0001	1.73
YQI-04	1,147.62	2.66	1.42	0.0001	4.06
YQI-05	1,152.60	2.65	1.71	< 0.0001	1.92
YQI-06	1,155.13	2.61	1.45	0.0286	5.17
YQI-07	1,159.17	2.68	1.78	0.0001	2.01
YQI-08	1,163.11	2.64	1.58	0.0020	2.45
YQI-09	1,164.55	2.67	1.46	0.0001	2.10
YQI-10	1,166.00	2.64	1.23	0.0097	1.22
QQ1-01	707.20	2.64	1.70	0.0312	-
QQ1-02	709.30	2.65	2.00	0.0071	-
QQ1-03	711.49	2.64	1.80	0.0077	-
QQ1-04	713.00	2.64	1.30	0.0085	-
QQ1-05	715.15	2.62	1.80	0.0213	-
QQ1-06	717.80	2.62	0.90	0.0056	-
QQ1-07	719.50	2.63	2.00	0.4699	-
QQ1-08	721.50	2.64	1.00	0.1263	-
QQ1-09	712.70	2.61	2.80	0.0089	-
QQ1-10	725.00	2.60	2.50	0.0058	-
QQ1-11	727.12	2.63	0.90	0.0079	-
QQ1-12	729.92	2.60	1.80	0.0091	-
QQ1-13	732.75	2.59	1.90	0.0076	-
QQ1-14	735.36	2.62	1.30	0.0168	-
QQ1-15	738.50	2.60	2.20	0.0076	-
QQ1-16	740.60	2.61	1.70	0.0074	-
QQ1-17	741.50	2.64	1.50	0.0993	-
QQ1-18	744.10	2.64	1.00	0.0322	-
QQ1-19	747.10	2.63	1.20	0.0104	-
QQ1-20	749.50	2.59	1.80	0.0087	-
QQ1-21	750.50	2.60	1.40	0.1754	-
QQ1-22	752.57	2.63	0.80	0.0093	-
QQ1-23	754.63	2.63	1.70	0.0240	-
QQ1-24	756.70	2.62	0.90	0.0105	-
QQ1-25	758.77	2.62	1.20	0.3384	-
QQ1-26	760.83	2.61	1.20	0.0103	-
QQ1-27	762.90	2.64	1.10	0.0106	-
QQ1-28	764.97	2.62	1.10	0.0192	-
QQ1-29	767.03	2.61	2.00	0.0881	-
QQ1-30	769.10	2.60	1.50	0.0088	-
QQ1-31	771.17	2.59	1.40	0.0096	-
QQ1-32	773.23	2.61	0.90	0.0082	-
QQ1-33	775.30	2.60	0.90	0.0081	-
QQ1-34	777.37	2.59	0.60	0.0089	-
QQ1-35	779.43	2.58	1.30	0.0061	-
QQ1-36	781.50	2.56	1.30	0.0185	-
QQ1-37	785.50	2.52	1.80	0.0064	-
QQ1-38	783.30	2.53	1.80	0.0129	-
QQ1-39	787.50	2.48	1.10	0.0265	-
QQ1-40	789.60	2.42	2.10	0.0055	-
QQ1-41	791.60	2.43	3.40	0.0792	-
QQ1-42	793.60	2.54	0.70	0.0046	-
QQ1-43	795.60	2.65	1.20	0.0092	-

Note that en dash indicates that the measurement is not available.

in the Longmaxi Formation shale, the pore connectivity of which was much higher than other pore types (**Figures 4I–L**).

The densities of the Longmaxi Formation shale generally vary from 2.42 to 2.69 g/cm^3 (average, 2.61 g/cm^3) (**Table 4**). The porosity of the Longmaxi Formation shale mainly ranges from 1 to 2% (average, 1.51%) (**Table 4** and **Figure 5A**), and permeability ranges from 0.001 to 0.05 $\times$ 10^{-3} μm^2 (average, 0.035 $\times$ 10^{-3} μm^2) (**Table 4** and **Figure 5B**). The specific surface of the Longmaxi Formation shale ranges from 1.22 to 5.17 m^2/g (**Table 4**).

DISCUSSION

Diagenetic Evolution History

Diagenetic evolution was closely related to sedimentary processes and structural evolution, because rapid deposition can accelerate diagenetic evolution, whereas a structural uplift can weaken or even stop diagenetic evolution (Curtis, 1978; Dong et al., 2015). The Sichuan Basin is a polyhistory basin, which experienced multi-stage tectonic movements (Liu et al., 2011). The diagenetic products and geochemistry can reconstruct the diagenetic evolution history of the Longmaxi Formation (**Figure 6**), in which structural history, burial history, thermal history, and Ro evolution were based on previous research (Xu et al., 2015; Liu et al., 2020).

According to the diagenetic division regime of Morad et al. (2000), diagenetic events can be divided into three regimes: eodiagenesis (0–2 km depth and <70°C), mesodiagenesis (>2 km depth and >70°C), and teleodiagenesis (uplift to near-surface exposure and weathering).

The Longmaxi Formation shale has undergone a rapid subsidence period, a rapid uplift period, and a stabile period during burial processes, which have resulted in a complicated diagenetic evolution in different burial stages (Liu et al., 2011; Wang et al., 2017b; **Figure 6**). Besides, the Longmaxi Formation shale experienced different burial and structural history in the basin margin and center (**Figure 6**). Therefore, the eodiagenesis was subdivided into two evolution stages and the mesodiagenesis (burial diagenesis) was subdivided into three evolution stages, respectively, in the basin margin and center (**Table 1** and **Figure 6**).

Diagenetic Evolution History in the Sichuan Basin Margin

Stage A of the eodiagenesis

During stage A of the eodiagenesis, the overlying Silurian system was widely deposited in the Sichuan Basin, such that the Longmaxi Formation shale was rapidly deposited and buried. The paleo-geotemperature was <60°C and the Ro values, which were calculated in a previous research of Xu et al. (2015), was <0.35% during this stage (**Figure 6**). Shale with immature organic matter was quickly isolated from surface water and gradually evolved into the eodiagenesis stage. The shale became tight with authigenic siderite and orientated minerals due to strong mechanical compaction and dehydration. Clay minerals were dominated by smectite. The pore space mainly consisted of primary pores (**Figure 3E**). The organic matter was immature, but it started to form some biogenic gas during this stage (Peters and Cassa, 1994).

Stage B of the eodiagenesis

During stage B of the eodiagenesis, the Longmaxi Formation rapidly subsided from 1,500 to 2,200 m and then slowly uplifted from 2,200 to 2,000 m (**Figure 6**). The paleo-geotemperature increased from 60 to 70°C, and the Ro reached up to 0.5% (Xu et al., 2015; **Figure 6**). The organic matter was still immature, although some more biogenic gas was formed during this stage (Peters and Cassa, 1994). The organic acids were formed by the thermal evolution before the extensive generation of hydrocarbon, so many secondary pores were formed as the result of strong acidic dissolution. Shale changed from semi-consolidated into a consolidated state due to strong mechanical compaction (**Figure 6**). Smectite gradually transformed into an illite–smectite mixed layer that was dominated by smectite (**Figure 6**). Sheet-like authigenic kaolinite was pervasive (**Figure 3F**), and authigenic quartz began to occur (**Figures 3D,E**). Some authigenic quartz gradually occurred due to clay mineral transformation and dissolution (**Figures 3C–E**, **4A**, **6**).

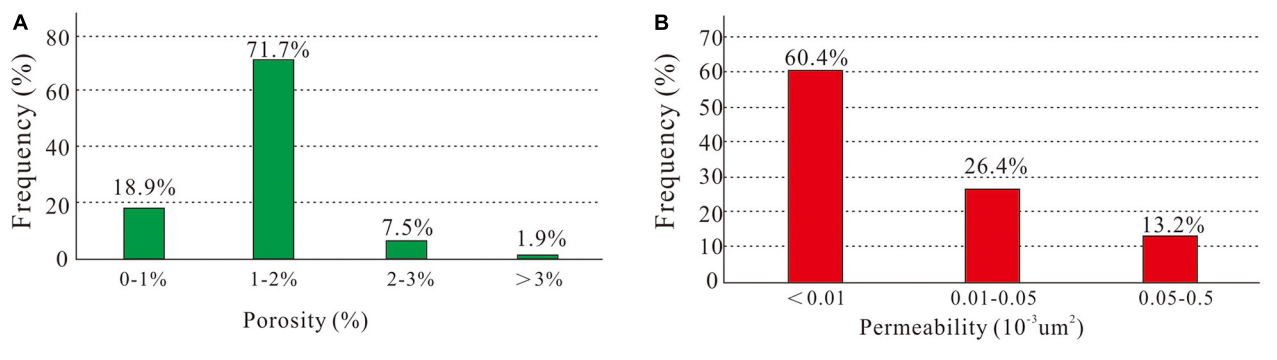

FIGURE 5 | Porosity **(A)** and permeability **(B)** histograms of the Longmaxi Formation shale in the Sichuan Basin.

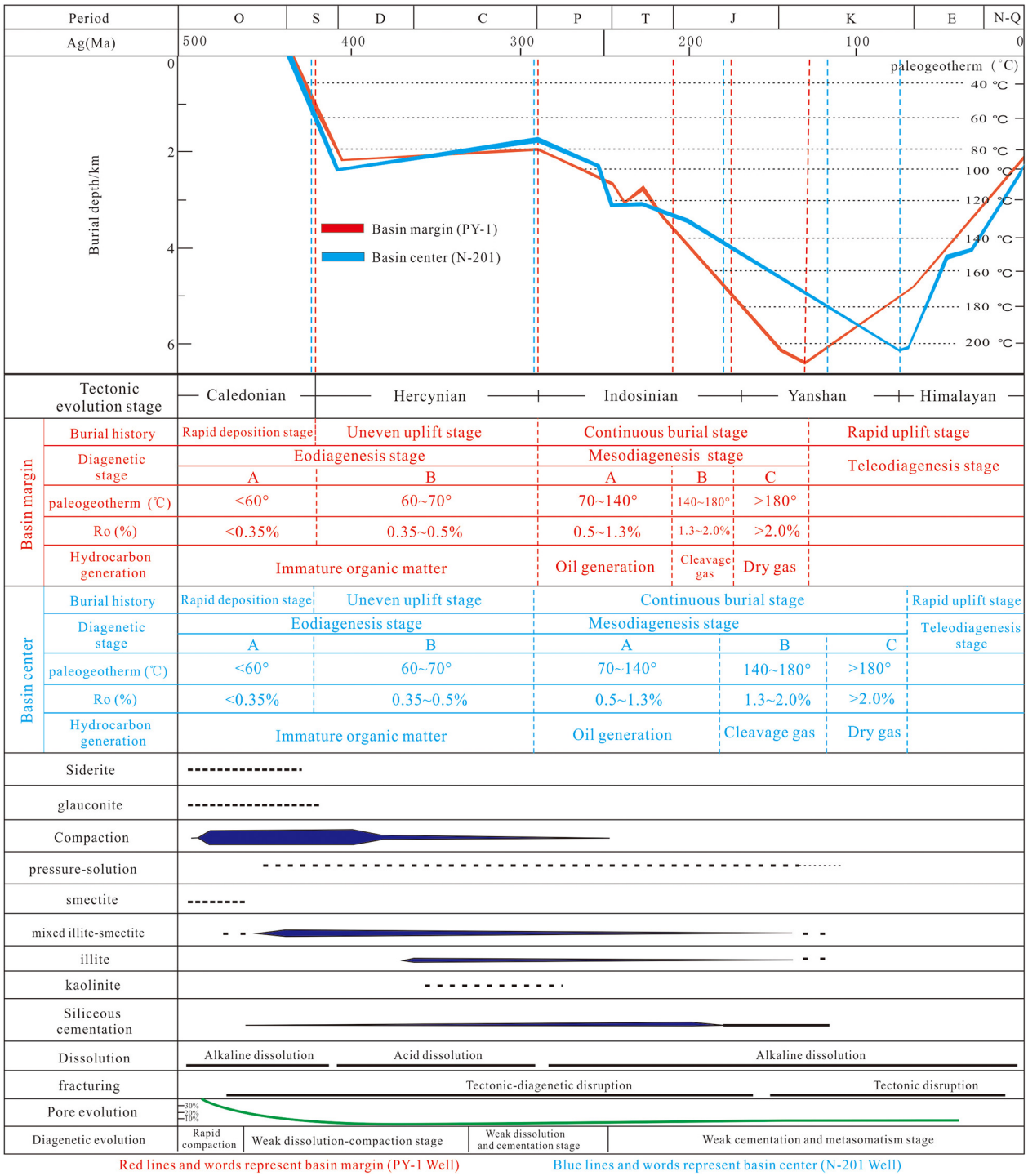

FIGURE 6 | Burial history, thermal history, and diagenetic evolution sequence of the Longmaxi Formation shale in the Sichuan Basin (the burial evolution and thermal history of well PY-1 referenced from Xu et al. (2015); the burial evolution and thermal history of well N-201 referenced from Liu et al. (2020); the diagenetic evolution sequence is modified after Wang et al. (2015)). Based on the burial history, combined with the characteristics of burial depth, temperature, thermal maturity of organic matter, authigenic mineral groups and relationships, and diagenesis, the diagenetic evolution process of different areas in Sichuan Basin is established.

Stage A of the mesodiagenesis

A large-scale relative sea level rise and marine transgression occurred from the Permian to the Early Triassic, which indicated the sustained subsidence of the Sichuan Basin (**Figure 6**) (Wang et al., 2017a). Consequently, the burial depth of the Longmaxi Formation increased from 2,000 to 4,000 m with slight fluctuation

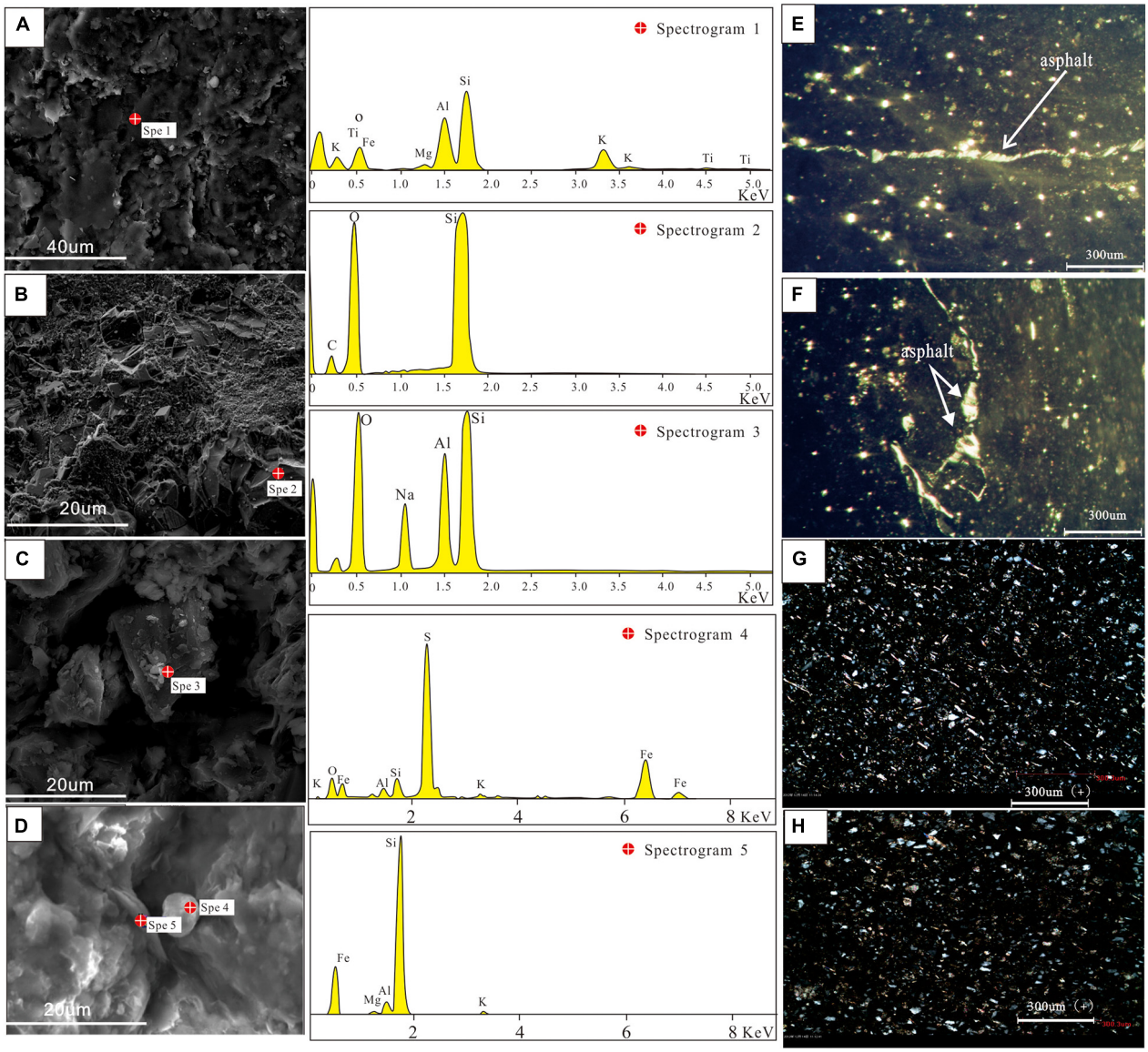

FIGURE 7 | Microscopic minerals and diagenetic characteristics of the Longmaxi Formation shale in the Sichuan Basin margin [scanning electron microscope (SEM) and energy-dispersive spectroscopy (EDS)]. **(A)** An SEM image showing the clay minerals; the right image of **(A)** is the corresponding EDS (spectrogram 1), the Shizhu section, layer 2. **(B)** An SEM image showing authigenic quartz; the right image is the corresponding EDS (spectrogram 2), the Shizhu section, layer 8. **(C)** An SEM image showing clay minerals grow on the surface of authigenic quartz; the right image is the corresponding EDS (spectrogram 3), the Shizhu section, layer 11. **(D)** An SEM image showing illite and pyrit; the right image is the corresponding EDS (spectrograms 4 and 5), the Shizhu section, layer 11. **(E)** A fluorescence microscope image showing asphalt in micro-cracks, well QQ-1, 756.13 m. **(F)** A fluorescence microscope image showing asphalt in micro-cracks, well QQ-1, 765.52 m. **(G)** Micrographs of thin sections (MTS) showing the quartz in shale, well YQ-1, 1,126.44 m. **(H)** Micrographs of thin sections (MTS) showing the quartz in shale, well YQ-1, 1,130.38 m.

during stage A of mesodiagenesis (**Figure 6**). Meanwhile, the paleo-geotemperature and Ro values, respectively, increased from 70 to 140°C and 0.5% to 1.3% (**Figure 6**). Organic matter evolved from early mature to peak mature and late mature (Peters and Cassa, 1994). Some more authigenic quartz gradually occurred due to clay mineral transformation and dissolution (**Figures 3C–E, 4A,I,J, 6**). Therefore, the Longmaxi Formation shale generated a large quantity of hydrocarbon, which was the main oil source of ancient oil reservoirs in the Sichuan Basin (Liu et al., 2011).

Phase B of the mesodiagenesis

During stage B of the mesodiagenesis, the Longmaxi Formation rapidly subsided to 5,000 m (**Figure 6**). Meanwhile, the paleo-geotemperature and the Ro, respectively, increased to 180°C and 2.0% (Xu et al., 2015; **Figure 6**). Most of organic matter transformed from late mature to postmature with the generation of pyrolysis gas (Peters and Cassa, 1994). The content of smectite in the illite–smectite mixed layer decreased obviously (**Table 3**). Clay mineral transformation accelerated the generation

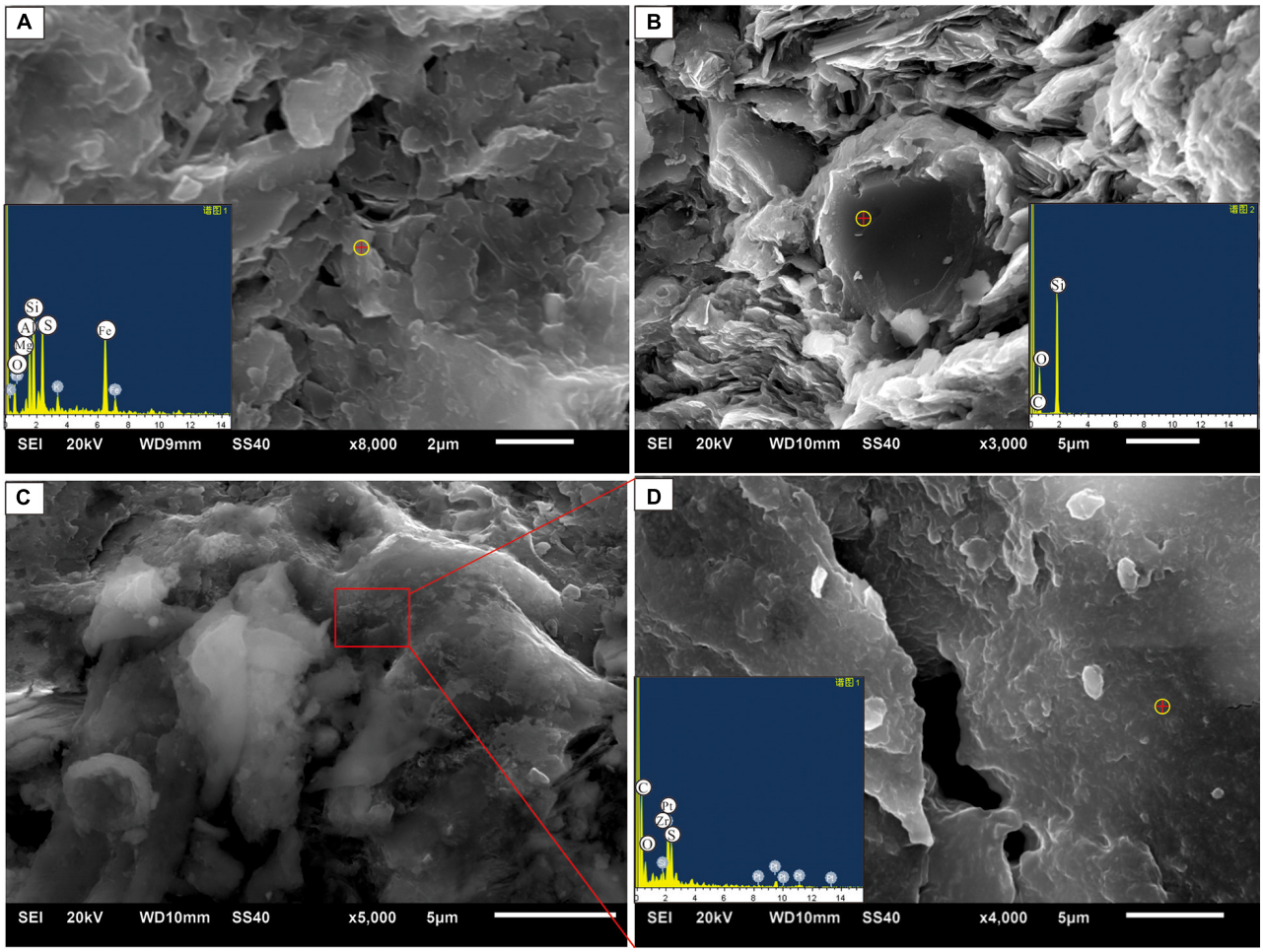

FIGURE 8 | Microscopic minerals and diagenetic characteristics of the Longmaxi Formation shale in the Sichuan Basin center (SEM and EDS). **(A)** An SEM image showing the clay minerals; the small picture in the lower left corner is the corresponding EDS, well JY-2, 2,459.36 m. **(B)** An SEM image showing authigenic quartz; the small picture in the lower right corner is the corresponding EDS, well JY-2, 2,459.36 m. **(C)** An SEM image showing asphalt organic matter in micro-cracks, well W-201, 2,678.61 m. **(D)** An SEM image that is a partial enlargement of image **(C)**; the small picture in the lower left corner is the corresponding EDS.

of authigenic quartz (**Figures 7A–D**) (Wang et al., 2017b) and authigenic grain-coating illite around detrital quartz (**Figure 7C**). The quartz was dissolved in the alkaline diagenetic environment due to depletion–expulsion of organic acids and generation–expulsion of hydrocarbon (**Figure 4F**).

Stage C of the Mesodiagenesis

The Longmaxi Formation shale was at stage C of the mesodiagenesis after the Middle Jurassic and before the Early Cretaceous. The Longmaxi Formation rapidly subsided before 130 Ma (Early Cretaceous) with a burial depth of 5,000–6,300 m and paleo-geotemperature of 180–210°C (**Figure 6**). Besides, the Ro values, which were calculated by paleo-geotemperature and burial depth in a previous research (Xu et al., 2015), were generally more than 2.0%. These indicate that the Longmaxi Formation shale was at a postmature stage of organic matter with generation of dry gas and experienced a large-scale generation-expulsion process of hydrocarbons (**Figure 6**; Wang et al., 2017a). Many microfractures were filled by a residual asphalt of organic matter evolution (**Figures 6E,F**), and a large amount of organic nanopores were formed within the organic matter (**Figures 4I–L**). The illite–smectite mixed layer nearly disappeared due to the complete transformation of clay minerals (**Table 3** and **Figure 6**).

Telediagnosis

The Sichuan Basin has gradually uplifted since the Early Cretaceous (130 Ma) because of Yanshan and Himalayan movement, which generated many large faults (**Figure 6**; Liu et al., 2011). The paleo-geotemperature subsequently decreased from 200 to 80°C due to an uplift from 6,300 to 2,000 m, which could have slowed down or stopped mesodiagenesis (Wang et al., 2017b). A relatively open-pressure system, which was caused by some large vertical faults, resulted in a massive loss of conventional oil and gas reservoirs in the Sichuan Basin (Liu et al., 2011; Wang et al., 2017a). Therefore, many secondary pores and micro-fractures were formed in the open system of uplift zone (**Figures 4E–H**).

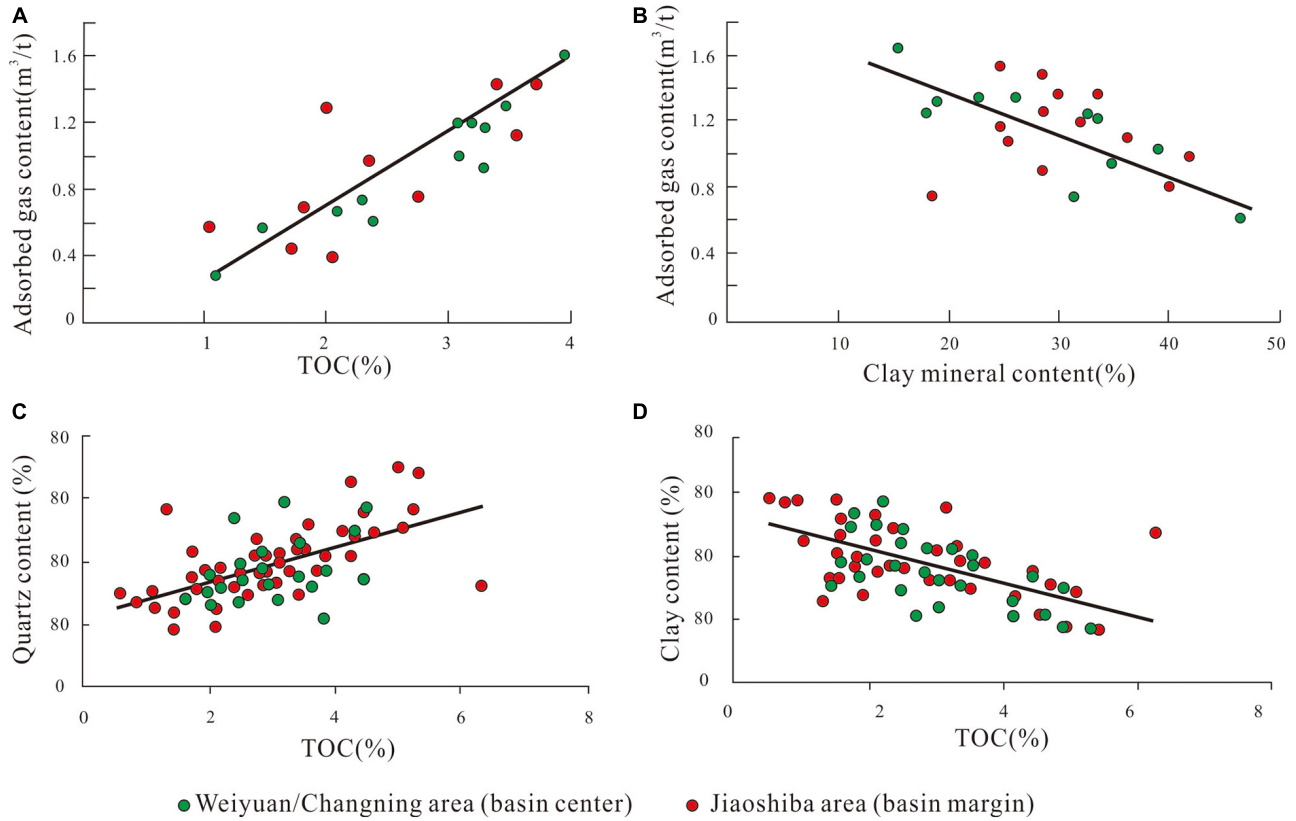

FIGURE 9 | Relationship maps between absorbed gas content and total organic carbon (TOC) and mineral content in the Sichuan Basin (the data of Jiaoshiba area was referenced from Guo et al. (2014)). **(A)** A scatter diagram of TOC and absorbed gas content. **(B)** A scatter diagram of absorbed gas and clay mineral content. **(C)** A scatter diagram of quartz content and TOC. **(D)** A scatter diagram of clay mineral content and TOC.

Diagenetic Evolution History in the Sichuan Basin Center

There are some differences in the burial evolution history between the central and marginal areas of the Sichuan Basin (**Figure 5**). According to the burial depth, paleo-temperature, Ro, and diagenesis characteristics of the Longmaxi Formation shale in well N-201 (Liu et al., 2020; **Figure 6**), combined with the diagenetic division regime of Morad et al. (2000), the diagenetic evolution of the Longmaxi Formation in the central Sichuan Basin can also be divided into six different stages (**Figure 6**).

There are no differences in the burial, thermal, and diagenetic history between the central and marginal Sichuan Basin during phase A and B of the eodiagenesis (**Figure 6**). However, the Longmaxi Formation shale in the central basin contains more carbonate minerals (average, 13.34%) and less feldspars (average, 3.35%) than the basin margin due to the early different sedimentary environment (**Table 2**).

The Longmaxi Formation continuously subsided from 300 to 80 Ma during phase A–C of the mesodiagenesis in the central basin, whose subsidence duration was longer than that in the basin margin (**Figure 6**). Besides, the average contents (23.3–33.0%) of mixed illite–smectite are obvious less than those of the basin margin (40.9–67.9%) (**Table 3**). Therefore, the compaction and clay mineral transformation of the Longmaxi Formation were stronger in the central basin than the basin margin (**Figure 8A**). The average quartz content in the central basin (50.0%) is generally higher than that in the basin margin (35.8–52.3%), indicating stronger silicification (**Table 2** and **Figure 8B**). The organic matter experienced more intense thermal evolution due to a longer subsidence duration. Besides, there are a lot of asphalt in pore space (**Figures 8C,D**). The existence of organic acids inhibits abundant quartz dissolution in the Longmaxi Formation of the central basin (Wang et al., 2017b).

The Longmaxi Formation has been uplifting since the Late Cretaceous (80 Ma) in the central basin (**Figure 6**). The relative closed diagenetic system of the central basin owing to shorter uplift duration resulted in the absence of fresh water leaching and fractures in the central basin compared to the basin margin.

Main Controlling Factors of Diagenesis

The low-energy, anoxic marine shelf environment is favorable for the sedimentation of black mud with abundant organic matter, which is the source of biogenic quartz cementation (**Figure 3C**). Clay mineral transformation and compaction were influenced by clay and brittle mineral composition of primary sediments. Besides, abundant soluble constituents of shale, which mainly derived from provenance, were material basis of dissolution (**Figures 4E,F**). The composition of shale was determined

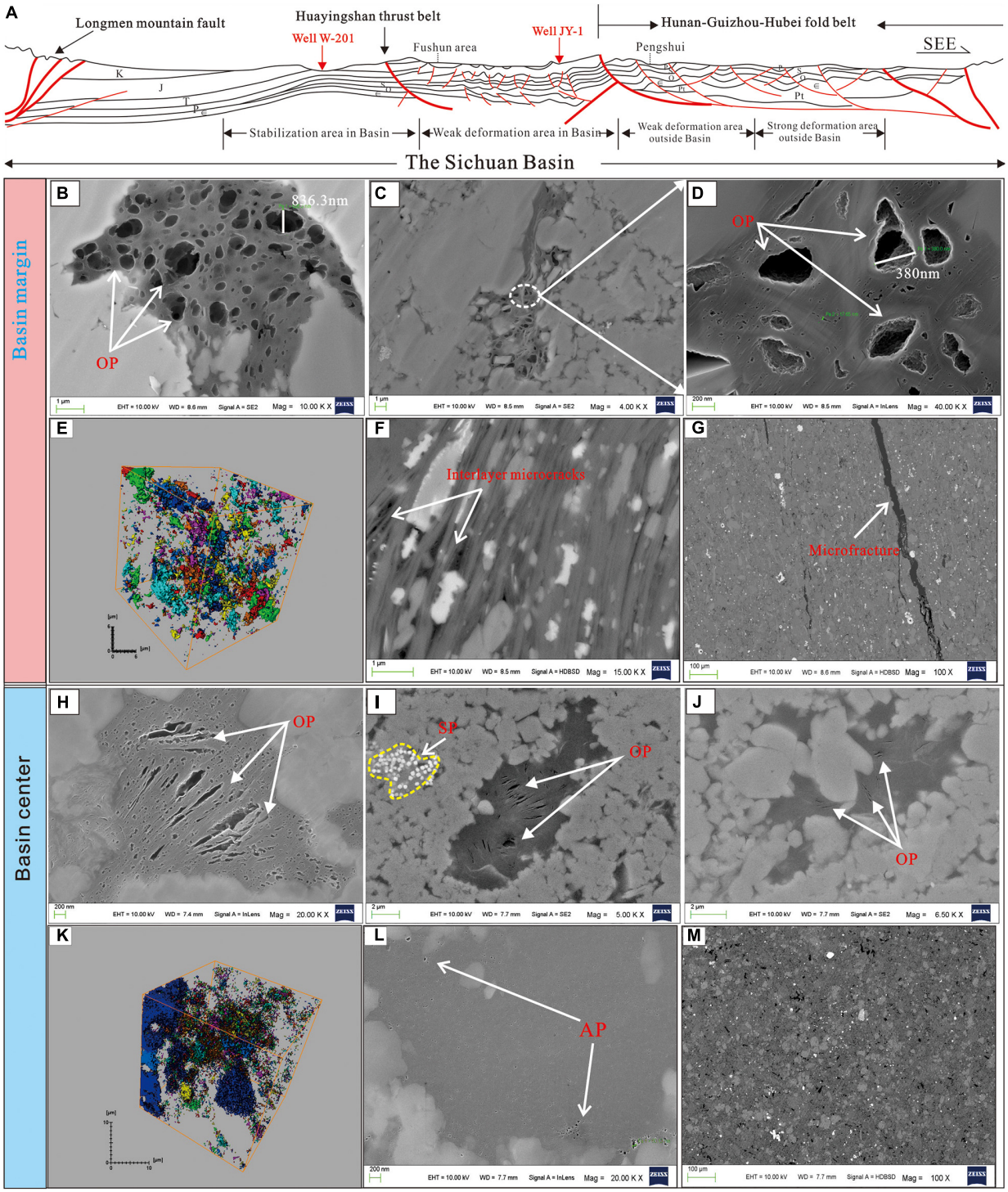

FIGURE 10 | Microscopic characteristics of reservoirs in different structural regions in the Sichuan Basin. **(A)** Different structural characteristics of the central and marginal areas in the Sichuan Basin. **(B)** An FESEM image showing the organic pores (OPs), well JY-2, 2,459.36 m. **(C)** An FESEM image showing the organic pores (OPs), well JY-2, 2,459.36 m. **(D)** An FESEM image showing the organic pores (OPs), which is a partial enlargement of image **(C)**, well JY-2, 2,459.36 m. **(E)** A field emission scanning electron microscope combined with a focused ion beam (FIB-FESEM) image showing the 3-D structure of pore spaces (different colors represent different types of pore spaces), well JY-2, 2,459.36 m. **(F)** FESEM images showing interlayer micro-cracks, well JY-2, 2,459.36 m. **(G)** FESEM images showing a micro-fracture of shale, well JY-2, 2,459.36 m. **(H)** An FESEM image showing the organic pores (OPs), well N-203, 2,325.64 m. **(I)** An FESEM image showing the organic pores (OPs) and strawberry pyrite (SP), well W-201, 2,678.61 m. **(J)** An FESEM image showing the organic pores (OPs), well W-201, 2,678.61 m. **(K)** An FIB-FESEM image showing the 3-D structure of pore spaces (different colors represent different types of pore spaces), well W-201, 2,678.61 m. **(L)** An FESEM image showing intragranular pore spaces (APs), well W-201, 2,678.61 m. **(M)** An FESEM image of the overall micro-characteristics of shale, well W-201, 2,678.61 m.

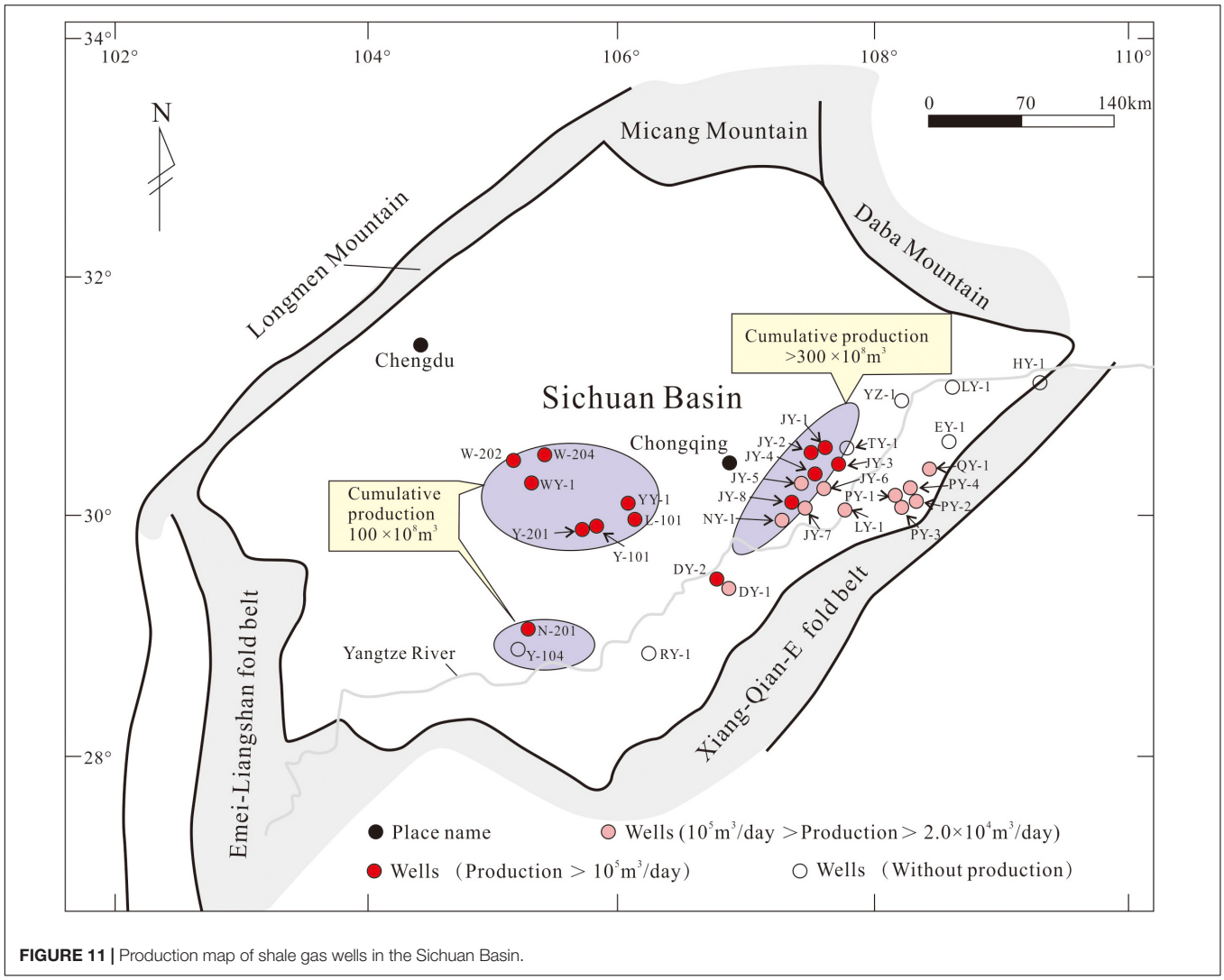

FIGURE 11 | Production map of shale gas wells in the Sichuan Basin.

by the provenance and sedimentary environment. Therefore, sedimentology characteristics is one of the most important controlling factors of diagenesis (Boles and Franks, 1979; Li and Liu, 2009).

The clay mineral transformation, compaction, and thermal evolution of organic matter were controlled by the burial depth and paleo-geotemperature during different diagenetic stages (**Figure 6**). Besides, the organic acids of dissolution were derived from the thermal evolution of organic matter. The burial depth and paleo-geotemperature were generally determined by the structural evolution (**Figure 6**). Therefore, the complex diagenetic evolution of the Longmaxi Formation shale was the result of a complicated structural history.

Influence of Diagenetic Evolution on Shale Gas Exploration and Development

Mineral Composition of Shale Reservoir

Absorbed gas, which is mainly stored within organic matter, is the most important occurrence of shale gas (Curtis, 2002). There are positive correlations between TOC and absorbed capacity of gas in the Longmaxi Formation shale of Sichuan Basin (**Figure 9A**). Besides, there is a negative correlation between clay mineral content and absorbed gas content (**Figure 9B**). In general, the TOC content of organic-rich shale increases with increasing content of clay mineral and decreasing content of quartz (Mou et al., 2011). However, there is a positive correlation between TOC and quartz content (**Figure 9C**) and an obvious negative correlation between TOC and clay minerals (**Figure 9D**). These indicate that some biogenetic silicification (**Figure 3C**; Wang S. F. et al., 2014) and clay mineral transformation added to the quartz content by forming authigenic quartz (**Figures 3D,E**, **4A**; Wang et al., 2017b). Therefore, the absorbed capacity of the Longmaxi Formation shale gas was related to mineral composition, which was influenced by the sediment characteristics and diagenetic evolution. The high contents of quartz and low content of the Longmaxi Formation suggest a strong absorbed capacity of shale both in the basin margin and center (**Table 2**).

Artificial fracturing is the most important method for shale gas development, which was influenced by the contents of

brittle minerals (Curtis, 2002; Jarvie et al., 2007). The high contents of brittle minerals both in the basin margin and center (**Table 1**), which was determined by sediment characteristics and silicification, were beneficial for artificial fracturing of shale gas development.

Reservoir Characteristics of Shale

A methane molecule is only 0.38 nm, which is comparable to a water molecule and thus easily enriched in shale (Jarvie, 2008). Organic matter volume can occupy 14% of the total shale volume when TOC content reached 7% in shale (Jarvie, 2008). Meanwhile, the shale porosity can increase by 4.9%, if 35% of the organic matter undergoes thermal evolution (Jarvie, 2008). Thus, the mass transfer of diagenetic system may be related to organic matter evolution, which resulted in the formation of secondary pores (**Figures 4D–F**) and organic pores (**Figures 4J–L**).

The organic micropores mainly occur as honeycomb-like subrounded nanopores (**Figures 10B,D**) in the Longmaxi Formation shale of the basin margin. In contrast, organic nanopores space of the Longmaxi Formation shale are generally long strip in the central basin (**Figures 10H–J**). The feldspar contents of the basin margin are obviously more than those in the central basin (**Table 2**), which provided more soluble constitute for the dissolution in the basin margin. Besides, micro-fractures of the Longmaxi Formation shale mainly developed in the basin margin (**Figures 10A,E-G**) but rarely in the central basin (**Figures 10A,L,M**). These suggest that the more open diagenetic system was in favor for the formation and preservation of secondary dissolved pores and organic pores in the basin margin and that the relatively stronger compaction resulted in the deformation of pore space in the central basin due to different burial history and diagenetic evolution (**Figures 6**, **10**).

Results of Shale Gas Development

More shale gas wells were drilled in the basin margin than the central basin (**Figure 11**). Besides, the cumulative gas production of the Longmaxi Formation shale is more than 300×10^8 m^3 in the basin margin and just 100×10^8 m^3 in the central basin (**Figure 11**). These also suggest and prove that the Longmaxi Formation shale in the basin margin with late weak tectonic reformation might have a better exploration and development potential of shale gas than the central basin.

CONCLUSION

The diagenetic evolution can be divided into three regimes: eodiagenesis, mesodiagenesis, and telediagnosis. The eodiagenesis was subdivided into two evolution stages and the mesodiagenesis was subdivided into three evolution stages, respectively, in the basin margin and center.

Provenance and sedimentary environment control the material basis of diagenetic evolution. Structural evolution determined the diagenetic evolution by influencing burial and thermal history. The diagenetic system in the basin margin was more open than that in the basin center due to a different structural and burial history.

The absorbed capacity and artificial fracturing effect of the Longmaxi Formation shale gas were related to mineral composition, which was influenced by the sediment characteristics and diagenetic evolution. The high contents of quartz (brittle minerals) and low clay mineral content of the Longmaxi Formation suggest a strong absorbed capacity and good artificial fracturing of shale both in the basin margin and center.

The mass transfer of diagenetic system may be related to organic matter evolution, which resulted in the formation of secondary pores and organic pores. The more open diagenetic system consisting of more micro-fractures and soluble constitute (e.g., feldspar) was in favor for the formation and preservation of secondary dissolved pores and organic pores in the basin margin. The relatively closed diagenetic system with stronger compaction resulted in the deformation of pore space in the central basin due to a different burial history and diagenetic evolution.

DATA AVAILABILITY STATEMENT

The original contributions presented in the study are included in the article/supplementary material, further inquiries can be directed to the corresponding author/s.

AUTHOR CONTRIBUTIONS

JW contributed as the major author of the manuscript. XT and JT did a part of writing and coding works. LL, XG, CL, and CZ provided some interesting ideas. LZ provided the suggestions. LZ and WX gave analysis on results. CL and WX collected the data. All authors contributed to the article and approved the submitted version.

FUNDING

This work was financially supported by the National Natural Science Foundation of China (Grant Numbers 42072140 and 41902153) and the Natural Science Foundation Project of CQ CSTC (Grant Numbers cstc2018jcyjAX0523 and cstc2020jcyj-msxm0778).

ACKNOWLEDGMENTS

We greatly thank the Exploration and Development Research Institute of Southwest Oil and Gas Field Company and Chongqing Institute of Geology and Mineral Resources for providing all the related core samples, geological data, and permission to publish these data. We thank our scientific research team for their help and guidance in the field investigation.

REFERENCES

Allen, P. A., and Allen, J. R. (1990). *Basin Analysis: Principles and Applications to Petroleum Play Assessment*. Oxford: Wiley-Blackwell, 263–308.

Archer, S. G., Wycherley, H. L., Watt, G. R., and Chen, H. (2004). Evidence for focused hot fluid flow within the Britannia Field, offshore Scotland, UK. *Basin Res.* 16, 377–395. doi: 10.1111/j.1365-2117.2004.00240.x

Bjørlykke, K. (1993). Fluid flow in sedimentary basins. *Sediment. Geol.* 86, 137–158. doi: 10.1016/0037-0738(93)90137-t

Bjørlykke, K. (2014). Relationship between depositional environments, burial history and rock properties. Some principal aspects of diagenetic process in sedimentary basins. *Sediment. Geol.* 301, 1–14. doi: 10.1016/j.sedgeo.2013.12.002

Bjørlykke, K., and Jahren, J. (2012). Open or closed geochemical systems during diagenesis in sedimentary basins: Constraints on mass transfer during diagenesis and the prediction of porosity in sandstone and carbonate reservoirs. *AAPG Bull.* 96, 2193–2214. doi: 10.1306/04301211139

Boles, J. R., and Franks, S. G. (1979). Clay diagenesis in wilcox sandstones of southwest texas–implications of smectite-illite reaction for sandstone cementation: abstract. *J. Sediment. Petrol.* 49, 55–70.

Buhman, C. (1992). Smectite-to-Illite conversion in a geothermally and lithologically complex Permian sedimentary sequence. *Clay Clay Miner.* 40, 53–64. doi: 10.1346/ccmn.1992.0400107

Burtner, R. L., and Warner, M. A. (1986). Relationship between illite/smectite diagenesis and hydrocarbon generation in Lower Cretaceous Mowry and Skull Creek shales of Northern Rocky Muntain Area. *Clay Clay Miner.* 34, 390–402. doi: 10.1346/ccmn.1986.0340406

Curtis, C. D. (1978). Possible links between sandstone diagenesis and depth-related geochemical reactions occurring in enclosing mudstones. *J. Geol. Soc. Lond.* 135, 107–114. doi: 10.1144/gsjgs.135.1.0107

Curtis, J. B. (2002). Fractured shale-gas systems. *AAPG Bull.* 86, 1921–1938.

Day-Stirrat, R. J., Milliken, K. L., Dutton, S. P., Loucks, R. G., Hillier, S., Aplin, A. C., et al. (2010). Open-system chemical behavior in deep Wilcox Group mudstones, Texas Gulf Coast, USA. *Mar. Pet. Geol.* 27, 1804–1818. doi: 10.1016/j.marpetgeo.2010.08.006

Dickinson, W. R. (1993). Basin geodynamics. *Basin Res.* 5, 195–196. doi: 10.1111/j.1365-2117.1993.tb00066.x

Dickinson, W., Anderson, R. N., and Biddle, K. T. (1997). *The Dynamics of Sedimentary Basins. USGC*. Washington, DC: The National Academies Press, 43.

Dong, C. M., Ma, C. F., Luan, G. Q., Lin, C. Y., Zhang, X. G., and Ren, L. H. (2015). Pyrolysis simulation experiment and diagenesis evolution pattern of shale. *Acta Sedimentol. Sin.* 33, 1053–1061. (in Chinese),

Guo, X. S., Hu, D. F., Wen, Z. D., and Liu, R. B. (2014). Major factors controlling the accumulation and high productivity in marine shale gas in the Lower Paleozoic of Sichuan Basin and its periphery: a case study of the Wufeng-Longmaxi Formation of Jiaoshiba area. *Geol. China* 41, 893–901. (in Chinese),

He, D. F., Zhao, W. Z., Lei, Z. Y., Qu, H., and Chi, Y. L. (2000). Characteristics of composite petroleum systems of superimposed basins in China. *Earth Sci. Front.* 7, 23–37. (in Chinese),

Jacob, H. (1985). Disperse solid bitumens as an indicator for migration and maturity in prospecting for oil and gas. *Erdöl Und Kohle-Erdgas-Petrochemie* 38, 364–366.

Jarvie, D. M. (2008). *Unconventional Shale Resource Plays: Shale Gas Shale Oil Opportunities. Fort Worth Buiness Press Meeting*. Texas, TX: Fort Worthenss Press, 7–17.

Jarvie, D. M., Hill, R. J., Ruble, T. E., and Pollastro, R. M. (2007). Unconventional shale-gas systems: the Mississippian Barnett Shale of north-central Texas as one model for thermogenic shale-gas assessment. *AAPG Bull* 91, 475–499. doi: 10.1306/12190606068

Jia, D., Qiu, Y., Li, C., and Cai, Y. (2019). Propagation of pressure drop in coalbed methane reservoir during drainage stage. *Adv. Geo Energy Res.* 3, 387–395. doi: 10.26804/ager.2019.04.06

Kong, L. M., Wan, M. X., Yan, Y. X., Zou, C. M., Liu, W. P., Tian, C., et al. (2015). Reservior diagenesis research of Silurian Longmaxi Formation in Sichuan Basin. *Nat. Gas Geosci.* 26, 1547–1555. (in Chinese),

Lai, J., Wang, G., Cao, J., Xiao, C., Wang, S., Pang, X., et al. (2018). Investigation of pore structure and petrophysical property in tight sandstones. *Mar. Pet. Geol* 91, 179–189. doi: 10.1016/j.marpetgeo.2017.12.024

Lai, J., Wang, G., Chai, Y., Xin, Y., Wu, Q., Zhang, X., et al. (2017). Deep burial diagenesis and reservoir quality evolution of high-temperature, high-pressure sandstones: examples from Lower Cretaceous Bashijiqike Formation in Keshen area, Kuqa depression, Tarim basin of China. *AAPG Bull.* 101, 829–862. doi: 10.1306/08231614008

Lai, J., Wang, G., Ran, Y., and Zhou, Z. (2015). Predictive distribution of high quality reservoirs of tight gas sandstones by linking diagenesis to depositional facies: evidences from Xu-2 sandstones in Penglai area of central Sichuan Basin, China. *J. Nat. Gas Sci. Eng.* 23, 97–111. doi: 10.1016/j.jngse.2015.01.026

Lai, J., Wang, G., Ran, Y., Zhou, Z., and Cui, Y. (2016). Impact of diagenesis on the reservoir quality of tight oil sandstones: the case of Upper TriassicYanchang Formation Chang 7 oil layers in Ordos Basin, China. *J. Petrol. Sci. Eng.* 145, 54–65. doi: 10.1016/j.petrol.2016.03.009

Law, B. E., and Curtis, J. B. (2002). Introduction to unconventional petroleum systems. *AAPG Bull.* 86, 1851–1852.

Li, D. S. (2013). China's multicycle superimposed petroliferous basins: theory and explorative practices. *Xinjiang Petrol. Geol.* 34, 497–503. (in Chinese)

Li, S. T. (1995). Geodynamics of sedimentary basins—the main trend of basin research. *Earth Sci. Front.* 2, 1–8. (in Chinese)

Li, Z., and Li, H. S. (1994). An Approach to genesis and evolution of secondary porosity in deeply buried sandatone reservoirs, Dongpu Deprseeion. *Chin. J. Geol.* 29, 1267–1275. (in Chinese)

Li, Z., and Liu, J. Q. (2009). Key problems and research trend of diagenetic geodynamic mechanism and spatio-temporal aistrbution in sedimentary basins. *Acta Sedimentol. Sin.* 27, 837–847. (in Chinese)

Li, Z., Fei, W. H., Shou, J. F., and Wang, S. L. (2003). Overpressure and fluid in the Dongpu Depression, North China: their constraints on diagenesis of reservoir scndstones. *Acta Geol. China* 77, 126–134. (in Chinese)

Liang, D. G., Guo, T. L., Che, J. P., Bian, L. Z., and Zhao, J. (2008). Distribution of four suits of regional marine source rocks, South China. *Mar. Origin Petrol. Geol.* 13, 1–16. (in Chinese)

Liu, S. G., Li, Z. W., Sun, W., Deng, B., Luo, Z. L., Wang, G. Z., et al. (2011). Basic geological features of superimposed baisn and hydrocarbon accumulatuion in Sichuan Basin, China. *Chin. J. Geol.* 46, 233–257. (in Chinese)

Liu, W. P., Zhou, Z., Wu, J., Luo, C., Wu, W., Jiang, L., et al. (2020). Hydrocarbon generation and shale gas accumulation in the Wufeng?Longmaxi formations, Changning shale?gas field, Southern Sichuan Basin. *J. Nanjing Univ. Nat. Sci.* 56, 393–404. (in Chinese)

Loucks, R. G., Reed, R. M., Ruppel, S. C., and Jarvie, D. M. (2009). Morphology, genesis, and distribution of nanometer-scale pores in siliceous mudstones of the Mississippian Barnett Shale. *J. Sediment. Res.* 79, 848–861.

Luan, G. Q., Dong, C. M., Ma, C. F., Lin, C. Y., Zhang, J. Y., Lv, X. W., et al. (2016). Pyrolysis simulation experiment study on diagenesis and evolution of organic-rich shale. *Acta Sedimentol. Sin.* 34, 1208–1216. (in Chinese)

Luo, L., Gao, X., Gluyas, J., Tan, X., Cheng, C., Kong, X., et al. (2019). Reservoir quality prediction of deeply buried tight sandstones in extensively faulted region: a case from the Middle-Upper Jurassic Shishugou Group in central Junggar Basin, NW China. *J. Petrol. Sci. Eng.* 175, 22–45. doi: 10.1016/j.petrol.2018.12.027

Lv, D. W., Li, Z. X., Feng, T. T., Li, Y., Wang, D. D., Liu, H. Y., et al. (2015). The characteristics of coal bed 1 and oil shale 2 qualities in the sea areas of Huangxian Coalfield, Eastern China. *Oil Shale* 32, 204–217. doi: 10.3176/oil.2015.3.02

Lv, D. W., Li, Z. X., Wang, D. D., Li, Y., Liu, H. Y., Liu, Y., et al. (2019). Sedimentary model of coal and shale in the Paleogene Lijiaya Formation of the Huangxian Basin: insight from Petrological and Geochemical Characteristics of Coal and Shale. *Energy Fuels* 33, 10442–10456. doi: 10.1021/acs.energyfuels.9b01299

Lv, D. W., Song, Y., Shi, L. Q., Wang, Z. L., Cong, P. Z., and Loon, A. J. V. (2020). The complex transgression and regression history of the northern margin of the Palaeogene Tarim Sea (NW China), and implications for potential hydrocarbon occurrences. *Mar. Petrol. Geol.* 112:104041. doi: 10.1016/j.marpetgeo.2019.104041

Meng, Y. L., Wei, W., Wang, W. A., Jie, X. L., Xiao, L. H., Gao, Y. T., et al. (2012). An optimization model of clay mineral transformation under overpressure setting. *J. Jilin Univ. Earth Sci. Ed.* 42, 145–152. (in Chinese)

Milliken, K. L., Esc, W. L., Reed, R. M., and Zhang, T. W. (2012). Grain assemblages and strong diagenetic overprinting in siliceous mudrocks, Barnett Shale (Mississippian), Fort Worth Basin, Texas. *AAPG Bull.* 96, 1553–1578. doi: 10.1306/12011111129

Morad, S., Ketzer, J. M., and Deros, L. F. (2000). Spatial and temporal distribution of diagenetic alterations in siliciclasticrocks: implications for mass transfer in sedimentary basins. *Sedimentology* 47, 95–120. doi: 10.1046/j.1365-3091.2000.00007.x

Mou, C. L., Zhou, K. K., Liang, W., and Guo, X. Y. (2011). Early paleozoic sedimentary environment of hydrocarbon source rocks in the middle-upper yangtze region and petroleum and gas exploration. *Acta Geol. Sin.* 85, 526–532. (in Chinese)

Peters, K. E., and Cassa, M. R. (1994). Applied source rock geochemistry. *AAPG Bull.* 60, 93–120. doi: 10.1306/m60585c5

Robert, L. L., Robert, M. R., Stephen, R., and Daniel, M. J. (2009). Morphology, genesis, and distribution of nanometer-scale pores in siliceous mudstones of the Mississippian Barnett shale. *J. Sediment. Res.* 79, 848–861. doi: 10.2110/jsr.2009.092

Schmoker, J. M. (1993). Use of formation-density logs to determine organic-carbon content in Devonian shales of the western Appalachian Basin and an additional example based on the Bakken Formation of the Williston Basin. *US Geol. Survey Bull.* 19, 1–14.

Schoenherr, J., Littke, R., Urai, J. L., Kukla, P. A., and Rawahi, Z. (2007). Polyphase thermal evolution in the Infra-Cambrian Are Group (South Oman Salt Basin) as deduced by maturity of solid reservoir bitumen. *Org. Geochem.* 38, 1293–1318. doi: 10.1016/j.orggeochem.2007.03.010

Seiver, R. (1979). Plate tectonic controls on diagenesis. *J. Geol.* 82, 127–155. doi: 10.1086/628405

Surdam, R. C. (1989). Organic-inorganic interactions and sandstone diagenesis. *Am. Assoc. Petrol. Geol. Bull.* 73, 1–23. doi: 10.1002/9781444304459.ch

Surdam, R. C., Boese, S. W., and Crossey, L. J. (1984). The chemistry of secondary porosity. *AAPG Mem.* 37, 183–200.

Wang, J., Huang, W. M., and Li, X. G. (2014). The shale Gas exploration prospect assess of the Niutitang Formation in Western Hubei and Hunan-Eastern Chongqing. *Geol. Sci. Technol. Inform.* 33, 98–103. (in Chinese)

Wang, J., Liu, S. G., Huang, W. M., Zhang, C. J., and Zeng, X. L. (2011). Oil and gas exploration prospects of Cambrian in Southern Sichuan Basin. *Geol. Sci. Technol. Inform.* 30, 74–82. (in Chinese)

Wang, J., Tan, X. F., Tian, J. C., Luo, C., Ran, B., Chen, Q., et al. (2017a). Constraints of hydrocarbon migration in Longmaxi shale in Sichuan Basin on shale gas accumulation. *Petrol. Geol. Exp.* 39, 755–762. (in Chinese with English abstract)

Wang, J., Tan, X. F., Zeng, C. L., Chen, Q., Ran, T., Xue, W. W., et al. (2017b). Process of diagenetic system in shale and its restrict on occurrence of SiO_2: a case study of the Longmaxi Formation in the southeast district of Chongqing. *Adv. Earth Sci.* 32, 292–306. (in Chinese),

Wang, R. Y., Hu, Z. Q., Dong, L., Gao, B., Sun, C. X., Yang, T., et al. (2020a). Advancemnet and trends of shale reservoir charactization and evaluation. *Oil Gas Geol.* 42, 54–65. (in Chinese),

Wang, R. Y., Hu, Z. Q., Long, S. X., Zhao, J. H., Dong, L., Du, W., et al. (2019). Differential characteristics of the Upper Ordovician-Lower Silurian Wufeng-Longmaxi shale reservoir and its implications for exploration and development of shale gas in/around the Sichuan Basin. *Acta Geol. Sin. (English Edition)* 93, 520–535. doi: 10.1111/1755-6724.13875

Wang, R. Y., Hu, Z. Q., Sun, C. X., Liu, Z. B., Zhang, C. C., Gao, B., et al. (2018). Comparative analysis of shale reservoir characteristics in the Wufeng-Longmaxi (O3w-S1l) and Niutitang (ε_1n) Formations: a case study of the Wells JY1 and TX1 in southeastern Sichuan Basin and its periphery, SW China. *Interpretation* 6, 31–45.

Wang, R. Y., Nie, H. K., Hu, Z. Q., Liu, G. X., Xi, B. B., and Liu, W. X. (2020b). Controlling effect of pressure evolution on shale reservoirs: a case study of the Wufeng-Longmaxi Formation in the Sichuan Basin. *Nat. Gas Ind.* 40, 1–11. (in Chinese)

Wang, S. F., Zo, C. N., Dong, D. Z., Wang, Y. M., Huang, J. L., and Guo, Z. J. (2014). Biogenic silica of organic-rich shale in Sichuan Basin and Its significance for shale gas. *Acta Scientianrum Nat. Universitatis Pekinensis* 50, 476–486. (in Chinese)

Wang, X. P., Mou, C. L., Wang, Q. Y., Ge, X. Y., Chen, X. W., Zhou, K. K., et al. (2015). Diagenesis of black shale in Longmaxi Formation, southern Sichuan Basin and its periphery. *Acta Petrol. Sin.* 36, 1035–1047. (in Chinese)

Wang, X., Yin, H., Zhao, X., Li, B., and Yang, Y. (2019). Microscopic remaining oil distribution and quantitative analysis of polymer flooding based on CT scanning. *Adv. Geo Energy Res.* 3, 448–456. doi: 10.26804/ager.2019.04.10

Wu, Q. M. (2018). *Shale Gas Geological Characteristics of the Lower Silurian Longmaxi formation in Weiyuan area, South Sichuan.* Master's thesis. Chengdu: Southwest Petroleum University. 31–35. (in Chinese).

Xu, E. S., Li, Z. M., and Yang, Z. H. (2015). Thermal and hydrocarbon generation history of Wufeng and Longmaxi shales in Pengshui area, eastern Sichuan Basin: a well PY1 case study. *Exp. Petrol. Geol.* 37, 494–499. (in Chinese)

Yuan, G. H., Cao, Y. C., Zan, N. M., Schula, H. M., Gluyas, J., Hao, F., et al. (2019). Coupled mineral alteration and oil degradation in thermal oil-water-feilspar systems and implications for organic-inorganic interactions in hydrocarbon reservoirs. *Geochim. Cosmochim. Acta* 248, 61–87. doi: 10.1016/j.gca.2019.01.001

Yuan, G. H., Cao, Y. C., Zhang, Y., and Gluya, J. (2017). Diagenesis and reservoir quality of sandstones with ancient "deep" incursion of meteoric freshwater –An example in the Nanpu Sag, Bohai Bay Basin, East China. *Mar. Petrol. Geol.* 82, 444–464. doi: 10.1016/j.marpetgeo.2017.02.027

Yuan, G. H., Gluya, J., Cao, Y. C., Oxtoby, H. N., Jia, Z. Z., and Wang, Y. Z. (2015). Diagenesis and reservoir quality evolution of the Eocene sandstones in the northern Dongying Sag, Bohai Bay Basin, East China. *Mar. Petrol. Geol.* 22, 77–89. doi: 10.1016/j.marpetgeo.2015.01.006

Zhang, J. C., Xu, B., Nie, H. K., Wang, Z. Y., and Lin, T. (2008). The issue of intellectual property protection in contracts management by oil and gas enterprises. *Nat. Gas Ind.* 28, 136–140. (in Chinese)

Zhao, D. F., Guo, Y. H., Yang, Y. J., Wang, S. Y., Mao, X. X., and Li, M. (2016). Shale reservoir diagenesis and its impacts on pores of the Lower Silurian Longmaxi Formation in southeastern Chongqing. *J. Palaeogeogr.* 18, 843–856. (in Chinese),

Zhao, W. Z., Zhang, G. Y., Wang, H. J., Wang, S. J., and Wang, Z. C. (2003). Basic features of petroleum geology in the superimposed petroliferous basins of China and their research methodologies. *Petrol. Explor. Dev.* 30, 1–7. (in Chinese) doi: 10.1007/s12182-015-0014-0

Zou, C. N., Yang, Z., Pan, S. Q., Chen, Y. Y., Lin, S. H., Huang, J. L., et al. (2016). Shale gas formation and occurrence in China: an overview of the current status and future potential. *Acta Geol. Sin. Engl. Ed.* 90, 1249–1283. doi: 10.1111/1755-6724.12769

Conflict of Interest: CL was employed by the company PetroChina.

The remaining authors declare that the research was conducted in the absence of any commercial or financial relationships that could be construed as a potential conflict of interest.

frontiers in Earth Science

ORIGINAL RESEARCH
published: 30 April 2021
doi: 10.3389/feart.2021.664330

Total Scanning Fluorescence Characteristics and Implications of Shale Oil in the Lucaogou Formation, Jimsar Sag, Junggar Basin, NW China

Zhongying Zhao, Lianhua Hou, Xia Luo*, Feifei Sun, Senhu Lin and Lijun Zhang*

Research Institute of Petroleum Exploration and Development, PetroChina, Beijing, China

OPEN ACCESS

Edited by:
Dawei Lv,
Shandong University of Science and Technology, China

Reviewed by:
Xianfeng Tan,
Chongqing University of Science and Technology, China
Bo Liu,
Northeast Petroleum University, China

***Correspondence:**
Lianhua Hou
houlh@petrochina.com.cn
Xia Luo
luoxia69@petrochina.com.cn

Specialty section:
This article was submitted to Economic Geology, a section of the journal Frontiers in Earth Science

Received: *05 February 2021*
Accepted: *07 April 2021*
Published: *30 April 2021*

Citation:
Zhao Z, Hou L, Luo X, Sun F, Lin S and Zhang L (2021) Total Scanning Fluorescence Characteristics and Implications of Shale Oil in the Lucaogou Formation, Jimsar Sag, Junggar Basin, NW China. Front. Earth Sci. 9:664330. doi: 10.3389/feart.2021.664330

The Lucaogou Formation in the Jimsar Sag is a typical lacustrine shale oil development area where the first large-scale shale oil field in China was discovered, and a large number of studies have been conducted on the genesis and distribution of the shale oil in this formation. However, few detailed studies have been conducted on the comparison between the characteristics of the hydrocarbons in the shale and the adjacent tight reservoirs in the same shale sequence package. In this study, the total scanning fluorescence (TSF) quantitative fluorescence technique, which has been rarely applied to and studied in the Lucaogou Formation in the Jimsar Sag, was used to conduct systematic quantitative fluorescence analysis of the shale, tight reservoirs, and crude oils in the Lucaogou Formation. The geochemical analysis was also carried out for all samples. The results revealed that the shale, tight reservoirs, and oils have similar single-peak TSF spectrograms, and different values of the TSF parameters in the Lucaogou Formation. The TSF parameters R_1 and R_2 values of the blocky shale, fractured shale, tight reservoirs, and produced oils are decreased successively. The TSF parameters can be used as indicators of hydrocarbon composition, physical properties, thermal maturity, migration, and oil-producing layers. The values of TSF parameters R_1 and R_2 are generally smaller in the upper section of the Lucaogou Formation (P_2l_2) than in the lower section (P_2l_1), indicating that the hydrocarbons in the upper section have better physical properties and higher thermal maturity. The distribution of TSF parameters R_1 and R_2 in the upper section of the Lucaogou Formation is relatively scattered, indicating that the hydrocarbons have undergone obvious lateral migration. Based on the TSF parameter comparison of core and oil samples, it was preliminarily determined that the shale oil in the upper and lower sections of the Lucaogou Formation was mainly produced from the tight reservoirs in the shale sequence. The results of this study provide new data and ideas for fine studies of the shale oil in the Lucaogou Formation in the Jimsar Sag.

Keywords: total scanning fluorescence, lacustrine shale oil, lucaogou formation, Jimsar sag, Junggar basin

INTRODUCTION

Following the shale revolution in North America, the shale oil industry has flourished in the Mesozoic-Cenozoic lacustrine shale in China (Zou et al., 2013; Li et al., 2015; Liu et al., 2017, 2021; Zhao et al., 2018; Hou et al., 2020a,b,c; Ma et al., 2020; Wang et al., 2020). The Junggar Basin has abundant shale oil resources and is the first basin in China in which shale oil has been developed on a large scale. China's first large-scale shale oil field was discovered in the Jimsar Sag, and the first national-level shale oil demonstration area in China was built there (Wang et al., 2019). Well J174 was drilled in the Jimsar Sag, and it was the first well in China to collect core samples of an entire set of the shale strata of the Lucaogou Formation (over 200 m). The shale oil in the Lucaogou Formation in the Jimsar Sag has been developed for more than 10 years, and numerous studies have been carried out on the sedimentary environment, shale oil genesis, source rock evaluation, reservoir characterization, the patterns of shale oil enrichment and distribution, and shale oil sweet spot identification in this area (Kuang et al., 2012; Gao et al., 2016; Qiu et al., 2016; Chen et al., 2018; Pang et al., 2018; Liu C. et al., 2019; Zha et al., 2019; Hou et al., 2021a,b). However, few detailed studies have been conducted on the comparison between the characteristics of the hydrocarbons in the shale and the adjacent tight reservoirs in the same shale sequence.

The total scanning fluorescence (TSF) technique has been widely used in conventional oil and gas research. It is an important method for fine oil source correlation, exploring reservoir oil and gas properties, identifying current and ancient oil layers, and for the fine analysis of oil and gas properties and migration characteristics (Brooks et al., 1983; Reyes, 1993; Li et al., 2007; Liu et al., 2014, 2016; Fan et al., 2015; Kong et al., 2019). However, TSF research results are rarely reported for the shale oil in the Lucaogou Formation in the Jimsar Sag. TSF is a new quantitative fluorescence analysis technique that was developed based on fluorescence spectroscopy in the 1980s. It uses the emission spectrum obtained by scanning the excitation light with a continuously changing wavelength, and it is an effective method of measuring the distribution and concentration of the aromatic hydrocarbon components (Brooks et al., 1983; Fan et al., 2015; Liu et al., 2016). The hydrocarbons of different origins or extracted from different rocks have different TSF fluorescence spectral characteristics, which are mainly manifested as different indicators, such as the profile of the spectrogram, the position of the main peak, the fluorescence intensity of the specific peak, and the ratio of the fluorescence intensity of two specific peaks. The TSF technique has a fast speed, high sensitivity, small amount of sample required, and fine quantitative and comparative analysis of micro-areas. This technique can be used to perform systematic, continuous quantitative fluorescence analysis of the shale and the adjacent tight reservoirs and for the fine comparison of the fluorescence characteristics of the shale and the adjacent tight reservoirs in the same shale sequence package. Therefore, it provides a good method for studying the factors that control the formation and enrichment of lacustrine shale oil.

In this study, the TSF technique was used to quantitatively analyze the fluorescence characteristics of the shale oil in the Lucaogou Formation in the Jimsar Sag. The shale and the adjacent tight reservoirs in the upper and lower sections of the Lucaogou Formation in Well J174 were systematically and continuously sampled. Oil samples were collected from oil-producing wells in the Lucaogou Formation in the Jimsar Sag. The TSF quantitative fluorescence characteristics of the Lucaogou Formation shale, its adjacent tight reservoirs, and the crude oil samples were systematically analyzed. In addition, all the samples were subjected to geochemical analysis. The relationship between TSF parameters and geochemical parameters were discussed in order to further explore the TSF characteristics of the Lucaogou Formation and their use in guiding shale oil exploration. The results of this study provide new data for the fine studies of the shale oil in the Lucaogou Formation in the Jimsar Sag and new ideas for the detailed studies of shale oil in other lacustrine basins.

GEOLOGIC SETTING

The Jimsar Sag is located in the southeastern edge of the Junggar Basin in northwestern China. It is a half-graben depression that is deep in the west and shallow in the east, with an area of 1278 km^2 (Graham et al., 1990; Gao et al., 2016; Hu et al., 2018; **Figure 1**). The Permian Lucaogou Formation is the main source rock in the Jimsar Sag and the main stratum for shale oil exploration. The 100–300 m thick Lucaogou Formation was deposited in a semi-deep to deep lake environment with an arid climate and a high salinity (Cao et al., 2016; Ding et al., 2020). The Lucaogou Formation has a complex lithology and strong heterogeneity. The multiple sets of interbedded high-quality source rocks are mainly composed of siliceous and carbonate shales; while the tight reservoirs are mainly composed of siliceous and carbonate siltstones (Kuang et al., 2012; Yang et al., 2019). The Lucaogou Formation consists of an upper section (P_2l_2) and a lower section (P_2l_1), each of which contains a set of shale oil sweet spots. The thickness of the upper Lucaogou Formation shale oil sweet spot is about 41 m, and the main part is located in the middle of the depression, with an area of 640 km^2. The shale oil sweet spots in the lower Lucaogou Formation are distributed in the sag, with an area of 1096 km^2 and a relatively large thickness in the southern part of the sag (Zhi et al., 2019).

The exploration of the Lucaogou Formation in the Jimsar Sag was divided into three stages: In the 2010–2011 exploration and discovery stage, well J25 was discovered, with a daily oil production of 18.25 t and a cumulative oil production of 264.94 t. In the 2012–2015 pilot test stage, the drilling of 22 wells was completed, and 15 wells achieved industrial oil flow. In the key breakthrough stage from 2016 to 2017, 31 horizontal wells were deployed, with a new production capacity of 31.95×10^4 t, achieving an overall breakthrough in the exploration and development of shale oil in the Lucaogou Formation in the Jimsar Sag (Wang et al., 2019). Currently, the upper sweet spot has oil reserves of over 4.5×10^8 t and the lower sweet spot has oil reserves of over 6.7×10^8 t (Zhao et al., 2020).

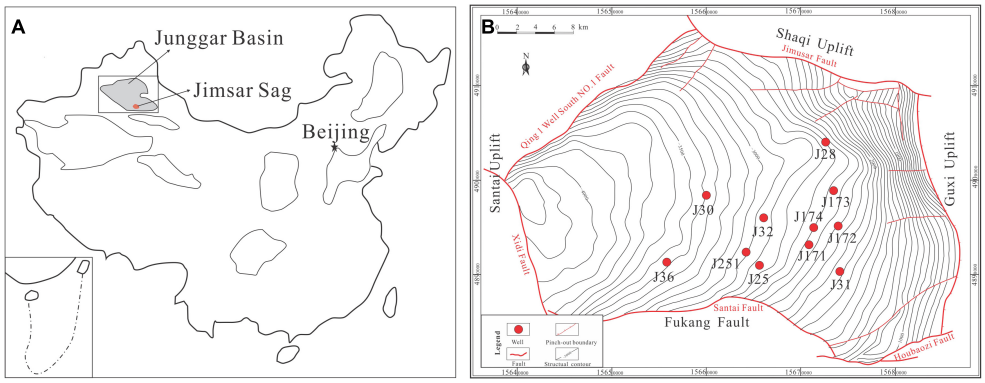

FIGURE 1 | Location of the sampling wells in the Jimsar Sag, Junggar Basin. **(A)** Locations of Junggar Basin and the Jimsar Sag. **(B)** Locations of oil wells, with a contour map of the Lucaogou Formation.

SAMPLES AND METHODS

In this study, 22 core samples from the upper and lower sections of the Lucaogou Formation were collected from Well J174 in the Jimsar Sag. The basic information for these samples is presented in **Table 1**. 11 oil samples were collected from the main oil-producing wells in the Lucaogou Formation in the Jimsar Sag. The locations of these wells are shown in **Figure 1B**, and the basic information for the oil samples is presented in **Table 2**. The core samples were subjected to thin section analysis, X-ray diffraction (XRD) analysis, rock pyrolysis analysis, total organic carbon (TOC) determination, and TSF analysis. An extraction experiment was carried out on the core sample, and the extract was subjected to group component analysis, gas chromatography (GC) analysis, and gas chromatography-mass spectrometry (GC-MS) analysis. Physical property determination, group component analysis, GC analysis, GC-MS analysis, and TSF analysis were conducted on the crude oil samples. The TSF analysis was performed in the Australian Commonwealth Scientific and Industrial Research Organization (CSIRO) laboratory. The determination of the physical properties of the crude oil was completed at the Institute of Experiment and Analysis of the Xinjiang Oilfield Company. The other analyses were conducted by the Research Institute of Petroleum Exploration and Development, China National Petroleum Corporation, Beijing.

The thin section analyses were performed using a Leica DM4500 microscope equipped with light emitting diode (LED) illumination and a LAS V4.2 digital camera detection system. The XRD analyses were conducted using a Rigaku TTR diffractometer according to Standard No. SY/T 5163-2010 *X-ray Diffraction Analysis Method of Clay Minerals and Common Non-clay Minerals in Sedimentary Rocks*. The rock pyrolysis analyses and TOC measurements were conducted on original and after-extracted core samples in parallel. The rock pyrolysis analyses were completed using a Rock Eval-6 Standard analyzer, and the amounts of free hydrocarbons (S_1) and pyrolysis hydrocarbons (S_2), and the temperature of the maximum pyrolysis yield (Tmax) were obtained. The TOC determination was performed using a LECO CS230HC analyzer. The standard procedures of the rock pyrolysis analyses and TOC measurements reported by Espitalié et al. (1984) were used. The density of the oil was measured using a DMA4500M digital densitometer. The viscosity was measured using a MCR101 rheometer. The wax content was determined using a DSC204F1 differential scanning calorimeter. The freezing point was determined using a JRS0919A freezing point instrument. Soxhlet extraction was conducted on the core samples using chloroform for 72 h. The core extracts and oil samples were fractionated via column chromatography into saturated hydrocarbons, aromatic hydrocarbons, non-hydrocarbons, and asphaltenes. The GC analyses were performed using an Agilent 6890N instrument with the flame ionization detector (FID). The GC-MS analyses were performed using an Agilent 6890N gas chromatography interfaced with a 5973C mass spectrometer for biomarker analysis.

The TSF analysis was performed using a Varian Cary-Eclipse fluorescence analyzer. The fluorescence analyzer was mainly composed of a spectrophotometer, a specially designed sample stage, optical filters, and special data analysis software. The analyzed samples were the hydrocarbons extracted from the core samples, and the details of the experimental procedure have been described by Fan et al. (2015) and Liu et al. (2016). The experimental parameters were as follows: the excitation wavelength range was 220:2:340 nm and the emission wavelength range was 250:5:540 nm. To avoid Rayleigh scattering interference, the starting emission wavelength was set to lag behind the starting excitation wavelength by 30 nm, and the experiments were performed at room temperature. The TSF parameters TSF Max, E_x, E_m, R_1, and R_2 were obtained via the TSF analysis. TSF Max is the maximum fluorescence intensity; E_x is the maximum excitation wavelength; E_m is the maximum emission wavelength; R_1 is the ratio of the emission intensities at 360 nm over 320 nm, corresponding to an excitation wavelength of 270 nm; and R_2 is the ratio of the emission intensities at 360 nm over 320 nm, corresponding to an excitation wavelength of 260 nm (Brooks et al., 1983; Liu et al., 2016). In order to eliminate the influence of the uneven oil contents of core samples, multiple

TABLE 1 | Characteristics of core samples from the Lucaogou Formation, Jimsar Sag.

Sample number	Depth (m)	Formation	Lithology	Before extraction				After extraction				Mineral composition (%)					
				TOC (%)	Tmax (°C)	S_1 (mg/g)	S_2 (mg/g)	TOC (%)	Tmax (°C)	S_1 (mg/g)	S_2 (mg/g)	Quartz	K-feldspar	Plagioclase	Calcite	Dolomite	Clay
1	3113.34	P_2l_2	SS	1.89	436.00	8.21	8.17	0.61	437.00	0.11	2.87	27.60	0.00	23.90	48.50	0.00	0.00
2	3114.07	P_2l_2	SSh*	3.39	439.00	4.04	28.40	2.69	438.00	0.26	7.96	40.20	0.00	42.10	0.00	3.10	14.60
3	3115.47	P_2l_2	CR	1.45	431.00	6.24	6.53	0.53	448.00	0.02	0.21	12.90	1.00	12.60	0.00	70.10	3.40
4	3119.00	P_2l_2	SSh	10.09	436.00	3.57	13.75	2.15	437.00	1.11	15.18	49.70	0.00	38.10	0.00	2.40	9.80
5	3119.20	P_2l_2	SS	0.81	440.00	3.92	4.27	0.31	439.00	0.08	1.52	29.00	26.50	26.60	0.00	11.60	6.30
6	3143.30	P_2l_2	SS	1.49	439.00	6.14	5.72	0.07	438.00	0.04	1.61	34.30	12.30	32.00	0.00	11.30	10.10
7	3145.19	P_2l_2	CR	1.87	439.00	7.09	7.94	0.61	440.00	0.04	2.19	18.80	0.00	14.60	0.00	63.00	3.60
8	3146.10	P_2l_2	SSh*	2.06	438.00	2.68	13.50	1.95	437.00	0.09	9.38	27.50	13.40	23.20	6.60	15.10	14.20
9	3199.99	P_2l_2	SS	1.15	433.00	5.63	5.28	0.20	435.00	0.12	1.16	30.30	8.50	40.70	9.70	10.80	0.00
10	3242.85	P_2l_1	CR	0.90	432.00	5.79	6.86	0.67	434.00	0.23	1.60	17.80	0.00	12.30	0.00	69.90	0.00
11	3263.36	P_2l_1	CS	3.34	430.00	28.42	22.98	0.75	435.00	0.12	1.93	27.80	0.00	26.90	0.00	45.30	0.00
12	3272.60	P_2l_1	SS	1.57	428.00	14.78	13.79	0.23	435.00	0.10	1.04	33.20	9.70	38.00	0.00	9.60	9.50
13	3274.30	P_2l_1	SS	4.61	436.00	22.46	17.23	0.65	437	0.19	0.88	17.60	4.10	42.00	8.30	28.00	0.00
14	3275.25	P_2l_1	CS	2.06	435.00	30.74	27.71	0.27	437.00	0.08	1.11	24.40	0.00	50.30	0.00	25.30	0.00
15	3275.68	P_2l_1	CSh	10.03	439.00	1.71	78.67	9.50	437.00	0.42	54.08	12.40	0.90	12.30	41.10	27.20	6.10
16	3282.99	P_2l_1	SS	2.90	433.00	28.55	32.04	0.12	436.00	0.08	1.14	26.40	18.00	31.20	0.00	16.00	8.40
17	3286.00	P_2l_1	CS	3.62	431.00	31.51	22.01	0.34	435.00	0.09	1.69	17.20	0.00	18.10	0.00	64.70	0.00
18	3302.13	P_2l_1	CS	2.13	435.00	19.05	17.28	0.12	437.00	0.11	0.88	27.00	0.00	38.40	0.00	34.60	0.00
19	3303.31	P_2l_1	SS	1.52	443.00	11.10	22.58	0.90	438.00	0.38	6.15	20.80	10.40	28.40	6.50	18.50	15.40
20	3304.80	P_2l_1	CR	1.81	433.00	11.37	11.23	0.37	442.00	0.29	1.17	20.60	0.00	15.30	0.00	64.10	0.00
21	3304.86	P_2l_1	CSh	5.65	440.00	10.55	31.40	3.64	440.00	0.18	11.61	17.40	0.00	11.10	35.40	19.50	16.60
22	3313.28	P_2l_1	CSh	9.56	441.00	2.86	112.83	7.44	440.00	0.74	50.99	25.90	2.00	13.30	6.80	30.10	21.90

*SS, siliceous sandstone; SSh, siliceous shale; CR, carbonate rock; CS, carbonate sandstone; CSh, carbonate shale; *, shale with obvious vertical fractures.*

TABLE 2 | Characteristics of crude oil samples from the Lucaogou Formation, Jimsar Sag.

Sample number	Well name	Depth (m)	Formation	Density (g/cm^3)	Viscosity (50°C Mpa·s)	Wax content (%)	Freezing point (°C)
23	J172	2920-2970	P_2l_2	0.88	59.90	14.39	32.00
24	J25	3403-3425	P_2l_2	0.89	55.20	10.91	26.00
25	J171	3074-3090	P_2l_2	0.89	55.20	8.31	15.00
26	J31	2742-2746	P_2l_2	0.89	47.60	8.20	20.00
27	J28	3198-3255	P_2l_2	0.89	52.61	8.39	15.00
28	J173	3088-3109	P_2l_2	0.88	49.91	14.40	28.00
29	J32	3755-4988	P_2l_2	0.89	53.03	8.73	22.00
30	J174	3255-3314	P_2l_1	0.92	196.20	4.77	4.00
31	J251	4361-4976	P_2l_1	0.89	56.10	3.50	10.00
32	J36	4209-4255	P_2l_1	0.90	67.00	2.20	8.00
33	J30	4018-4184	P_2l_1	0.89	44.36	6.81	14.00

TSF experiments were carried out at different oil-content locations on the same core sample. The average values of the multiple experimental results were used as the TSF parameters values of the sample in order to compare with geochemical parameters.

RESULTS

Lithology and Hydrocarbon Generation Potential Characteristics

The core observations, thin section analysis, and XRD analysis reveal that the lithology of the collected core samples can mainly be classified into two categories and five subcategories. The shale includes carbonate shale (CSh) and siliceous shale (SSh). The tight reservoirs include carbonate rock (CR), carbonate sandstone (CS), and siliceous sandstone (SS). Apparent vertical fractures are developed in samples No. 2 and No. 8. In this study, the shale with obvious vertical fractrures is named fractured shale, on the contrary, the shale without obvious vertical fractures is named blocky shale. **Table 1** shows the XRD, rock pyrolysis, and TOC analysis results of the core samples. The XRD results reveal that the shale and tight reservoirs contain similar minerals (**Figure 2**). In comparison, the shale has a relatively high clay content, and the tight reservoirs have a relatively high dolomite content. The clay contents of the shale range from 6.10% to 21.90% (average 13.87%), and the dolomite contents of the tight reservoirs range from 0% to 70.10% (average 33.93%).

Table 1 shows the TOC and pyrolysis data for the core samples before and after extraction. The experimental results indicate that the shale samples are superior to tight-reservoir samples in terms of organic-matter content and potential for hydrocarbon generation. For shale samples, TOC is in the range of 2.06%–10.09% (average 6.80%) for original samples and 1.95%–9.50% (average 4.56%) for after-extracted samples. S_1 is in the range of 1.71–10.55 mg/g (average 4.24), and S_2 13.50–112.83 mg/g (average 46.43) for original shale samples. S_1 is in the range of 0.09–1.11 mg/g (average 0.47), and S_2 7.96–54.08 mg/g (average 24.87) for after-extracted shale samples. For tight reservoir samples, TOC is in the range of 0.81%–4.61% (average 2.10%) for original samples and 0.07%–1.22% (average 0.44%) for after-extracted samples. S_1 is in the range of 3.92–31.51 mg/g (average 14.74), and S_2 4.27–32.04 mg/g (average 14.08) for original tight reservoir samples. S_1 is in the range of 0.02–0.41 mg/g (average 0.13), and S_2 0.21–6.53 mg/g (average 1.72) for after-extracted tight reservoir samples.

Bulk Properties of the Hydrocarbons

The group components of the core extracts and crude oil samples are presented in **Table 3**. The group components of the upper and lower sections of the Lucaogou Formation are vastly different (**Figure 3**). The upper section of the Lucaogou Formation has relatively high saturated hydrocarbon contents of 51.32% to 69% (average 58.92%); relatively low aromatic hydrocarbon contents of 12.30% to 18.61% (average 15.36%); and relatively low non-hydrocarbon contents of 14.62% to 30.22% (average 23.39%). The lower section of the Lucaogou Formation has relatively low saturated hydrocarbon contents of 38.42% to 59.80% (average 48.31%); relatively high aromatic hydrocarbon contents of 13.99% to 20.26% (average 16.17%); and relatively high non-hydrocarbon contents of 15.81% to 43.78% (average 31.39%).

The experimental results of the physical property parameters of the crude oil are presented in **Table 2**. The physical quality of the crude oil in the upper section of the Lucaogou Formation is considerably better than that in the lower section. The density of the crude oil in the lower section of the Lucaogou Formation is relatively low, with an average value of 0.89 g/cm^3; the viscosity is relatively low, with an average value of 53.35 Mpa·s (50°C); the wax content is relatively high, with an average value of 10.48%; and the freezing point is relatively high, with an average of 22.57°C. The crude oil in the lower section of the Lucaogou Formation has a relatively high density, with an average value of 0.90 g/cm^3; a relatively high viscosity, with an average value of 90.92 Mpa·s (50°C); a relatively low wax content, with an average value of 4.32%; and a relatively low freezing point, with an average value of 9.00°C.

Biomarker Characteristics

Biomarkers can be used to study the depositional environment, source, and thermal maturity of organic matter. The key

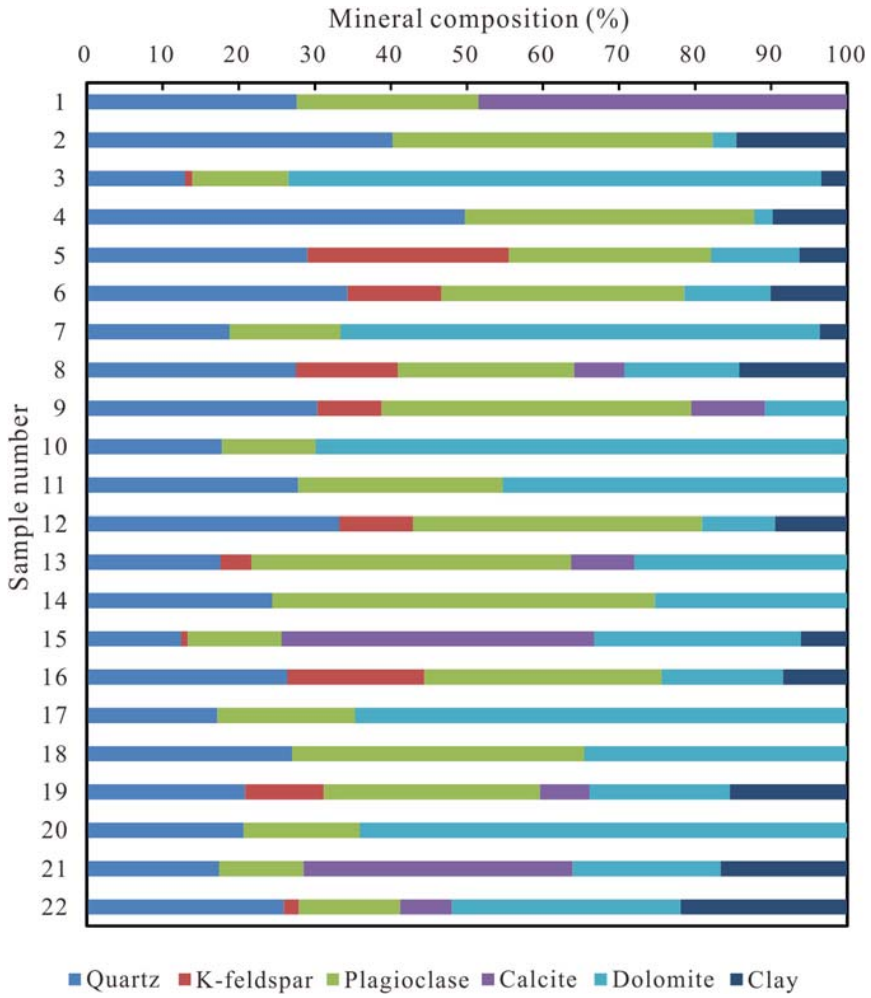

FIGURE 2 | Mineral composition of core samples in the Lucaogou Formation, Jimsar Sag.

biomarker parameters of the core and crude oil samples obtained from the GC and GC-MS analysis are presented in **Table 3**.

The Pr/Ph, Pr/nC_{17}, and Pr/nC_{18} ratios are excellent indicators of depositional environment. The Pr/Ph ratio of less than 1 indicates a suboxic or anoxic depositional environment, and a ratio of greater than 1 indicates an oxidizing depositional environment (Didyk et al., 1978). The Pr/Ph ratios of the upper section of the Lucaogou Formation range from 1.04% to 1.52% (average 1.24%), indicating a suboxic or anoxic depositional environment. The Pr/Ph ratios of the lower section of the Lucaogou Formation range from 0.74% to 1.24% (average 1.00%), indicating a mildly oxic or suboxic depositional environment. **Figure 4** presents a plot of Pr/nC_{17} versus Pr/nC_{18}, which also indicates that the upper section of the Lucaogou Formation was deposited in a more oxidative environment than the lower section. This finding is consistent with the results of previous studies (Ding et al., 2019; Su et al., 2019).

The compositions of regular steranes are usually used as indicators of organic matter origin (Seifert and Moldowan, 1978; Huang and Meinschein, 1979). **Figure 5** presents a ternary plot of the regular steranes compositions of the core and oil samples from the Lucaogou Formation. The relative abundances of the C_{27}, C_{28}, and C_{29} steranes are 10.02-23.79%, 31.86-43.85%, and 41.24-53.60%, respectively (**Table 3**), indicating that the organic matter was mainly derived from bacteria and advanced plants (**Figure 5**). There is a slight difference in the sources of the organic matter in the samples from the upper and lower sections of the Lucaogou Formation. In comparison, more organic matter from advanced plants was input in the lower section of the Lucaogou Formation. This finding is consistent with the results of previous studies reported by Ding et al. (2019) and Su et al. (2019).

The C_{29}ααα20S/(20S + 20R) and C_{29}ββ/(αα + ββ) ratios have always been considered to be effective indicators of thermal maturity (Mackenzie et al., 1980; Seifert and Moldowan, 1980, 1986; Peters and Moldowan, 1993). Larger C_{29}ααα20S/(20S + 20R) and C_{29}ββ/(αα + ββ) ratios indicate a higher thermal maturity. **Figure 6** shows the Lucaogou Formation hydrocarbons are in the mature stage. The thermal maturity of the shale hydrocarbons in the upper section of

TABLE 3 | Group component and biomaker parameters in the Lucaogou Formation core extracts and oils, Jimsar Sag.

Sample number	Formation	Rock type	Group component (%)				Pr/nC_{17}	Ph/nC_{18}	Pr/Ph	C_{29} ααα20S/(S + R)	C_{29} ββ/(αα + ββ)	Ts/(Ts + Tm)	Sterane abundance (%)		
			Sat. HC (%)	Aro. HC (%)	NSO (%)	Asph. (%)							C_{27}	C_{28}	C_{29}
1	P_2l_2	T	58.84	16.72	22.51	1.93	0.93	0.84	1.15	0.49	0.37	0.10	13.53	42.08	44.38
2	P_2l_2	FS	56.73	13.46	24.36	5.45	0.99	1.04	1.09	0.41	0.24	0.10	23.79	31.86	44.35
3	P_2l_2	T	54.17	17.34	27.55	0.95	1.41	1.03	1.52	0.44	0.33	0.08	17.17	35.41	47.43
4	P_2l_2	BS	61.06	14.95	23.05	0.94	2.02	1.62	1.24	0.41	0.26	0.09	20.99	33.88	45.13
5	P_2l_2	T	51.32	15.56	27.48	5.63	1.26	1.36	1.15	0.49	0.31	0.09	12.83	41.77	45.39
6	P_2l_2	T	54.35	14.42	29.72	1.50	1.23	1.33	1.04	0.48	0.31	0.06	11.76	42.29	45.95
7	P_2l_2	T	54.81	12.30	30.21	2.68	1.16	1.23	1.08	0.47	0.31	0.09	12.20	42.52	45.28
8	P_2l_2	FS	53.38	15.43	30.22	0.97	0.51	0.42	1.20	0.40	0.26	0.08	19.48	36.34	44.19
9	P_2l_2	T	56.18	18.26	25.00	0.56	1.30	1.24	1.24	0.45	0.32	0.06	15.98	34.86	49.16
10	P_2l_1	T	41.85	15.17	36.80	6.18	1.77	2.39	1.05	0.40	0.21	0.05	16.68	36.00	47.32
11	P_2l_1	T	49.54	15.20	30.69	4.56	1.70	2.37	1.00	0.46	0.29	0.05	10.20	41.52	48.28
12	P_2l_1	T	52.11	15.96	28.01	3.92	2.24	3.49	0.86	0.44	0.28	0.05	14.50	33.52	51.98
13	P_2l_1	T	51.20	14.76	27.41	6.63	1.59	2.24	1.00	0.47	0.30	0.05	10.02	41.50	48.48
14	P_2l_1	T	40.35	16.14	41.21	2.31	1.13	1.58	0.97	0.45	0.27	0.05	11.14	41.54	47.32
15	P_2l_1	BS	48.11	15.07	31.88	4.93	1.04	1.46	0.98	0.46	0.28	0.06	11.12	42.39	46.49
16	P_2l_1	T	50.00	16.34	30.00	3.67	1.89	3.20	0.91	0.43	0.25	0.04	13.73	32.67	53.60
17	P_2l_1	T	52.20	15.09	31.76	0.94	1.99	3.37	0.74	0.43	0.25	0.04	17.09	31.97	50.94
18	P_2l_1	T	44.41	17.39	32.92	5.27	1.87	2.64	0.93	0.43	0.27	0.10	11.76	43.85	44.39
19	P_2l_1	T	45.08	14.08	38.87	1.97	1.61	2.27	1.02	0.43	0.28	0.14	14.97	40.77	44.26
20	P_2l_1	T	46.43	13.99	38.39	1.19	2.25	3.05	1.00	0.40	0.26	0.07	11.51	40.88	47.61
21	P_2l_1	BS	38.42	15.82	43.78	1.98	2.25	3.05	1.00	0.42	0.27	0.11	13.45	42.56	43.99
22	P_2l_1	BS	43.99	20.26	34.49	1.27	1.02	1.48	0.94	0.41	0.22	0.10	14.54	34.98	50.47
23	P_2l_2	/	64.78	14.28	18.28	2.66	0.96	0.82	1.20	0.45	0.30	0.12	13.96	42.12	43.91
24	P_2l_2	/	59.36	15.20	22.80	2.64	0.80	0.64	1.27	0.48	0.32	0.16	13.93	41.00	45.07
25	P_2l_2	/	62.50	18.61	15.83	3.05	1.06	0.94	1.23	0.48	0.34	0.12	12.29	42.16	45.55
26	P_2l_2	/	65.21	15.33	18.25	1.21	1.14	0.80	1.44	0.42	0.28	0.12	17.24	40.43	42.33
27	P_2l_2	/	69.00	14.04	14.62	2.34	1.45	1.17	1.34	0.45	0.28	0.15	15.02	41.10	43.87
28	P_2l_2	/	58.68	14.67	25.15	1.50	1.17	0.95	1.30	0.42	0.28	0.18	18.49	40.28	41.24
29	P_2l_2	/	62.42	15.22	19.25	3.10	0.97	0.81	1.30	0.49	0.35	0.13	16.16	39.12	44.72
30	P_2l_1	/	46.56	18.36	29.84	5.24	1.71	2.32	1.08	0.41	0.26	0.05	14.71	33.54	51.75
31	P_2l_1	/	58.79	16.55	19.93	4.73	1.19	1.26	1.15	0.50	0.34	0.10	12.63	40.82	46.55
32	P_2l_1	/	52.47	16.50	21.78	9.24	1.31	1.56	1.05	0.51	0.35	0.09	12.89	41.08	46.03
33	P_2l_1	/	59.80	18.21	15.81	6.18	0.80	0.76	1.16	0.52	0.42	0.15	12.65	40.20	47.15

T, tight reservoirs; BS, blocky shale; FS, fractured shale.

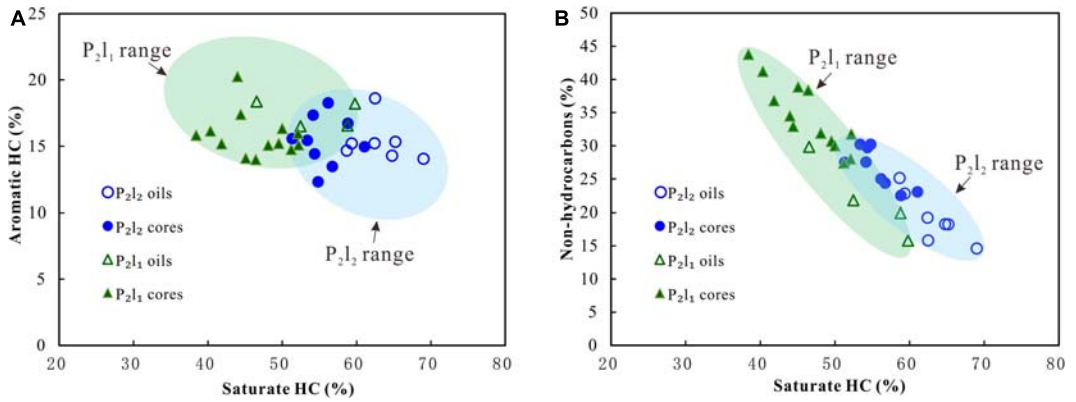

FIGURE 3 | Group component plots for the Lucaogou Formation core extracts and oils, Jimsar Sag. **(A)** Aromatic HC *vs.* Saturate HC; **(B)** Non-hydrocarbons *vs.* Saturate HC.

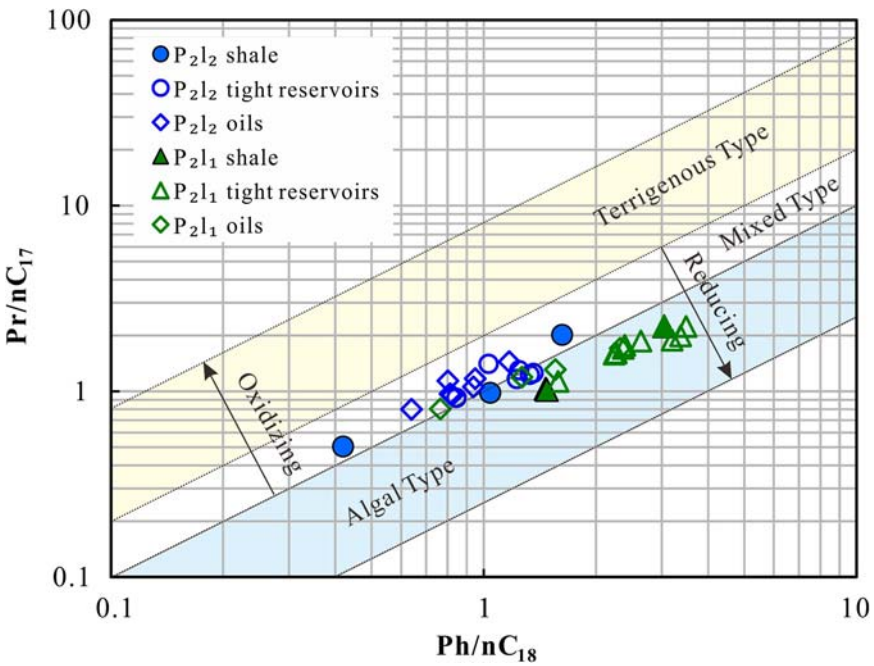

FIGURE 4 | Pr/nC_{17} *vs.* Ph/nC_{18} plot for the core extracts and oils in the Lucaogou Formation, Jimsar Sag (Modified after Peters et al., 1999).

the Lucaogou Formation is slightly lower than that the shale hydrocarbons in the lower section. The average values of the $C_{29}\alpha\alpha\alpha20S/(20S + 20R)$ and $C_{29}\beta\beta/(\alpha\alpha + \beta\beta)$ ratios of the shale in the upper section of the Lucaogou Formation are 0.41 and 0.25, respectively. The average values of the $C_{29}\alpha\alpha\alpha20S/(20S + 20R)$ and $C_{29}\beta\beta/(\alpha\alpha + \beta\beta)$ ratios of the shale in the lower section of the Lucaogou Formation are 0.43 and 0.26, respectively. The thermal maturity of the hydrocarbons in the tight reservoirs in the lower section of the Lucaogou Formation is similar to that of the adjacent shale hydrocarbons. The average values of the $C_{29}\alpha\alpha\alpha20S/(20S + 20R)$ and $C_{29}\beta\beta/(\alpha\alpha + \beta\beta)$ ratios of the tight reservoirs in the lower section of the Lucaogou Formation are the same as those of the shale, i.e., 0.43 and 0.26, respectively. The above results show that the oil in the tight reservoirs in the lower section of the Lucaogou Formation mainly came from the adjacent shale, and the oil did not migrate over a long distance. In comparison, the thermal maturity of the hydrocarbons in the tight reservoirs in the upper section of the Lucaogou Formation is significantly higher than that of the nearby shale hydrocarbons. The average values of the $C_{29}\alpha\alpha\alpha20S/(20S + 20R)$ and $C_{29}\beta\beta/(\alpha\alpha + \beta\beta)$ ratios of the upper-section shale in the Lucaogou Formation are 0.47 and 0.32, respectively. It is inferred that the oil in the tight reservoirs in the upper section of the Lucaogou Formation may be partially derived from the relatively high maturity shale in the deep part of the sag. Compared with that of the lower section of the Lucaogou Formation, the oil

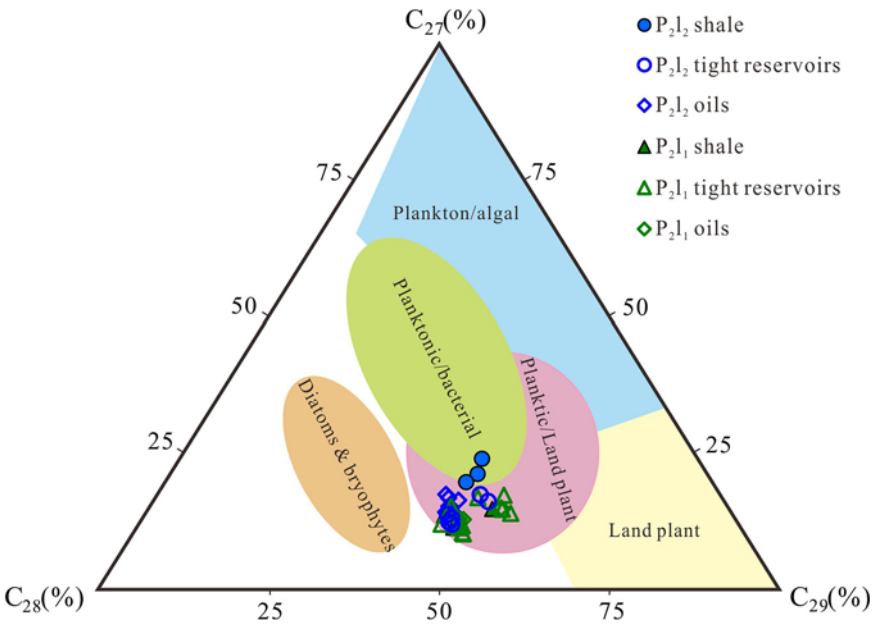

FIGURE 5 | Ternary plot of C_{27}-C_{28}-C_{29} steranes for the core extracts and oils in the Lucaogou Formation, Jimsar Sag (Modified after Huang and Meinschein, 1979).

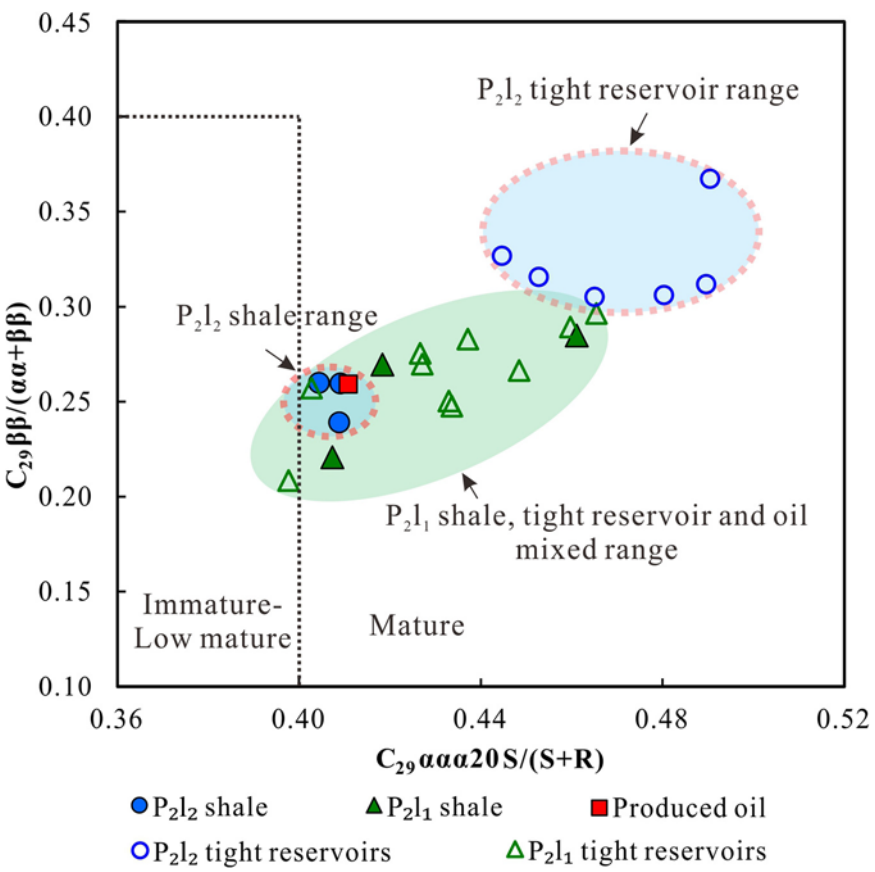

FIGURE 6 | C_{29}ααα20S/(20S + 20R) *vs.* C_{29}ββ/(αα + ββ) plot for the Lucaogou Formation core extracts and oils in Well J174, Jimsar Sag.

TABLE 4 | TSF parameters of cores and oils in the Lucaogou Formation, Jimsar Sag.

Sample number	Formation	Rock type	Analysis ID	TSF Max (p.c)	E_x (nm)	E_m (nm)	R_1	R_2
1	P_2l_2	T	#1	396.79	253.96	368.96	4.41	5.70
2	P_2l_2	FS	#2	503.55	260.00	370.00	5.52	7.04
3	P_2l_2	T	#3-1	1002.46	262.03	377.03	4.02	5.82
			#3-2	913.88	262.03	382.03	4.62	6.62
			Average	958.17	262.03	379.53	4.32	6.22
4	P_2l_2	BS	#4-1	337.22	262.03	372.03	7.03	9.22
			#4-2	293.66	262.03	377.03	6.35	8.90
			Average	315.44	262.03	374.53	6.69	9.06
5	P_2l_2	T	#5-1	239.44	256.03	371.03	6.18	7.46
			#5-2	394.85	256.03	371.03	5.76	7.20
			Average	317.15	256.03	371.03	5.97	7.33
6	P_2l_2	T	#6-1	910.43	262.03	367.03	5.55	7.15
			#6-2	551.69	253.96	373.96	5.60	7.17
			#6-3	351.65	253.96	368.96	5.70	7.26
			Average	604.59	256.65	369.98	5.62	7.20
7	P_2l_2	T	#7-1	327.89	253.96	378.96	5.52	6.82
			#7-2	403.95	260.00	370.00	5.48	6.88
			#7-3	317.96	253.96	368.96	5.88	7.46
			#7-4	318.89	260.00	375.00	5.85	7.50
			#7-5	579.64	253.96	373.96	5.92	7.95
			Average	389.67	256.38	373.38	5.73	7.32
8	P_2l_2	FS	#8	660.33	265.93	375.93	5.74	7.49
9	P_2l_2	T	#9-1	209.59	260.00	370.00	4.38	6.36
			#9-2	310.28	262.03	372.03	4.53	5.99
			#9-3	2456.79	262.03	372.03	4.77	6.39
			Average	992.22	261.35	371.35	4.56	6.25
10	P_2l_1	T	#10	313.07	262.03	367.03	5.53	7.00
11	P_2l_1	T	#11-1	257.45	262.03	372.03	5.35	6.92
			#11-2	315.31	260.00	375.00	5.55	7.13
			#11-3	298.56	262.03	372.03	5.39	6.97
			Average	290.44	261.35	373.02	5.43	7.00
12	P_2l_1	T	#12-1	553.76	260.00	375.00	5.66	7.54
			#12-3	1663.40	264.06	374.06	5.56	7.24
			#12-4	947.91	262.03	372.03	5.64	7.56
			Average	1055.02	262.03	373.70	5.62	7.45
13	P_2l_1	T	#13-1	243.76	262.03	372.03	5.62	6.88
			#13-2	223.19	262.03	372.03	5.27	7.01
			Average	233.47	262.03	372.03	5.45	6.95
14	P_2l_1	T	#14-1	811.08	260.00	370.00	5.42	6.94
			#14-2	323.45	260.00	370.00	5.55	7.16
			Average	567.26	260.00	370.00	5.49	7.05
15	P_2l_1	BS	#15-1	110.22	262.03	372.03	7.46	10.61
			#15-2	148.12	260.00	375.00	7.56	10.64
			Average	129.17	261.01	373.51	7.51	10.63
16	P_2l_1	T	#16-1	394.96	262.03	372.03	5.31	6.87
			#16-2	230.93	262.03	372.03	5.60	7.32
			#16-3	729.21	253.96	373.96	5.27	7.21
			Average	451.70	259.34	372.67	5.39	7.13
17	P_2l_1	T	#17-1	1999.86	262.03	372.03	5.05	6.58
			#17-2	250.71	262.03	372.03	5.34	7.05
			#17-3	256.57	260.00	370.00	5.30	7.11
			#17-4	160.24	262.03	372.03	5.54	6.66
			Average	666.85	261.52	371.52	5.31	6.85

(Continued)

TABLE 4 | Continued

Sample number	Formation	Rock type	Analysis ID	TSF Max (p.c)	E_x (nm)	E_m (nm)	R_1	R_2
18	P_2l_1	T	#18-1	316.81	260.00	375.00	5.39	6.94
			#18-2	575.87	262.03	372.03	5.70	6.71
			#18-3	275.11	247.96	362.96	5.23	6.74
			Average	389.27	256.66	370.00	5.44	6.80
19	P_2l_1	T	#19-1	46.40	260.00	370.00	5.35	7.58
			#19-2	20.47	253.96	363.96	5.52	6.83
			#19-3	101.82	260.00	370.00	5.93	7.34
			Average	56.23	257.99	367.99	5.60	7.25
20	P_2l_1	T	#20	24.37	253.96	368.96	4.97	6.47
21	P_2l_1	BS	#21	151.14	262.03	372.03	7.23	9.22
22	P_2l_1	BS	#22	741.39	275.93	400.93	7.71	8.40
23	P_2l_2	/	#23	59.18	260.00	375.00	4.15	5.85
24	P_2l_2	/	#24	207.16	262.03	377.03	3.99	4.96
25	P_2l_2	/	#25	329.43	262.03	377.03	4.67	6.17
26	P_2l_2	/	#26	188.61	262.03	377.03	4.30	5.46
27	P_2l_2	/	#27	248.12	262.03	372.03	3.85	5.17
28	P_2l_2	/	#28	214.10	262.00	367.00	4.10	5.30
29	P_2l_2	/	#29	162.81	260.00	375.00	4.52	5.91
30	P_2l_1	/	#30	392.11	262.03	372.03	5.16	6.60
31	P_2l_1	/	#31	91.43	262.03	372.03	4.58	6.25
32	P_2l_1	/	#32	545.23	260.00	375.00	4.89	6.52
33	P_2l_1	/	#33	595.74	262.03	377.03	4.86	6.38

T, tight reservoirs; BS, blocky shale; FS, fractured shale.

in the tight reservoirs in the upper section underwent a longer distance migration.

TSF Characteristics

The key fluorescence parameters obtained from the TSF analysis of the core and oil samples are presented in **Table 4**. **Figure 7** depicts the TSF parameters and spectrograms of the shale, tight reservoir, and oil samples from the upper and lower sections of the Lucaogou Formation. The shale, tight reservoir, and oil samples from the Lucaogou Formation have very similar TSF spectrogram characteristics. The TSF spectrograms of the shale, tight reservoir, and oil samples from the Lucaogou Formation all exhibit a single peak, which is very similar to the TSF spectrograms of the shale and oil samples from the Qingshankou Fromation in Songliao Basin (Liu B. et al., 2019).

The shale, tight reservoir, and oil samples have different value ranges of TSF parameters (**Figure 7** and **Table 4**). For the shale in the upper section of the Lucaogou Formation, the TSF Max values range from 293.66 to 660.33 p.c (average 448.69 p.c), the E_x values range from 260.00 to 265.93 nm (average 262.50 nm), the E_m values range from 370.00 to 377.03 nm (average 373.75 nm), the R_1 values range from 5.52 to 7.03 (average 6.16), and the R_2 values range from 7.04 to 9.22 (average 8.16). For the shale in the lower section, the TSF Max values range from 110.22 to 741.39 p.c (average 287.72 p.c), the E_x values range from 260.00 to 275.93 nm (average 265.00 nm), the E_m values range from 372.03 to 400.93 nm (average 380.00 nm), the R_1 values range from 7.23 to 7.71 (average 7.49), and the R_2 values range from 8.40 to 10.64 (average 9.72).

For the tight reservoirs in the upper section of the Lucaogou Formation, the TSF Max values range from 209.59 to 2456.79 p.c (average 605.39 p.c), the E_x values range from 253.96 to 262.03 nm (average 257.87 nm), the E_m values range from 367.03 to 382.03 nm (average 372.56 nm), the R_1 values range from 4.02 to 6.18 (average 5.26), and the R_2 values range from 5.70 to 7.95 (average 6.86). For the tight reservoirs in the lower section, the TSF Max values range from 20.47 to 1999.86 pc (average 453.37 pc), the E_x values range from 247.96 to 264.06 nm (average 259.93 nm), the E_m values range from 362.96 to 375.00 nm (average 371.13 nm), the R_1 values range from 4.97 to 5.93 (average 5.44), and the R_2 values range from 6.47 to 7.58 (average 7.03).

For the crude oils in the upper section of the Lucaogou Formation, the TSF Max values range from 59.18 to 329.43 p.c (average 201.35 p.c), the E_x values range from 260.00 to 262.03 nm (average 261.45 nm), the E_m values range from 367.00 to 377.03 nm (average 374.30 nm), the R_1 values range from 3.85 to 4.67 (average 4.23), and the R_2 values range from 4.96 to 6.17 (average 5.55). For the crude oil in the lower section, the TSF Max values range from 91.43 to 595.74 p.c (average 406.13 pc), the E_x values range from 260.00 to 262.03 nm (average 261.52 nm), the E_m values range from 372.03 to 377.03 nm (average 374.02 nm), the R_1 values range from 4.58 to 5.16 (average 4.87), and the R_2 values range from 6.25 to 6.60 (average 6.44).

Formation	Rock type	TSF parameters	TSF crossplot	TSF contour map
P_2l_2	Shale	TSF Max=294-660 p.c E_x=260-266 nm E_m=370-377 nm R_1=5.52-7.03 R_2=7.04-9.22	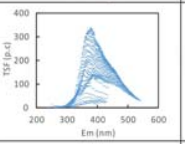	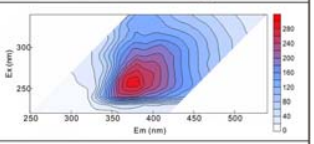
	Tight reservoir	TSF Max=210-2457 p.c E_x=254-262 nm E_m=367-382 nm R_1=4.02- 6.18 R_2=5.70-7.95	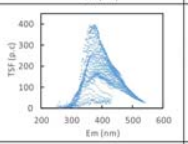	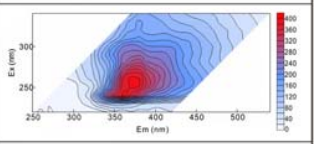
	Oil	TSF Max=59-329 p.c E_x=260-262 nm E_m=367-377 nm R_1=3.85-4.67 R_2=4.96-6.17	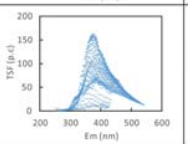	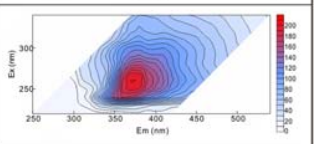
P_2l_1	Shale	TSF Max=110-741 p.c E_x=260-276 nm E_m=372-401 nm R_1=7.23-7.71 R_2=8.40-10.64	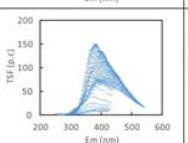	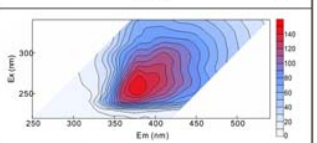
	Tight reservoir	TSF Max=20-2000 p.c E_x=248-264 nm E_m=363-375 nm R_1=4.97-5.93 R_2=6.47-7.58	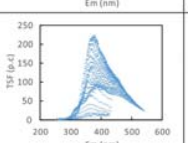	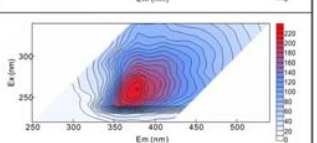
	Oil	TSF Max=91-596 p.c E_x=260-262 nm E_m=372-377 nm R_1=4.58-5.16 R_2=6.25-6.60	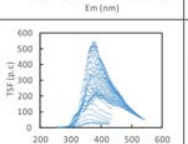	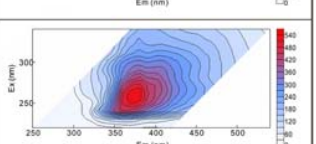

FIGURE 7 | TSF characteristics of shale, tight reservoirs, oils in the Lucaogou Formation, Jimsar Sag.

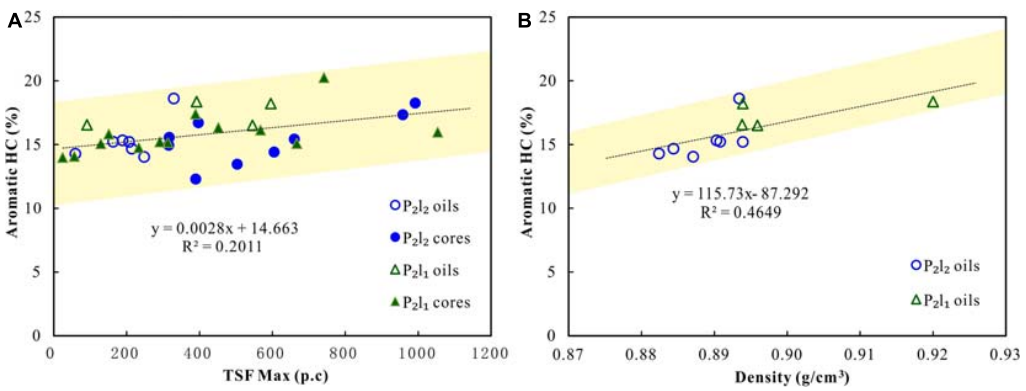

FIGURE 8 | Plots of Aromatic HC *vs.* TSF Max **(A)** and Aromatic HC *vs.* Density **(B)** in the Lucaogou Formation, Jimsar Sag.

DISCUSSION

TSF Parameters vs. Bulk Properties of the Hydrocarbons

The TSF Max of the core and oil samples are positively correlated with the aromatic hydrocarbon content (**Figure 8A**) but are not significantly correlated with the saturated hydrocarbon, non-hydrocarbon, and asphaltene contents. The above results demonstrate that the fluorescent substances of the shale oil in the Lucaogou Formation are mainly aromatic compounds. There is also a positive correlation between the TSF Max and the aromatic hydrocarbon content of the conventional oil from the North Sea and the Bohai Bay Basin in China (Barwise and Hay, 1996; Li et al., 2007). Therefore, in a sense, all of the factors related to

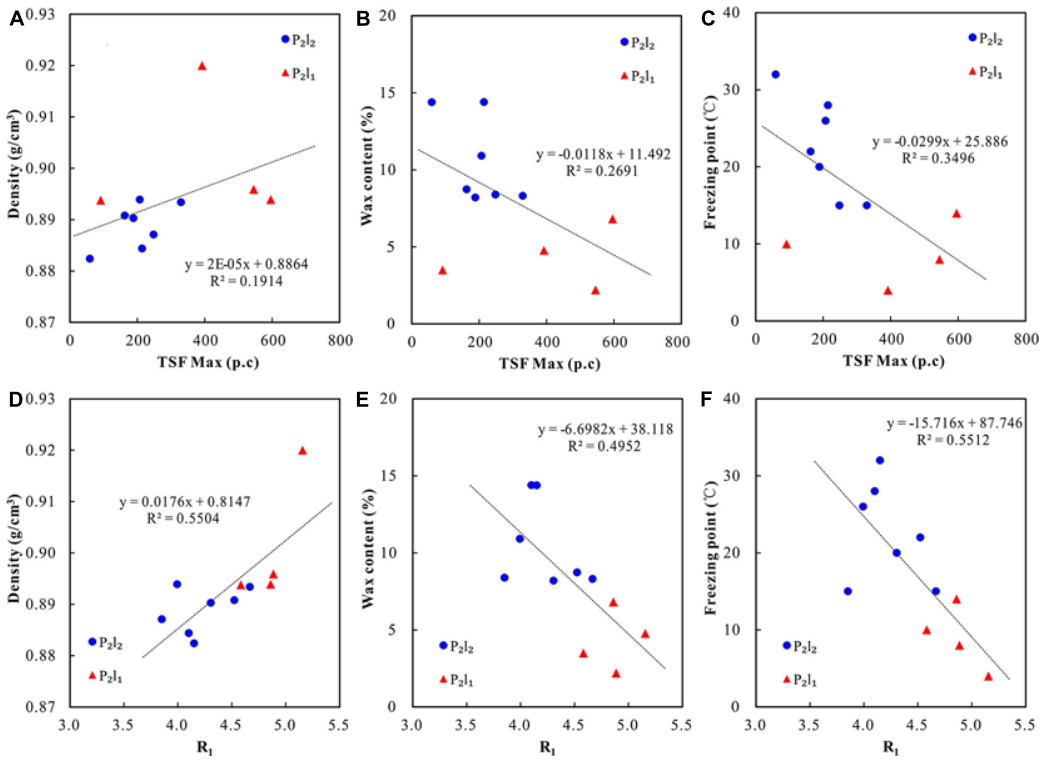

FIGURE 9 | Plots of physical properties *vs.* TSF parameters for oils in the Lucaogou Formation, Jimsar Sag. **(A)** Density *vs.* TSF Max; **(B)** Wax content *vs.* TSF Max; **(C)** Freezing point *vs.* TSF Max; **(D)** Density *vs.* R_1; **(E)** Wax content *vs.* R_1; **(F)** Freezing point *vs.* R_1.

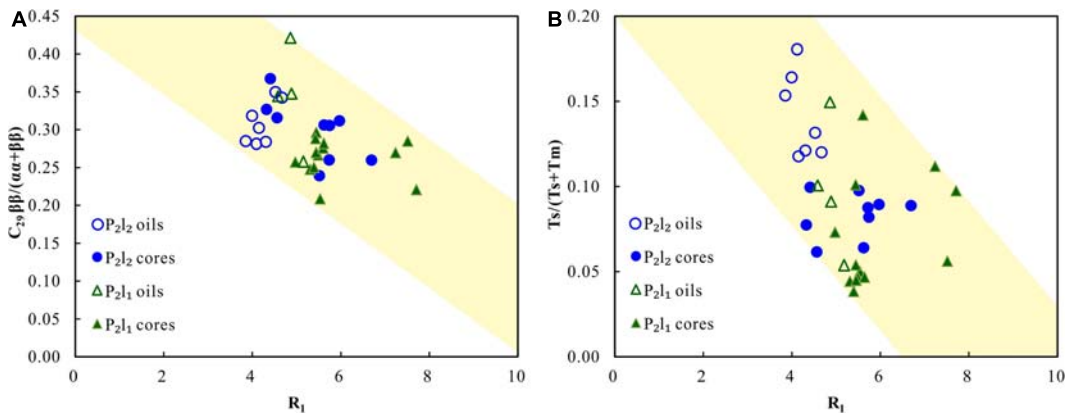

FIGURE 10 | Plots of C_{29} ββ/(αα + ββ) *vs.* R_1 **(A)** and Ts/(Ts + Tm) *vs.* R_1 **(B)** for cores and oils in the Lucaogou Formation, Jimsar Sag.

the aromatic hydrocarbon content will have a certain impact on the TSF parameters.

The physical properties of the crude oil samples are strongly correlated with the aromatic content (**Figure 8B**). Therefore, the TSF parameters exhibit significant correlations with the physical properties of the oil (**Figure 9**). The TSF Max and R_1 values are positively correlated with the oil density, negatively correlated with the wax content, and negatively correlated with the freezing point. The lower TSF Max and R_1 values indicate a lower oil density, a higher wax content, a higher freezing point, and a better quality of the crude oil. The TSF Max and R_1 values in the upper section of the Lucaogou Formation are lower than those in the lower section (**Figure 9**), indicating that the physical properties of the oil in the upper section of the Lucaogou Formation are better than those of the oil in the lower section. This result is consistent with the actual exploration results (**Table 2**). It can be concluded that the quality of the crude oil affects its TSF characteristics. Therefore, the TSF Max and R_1 values can be used to predict the quality of the oil to a certain extent.

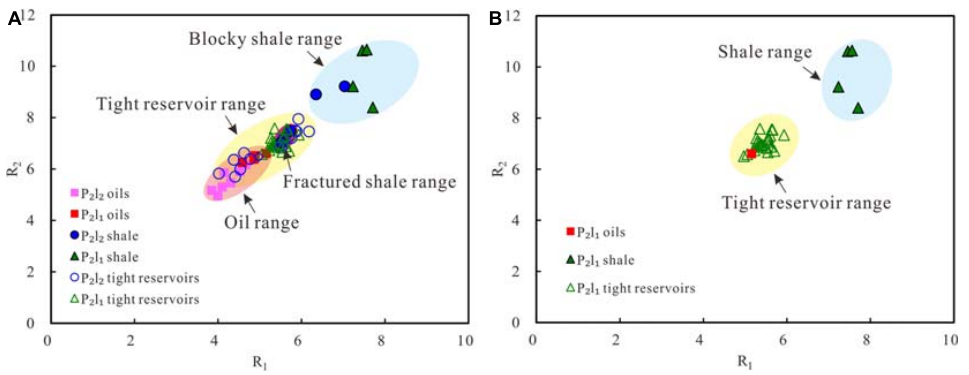

FIGURE 11 | R_2 *vs.* R_1 plot for shale, tight reservoirs and oils in the Lucaogou Formation, Jimsar Sag. **(A)** all the samples; **(B)** the lower section of the Lucaogou Formation samples in the Well J174.

TSF Parameters vs. Thermal Maturity

Previous studies have shown that maturity is an important factor affecting the fluorescent fingerprint characteristics of crude oil (Barwise and Hay, 1996; Li et al., 2006, 2007; Liu et al., 2014; Wu et al., 2016). The TSF parameter R_1 values mainly increase with decreasing thermal maturity, which has been reported for conventional oil from Europe, Australia, and eastern China (Barwise and Hay, 1996; Li et al., 2007; Liu et al., 2014). The emission wavelength of 360 nm mainly represents three-ring aromatics (such as the phenanthrene series), the emission wavelength of 320 nm mainly represents two-ring aromatics (such as the naphthalene series). The R_1 and R_2 values represent the ratio of the heavy fraction to the light fraction in the sample (Li et al., 2007; Liu et al., 2014, 2016). Therefore, in theory, the lower the values of R_1 and R_2, the less the heavy fraction and the greater the light fraction, indicating a higher degree of maturity. In this study, the relationships between the R_1 values and the C_{29} ββ/(αα + ββ) and Ts/(Ts + Tm) ratios were analyzed (**Figure 10**). The results reveal that the R_1 values are negatively correlated with thermal maturity. As the R_1 values increase, the C_{29}ββ/(αα + ββ) and Ts/(Ts + Tm) ratios decrease (**Figure 10** and **Table 3**). Although there are some differences in depositional environment and organic matter origin between the upper and lower sections of the Lucaogou Formation, the variation trends of the R_1 values and the biomarker maturity parameters still exist in the two sections, respectively. As above mentioned, the thermal maturity of the tight reservoirs in the upper section is higher than that of the tight reservoirs in the lower section (**Figure 6**), which may result in better physical properties, lower aromatic hydrocarbon contents, and smaller R_1 values in the upper section than in the lower section of the Lucaogou Formation (**Figures 3**, **9** and **Tables 2**–**4**). It can be concluded that the TSF parameter is a good indicator of the thermal maturity of the shale oil in the Lucaogou Formation in the Jimsar Sag.

TSF Parameters vs. Hydrocarbon Migration and Oil-Producing Layer Type

The lacustrine shale sequence in China are characterized by complex lithology, strong heterogeneity, and frequent interbedding of shale and thin tight reservoir layers (Kuang et al., 2012; Zou et al., 2015; Zhao et al., 2020; Hou et al., 2021a), which makes it difficult to determine whether the shale oil is mainly produced from tight reservoirs or the shale in the same shale sequence package. Previous studies have shown that there is an obviously positive correlation between TSF fluorescence intensity and oil content for shale (Liu B. et al., 2019), indicating that the TSF parameters may be used to predict the oil-producing layer. In this study, it was found that on the condition of similar depositional environment, organic matter origin, and maturity, the TSF parameters may be effective indicators for determining the oil-producing layer is the tight reservoirs or the adjacent shale in the same shale sequence package. For a set of shale strata with similar sedimentary environment, organic matter origin, and maturitiy, the largest difference between the oil in the shale and tight reservoirs may be the difference in the oil migration distance. The oil in shale is generated and accumulated *in situ*, and the oil basically does not migrate. The oil in tight reservoirs originates from adjacent shale and migrates a distance, but the oil migration distance in tight reservoirs is shorter than that in conventional reservoirs. The light fraction of the hydrocarbons migrates more easily than the heavy fraction, so as the migration distance increases, the R_1 and R_2 values decrease. Therefore, it can be inferred that there may be some differences between the TSF parameters of the shale and tight reservoirs.

Comparisons of the TSF parameter characteristics of the blocky shale, fractured shale, tight reservoirs, and produced oil in the upper and lower sections of the Lucaogou Formation were carried out. The results reveal that the TSF parameter characteristics of the oil in the different reservoirs in the Lucaogou Formation are significantly different. The R_1 and R_2 values of the blocky shale, fractured shale, tight reservoirs, and produced oils are decreased successively (**Figure 11A**). The distributions of the R_1 and R_2 values of the tight reservoir and oil samples from the upper section of the Lucaogou Formation are scattered. In contrast, the distributions of the R_1 and R_2 values of the tight reservoir and oil samples from the lower section of the Lucaogou Formation are more concentrated. This shows that the hydrocarbons in the tight reservoirs in the upper section of the Lucaogou Formation have migrated over a long distance, and the fractionation effects are more distinct. In comparison,

the hydrocarbons in the tight reservoirs in the lower section of the Lucaogou Formation migrated only a short distance, so the fractionation effects are not distinct. These findings are consistent with the above mentioned results revealed by the biomarker characteristics. By comparing the R_1 and R_2 values of the core and oil samples, it is preliminarily determined that the shale oil in the upper and lower sections of the Lucaogou Formation is mainly produced from the tight reservoirs in the shale sequence (**Figure 11**). However, since all of the core samples were collected from Well J174, there is a lack of core samples from the wells with higher maturity in the deep part of the Jimsar Sag. Therefore, further studies on the identification of oil-producing layer type of the Lucaogou Formation in other wells are needed.

CONCLUSION

The TSF analysis of the shale, tight reservoirs, and oils in the Lucaogou Formation in the Jimsar Sag were carried out. The relationship between the TSF parameters and geochemical parameters were discussed. The shale, tight reservoir, and oil samples from the Lucaogou Formation have very similar TSF spectrogram characteristics, but different TSF parameter characteristics. The TSF parameters are good indicators of the hydrocarbon composition, physical properties, thermal maturity, migration, and oil-producing layers. The TSF Max and R_1 values are correlated with the aromatic hydrocarbon contents and oil physical parameters. The R_1 values increase with decreasing thermal maturity and migration distance. The hydrocarbons have lower aromatic hydrocarbon contents, better physical properties, higher thermal maturity, and longer migration distance in the upper section than in the lower section of the Lucaogou Formation. It is preliminarily concluded that the shale oil was mainly produced from the tight reservoirs in the shale sequence of the Lucaogou Formation, Jimsar Sag.

DATA AVAILABILITY STATEMENT

The original contributions presented in the study are included in the article/supplementary material, further inquiries can be directed to the corresponding author/s.

AUTHOR CONTRIBUTIONS

All authors contributed to the article and approved the submitted version.

FUNDING

This work was supported by the CNPC International Science and Technology Cooperation Development Project (2012A-4802-02 and 2015D-4810-02).

ACKNOWLEDGMENTS

We acknowledge the Xinjiang Oilfield for sample collection.

REFERENCES

Barwise, T., and Hay, S. (1996). "Predicting oil properties from core fluorescence," in *Hydrocarbon Migration and Its Nearsurface Expression*, eds D. Schumacher and M. A. Abrams (Tulsa: AAPG Memoir.), 363–371.

Brooks, J., Kennicutt, M. II, Barnard, L., Denoux, G., and Carey, B. (1983). "Applications of total scanning fluorescence to exploration geochemistry," in *Proceedings of the Offshore Technology Conference*, London, 393–400.

Cao, Z., Liu, G., Kong, Y., Wang, C., Niu, Z., Zhang, J., et al. (2016). Lacustrine tight oil accumulation characteristics: Permian Lucaogou Formation in Jimusaer Sag, Junggar Basin. *Int. J. Coal Geol.* 153, 37–51. doi: 10.1016/j.coal.2015.11.004

Chen, J., Pang, X., Pang, H., Chen, Z., and Jiang, C. (2018). Hydrocarbon evaporative loss evaluation of lacustrine shale oil based on mass balance method: permian lucaogou formation in jimusaer depression, junggar basin. *Mar. Pet. Geol.* 91, 422–431. doi: 10.1016/j.marpetgeo.2018.01.021

Didyk, B., Simoneit, B., and Brassell, C. (1978). Organic geochemical indicators of palaeoenvironmental conditions of sedimentation. *Nature* 272, 216–222. doi: 10.1038/272216a0

Ding, W., Hou, D., Jiang, L., Jiang, Y., and Wu, P. (2020). High abundance of carotanes in the brackish-saline lacustrine sediments: a possible cyanobacteria source. *Int. J. Coal Geol.* 219:103373. doi: 10.1016/j.coal.2019.103373

Ding, X., Qu, J., Imin, A., Zha, M., Su, Y., Jiang, Z., et al. (2019). Organic matter origin and accumulation in tuffaceous shale of the lower permian lucaogou formation, Jimsar Sag. *J. Pet. Sci. Eng.* 179, 696–706. doi: 10.1016/j.petrol.2019.05.004

Espitalié, J., Marquis, F., and Barsony, I. (1984). "Geochemical logging," in *Analytical Pyrolysis*, ed. K. J. Voorhess (Boston: Butterworths), 53–79.

Fan, J., Liu, S., Liu, K., Ma, X., and Liu, R. (2015). Preliminary study on determining coal maturity using total scanning fluorescence technique. *Sci. Technol. Eng.* 34, 139–143.

Gao, G., Zhang, W., Xiang, B., Liu, G., and Ren, J. (2016). Geochemistry characteristics and hydrocarbon-generating potential of lacustrine source rock in Lucaogou Formation of the Jimusaer Sag, Junggar Basin. *J. Pet. Sci. Eng.* 145, 168–182. doi: 10.1016/j.petrol.2016.03.023

Graham, S., Brassell, S., Carroll, A., Xiao, X., Demaison, G., Mcknight, C., et al. (1990). Characteristics of selected petroleum source rocks, Xinjiang Uygur Autonomous Region, Northwest China. *AAPG Bull.* 74, 493–512.

Hou, L., Luo, X., Han, W., Lin, S., Pang, Z., and Liu, J. (2020a). Geochemical evaluation of the hydrocarbon potential of shale oil and its correlation with different minerals-a case study of the TYP shale in the Songliao Basin, China. *Energy Fuels* 34, 11998–12009. doi: 10.1021/acs.energyfuels.0c01285

Hou, L., Luo, X., Zhao, Z., and Zhang, L. (2021a). Identification of oil produced from shale and tight reservoirs in the Permian Lucaogou Shale Sequence, Jimsar Sag, Junggar Basin, NW China. *ACS Omega* 6, 2127–2142. doi: 10.1021/acsomega.0c05224

Hou, L., Ma, W., Luo, X., Liu, J., Lin, S., and Zhao, Z. (2021b). Hydrocarbon generation-retention-expulsion mechanism and shale oil producibility of the permian lucaogou shale in the Junggar Basin as simulated by semi-open pyrolysis experiments. *Mar. Petrol. Geol.* 125:104880. doi: 10.1016/j.marpetgeo.2020.104880

Hou, L., Ma, W., Luo, X., Tao, S., Guan, P., and Liu, J. (2020b). Chemical structure changes of lacustrine Type-II kerogen under semi-open pyrolysis as investigated by solid-state 13C NMR and FT-IR spectroscopy. *Mar. Pet. Geol.* 116:104348. doi: 10.1016/j.marpetgeo.2020.104348

Hou, L., Ma, W., Luo, X., Tao, S., Guan, P., Liu, J., et al. (2020c). Characteristics and quantitative models for hydrocarbon generation-retention-production of shale

under ICP conditions: example from the Chang 7 member in the Ordos Basin. *Fuel* 279:118497. doi: 10.1016/j.fuel.2020.118497

Hu, T., Pang, X., Jiang, S., Wang, Q., Zheng, X., Ding, X., et al. (2018). Oil content evaluation of lacustrine organic-rich shale with strong heterogeneity: a case study of the Middle Permian Lucaogou Formation in Jimusaer Sag, Junggar Basin, NW China. *Fuel* 222, 196–205. doi: 10.1016/j.fuel.2018.02.082

Huang, W., and Meinschein, G. (1979). Sterols as ecological indicators. *Geochem. Cosmochim. Acta* 43, 739–745. doi: 10.1016/0016-7037(79)90257-6

Kong, D., Cui, Y., Kong, L., Wang, S., and Shi, H. (2019). The application of digital image recognition to the analysis of three-dimensional fluorescence spectra of mixed oil. *Spectrosc. Spectr. Anal.* 39, 3407–3413.

Kuang, L., Tang, Y., Lei, D., Chang, Q., Ouyang, M., Hou, L., et al. (2012). Formation conditions and exploration potential of tight oil in the Permian saline lacustrine dolomitic rock, Junggar Basin, NW China. *Pet. Explor. Dev.* 39, 700–711. doi: 10.1016/s1876-3804(12)60095-0

Li, J., Wang, W., Cao, Q., Shi, Y., Yan, X., and Tian, S. (2015). Impact of hydrocarbon expulsion efficiency of continental shale upon shale oil accumulations in eastern China. *Mar. Pet. Geol.* 59, 467–479. doi: 10.1016/j.marpetgeo.2014.10.002

Li, S., Pang, X., Liu, K., and Jin, Z. (2006). Characteristics and application of total scanning fluorescence for oils and reservoir rock extracts from the dongying depression. *Acta Geol. Sin.* 80, 439–445.

Li, S., Pang, X., and Sun, A. (2007). Total scanning fluorescence for oils with different genetic types and controlling factors. *Acta Geol. Sin.* 81, 230–235.

Liu, B., Bai, L., Chi, Y., Jia, R., Fu, X., and Yang, L. (2019). Geochemical characterization and quantitative evaluation of shale oil reservoir by two-dimensional nuclear magnetic resonance and quantitative grain fluorescence on extract: a case study from the Qingshankou Formation in Southern Songliao Basin, northeast China. *Mar. Pet. Geol.* 109, 561–573. doi: 10.1016/j.marpetgeo.2019.06.046

Liu, B., Bechtel, A., Sachsenhofer, R. F., Gross, D., Gratzer, R., and Chen, X. (2017). Depositional environment of oil shale within the second member of Permian Lucaogou Formation in the Santanghu Basin, Northwest China. *Int. J. Coal Geol.* 175, 10–25. doi: 10.1016/j.coal.2017.03.011

Liu, B., Sun, J., Zhang, Y., He, J., Fu, X., Yang, L., et al. (2021). Reservoir space and enrichment model of shale oil in the first member of Cretaceous Qingshankou Formation in the Changling sag, southern Songliao Basin, NE China. *Pet. Explor. Dev.* 48, 1–16.

Liu, C., Liu, K., Wang, X., Wu, L., and Fan, Y. (2019). Chemostratigraphy and sedimentary facies analysis of the Permian Lucaogou Formation in the Jimusaer Sag, Junggar Basin, NW China: implications for tight oil exploration. *J. Asian Earth Sci.* 178, 96–111. doi: 10.1016/j.jseaes.2018.04.013

Liu, K. Y., Lu, X., Gui, L., Fan, J., Gong, Y., and Li, X. (2016). Quantitative fluorescence techniques and their application in hydrocarbon accumulation studies. *Earth Sci.* 41, 373–384.

Liu, K. Y., Simon, C. G., Lu, X., Gong, S., Tian, H., and Gui, L. (2014). Innovative fluorescence spectroscopic techniques for rapidly characterising oil inclusions. *Organ. Geochemistr.* 72, 34–45. doi: 10.1016/j.orggeochem.2014.04.010

Ma, W., Hou, L., Luo, X., Liu, J., Tao, S., Guan, P., et al. (2020). Generation and expulsion process of the Chang 7 oil shale in the Ordos Basin based on temperature-based semi-open pyrolysis: implications for in-situ conversion process. *J. Pet. Sci. Eng.* 190:107035. doi: 10.1016/j.petrol.2020.107035

Mackenzie, A., Patience, L., Maxwell, R., Vandenbroucke, M., and Durand, B. (1980). Molecular parameters of maturation in the Toarcian shales, Paris Basin, France—I. Changes in the configurations of acyclic isoprenoid alkanes, steranes and triterpanes. *Geochim. Cosmochim. Acta* 44, 1709–1721. doi: 10.1016/0016-7037(80)90222-7

Pang, H., Pang, X., Dong, L., and Zhao, X. (2018). Factors impacting on oil retention in lacustrine shale: permian Lucaogou Formation in Jimusaer Depression, Junggar Basin. *J. Pet. Sci. Eng.* 163, 79–90. doi: 10.1016/j.petrol.2017.12.080

Peters, K., Fraser, H., and Amris, W. (1999). Geochemistry of crude oils from eastern Indonesia. *AAPG Bull.* 83, 1927–1942.

Peters, K., and Moldowan, J. (1993). *The Biomarker Guide: Interpreting Molecular Fossils in Petroleum and Ancient Sediments*. Englewood Cliffs, NJ: Prentice Hall.

Qiu, Z., Tao, H., Zou, C., Wang, H., Ji, H., and Zhou, S. (2016). Lithofacies and organic geochemistry of the middle Permian Lucaogou Formation in the Jimusar sag of the Junggar Basin, NW China. *J. Pet. Sci. Eng.* 140, 97–107. doi: 10.1016/j.petrol.2016.01.014

Reyes, M. (1993). "The application of fluorescence techniques for mudlogging analysis of oil drilled with oil-based muds," in *Proceedings of the 22nd Annual Convention Proceedings*, Vol. 2, (Tulsa: AAPG), 157–170.

Seifert, K., and Moldowan, M. (1978). Applications of steranes, terpanes and monoaromatics to the maturation, migration and source of crude oils. *Geochem. Cosmochim. Acta* 42, 77–95. doi: 10.1016/0016-7037(78)90219-3

Seifert, W., and Moldowan, J. (1980). The effect of thermal stress on source-rock quality as measured by hopane stereochemistry. *Phys. Chem. Earth* 12, 229–237. doi: 10.1016/0079-1946(79)90107-1

Seifert, W., and Moldowan, J. (1986). Use of biological markers in petroleum exploration. *Methods Geochem. Geophys.* 24, 261–290.

Su, Y., Zha, M., Ding, X., Qu, J., Gao, C., Jin, J., et al. (2019). Petrographic, palynologic and geochemical characteristics of source rocks of the Permian Lucaogou formation in Jimsar Sag, Junggar Basin, NW China: origin of organic matter input and depositional environments. *J. Pet. Sci. Eng.* 183:106364. doi: 10.1016/j.petrol.2019.106364

Wang, X., Yang, Z., Guo, X., Wang, X., Feng, Y., and Huang, L. (2019). Practices and prospects of shale oil exploration in Jimsar Sag of Junggar Basin. *Xinjiang Petrol. Geol.* 40, 402–413.

Wang, Y., Cao, J., Tao, K., Li, E., Ma, C., and Shi, C. (2020). Reevaluating the source and accumulation of tight oil in the middle Permian Lucaogou Formation of the Junggar Basin, China. *Mar. Pet. Geol.* 117:104384. doi: 10.1016/j.marpetgeo.2020.104384

Wu, H., Zhao, M., Zhuo, Q., Lu, X., Li, W., Zeng, F., et al. (2016). Palaeofluid evolution process in Well Block Tubei 1 in the Kuqa Depression, Tarim Basin. *Nat. Gas Ind. B* 3, 129–138. doi: 10.1016/j.ngib.2016.03.007

Yang, Z., Zou, C., Hou, L., Wu, S., Lin, S., Luo, X., et al. (2019). Division of fine-grained rocks and selection of "sweet sections" in the oldest continental shale in China: taking the coexisting combination of tight and shale oil in the Permian Junggar Basin. *Mar. Pet. Geol.* 109, 339–348. doi: 10.1016/j.marpetgeo.2019.06.010

Zha, M., Wang, S., Ding, X., Feng, Q., Xue, H., and Su, Y. (2019). Tight oil accumulation mechanisms of the Lucaogou Formation in the Jimsar Sag, NW China: insights from pore network modeling and physical experiments. *J. Asian Earth Sci.* 178, 204–215. doi: 10.1016/j.jseaes.2018.05.037

Zhao, W., Hu, S., and Hou, L. (2018). Connotation and strategic role of in-situ conversion processing of shale oil underground in the onshore China. *Pet. Explor. Dev.* 45, 563–572. doi: 10.1016/s1876-3804(18)30063-6

Zhao, W., Hu, S., Hou, L., Yang, T., and Yang, Z. (2020). Types and resource potential of continental shale oil in China and its boundary with tight oil. *Pet. Explor. Dev.* 47, 1–11. doi: 10.1016/s1876-3804(20)60001-5

Zhi, D., Tang, Y., Yang, Z., Guo, X., Zheng, M., Wan, M., et al. (2019). Geological characteristics and accumulation mechanism of continental shale oil in Jimusaer sag, Junggar Basin. *Oil Gas Geol.* 40, 524–535.

Zou, C., Yang, Z., Cui, J., Zhu, R., Hou, L., and Tao, S. (2013). Formation mechanism, geological characteristics, and development strategy of nonmarine shale oil in China. *Petrol. Exploration Dev.* 40, 15–27. doi: 10.1016/s1876-3804(13)60002-6

Zou, C., Yang, Z., and Zhu, R. (2015). Progresses in China's unconventional oil & gas exploration and theoretical technologies. *Acta Geol. Sin. Engl.* 89, 938–971.

Conflict of Interest: All authors are employed by the company PetroChina.

frontiers in Earth Science

ORIGINAL RESEARCH
published: 05 May 2021
doi: 10.3389/feart.2021.661706

Characteristics and Genetic Mechanisms of Normal-Pressure Fractured Shale Reservoirs: A Case Study From the Wufeng–Longmaxi Formation in Southeastern Chongqing, China

Jinxi Wang[1,2], Xianfeng Tan[3], Jia Wang[3]*, Hualian Zhang[2], Ye Zhang[1,2], Dongxin Guo[2], Xiaofeng Wang[4], Zhian Lei[5], Chunlin Zeng[1] and Guanghua Yao[6]*

[1] National and Local Joint Engineering Research Center of Shale Gas Exploration and Development, Chongqing Institute of Geology and Mineral Resources, Chongqing, China, [2] Key Laboratory of Shale Gas Exploration, Ministry of Natural Resources, Chongqing Institute of Geology and Mineral Resources, Chongqing, China, [3] Chongqing Key Laboratory of Complex Oil and Gas Exploration and Development, Chongqing, China, [4] Chongqing Institute of Geological Survey, Chongqing, China, [5] Chongqing Shale Gas Exploration and Development Company Limited, Chongqing, China, [6] China Huaneng Group Co., Ltd., Chongqing, China

Compared with the overpressure conditions of shale reservoirs in the Jiaoshiba area, exploring the controlling factors of changes in shale reservoir physical properties under normal-pressure accumulation is of great significance to shale gas exploration. To achieve this, X-ray powder diffraction, nitrogen adsorption, and scanning electron microscopy were carried out to determine mineral content, permeability, porosity, and pore structure for well core and outcrop samples of the Wufeng–Longmaxi Formation in southeastern Chongqing, China. Field observations and drilling cores revealed abundant structural fractures in southeastern Chongqing, offering potential main storage space for shale gas. Findings also determined that high-quality source rocks are located in the lower part of the Wufeng–Longmaxi Formation, which features low porosity and low permeability, yet existing structural fractures could potentially improve permeability to a certain extent. The main factors controlling the shale reservoir with the above characteristics include the depositional environment, mineral components, total organic carbon content, and tectonic movement. The deep-water anoxic depositional environment was conducive to the complete preservation of organic matter and sedimentation of the biogenic siliceous minerals, which had a strong effect on improving the porosity of organic matter and brittleness of the rocks. The high content of quartz was found to improve rock compression resistance and brittleness, and increasing clay proportion was found to enhance the interlayer pores of clay minerals. Total organic carbon content, specific surface area, pore volume, and fracture development were all

OPEN ACCESS

Edited by:
Dawei Lv,
Shandong University of Science and Technology, China

Reviewed by:
Yanbin Yao,
China University of Geosciences, China
Ruyue Wang,
SINOPEC Exploration & Production Research Institute, China

***Correspondence:**
Xianfeng Tan
xianfengtan8299@163.com
Jia Wang
wangjia@cqust.edu.cn.com

Specialty section:
This article was submitted to Economic Geology, a section of the journal Frontiers in Earth Science

Received: *31 January 2021*
Accepted: *26 March 2021*
Published: *05 May 2021*

Citation:
Wang J, Tan X, Wang J, Zhang H, Zhang Y, Guo D, Wang X, Lei Z, Zeng C and Yao G (2021) Characteristics and Genetic Mechanisms of Normal-Pressure Fractured Shale Reservoirs: A Case Study From the Wufeng–Longmaxi Formation in Southeastern Chongqing, China. Front. Earth Sci. 9:661706. doi: 10.3389/feart.2021.661706

found to have direct contributions to shale gas entrapment. Overall, the most important factor resulting in normal-pressure accumulation in southeastern Chongqing was the intense tectonic movements since the Late Jurassic period which destroyed the original overpressure accumulation conditions.

Keywords: shale reservoir, physical characteristics, the Wufeng formation, the Longmaxi formation, southeastern Chongqing

INTRODUCTION

As an unconventional gas, shale gas is of great significance to the global energy supply. China's shale gas exploration blocks are concentrated in the Upper Yangtze Fuling, Weiyuan, Pengshui, and Changning areas. The main strata for exploration and development are located in the Upper Ordovician Wufeng Formation (O_3w)–Lower Silurian Longmaxi Formation (S_1l), which are rich in organic black shale and have been commercialized (Wang et al., 2013; Guo and Zhang, 2014; He Z. et al., 2017). Among them, the Fuling gas field has reserves amounting to $7{,}685.16 \times 10^8$ m^3, making it the second-largest shale gas field in the world after one field located in North America (Jiang et al., 2016; Dai et al., 2017). Therefore, the black shale of the Wufeng–Longmaxi Formation in the Upper Yangtze District has good prospects for exploration and development. Previous research on this area's black shale has mainly been concentrated on the Sichuan Basin. The Changning–Weiyuan block is mainly composed of organic-rich black shales enriched in graptolites, brachiopods, and other fossils, along with good organic matter types, relatively high thermal maturity, moderate content of brittle mineral components in shale matrix, and the presence of diverse types of pores and fractures, all of which make the Longmaxi Formation shale favorable for shale gas accumulation (Pu et al., 2010; Pan et al., 2016). Most research into black shale has focused on the Jiaoshiba shale gas reservoir in Fuling, southeastern Sichuan, including studies on the division of graptolite belts, sedimentary responses, shale distribution laws, accumulation models, and structural influences (Su et al., 2007; Mu et al., 2011; Guo, 2014; Guo et al., 2014a; Chen et al., 2015; Wang, 2015; Nie et al., 2016; Jin et al., 2018; Zhou et al., 2018; Gao et al., 2019; Gou and Xu, 2019; Liang et al., 2018; Lv et al., 2019, 2020; Tang et al., 2019; Wang Q. et al., 2019; Wang R. Y. et al., 2019; Wang et al., 2020). Overall conclusions agree that Jiaoshiba experiences overpressure, with a pressure coefficient of more than 1.74 and a burial depth of >6,200 m. The reservoir space mainly consists of pores, and the thermal evolution of organic matter hydrocarbon-generation pressurization is the main mechanism of overpressure formation (Gao et al., 2019; Wang Q. et al., 2019). Gao et al. (2019) divided the evolution of the Jiaoshiba overpressure conditions into four stages: (i) the rapid pressurization stage caused by the generation of thermal catalytic dry gas, (ii) the rapid pressure release stage, (iii) the overpressure preservation stage, and (iv) the slow-release pressure stage. Regarding this last stage, researchers have suggested that pressure has been released since the initial overpressure was first formed. Guo and Zhang (2014) proposed that the shale gas in the Longmaxi Formation of Jiaoshiba has undergone three stages of accumulation: (i) the early-stage formation of a small amount of carbohydrates, (ii) deep burial and massive carbohydrate formation, and (iii) uplift, denudation, and fracture development, all of which correspond well with Gao et al.'s (2019) perspective. In contrast, although southeastern Chongqing is located relatively close to Jiaoshiba, the Wufeng–Longmaxi Formation shale is situated within a different atmospheric environment with a pressure coefficient between 0.8 and 1.2 (He X. et al., 2017). Yuan et al. (2020) proposed that the Pengshui–Longmaxi Formation shale gas reservoir also experienced overpressure during its geological formation period, yet during uplift, the overpressure caused ruptures and fractures, resulting in the loss of shale gas and release of overpressure, ultimately transitioning the pressure environment to atmospheric. This is because the tectonic deformation experienced in the periphery of the Sichuan Basin was earlier and more intense than that in the interior of the basin, which resulted in the formation of distinctly contrasting accumulation environments between Jiaoshiba and Pengshui (Fan et al., 2019). Therefore, owing to a lack of relevant research, the characteristics, vertical evolution laws, and main controlling factors of normal-pressure Wufeng–Longmaxi Formation shale reservoirs in southeastern Chongqing need to be determined. This study therefore uses petrographic observations, low-temperature nitrogen adsorption, and scanning electron microscopy to better evaluate shale gas reservoir characteristics and guide the division of shale gas-favorable blocks in southeastern Chongqing.

GEOLOGICAL SETTING

Parts of southeastern Chongqing are adjacent to the southeastern margin of the Sichuan Basin, western Hunan, and northern Guizhou (**Figure 1A**). This area has undergone the superimposition and transformation of multiple tectonic movements (Guangxi, Indo-China, Yanshan, and Himalayan), forming the upper Yangtze intra-platform depression structural unit, with folds and faults trending north–northeast (Xie et al., 2013). According to the changes in structural styles, the northwestern part of the area is classified as a trough-fold belt, the middle part as a transitional fold belt, and the southeastern part as a barrier-fold belt (**Figure 1B**). The partition and trough structure are successively controlled by the Yanshan and Himalayan movements (Wang et al., 2017). The outcropping strata in the area are dominated by Paleozoic-age rocks, lacking the Carboniferous, Cretaceous, and Tertiary eras. The basement of the strata is the Precambrian Banxi Group, and the total thickness of deposits of Sinian to Jurassic-age is nearly 10,000 m

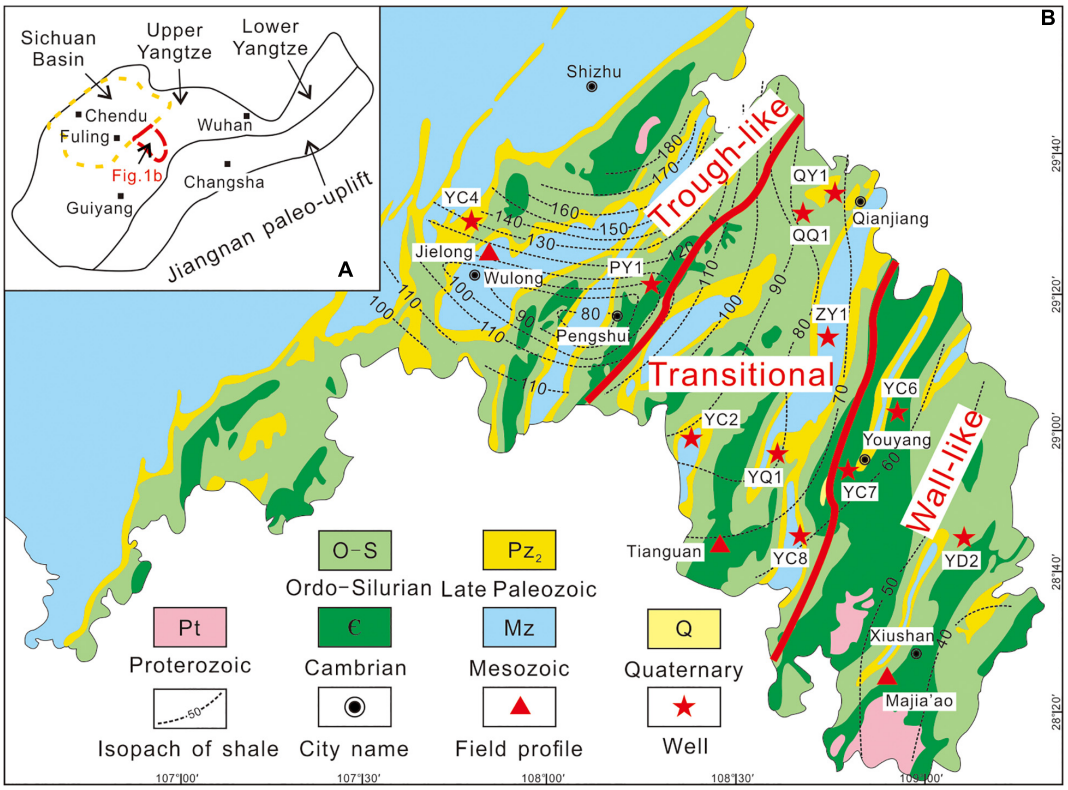

FIGURE 1 | (A) Map of the study area; **(B)** geological map of southeastern Chongqing and sampling points (refer to Wu et al., 2011; Tan et al., 2015; Luo et al., 2016).

(Xu et al., 2015). This area developed two main source rocks: the Lower Cambrian Niutitang Formation ($\epsilon_1 n$) and Upper Ordovician Wufeng Formation–Lower Silurian Longmaxi Formation ($O_3 w$–$S_1 l$) (i.e., the Wufeng–Longmaxi Formation or separate formations thereof) (Wang et al., 2017). The sedimentation of the Niutitang shale most likely occurred in a weak hydrodynamic, deep water, oxygen-deficient reducing environment, sourced from continental margins (Liu et al., 2016a). The Wufeng and Longmaxi formations are the main horizons for marine shale gas exploration and development in the Sichuan–Chongqing area. The two sets of shale have relatively similar characteristics, such as "high organic carbon content, high thermal evolution, and deep burial," and are generally incorporated into an overall stratum for research (Liang et al., 2018). The original thickness of the Wufeng–Longmaxi Formation varies between 300 and 4,500 m. Owing to the influence of structural uplift and denudation, the current residual thickness is 20–120 m (70 m on average), which is thinner in the southeast and thicker in the northwest (Tan et al., 2015; Wang et al., 2017; **Figure 1B**). He X. et al. (2017) proposed that the Wufeng–Longmaxi Formation in the Pengshui area of southeastern Chongqing is under normal pressure, with a pressure coefficient between 0.8 and 1.2 which is far below that of the Jiaoshiba area. During the Late Ordovician–Early Silurian, the Sichuan Basin and its periphery were affected by the Guangxi Movement in which an intracontinental depression occurred under a background of compression, forming a large-scale deep-water shelf environment. The long-term closed and stable anaerobic environment was conducive to the preservation of organic matter, which provided superior conditions for high shale gas production (Mu et al., 2011; He et al., 2016; Fan et al., 2019). The argillaceous limestone and calcareous mudstone of the Guanyinqiao section are locally deposited, conforming to the overlying Longmaxi Formation and underlying Wufeng Formation (Liang et al., 2018; Zhao et al., 2020).

SAMPLES AND METHODS

Samples of the Wufeng–Longmaxi Formation were collected from nine wells: Yushen 4, Yushen 6, Yushen 7, Yushen 8, Zhuoye 1, Qianqian 1, Youqian 1, Youshen 2, and Youdi 2 (**Figure 1B**).

TOC Content Analysis

Two grams of a powder sample was placed into a centrifuge tube, and 10% dilute hydrochloric acid was added. The sample was then dissolved by shaking and allowed to stand for 24 h. Then, the supernatant was poured out, and deionized water was added. This step was repeated several times until the supernatant was neutral, and then the sample was dried. Finally, a Leco CS-230 carbon and sulfur analyzer was used to determine the total organic carbon (TOC) content.

Mineral Composition Analysis

Quantitative analysis of the mineral composition was carried out using a Rigaku D/MAX RAPID II diffractometer for X-ray powder diffraction, and the experimental conditions used a Mo target. The rotation angle was 2.5–60°, the tube pressure was 40 kV, the tube flow was 100 mA, the incident spot diameter was 0.1 mm, and the sample tube diameter was 0.5 mm; no background sample tube was utilized.

Scanning Electron Microscopy

Scanning electron microscopy analysis was performed using a Quanta 200F (Field Electron and Ion Company, FEI; Oregon, United States). Secondary electron imaging was performed in high-vacuum mode at 3.0 nm and 30 kV, and at 8 nm and 3 kV; in high-vacuum deceleration mode at 7 nm and 3 kV; in low-vacuum mode at 3.0 nm and 30 kV, and at 10 nm and 3 kV; and in ambient-vacuum mode at 3.0 nm and 30 kV. The backscattered electron (BSE) imaging passes were conducted at 4.0 nm and 30 kV, the sample chamber pressure extended up to 2600 Pa, the acceleration voltage was between 200 V and 30 kV, and the moving range of the sample stage was continuously adjusted (Quanta 200F X = Y = 100 mm).

Porosity and Permeability Analysis

The analysis of porosity and permeability was performed with a CMS-300 (Temco, United States). Before the experiment, the core samples were dried at 104.4°C for 2 days, and the permeability was measured at a confining pressure of 1000 to 6000 psia. The instrument uses a pressure attenuation method to measure the permeability and porosity according to Boyle's law, with a permeability range of 0.00005–15 mD and porosity range of 0.01–40%.

Pore Structure Analysis

Pore structure analysis was performed on the Autosorb-1 specific surface area and pore size measuring instrument (Quantachrome Company, United States). The instrument utilizes the isothermal physical adsorption static volume method, with a minimum resolvable relative pressure of 2.6×10^{-7}, specific surface area of $\geq$0.0005 m^2/g, test pore size range of 0.35–500 nm, and test pore volume of $<$0.0001 cm^3/g. The test requires degassing, which was performed at a temperature of 97°C for 5 h. The Brunauer–Emmett–Telle (BET) model (Brunauer et al., 1938) was used to calculate the specific surface area of shale and determine the pore size distribution characteristics, including pore volume calculation of mesopores and some macropores (Barratt et al., 1951).

RESULTS

Material Composition

Petrology

The Wulong–Jielong section in the northwest of the area reveals the complete profile of the Wufeng Formation–Guanyinqiao Section–Longmaxi Formation (**Figure 2A**). The lithology of the Wufeng Formation is mainly black siliceous shale, carbonaceous shale, and silty shale with a deposition thickness of 10.4 m (**Figure 2B**). The lithology of the Guanyinqiao section (in the upper part of the Wufeng Formation) is mainly marl and lime shale, and the thickness is very thin at only 31 cm (**Figure 2B**). The lower Longmaxi Formation comprises black shale with extremely thick deposits, and the silty content increases upward.

The Youyang–Tianguan section (**Figure 2C**) in the central part of the study area outcrops black carbonaceous shale and carbonaceous siliceous shale at the bottom of the Wufeng–Longmaxi Formation (**Figure 2D**), where many graptolite fossils can be seen and with horizontal bedding of 22.39 m thickness. The upper lithology is black and gray-black carbon-bearing silt shale and silt stone, and the overall silt content increases upward, with a thickness of 36.79 m.

At the Xiushan–Majiaao section in the southeastern part of the study area (**Figures 1B**, **2E**), the organic-rich mud shale at the bottom of the Wufeng–Longmaxi Formation is thinner, having a thickness of 10.2 m (**Figure 2F**). The lithology is mainly black and gray-black carbonaceous shale and carbonaceous siliceous shale with a large number of graptolite fossils and pyrite and reduced carbon content after weathering. The lithology in the central part is mainly gray-black and black argillaceous siltstone with occasional gray-white ultra-thin layered porphyrite and a thickness of 6.53 m. In the upper part, the argillaceous content is increased, and the lithology is mainly gray-black and gray silty mudstone. The local carbon content is high, and a large number of graptolite fossils can be seen with a thickness of 28.19 m.

Mineralogy

The Wufeng–Longmaxi Formation shale in the area is mainly composed of brittle minerals and clay minerals and a small amount of pyrite (**Table 1**). The content of the brittle minerals is between 39.5 and 90.7% (65.5% on average), which mainly consists of quartz (22–79%, average 41.1%), followed by feldspar (1.7–28.7%, average 14.9%), and a small amount of carbonate minerals (0–27.9%, average 9.3%). The content of the clay minerals is 7.1–58.2% with an average of 30.3%, which is mainly illite (7–68%, 29.9% on average) and illite/smectite minerals (8–85%, 54.1% on average) (**Figure 3D**). A small amount of chlorite (1–42%, average 11.5%) and a chlorite/smectite layer (0–17%, average 3.7%) are present, and the illite/smectite layer mainly reflects the properties of illite. The pyrite content ranges from 0 to 14.6%, with an average of 3%. Vertically, the content of the brittle minerals such as quartz feldspar in the lower shale section is highest, generally reaching more than 60% and gradually decreasing upward; the content of the clay minerals gradually increases upward (**Figures 3A,B**). Horizontally, the quartz content gradually decreases from the barrier-fold belt to trough-fold belt. The content of feldspar and carbonate minerals gradually increases, and the clay mineral content gradually decreases (**Figures 3C,D**).

Organic Matter Characteristics

The overall TOC content of Wufeng–Longmaxi Formation shale in the research area has a large variation range of 0.29–8.49%. In terms of total TOC content of the samples, samples with

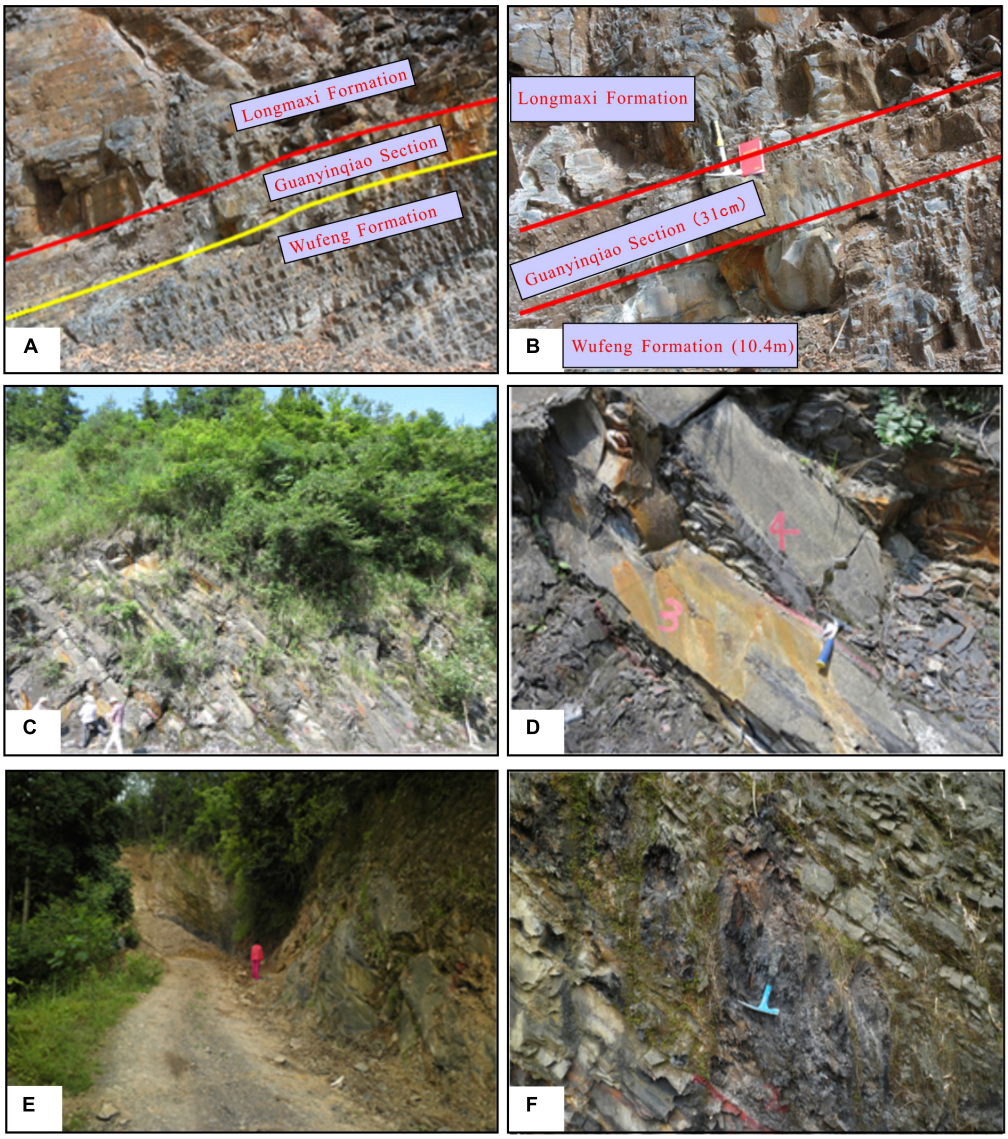

FIGURE 2 | Field sedimentary characteristics of the Wufeng–Longmaxi Formation shale. **(A)** shale at the Wulong–Jielong Section; **(B)** interface of Wufeng–Guanyinqiao Section–Longmaxi Formation at the Wulong–Jielong Section; **(C)** shale of the Youyang–Tianguan Section; **(D)** black carbonaceous mud shale at the bottom of the formation at the Tianguan Section in Youyang; **(E)** shale at the Majiaao Section in Xiushan; and **(F)** black carbon at the bottom of the formation at the Majiaao Section in Xiushan mudstone.

TABLE 1 | Mineral composition of organic-rich shale from the Wufeng–Longmaxi Formation.

Well	Quartz (min–max/average, %)	Feldspar (min–max/average, %)	Carbonate (min–max/average, %)	Pyrite (min–max/average, %)	Clay minerals (min–max/average, %)	Brittle minerals (min–max/average, %)
Qianqian 1	32–70/45.9	3–20/12.6	0–12/6.4	0–8/2.3	16–58/35.18	40–81/64.91
Youdi 2	30.8–70/41.6	4.6–25/14.8	2.1–19.8/10	1.5–6.5/3.1	16.6–42.2/29.6	53.7–79.2/66.4
Yucan 2	33.1–71/42.2	5–21.8/14.7	0–13.6/8.7	0.8–5.1/2.4	15–50.9/29.7	45.6–82.5/65.6
Youqian 1	33.7–65.2/44.8	8–26.7/18.9	0.2–18.7/9.1	0.6–3.7/1.7	12–49.3/24.4	48.4–85.9/72.8
Yucan 4	25.9–69.7/38.4	3–20.1/12.7	1–24.6/11	1.3–14.6/4.5	9.6–50.9/32.3	45–88.2/62
Yucan 6	27.9–56.8/39.9	4.7–28.1/16.5	2.3–19.9/10.8	0–7.3/2.6	14–50.1/28.4	40.9–84/67.2
Yucan 7	22–72.1/42.3	3.2–23.6/13.7	0–27.9/10.3	0–12.7/3.5	12.9–52.1/28.4	42.2–83/66.3
Yucan 8	25.7–52.2/40.8	1.7–28.7/16.9	0.2–23.5/9.4	0–7/2.5	7.1–58.2/29.28	39.5–90.7/67.1
Zhuoye 1	31.7–79/50	3.3–23.3/13.3	0–24.5/7.3	0.8–11.2/3.7	8.8–50.5/25.8	42.8–90/70.6

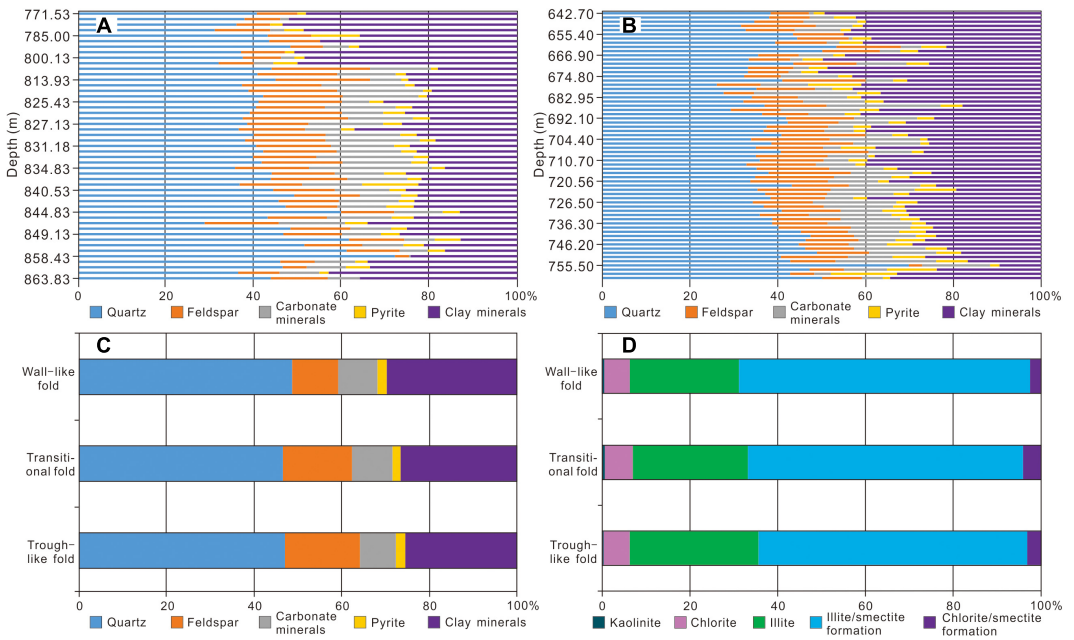

FIGURE 3 | Variation trend of mineral composition in the Wufeng–Longmaxi Formation shale: **(A)** Vertical distribution map of the shale mineral composition in the Yucan 7 well; **(B)** vertical distribution map of the shale mineral composition in the Yucan 4 well; **(C)** shale mineral composition distribution map according to structural style; and **(D)** shale clay mineral composition distribution map according to structural style.

TOC greater than 1% account for 50.92%, and those greater than 2% account for 24.51%. According to the vertical lithology changes, the Wufeng–Longmaxi Formation shale is divided into three sections in the northwestern part of the area, characterized by high TOC (first section; 2.0–8.49%, average 3.43%); low TOC (second section; 0.63–1.97%, average 1.37%); and moderate TOC (third section; 1.28–2.64%, average 2.07%). However, the lithological changes of the Wufeng–Longmaxi Formation in the research area are not obvious, nor is the vertical change in TOC. These phenomena may be related to the distribution of sedimentary facies.

Based on the classification criterion of kerogen type index from Shen et al. (2013), the Wufeng–Longmaxi Formation kerogen type in the area is mainly saprolite I (**Table 2**). The organic-rich shale has a relatively high degree of evolution with a maturity of 1.6–3.38% (average 2.56%). The overall Ro did not change much (1.8–2.8%). The Youyang East–Xiushan area has the characteristics of thin deposits, low maturity, and Ro values of less than 2.0%. The Wulong–Pengshui area has the characteristics of thick deposits, high maturity, and Ro values of greater than 2.5%.

Reservoir Characteristics

Type of Storage Space

According to the observational statistics of scanning electron microscopy and core samples, the Wufeng–Longmaxi Formation mud shale developed organic matter pores, clay mineral interlayer pores, intragranular and intergranular pores, and structural fractures. Of these, the structural fractures are the main storage space for shale gas, followed by organic pores, which have the lowest proportion of intragranular pores. There appears to be no change in the type of storage space from the southeast to the northwest of the study area.

(1) Organic pores

The shale in the formation considered herein has well-developed organic pores, which are circular or elliptical in shape and distributed in a honeycomb shape; the pore diameters are concentrated at 30–100 nm (**Figures 4A,B**). The facies ratios of the organic matter in the shale show that the separate Wufeng and Longmaxi formations account for 19.67% and 9.84% respectively, and that of the Wufeng–Longmaxi Formation shale accounts for 39.9% of the total pores.

(2) Clay mineral interlayer pores

The shale structure of the Longmaxi Formation is relatively dense with fewer intergranular and intragranular pores of inorganic minerals, but large-scale interlayer pores of clay minerals are observed, distributed among clay minerals such as the filamentous and curly, flaky illite (**Figure 4C**). The width of these interlayer pores varies from tens of nanometers to several micrometers with good connectivity and the pores are linear and parallel to each other, accounting for 28% of the total pores.

(3) Intergranular pores

The intergranular pores of the Wufeng–Longmaxi Formation shale mainly include mineral pores and intermediate pores of organic matter and minerals, accounting for 20.2% of the total

TABLE 2 | Microscopic content distribution of shale samples in different parts of the study area.

Well	Level	Sample number	Sapropelite (min–max/average, %)	Exinite (min–max/average, %)	Vitrinite (min–max/average, %)	Inertinite (min–max/average, %)	Ti (min–max/average, %)	Organic matter type
Youdi 2	O_3w–S_1l	7	95–98/96.75	0	1–3/1.63	1–3/1.63	90.50–96.25/93.91	I
Youqian 1	O_3w–S_1l	10	95–99/96.8	0	1–5/3.2	0	87.75–98.25/94.4	I
Yucan 4	O_3w–S_1l	25	94–98/96	0	2–6/4	0	89. 5–96. 5/93	I
Yucan 6	O_3w–S_1l	17	94–98/96.24	0	1–3/2.0	1–3/1.76	88.75–96.25/92.97	I
Yucan 7	O_3w–S_1l	5	80–96/89.2	0	1–10/5	2–10/5.8	62.5–92.5/79.7	I–II$_1$
Yucan 8	O_3w–S_1l	13	80–95/88.15	0	2–8/5.0	2–15/6.85	61.25–90.5/77.56	I–II$_1$

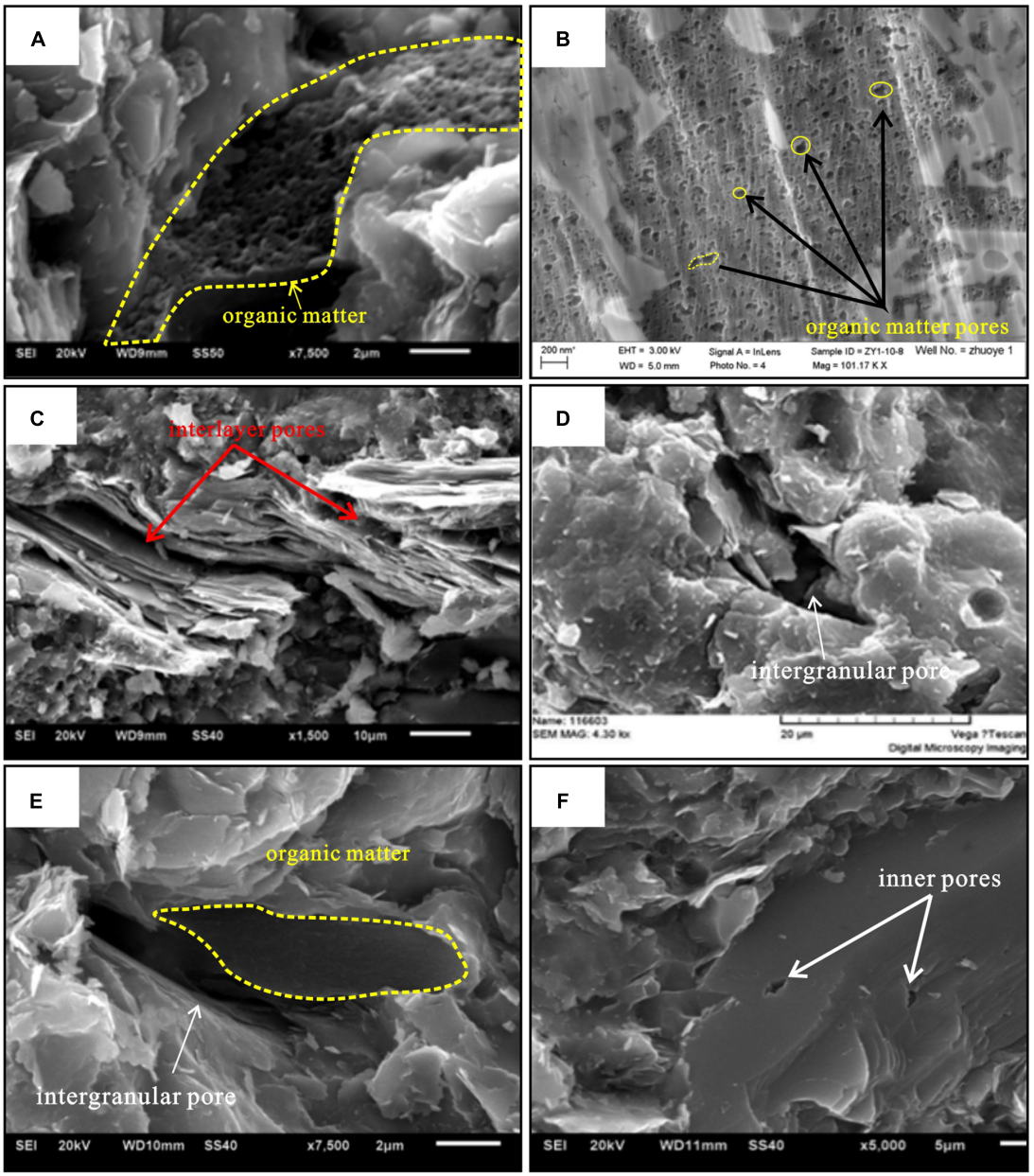

FIGURE 4 | Types and characteristics of pore spaces of the Longmaxi Formation shale in the study area (scanning electron microscopy). **(A)** Nano-scale organic pores, Yucan 4 well; **(B)** nano-scale organic pores, Zhuoye 1 well; **(C)** interlayer pores of clay minerals, Youdi 2 well; **(D)** intergranular pores, Qianqian 1 well; **(E)** micron-scale organic matter and mineral intergranular pores, Yucan 6 well; **(F)** nano-scale feldspar grain inner pores, Yucan 6 well.

FIGURE 5 | Distribution characteristics of fractures in field section and drilling cores. **(A)** Wufeng–Longmaxi Formation structural fractures in the Majiaao section of Xiushan; **(B)** multi-stage structural fractures in the lower part of the Wufeng–Longmaxi Formation, Yucan 4 well; **(C,D)** attachment and detachment zones in the lower part of the Wufeng–Longmaxi Formation scratches, Yucan 6 well.

pores. The larger the mineral particles, the larger the inter-particle pores, and the pore diameters range from nanometers to 5 μm (**Figure 4D**). Organic matter and mineral intermediate pores only account for a small part of the shale pores (**Figure 4E**), but such pores open up organic matter pores and mineral pore channels, enabling natural gas to migrate to mineral pores. The Wufeng Formation shale structure is relatively fragmented, and a large number of intergranular pores are developed between quartz grains and between quartz and clay minerals, which are usually distributed linearly along the grain edges.

(4) Intragranular pores

The edges of the dissolved pores are irregular harbors or zigzags (**Figure 4F**), and the pore walls are curved and developed in groups. The pores are nanometer-sized, accounting for 11.9% of the total pores.

(5) Structural fractures

The Wufeng–Longmaxi Formation shale has structural fractures that formed in the Yanshanian and Himalayan movement periods (**Figures 5A,B**); these fractures are the main storage space for shale gas. The width of typical open fractures is large, while the extension is short, and the fracture surface is non-straight. In contrast, shear fractures have a relatively straight fracture surface and high density. The same group of fractures has better equidistance, and the different groups of fractures cut through one another. The surface of the slippage fracture is non-smooth, yet the scratches, steps, and mirror features are visible (**Figures 5C,D**).

The fracture length is dominated by short fractures (<10 cm), which represent close to 90% of the total length (**Figure 6A**). The longest fracture was observed to be up to 88 cm. The fractures with openings ≤0.2 mm and 0.5–1 mm represent 40% of the total, while fractures with openings of 0.2–0.5 mm are not developed (**Figure 6B**). Low-angle oblique fractures and high-angle cutting joints are roughly the same, accounting for 34.95 and 33.49% of the total, respectively. The frequencies of occurrence of the horizontal and vertical slits were also very close at 15.73 and 15.83%, respectively (**Figure 6C**).

The Wufeng–Longmaxi Formation has a relatively high degree of fracture filling. More than half of the fractures are completely filled, and unfilled fractures account for 40.81% of the total number of fractures measured; semi-filled fractures are basically not developed and are characterized by a large amount of pyrite and calcite filled together. These types of fractures are widely distributed in the stratum, with stable extension and spreading.

Porosity and Permeability Characteristics

The porosity and permeability of the Wufeng–Longmaxi shale in the study area were lower than those in the Jiaoshiba area (**Figure 7A**), indicating a low-porosity and low-permeability reservoir. The study area porosity ranges from 0.05% to 5.61% (average 1.25%), while the porosity of 81.1% of the region ranges from 0 to 2%. Likewise, the study area permeability is

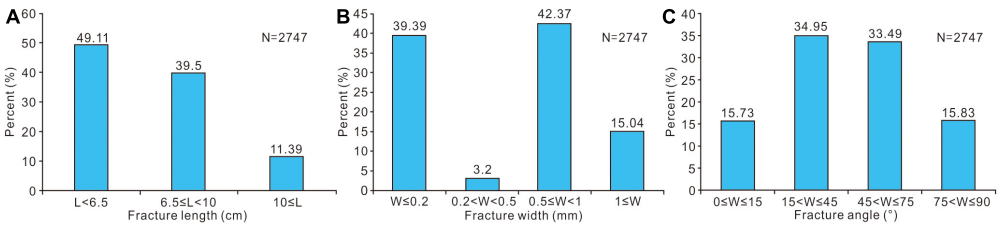

FIGURE 6 | (A) Percent of fracture length with the different scale from the Wufeng-Longmaxi Formation, southeastern Chongqing. **(B)** Percent of different fracture width in the Wufeng-Longmaxi Formation, southeastern Chongqing. **(C)** Percent of different Fracture angle in the Wufeng-Longmaxi Formation, southeastern Chongqing. N denotes the number of fractures.

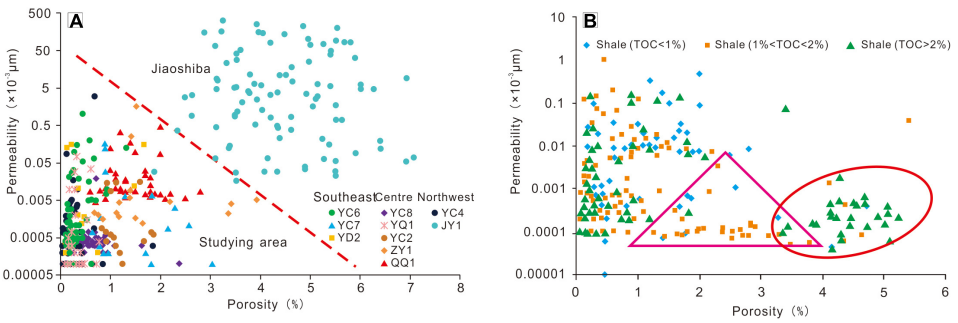

FIGURE 7 | (A) Pore-permeability intersection diagram of shale from the Wufeng-Longmaxi Formation in southeastern Chongqing,compared with those in Jiaoshiba area (data from JY 1 well were obtained from Guo et al., 2014b). **(B)** Pore-permeability intersection diagram of shale with different percent of TOC content from the Wufeng-Longmaxi Formation in southeastern Chongqing. YC6 denotes the serial number of well drilling.

between 5×10^{-7} and 16.26×10^{-3} μm^2, while the permeability of 72.1% of the region is 1×10^{-4} to 1×10^{-5} μm^2. Therefore, the correlation between the porosity and permeability of the Wufeng–Longmaxi Formation in the study area is not obvious; however, the southeastern Yucan 6 well, the central Qianqian 1 well, and the northwestern Yucan 4 well all show the characteristics of low porosity and high permeability (**Figure 7A**). Further, Liu et al. (2017a) previously revealed the vertical heterogeneity of the physical properties of the Longmaxi shale reservoir resulting from diagenesis based on the comparison of the single well. According to TOC content, the shale in the study area is divided into organic-rich shale (TOC > 2%), organic shale (1% < TOC < 2%), and organic-poor shale (TOC < 1%). From the cross-plot of porosity and permeability of different lithofacies (**Figure 7B**), the permeability of all three lithofacies is the same, in that the porosity of organic-rich shale is the largest, followed by organic shale, and that of organic-poor shale is the smallest. This shows that the higher TOC content of shale, the more developed the organic porosity and the higher the porosity.

Pore Structure

According to the nitrogen gas adsorption/desorption curves (**Figure 8**), the internal pore structure of the particles has the characteristics of slit-like pores with parallel walls and contains other pores with multiple morphologies. The pores are in an open state and have mainly cylindrical holes with open ends and parallel plate-shaped holes with four sides open. The average pore size of specific surface area (as determined using the method of Barrett, Joyner, and Halenda) (hereafter referred to as BJH) ranges from 2.97 to 8.21 nm (average 5.28 nm). The average diameter of the pores in the Yucan 6 well is the largest (6.58 nm); the average pore diameter in the Zhuoye 1 well is the smallest (3.65 nm) (**Figure 9**). The average pore size of the lower part of the Wufeng-longmaxi Formation was smaller than that of the upper part (**Figure 9**). Pore properties can affect the specific surface area of shale and the relative abundance of micropores. The results of nitrogen adsorption experiments show that the specific surface area (i.e., BET) of the Wufeng–Longmaxi Formation shale is large, ranging from 2.1 to 35.1 m^2/g (average 9.2 m^2/g). Horizontally, the BET-specific surface area of the Zhuoye 1 well is the largest, with a distribution range of 12.1–35.1 m^2/g (20.2 m^2/g on average). The Yucan 6 well BET-specific surface area is the smallest, ranging from 2.8–7.7 m^2/g (5.2 m^2/g on average) (**Figure 9**). Vertically, the BET-specific surface area of the lower Wufeng-longmaxi Formation is relatively large, and the micropores are more developed but gradually decrease upward (**Figure 9**). The Wufeng–Longmaxi Formation shale BJH has a relatively large pore volume, ranging from 0.0012–0.026 ml/g (0.0064 ml/g on average). The BJH pore volume of the Zhuoye 1 well is largest, distributed between 0.0122–0.026 ml/g (average 0.018 ml/g). The BJH pore volumes of the Yushen 7 and Yushen 8 wells are similar in size, with an average of ∼0.0045 ml/g. The BJH pore volume of the Youdi 2 well is the smallest at 0.0012–0.0048 ml/g, with an average of 0.0026 ml/g (**Figure 9**). Among the different types of pores, the mesopore volume (2–50 nm) accounts for 90.8–97.2% of the total pore volume (average 94.9%). Micropores smaller than 2 nm account for 2.8–9.3% (average 5.1%), with almost no large holes (>50 nm) present.

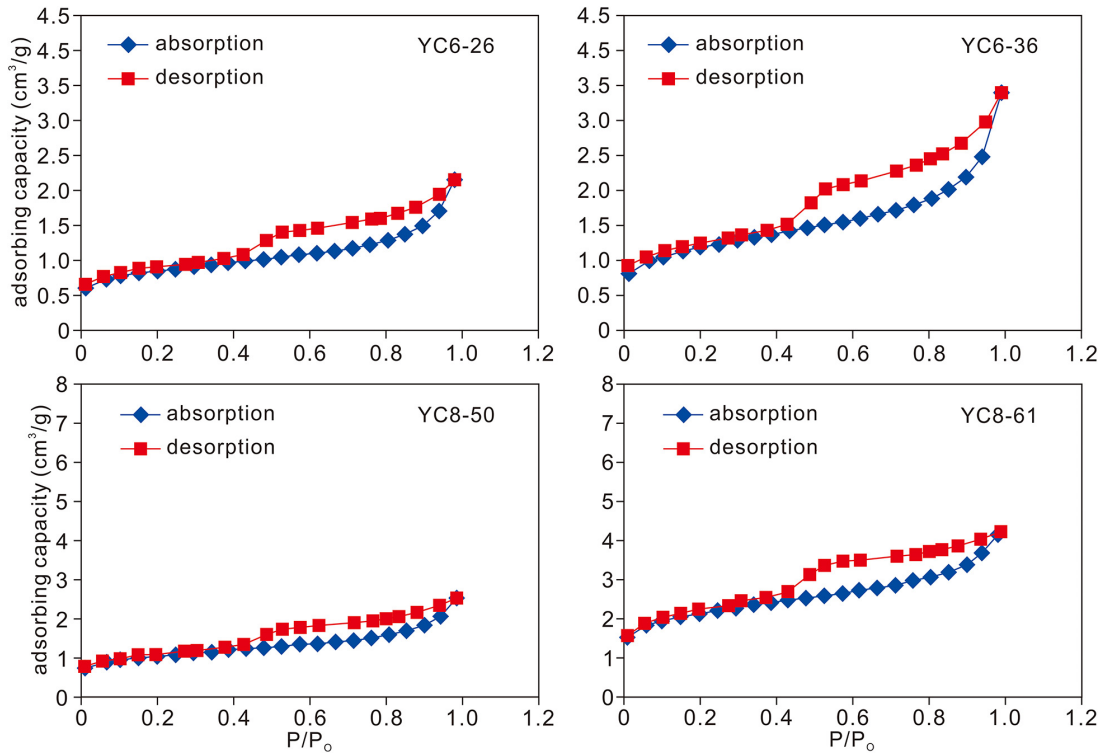

FIGURE 8 | Nitrogen gas adsorption/desorption curves of representative samples from YC 6 well and YC 8 well in the Wufeng–Longmaxi Formation.

DISCUSSION

Mud shale gas reservoirs are self-generating, self-storing, and self-covering. The physical characteristics of the reservoir determine whether it can become an industrial gas flow; however, the physical properties of shale reservoirs are constrained by multiple factors, and identifying the formation mechanisms of reservoir physical characteristics can provide guidance for the determination and categorization of shale gas-favorable areas. The Wufeng–Longmaxi Formation shale reservoir in southeastern Chongqing is of low porosity and low permeability. Structural fractures are the main storage space for shale gas, followed by organic pores. The main factors controlling its physical properties include the sedimentary environment, mineral composition, organic carbon content, and tectonic movement. The difference in the depositional environment determines the changes in the mineral composition and TOC content of the Wufeng–Longmaxi Formation in the southeast and northwest areas of southeastern Chongqing, which controls the anti-compaction ability, degree of fracture development, and organic matter pore ratio of the shale reservoir, as well as the tectonic movement. The depositional environment is a power source that affects the physical properties of shale reservoirs.

Depositional Environment

The Late Cambrian Niutitang Formation was deposited in a neritic-to-slope environment with a weak hydrodynamic and oxygen-deficient reducing environment (Liu et al., 2016a). In the Late Ordovician–Early Silurian period, a famous intracontinental orogeny occurred in the South China Plate (Shu, 2012). During this, the continuous compression of the Yangtze and Cathaysia landmass formed the Middle–Upper Yangtze Craton into a rugged and uneven sedimentary terrain, and a deformed depression area developed in eastern Chongqing and northern Guizhou (Mou et al., 2014). Previous research has been conducted thoroughly on the depositional environment of the Middle–Upper Yangtze Region in the Late Ordovician–Early Silurian period. Mou et al. (2014) proposed that the topographic depression area was a deep-water basin facies in the late Kaidi–Henantian period, which developed black carbonaceous shale and radiolarian siliceous shale. Wang G. et al. (2019) suggested that the late Hernnant period corresponds to the global ice age, which caused an eventual regression of global sea levels, allowing limestone and argillaceous siltstone to be deposited in the Guanyinqiao section. During the Early Silurian period, the climate warmed and the ice caps melted, and this rapid event transgression deposited the graptolite-rich carbonaceous shale at the bottom of the Longmaxi Formation. After that, the area was affected by structural uplift, and the sea level gradually declined. Fan et al. (2019) indicated that northeastern Sichuan entered a rapid transgression stage during the Late Ordovician–Early Silurian period, forming a large-scale and deep-water shelf sedimentary environment. Lower microorganisms began to proliferate in large numbers, and lower planktonic microalgae settled out in the deep-water environment after death, which transformed the deepened

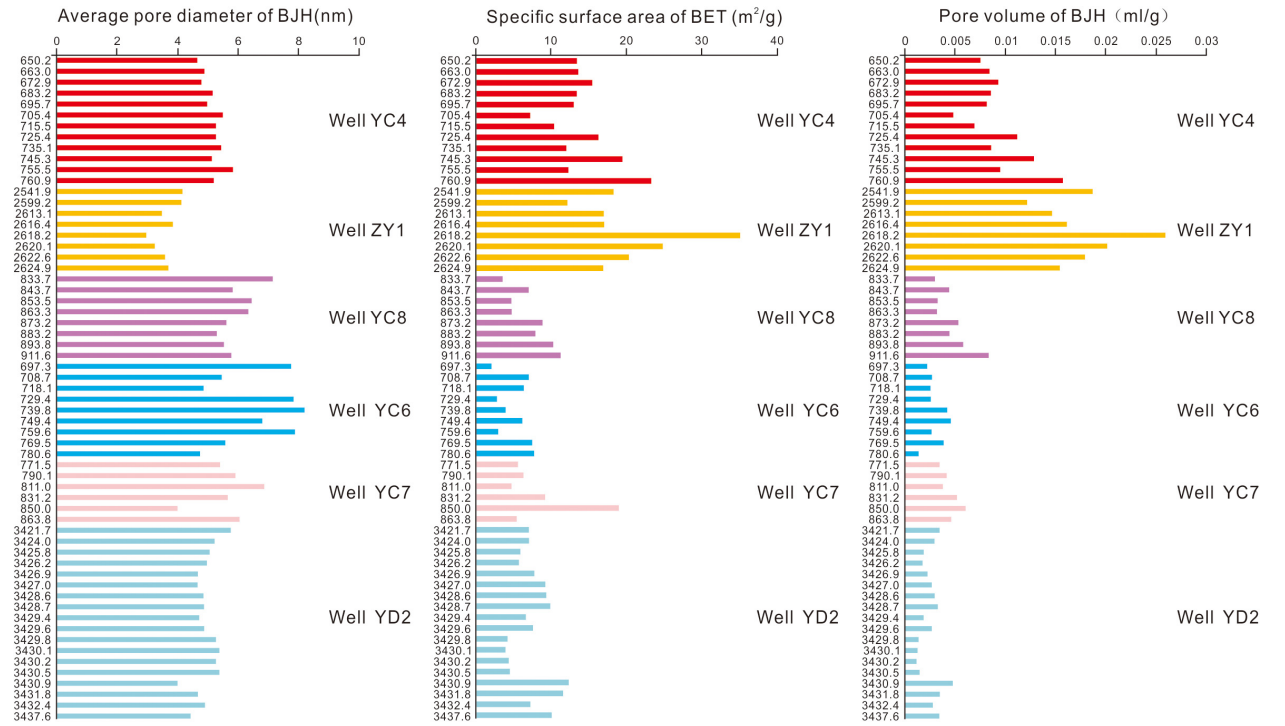

FIGURE 9 | Vertical distribution map of pore parameters in the Wufeng–Longmaxi Formation shale.

and blocked deep-water shelf environment into a reducing environment. This was conducive to the burial and preservation of microbial remains and allowed for organic matter-rich shale layers in this area. Earlier research on the sequence stratigraphy in the Wufeng–Longmaxi Formation in southeast Chongqing showed that the deep-water shelf facies occurred in the Wufeng period. Since the Longmaxi period, the sea level gradually receded to the northwest, and the depositional environment evolved into deep-water shelf, shallow-water shelf, and shallow sandy shelf facies (Liang et al., 2018). In addition, previous researchers have also used geochemical methods to define and further verify the depositional environment. Zhang et al. (2013) used nutrient elements and redox indicators to demonstrate that the bottom of the Longmaxi Formation was deposited in a reducing environment, and the middle–upper spherical chemical indicators were mainly in the oxygen-poor stage, indicating the transition from a reducing to an oxidizing environment. This effectively confirmed that the southeastern Sichuan to northern Guizhou region during the early Longmaxi period mainly experienced deep cementitious shelf deposition and that the middle–late period was a shallow-water shelf depositional environment. Therefore, the high-quality source rocks of the Longmaxi Formation mainly developed at its bottom. Moreover, Fan et al. (2019) have suggested that the Longmaxi Formation in the Dingshan area was deposited in a weakly oxidizing–strongly reducing environment, mainly in sub–high energy and low-energy sedimentary water bodies. Zhou et al. (2011) studied the Mo isotope of the Longmaxi Formation and concluded that the Longmaxi Formation black shale was deposited in an anaerobic-poor environment. Therefore, southeastern Chongqing was in a deep-water shelf and shallow-water shelf environment during the Late Ordovician Wufeng period–Early Silurian–Longmaxi period (**Figure 9**). In addition, the Wufeng–Longmaxi Formation mud shale in the study area has sedimentary characteristics of thickening from the southeast to northwest and increasing sand content from the bottom to top, which may be related to changes in the depositional environment. A set of organic-rich black siliceous shale and carbonaceous shale was deposited at the bottom of the Wufeng and Longmaxi formations in the area, which corresponds well to the deep-water shelf environment; however, the increase in upward sand content and the decrease in organic matter content may be effects of the collision orogeny between the Yangtze and Cathaysia plates, resulting in large-scale northwestward regression (**Figure 10A**). The Youyang–Xiushan area in the southeast of the study area is characterized by thin sediment thickness, low TOC (average 1.69%), and average siliceous mineral content of 35.8%, suggesting that the region may belong to a shallow-water shelf environment (**Figure 10B**). The Beixi Shizhu–Pengshui-Qianjiang area has the characteristics of thick deposit thickness and high TOC, which suggests that it may belong to a deep-water shelf environment (**Figure 10B**) with an average TOC of 3.6% and an average composition of 49% siliceous minerals. Tang et al. (2019) proposed that the Wufeng–Longmaxi Formation deposition center in southeastern Chongqing has high porosity, high TOC, and high quartz content. Based on this, the deposition center is located in the northwest of the study area, and the provenance area may be the Xuefeng Mountain uplift area in

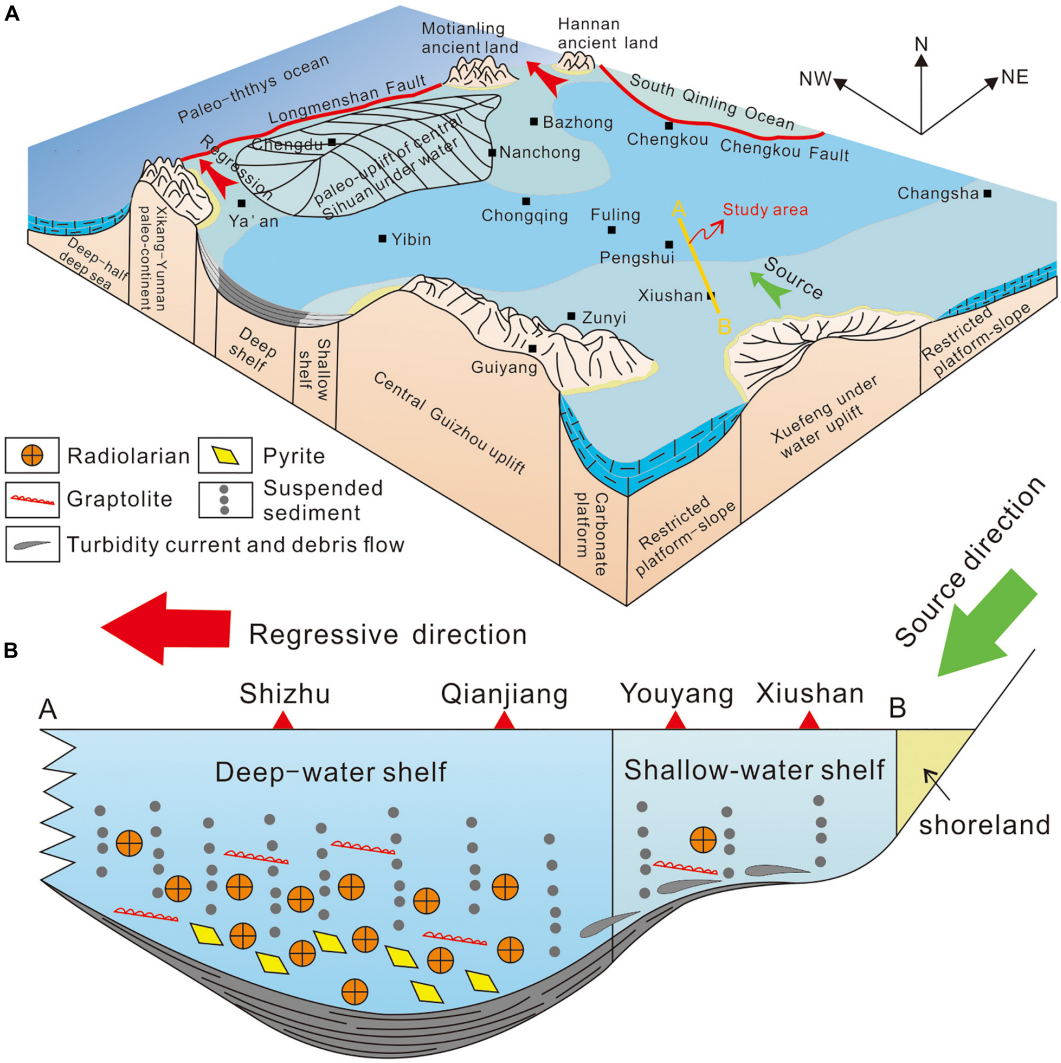

FIGURE 10 | (A) Late Ordovician–Early Silurian sedimentary environment model map of the Sichuan Basin and its periphery (modified from Fan et al., 2019); **(B)** sedimentary environment distribution model map of the Wufeng–Longmaxi Formation in southeastern Chongqing (modified from Liang et al., 2018).

the southeast (**Figure 10B**). Mud shale with high TOC and high brittle mineral content not only has significantly greater adsorption capacity for methane, but it also helps to improve the physical properties of mud reservoirs.

Mineral Composition

The Wufeng–Longmaxi Formation organic-rich shale contains two main mineral groups: brittle minerals and clay minerals, consistent with the viewpoint of Liu et al. (2016b). The brittle minerals are mainly quartz, and the clay minerals are mainly illite and illite/smectite (**Figure 3**). The deep-water anoxic depositional environment is conducive to the complete preservation of microorganisms and plankton. The Wufeng–Longmaxi Formation deposited in the deep-water shelf environment has higher TOC and quartz content (Tang et al., 2019), indicating that SiO_2 mainly comes from the slow sedimentation of seawater rather than terrigenous debris, which is consistent with the view of biogenic siliceous minerals (Guo et al., 2020).

The high content of brittle minerals not only improves the anti-compaction ability of pores but also allows for easier shale fracturing, producing a large number of fractures and microfractures, which is conducive to the preservation of shale gas (oil). According to the statistics of quartz content and fractures in the Longmaxi Formation of the Yucan 8 well from 789 to 860 m (**Figure 11**), there is a clear exponential relationship between the quartz content and fracture line density. The higher the quartz content, the greater the fracture line density. Combined with the characteristics of high permeability but low porosity in the study area (**Figure 7**), this indicates that incompletely filled natural fractures in the shale layer likely improve the permeability of the shale reservoir. Vertically, the bottom of the Wufeng–Longmaxi Formation has a higher content of brittle minerals (**Figures 3A,B**), indicating that the

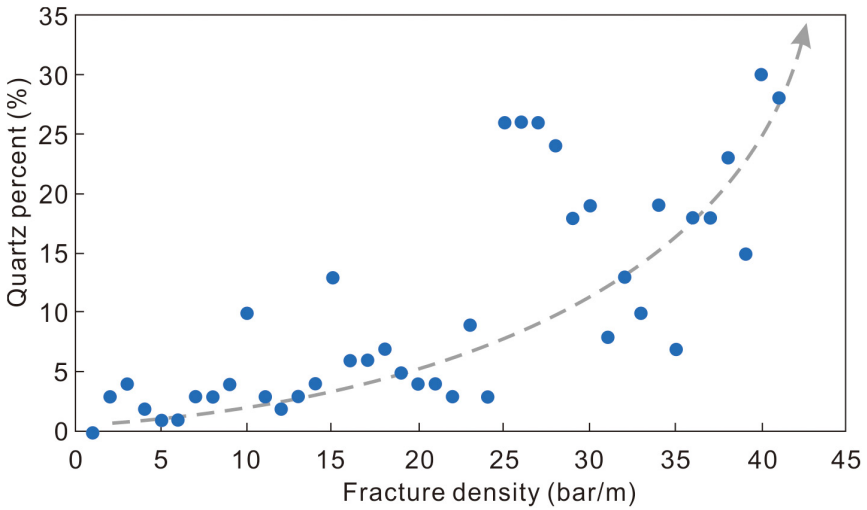

FIGURE 11 | Relationship between fracture development and quartz content in the Longmaxi Formation shale at the Yushen 8 well.

bottom is more prone to fractures and has better permeability. Horizontally, the northwest has the highest content of brittle minerals, and the southeast has the lowest content (**Figure 3C**), indicating that the northwestern area has more developed fractures and better permeability.

Ross and Bustin (2008) suggested that clay minerals in shale gas reservoirs have higher micropore volumes and larger specific surface areas. The analysis of clay minerals, pore volume, and specific surface area in the Longmaxi Formation shale of the Yushen 6 and Yushen 8 wells in southeastern Chongqing in this study shows a definite positive correlation between these characteristics, indicating that the pore-specific surface area and pore volume of organic-rich mud shale vary with the increase in clay mineral content (**Figures 12A,B**). However, the crystal layer and pore structure of different clay minerals are distinct, and the pore-specific surface area is also very different (Ji et al., 2013). The clay minerals contained in the organic-rich shale of the Longmaxi Formation in southeastern Chongqing are mainly illite and an illite/smectite mixed layer (**Figure 3D**). There is a good exponential relationship between the illite/smectite mixed-layer mineral content and the pore volume and specific surface area of the Yushen 6 and Yushen 8 wells (**Figures 12C,D**), indicating that the organic-rich shale pore volume and pore-specific surface area increase as the mineral content of the illite/smectitemixed layer increases. Therefore, the mineral content of the illite/smectite mixed layer is one of the main factors controlling the microscopic pore volume and pore-specific surface area of the organic-rich shale of the Longmaxi Formation.

TOC Content

The TOC content of shale is an important parameter for measuring the hydrocarbon-generation potential of source rocks, and also an important controlling factor for the development of organic matter pores. A large number of nano-scale pores develop in organic matter, providing the specific surface area and pore volume (Bustin et al., 2008). From this study, according to the correlation analysis between the TOC and the specific surface area and pore volume of the Longmaxi Formation in southeastern Chongqing (**Figures 13A,B**), TOC has a significant positive correlation with both characteristics, indicating that as the TOC value increases, the pore volume and pore-specific surface area of organic-rich shale also increase accordingly. Generally, organic matter pores have a complicated internal structure with rough pore surfaces and diverse internal morphologies. This special structure can increase the specific surface area and pore volume, thereby improving the adsorption and storage capacity. The lower part of the Wufeng–Longmaxi Formation in the study area has a high TOC content which gradually decreases upward. In addition, the TOC content in the northwest is high (>2.4%), and that in the southeast is low. The corresponding specific surface area and pore volume also have the same characteristics (**Figure 8**). Therefore, TOC is one of the important factors controlling the micropores of organic-rich shale in the Longmaxi Formation, which plays an important role in shale gas enrichment.

In addition, TOC can also control the development of shale fractures to a certain extent. This is mainly due to the fact that the deep-water reduced depositional environment could completely preserve siliceous organisms (such as radiolarians) and biological skeleton remains, which increases the siliceous content of shale reservoirs. Shales with high organic matter and quartz content are more brittle, making it easy to form natural fractures and induce fractures under tectonic stress, which is conducive to the desorption of shale gas as well as free gas accumulation and seepage. According to the correlation statistics between the fracture line density and TOC in the Yucan 7 well (**Figure 13C**), the TOC is lower than 1.6% in the 786–836 m well section, the fracture line density and TOC are not high, and there is no obvious change trend. In the 838–849 m well section, the organic matter content is between 1.6 and 2.5%, and the fracture line density increases from 13 to 28 lines/m, indicating that, when the TOC is greater than 1.6%, the fracture density is largely

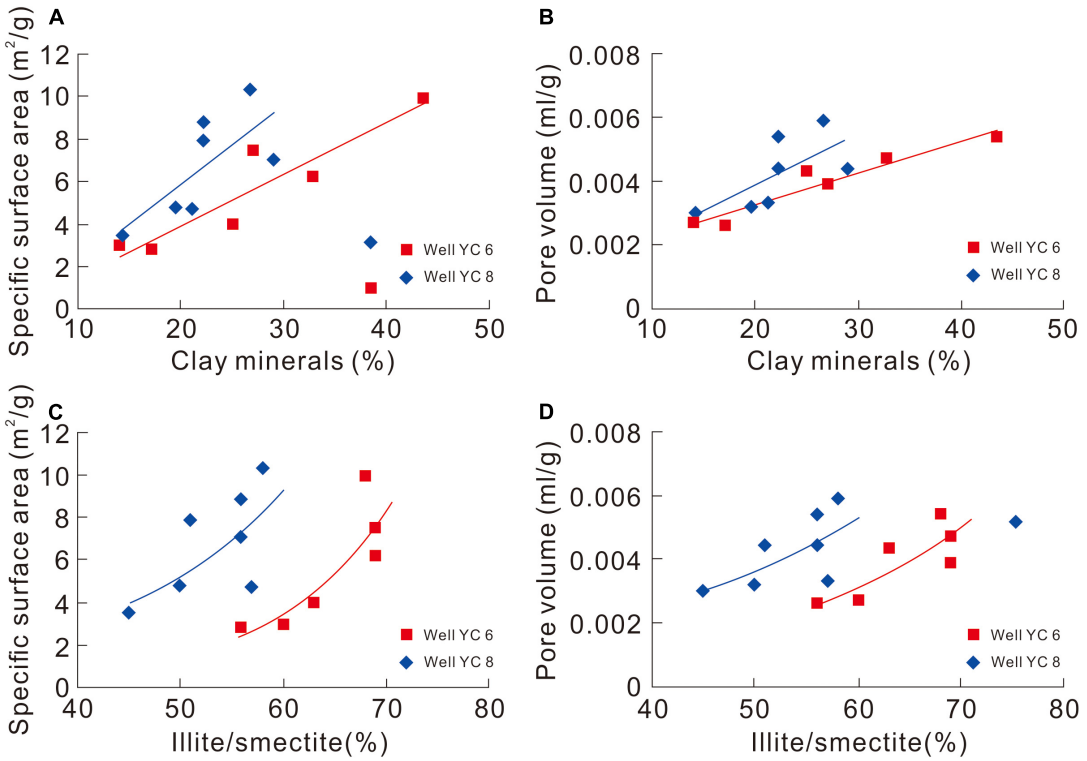

FIGURE 12 | (A,B) Correlation diagram of the clay mineral content, specific surface area, and pore volume of the Longmaxi Formation shale in southeastern Chongqing; **(C,D)** correlation diagram of the mineral content, specific surface area, and pore volume of the shale illite/smectite layer of the same formation.

affected by the TOC changes. Regarding the regional tectonics, Tang et al. (2019) proposed that the natural fractures in the upper Yangtze area mainly developed in the Qiyaoshan fault zone in the northwest and the Xuefengshan fault zone in the southeast. The TOC content was the highest (>2.4) in the northwest of the study area and was low in the southeast, which has a good corresponding relationship with the fracture development area. Therefore, the TOC can affect the physical properties of shale reservoirs by controlling the degree of fracture development.

Tectonic Movement

Shale gas belongs to the "self-generation and self-storage" accumulation model. Based on the characteristics of rock compactness of the study area, as well as the low porosity, degree of development, and distribution characteristics of fractures, these factors can have important geological significance for the accumulation and preservation of shale gas. However, tectonic movement has a larger significance on the reformation of the reservoir, in dual effect. On one hand, uplifting and squeezing are beneficial to the formation of fractures, increasing the storage space, connecting isolated pores, and constituting the main channel for shale gas desorption and flow. On the other hand, tectonic movement can also destroy the reservoir structure, transforming structural fractures into channels for shale gas to escape, causing the shale reservoirs to be invalidated. Therefore, determining whether the tectonic movement has been constructive or destructive to the Wufeng–Longmaxi Formation high-quality shale reservoir in southeastern Chongqing is a particularly important question.

Southeastern Chongqing has undergone multiple periods of tectonic movement after the deposition during the Early Silurian, presenting an NNE-trending tectonic pattern and developing a large number of fault zones. Combined with the characteristics of rich brittle minerals in the Wufeng–Longmaxi Formation, a large number of structural fractures have easily formed. The Wufeng–Longmaxi shales in the southeastern Chongqing show high porosity and permeability resulting from the developed pores and fracture systems (Liu et al., 2017b). Wu et al. (2011) predicted the fracture distribution in the black shale of the Longmaxi Formation in southeastern Chongqing and divided the fracture-favorable areas into three types. The first type of fracture-favorable area is mostly located in the large-scale fault development area and the axis of the anticline; the second type is located in the vicinity of some secondary faults and the axis of the syncline; and the third type is mostly located on the two wings of anticlines and synclines as well as on some small synclines and anticlines with weak structural deformations. Tang et al. (2019) indicated that a large number of natural fractures developed around the Qiyaoshan and Xuefengshan fault zones, which agrees with the findings of Wu et al. (2011).

The well-known large-scale Fuling shale gas field is the result of overpressure accumulation. Overpressure is a direct sign of a well-preserved shale gas reservoir, and the thermal evolution of organic matter and the pressurization of hydrocarbon generation

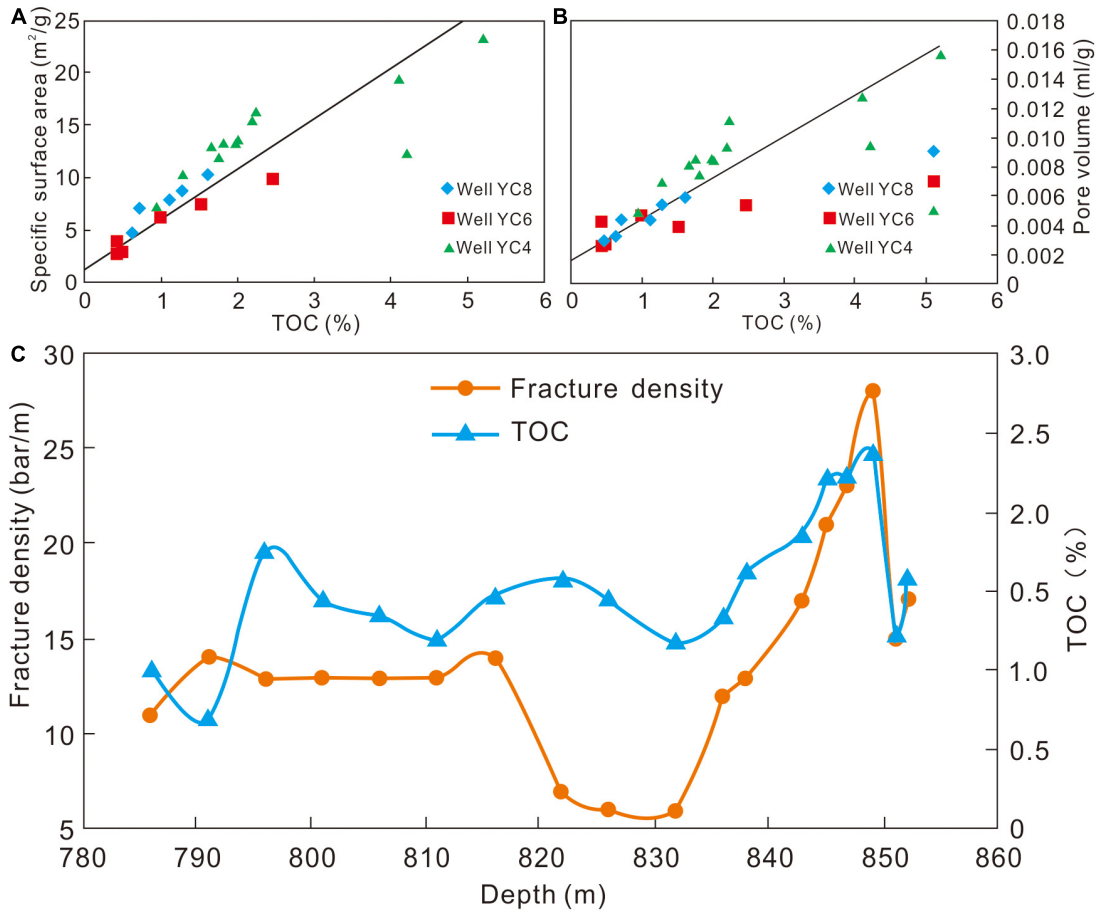

FIGURE 13 | (A,B) Correlation between the TOC and the specific surface area and pore volume of the Longmaxi shale in southeastern Chongqing; **(C)** correlation between the vertical fracture development and TOC of the Longmaxi shale at the Yushen 7 well.

are the main reasons for the abnormally high pressure in this area (Gao et al., 2019; Wang Q. et al., 2019). However, the Wufeng–Longmaxi Formation in the Pengshui area of southeastern Chongqing is under normal pressure, with a pressure coefficient between 0.8 and 1.2 (He X. et al., 2017). Nie et al. (2019) suggested that atmospheric shale gas reservoirs can be divided into four main types: (i) high-quality shale missing/thinning, (ii) early escape, (iii) fault failure, and (iv) residual syncline types, and their distribution and enrichment are mainly controlled by tectonic processes. Li et al. (2016) proposed that early and late tectonic uplift, the superimposition of multi-stage stress fields, and the development of high-angle fractures are the controlling factors that affect the maintenance of shale gas overpressure in the later stages. Yuan et al. (2020) then studied the atmospheric formation mechanism of the Longmaxi Formation in Pengshui and revealed that the Longmaxi Formation shale gas reservoir experienced overpressure during its geological development period. During the uplifting process, an overpressure rupture occurred, resulting in fractures that led to the loss of shale gas and the release of overpressure, transitioning the area from overpressure to normal pressure. It is therefore unclear why the Fuling and Pengshui areas are located so geographically close together with starkly opposing accumulation environments. One explanation may be related to the fact that since the Late Jurassic period, the South China Plate has been affected by the subduction of the Pacific slab, causing an intracontinental uplift movement from the southeast to northwest (Shu, 2012). The southeastern area of Chongqing is located in the periphery of the Sichuan Basin; therefore, it was uplifted and suffered strong denudation and deformation at ∼125 Ma. That tectonic movement was relatively long-lived, leading to the destruction of the preservation conditions of the Wufeng–Longmaxi Formation shale reservoir (Fan et al., 2019). However, the Fuling Jiaoshiba is located in the Sichuan Basin, and the structural uplift occurred at ∼80 Ma, with short duration, weak deformation, and thin denudation thickness (Fan et al., 2019). Therefore, it is likely that earlier structural uplift and longer-term and more intense denudation and deformation are the main factors that caused the two completely opposite accumulation environments. The structural fractures that have often developed in southeastern Chongqing are generally destructive to shale reservoirs.

Nevertheless, some structural fractures in southeastern Chongqing still exhibit constructive performance. As mentioned above, the Wufeng–Longmaxi Formation in southeastern

Chongqing is divided into three sections, of which the optimal section for comprehensive evaluation of shale gas enrichment conditions is the first section: the black organic shale section at the bottom of the formation. An obvious detachment zone can be seen in the first section of the Wufeng–Longmaxi Formation in the Yucan 4 and Yucan 6 wells, and obvious scratches, steps, or smooth mirror surface characteristics can be seen in the core observations with well-developed fractures (**Figures 5B–D**). In addition, the on-site analytical gas content of the Wufeng–Longmaxi Formation in the Yucan 4 well is 0.96–2.7 m^3/t, with an average of 1.62 m^3/t, indicating that fractures still have a beneficial effect on the gas-bearing properties of shale and confirming the constructive effect of fracture development on shale gas enrichment.

CONCLUSION

The Wufeng–Longmaxi Formation mud shales in the northwestern part of the study area have a higher content of brittle minerals and organic carbon than those in the southeastern part in the southeastern Chongqing. The types of storage spaces include organic pores, clay mineral interlayer pores, intergranular pores, intragranular pores, and structural fractures. The high-quality shale reservoir is located in the lower part of the Wufeng–Longmaxi Formation, and features low porosity and low permeability. Tectonic fractures are the main shale gas storage spaces, and effectively improve the permeability of the reservoir to a certain extent.

The depositional environment, mineral component, TOC content, and tectonic movement are the main factors that cause the obvious differences from shale gas productions in the Jiaoshiba area. The deep-water anoxic depositional environment is conducive to the complete preservation of organic matter and has an important effect on improving the pores of organic matter and the brittleness of rocks. A high content of quartz was found to improve the rock compression resistance, brittleness, and a high proportion of clay minerals was found to enhance the interlayer pores of clay minerals. Specific surface area, pore volume, and degree of fracture development all have a positive correlation with the TOC content. As the most important factor controlling the shale reservoir environment of normal-pressure accumulation, tectonic movement destroyed the original overpressure accumulation that would have been similar to that of the modern Jiaoshiba area, yet also improved the permeability of the reservoir. Overall, tectonic movement was ultimately destructive to the reservoir.

DATA AVAILABILITY STATEMENT

The original contributions presented in the study are included in the article/supplementary material, further inquiries can be directed to the corresponding author/s.

AUTHOR CONTRIBUTIONS

JinW completed the writing and editing of the manuscript. XT and JiaW focused on the scientific issues involved in the manuscript. HZ, YZ, and DG were responsible for the physical property analysis of shale reservoir involved in the manuscript. XW, ZL, CZ, and GY have carried out the data analysis of shale mineral composition and sedimentary environment. All authors contributed to the article and approved the submitted version.

FUNDING

We are grateful to all teachers at the Chongqing University of Science and Technology for the analysis and guidance of experimental samples. This work was financially supported by the National Science Foundation of China (Grant Numbers 42072140 and 41502150), Natural Science Foundation Project of CQ CSTC (Grant Numbers cstc2018jcyjAX0523 and cstc2020jcyj), the Performance Incentive and Guidance Project for Scientific Research Institutions in Chongqing (Grant Number cstc2020jxjlX0002), the Special Project of performance incentive and guidance for scientific research institutions in Chongqing (Grant Number cstc2019jxjl90001), and the Pre-project of Chongqing Shale Gas Exploration and Development Company Limited (Grant Number CYS-FW-2020-0047).

ACKNOWLEDGMENTS

We thank our scientific research team for their help and guidance in the field investigation.

REFERENCES

Barratt, E., Joyner, L., and Halenda, P. (1951). The determination of pore volume and area distributions in porous substances. I.Computations from nitrogen isotherms. *J. Manag. Eng.* 24, 373–380. doi: 10.1021/ja01145a126

Brunauer, S., Emmet, P., and Teller, E. (1938). Adsorption of gases in multimolecular layers. *J. Am. Chem. Soc.* 60, 309–319. doi: 10.1021/ja01269a023

Bustin, R., Bustin, A., Cui, X., Ross, D., and Pathi, V. (2008). Impact of shale properties on pore structure and storage characteristics. *Paper Presented at the Society of Petroleum Engineers shale Gas Production Conference in Fort Worth, Texas, SPE Paper 119892*, Fort Worth, TX.

Chen, X., Fan, J., Zhang, Y., Wang, D., Chen, Q., Wang, W., et al. (2015). Subdivision and delineation of the Wufeng and Lungmachi black shales in the subsurface areas of the Yangtze platform. *J. Stratigr.* 39, 351–358.

Dai, J., Ni, Y., Gong, D., Feng, Z., and Han, W. (2017). Geochemical characteristics of gases from the largest tight sand gas field (Sulige) and shale gas field (Fuling) in China. *Mar. Petrol. Geol.* 79, 426–438. doi: 10.1016/j.marpetgeo.2016.10.021

Fan, C., Zhong, C., Zhang, Y., Qin, Q., and He, S. (2019). Geological factors controlling the accumulation and high yield of marine–facies shale gas: case study of the wufeng– longmaxi formation in the dingshan area of southeast sichuan china. *Acta Geol. Sin. (Eng. Ed.)* 3, 536–560. doi: 10.1111/1755-6724.13857

Gao, J., Zhang, J., He, S., Zhao, J., He, Z., Wo, J., et al. (2019). Overpressure generation and evolution in Lower Paleozoic gas shales of the Jiaoshiba region

China: implications for shale gas accumulation. *Mar. Petrol. Geol.* 102, 844–859. doi: 10.1016/j.marpetgeo.2019.01.032

Gou, Q., and Xu, S. (2019). Quantitative evaluation of free gas and adsorbed gas content of Wufeng-Longmaxi shales in the Jiaoshiba area, Sichuan Basin, China. *Adv. Geo Ener. Res.* 3, 258–267. doi: 10.26804/ager.2019.03.04

Guo, T., and Zhang, H. (2014). Formation and enrichment mode of jiaoshiba shale gas field Sichuan Basin. *Petrol. Expl. Dev.* 41, 28–36. (in Chinese).

Guo, X. (2014). Rules of two-factor enrichment for marine shale gas in southern china—understanding from the longmaxi formation shale gas in sichuan basin and its surrounding area. *Acta Geol. Sin.* 88, 1209–1218. (in Chinese).

Guo, X., Hu, D., Li, Y., Liu, R., and Wang, Q. (2014a). Geological features and reservoiring mode of shale gas reservoirs in longmaxi formation of the jiaoshiba area. *Acta Geol. Sin. (Eng. Ed.)* 88, 1811–1821. doi: 10.1111/1755-6724.12347

Guo, X., Hu, D., Wen, Z., and Liu, R. (2014b). Major factors controlling the accumulation and high productivity in marine shale gas in the Lower Paleozoic of Sichuan Basin and its periphery: a case study of the Wufeng-Longmaxi Formation of Jiaoshiba area. *Geol. China* 41, 893–901. (in Chinese).

Guo, X., Li, Y., Tenger, B., Wang, Q., Yuan, T., Shen, B., et al. (2020). Hydrocarbon generation and storage mechanisms of deep–water shelf shales of Ordovician Wufeng Formation–Silurian Longmaxi Formation in Sichuan Basin China. *Petrol. Explor. Dev.* 47, 1–9. (in Chinese).

He, X., Gao, Y., Tang, X., Zhang, P., and He, G. (2017). Analysis of major factors controlling the accumulation in normal pressure shale gas in the southeast of Chongqing. *Nat. Gas Geosci.* 28, 654–664. (in Chinese).

He, Z., Hu, Z., Nie, H., Li, S., and Xu, J. (2017). Characterization of shale gas enrichment in the Wufeng Formation–Longmaxi Formation in the Sichuan Basin of China and evaluation of its geological construction–transformation evolution sequence. *J. Nat. Gas Geosci.* 28, 724–733. (in Chinese).

He, Z., Nie, H., and Zhang, Y. (2016). The main factors of shale gas enrichment of Ordovician Wufeng Formation–Silurian Longmaxi Formation in the Sichuan Basin and its adjacent area. *Earth Sci. Front.* 23, 8–17. (in Chinese).

Ji, L., Qiu, J., and Xia, Y. (2013). Micro-pore characteristics and methane adsorption properties of common clay minerals by electron microscope scanning. *Acta Petrol. Sin.* 2, 249–256.

Jiang, S., Peng, Y., Gao, B., Zhang, J., Cai, D., Xue, G., et al. (2016). Geology and shale gas resource potentials in the Sichuan Basin China. *Ener. Explor. Expl.* 34, 689–710. doi: 10.1177/0144598716657442

Jin, Z., Nie, H., Liu, Q., Zhao, J., and Jiang, T. (2018). Source and seal coupling mechanism for shale gas enrichment in upper Ordovician Wufeng Formation – Lower Silurian Longmaxi Formation in Sichuan Basin and its periphery. *Mar. Petrol. Geol.* 97, 78–93. doi: 10.1016/j.marpetgeo.2018.06.009

Li, S., Yuan, Y., Sun, W., Sun, D., and Jin, Z. (2016). The formation and destroyment mechanism of shale gas overpressure and its main controlling factors in Silurian of Sichuan Basin. *Nat. Gas Geosci.* 27, 924–931. (in Chinese).

Liang, M., Tan, X., Chen, X., Wang Ran, T., Wang, P., Tan, D., et al. (2018). Sequence stratigraphy of Wufeng–Longmaxi Formation in the southeastern Chongqing area and its geological significance. *Coal Geol. Explor.* 46, 40–51. (in Chinese).

Liu, J., Yao, Y., Elsworth, D., Liu, D., Cai, Y., and Dong, L. (2017a). Vertical heterogeneity of the shale reservoir in the lower Silurian Longmaxi Formation: Analogy between the southeastern and northeastern Sichuan Basin, SW China. *Minerals* 7:151. doi: 10.3390/min7080151

Liu, J., Yao, Y., Elsworth, D., Pan, Z., Sun, X., and Ao, W. (2016a). Sedimentary characteristics of the Lower Cambrian Niutitang shale in the southeast margin of Sichuan Basin, China. *J. Nat. Gas Sci. Eng.* 36, 1140–1150. doi: 10.1016/j.jngse.2016.03.085

Liu, J., Yao, Y., Liu, D., Pan, Z., and Cai, Y. (2017b). Comparison of three key marine shale reservoirs in the southeastern margin of the Sichuan basin, SW China. *Minerals* 7:179. doi: 10.3390/min7100179

Liu, J., Yao, Y., Zhu, Z., Cheng, L., and Wang, G. (2016b). Experimental investigation of reservoir characteristics of the upper Ordovician Wufeng Formation shale in middle–upper Yangtze region, China. *Ener. Explor. Expl.* 34, 527–542. doi: 10.1177/0144598716650553

Luo, Q., Zhong, N., Dai, N., and Zhang, W. (2016). Graptolite-derived organic matter in the Wufeng–Longmaxi Formations (Upper Ordovician–Lower Silurian) of southeastern Chongqing China: implications for gas shale evaluation. *Int. J. Coal Geol.* 153, 87–98. doi: 10.1016/j.coal.2015.11.014

Lv, D. W., Li, Z. X., Wang, D. D., Li, Y., Liu, H. Y., Liu, Y., et al. (2019). Sedimentary model of coal and shale in the paleogene lijiaya formation of the huangxian basin: insight from petrological and geochemical characteristics of coal and shale. *Ener. Fuels* 33, 10442–10456. doi: 10.1021/acs.energyfuels.9b01299

Lv, D. W., Song, Y., Shi, L. Q., Wang, Z. L., Cong, P. Z., and Loon, A. J. V. (2020). The complex transgression and regression history of the northern margin of the Palaeogene Tarim Sea (NW China), and implications for potential hydrocarbon occurrences. *Mar. Petrol. Geol.* 112:104041. doi: 10.1016/j.marpetgeo.2019.104041

Mou, C., Ge, X., Xu, X., Zhou, K., Liang, W., and Wang, X. (2014). Lithofacies palaeogeography of the late ordovician and its petroleum geological significance in middle-upper yangtze region. *J. Palaeogeogr.* 16, 427–440. (in Chinese).

Mu, C., Zhou, K., and Liang, W. (2011). Early paleozoic sedimentary environment of hydrocarbon source rocks in the middle–upper yangtze region and petroleum and gas exploration. *Acta Geol. Sin.* 85, 526–532. (in Chinese).

Nie, H., Jin, Z., Bian, R., and Du, W. (2016). The "source-cap hydrocarbon-controlling" enrichment of shale gas in Upper Ordovician Wufeng Formation-Lower Silurian Longmaxi Formation of Sichuan Basin and its periphery. *Acta Petrol. Sin.* 37, 557–571. (in Chinese).

Nie, H., Wang, H., He, Z., Wang, R., Zhang, P., and Peng, Y. (2019). Formation mechanism distribution and exploration prospect of normal pressure shale gas reservoir: a case study of Wufeng-Longmaxi Formation in Sichuan Basin and its periphery. *Acta Petrol. Sin.* 40, 131–143. (in Chinese).

Pan, R., Gong, Q., Yan, J., and Jin, J. (2016). Elements and gas enrichment laws of sweet spots in shale gas reservoir: a case study of the Longmaxi Fm in Changning Block, Sichuan Basin. *Nat. Gas Industr. B* 3, 195–201. doi: 10.1016/j.ngib.2016.05.003

Pu, B., Jiang, Y., Wang, Y., Bao, S., and Liu, X. (2010). Reservoirforming conditions and favorable exploration zones of shale gas in lower Silurian Longmaxi formation of Sichuan Basin. *Acta Petrol. Sin.* 31, 225–230. (in Chinese).

Ross, D., and Bustin, R. (2008). Characterizing the shale gas resource potential of Devonian–Mississippian strata in the Western Canada sedimentary basin: application of an integrated formation evaluation. *AAPG Bull.* 92, 87–125. doi: 10.1306/09040707048

Shen, J., Yang, J., Zhou, F., Zhang, J., Yang, G., Qiu, Y., et al. (2013). Study of kerogen type index through the calculation of organic elements. *J. North. Petrol. Univ.* 37, 24–31.

Shu, L. (2012). Liangshu. an analysis of principal features of tectonic evolution in South China Block. *Geol. Bull. China* 31, 1035–1053. (in Chinese).

Su, W., Li, Z., Ettensohn, F., Johson, M., Huff, W., Wang, W., et al. (2007). Tectonic and eustatic control on the distribution of black–shale source beds in the Wufeng and Longmaxi formations (Ordovician–Silurian), South China. *Front. Earth Sci. China* 1, 470–481. doi: 10.1007/s11707-007-0058-6

Tan, L., Xu, Y., Li, D., Cheng, L., and Zeng, C. (2015). Geological condition of shale gas accumulation and favorable area prediction for the wufeng-longmaxi formations in southeastern chongqing. *Acta Geol. Sin.* 89, 1308–1317. (in Chinese).

Tang, X., Jiang, S., Jiang, Z., Li, Z., He, Z., and Zhu, D. (2019). Heterogeneity of paleozoic wufeng–longmaxi formation shale and its effects on the shale gas accumulation in the Upper Yangtze Region China. *Fuel* 239, 387–402. doi: 10.1016/j.fuel.2018.11.022

Wang, G., Zhu, T., Wang, H., Wu, J., Du, W., Feng, D., et al. (2019). Integrated Sequence stratigraphic division and vertical distribution characteristics of marine shale: a case study of the wufeng formation–longmaxi formation in southeastern sichuan basin. *Acta Sedimentol. Sin.* 37, 330–344. (in Chinese).

Wang, H., Liu, Y., Dong, D., Zhao, Q., and Du, D. (2013). Scientific issues on effective development of marine shale gas in southern China. *Petrol. Explor. Dev.* 40, 574–579. (in Chinese).

Wang, Q., Wei, X., Wei, F., Yan, J., and Wan, L. (2019). Overpressure in shale gas reservoirs of Wufeng–Longmaxi formations Fuling area southeastern Sichuan Basin. *Petrol. Geol. Exp.* 41, 333–340. (in Chinese).

Wang, R. Y., Hu, Z. Q., Long, S. X., Zhao, J. H., Dong, L., Du, W., et al. (2019). Differential characteristics of the Upper Ordovician-Lower Silurian Wufeng-Longmaxi shale reservoir and its implications for exploration and development of shale gas in/around the Sichuan Basin. *Acta Geol. Sin. (Eng. Ed.)* 93, 520–535. doi: 10.1111/1755-6724.13875

Wang, R. Y., Nie, H. K., Hu, Z. Q., Liu, G. X., Xi, B. B., and Liu, W. X. (2020). Controlling effect of pressure evolution on shale reservoirs: a case study of the

Wufeng-Longmaxi Formation in the Sichuan Basin. *Nat. Gas Indust.* 40, 1–11. (in Chinese).

Wang, S., Jiao, W., Fang, G., Wang, F., Zhang, Z., Wang, Q., et al. (2017). Geochemical features and genesis of shale gas of Wufeng–Longmaxi formation in southeastern chongqing. *Mar. Origin Petrol. Geol.* 22, 77–84. (in Chinese).

Wang, Z. (2015). Breakthrough of Fuling shale gas exploration and development and its inspiration. *Oil Gas Geol.* 36, 1–6. (in Chinese).

Wu, L., Ding, W., Zhang, J., Li, Y., Zhao, S., and Hu, L. (2011). Fracture prediction of organic–enriched shale reservoir in lower silurian longmaxi formation of southeastern chongqing area. *J. Oil Gas Technol.* 33, 43–46. (in Chinese).

Xie, C., Zhang, J., Li, Y., and Wang, X. (2013). Characteristics and gas content of the lower cambrian dark shale in well yuke 1 southeast chongqing. *Oil Gas Geol.* 34, 11–15. (in Chinese).

Xu, E., Li, Z., and Yang, Z. (2015). Thermal and hydrocarbon generation history of Wufeng and longmaxi shales in pengshui area eastern sichuan basin: a well PY1 case study. *Etrol. Geol. Exp.* 37, 494–499. (in Chinese).

Yuan, Y., Fang, Z., He, X., Li, S., Peng, Y., and Long, S. (2020). Normal pressure formation mechanism of longmaxi shale gas in Pengshui and its adjacent areas. *Reserv. Eval. Dev.* 10, 9–16. (in Chinese).

Zhang, C., Jiang, Z., Guo, Y., and Zhang, W. (2013). Geochemical Characteristics and paleoenvironment reconstruction of the longmaxi formation in southeast sichuan and northern guizhou. *Geol. Sci. Technol. Inform.* 32, 124–130. (in Chinese).

Zhao, D., Guo, Y., Wang, G., Bai, W., Zeng, C., Jiao, W., et al. (2020). Sedimentary characteristics of shales graptololite and Its implications for high–quality shale gas reservoirs in the Wufeng-Longmaxi formation shales in southeast Chongqing. *J. Henan Polyt. Univ. (Nat. Sci.)* 39, 26–36. (in Chinese).

Zhou, L., Su, J., Huang, J., Yan, J., Xie, X., Gao, S., et al. (2011). A new paleoenvironmental index for anoxic events—Mo isotopes in black shales from Upper Yangtze marine sediments. *Sci. China Earth Sci.* 41, 309–317. (in Chinese).

Zhou, S., Ning, Y., Wang, H., Liu, H., and Xue, H. (2018). Investigation of methane adsorption mechanism on Longmaxi shale by combining the micropore filling and monolayer coverage theories. *Adv. Geo Ener. Res.* 2, 269–281. doi: 10.26804/ager.2018.03.05

Conflict of Interest: ZL was employed by the Chongqing Shale Gas Exploration and Development Company Limited and GY was employed by the China Huaneng Group Co., Ltd.

The remaining authors declare that the research was conducted in the absence of any commercial or financial relationships that could be construed as a potential conflict of interest.

frontiers in Earth Science

ORIGINAL RESEARCH
published: 12 May 2021
doi: 10.3389/feart.2021.664629

The Effect of Multi-Scale Faults and Fractures on Oil Enrichment and Production in Tight Sandstone Reservoirs: A Case Study in the Southwestern Ordos Basin, China

Lianbo Zeng[1,2], Wenya Lyu[1,2], Yunzhao Zhang[1,2], Guoping Liu[1,2] and Shaoqun Dong[1,2,3]*

[1] State Key Laboratory of Petroleum Resources and Prospecting, China University of Petroleum, Beijing, China, [2] College of Geosciences, China University of Petroleum, Beijing, China, [3] College of Science, China University of Petroleum, Beijing, China

OPEN ACCESS

Edited by:
Dawei Lv,
Shandong University of Science and Technology, China

Reviewed by:
Hu Li,
Southwest Petroleum University, China
Shuai Yin,
Xi'an Shiyou University, China

***Correspondence:**
Lianbo Zeng
lbzeng@sina.com

Specialty section:
This article was submitted to Sedimentology, Stratigraphy and Diagenesis, a section of the journal Frontiers in Earth Science

Received: *09 February 2021*
Accepted: *07 April 2021*
Published: *12 May 2021*

Citation:
Zeng L, Lyu W, Zhang Y, Liu G and Dong S (2021) The Effect of Multi-Scale Faults and Fractures on Oil Enrichment and Production in Tight Sandstone Reservoirs: A Case Study in the Southwestern Ordos Basin, China. Front. Earth Sci. 9:664629. doi: 10.3389/feart.2021.664629

The Chang 8 Member of the Upper Triassic Yanchang Formation in the southwestern Ordos Basin is a typical tight sandstone reservoir and has an average porosity of 8.60% and air permeability 0.20 mD. Multi-scale faults and fractures are widely developed in these reservoirs. In this study, three-dimensional seismic data, outcrops, cores, imaging logs, and thin sections were used to classify faults and fractures at multiple scales. Combined with the oil production data, the influence of multi-scale faults and fractures on the oil enrichment and production was analyzed. The results show multi-scale faults and fractures can be divided into six levels: type-I faults, type-II faults, large-scale fractures, mesoscale fractures, small-scale fractures, and micro-scale fractures. As the scale decreases, the number of fractures increases in a power function. Type-I faults cut the caprocks and are not conducive to the preservation of oil. Type-II faults connect the source rocks and reservoirs and are migration channels of the oil source. Large-scale fractures cut the mudstone interlayer and are the seepage channel inside the reservoir. Mesoscale fractures are controlled by thick interlayers, and small-scale fractures are restricted by thin interlayers or layer interfaces. These fractures are the main seepage channels and effective storage spaces. Micro-scale fractures serve as important storage spaces for these reservoirs. The case study of oil reservoir development proves that type-I faults have the greatest impact on fluid flow, while wells drilled into the type-II faults zone have a higher oil production capacity. The oil production changes with the development degree of fractures in different scales, strikes, and positions of faults. Meso- and small-scale fractures are the key to influencing the early single-well production, and micro-scale fractures are conducive to the stable production of single wells. Consequently, multi-scale faults and fractures have significantly different effects on the oil enrichment and production of tight sandstone reservoirs, and the research conclusions can guide to the exploration and development of such similar reservoirs.

Keywords: multi-scale faults and fractures, oil enrichment and production, tight sandstone reservoir, Yanchang formation, Ordos Basin

INTRODUCTION

Tight sandstones of the Upper Triassic Yanchang Formation with a matrix permeability of less than 0.1 mD under subsurface conditions are the primary targets for tight oil exploration and development in the Ordos Basin (Han et al., 2017; Jia, 2017). These tight sandstone reservoirs have low porosity and permeability, strong heterogeneity, and widely developed natural fractures (Ameen et al., 2012; Gong et al., 2019). Natural fractures, which can provide effective storage space and improve the seepage capacity, are an essential factor influencing the oil and gas distribution in tight sandstone reservoirs (Laubach et al., 2010; Zeng et al., 2013; Liu et al., 2020a). Therefore, the study of natural fractures is of great significance to the exploration and development of tight oil and gas.

The development and distribution of natural fractures are controlled by rock mechanical units (Gross et al., 1995; Strijker et al., 2012; Liu et al., 2020b). Differences in the mechanical properties and thickness of the rock mechanical unit determine the extension and termination of fractures, making natural fractures characterized with multi-scale (Cooke et al., 2006; Larsen et al., 2010). The quantitative statistics of fracture parameters, such as the density, aperture, and length, need to be considered under multiple-scale. The aperture and length of multi-scale fractures obey the power-law distribution (Berkowitz, 2002; Olson, 2003; Laubach and Ward, 2006). Fractures with different scales have various contributions to tight sandstone reservoirs. Large-scale fractures with low porosity but high permeability are effective migration channels, while small and micro-scale fractures with low permeability can provide important storage spaces for these reservoirs on account of the high porosity (Zeng et al., 2020). The study of multi-scale fractures is useful to better understand the contribution of natural fractures to the distribution and development of oil and gas in tight sandstone reservoirs.

The genetic types of natural fractures include tectonic, diagenetic, and overpressure-related fractures in tight sandstone in the Upper Triassic Yanchang Formation of the Ordos Basin. Among them, the tectonic fractures developed during the Late Jurassic to Early Cretaceous and Paleogene are the dominant ones (Zeng et al., 2007). The fracture development is controlled by lithology, rock mechanical units, sedimentary microfacies, diagenetic facies, and reservoir heterogeneity (Zeng et al., 2008; Gong et al., 2019). Besides, the contribution of natural fractures to reservoir permeability and their influence on oil and gas development are also discussed (Lyu et al., 2019). However, there is a lack of research and understanding of fracture scales and the differences in the effects of multi-scale fractures on reservoirs.

In this paper, various data including outcrops, 3D seismic data, imaging logs, cores, and thin sections were used to conduct research. Based on the development characteristics, the faults and fractures are divided into different levels, and the influence of multi-scale fault-fractures on the oil and gas accumulation and productivity of tight sandstone reservoirs is also discussed. The research results provide an example for understanding the role of multi-scale fault-fractures in tight oil and gas exploration and development.

GEOLOGICAL SETTING

Location and Structure

The Ordos Basin is located in the central of China and has an area of about 37×10^4 km^2 (**Figure 1A**). It is separated from the Yinshan Mountains by the Hetao Graben in the north, faces the Qinling Mountains by the Weihe Graben in the south, reaches Liupan Mountain in the west, and reaches Lvliang Mountain in the east. This basin can be divided into six first-level structural units (**Figure 1B**), including the Yimeng Uplift, Weibei Uplift, West Margin Thrust Belt, Yishan Slope, Tianhuan Depression, and Jinxi Flexfold Belt (Han et al., 2014; Wang et al., 2017). The study area is located in the southern of the Tianhuan Depression and is a west-dipping monoclinic structure as a whole. Some small uplifts of low amplitude and NEE-SWW, NWW-SEE, NW-SE, and near E-W strike faults are developed in the study area (**Figure 1C**).

Stratigraphy

The Ordos Basin developed Paleozoic marine and Mesozoic-Cenozoic terrestrial strata (**Figure 2**). The Paleozoic marine strata are generally natural gas reservoirs, while the Mesozoic terrestrial strata are mainly oil reservoirs (Zeng and Li, 2009). The Yanchang Formation of the Upper Triassic is one of the most important oil-bearing formations in the Ordos Basin (Duan et al., 2008). The Yanchang Formation consists of Chang 1 to Chang 10 oil layer groups from top to bottom (Tang et al., 2014), with a thickness of about 430–620 m. Among them, the Chang 8 sandstones are the major target for the tight oil (Hao et al., 2017; Wang et al., 2020).

Reservoir

The Chang 8 member of the southwestern Ordos Basin comprises shallow braided river delta deposits, with dominant sedimentary microfacies of distributary channel, estuary bar, sheet sand, and distributary bay. The reservoir lithology is debris feldspar sandstones with fine, fine-medium, and silty-fine grains. The storage space is mainly intergranular dissolved pores, residual primary pores, and microfractures, in addition to a small amount of intragranular dissolved pores, mold pores, and intercrystalline pores (Liang and Guo, 2017). The reservoir porosity distribution ranges from 4.4 to 12%, with an average of 8.6%, and the air permeability of these reservoirs is between 0.10 and 0.65 mD, with an average of 0.20 mD, which is a typical tight oil sandstone reservoir (Lyu et al., 2017b).

In situ Stress

The direction of present *in situ* stress can be obtained from borehole breakouts and drilling-induced fractures from imaging logs, and the value of present *in situ* stress comes from rock acoustic emission experiment, hydraulic fracturing, and acoustic logging data (Hillis and Reynolds, 2003; Zoback et al., 2003; Rajabi et al., 2016; Ju et al., 2017). Based on the above methods, the maximum and minimum principal stresses are in the horizontal direction, and the intermediate principal stress is vertical in the southwest of Ordos Basin. The dominant direction of the maximum

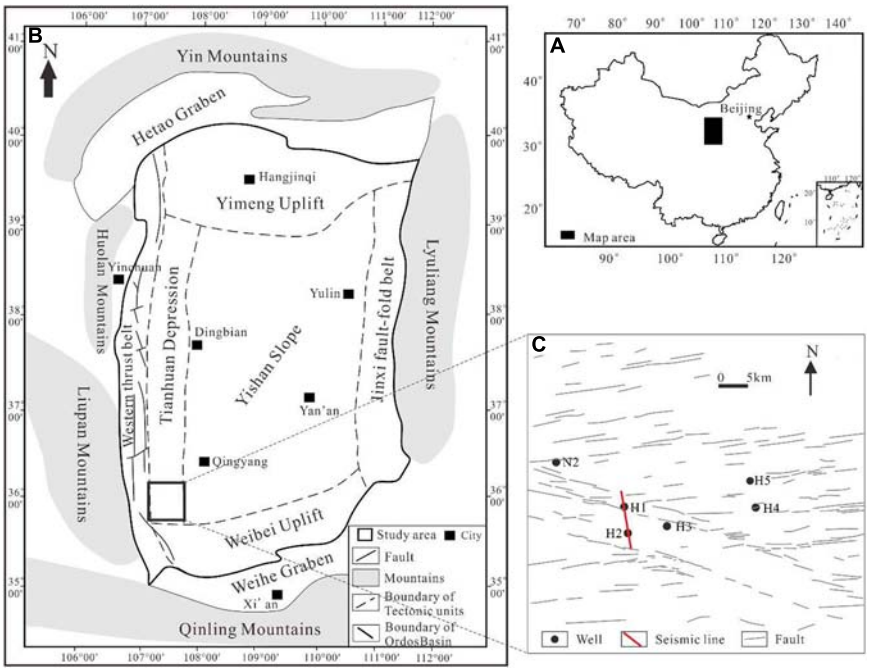

FIGURE 1 | Location map of the Ordos Basin, study area, wells, and fault systems (modified from Zeng and Li, 2009; Lyu et al., 2016; Lyu et al., 2017a, 2019). **(A)** Location of the Ordos Basin. **(B)** Location of the study area and tectonic units of the Ordos Basin. **(C)** Location of wells, seismic line, and fault systems in the study area.

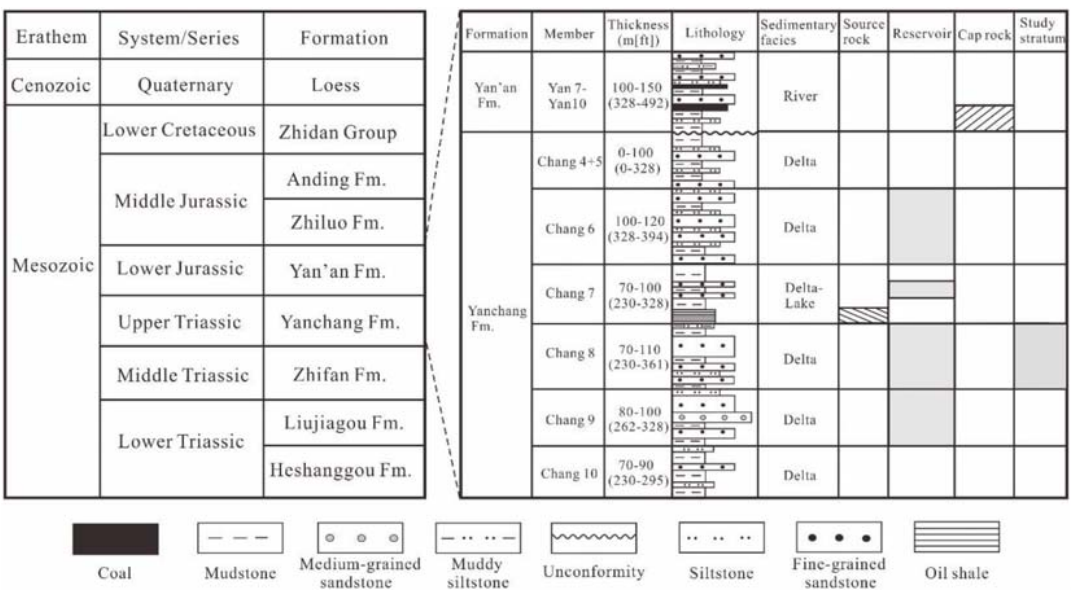

FIGURE 2 | Schematic stratigraphy and hydrocarbon potential of the southwestern Ordos Basin (modified from Lyu et al., 2019). Fm.= Formation.

horizontal compressive stress is 60–70°. The value of present *in situ* stress has a good linear relationship with buried depth, and the stress gradients of the maximum, intermediate, and minimum principal stresses are 0.0301, 0.0212, and 0.0165 MPa·m^{-1}, respectively (Zeng and Li, 2009; Lyu et al., 2019).

DATA SET AND METHODOLOGY

This study uses cores of 2,413.33 m from 127 wells, micro-resistivity imaging logs from nine wells, 225 thin sections, and oil test data from more than 200 wells in the tight sandstones of the Upper Triassic Yanchang Formation in the southwestern Ordos

Basin. Various materials, including 3D seismic data, outcrops, cores, imaging logs, and thin sections, are integrated for multi-scale fault-fracture evaluation, reducing the uncertainty caused by a single data.

Fault parameters, including length, fault displacement, and occurrence, are obtained by interpreting 3D seismic data. Large-scale fractures come from the outcrops and post-stack attributes (coherence, curvature, and variance) of 3D seismic data (Chen et al., 2016; Xu et al., 2020). Meso- and small-scale fracture parameters, including strike, dip, density, aperture, and length, are obtained through outcrops, cores, and imaging logs (Hennings et al., 2000; Khoshbakht et al., 2012). The density of meso- and small-scale fractures refers to linear density, which is the number of fractures per unit length in the normal direction of the fracture surface (Shi et al., 2020). Micro-scale fracture parameters such as length, aperture, and density are derived from thin section observation (Ameen and Hailwood, 2008). Micro-scale fracture density means the areal density, the total length of fractures per unit area (Zeng et al., 2008).

The micro-resistivity imaging logs can provide high-resolution two-dimensional images of the surrounding wellbore containing petrophysical information. These images convert the difference in resistivity or acoustic impedance caused by meso- and small-scale fractures into different colors, which can accurately characterize fracture properties such as aperture, length, and occurrence (Ameen and Hailwood, 2008; Barton et al., 2009).

RESULTS

Fault-Fracture Scale Division

According to the development characteristics and distribution scale, the faults and fractures in the tight sandstones of the Upper Triassic Yanchang Formation in the Ordos Basin can be divided into six levels: type-I faults, type-II faults, large-scale fractures, mesoscale fractures, small-scale fractures, and micro-scale fractures (**Figure 3** and **Table 1**). In this article, we mainly discuss the classification of tectonic fractures.

The interpretation of 3D seismic data shows that these faults are mainly strike-slip faults, with a nearly upright dip angle, a small fault displacement, and an echelon arrangement on the plane. Type-I faults cut the Yanchang Formation and the bottom coal and mudstone strata of the Yan'an Formation on the section and have the fault displacement greater than 40 m (**Figures 3**, **4**). Their extension length is generally greater than 4.0 km on the plane and their directions are mainly NW-SE strikes. Type-II faults cut the Chang 7 source rock and Chang 8 reservoirs on the section, and their fault displacement is generally less than 40 m (**Figures 3**, **4**). The extension length of these

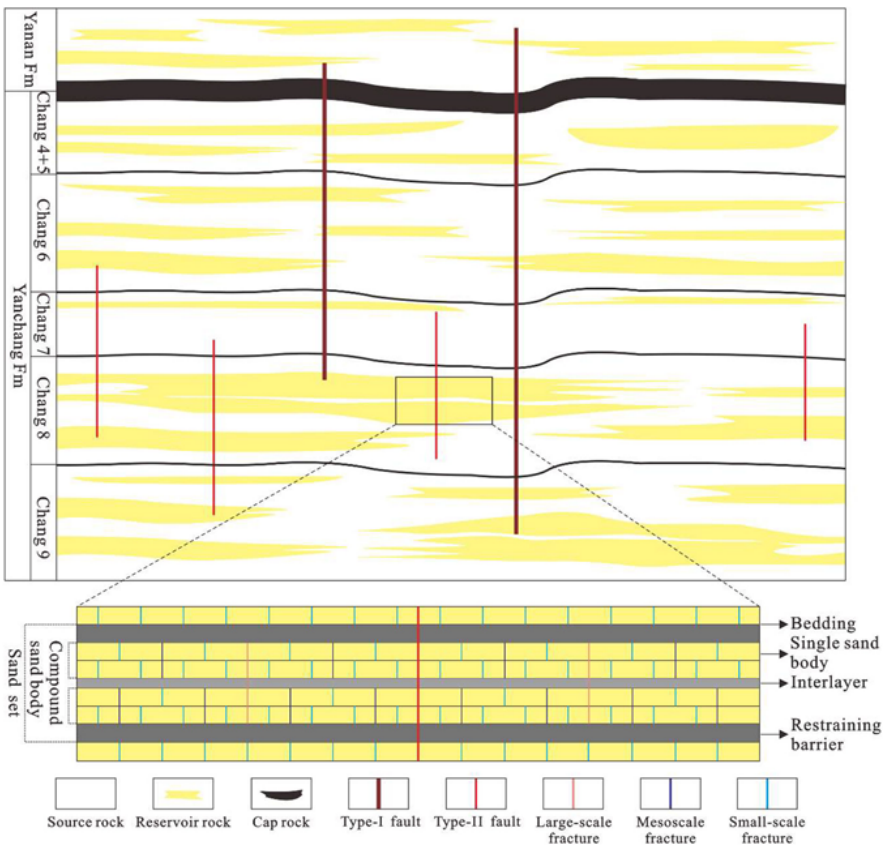

FIGURE 3 | Schematic diagram of different scale fault and fracture distribution patterns.

TABLE 1 | Multi-scale fault and fracture classification and their characteristics.

Classification	Development characteristics	Scale	Function
Type-I faults	Cutting through the bottom coal seam and mud-shale of Jurassic Yan'an Formation	With the plane propagation over 4.0 km; fault displacement over 40 m	Against for oil storage
Type-II faults	Cutting through the Chang 7 mudstones and Chang 8 reservoir of the Upper Triassic Yanchang Formation	With propagation less than 4.0 km; fault displacement less than 40 m	The fault of oil source, oil migration channel
Large-scale fractures	Developed within the Chang 8 of the Upper Triassic Yanchang Formation, cutting through interlayers of sandstones and mudstones and restricted by the Chang 7 mudstones of the Yanchang Formation	With propagation ranging from hundreds of meters to thousands of meters, the height is over tens of meters	Seepage channels
Mesoscale fractures	Developed within composite sandstone layers, cutting through thin interlayers and restricted by interlayers of mudstone	With propagation ranging from tens to hundreds of meters; height ranging from meters to tens of meters	Seepage channels
Small-scale fractures	Developed within a single sandstone layer and controlled by thin interlayers or layer interfaces	With propagation ranging from several meters to tens of meters; the height of several decimeters	Storage spaces and seepage channels
Micro-scale fractures	Developed within a single sandstone layer	With the propagation of less than several centimeters, and aperture less than 50 μm	Storage space

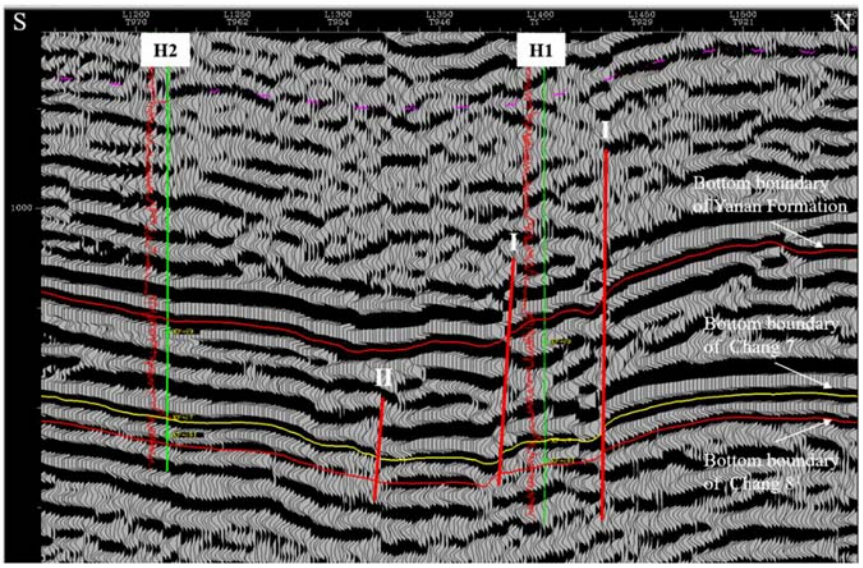

FIGURE 4 | Type-I and type-II faults on the seismic cross-section. I refers to the type-I fault. II refers to the type-II fault. H1 and H2 refer to drilling wells, see **Figure 1** for the well location.

faults on the plane is less than 4.0 km, and their directions are NEE-SWW and NWW-SEE strikes. The statistical results of seismic data interpretation show that the number of type-I faults is significantly less than that of type-II faults, reflecting that the number of faults decreases as the fault scale increases. Generally, the larger the fault scale, the greater the energy, and the more secondary faults will be formed.

Large-scale fractures are mainly identified by outcrops and the post-stack attributes such as coherence, curvature, and variance from 3D seismic data, and some large-scale fractures can be observed on the core (**Figure 5a**). These fractures are developed in the Chang 8 reservoirs, cutting the mudstone interlayer on the section, and were restricted by the Chang 7 mudstone (Zeng et al., 2020). The extension length of this kind of fracture ranges from several hundred meters to thousands of meters, and they are arranged in an echelon on the plane. Their height is tens of meters, and their directions are NEE-SWW and NWW-SEE strikes. Outcrops, cores, and imaging logs show that mesoscale fractures are developed in the composite sandstone layers and terminated in the thick mudstone interlayers, which can cut through thin interlayers and has a height of several meters to tens of meters on the section (**Figures 5b**, **6**). Outcrops and imaging logs indicate that the main directions of these fractures are NEE-SWW and NWW-SEE (**Figure 7**). Small-scale fractures are developed in a single sandstone layer and are controlled by thin interlayers or layer interfaces. These fractures intersect with the layer interface nearly perpendicularly, with a height of tens of centimeters, extending from several meters to tens of meters on the plane (**Figure 5c**). Micro-scale fractures are observed in the casting thin sections (**Figure 5d**). Their length is generally less than one centimeter, and their aperture is less than 50 μm, concentrated in 10–20 μm. The

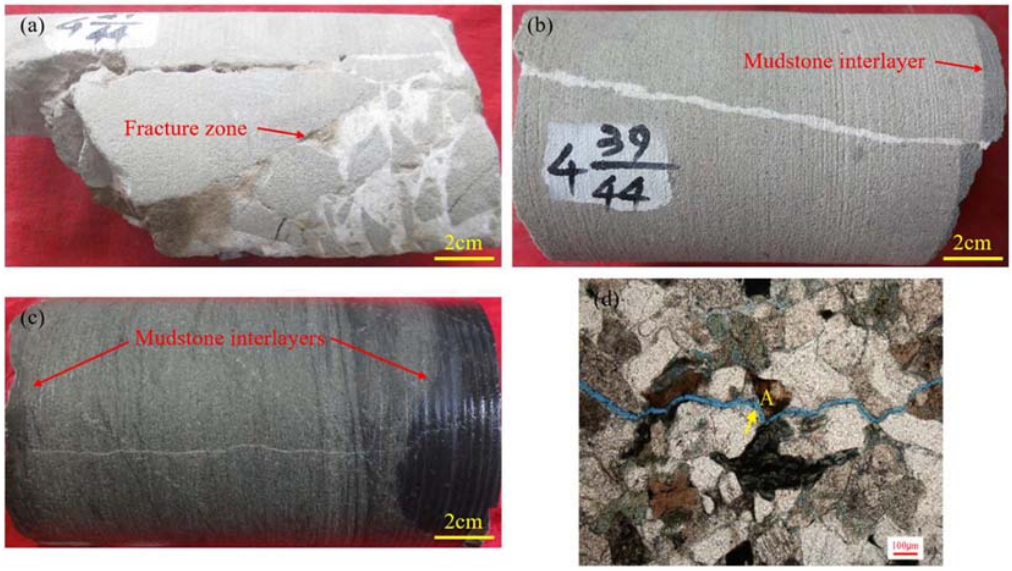

FIGURE 5 | Large-scale fracture, mesoscale fracture, small-scale fracture, and micro-scale fracture in cores and thin sections. **(a)** Large-scale fracture shows fracture zone, Well N2, depth of 2,309.90 m. **(b)** Mesoscale fracture cuts mudstone interlayer, Well N2, depth of 2,303.27 m (from Lyu et al., 2016). **(c)** Small-scale fracture is restricted by mudstone interlayer, Well H4, depth of 2,091.76 m, **(d)** Micro-scale fracture, Well H3, depth of 2,268.90 m. "A" refers to the micro-scale fracture.

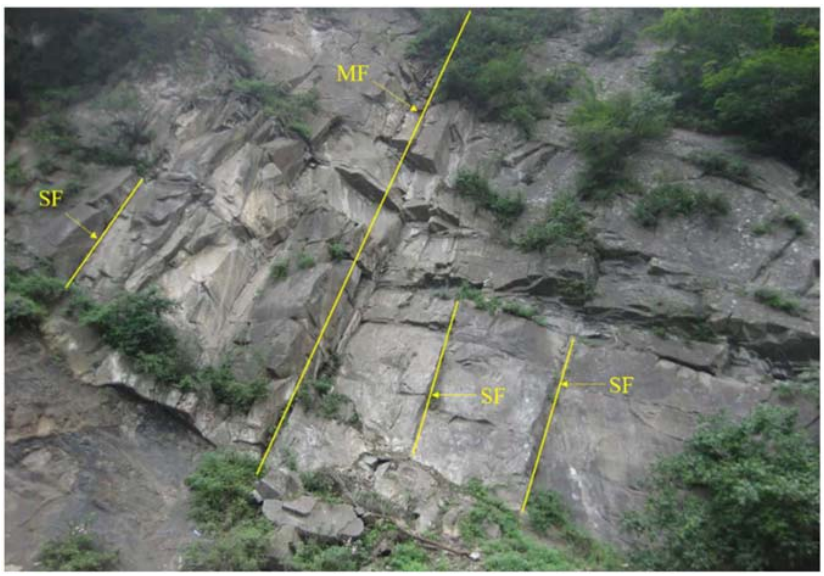

FIGURE 6 | Mesoscale and small-scale fractures in outcrops. MF refers to the mesoscale fracture; SF refers to the small-scale fracture.

statistical results show that as the fracture size increases, the density of fracture decreases, and the density of micro-scale fractures is the largest.

Relationship Between Faults and Fractures

Outcrops, cores, and imaging logs show that the development intensity of fractures is closely related to faults. As the distance from the fault plane increases, the fracture density gradually decreases (**Figure 8**). There is a fracture development zone near the fault plane, namely the fault damage zone (Torabi and Berg, 2011). The width of the fault damage zone is related to the scale of the fault. As the scale of the fault increases, the width of the fault damage zone becomes larger (Lyu et al., 2017b). In addition, due to the control of faults on fracture development, the degree of fracture development at different fault positions also varies. Generally, the fractures in the hanging wall are more developed

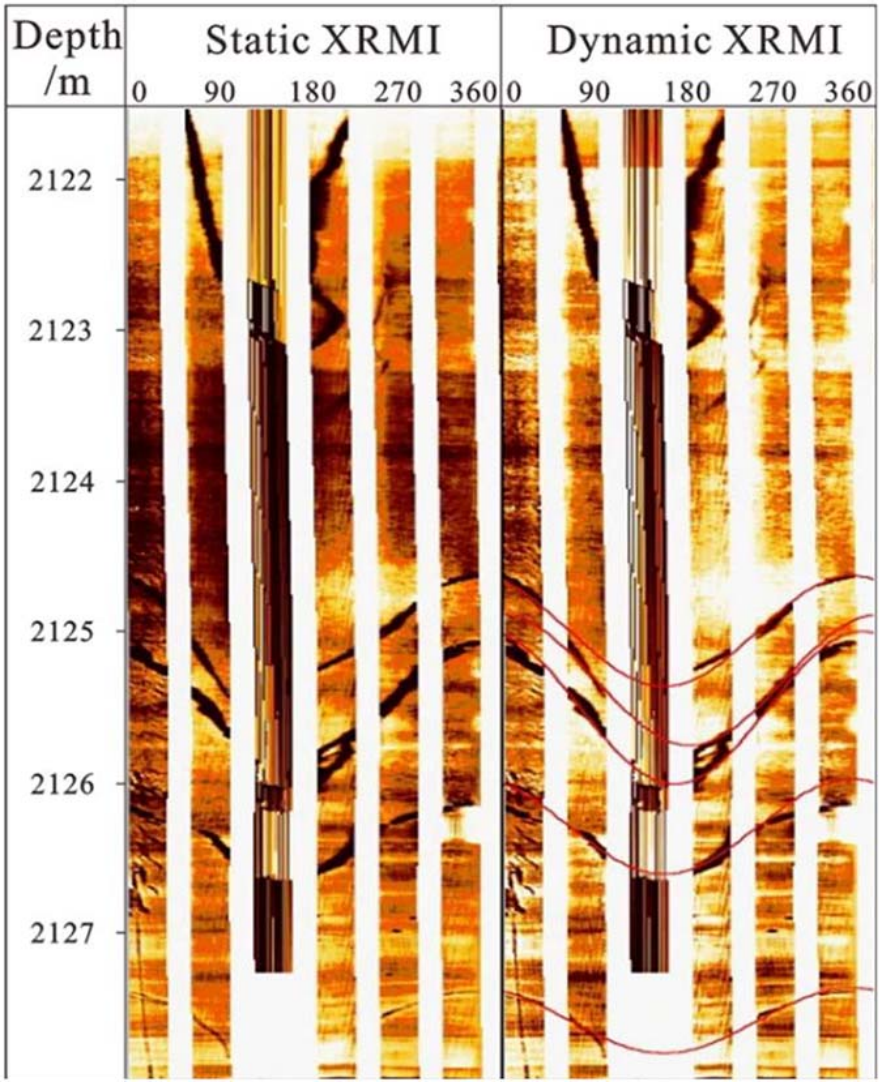

FIGURE 7 | Fractures detected by micro-resistivity imaging log in the Well H5. See **Figure 1** for the location of Well H5.

than those in the footwall (Zeng, 2008). The fractures at the end of the fault are more developed than in the middle part, and the fractures at the intersection of faults and the overlapping part of echelon faults are more developed.

DISCUSSION

Influence of Different Scale Faults on Oil Enrichment and Production

The source rock of the Upper Triassic Yanchang Formation in the Ordos Basin is the Chang 7 mudstone. The reservoir is the Chang 8 sandstones. The regional caprock is the Yan 10 coal-measure strata at the bottom of the Yan'an Formation. Type-I faults cut reservoirs, source rocks, and regional caprocks, and easily cause the loss of oil and gas. The analysis of geochemical data shows that the geochemical characteristics of the crude oils of the Mesozoic oil layer groups in the Honghe Oilfield are similar (Ma et al., 2015), reflecting that they come from the same oil source. The oil in the tight reservoirs at the bottom of the Yan'an Formation are a hydrocarbon generated from the Chang 7 source rocks of the Yanchang Formation (Xing et al., 2016), which is powerful evidence that the type-I faults zone are not conducive to the oil and gas preservation of the Chang 8 sandstone reservoir. Moreover, although the fluid production of the wells drilled through type-I faults is high, the oil production of these wells is low, mainly water production (**Figure 9**). Therefore, type-I faults contribute the most to the fluid flow in the reservoirs but are not conducive to the enrichment and production of tight oil in the Chang 8.

Type-II faults connect the Chang 7 source rocks and the Chang 8 reservoirs in the study area and are oil source faults and the main migration channels for oil. In addition, due to the more developed fractures near the fault, tight oil production

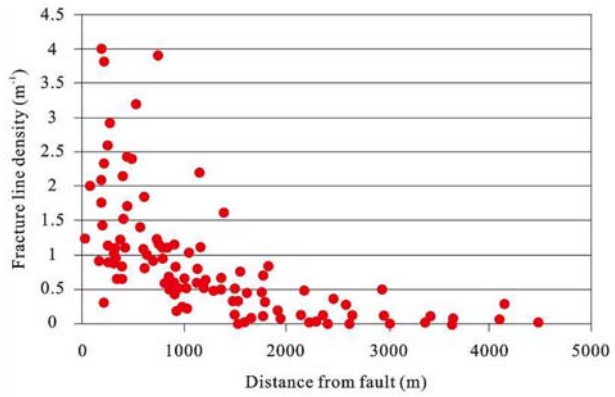

FIGURE 8 | The relationship between fracture density and distance from the fault.

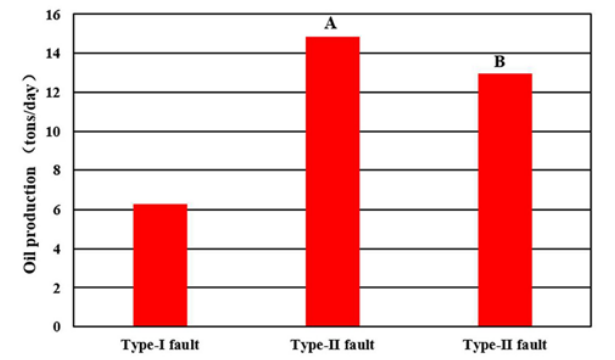

FIGURE 9 | The oil production in the wells drilled different scale of fault. **(A)** Cutting the fault of Chang 7, with a larger fault scale; **(B)** Cutting the fault of Chang 8, with a smaller fault scale.

is generally high when drilling through the type-II faults zone. According to the oil test data in the reservoirs, although the fluid output of wells drilling through the type-II faults zone is not as high as that drilling through that of type-I faults, the oil production of wells drilling through the type-II faults zone is significantly higher than that drilling through that of type-I faults. The average oil production of wells drilled through the type-II faults zone with an extension length of 1,000–4,000 m exceeds 12 tons per day, while the average oil production of wells drilled through that of type-I faults is less than six tons per day (**Figure 10**).

There are apparent differences in the impact of faults with different directions on oil production. There are two sets of nearly upright faults in the NWW-SEE and NEE-SWW directions in the tight sandstones of the Upper Triassic Yanchang Formation in the southwestern Ordos Basin. According to the statistics of oil test data, the average oil production of wells drilled into the NWW-SEE fault is greater than 10 tons per day, while the average oil production of the wells drilled into the NEE-SWW fault is less than six tons per day (**Figure 11**). It indicates that the oil production of wells with NWW-SEE faults that are nearly parallel to the present maximum principal stress direction is higher than that of wells with NWW-SEE faults. This is because under the influence of the present *in situ* stress in the NEE-SWW direction, the NEE-SWW fault is in a state of tension currently, and the faults and their related fractures have larger apertures, better effectiveness and connectivity, and higher permeability (Liu et al., 2020b). On the contrary, the NWW-SEE fault is in a compressed state currently, and these faults and their related fractures have smaller apertures, poorer effectiveness and connectivity, and lower permeability. Therefore, the multi-scale faults and fractures that are nearly parallel to the present maximum principal stress direction significantly contribute to the oil productivity of tight sandstone reservoirs.

In different positions of the fault, the development degree of fractures is diverse, and oil production also varies greatly. Based on the statistical results of the oil test data, the oil production of wells on the fault hanging wall is higher than that of wells on the fault footwall (**Figure 12**). In the same fault, the wells' oil production at the end part of the fault is higher than that of the wells in the middle part of the fault. Additionally, the oil production is highest at the intersection of faults (cross part)

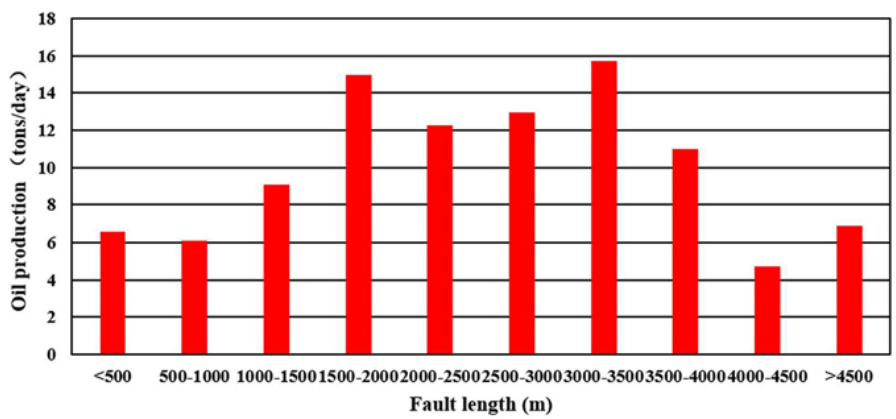

FIGURE 10 | The oil production in the wells drilled different length of fault.

FIGURE 11 | The oil production in the wells drilled different strike of fault.

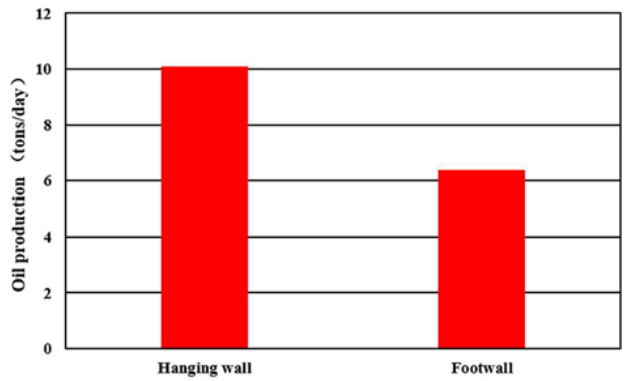

FIGURE 12 | The oil production in the wells located at hanging wall and foot wall of fault.

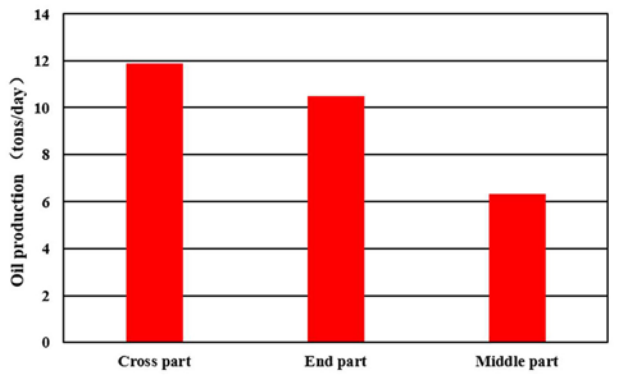

FIGURE 13 | The oil production in the wells located at different parts of fault (data from Lyu et al., 2019).

with different strikes and the overlaps of faults (cross part) with the same strike in an echelon arrangement (**Figure 13**). This proves that the difference in fracture development at different fault positions controls the difference in oil enrichment of tight sandstones and the production of single wells.

Influence of Different Scale Fractures on Oil Production

Different scale fractures are developed and distributed variedly in the tight sandstone reservoirs, which are effective storage spaces and main seepage channels and have variously effects on oil production. The tight oil in the Chang 8 reservoir is generated from the overlying Chang 7 source rocks. Due to the existence of near-upright type-II faults and large-scale fractures, tight oil preferentially charged and accumulated into reservoirs locally, showing the characteristics of "near-source vertical short distance" enrichment (Guo, 2017). The distribution of mesoscale fractures is controlled by thick interlayers, and small-scale fractures are controlled by thin interlayers or layer interfaces. Besides, the fluid flow in the tight-oil sandstones may have been largely controlled by intraformational natural fractures, which provide major fluid-flow channels. Therefore, meso- and small-scale fractures still control the internal flow of fluid in Chang 8 reservoir. Meso- and small-scale fractures include near vertical, high, medium, low, and nearly horizontal dip angles (Lyu et al., 2016). Meso- and small-scale fractures with various dip angles are intertwined to form a fracture network system with good connectivity and permeability. This system significantly improves the seepage capacity and effectiveness of storage space in tight sandstone reservoirs, showing that the cumulative oil production of the wells drilled fracture zone is much greater than that of wells not drilled into fracture zones. There is a positive correlation between the density of meso- and small-scale fractures and initial production (R^2 = 0.838) (Lyu et al., 2019). As the density of meso- and small-scale fractures increases, the initial production of wells increases. Besides, away from the fault damage zones, the initial oil production decreases. This decrease law could also be ascribed to the decreasing fracture intensity away from faults. The exploration and development status mentioned above reflects that meso- and small-scale fractures are the key factors to control the oil production of tight sandstone reservoirs.

The porosity and permeability of fractures can characterize the migration and storage capacity of fluids (Gong et al., 2021). According to the calculation results of porosity and permeability, small-scale fractures can increase the permeability of tight sandstone reservoirs by 1–2 orders of magnitude, and their porosity is similar to the reservoir matrix (Lyu et al., 2019). This means that the small-scale fractures mainly improve the reservoir permeability and secondly serve as the reservoir storage space. The micro-scale fractures are distributed in the tight sandstones with the largest number, and their fracture porosity is also the largest. Micro-scale fractures can be regarded as relatively large-scale pores, it is used as a storage space first, and then as a migration channel. As the distance from the fault plane decreases, the density of micro-scale fractures increases. Type-II faults migrate oil and gas to the Chang 8 reservoir, and preferentially enrich and accumulate in the micro-fractures near the faults. Or oil and gas migrate from large-scale, mesoscale, and small-scale fractures, and enrich in micro-scale fractures near these fractures. The above reasons enable the micro-scale fractures to have considerable oil storage

capacity, which is an important factor influencing the stable production of tight sandstone reservoirs. Besides, micro-scale fractures nucleate at stress concentrations that occur at the grain scale. Once micro-scale fractures become longer than that length scale, i.e., become transgranular, they may continue to propagate by virtue of the stress concentration at the tip and become macro-fractures (Anders et al., 2014). From this perspective, some fractures may grow into cracks microscale larger scale potential as migration pathways of hydrocarbon and have considerable capacity enrichment. A parallelism between the orientation of micro-scale fractures and larger micro-scale fractures (Laubach and Diaz-Tushman, 2009), we can take advantage of the distribution law and development characteristics of larger-scale fractures to determine well pattern deployment and fracturing plans to further achieve high and stable production of tight oil.

CONCLUSION

The faults and fractures of the tight oil sandstone reservoirs of the Upper Triassic Yanchang Formation in the southwestern Ordos Basin are divided into six levels: type-I faults, type-II faults, large-scale fractures, mesoscale fractures, small-scale fractures, and micro-scale fractures. Type-I faults cut through the regional caprocks and cause the loss of oil. Type-II faults connect the source rocks and the reservoirs and act as oil migration channels. Large-scale fractures are developed in the reservoirs, cut the mudstone interlayer, and are the seepage channel inside the reservoir. Mesoscale fractures are developed in the composite sandstone layers and are controlled by thick mudstone interlayers. Small-scale fractures are developed in a single sandstone layer and are restricted by thin interlayers or layer interfaces. Meso- and small-scale fractures are the main seepage channels and effective storage spaces for tight reservoirs. The micro-scale fractures are observed in the casting thin sections and are important storage space for tight oil sandstone reservoirs.

The scale, strike, and position of the fault will change the development degree of fractures, leading to different oil production in a single well of tight sandstone reservoirs. Type-I faults contribute the most to regional fluid flow but are not conducive to the enrichment and high oil production in the Chang 8 tight sandstone reservoirs. Fractures near type-II faults are more developed, which is favorable to oil enrichment and generally has higher oil production. The faults and fractures that are nearly parallel to the present maximum principal stress direction greatly contribute to the oil productivity of tight sandstones. In the intersections and overlaps (cross parts), and end parts of faults, fractures are more developed, and single well oil production is higher. The development degree of meso- and small-scale fractures is the key to influencing the early single-well production in tight sandstone reservoirs. The more meso- and small-scale fractures are developed, the higher the single-well production is. The development of micro-scale fractures is conducive to the stable production of single wells in tight sandstone reservoirs.

Multi-scale faults and fractures have significantly different effects on the oil enrichment and production of tight sandstone reservoirs. Consequently, it is necessary to pay more attention to their development and distribution law to better refer to the exploration and development of tight oil sandstone reservoirs.

DATA AVAILABILITY STATEMENT

The original contributions presented in the study are included in the article/Supplementary Material, further inquiries can be directed to the corresponding author/s.

AUTHOR CONTRIBUTIONS

LZ and WL contributed to conception and design of the study, organized the database, and performed the statistical analysis. LZ, WL, YZ, and GL wrote the first draft of the manuscript. SD wrote sections of the manuscript. All authors contributed to manuscript revision, read, and approved the submitted version.

FUNDING

This study was financially supported by the National Natural Science Foundation of China (Grant No. 42002135) and the Science Foundation of China University of Petroleum, Beijing (2462017YJRC057).

ACKNOWLEDGMENTS

We are particularly grateful to Frontiers in Earth Science editor and reviewers for their thorough and constructive comments, which will improve the manuscript significantly.

REFERENCES

Ameen, M. S., and Hailwood, E. A. (2008). A new technology for the characterization of microfractured reservoirs (test case: Unayzah reservoir, Wudayhi field, Saudi Arabia). *Am. Assoc. Pet. Geol. Bull.* 92, 31–52. doi: 10.1306/08200706090

Ameen, M. S., MacPherson, K., Al-Marhoon, M. I., and Rahim, Z. (2012). Diverse fracture properties and their impact on performance in conventional and tight-gas reservoirs, Saudi Arabia: The Unayzah, South Haradh case study. *Am. Assoc. Pet. Geol. Bull.* 96, 459–492. doi: 10.1306/06011110148

Anders, M. H., Laubach, S. E., and Scholz, C. H. (2014). Microfractures: a review. *J. Struct. Geol.* 69, 377–394. doi: 10.1016/j.jsg.2014.05.011

Barton, C., Moos, D., and Tezuka, K. (2009). Geomechanical wellbore imaging: implications for reservoir fracture permeability. *Am. Assoc. Pet. Geol. Bull.* 93, 1551–1569. doi: 10.1306/06180909030

Berkowitz, B. (2002). Characterizing flow and transport in fractured geological media: a review. *Adv. Water Resour.* 25, 861–884. doi: 10.1016/S0309-1708(02)00042-8

Chen, S. Q., Zeng, L. B., Huang, P., Sun, S. H., Zhang, W. L., and Li, X. Y. (2016). The application study on the multi-scales integrated prediction method to

fractured reservoir description. *Appl. Geophys.* 13, 80–92. doi: 10.1007/s11770-016-0531-7

Cooke, M. L., Simo, J. A., Underwood, C. A., and Rijken, P. (2006). Mechanical stratigraphic controls on fracture patterns within carbonates and implications for groundwater flow. *Sediment. Geol.* 184, 225–239. doi: 10.1016/j.sedgeo.2005.11.004

Duan, Y., Wang, C. Y., Zheng, C. Y., Wu, B. X., and Zheng, G. D. (2008). Geochemical study of crude oils from the Xifeng oilfield of the Ordos basin, China. *J. Asian Earth Sci.* 31, 341–356. doi: 10.1016/j.jseaes.2007.05.003

Gong, L., Fu, X., Wang, Z., Gao, S., Jabbari, H., Yue, W., et al. (2019). A new approach for characterization and prediction of natural fracture occurrence in tight oil sandstones with intense anisotropy. *Am. Assoc. Pet. Geol. Bull.* 103, 1383–1400. doi: 10.1306/12131818054

Gong, L., Wang, J., Gao, S., Fu, X., Liu, B., Miao, F., et al. (2021). Characterization, controlling factors and evolution of fracture effectiveness in shale oil reservoirs. *J. Pet. Sci. Eng.* 203:108655. doi: 10.1016/j.petrol.2021.108655

Gross, M. R., Fischer, M. P., Engelder, T., and Greenfield, R. J. (1995). Factors controlling joint spacing in interbedded sedimentary rocks: integrating numerical models with field observations from the Monterey Formation, USA. *Geol. Soc. Spec. Publ.* 92, 215–233. doi: 10.1144/GSL.SP.1995.092.01.12

Guo, K. (2017). Active source rocks of Chang 7 member and hydrocarbon generation and expulsion characteristics in Longdong area, Ordos Basin. *Pet. Geol. Exp* 39, 15–23.

Han, S., Horsfield, B., Zhang, J., Chen, Q., Mahlstedt, N., Di Primio, R., et al. (2014). Hydrocarbon generation kinetics of lacustrine Yanchang shale in Southeast Ordos Basin. North China. *Energy Fuels* 28, 5632–5639. doi: 10.1021/ef501011b

Han, Y., Horsfield, B., Wirth, R., Mahlstedt, N., and Bernard, S. (2017). Oil retention and porosity evolution in organic-rich shales. *Am. Assoc. Pet. Geol. Bull.* 101, 807–827. doi: 10.1306/09221616069

Hao, L., Tang, J., Wang, Q., Tao, H., Ma, X., Ma, D., et al. (2017). Fractal characteristics of tight sandstone reservoirs: a case from the Upper Triassic Yanchang Formation, Ordos Basin, China. *J. Pet. Sci. Eng.* 158, 243–252. doi: 10.1016/j.petrol.2017.08.060

Hennings, P. H., Olson, J. E., and Thompson, L. B. (2000). Combining outcrop data and three-dimensional structural models to characterize fractured reservoirs: an example from Wyoming. *Am. Assoc. Pet. Geol. Bull.* 84, 830–849. doi: 10.1306/a967340a-1738-11d7-8645000102c1865d

Hillis, R. R., and Reynolds, S. D. (2003). In situ stress field of Australia. *Spec. Pap. Geol. Soc. Am.* 372, 49–58. doi: 10.1130/0-8137-2372-8.49

Jia, C. (2017). Breakthrough and significance of unconventional oil and gas to classical petroleum geological theory. *Pet. Explor. Dev.* 44, 1–11. doi: 10.11698/PED.2017.01.01

Ju, W., Shen, J., Qin, Y., Meng, S., Wu, C., Shen, Y., et al. (2017). In-situ stress state in the Linxing region, eastern Ordos Basin, China: implications for unconventional gas exploration and production. *Mar. Pet. Geol.* 86, 66–78. doi: 10.1016/j.marpetgeo.2017.05.026

Khoshbakht, F., Azizzadeh, M., Memarian, H., Nourozi, G. H., and Moallemi, S. A. (2012). Comparison of electrical image log with core in a fractured carbonate reservoir. *J. Pet. Sci. Eng.* 8, 289–296. doi: 10.1016/j.petrol.2012.03.007

Larsen, B., Gudmundsson, A., Grunnaleite, I., Sælen, G., Talbot, M. R., and Buckley, S. J. (2010). Effects of sedimentary interfaces on fracture pattern, linkage, and cluster formation in peritidal carbonate rocks. *Mar. Pet. Geol.* 27, 1531–1550. doi: 10.1016/j.marpetgeo.2010.03.011

Laubach, S. E., and Diaz-Tushman, K. (2009). Laurentian palaeostress trajectories and ephemeral fracture permeability, Cambrian Eriboll Formation sandstones west of the Moine Thrust Zone, NW Scotland. *J. Geol. Soc. London.* 166, 349–362. doi: 10.1144/0016-76492008-061

Laubach, S. E., Eichhubl, P., Hilgers, C., and Lander, R. H. (2010). Structural diagenesis. *J. Struct. Geol.* 32, 1866–1872. doi: 10.1016/j.jsg.2010.10.001

Laubach, S. E., and Ward, M. E. (2006). Diagenesis in porosity evolution of opening-mode fractures, Middle Triassic to Lower Jurassic La Boca Formation, NE Mexico. *Tectonophysics* 419, 75–97. doi: 10.1016/j.tecto.2006.03.020

Liang, C., and Guo, J. (2017). Diagenesis and reservoir characteristics of tight sandstones of Chang 8_1 member of Yanchang Formation in Honghe oilfield,Ordos Basin. *Pet. Geol. Recover. Effic* 24, 57–63.

Liu, G. P., Zeng, L. B., Han, C. Y., Mehdi, O., Lyu, W. Y., Wang, Q. Q., et al. (2020a). Natural Fractures in Carbonate Basement Reservoirs of the Jizhong Sub-Basin, Bohai Bay Basin, China: key Aspects Favoring Oil Production. *Energies* 13:4635. doi: 10.3390/en13184635

Liu, G. P., Zeng, L. B., Sun, G., Zu, K., Qin, L., Mao, Z., et al. (2020b). Natural fractures in tight gas volcanic reservoirs and their influences on production in the Xujiaweizi Depression, Songliao Basin, China. *Am. Assoc. Pet. Geol. Bull.* 104, 2099–2123. doi: 10.1306/05122017169

Lyu, W., Zeng, L., Liu, Z., Liu, G., and Zu, K. (2016). Fracture responses of conventional logs in tight-oil sandstones: a case study of the Upper Triassic Yanchang Formation in southwest Ordos Basin, China. *Am. Assoc. Pet. Geol. Bull.* 100, 1399–1417. doi: 10.1306/04041615129

Lyu, W., Zeng, L., Liao, Z., Ji, Y., Lyu, P., Dong, S., et al. (2017a). Fault damage zone characterization in tight-oil sandstones of the Upper Triassic Yanchang formation in southwest Ordos Basin, China: Integrating cores, image logs and conventional logs. *Interpretation* 5. doi: 10.1190/int-2016-0231.1

Lyu, W., Zeng, L., Zhang, B., Miao, F., Lyu, P., and Dong, S. (2017b). Influence of natural fractures on gas accumulation in the Upper Triassic tight gas sandstones in the northwestern Sichuan Basin, China. *Mar. Pet. Geol.* 83, 60–72. doi: 10.1016/j.marpetgeo.2017.03.004

Lyu, W., Zeng, L., Zhou, S., Du, X., Xia, D., Liu, G., et al. (2019). Natural fractures in tight-oil sandstones: a case study of the upper triassic yanchang formation in the southwestern ordos basin, China. *Am. Assoc. Pet. Geol. Bull.* 103, 2343–2367. doi: 10.1306/0130191608617115

Ma, L., Yin, H., Chen, C., and Yin, W. (2015). Research of geochemistry characteristics and source of crude oils from the Honghe Oilfield in the Ordos Basin. *Acta Sedimentol. Sin.* 33, 416–425.

Olson, J. E. (2003). Sublinear scaling of fracture aperture versus length: an exception or the rule? *J. Geophys. Res: Solid Earth.* 108:B9. doi: 10.1029/2001jb000419

Rajabi, M., Tingay, M., and Heidbach, O. (2016). The present-day state of tectonic stress in the Darling Basin, Australia: implications for exploration and production. *Mar. Pet. Geol.* 77, 776–790. doi: 10.1016/j.marpetgeo.2016.07.021

Shi, J., Zeng, L., Zhao, X., Zhang, Y., and Wang, J. (2020). Characteristics of natural fractures in the upper Paleozoic coal bearing strata in the southern Qinshui Basin, China: implications for coalbed methane (CBM) development. *Mar. Pet. Geol.* 113:104152. doi: 10.1016/j.marpetgeo.2019.104152

Strijker, G., Bertotti, G., and Luthi, S. M. (2012). Multi-scale fracture network analysis from an outcrop analogue: a case study from the Cambro-Ordovician clastic succession in Petra, Jordan. *Mar. Pet. Geol.* 38, 104–116. doi: 10.1016/j.marpetgeo.2012.07.003

Tang, X., Zhang, J., Wang, X., Yu, B., Ding, W., Xiong, J., et al. (2014). Shale characteristics in the southeastern Ordos Basin, China: implications for hydrocarbon accumulation conditions and the potential of continental shales. *Int. J. Coal Geol.* 12, 32–46. doi: 10.1016/j.coal.2014.03.005

Torabi, A., and Berg, S. S. (2011). Scaling of fault attributes: a review. *Mar. Pet. Geol.* 28, 1444–1460. doi: 10.1016/j.marpetgeo.2011.04.003

Wang, Y., Chang, X., Sun, Y., Shi, B., and Qin, S. (2020). Investigation of fluid inclusion and oil geochemistry to delineate the charging history of Upper Triassic Chang 6, Chang 8, and Chang 9 tight oil reservoirs, Southeastern Ordos Basin, China. *Mar. Pet. Geol* 113:104115. doi: 10.1016/j.marpetgeo.2019.104115

Wang, Y., Liu, L., Li, S., Ji, H., Xu, Z., Luo, Z., et al. (2017). The forming mechanism and process of tight oil sand reservoirs: a case study of Chang 8 oil layers of the Upper Triassic Yanchang Formation in the western Jiyuan area of the Ordos Basin, China. *J. Pet. Sci. Eng.* 158, 29–46. doi: 10.1016/j.petrol.2017.08.026

Xing, L., Xu, L., Zhao, Y., Wang, X., and Zhou, D. (2016). Hydrocarbon Accumulation of Linzhen Yanan Formation in Ordos Basin. *Spec. Oil Gas Reserv* 23, 14–18.

Xu, S., Hao, F., Gou, Q., Liu, R., Liu, J., and Tian, J. (2020). Multiscale Faults and Fractures Characterization and Their Effects on Shale Gas Accumulation in the Jiaoshiba Area, Sichuan Basin, China. *J. Pet. Sci. Eng* 189:107026. doi: 10.1130/abs/2019am-338586

Zeng, L. (2008). *Formation and Distribution of Fractures in Low-permeability Sandstone Reservoirs*. Beijing: Science Press.

Zeng, L., and Li, X. (2009). Fractures in sandstone reservoirs with ultra-low permeability: a case study of the Upper Triassic Yanchang Formation in the Ordos Basin, China. *Am. Assoc. Pet. Geol. Bull.* 93, 461–477. doi: 10.1306/09240808047

Zeng, L., Li, Z., Shi, C., Wang, Z., Zhao, J., and Wang, Y. (2007). Characteristics and origin of fractures in the extra low-permeability sandstone reservoirs of the Upper Triassic Yanchang Formation in the Ordos Basin. *Acta Geol. Sin.* 81, 174–180.

Zeng, L., Lyu, P., Qu, X., and Fan, J. (2020). Multi-scale fractures in tight sandstone reservoirs with low permeability and geological conditions of their development. *Oil Gas Geol.* 41, 449–454. doi: 10.11743/ogg20200301

Zeng, L., Su, H., Tang, X., Peng, Y., and Gong, L. (2013). Fractured tight sandstone oil and gas reservoirs: a new play type in the Dongpu depression, Bohai Bay Basin, China. *Am. Assoc. Pet. Geol. Bull.* 97, 363–377. doi: 10.1306/09121212057

Zeng, L. B., Gao, C. Y., Qi, J. F., Wang, Y. K., Li, L., and Qu, X. F. (2008). The distribution rule and seepage effect of the fractures in the ultra-low permeability sandstone reservoir in east Gansu Province, Ordos Basin. *Sci. China Ser. D Earth Sci.* 51, 44–52. doi: 10.1007/s11430-008-6015-8

Zoback, M. D., Barton, C. A., Brudy, M., Castillo, D. A., Finkbeiner, T., Grollimund, B. R., et al. (2003). Determination of stress orientation and magnitude in deep wells. *Int. J. Rock Mech. Min. Sci.* 40, 1049–1076. doi: 10.1016/j.ijrmms.2003.07.001

Conflict of Interest: The authors declare that the research was conducted in the absence of any commercial or financial relationships that could be construed as a potential conflict of interest.

frontiers in Earth Science

ORIGINAL RESEARCH
published: 16 June 2021
doi: 10.3389/feart.2021.663401

Reservoir Characteristics and Main Controlling Factors of the Mesozoic Volcanic Rocks in the D Oilfield in Southern Gentle Slope Zone of the Laizhouwan Sag

Jun Xie[1], *Xiao Hu*[1], *Baichuan Li*[1], *Yajun Duan*[1], *Huizhen Liang*[2]*, *Yanchun Su*[3], *Wuchao Cai*[1] *and Rui Wang*[1]

[1]College of Earth Science and Engineering, Shandong University of Science and Technology, Qingdao, China, [2]College of Mechanical and Electronic Engineering, Shandong University of Science and Technology, Qingdao, China, [3]CNOOC China Limited, Tianjin Branch, Tianjin, China

The Mesozoic volcanic rocks are widely developed in the Bohai Bay basin. The D oilfield, located in the southeast of the Bohai Bay Basin, is a Cenozoic depression developed on the base of the Mesozoic. The types of the volcanic rocks are complex and the reservoir space is diverse. According to the characteristics of the volcanic reservoir, such as vertical multi-stage and strong heterogeneity, and based on the analysis of the volcanic core observation, thin section identification, logging data and seismic data, we analyzed the reservoir space type, physical property characteristics and reservoir physical property control factors of volcanic reservoir in the study area. The results show that the volcanic rocks in the study area are mainly volcanic breccia, andesite and tuff; the lithofacies types mainly include volcanic eruption facies, effusion facies and volcanic sedimentary facies, and the volcanic eruption facies is the most developed. Four types of volcanic reservoirs and 14 effective storage space types have been identified from the macroscopic and microscopic multi-scale, mainly intergranular pores, intergranular dissolution pores, intracrystalline pores, structural fractures and weathering dissolution fractures. Reservoir performance is mainly affected by lithology, lithofacies, tectonic activity and diagenesis. The primary pores in the upper part of exhalative and explosive facies are the most developed. Early cement filling is beneficial to the preservation of primary intergranular pore space and is an important prerequisite for the formation of secondary dissolution pores. Under the action of multi-stage tectonic movement and weathering leaching, the reservoir performance of volcanic rocks has been greatly improved, and the volcanic rocks with superimposed fractures and porosities are effective volcanic reservoirs.

Keywords: laizhouwan sag, mesozoic, volcanic rock, reservoir characteristics, main controlling factors

OPEN ACCESS

Edited by:
Jon Jincai Zhang,
Sinopec Tech Houston Center,
United States

Reviewed by:
Chao Liang,
China University of Petroleum, China
Jinliang Zhang,
Beijing Normal University, China
Suhua Jiang,
Ocean University of China, China

****Correspondence:***
Huizhen Liang
2823451361@qq.com

Specialty section:
This article was submitted to Sedimentology, Stratigraphy and Diagenesis, a section of the journal Frontiers in Earth Science

Received: *02 February 2021*
Accepted: *31 May 2021*
Published: *16 June 2021*

Citation:
Xie J, Hu X, Li B, Duan Y, Liang H, Su Y, Cai W and Wang R (2021) Reservoir Characteristics and Main Controlling Factors of the Mesozoic Volcanic Rocks in the D Oilfield in Southern Gentle Slope Zone of the Laizhouwan Sag. Front. Earth Sci. 9:663401. doi: 10.3389/feart.2021.663401

INTRODUCTION

In the middle and late last century, the comprehensive geology of volcanic oil and gas reservoirs began to be studied. The main research methods of volcanic reservoir include core analysis, logging analysis, geophysical experiment and so on (Fang et al., 2011; Zhang, 2011; Xiong et al., 2012). The reservoir space of volcanic rocks is more complex than that of sedimentary rocks, and the study of reservoir performance is an important part of volcanic reservoirs (Somasundaram et al., 2017; Leng et al., 2020). According to pore genesis, volcanic reservoir space can be divided into four types: primary pore, secondary pore, primary fracture and secondary fracture, and can be divided into three types: pore, cave and fracture (Hawlander, 1990; Fan et al., 2018; Yu, 2019). The combination of different types of reservoir space leads to the diversity of igneous reservoir space (Jansa, 1988; He et al., 2019; Kong, 2020; Xie, 2020). Among them, fractures play the main role of connectivity and seepage in volcanic reservoir space, which is the focus of reservoir space research. The methods used to identify fractures include conventional logging curve identification method, fracture index method, curvature change rate method, saturation ratio method, discriminant analysis method, fuzzy mathematics method, neural network method, MFI imaging logging method and so on (Wang et al., 2007; Liu et al., 2008; Zhang, 2012). Diagenesis plays a very important role in the evolution of volcanic pores and is an important factor in the development of primary and secondary pores in volcanic reservoirs (Levin, 1995; Liu Y. et al., 2018; Liyao et al., 2018; Hu et al., 2020). The Mesozoic volcanic rocks are widely distributed in the Bohai Bay Basin, covering the whole basin (Jin et al., 2012; Cai et al., 2018; Liu X.J. et al., 2018). In 2014, a high abundance reservoir was found in the Mesozoic of the D oilfield in the South gentle slope of the Laizhouwan sag (Jin et al., 2013; Yang et al., 2017; Wang B. Q. et al., 2020). However, in the research and exploration of volcanic rocks in the Bohai Bay oilfield for many years, due to the high exploration cost of offshore platform, limited data collection, difficult identification of volcanic lithofacies, complex lithology and strong reservoir heterogeneity, the degree of exploration is restricted. Therefore, it is urgent to study the types of reservoir space, porosity and permeability characteristics, pore structure and main controlling factors of the Mesozoic volcanic reservoir, so as to provide certain basis and guidance for later exploration and development as well as favorable area selection. This work can provide ideas for volcanic reservoir prediction and oil and gas reservoir exploration in the Bohai Bay Basin, and provide supplementary for research results of Mesozoic volcanic rocks in offshore oilfields of China, and also has certain reference value for exploration of similar reservoirs.

GEOLOGICAL BACKGROUND

The Laizhouwan sag is located in the southeast of the Bohai Sea. It is adjacent to the north sag of the Laizhouwan sag in the north and the south sub sag of the Laizhouwan sag in the East. It is a Cenozoic sag developed on the Mesozoic base. Under the influence of the Indosinian movement and the Yanshanian movement, strong volcanic activities occurred in the Mesozoic rifting process (Cai et al., 2001; Duan et al., 2020a). D oilfield is located in the southern slope zone of the Laizhou Bay (**Figure 1**), and its structure is a fault semi anticline. Due to the complexity of fault development, the oilfield has the characteristics of multiple fault blocks and multiple highs. Its strike is mainly east-west and its dip is due north. The strata revealed by drilling in the study area are the Quaternary Pingyuan formation, Neogene Minghuazhen Formation and Guantao formation, Paleogene Dongying Formation and Shahejie Formation and Mesozoic (not penetrated) from top to bottom (Lu et al., 2018; Wang et al., 2019). The Mesozoic buried hill in the study area is located in the high part, close to the hydrocarbon generation center of the Laizhouwan sag, with good trap conditions, well-developed fractures and good reservoir forming conditions of volcanic rocks. Drilling revealed that the Mesozoic in this area mainly developed volcanic strata of the Cretaceous Yixian formation.

Based on the analysis of drilling data and seismic data, the Mesozoic, the target interval of this study, is revealed by drilling of D-4, D-6, D-7, D-9, and D-10 within the scope of the oilfield

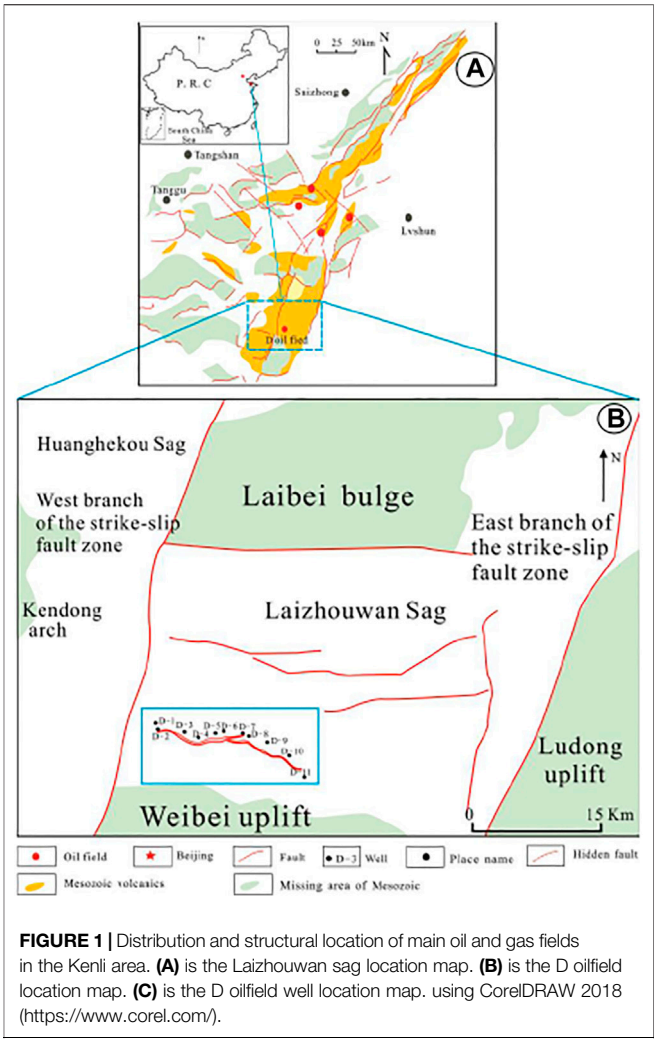

FIGURE 1 | Distribution and structural location of main oil and gas fields in the Kenli area. **(A)** is the Laizhouwan sag location map. **(B)** is the D oilfield location map. **(C)** is the D oilfield well location map. using CorelDRAW 2018 (https://www.corel.com/).

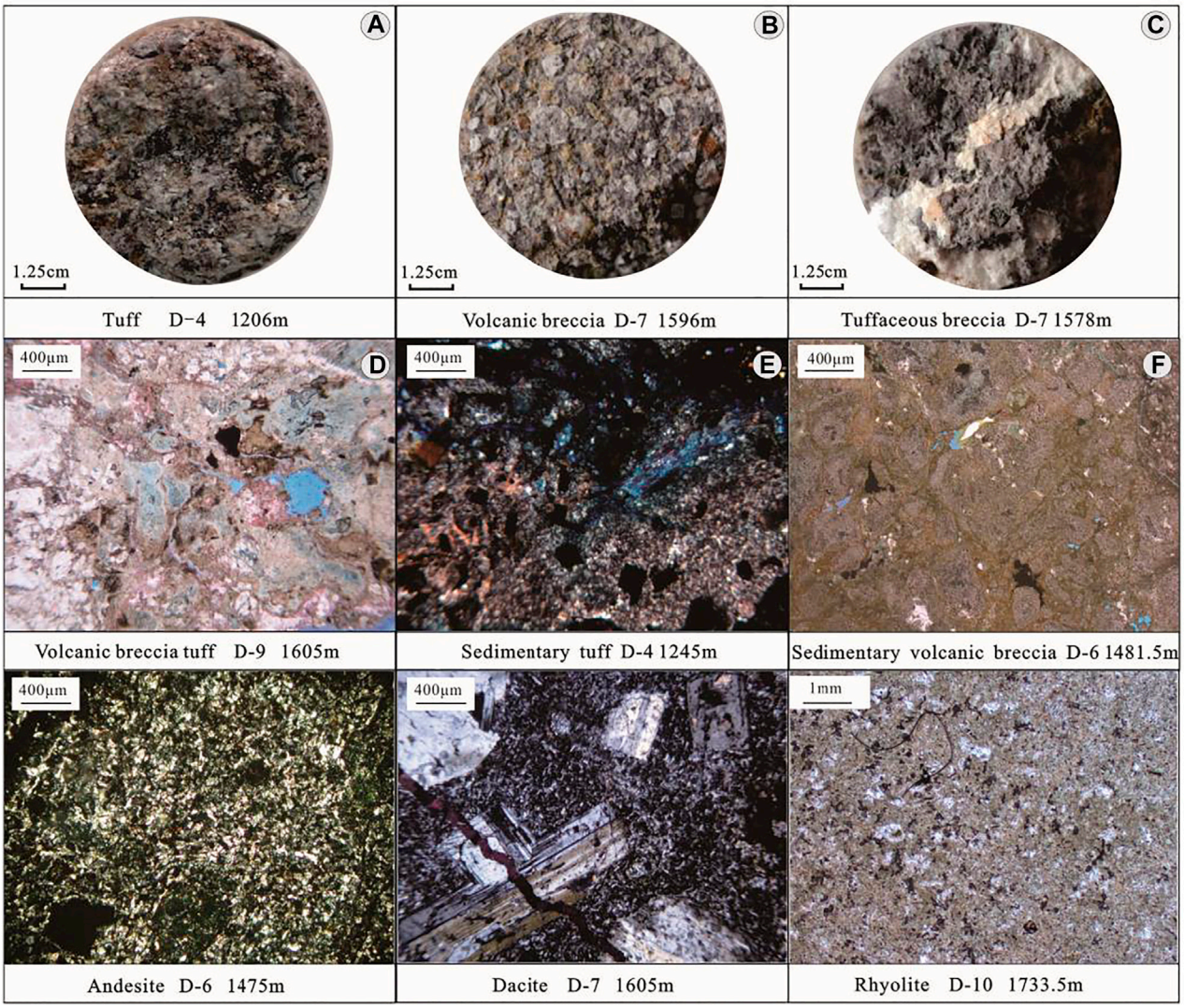

FIGURE 2 | Lithology photos of volcanic rocks in the D Oilfield.

(**Figure 2C**). However, the drilling did not drill through the formation, and the thickness of the revealed formation is 11.8–215.0 m. The lithology of the study area mainly includes pyroclastic rock, lava and sedimentary pyroclastic rock (Duan et al., 2020b). This area belongs to low exploration area and has great exploration potential.

SAMPLES AND METHODS

We have collected eight logging curves from each well in the core bank of the D oilfield. Reservoir evaluation method requires qualitative analysis of sedimentation and diagenesis, and quantitative analysis of physical properties and pore structure. A total of 68 core samples were processed by scanning electron microscope (Evo) to identify clay mineral distribution and secondary pore size. In order to identify the clay minerals in volcanic rocks, X-ray diffraction analysis of clay with size less than 2 μm was carried out in Rigaku RU 200 diffractometer. The sample used for diffractometer was air dried, ethylene glycol was saturated and heated at 490°C for 4 h. According to the Darcy's law, a total of 123 samples were collected from the target reservoir for conventional petrophysical analysis, and gas porosity and permeability were measured by instruments. We identified 136 samples from the study area by conventional rock and mineral methods by polarizing microscope (POROTm300). In addition, a total of 78 samples were made into thin cast sheets, and the samples were vacuum impregnated with alizarin epoxy resin and potassium ferricyanide, so that the pores could be clearly seen and the carbonates could be identified (Dickson, 1965). The Dickson's method helps to distinguish between pores and grains. Put the full diameter core into GE vtomx m 300 nm CT equipment, adjust the equipment parameters for scanning, and get pore data table, pore throat data table and scanning slice.

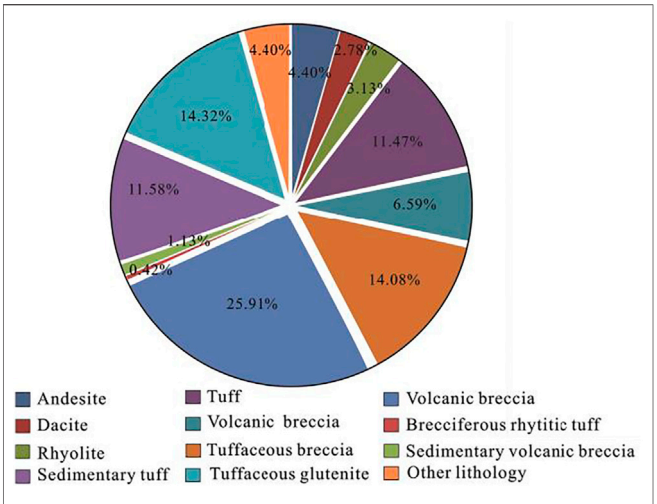

FIGURE 3 | Lithologic content ratio of the Mesozoic volcanic rocks in the D oilfield of the Laizhouwan sag.

RESULTS

Types and Characteristics of Volcanic Rocks

Based on the analysis of cuttings, logging data, core thin section data and borehole wall coring data of each well in the study area, the main types of Mesozoic volcanic rocks in the study area are pyroclastic rocks, volcanic lava and sedimentary pyroclastic rocks. A small amount of pyroclastic sedimentary rocks, mainly tuffaceous glutenite, can be seen in the lower part of D-7 and D-10.

Pyroclastic rocks include volcanic breccia, tuff, tuffaceous volcanic breccia, volcanic breccia tuff, and breccia bearing rhyolitic tuff. The Volcanic lava can be seen andesite, rhyolite, dacite. The tuff is mostly light gray, light brown and gray, mainly composed of fine volcanic ash and volcanic dust, containing a small amount of quartz, hornblende and biotite, with massive structure and tuff structure, dense and hard, and some of them are altered. The Volcanic breccia is mainly gray, grayish green and reddish brown. The gravel is mainly composed of volcanic rock block and feldspar. The rock debris is mainly andesite and rhyolite. The crystal debris is mainly composed of neutral plagioclase and subangular. The separation is poor, with fracture development and volcanic breccia structure. The Volcanic breccia tuff is mainly grayish green and variegated. Its rock composition is mainly composed of volcanic breccia, cuttings and tuffaceous. The Volcanic breccia is rhyolite and tuff, and crystal cuttings are quartz and feldspar. The rock pores are not developed. The main reservoir space is microcracks or dissolution pores, and most of them are tuff structure. The andesite is mainly brownish gray and dark brown, with porphyritic texture. The phenocrysts are feldspar and plagioclase, and the matrix is fine lath plagioclase, showing interwoven structure. The development of rock pores is poor, with fracture development, a small amount of chlorite and argillaceous filling, and a small amount of phenocryst corrosion pores. The tuff is mainly variegated, and the rock is mainly composed of cuttings and volcanic dust. The cuttings are mainly quartz and feldspar of medium and fine sand grade. Most of the cuttings are altered, and some of them are argillized. The matrix is mainly siliceous formed by volcanic dust under high temperature and high pressure, evenly distributed among rock cuttings, with medium development of fractures and pores and tuff structure (**Figure 2**).

Among the volcanic rocks in the study area, the content of pyroclastic rocks is the highest, followed by sedimentary pyroclastic rocks. Among the pyroclastic rocks, the content of volcanic breccia is the highest, followed by tuffaceous volcanic breccia. Among the volcanic lava, andesite has the highest content. Among the sedimentary pyroclastic rocks, the content of tuff is the highest. Other lithology is mainly mudstone, dolomite and a small amount of mixed rock (**Figure 3**).

Volcanic Lithofacies

On the basis of lithology identification of the Mesozoic D oilfield in the Laizhouwan sag, combined with volcanic eruption characteristics (Cas and Wright, 1987), volcanic rock types, production morphology and core thin section characteristics of the Bohai Bay Basin, it is divided that the main development of Mesozoic strata is explosive facies accounting for 61.8%, overflow facies accounting for 10.09% and volcanic sedimentary facies accounting for 28.11% (**Table 1**).

It can be seen from the lithofacies model of the Mesozoic volcanic rocks (**Figure 4**) that the study area is mainly composed of eruptive facies and effusive facies. Vertically, it is mainly a volcanic cycle. From bottom to top, the cycle is mainly composed of eruptive facies, exhalative facies and volcanic sedimentary facies, and a few of them are composed of eruptive facies and overflow facies.

Physical Properties and Reservoir Space Characteristics of Volcanic Rocks

Physical Properties of Volcanic Rocks

According to the data of core, imaging logging and thin section, the Mesozoic reservoir is mainly of pore type, followed by the development of microfractures and dissolution pores, with fracture width of 0.03–0.20 mm and cross connection, forming an effective seepage channel. According to the log interpretation results, the distribution range of reservoir porosity is 2–31.1%, the average value is 14.01%, mainly distributed in 5–20%. The fracture porosity ranges from 0.01 to 1.52%, which shows the reservoir characteristics of high porosity and dual porosity medium. The permeability distribution ranges from 0.003 to 79.3 mD, with a large span, which is mainly caused by the complex lithology. The overall lithology is relatively dense, and the permeability is small, with an average permeability of 6.16 mD (**Figure 5**).

From the relationship between permeability and buried depth, it can be seen that the permeability decreases with the increase of depth. It can be seen from the relationship between porosity and permeability (**Figure 6**) that the correlation coefficient of porosity and permeability is only 0.1067, which is poor. Therefore,

TABLE 1 | Lithology and structural characteristics of the Mesozoic volcanic rocks in the D Oilfield.

Lithofacies	Characteristic lithology of the study area	Structure
Eruption facies	Volcanic breccia, Volcanic breccia tuff, Tuffaceous breccia, Tuff	Volcanic breccia texture, Tuff structure
Effusive facies	Andesite, Dacite, Rhyolite	Porphyritic structure, Interwoven structure, Multi-spot structure, Cryptocrystalline structure, Cataclastic structure
Volcanic sedimentary facies	Sedimentary tuff, Sedimentary volcanic breccia, Tuffaceous sandstone, Tuffaceous conglomerate, Tuffaceous fine sandstone	Tuff structure, Medium coarse sandy texture, Settled breccia structure

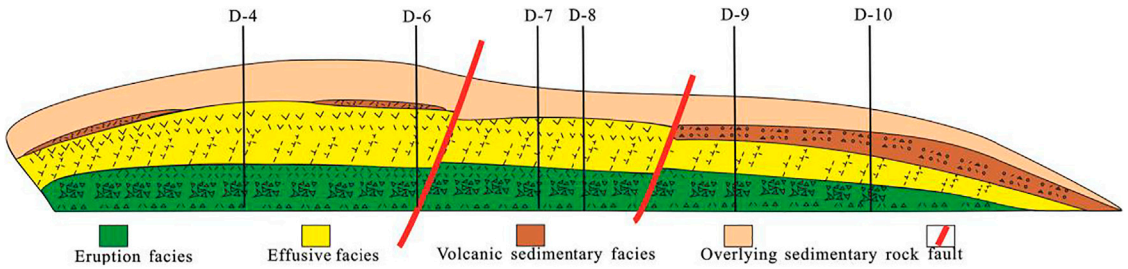

FIGURE 4 | Lithofacies model of the Mesozoic volcanic rocks in the D oilfield of the Laizhouwan sag.

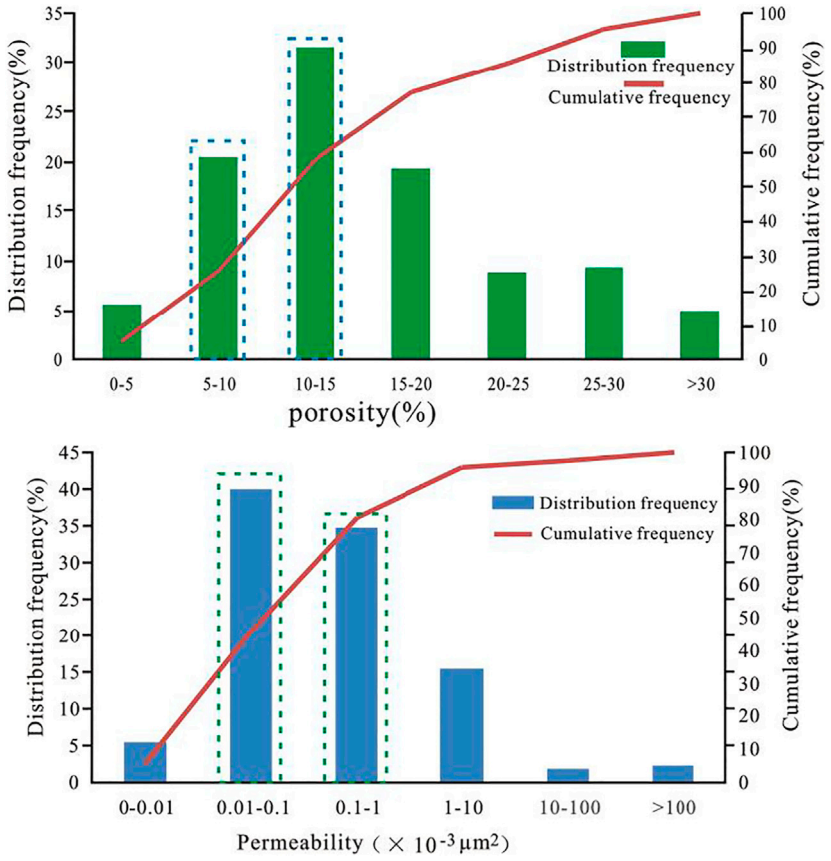

FIGURE 5 | Distribution frequency of porosity and permeability of the Mesozoic volcanic rocks in the D oilfield of the Laizhouwan sag.

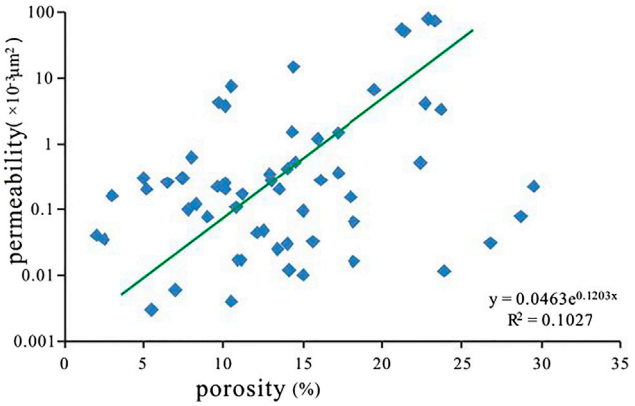

FIGURE 6 | Relationship between porosity and permeability of the Mesozoic volcanic rocks in the D oilfield of the Laizhouwan sag.

fractures have a certain impact on the reservoir space and belong to the pore fracture type reservoir.

Types of Volcanic Reservoir Space

The volcanic rocks in the study area are affected by tectonism, weathering leaching and diagenesis. The types of reservoir space include primary pore, secondary pore, primary fracture and secondary fracture (**Table 2**). The Mesozoic reservoir is dominated by pore type, followed by microfractures and dissolution pores, with fracture width of 0.03–0.20 mm and cross connection, forming an effective seepage channel (**Figure 7**).

Pore Structure of Volcanic Reservoir

Through the analysis of capillary pressure curves measured by mercury injection method (Wang M.Q. et al., 2020) in each well in the study area, it can be seen that the pore throat of the reservoir in the study area belongs to the reservoir with good sorting and fine skewness. According to the shape and parameters of capillary pressure curves of different rock samples, the micro pore structure of the reservoir in the study area can be divided into three categories (**Figure 8**).

Type I pore structure: the displacement pressure of this kind of reservoir is very low, the median pressure value of mercury saturation is low, the maximum mercury saturation value is relatively high, and the curve platform is good. It is the best pore structure of volcanic reservoir in the study area because of the coarseness of pore throat, the best physical property, the largest pore throat radius and the largest average capillary pore radius.

Type II pore structure: the displacement pressure of this kind of reservoir is relatively low, the median pressure of mercury saturation is relatively low, the maximum mercury saturation is relatively high, and the curve has no obvious platform. This kind of reservoir has smaller physical properties, smaller maximum pore throat radius and average capillary radius, which is a relatively good pore structure of volcanic reservoirs in the study area.

Type III pore structure: this kind of reservoir has relatively high displacement pressure, relatively high median pressure of mercury saturation, low maximum mercury saturation and good curve platform. This kind of reservoir has the worst physical property, the average value of maximum pore throat radius and capillary pore radius is the smallest, and the displacement

TABLE 2 | Types and characteristics of the Mesozoic volcanic reservoir space in the D Oilfield.

Cause type		Types of reservoir space	Formation mechanism	Characteristic
Pore	Primary pore	Stoma	Pores formed by gas expansion during diagenesis	Most of them are distributed at the top and bottom of rock strata, round or oval
		Amygdala foramen	Pores between minerals after filling	Most of them are distributed on the top of the rock, irregular
		Intergranular pore	Residual pores between clastic grains after diagenesis and compaction	Most of them are found in pyroclastic rocks with irregular shape and different sizes
	Secondary pore	Intergranular dissolved pore	The pores formed by the dissolution of the interstitial materials between pyroclastic particles	It is common in pyroclastic rocks and has irregular shape
		Intercrystalline dissolution pore	Pores formed by phenocrysts, dissolution of mineral crystals and mineral transformation	Between phenocrysts, irregular shape
		Intracrystalline dissolution pore	Pores formed by phenocrysts, dissolution of mineral crystals and mineral transformation	Intracrystalline growth of authigenic minerals
		Devitrification pore	Pores formed by glass devitrification	In chlorite and zeolite minerals
		Pores between gravels	Pores formed by leaching and dissolution of pyroclastic particles	Between breccia, irregular shape
		Pores in gravel	Pores formed by dissolution in breccia	In breccia, irregular shape
Fracture	Primary fracture	Condensation contraction joint	Cracks caused by condensation shrinkage	The edge of rock mass is high low angle
		Fried cracks	Cracks formed by self breaking or concealed blasting	In the middle and lower part of the rock mass, there is a high angle
	Secondary fracture	Structural fracture	Fractures formed by tectonic stress	Near the fault, it is directional and appears in groups
		Dissolution fracture	Cracks formed by dissolution	It is widely distributed and irregular in shape
		Weathering fracture	Cracks formed by weathering	Rock surface

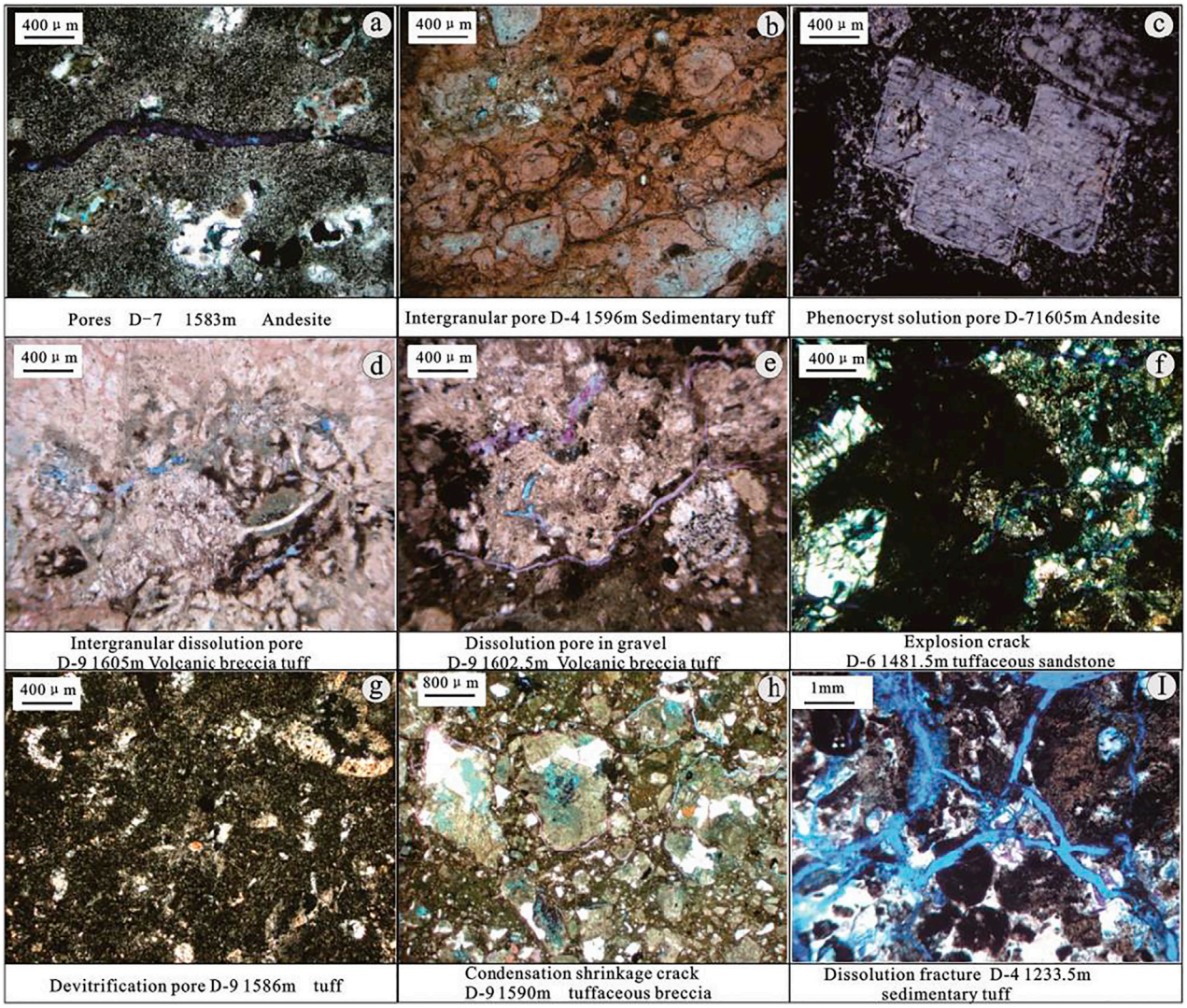

FIGURE 7 | Photos of the Mesozoic volcanic reservoir space types in the D oilfield of the Laizhouwan sag.

pressure is the highest, which is the relatively poor pore structure of volcanic reservoir in the study area.

Characteristics of Reservoir Fractures in the Study Area

According to the statistics of the fractures identified in the study area, it can be seen that the filled fractures account for 48.32% of the total fractures, nearly half of them, the half-filled fractures account for 32.55%, the unfilled fractures account for 19.12%, and the fracture width is mainly distributed between 0.01 and 0.5 mm. According to the core photos and core description statistics, the low angle fractures of volcanic rocks in the study area are the most developed, accounting for 34.88%, followed by oblique fractures, accounting for 32.56%, and high angle fractures, accounting for 23.26%. The vertical fractures and horizontal fractures were the least developed, accounting for 6.98 and 2.33%, respectively. Low angle fractures and oblique fractures are the main types of fractures in the study area (**Figure 9**). The fracture strikes in the study area are mainly northeast-southwest, and a small part of the fractures are near east-west. The fracture porosity in the study area was calculated to be 0.2% (**Figure 10**).

Diagenesis

The evolution of reservoir pore is affected by lithology, diagenesis and tectonism of volcanic rocks, and goes through the whole process of volcanic reservoir formation. During the Mesozoic Jurassic, the Bohai Bay Basin entered the rift basin development stage, accompanied by a large number of volcanic activities. The magma erupted and deposited in the rift basin. After the volatilization and dissipation of gas, a large number of pores are formed in volcanic rocks. At the same time, due to the gradual decrease of temperature, the rock condenses and shrinks to produce condensing contraction joints, which makes the

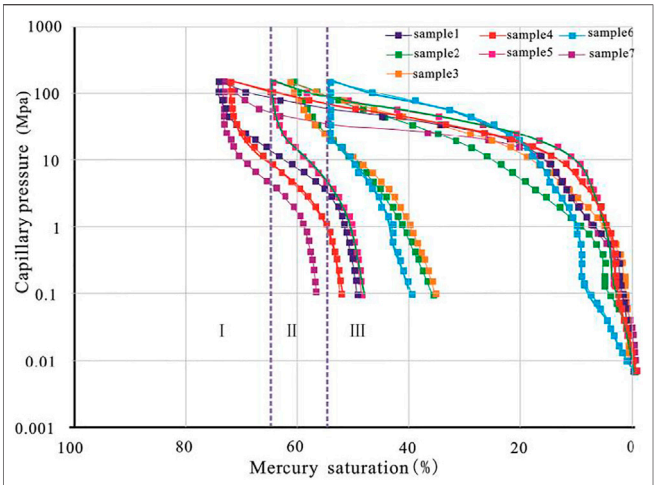

FIGURE 8 | Pore types of the Mesozoic volcanic reservoir in the D oilfield of the Laizhouwan sag.

reservoir performance better. In the later stage of magmatism, amygdaloid was formed due to hydrothermal alteration. With the continuous deposition of volcanic rocks, the primary pores decrease due to filling and crystallization. At the same time, with the deepening of burial depth, the porosity will also decrease under the influence of compaction. Under the weathering and leaching process, some previously deposited strata exposed to the surface due to the continuous uplift of the later strata produce secondary pores. Under the dissolution caused by the infiltration of acidic liquid into the reservoir, the porosity is continuously expanded and the reservoir capacity is increased. But at the same time, the porosity will decrease because the fractures and pores are filled by quartz or feldspar again, with the influence of metasomatism and filling. With the continuous progress of tectonic movement, a large number of fractures are produced in the rock after diagenesis due to the late structural fragmentation, which increases the reservoir performance. After the continuous change of pore evolution, the volcanic reservoir pores are finally and stably formed (**Figures 11**, **12**).

DISCUSSION

The formation of volcanic reservoir is complex and the types of reservoir space are various, and its formation process is controlled by many factors (Zhang et al., 2018; Zheng et al., 2018; Yang et al., 2020). Through the study of the Mesozoic volcanic reservoir in the D oilfield of the Laizhouwan sag, it is considered that the reservoir development is mainly affected by lithology, tectonic movement and diagenesis.

Influence of Lithology and Lithofacies

Combined with previous studies, we can know that any volcanic rock lithology can form reservoir, but the enrichment degree of volcanic rocks with different lithology is different, which mainly depends on the influence of volcanic eruption intensity, lithofacies, tectonism, and diagenesis on the reservoir space type and development degree of volcanic rocks (Ran et al., 2005; Tang and Ji, 2006; Zhu et al., 2019).

According to the statistical results of physical properties of different lithology, the physical properties of different types of volcanic rocks are obviously different, and the best physical properties are tuff, volcanic breccia and andesite. The porosity of the Tuff is mainly distributed in 7.9–31.1%, and the average porosity is 17.72%. The permeability is mainly distributed in 0.004–79.3 mD, and the average permeability is 14.19 mD. The porosity of volcanic breccia ranges from 2.2 to 30.3%, and the average porosity is 16.185%. The permeability is 0.006–40 mD, and the average permeability is 5.2 mD. The porosity of andesite is mainly distributed in 7.5–16.1%, the average porosity is 14.2%. The permeability is mainly distributed in 0.2–14.9 mD, and the average permeability is 3.5 mD (**Figure 13**).

According to the statistics of the face rate of different lithology in the study area (**Figure 14**), the average face rate of tuff in the study area is the highest, which is 7.29%, followed by volcanic breccia and andesite, which are 5.82 and 4.92%, respectively. The face ratios of volcanic breccia, tuff, tuff and tuffaceous volcanic breccia are 4.12, 4.03, 3.46, and 3.28%, respectively. The dacite and rhyolite have the lowest average face rate of 2.87 and 2.23%, respectively. In general, the best lithology in the study area is tuff, andesite and volcanic breccia.

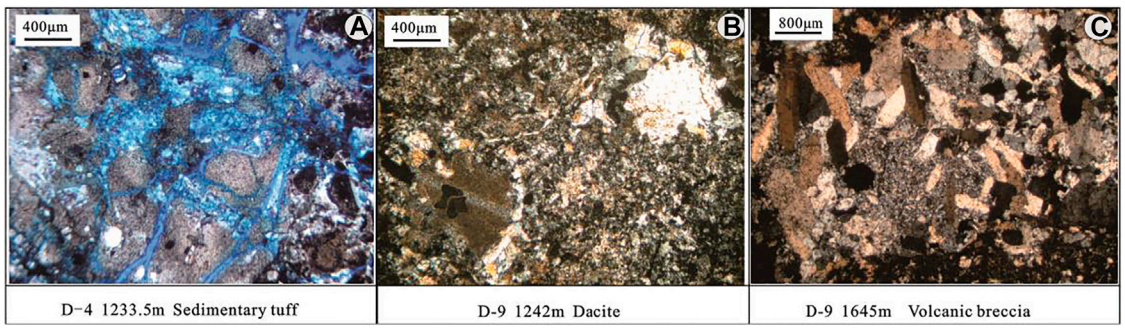

FIGURE 9 | Photos of fractures in the study area.

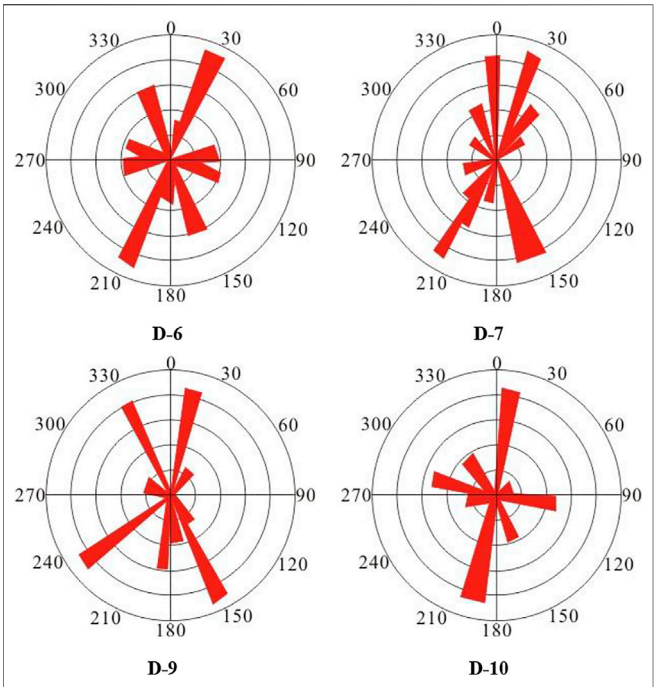

FIGURE 10 | Rose diagram of fracture strike of the Mesozoic volcanic rocks in the D oilfield of the Laizhouwan sag.

Influence of Tectonic Movement

The tectonic movement controls the volcanic activity and the distribution of volcanic rocks, and improves the performance of volcanic reservoir space. The Tectonic movement can cause a large number of fractures in the originally dense volcanic reservoir, which further improves the original reservoir performance (Su et al., 2020).

In the Bohai Sea area, the Mesozoic volcanic activity occurred in the late Jurassic Early Cretaceous, mainly in the early Cretaceous. The Cretaceous volcanic rocks are mainly developed in the low uplift of the northern Laizhou Bay. The southern section of the Bohai Sea is the most active area of the Mesozoic volcanic activity in the Bohai Sea. The Seismic data show that strike slip and extension fault systems are developed in the gentle slope zone of the southern the Laizhouwan sag. A large fault nose is developed in the basement of the Mesozoic, which is controlled by two first type faults. The degree of rock brittleness affects the formation of fractures. Under the same tectonic stress, the more brittle the rock is, the more likely it is to produce fractures. The Volcanoes with less brittleness are prone to deformation and fractures are not developed. Many primary pores in volcanic rocks are not connected with each other, so the permeability of volcanic rocks is very poor. The Tectonic action can form a large number of fractures, which connect the original isolated primary pores in volcanic rocks and increase the reservoir space of volcanic rocks. Moreover, structural fractures are also an important channel for groundwater and organic acids, which is the key to form secondary dissolution pores and improve the seepage capacity of reservoirs (Deng et al., 2002).

The development degree of structural fractures in the study area is andesite, volcanic breccia tuff, volcanic breccia, sedimentary tuff, rhyolite, dacite, tuff, tuffaceous volcanic breccia, rhyolitic tuff, and sedimentary volcanic breccia (**Figure 15**).

Influence of Diagenesis

Diagenesis is one of the important factors affecting the reservoir performance of volcanic rocks (Wang et al., 2017; Miao et al., 2020). In the epidiagenetic stage, the constructive diagenesis is mainly structural fragmentation, weathering leaching and dissolution. In the study area, faults are relatively developed, and groundwater or acidic liquid can penetrate into volcanic reservoir through faults, so as to dissolve the reservoir and improve the reservoir performance. Weathering leaching mainly occurs when the volcanic rocks are exposed to the surface, and the soluble components in the rocks are weathered and dissolved, which improves the reservoir performance. The tectonic process can produce a large number of fractures and connect the originally disconnected pore volume, which greatly improves the reservoir performance. In the stage of burial diagenesis, the main constructive effects on reservoir performance are dissolution and tectonism. At the same time, the mechanical compaction can also improve the reservoir performance to a certain extent, because the mechanical compaction can make the clastic particles in the volcanic rocks break up and improve the reservoir, and the secondary dissolution can make the phenocryst, matrix and various fillers in the pores be dissolved, thus forming secondary pores and improving the reservoir performance. According to the statistics of the distance between the oil producing section and the top of the Mesozoic, the oil layer has a large vertical span, oil-bearing as a whole and local enrichment. However, the vertical enrichment intervals of each fault block are different. The well depth of oil-bearing interval is generally 1,200–1,700 m, and the oil layer is mainly developed within 100 m below the weathering crust at the top of the Mesozoic (**Figure 16**).

In the process of syngenetic magmatic fusion, the crystal chips and glass chips in the rocks are flattened and arranged. The fusion structure of the rocks makes the arrangement more compact and the primary pores smaller. Thermal alteration changes mineral composition and structure and reduces primary reservoir space. In the stage of epigenetic diagenesis, filling and cementation are the main destructive factors. Microcrystalline siliceous aggregate is filled in the breccia, quartz, iron calcite, siliceous, feldspar and other materials are filled in the pores and fractures, making the pores smaller. The chlorite and carbonate minerals produced during cementation also make primary or secondary pores smaller. Filling and compaction are the main destructive factors in burial diagenesis. Compaction can make the clastic particles in volcanic rocks arrange more closely and reduce the primary pores. Generally speaking, the porosity decreases with the increase of burial depth. Because the buried depth of the Mesozoic volcanic rocks in the Laizhouwan sag is relatively

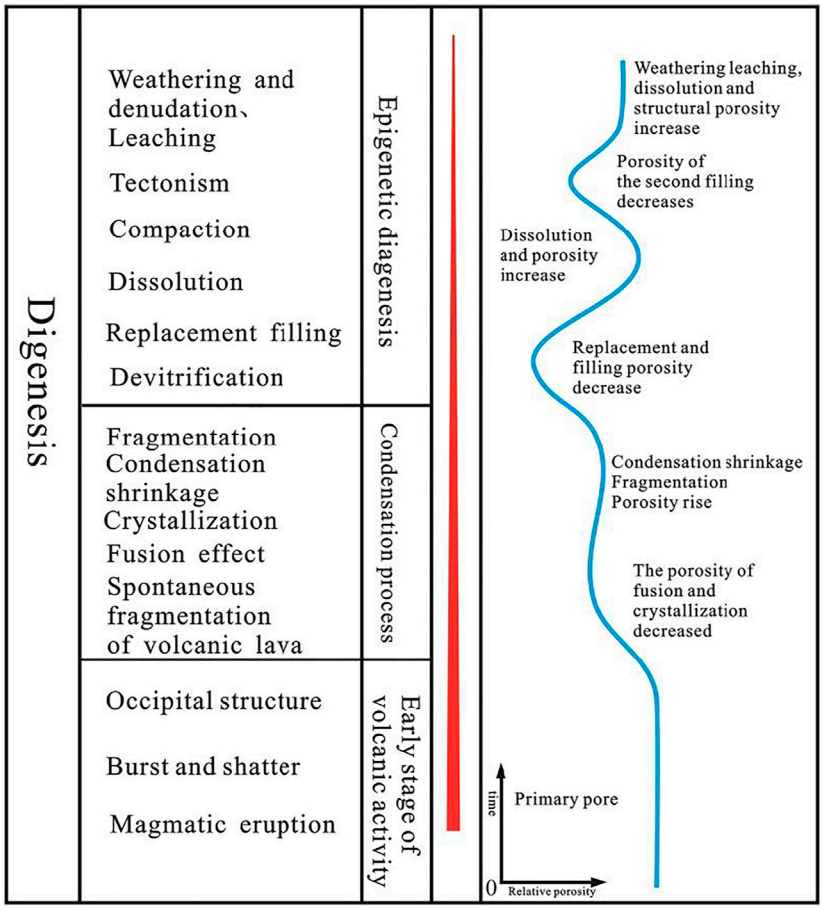

FIGURE 11 | Diagenesis and porosity evolution of volcanic reservoir in the D oilfield of the Laizhouwan sag.

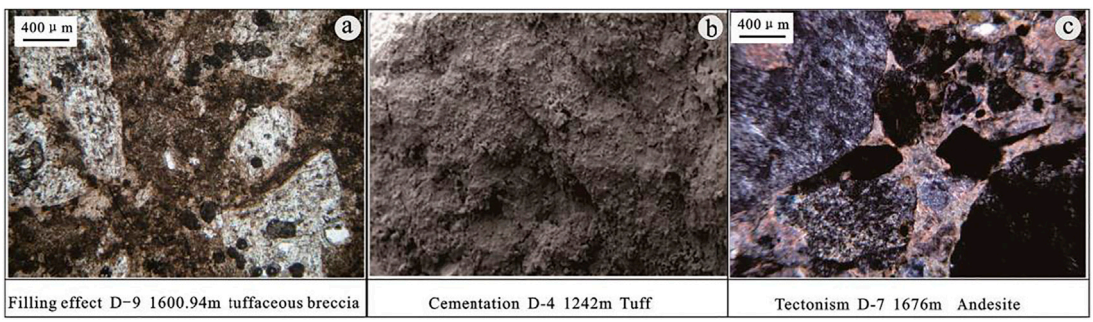

FIGURE 12 | Diagenesis and porosity evolution of volcanic reservoir in the D oilfield of the Laizhouwan sag.

shallow, the destructive effect of compaction on reservoir performance is relatively weak. From the relationship between porosity and burial depth (**Figure 17**), it can be seen that with the increase of burial depth, porosity gradually decreases and reservoir physical properties gradually deteriorate, but the change range is not large. And there will be a relatively high porosity development zone, the porosity gradually decreases from 1,200 to 1,800 m, but the porosity can still reach 27% in 1,580–1,800 m well section. This is because igneous rock is condensed rock, which is less affected by compaction, especially volcanic lava, so the relationship between volcanic rock reservoir and buried depth is small.

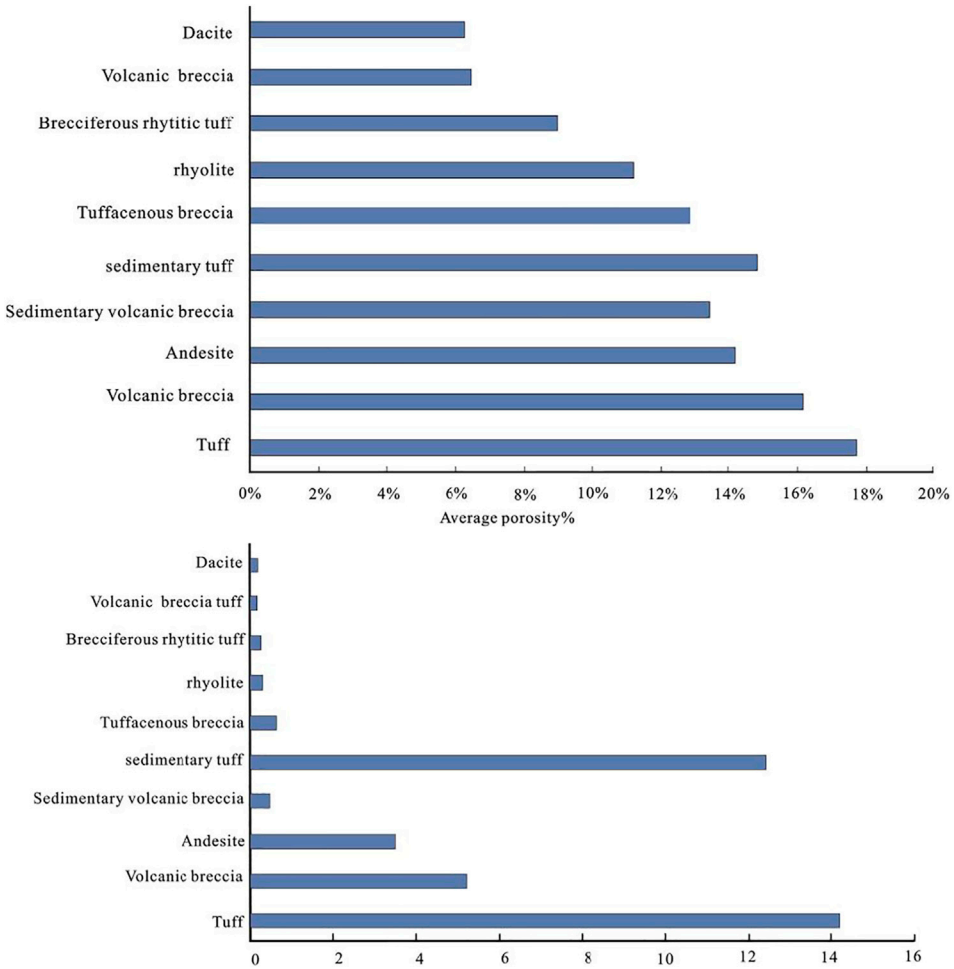

FIGURE 13 | Average values of porosity and permeability for different lithology of the Mesozoic in the D Oilfield.

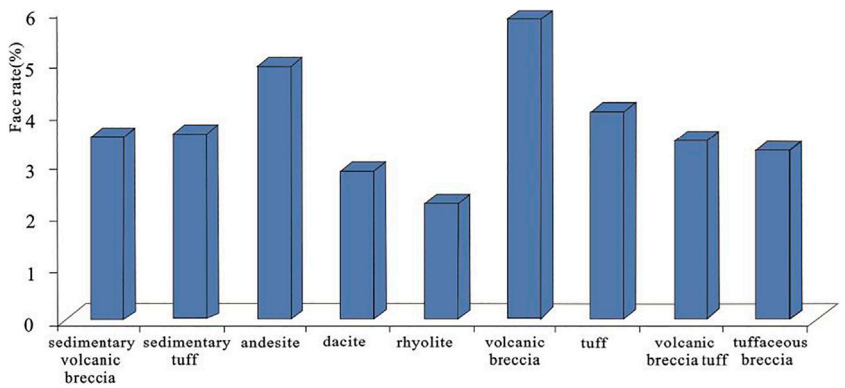

FIGURE 14 | Average face rate of different lithology in the Mesozoic of the D Oilfield.

It can be seen that the lithofacies of volcanic rocks in the study area is the basic factor affecting the reservoir development, weathering leaching and dissolution are the key factors to improve the physical properties of volcanic rocks, and tectonism is an important factor affecting the reservoir performance of volcanic rocks, which controls the development of structural fractures.

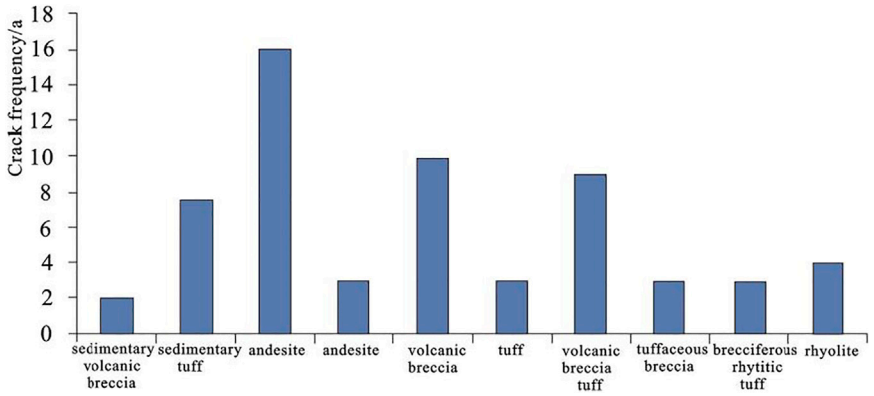

FIGURE 15 | Development frequency of structural fractures with different lithology in Mesozoic of D Oilfield.

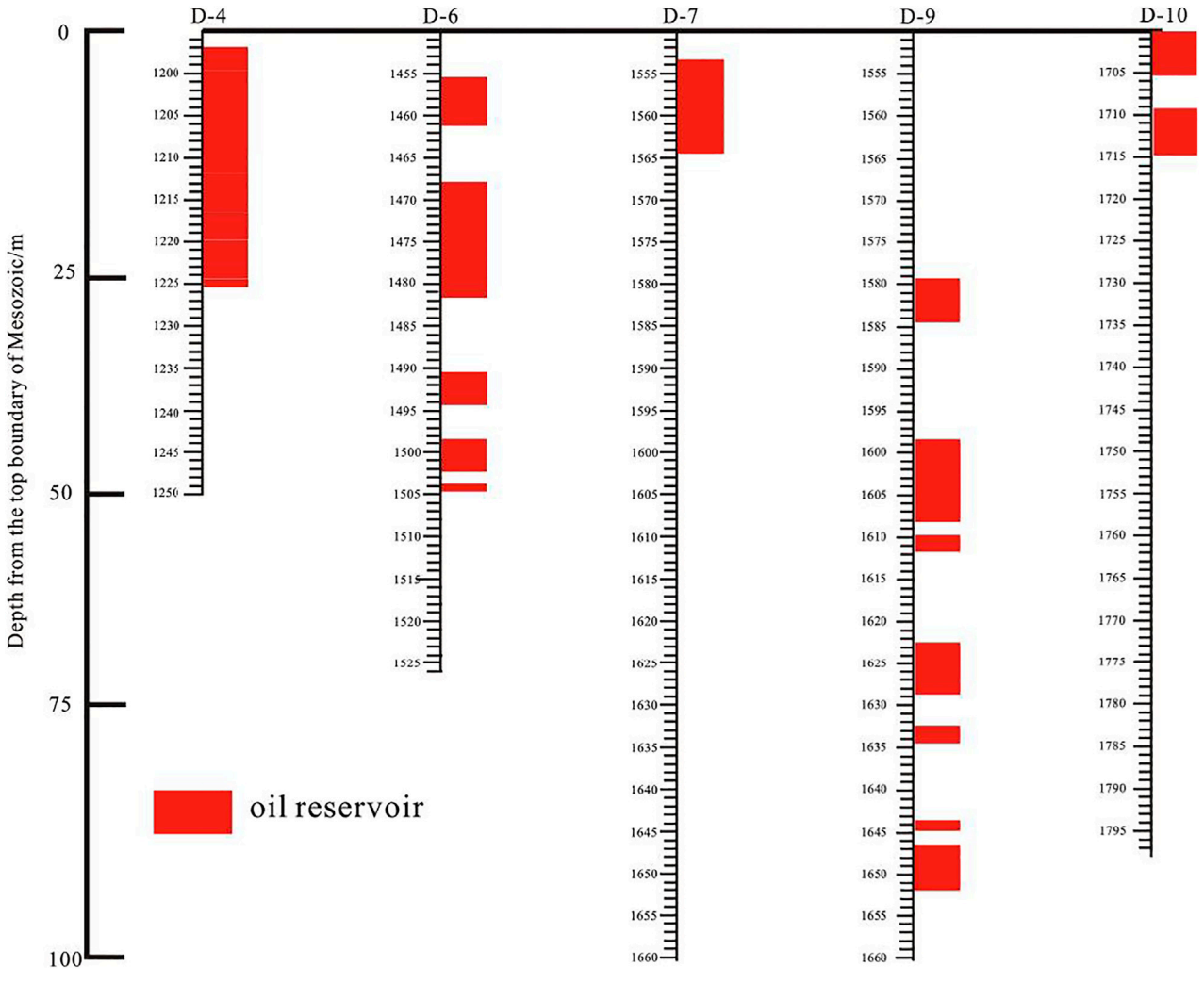

FIGURE 16 | The distance between the oil bearing section of oil wells and the top boundary of the Mesozoic in the study area.

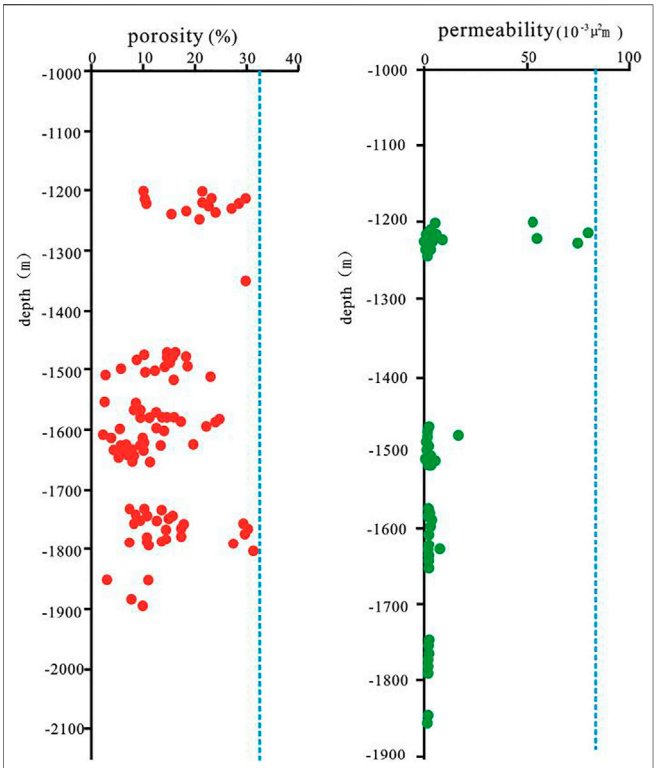

FIGURE 17 | Relationship between porosity, permeability and burial depth of Mesozoic volcanic rocks in D oilfield of the Laizhouwan sag.

CONCLUSION

(1) According to lithology identification, the study area mainly develops volcanic lava (andesite, dacite, and rhyolite), pyroclastic rock (tuff, volcanic breccia tuff, tuffaceous volcanic breccia, volcanic breccia, and rhyolitic volcanic breccia) and sedimentary pyroclastic rock (sedimentary volcanic breccia, and sedimentary tuff). There are three types of lithofacies: explosive facies, exhalative facies, and volcanic sedimentary facies, among which the most important one is explosive facies. According to logging and seismic data, the lithofacies types and distribution characteristics of volcanic rocks are identified. From the bottom to the top of the study area, there are explosive facies, exhalative facies and volcanic sedimentary facies.

(2) Combined with borehole coring and cast thin section data, the main reservoir space types in the study area are primary pore, secondary pore, primary fracture and secondary fracture. The porosity distribution ranges from 2 to 31.1%, with an average of 14.01%. The permeability distribution ranges from 0.003 to 79.3 mD, and the average permeability is 6.16 mD. The best physical properties are tuff, andesite and volcano breccia. According to the capillary pressure curve, the study area has three types of pore structure.

(3) Through the analysis of the reservoir in the study area, two kinds of diagenesis exist in the study area. The constructive diagenesis mainly includes condensation contraction, tectonism, weathering leaching, devitrification, dissolution, and alteration. The destructive effects include compaction, filling, crystallization, and metasomatism. Reservoir development is mainly affected by lithology, tectonic movement, and diagenesis.

DATA AVAILABILITY STATEMENT

The original contributions presented in the study are included in the article/Supplementary Material, further inquiries can be directed to the corresponding author.

AUTHOR CONTRIBUTIONS

JX and BL contributed to the conception of the study; XH and YD finished the first draft; YS and HL contributed significantly to analysis and manuscript preparation; BL, YD, WC, and RW conducted data preparation and experimental analysis; XH has made a lot of revisions to the paper revision, and through the constructive discussion help to carry on the analysis. All authors reviewed the manuscript.

FUNDING

This work was cofunded by the National Natural Science Foundation of China (Grant Nos.51674156 and 51504143) and the Innovation Team of Shandong University of Science and Technology (2015TDJH101).

ACKNOWLEDGMENTS

The authors thank the Bohai Petroleum Research Institute for supplying core samples and logging data. The authors also wish to thank the anonymous reviewers for their careful work and thoughtful suggestions and the editors for their valuable comments.

REFERENCES

Cai, D. M., Ye, T., Lu, F. T., Gao, K. S., and Ren, Y. P. (2018). Lithofacies Characteristics and Identification Methods of Mesozoic Volcanic Rocks in Bohai Sea. *Lithologic Reservoirs*. 30, 112–120. doi:10.3969/j.issn.1673-8926.2018.01.011

Cai, D. S., Luo, Y. H., and Yao, C. H. (2001). Strike-slip and Pull-Apart Structure Study and its Significance to Petroleum Exploration on Laizhouwan Sag, Bohai Area. *Acta Petrolei. Sinica.* 22 (02), 19–25. doi:10.3321/j.issn:0253-2697.2001.02.004

Cas, R. A. F., and Wright, J. V. (1987). Volcanic Successions, Modern and Ancient: a Geological Approach to Processes, Products, and Successions. *Allen&Unwin*, 528. doi:10.1007/978-94-009-3167-1

Deng, P., Chen, M. J., and Gao, Z. R. (2002). Log Response and Explanation of Structural Fractures in Volcanic Rock Reservoir. *Acta Petrolsi. Sinica.* 23 (6), 32–36. doi:10.1007/s11769-002-0037-5

Dickson, J. A. D. (1965). A Modified Staining Technique for Carbonates in Thin Section. *Nature* 205, 587. doi:10.1038/205587a0

Duan, Y. J., Xie, J., Li, B. C., Wang, M. Q., Zhang, T. Q., and Zhou, Y. W. (2020a). Lithology Identification and Reservoir Characteristics of the Mixed Siliciclastic-Carbonate Rocks of the Lower Third Member of the Shahejie Formation in the South of the Laizhouwan Sag, Bohai Bay Basin, China. *Carbonates and Evaporites* 35 (2). doi:10.1007/s13146-020-00583-8

Duan, Y., Xie, J., Su, Y., Liang, H., Hu, X., Wang, Q., et al. (2020b). Application of the Decision Tree Method to Lithology Identification of Volcanic Rocks-Taking the Mesozoic in the Laizhouwan Sag as an Example. *Sci. Rep.* 10 (05), 19209. doi:10.1038/s41598-020-76303-y

Fan, C., Qin, Q., Liang, F., Fan, Z., and Li, Z. (2018). Fractures in Volcanic Reservoir: a Case Study of Zhongguai Uplift in Northwestern Margin of Junggar Basin, China. *Earth Sci. Res. J.* 22 (3), 169–174. doi:10.15446/esrj.v22n3.75426

Fang, J., Jia, C. Z., Ran, Q. Q., Zhou, X. M., and Hui, G. (2011). *The Study of Fracture in Volcanic Reservoir. CPS/SPE International Oil&Gas Conference and Exhibition*. Beijing, China: Jilin University. 2000, 8–10. doi:10.2523/131813-MS

Hawlander, H. M. (1990). Digenesis and Reservoir Potential of Volcanogenic Sandstones-Cretaceous of the Surat Basin, Australia. *Sediment. Geology.* 66 (4), 181–195. doi:10.1016/0037-0738(90)90059-3

He, J., Wang, H., Zhang, C., Yang, X., Shangguan, Y., Zhao, R., et al. (2019). A Comprehensive Analysis of the Sedimentology, Petrography, Diagenesis and Reservoir Quality of Sandstones from the Oligocene Xiaganchaigou (E3) Formation in the Lengdong Area, Qaidam Basin, China. *J. Petrol. Explor Prod. Technol.* 9 (2), 953–969. doi:10.1007/s13202-018-0571-z

Hu, X., Xie, J., Cai, W. C., Wang, R., and Davarpanah, A. (2020). Thermodynamic Effects of Cycling Carbon Dioxide Injectivity in Shale Reservoirs. *J. Pet. Sci. Eng.* 195, 107717. doi:10.1016/j.petrol.2020.107717

Jansa, L. F. (1988). Pe-Piper G. Middle Jurassic to Early Cretaceous Igneous Rocks along Eastern North American continental Margin. *Aapg Bull. Am. Assoc. Pet. Geologists* 72 (3), 347–366. doi:10.1306/703C8C27-1707-11D7-8645000102C1865D

Jin, C., Pan, W., and Qiao, D. (2013). Volcanic Facies and Their Reservoirs Characteristics in Eastern China Basins. *J. Earth Sci.* 24 (6), 935–946. doi:10.1007/s12583-013-0380-8

Jin, C. S., Qiao, D. W., and Dan, W. N. (2012). Meso-Cenozoic Volcanic Rock Distribution and Reservoir Characteristics in the Bohai Bay Basin. *OIL GAS GEOLOGY.* 033 (001), 19–29. doi:10.11743/ogg20120103

Kong, C. X., Xiao, Y., Chen, L. C., Jia, J. F., and Zhang, H. Y. (2020). Research on Volcanic Reservoir Prediction in Jinlong. *J. Phys. Conf. Ser.* 1549 (4). doi:10.1088/1742-6596/1549/4/042027

Leng, Q. L., Huang, Y. L., Ran, B., Zhang, J. M., and Wang, P. J. (2020). Development Characteristics and Controlling Factors of Dissolution Pores in Pyroclastic Reservoirs: A Case Study of the Lower Cretaceous in Lujiapu Sag, Southern Songliao Basin. *Glob. Geology.* 39 (02), 1–10. doi:10.3969/j.issn.1004-5589.2020.02.011

Levin, L. E. (1995). Volcanogenic and Volcaniclastic Reservoir Rocks in Mesozoic-Cenozoic Island Arcs: Examples from the Caucasus and the Nw Pacific. *J. Pet. Geol.* 18 (3), 267–288. doi:10.1111/j.1747-5457.1995.tb00906.x

Liu, X. J., W, Q. B., Dai, L. M., and Hao, Y. W. (2018). Relationship between Lithofacies Characteristics and Reservoirs of Mesozoic Volcanic Rocks in Laizhouwan Sag. *Pet. Geology. Eng.* 032 (003), 1–6. doi:10.3969/j.issn.1673-8217.2018.03.001

Liu, Y., Hu, W., Cao, J., Wang, X., Tang, Q., Wu, H., et al. (2018). Diagenetic Constraints on the Heterogeneity of Tight sandstone Reservoirs: A Case Study on the Upper Triassic Xujiahe Formation in the Sichuan Basin, Southwest China. *Mar. Pet. Geology.* 92 (92), 650–669. doi:10.1016/j.marpetgeo.2017.11.027

Liu, Z. D., Liu, H. Q., Dai, S. H., Wang, H. L., and Yu, H. G. (2008). Study on Volcanic Rock Fracture Quantitative Identificantion Method Using Logging Data. *PGODD* 27 (5), 132–134. doi:10.3969/j.issn.1000-3754.2008.05.035

Liyao, L., Jiuchuan, W., and Huiyong, Y. (2018). Influence of Sedimentary Facies on Reservoir Quality and Distribution of Diagenetic Features in the Funing Formation, Wanglongzhuang Oilfield, Subei Basin, Eastern China. *Arabian J. Geosciences* 11 (15), 432–445. doi:10.1007/s12517-018-3745-6

Lu, C., Liu, Z., Jia, H., Dai, Q., Li, M., Ren, M., et al. (2018). The Controls of Geomorphology and Sediment Supply on Sequence Stratigraphic Architecture and Sediment Partitioning of the Lacustrine Rift basin in the Es3 of Liuzan Area, Nanpu Sag, Bohai Bay Basin, China. *Aust. J. Earth Sci.* 65, 275–301. doi:10.1080/08120099.2018.1413594

Miao, C. S., Xu, W., Liu, Y. H., and Xie, R. X. (2020). Characteristics of Volcanic Rock Reservoir in Southern Songliao Basin. *J. Jilin Univ. (Earth Sci. Edition)* 50 (02), 635–643. doi:10.13278/j.cnki.jjuese.20190253

Ran, Q. Q., Hu, Y. L., and Ren, B. S. (2005). A Lithologic Identification Method of Igneous Rocks and its Application:a Case of the Igneous Reservoir in Block Zao-35. *China of Fsh Ore Oil and Gas* 17 (1), 25–30. doi:10.3969/j.issn.1673-1506.2005.01.006

Somasundaram, S., Mund, B., Soni, R., and Sharda, R. (2017). Seismic Attribute Analysis for Fracture Detection and Porosity Prediction: A Case Study from Tight Volcanic Reservoirs, Barmer Basin, India. *The Leading Edge* 36 (11), 947b1–947b7. doi:10.1190/tle36110947b1.1

Su, D. X., Wang, Z. Q., Yuan, Y. F., and Han, B. (2020). Weathered Volcanic Reservoir Characteristics and Their Controlling Factors on Permian Fengcheng Formation in Southern Mahu Depression, Junggar Basin. *Nat. Gas Geosci.* 31, 209–219. doi:10.11764/j.issn.1672-1926.2019.10.003

Tang, H., and Ji, H. (2006). Incorporation of Spatial Characteristics into Volcanic Facies and Favorable Reservoir Prediction. *SPE Reservoir Evaluation&Engineering* 9 (05), 565–573. doi:10.2118/90847-pa

Wang, G., Chang, X., Yin, W., Li, Y., and Song, T. (2017). Impact of Diagenesis on Reservoir Quality and Heterogeneity of the Upper Triassic Chang 8 Tight Oil Sandstones in the Zhenjing Area, Ordos Basin, China. *Mar. Pet. Geology.* 83, 84–96. doi:10.1016/j.marpetgeo.2017.03.008

Wang, B. Q., Wang, Z. P., Tang, G. M., and Yu, X. T. (2020). Characteristics and Main Controlling Factors of Mesozoic Volcanic Rock Reservoir in central Bohai Sea Area. *Mar. Geology. Front.* 36 (08), 36–42. doi:10.16028/j.1009-2722.2020.007

Wang, M. Q., Xie, J., Guo, F. J., Zhou, Y. W., Yang, X. D., and Meng, Z. A. (2020). Determination of NMR T 2 Cutoff and CT Scanning for Pore Structure Evaluation in Mixed Siliciclastic–Carbonate Rocks before and after Acidification. *Energies* 13 (6), 1338. doi:10.3390/en13061338

Wang, M. Q., Xie, J., Zhang, Q., Wang, Y. J., and Duan, Y. J. (2019). Characteristics and Sedimentary Model of a Reticular Shallow-Water delta with Distributary Channels: Lower Member of the Neogene Minghuazhen Formation in the Bozhong Area of the Huanghekou Sag, China. *Arabian J. Geosciences* 12, 760. doi:10.1007/s12517-019-4928-5

Wang, Y. J., Hu, Y. L., Ran, Q. J., Pang, Y. M., and Yu, S. Q. (2007). Fracture Development Evaluation for Deep Volcanic Gas Reservoir[J]. *Nat. Gas Industry* 2007 (8), 37. doi:10.3321/j.issn:1000-0976.2007.08.009

Xie, J., Hu, X., Liang, H. Z., Wang, M. Q., Guo, F. J., Zhang, S. J., et al. (2020). Cold Damage from Wax Deposition in a Shallow, Low-Temperature, and High-Wax Reservoir in Changchunling Oilfield. *Scientific Rep.* 10 (1), 14223. doi:10.1038/s41598-020-71065-z

Xiong, Y. X., Xi, A. H., Ran, Q. Q., Ge, Y. H., Liu, X. H., and Sun, Y. H. (2012). Characteristics and Distribution of Reservoir Spaces of the Carboniferous Volcanic Rocks in Dixi Area, Junggar Basin. *Geol. J. China Universities* 18 (1), 164–173. doi:10.16108/j.issn1006-7493.2012.01.002

Yang, C., Hou, L. H., Yang, F., Luo, X., and Wang, J. H. (2017). Controlling Factors of Volcanic Hydrocarbon Reservoirs in Bohai Bay Basin, China. *J. Nat. Gas Geosci.* 2 (4), 219–228. doi:10.1016/j.jnggs.2017.10.001

Yang, Z. D., Zhang, M. L., Zhang, Q., Qin, Y., and Zheng, Q. H. (2020). Characteristics and Main Controlling Factors of Igneous Reservoirs in Chepaizi Uplift, Junggar Basin. *J. Yunnan Univ. Nat. Sci. Edition* 42 (03), 507–514. doi:10.7540/j.ynu.20190499

Yu, H. Z. (2019). Development Characteristics and Genetic Model of Volcanic Reservoir in Complex Tectonic belt of Hashan Area,northwestern Margin of Junggar Basin. *Pet. Geology. Recovery Efficiency* 26 (03), 46–53. doi:10.13673/j.cnki.cn37-1359/te.2019.03.006

Zhang, X. F. (2011). *Study on Quantitative Characterization of Borehole Fractures and its Appiication*. Jilin University. doi:10.1109/appeec.2011.5748362

Zhang, C. G. (2012). *Study on Fracture Recognition and Extraction Based on Image Log Data Processing and Frcture Parameters Calculation*. Jilin University. doi:10.1109/cisp.2012.6470035

Zhang, X., Xia, Y., Zhang, Y., Chen, Y., Zhang, G., and Gao, W. (2018). Volcanic Reservoir Characteristics and Hydrocarbon Genesis of Jiamuhe Formation in Jinlong 2 Wellblock, Junggar Basin. *Pet. Sci. Technology* 36 (19), 1516–1523. doi:10.1080/10916466.2018.1471486

Zheng, H., Sun, X. M., Wang, J. P., Zhu, D. F., and Zhang, X. Q. (2018). Devitrification Pores and Their Contribution to Volcanic Reservoirs: A Case Study in the Hailar Basin, NE China. *Mar. Pet. Geology*. 98, 718–732. doi:10.1016/j.marpetgeo.2018.09.016

Zhu, X. E., Yang, S. F., and Si, C. Q. (2019). Lithology Identification and Lithofacies Distribution of Cenozoic Volcanic Rocks in Wichian Buri Sub-basin of Phetchabun Basin, Thailand. *Geological Surv. China* 6 (2) 48–57. doi:10.19388/j.zgdzdc.2019.02.06

Conflict of Interest: The author YS was employed by the company CNOOC China Limited.

The remaining authors declare that the research was conducted in the absence of any commercial or financial relationships that could be construed as a potential conflict of interest.

frontiers in Earth Science

METHODS
published: 28 June 2021
doi: 10.3389/feart.2021.684592

Evaluation Method of Movable Shale Oil Resource: A Case Study of the Shahejie Formation in the Dongying Sag, Jiyang Depression

Liang Xu[1], Min Wang[1], Jinbu Li[1]*, Ming Li[1], Zheng Li[2], Rifang Zhu[2] and Huimin Liu[2]*

[1]Key Laboratory of Deep Oil and Gas, China University of Petroleum (East China), Qingdao, China, [2]Geology Scientific Research Institute of Shengli Oilfield Company, Sinopec, Dongying, China

Although China has enormous shale oil resource potential, oil recovery is limited at present, largely because its movable resource is not evaluated. In this study, an evaluation method for movable shale oil resources is proposed. The process first evaluates the total shale oil resource (Q_{total}), and then two-dimensional nuclear magnetic resonance (NMR) technology is used to measure the free oil ratio (R_{free}) and further define the quantitative relationship (F) between the movable ratio (R_m) in the free oil and centrifugal force. The movable oil resource is calculated by the total shale oil resource, free oil ratio, and movable oil ratio ($Q_m = Q_{total} \times R_{free} \times R_m$). This method was applied to the Shahejie Formation of the Dongying Sag, Jiyang Depression, in Bohai Bay Basin, and the relationship between the free oil ratio (R_{free}) and depth was established based on several core 2D NMR data. Based on the formation pressure, flowing bottom hole pressure, and relationship (F), the movable shale oil ratio (R_m) in the target area was determined. The results showed that the movable shale oil ratio (R_m) of the lower Es3 is approximately 18.9–20% in the depth range of 3,200–3,700 m, and the movable shale oil resource is approximately 2.52×10^8 t.

Keywords: shale oil, movable oil, free oil, nuclear magnetic resonance, jiyang depression

OPEN ACCESS

Edited by:
Dawei Lv,
Shandong University of Science and Technology, China

Reviewed by:
Clive Francis Burrett,
Mahasarakham University, Thailand
Xianfeng Tan,
Chongqing University of Science and Technology, China

****Correspondence:***
Min Wang
wangm@upc.edu.cn
Jinbu Li
498891492@qq.com

Specialty section:
This article was submitted to Economic Geology, a section of the journal Frontiers in Earth Science

Received: *23 March 2021*
Accepted: *28 May 2021*
Published: *28 June 2021*

Citation:
Xu L, Wang M, Li J, Li M, Li Z, Zhu R and Liu H (2021) Evaluation Method of Movable Shale Oil Resource: A Case Study of the Shahejie Formation in the Dongying Sag, Jiyang Depression. Front. Earth Sci. 9:684592. doi: 10.3389/feart.2021.684592

INTRODUCTION

After decades of development, the global shale oil and gas boom led by the United States has entered an active period of discovery, and unconventional oil and gas has now become an important part of global oil and gas growth (Capuano, 2018; Us Eia, 2019). The successful exploitation of shale oil and gas has greatly improved the oil and gas self-sufficiency rates of the United States. In 2018, the total energy consumption of the United States was 28×10^8 t oil equivalent, total production was 21.1×10^8 t oil equivalent, and external dependence was only 8.3%. The country may achieve "Energy independence" in 2022 (Zou et al., 2020). In 2019, China's crude oil import volume reached 505.72 million tons, and its degree of dependence on foreign countries reached 70.8%. To meet national energy security needs, China must strengthen its oil exploration and development (CEP, 2020). Currently, China has achieved remarkable results in unconventional oil and gas exploration and development, especially the rapid growth in tight oil, tight gas, and shale gas production, which makes the exploration and development of shale oil rise to national strategic prominence (Li and Zhu, 2020a).

In recent years, China's Ministry of Natural Resources (Ministry of Land and Resources), PetroChina, Sinopec, and other companies have launched shale oil resource evaluations. In

2014, the shale oil resource in Sinopec's exploration area was approximately 204×10^8 t. In 2016, PetroChina estimated that the shale oil resource in its exploration area was approximately 145×10^8 t, and simultaneously, the evaluation by the Ministry of Land and Resources showed that the shale oil resource in China was 153×10^8 t. Specifically, continental shale oil in China is mainly developed in the Permian, Cretaceous, and Paleogene. The favorable shale oil area of the Permian Lucaogou Formation in the Jimusaer Sag, Junggar Basin is 11.12×10^8 t, where large-scale production began in 2019 (Wu B. C. et al., 2019; Guo et al., 2019; Lv et al., 2019; Zhi et al., 2019). The Paleogene Kongdian Formation and Shahejie Formation in the Cangdong Sag in Bohai Bay Basin also have good oil and gas resource potential, and the total shale oil resources of fifteen vertical wells in the second member of the Kongdian Formation are estimated to be 6.8×10^8 t (Pu et al., 2019; Zhao et al., 2019). Lu et al. (2016a) showed that the total amount of oil trapped in the Bonan Sag shale with an area of less than 1,000 km^2 in the Shengli oilfield is as high as 88×10^8 t. Moreover, Song et al. (2013) estimated the shale oil resource of the lower Es3 in the Bonan Sag to be 5.47×10^8 t. In addition, Daqing oilfield performed a geological evaluation of the shale of the first Qingshankou Formation member in the Qijia–Gulong to Sanzhao area of the Songliao Basin and obtained many industrial flowing oil wells, such as Guyeyouping 1 (Wu H. Y. et al., 2019). Although high initial production can be obtained using fracturing technology from shale oil exploration wells, with time, shale oil production decreases rapidly, resulting in poor economic benefits from those wells (Chen F. et al., 2019; Wang et al., 2019; Lv et al., 2020). This is because under geological conditions, shale oil in the pores is not completely movable due to the limitations in reservoir physical properties and formation pressure.

The marine shale oil mobility was characterized by the geochemical parameter OSI (oil saturation index) = S1/TOC × 100. Some scholars also use this method to characterize the mobility of continental shale oil. It is considered that there is a certain lower limit for OSI in the study area, and shale oil can flow only when it exceeds this value (Jarvie and Daniel, 2012; Wang et al., 2015; Xue et al., 2015; Jiang et al., 2016). Zhou et al. (2016) analyzed movable fluids in marine shale reservoirs in southern China through NMR-centrifugal experiments and discussed the fluid mobility under optimal centrifugal force conditions. Wang et al. (2010) discussed the mobility of crude oil in low-permeability reservoirs by NMR displacement experiments on cores from the Yanchang Formation in the Ordos Basin. Zhang et al. (2014) analyzed continental shale oil mobility from the perspective of formation energy. The above research methods accelerated the understanding of shale oil mobility to accurately evaluate movable shale oil resources. However, due to the constraints of geological data and geological conditions, some methods need to be improved. When analyzing shale oil mobility by NMR centrifugation, only considering shale oil mobility under the condition of optimal centrifugal force is not an actual geological condition. Different driving forces of shale oil under different formation overpressures lead to different mobilities. Because of the smaller pore throat structure and stronger hydrocarbon–rock interaction in shale reservoirs, the feasibility and effectiveness of the displacement experiment technology remain debatable.

In this study, a new method for evaluating movable shale oil resources is proposed. The movable shale oil resource (Q_m) was calculated using the total shale oil resource (Q_{total}), free oil ratio (R_{free}), and movable oil ratio (R_m). The application of this method is introduced by considering the Shahejie Formation in the Dongying Sag as an example. This method is of great significance for finding the "sweet spot" in shale oil, thereby guiding future exploration and development.

METHODS

The lacustrine shale reservoirs in China are characterized by large thickness, strong longitudinal heterogeneity, ultra-low porosity, ultra-low permeability, and ultra-strong hydrocarbon–rock interaction. Therefore, shale oil mobility should be fully considered while evaluating the degree of shale oil recovery (Lu et al., 2016a). For the above reasons, based on total shale oil resources (Q_{total}) and free shale oil resources (Q_{free}), a new method for evaluating movable shale oil resources (Q_m) is established in this study. The specific ideas are as follows.

First, combined with conventional logging curves and measured core data, an improved ΔlogR model was used to evaluate the organic heterogeneity and obtain the vertical variation in S_1 (Huang et al., 2014; Lu et al., 2017). Then, the total shale oil resources (Q_{total}) were calculated using S_1 light and heavy hydrocarbon corrections (Wang et al., 2014; Li et al., 2016; Xue et al., 2016). Second, after clarifying the total resource calculation results, to calculate free shale oil resources (Q_{free}), it was necessary to use the nuclear magnetic resonance (NMR) T_1–T_2 spectrum to evaluate the free oil ratio (R_{free}). Finally, the quantitative relationship (F) between the movable ratio (R_m) in free oil and centrifugal force (ΔP = formation overpressure—flowing bottom hole pressure) was further defined by a centrifugal experiment, and the movable oil resource was calculated using the total shale oil resource, free oil ratio, and movable oil ratio ($Q_m = Q_{total} \times R_{free} \times R_m$). The evaluation process is illustrated in **Figure 1**.

CASE STUDY

Geological Setting

The Dongying Sag is a secondary structural unit located in the Jiyang Depression in the Bohai Bay rift basin in eastern China, which is a typical dustpan structure with "north fault and south overlap" characteristics. The sag starts from Qingtuozi uplift in the east and ends at Qingcheng uplift in the west and starts from Luxi uplift in the south and ends at Chenjiazhuang uplift in the north. Overall, the sag trends east–west, and the northern fault activity is relatively developed, which controls the structural evolutionary characteristics of the entire sag (**Figure 3**). A large set of lacustrine shales in the lower sub-member of the Shahejie Formation (Es3x) developed in a brackish water environment (Zhang et al., 2014; Zhu et al., 2019). The

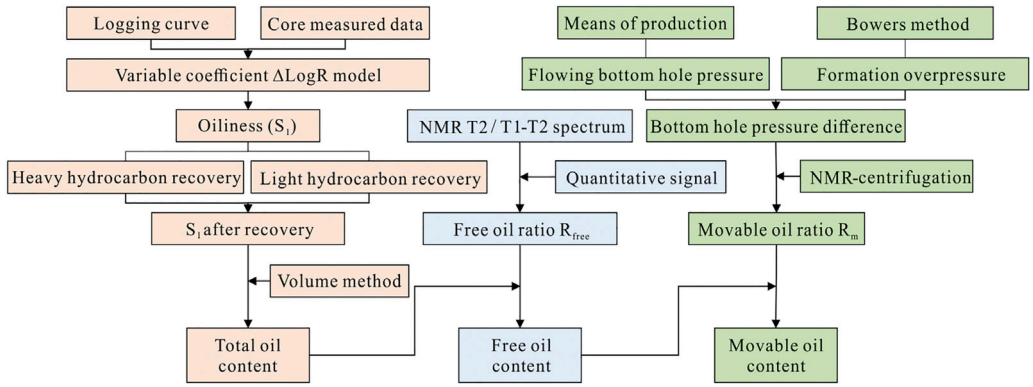

FIGURE 1 | Movable shale oil resources evaluation workflow.

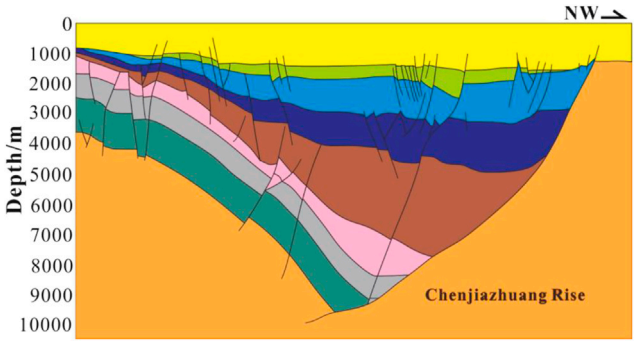

FIGURE 2 | Present day north to south structural section of Dongying Depression (modified after Song et al., 2014).

lithology is mainly layered with laminar shales of high carbonate content. The organic carbon content of Es3x shales ranges between 1 and 5% and contain type Ⅰ and type $Ⅱ_1$ organic matter, with a small amount of type $Ⅱ_2$ kerogen. The shale burial depth is between 1,500 and 4,000 m, and most shales are mature. These characteristics define a set of favorable source rocks with high abundance and good organic matter qualities (Wang et al., 2019).

According to the response characteristics of lithology and logging curves, the lower Es3 sub-member of the Dongying Sag is subdivided into four sub-layers (Li, 2012; Zhang S. et al., 2015; Liu, 2018). By estimating the thickness of each sub-layer, the thickness contour of each layer is established (**Figure 4**). **Figure 4** shows that the thick center is the center of each depression, and the maximum thickness is between 100 and 150 m. An area of approximately 2,468.21 km^2 is calculated as the effective area.

Experiment

Pressure Saturation Experiment

Rock samples were dried at 60°C for 24 h to remove impurities and placed in a vacuum pressure saturator. First, the rock sample was held at a 1×10^{-4} Pa vacuum for 24 h. The sample was then saturated with n-dodecane at 20 MPa. The saturated samples were measured at different times and when the quality was stable (the test variability was within 0.5%), the rock samples were considered to be saturated.

Nuclear Magnetic Resonance Experiment

NMR experiments were performed using a micromr23-060h-1 instrument from Shanghai Niumag Company. The instrument was operated at a resonance frequency of 21.36 MHz and magnetic strength of 0.5 T using a 25.4 mm coil diameter; the magnet temperature was maintained at 32°C. When testing the T_2 and the T_1-T_2 spectra, the Carr–Purcell–Meiboom–Gill (CPMG) sequence was used. For inversion recovery, the CPMG (IR-CPMG) sequence was detected for the T_1-T_2 spectrum. The measurement parameters used an echo time (TE) of 0.07 ms, waiting time (TW) of 1,000 ms, 90 pulse width (P90) of 5.4 μs, and included 32 scans and 6,000 echoes.

Centrifugation Experiment

In this centrifugal experiment, the saturated oil sample was placed in the rotor of a CSC-12 centrifuge for 8 h. The properties of the centrifuge were as follows: rotor radius, 13.5 cm; centrifugal temperature, 21°C; The centrifugal rotation speed was increased by 2000 rotations until the rotation speed was 12,000 rotations, and the corresponding centrifugal forces were 0.08, 0.33, 0.75, 1.34, 2.09, and 3.01 MPa. Six centrifugation experiments were performed.

Evaluation of Total Shale Oil Resource

The total shale oil resource is the total amount of shale oil contained in the shale reservoir. The total shale oil resource evaluation method is roughly divided into dynamic and static categories. The former uses the dynamic parameters during reservoir development to calculate shale oil resources through numerical simulation, decline curve calculations, and material balance, which uses static parameters to calculate the total shale oil resources. Because of the different calculation methods, they can be subdivided into analog, statistical, and genetic methods

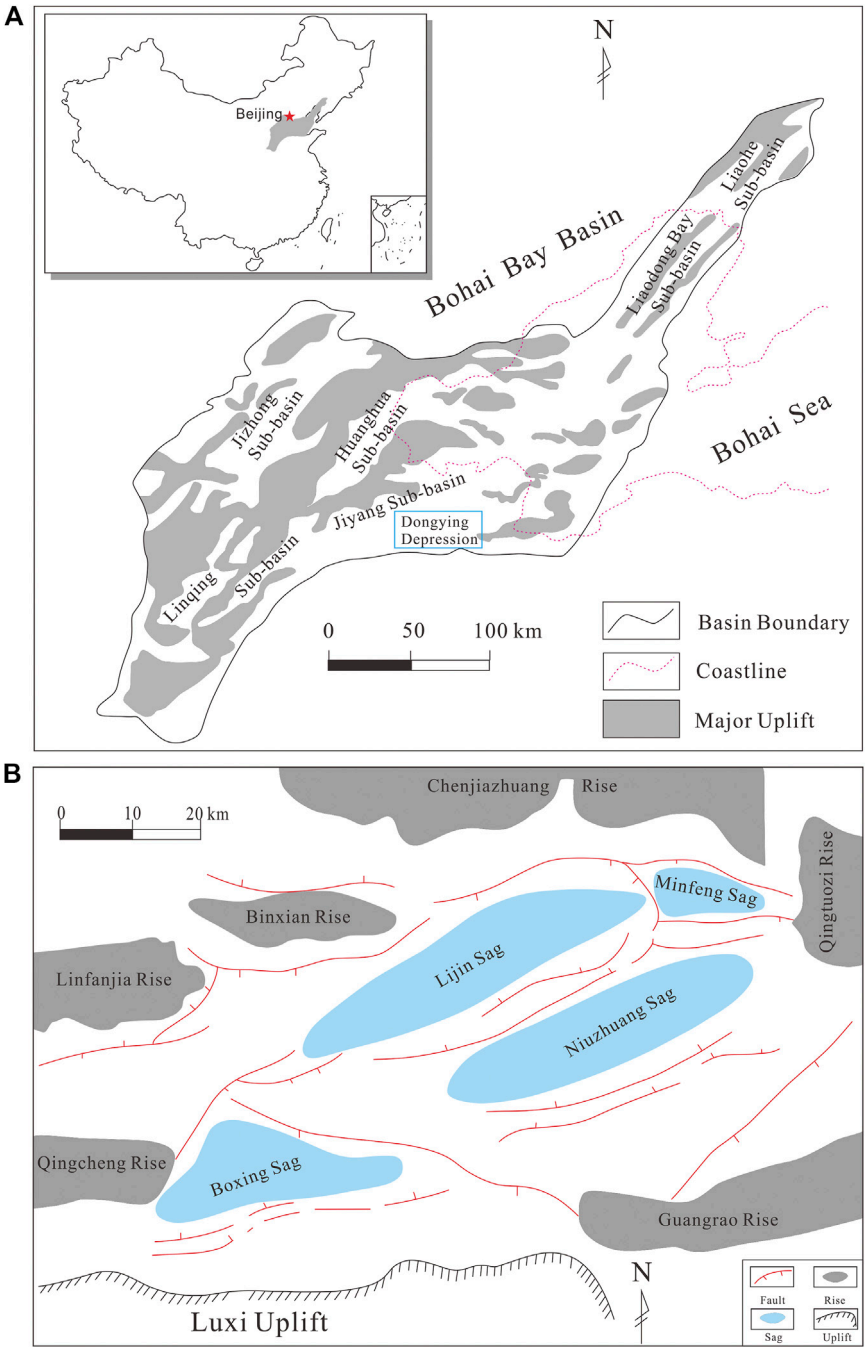

FIGURE 3 | Location map of study area **(A)** schematic map of Bohai Bay Basin and its location in China. **(B)** Location of Dongying Depression (modified after Zhang et al., 2020).

(Wang et al., 2014; Wright et al., 2015; Lu et al., 2016b; Chen et al., 2017).

The analog method is typically used to evaluate areas with low exploration degree. It considers an area with a high exploration degree as the analog area, mainly based on the estimated ultimate recoverable reserves (EUR) of production wells. It includes the FORSPAN model and its improved method from the U.S. Geological Survey (Schmoker, 2002; Salazar et al., 2010). In 2010, in Calgary, Canada, the Third International Symposium on oil and gas resource evaluation methods was held. Hood of ExxonMobil used this method to accurately evaluate reservoirs with continuous oil and gas distributions (Hood et al., 2012).

The statistical method, subdivided small area unit volume method, and stochastic simulation method are used to establish relevant mathematical models to predict future change processes according to the known system behavior. Among them, the small

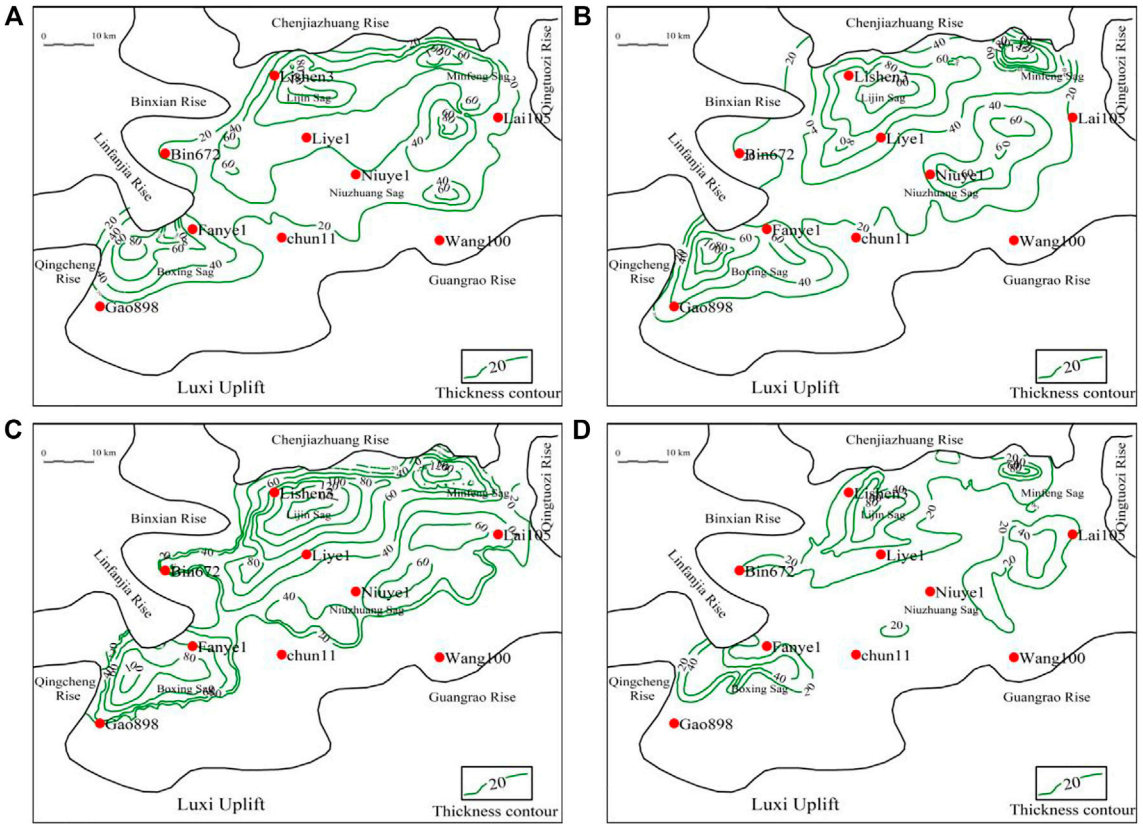

FIGURE 4 | Thickness contour map of each sub layer in Es3x **(A)**: first sub layer; **(B)**: second sub layer; **(C)**: third sub layer; **(D)**: fourth sub layer).

area unit volume method is often used by the International Energy Agency (EIA). Almanza used the small area unit volume method to evaluate the tight oil of the Bakken Formation in the Elm Coulee Oilfield in the Williston Basin in 2011 (Guo et al., 2015). In 2010, after summarizing the shortcomings of the traditional analog method, Olea et al. (2010) proposed a stochastic simulation method. Chen and Kirk (2013) used a stochastic simulation method to evaluate tight oil resources in the Cardium Formation of the Upper Cretaceous Colorado Group in the Western Canada Sedimentary Basin. The results showed that the total resources of tight oil in the work area were $29 \times 108\ m^3$.

The genetic method evaluation process embodies the principles of oil and gas generation, migration, and accumulation in reservoirs. The residual amount of oil and gas in the final stage is determined by calculating the generation, adsorption, discharge, and loss of hydrocarbons in the source rock. The genetic method can be divided into volume, material balance, and so on. The volume method is the most effective and applicable method for calculating shale oil resources by multiplying the residual hydrocarbon content in shale by the shale volume. Therefore, it is the most commonly used method in the shale oil exploration stage in China. Liu et al. (2013), Yang et al. (2013), Liu B. et al. (2014), Lu et al. (2016b) and Zhu et al. (2019) evaluated the shale oil resource of Malang sag of Santanghu basin, Ordos Basin, Qingshankou formation of Songliao Basin, Damintun Sag, and Dongying sag of Bohai Bay Basin, by volume method, respectively. To obtain the final resource amounts, the material balance method focuses on the calculation of hydrocarbon generation, expulsion, and loss through geochemical parameters (Jiang et al., 2002). Chen et al. (2020) evaluated the shale/tight oil resources of the Lucaogou Formation in the Jimusaer depression using the material balance method. However, the calculation models of hydrocarbon expulsion threshold, hydrocarbon generation conversion rate, and hydrocarbon expulsion efficiency involved in the material balance method are relatively complex, resulting in a low utilization rate of this method.

In practical applications, the volume method is subdivided into the chloroform pitch "A" method and pyrolysis S_1 method (Song et al., 2013; Zhu et al., 2015; Li et al., 2020c). In this study, the pyrolysis S_1 method was used to calculate the total shale oil resources. The pyrolysis parameter S_1 represents the thermal evaporation of the rock below 300 °C during pyrolysis heating. It is the hydrocarbon that has been generated in the source rock but has not been discharged, which is the object of shale oil evaluation and exploration. The calculation formula is as follows:

$$Q_{\text{total}} = S \times h \times \rho \times S_1 \times K_L \times K_H \quad (1)$$

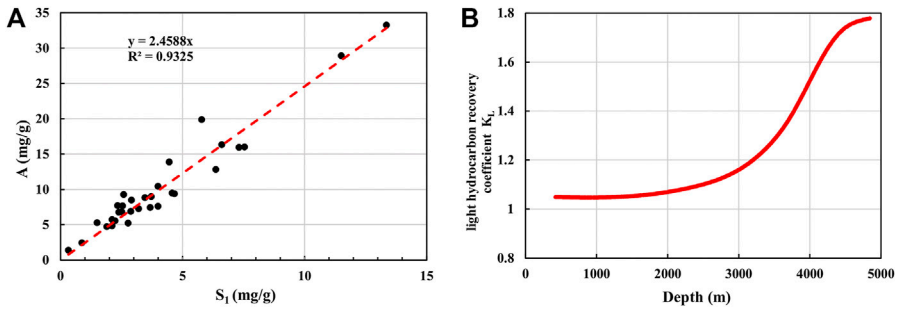

FIGURE 5 | Heavy hydrocarbon recovery coefficient **(A)** and light hydrocarbon recovery coefficient **(B)** [modified after Zhu et al. (2015)]

where Q_{total} is total shale oil resource, h is the effective shale thickness, S is effective shale area, ρ is shale density, measured density of the sample is 1.9–2.6 g/cm^3 (Zhu et al., 2019), S_1 is pyrolytic hydrocarbon content, K_L is the light hydrocarbon correction coefficient of S_1, and K_H is the heavy hydrocarbon correction factor of S_1.

In this study, the variable coefficient ΔlogR model was used to evaluate the vertical change in parameter S_1. This method is based on the minimum error between the core measured data and the predicted log value and automatically selects the baseline and optimizes the scale factor K (Liu C. et al., 2014). Huang et al. (2014) and Li et al. (2020c) used this method to evaluate the organic heterogeneity of the Shahejie Formation in the Songliao Basin Bonan and Qingshankou formations, and the results were in good agreement with the measured data. The variable coefficient ΔlogR model calculation was completed by a computer. The calculation model is as follows:

$$\Delta \log R = K \times \log(R/R_{baseline}) + (1 - K) \times (\Delta t - \Delta t_{baseline}) \quad (2)$$

$$S_1 = A \times \log R + B \quad (3)$$

where R and $R_{baseline}$ are the measured value and the baseline value of the resistivity log(Ω·m); Δt and $\Delta t_{baseline}$ are the measured value and the baseline value of the acoustic log(Ω·m); K is the proportion of the resistivity part in ΔlogR model, ranging from 0 to 1; and A and B are fitting coefficients.

Previous studies have shown that hydrocarbons with low molecular weights are lost during transportation, preservation, and sample preparation (Jarvie and Daniel, 2012; Michael, 2013; Wang et al., 2014). The methods of light hydrocarbon recovery include component hydrocarbon generation kinetics, formation volume coefficient, chromatography, experimental comparison, and material balance (Jarvie and Daniel, 2012; Michael, 2013; Wang et al., 2014; Zhu et al., 2015; Chen et al., 2018; Chen Z. et al., 2019). In addition, by comparing the pyrolysis experiments of the extracted and unextracted samples, it was found that when measured at 300°C, there were still some high carbon numbers that could not be pyrolyzed, resulting in a low measured S_1 value (Delvaux et al., 1990). Heavy hydrocarbon recovery methods include the comparison of pyrolysis parameters of shale before and after extraction, comparison of the cumulative sum of the FID curve of pyrolysis before and after extraction, and comparison of hydrocarbon generation kinetic parameters of shale organic matter before and after extraction (Wang and Zheng, 1987; Wang et al., 2014; Li et al., 2019).

The heavy hydrocarbon correction of S_1 is carried out by looking for the relationship between S_1 and chloroform pitch "A." As shown in **Figure 5A**, the heavy hydrocarbon correction coefficient (K_H) is 2.588 in this area. For the light hydrocarbon correction coefficient of S_1, this study adopts the relationship between the light hydrocarbon recovery coefficient (K_L) and depth established by Zhu et al. (2015). As shown in **Figure 5B**, with an increase in depth, the light hydrocarbon recovery coefficient gradually increases, which can be interpreted as the maturity of the source rock increases with the increase in depth, resulting in more light components, which are more likely to be lost in the process of handling and preservation.

Evaluation of Free Shale Oil Resource

It is generally considered that shale oil mainly exists in the adsorbed and free states in the reservoir, and the content of free shale oil plays a major role in shale oil productivity. Theoretically, the maximum movable shale oil resource is directly determined by the free oil content (Zhang et al., 2012; Zou et al., 2013; Jiang et al., 2016; Ning et al., 2017; Li et al., 2019; Wang et al., 2019). Therefore, the calculation of movable shale oil resources should first clarify the free oil content in shale reservoirs.

It is not easy to determine the free state of shale oil. Different scholars have analyzed extensively from different angles (Ribeiro et al., 2009; Zhang L. Y. et al., 2015; Jiang et al., 2016; Li et al., 2016; Qian et al., 2017; Li et al., 2018; Li et al., 2019). One approach is to directly determine the free state shale oil content through experimental methods such as stepwise solvent extraction, heating release, and NMR. The second method is to determine the adsorbed shale oil content and calculate the amount of free oil from the difference between the total and adsorbed oil contents. The main method in the laboratory is the adsorption experiment of an oil solution (swelling experiment). Compared with the complicated and cumbersome analytical process of the solvent stepwise extraction method, the heating release method is relatively simple and easy to implement (Jiang et al., 2016). However, it is debatable whether the thermally released hydrocarbons at a certain temperature in the heating

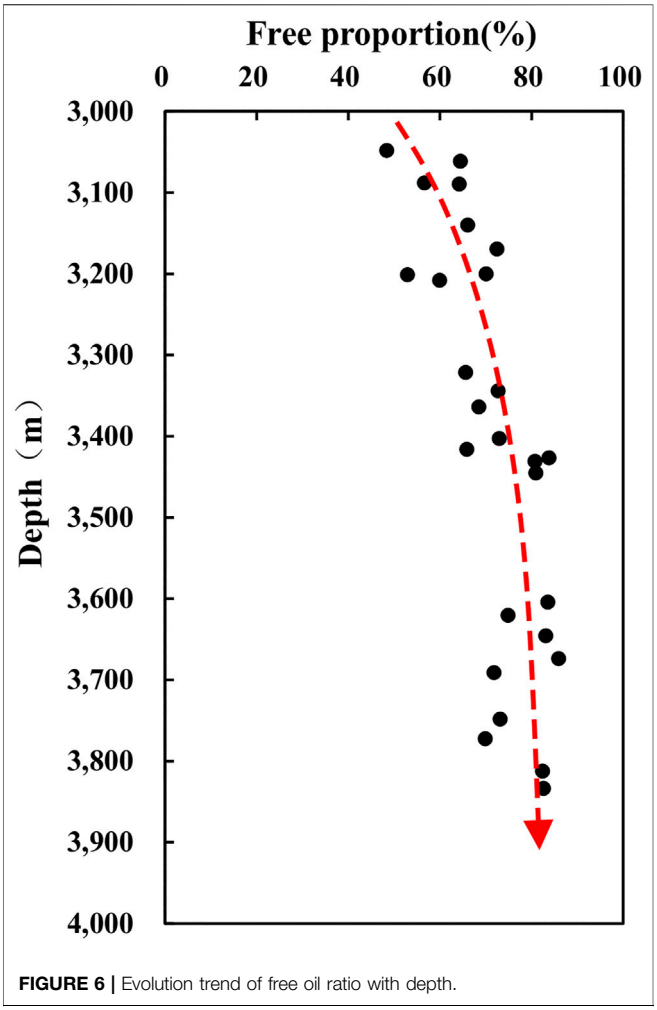

FIGURE 6 | Evolution trend of free oil ratio with depth.

release method are all adsorbed or free compounds are present (Li et al., 2019). In this study, the free shale oil content was determined using the NMR method according to the distribution position of different hydrogen components in the NMR T_2/T_1–T_2 spectrum (Li et al., 2018; Li et al., 2020b).

Because the rock samples are stored in the laboratory after extraction, light hydrocarbon loss will occur. To determine the free oil content of the saturated shale under the formation conditions, the rock sample needs to be pressurized and saturated, and then the free oil content of the saturated shale can be calculated according to the NMR T_1–T_2 spectrum. Due to the limitations in the experimental equipment, the NMR T_1–T_2 spectrum test time is long (40 min), and the light components can be lost during the test. To avoid the above situation, this study combines the NMR T_1 spectrum (1 min) and NMR T_1–T_2 spectrum technology to characterize the free oil content of saturated shale. The test process was as follows.

First, core samples with different lithofacies and maturity were selected to test the NMR T_1–T_2 spectrum, and the signal values of kerogen, adsorbed water, free water, and structural water were quantitatively evaluated. Second, the rock samples were saturated under pressure, and the samples after saturation were analyzed by NMR T_2 spectra. According to the signal difference of kerogen, adsorbed water, free water, and structural water evaluated by the NMR T_2 and NMR T_1–T_2 spectra, the adsorbed oil and free oil contents in saturated samples were obtained.

Based on the results of Li et al. (2020b), the 1-ms relaxation time in the T_2 spectrum was determined as the boundary between the adsorbed oil and free oil, and then the evolution chart between the free oil ratio (R_{free}) and the depth of saturated oil shale was established according to the relationship between oil/water signal intensity and volume/mass in the NMR T_2/T_1–T_2 spectrum (**Figure 6**). Finally, according to this chart and the total shale oil resources calculated above, the free shale oil resources were estimated.

Evaluation of Movable Shale Oil Resource

As mentioned above, the resource potential of free shale oil represents the theoretical maximum movable resource potential. However, restricted by factors such as the size and shape of pores throats, free shale oil cannot drain completely. Therefore, an accurate evaluation of the movable shale oil resource potential is of great significance in the exploration for "sweet spots." The important factor that restricts the evaluation accuracy of movable shale oil resources is shale oil mobility (Lu et al., 2016a; Chen F. et al., 2019). Hence, as the introduction describes, many scholars have conducted extensive research on shale oil mobility.

Based on previous research results and considering the actual formation conditions, to retain the residual oil and water in shale, this study performed the pressure saturation treatment on the unwashed oil shale samples and established an evolution chart of the shale oil movable ratio (movable oil/free oil) under different centrifugal forces according to the NMR centrifugal experiment. As shown in **Figure 7**, the relationship between the shale oil movable ratio and centrifugal force conforms to a Langmuir shape, that is, a curve passing through the origin. With the increase in centrifugal force, the shale oil movable ratio

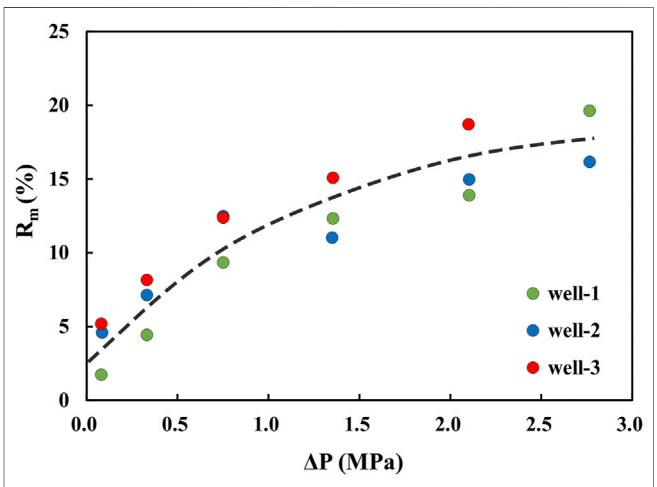

FIGURE 7 | Relationship between movable ratio and centrifugal force.

increases, and the rate of increase gradually decreases. The model can be expressed as follows:

$$R_{\mathrm{m}} = \frac{R_f \times \Delta P}{\Delta P + \Delta P_L} \tag{4}$$

where R_m is the movable ratio, ΔP is the centrifugal pressure, R_f is the theoretical maximum movable ratio, and ΔP_L is the median pressure.

The above equation is further rewritten as follows:

$$\frac{1}{R_{\mathrm{m}}} = \frac{\Delta P_L}{R_f}\frac{1}{\Delta P} + \frac{1}{R_f} \tag{5}$$

By plotting the relationship between 1/movable ratio and 1/centrifugal force, the theoretical maximum movable ratio (R_f) and median pressure (ΔP_L) of shale oil can be obtained. When applied to the target horizon in the study area, R_f was 20.83 and ΔP_L was 1.09. Therefore, the mathematical expression of the shale oil movable ratio is as follows (**Eq. 6**):

$$R_m = \frac{20.83 \times \Delta P}{\Delta P + 1.09} \tag{6}$$

Eq. 6 shows that the difference in production pressure, that is, the difference between the formation overpressure evaluation and flowing bottom hole pressure, needs to be determined when calculating movable shale oil resources by the movable ratio. Hence, this study performed a formation overpressure evaluation and bottom hole flow pressure evaluation. At present, some scholars have explored different quantitative evaluation methods for overpressure caused by different origins; however, they mainly rely on logging methods to analyze the relationship between porosity (acoustic curve, density) and stress (depth) to determine the reason of overpressure. The main methods for the quantitative overpressure prediction are direct estimation, effective vertical stress, effective horizontal stress (e.g., Eaton method), and other effective stress methods (e.g., Bowers method) (Hottmann and Johnson, 1965; Magara and Kinji, 1978; Bilgeri and Ademeno, 1982; Eaton and Eaton, 1997; Dutta, 2002; Xue et al., 2004; Wen, 2019). This study comprehensively analyzes the advantages and disadvantages of the above methods and their applicable conditions and combines the characteristics of the stratigraphic development in the study area to use the Bowers method for overpressure evaluation. The Bowers method is divided into loading and unloading curves. The normal compaction and under-compacted formations are on the loading curve, and the fluid expansion-causing formations are on the unloading curve. The corresponding mathematical expressions were established as follows:

Loading:

$$\begin{cases} v = 5000 + A\sigma^B \\ P_P = P_0 - \sigma \end{cases} \tag{7}$$

Unloading:

$$\begin{cases} v = 5000 + A\left[\sigma_{\max}\left(\dfrac{\sigma}{\sigma_{\max}}\right)^{1/U}\right]^B \\ P_P = P_0 - \sigma \end{cases} \tag{8}$$

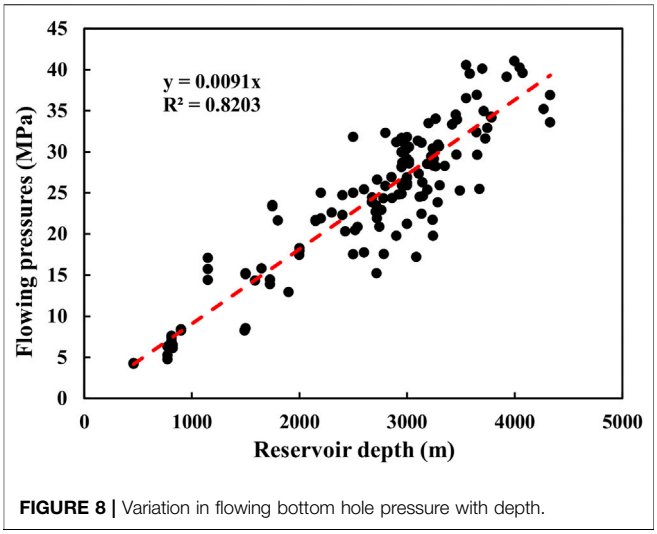

FIGURE 8 | Variation in flowing bottom hole pressure with depth.

$$\sigma_{\max} = \left[\frac{(v_{\max} - 5000)}{A}\right]^{\frac{1}{B}} \tag{9}$$

where v is acoustic velocity (m/s), v_{max} is acoustic velocity at the inflection point (m/s), σ is vertical effective stress (kPa), A and B are constant parameters, P_0 is overburden pressure, P_P is pore pressure, σ_{max} is effective stress at the unloading point (kPa), and U is the elastic coefficient.

Based on the above method combined with actual geological data, this study establishes an overpressure identification equation for the work area (**Eq. 10** and **Eq. 11**). Using this method, the formation pressure coefficient of each well position was calculated, and the formation pressure of the target layer was predicted.

Loading:

$$\begin{cases} v = 5000 + \left(4{*}10^{-15}\right)\sigma^{5.0255} \\ P_P = P_0 - \sigma \end{cases} \tag{10}$$

Unloading:

$$\begin{cases} v = 5000 + \left(4{*}10^{-15}\right)\left[\sigma_{\max}\left(\dfrac{\sigma}{\sigma_{\max}}\right)^{1/1.65}\right]^{5.0255} \\ P_P = P_0 - \sigma \end{cases} \tag{11}$$

The flowing bottom hole pressure is an important parameter for calculating the movable ratio. There has been considerable research on the evaluation of flowing bottom hole pressure in conventional gas and coalbed methane, and the common methods are the average temperature average deviation coefficient, Cullender–Smith, Chen Jialang–Yue Xiangan, Podio modified "s" curve, and Hasan Kabir analytical methods (Cullender and Smith, 1956; Aziz and Khalid, 1967; Hasan and Kabir, 1988; Mccoy et al., 1988; Chen et al., 1994). For the flowing bottom hole pressure calculation in shale oil wells, good correlation was observed between oil layer depth and flowing bottom hole pressure through intuitive statistics of several well test reports and completion reports in oilfield geological production data (**Figure 8**), thereby establishing the calculation formula for the flowing bottom hole pressure.

TABLE 1 | Statistics of resources of each small layer in Es3x.

Layer	Total oil content (× 10^8 t)	Free oil content (× 10^8 t)	Movable oil content (× 10^8 t)
First sub layer of Es3x	8.78	1.79	0.35
Second sub layer of Es3x	14.74	3.63	0.71
Third sub layer of Es3x	22.13	6.00	1.18
Fourth sub layer of lower Es3	5.06	1.45	0.28
Total	50.70	12.87	2.52

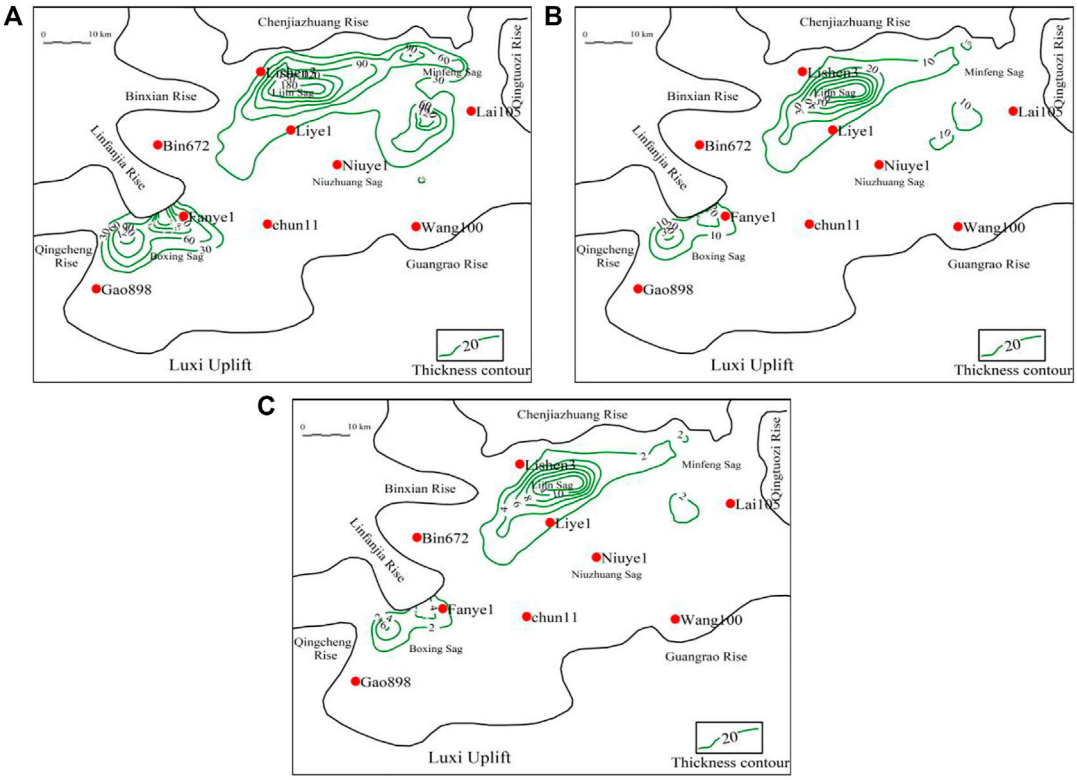

FIGURE 9 | Resource abundance contour map of the Shahejie Formation Es3x in the Dongying Sag **(A)**: total resource abundance; **(B)**: free resource abundance; **(C)**: movable resource abundance).

RESULTS AND DISCUSSION

The total shale oil, free shale oil, and movable shale oil resources were calculated through the above process. The results show that the total oil resource of the Es3x in the Dongying Sag was 50.7 × 10^8 t, free oil resource was 12.87 × 10^8 t, and movable oil resource was 2.52 × 10^8 t. The second and third layers were more abundant, accounting for 74% of Es3x (**Table 1**). The movable ratio of shale oil (movable oil/free oil) was approximately 18.9–20% within a buried depth of 3,200–3,700 m. According to the plane distribution characteristics of the total shale oil resource abundance in the Es3x in Dongying Sag (considering the first lower layer of Es3x as an example), shale oil resources were mainly distributed in each sag belt, gradually decreasing from the center to the edge of the sag, and Lijin Sag was the most abundant, with relatively small resource potential near the Boxing and Niuzhuang depressions (**Figure 9**). From the plane distribution characteristics of free resource and movable resource abundances, compared with the total shale oil resource abundance, the shale oil enrichment area basically remains unchanged.

CONCLUSION

(1) This study explores the relationship between different centrifugal forces and movable ratios through NMR

centrifugal experiments and proposes a new method for evaluating movable shale oil resources. When applied to geological conditions, the movable ratio of shale oil can be determined by evaluating the formation pressure and flowing bottom hole pressure, and then the movable oil resource can be estimated. The above method provides new insights for future shale oil resource evaluations.

(2) Considering the Dongying Sag as an example, this study calculates that the movable ratio of shale oil (movable oil/free oil) within the range of 3,200–3,700 m in Es3x is approximately 18.9–20%. The shale oil resource is 50.7×10^8 t, free shale oil resource is 12.87×10^8 t, and movable shale oil resource is 2.52×10^8 t, of which the resources of the second and third layers account for approximately 74% of the resources of the Es3x.

(3) From the distribution of Es3x in Dongying Sag, the movable shale oil resource is mainly concentrated in the Lijin Sag, and the potential of movable shale oil resources near Boxing and Niuzhuang sags is low. The Lijin Sag is a favorable exploration area in the Es3x of the Dongying Sag.

DATA AVAILABILITY STATEMENT

The raw data supporting the conclusion of this article will be made available by the authors, without undue reservation.

AUTHOR CONTRIBUTIONS

LX, MW, JL, and ML contributed to the conception and design of the study. LX wrote the first draft of the manuscript and led the data analysis and interpreted the results with MW, ZL, RZ, and HL. All authors contributed to manuscript revision, read and approved it for publication.

ACKNOWLEDGMENTS

This study was funded by the National Natural Science Foundation of China (41922015, 42072147), Fundamental Research Funds for the Central Universities (20CX06085A) and Qingdao Postdoctoral (ZX20210070).

REFERENCES

Aziz and Khalid (1967). Calculation of Bottom-Hole Pressure in Gas Wells. *J. Pet. Techn.* 19 (07), 897–899.

Bilgeri, D., and Ademeno, E. B. (1982). Predicting Abnormally Pressured Sedimentary Rocks*. *Geophys. Prospect* 30 (5), 608–621. doi:10.1111/j.1365-2478.1982.tb01329.x

Capuano, L. (2018). *International Energy Outlook 2018 (IEO2018)*. Washington, DC, USA: US Energy Information Administration (EIA), 21.

Chen, F., Zhao, H., Wang, S., Lu, S., Wang, M., and Ding, X. (2019a). Evaluation of Movable Shale Oil Reserves in the Es^{1L} of the Raoyang Sag, Jizhong Depression. *Oil Gas Geol.* 40 (03), 593–601. doi:10.11743/ogg20190314

Chen, G., Lu, S., Li, J., Xue, H., Wang, M., Tian, S., et al. (2017). A Method to Recover the Original Total Organic Carbon Content and Cracking Potential of Source Rocks Accurately Based on the Hydrocarbon Generation Kinetics Theory. *J. Nanosci. Nanotechnol.* 17 (9), 6169–6177. doi:10.1166/jnn.2017.14407

Chen, J., Pang, X., Pang, H., Chen, Z., and Jiang, C. (2018). Hydrocarbon Evaporative Loss Evaluation of Lacustrine Shale Oil Based on Mass Balance Method: Permian Lucaogou Formation in Jimusaer Depression, Junggar Basin. *Mar. Pet. Geol.* 91, 422–431. doi:10.1016/j.marpetgeo.2018.01.021

Chen, J., Pang, X., Wang, X., and Wang, Y. (2020). A New Method for Assessing Tight Oil, with Application to the Lucaogou Formation in the Jimusaer Depression, Junggar Basin, China. *Bulletin* 104 (6), 1199–1229. doi:10.1306/12191917401

Chen, J., Shi, Z., and Xu, J. (1994). Flow Patterns of Gas-Liquid Two-phase Upward Flow in Vertical Annuli. *J. Daqing Pet. Inst.* (04), 23–26.

Chen, Z., and Kirk, G. O. (2013). An Assessment of Tight Oil Resource Potential in the Upper Cretaceous Cardium Formation, Western Canada Sedimentary Basin. *Pet. Exploration Dev.* 40 (03), 320–328. doi:10.1016/s1876-3804(13)60041-5

Chen, Z., Li, M., Jiang, C., and Qian, M. (2019b). Shale Oil Resource Potential and its Mobility Assessment: A Case Study of Upper Devonian Duvernay Shale in Western Canada Sedimentary Basin. *Oil Gas Geol.* 40 (03), 459–468. doi:10.11743/ogg20190302

China Petroleum Enterprise Association (2020). China's Oil and Gas Industry Development Analysis and Outlook Report Blue Book (2019-2020). *China Pet. Enterprise* (04), 25–26.

Cullender, M. H., and Smith, R. V. (1956). Practical Solution of Gas-Flow Equations for Wells and Pipelines with Large Temperature Gradients. *Trans. AIME* 207 (1), 281–287. doi:10.2118/696-g

Delvaux, D., Martin, H., Leplat, P., and Paulet, J. (1990). Comparative Rock-Eval Pyrolysis as an Improved Tool for Sedimentary Organic Matter Analysis. *Org. Geochem.* 16 (4), 1221–1229. doi:10.1016/0146-6380(90)90157-U

Dutta, N. C. (2002). Geopressure Prediction Using Seismic Data: Current Status and the Road Ahead. *Geophysics* 67 (6), 2012–2041. doi:10.1190/1.1527101

Eaton, B. A., and Eaton, T. L. (1997). Fracture Gradient Prediction for the New Generation. *World Oil* 218 (10), 93–100.

Guo, Q. L., Chen, N. S., Liu, C. L., Xie, H. B., Wu, X. Z., Wang, S. J., et al. (2015). Research advance of Hydrocarbon Resource Assessment Method and a New Assessment Software. *Acta Petrolei Sinica* 36 (10), 1305–1314. doi:10.7623/syxb201510014

Guo, X. G., He, W. J., Yang, S., Wang, J. T., Feng, Y. L., Jia, X. Y., et al. (2019). Evaluation and Application of Key Technologies of "Sweet Area" of Shale Oil in Junggar Basin: Case Study of Permian Lucaogou Formation in Jimusar Depression. *Nat. Gas Geosci.* 30 (08), 1168–1179. doi:10.11764/j.issn.1672-1926.2019.05.020

Hasan, A. R., and Kabir, C. S. (1988). A Study of Multiphase Flow Behavior in Vertical wells. *Spede* 3 (02), 263–272. doi:10.2118/15138-pa

HoodYurewiczStefen, K. C. D. A. K. J., Yurewicz, D. A., and Stefen, K. J. (2012). Assessing Continuous Resources - Building the Bridge between Static and Dynamic Analyses. *Bull. Can. Pet. Geol.* 60 (3), 112–133. doi:10.2113/gscpgbull.60.3.112

Hottmann, C. E., and Johnson, R. K. (1965). Estimation of Formation Pressures from Log-Derived Shale Properties. *J. Pet. Techn.* 17 (06), 717–722. doi:10.2118/1110-pa

Huang, W. B., Deng, S. W., Lu, S. F., Yu, L., Hu, S., and Zhang, J. (2014). Shale Organic Heterogeneity Evaluation Method and its Application to Shale Oil Resource Evaluation—A Case Study from Qingshankou Formation, Southern Songliao Basin. *Oil Gas Geol.* 35 (05), 704–711. doi:10.11743/ogg201405

Jarvie, D. M., and Daniel, M. (2012). Shale Resource Systems for Oil and Gas: Part 1—Shale-Gas Resource Systems. Aapg Memoir, 89–119. doi:10.1306/13321446M973489

Jiang, Q. G., Li, M. W., Qian, M. H., Li, Z. M., Li, Z., Huang, Z. K., et al. (2016). Quantitative Characterization of Shale Oil in Different Occurrence States and its Application. *Pet. Geol. Exp.* 38 (6), 842–849. doi:10.11781/sysydz201606842

Jiang, Z. X., Pang, X. Q., Jin, Z. J., Zhou, H. Y., and Wang, X. D. (2002). Threshold Control over Hydrocarbons and its Application in Distinguishing Valid Source Rock. *Earth Sci.* (06), 689–695.

Li, G. X., and Zhu, R. K. (2020a). Progress, Challenges and Key Issues of Unconventional Oil and Gas Development of CNPC. *China Pet. Exploration* 25 (02), 1–13. doi:10.3969/j.issn.1672-7703.2020.02.001

Li, J. B., Lu, S. F., Chen, G. H., Shan, J. F., Hu, Y. J., Mao, J. L., et al. (2016). Correction of Light and Heavy Hydrocarbon Loss for Residual Hydrocarbon S_1

and its Significance to Assessing Resource Potential of $E_2s^{4(2)}$ Member in Damintun Sag, Bohai Bay Basin. *Oil Gas Geol.* 37 (04), 538–545. doi:10.11743/ogg20160410

Li, J., Huang, W., Lu, S., Wang, M., Chen, G., Tian, W., et al. (2018). Nuclear Magnetic Resonance T1-T2 Map Division Method for Hydrogen-Bearing Components in Continental Shale. *Energy Fuels* 32 (9), 9043–9054. doi:10.1021/acs.energyfuels.8b01541

Li, J., Jiang, C., Wang, M., Lu, S., Chen, Z., Chen, G., et al. (2020b). Adsorbed and Free Hydrocarbons in Unconventional Shale Reservoir: A New Insight from NMR T1-T2 Maps. *Mar. Pet. Geol.* 116, 104311. doi:10.1016/j.marpetgeo.2020.104311

Li, J. Q., Lu, S. F., Zhang, J., Zhang, P. F., and Xue, H. T. (2019). Quantitative Evaluation Models of Adsorbed and Free Shale Oil and its Microscopic Occurrence Mechanism. *Oil Gas Geol.* 40 (03), 583–592. doi:10.11743/ogg20190313

Li, J., Wang, M., Chen, Z., Lu, S., Jiang, C., Chen, G., et al. (2019). Evaluating the Total Oil Yield Using a Single Routine Rock-Eval experiment on As-Received Shales. *J. Anal. Appl. Pyrolysis* 144, 104707. doi:10.1016/j.jaap.2019.104707

Li, J., Wang, M., Lu, S., Chen, G., Tian, W., Jiang, C., et al. (2020c). A New Method for Predicting Sweet Spots of Shale Oil Using Conventional Well Logs. *Mar. Pet. Geol.* 113, 104097. doi:10.1016/j.marpetgeo.2019.104097

Li, W. J. (2012). *The Sedimentary System of Es_4-Es_{3x} Member of Shahejie Formation on the Southern Slope of Dongying Sag*. EastChina: China University of Petroleum.

Li, Z., Zou, Y.-R., Xu, X.-Y., Sun, J.-N., Li, M., and Peng, P. A. (2016). Adsorption of Mudstone Source Rock for Shale Oil - Experiments, Model and a Case Study. *Org. Geochem.* 92, 55–62. doi:10.1016/j.orggeochem.2015.12.009

Liu, B., Guo, X. B., Huang, Z. L., Tu, X. X., Shen, Y., and Wang, R. (2013). Discussion on Prediction Method for Hydrocarbon Resource Potential of Shale Oil: Taking Lucaogou Formation Shale Oil of Malang Sag as Case. *J. Cent. South Univ. (Science Technology)* 44 (04), 1472–1478.

Liu, B., He, J., Lv, Y. F., Ran, Q. C., Dai, C. L., and Li, M. (2014a). Parameters and Method for Shale Oil Assessment: Taking Qinshankou Formation Shale Oil of Northern Songliao Basin. *J. Cent. South Univ. (Science Technology)* 45 (11), 3846–3852.

Liu, C., Lu, S. F., and Xue, H. T. (2014b). Variable-coefficient ΔlogR Model and its Application in Shale Organic Evaluation. *Prog. Geophys.* 29 (01), 312–317. doi:10.6038/pg20140144

Liu, Y. (2018). *Study on Shale Oil Reservoir Characteristics of Shahejie Formation in Jiyang Depression, Bohai Bay Basin*. Chengdu, China: Chengdu University of Technology.

Lu, S. F., Chen, G. H., Wang, M., Li, J. B., Wang, X., Shan, J. F., et al. (2016a). Potential Evaluation of Enriched Shale Oil Resource of Member 4 of the Shahejie Formation in the Damintun Sag, Liaohe Depression. *Oil Gas Geol.* 37 (1), 8–14. doi:10.11743/ogg20160102

Lu, S. F., Xue, H. T., Wang, M., Xiao, D. S., Huang, W. B., Li, J. Q., et al. (2016b). Several Key Issues and Research Trends in Evaluation of Shale Oil. *Acta Petrolei Sinica* 37 (10), 1309–1322. doi:10.7623/syxb201610012

Lu, S., Liu, W., Wang, M., Zhang, L., Wang, Z., Chen, G., et al. (2017). Lacustrine Shale Oil Resource Potential of Es 3 L Sub-member of Bonan Sag, Bohai Bay Basin, Eastern China. *J. Earth Sci.* 28 (6), 996–1005. doi:10.1007/s12583-016-0945-4

Lv, D., Li, Z., Wang, D., Li, Y., Liu, H., Liu, Y., et al. (2019). Sedimentary Model of Coal and Shale in the Paleogene Lijiaya Formation of the Huangxian Basin: Insight from Petrological and Geochemical Characteristics of Coal and Shale. *Energy Fuels* 33 (11), 10442–10456. doi:10.1021/acs.energyfuels.9b01299

Lv, D., Song, Y., Shi, L., Wang, Z., Cong, P., van Loon, A. J., et al. (2020). The Complex Transgression and Regression History of the Northern Margin of the Palaeogene Tarim Sea (NW China), and Implications for Potential Hydrocarbon Occurrences. *Mar. Pet. Geol.* 112, 104041. doi:10.1016/j.marpetgeo.2019.104041

MagaraKinji (1978). *Compaction and Fluid Migration : Practical Petroleum Geology*. Elsevier Scientific Publishign Co.

Mccoy, J. N., Podio, A. L., and Huddleston, K. L. (1988). Acoustic Determination of Producing Bottomhole Pressure. *Spe Formation Eval.* 3 (03), 617–621. doi:10.2118/14254-pa

Michael, G. E., Packwood, J., Holba, A., and Houston, C. (2013). *Determination of* In-Situ *Hydrocarbon Volumes in Liquid Rich Shale Plays*. doi:10.1190/urtec2013-211

Ning, F. X., Wang, X. J., Hao, X. F., Yang, W. Q., Yin, Y., Ding, J. H., et al. (2017). Occurrence Mechanism of Shale Oil with Different Lithofacies in Jiyang Depression. *Acta PetroLei Sinica* 38 (02), 185–195. doi:10.7623/syxb201702006

Olea, R. A., Cook, T. A., and Coleman, J. L. (2010). A Methodology for the Assessment of Unconventional (Continuous) Resources with an Application to the Greater Natural Buttes Gas Field, Utah. *Nat. Resour. Res.* 19 (4), 237–251. doi:10.1007/s11053-010-9127-8

Pu, X. G., Jin, F. M., Han, Z. W., Shi, Z. F., Cai, A. B., Wang, A. G., et al. (2019). Sweet Spots Geological Characteristics and Key Exploration Technologies of continental Shale Oil: a Case Study of Member 2 of Kongdian Formation in Cangdong Sag. *Acta PetroLei Sinica* 40 (08), 997–1012. doi:10.7623/syxb201908011

Qian, M. H., Jiang, Q. G., Li, M. W., Li, Z. M., Liu, P., Ma, Y. Y., et al. (2017). Quantitative Characterization of Extractable Organic Matter in Lacustrine Shale with Different Occurrences. *Pet. Geol. Exp.* 39 (02), 278–286. doi:10.11781/sysydz201702278

Ribeiro, R. C., Correia, J. C. G., and Seidl, P. R. (2009). The Influence of Different Minerals on the Mechanical Resistance of Asphalt Mixtures. *J. Pet. Sci. Eng.* 65 (3), 171–174. doi:10.1016/j.petrol.2008.12.025

Salazar, J., Mcvay, D. A., and Lee, W. J. (2010). Development of an Improved Methodology to Assess Potential Unconventional Gas Resources. *Nat. Resour. Res.* 19 (4), 253–268. doi:10.1007/s11053-010-9126-9

Schmoker, J. W. (2002). Resource-assessment Perspectives for Unconventional Gas Systems. *AAPG Bull.* 86 (11), 1993–1999. doi:10.1306/61EEDDDC-173E-11D7-8645000102C1865D

Song, G. Q., Hao, X. F., and Liu, K. Q. (2014). Tectonic Evolution, Sedimentary System and Petroleum Distribution Patterns in Dustpan-Shaped Rift basin: a Case Study from Jiyang Depression, Bohai Bay Basin. *Oil Gas Geol.* 35 (03), 303–310. doi:10.11743/ogg201402

Song, G. Q., Zhang, L. Y., Lu, S. F., Xu, X. Y., Zhu, R. F., Wang, M., et al. (2013). Resource Evaluation Method for Shale Oil and its Application. *Earth Sci. Front.* 20 (4), 221–228.

Us Eia, U. (2019). *Annual Energy Outlook 2019 with Projections to 2050*. Technical Report.

Wang, A. Q., and Zheng, B. M. (1987). Calibration of Analytic Parameters for Pyrolytic Chromatography. *Exp. Pet. Geol.* (04), 342–350.

Wang, M., Ma, R., Li, J. B., Lu, S. F., Li, C. M., Guo, Z. Q., et al. (2019). Occurrence Mechanism of Lacustrine Shale Oil in the Paleogene Shahejie Formation of Jiyang Depression, Bohai Bay Basin, China. *Pet. Exploration Dev.* 46 (04), 789–802. doi:10.11698/PED.2019.04.1910.1016/s1876-3804(19)60242-9

Wang, M., Tian, S., Chen, G., Xue, H., Huang, A., and Wang, W. (2014). Correction Method of Light Hydrocarbons Losing and Heavy Hydrocarbon Handling for Residual Hydrocarbon (S1) from Shale. *Acta Geologica Sinica - English Edition* 88 (6), 1792–1797. doi:10.1111/1755-6724.12345

Wang, R. F., Sun, W., and Yang, H. (2010). Micro Mechanism of Water Drive in Ultra-low Permeability sandstone Reservoir. *J. Lanzhou Univ. (Natural Sciences)* 46 (06), 29–33. doi:10.13885/j.issn.0455-2059.2010.06.012

Wang, W. G., Zheng, M., Wang, M., Lu, S. F., Peng, J., Lu, K., et al. (2015). The Discussion of the Evaluation Method of Shale Oil Movable Resources Amount and Palaeogene Shahejie Formation Application Effect in the Northern of Dongpu Depression. *Nat. Gas Geosci.* 26 (4), 771–781. doi:10.11764/j.issn.1672-1926.2015.04.0771

Wen, C. X. (2019). *Identification and Quantitative Evaluation of Overpressure of Different Origin in Kuqa Depression*. Xi'an, China: Northwest University. doi:10.1109/iceaa.2019.8879378

Wright, M. C., Court, R. W., Kafantaris, F.-C. A., Spathopoulos, F., and Sephton, M. A. (2015). A New Rapid Method for Shale Oil and Shale Gas Assessment. *Fuel* 153, 231–239. doi:10.1016/j.fuel.2015.02.089

Wu, B. C., Li, J. M., Wu, Y. Y., Han, L., Zhao, T. F., and Zou, Y. S. (2019a). Development Practices of Geology-Engineering Integration on Upper Sweet Spots of Lucaogou Formation Shale Oil in Jimsar Sag, Junggar Basin. *China Pet. Exploration* 24 (05), 679–690. doi:10.3969/j.issn.1672-7703.2019.05.014

Wu, H. Y., Lin, T. F., Bai, Y. F., Zhang, J. Y., Liu, X., Huo, Q. L., et al. (2019b). Analyses of the Mudstone (Shale) Oil Exploration Potential in North Songliao Basin. *Pet. Geol. Oilfield Dev. Daqing.* 38 (05), 78–86. doi:10.19597/J.ISSN.1000-3754.201907007

Xu, G., Guan, L. P., Wang, L. S., Yang, Z. X., and Sun, C. L. (2004). The Technology for Detection of Overpressured Zones in Formations: an Example from the Tongnanba fold-belt, Sichuan basin, China. *Prog. Geophys.* (03), 645–651.

Xue, G., Guan, L. P., Wang, L. S., Yang, Z. X., and Sun, C. L. (1995). The Technology for Detection of Overpressured Zones in Formations: an Example From the Tongnanba Fold-Belt, Sichuan Basin, China. *Prog. Geophys.* (3), 645–651.

Xue, H. T., Tian, S. S., Lu, S. F., Zhang, W. H., Du, T. T., and Mu, G. D. (2015). Selection and Verification of Key Parameters in the Quantitative Evaluation of Shale Oil: A Case Study at the Qingshankou Formation, Northern Songliao Basin. *Bull. Mineral. Petrol. Geochem.* 34 (01), 70–78+2.

Xue, H. T., Tian, S. S., Wang, W. M., Zhang, W. H., Du, T. T., and Mu, G. D. (2016). Correction of Oil Content—One Key Parameter in Shale Oil Resource Assessment. *Oil Gas Geol.* 37 (01), 15–22. doi:10.11743/ogg20160103

Yang, H., Li, S. X., and Liu, X. Y. (2013). Characteristics and Resource Prospects of Tight Oil and Shale Oil in Ordos Basin. *Acta Petrolei Sinica* 34 (01), 1–11. doi:10.7623/syxb201301001

Zhang, H., Huang, H., Li, Z., and Liu, M. (2020). Comparative Study between Sequential Solvent-Extraction and Multiple Isothermal Stages Pyrolysis: A Case Study on Eocene Shahejie Formation Shales, Dongying Depression, East China. *Fuel* 263, 116591. doi:10.1016/j.fuel.2019.116591

Zhang, J. C., Lin, L. M., Li, Y. X., Tang, X., Zhu, L. L., Xing, Y. W., et al. (2012). Classification and Evaluation of Shale Oil. *Earth Sci. Front.* 19 (05), 322–331.

Zhang, L. Y., Bao, Y. S., Li, J. Y., Li, Z., Zhu, R. F., and Zhang, J. G. (2014). Movability of Lacustrine Shale Oil: A Case Study of Dongying Sag, Jiyang Depression, Bohai Bay Basin. *Pet. Exploration Dev.* 41 (06), 641–649. doi:10.1016/s1876-3804(14)60084-7

Zhang, L. Y., Bao, Y. S., Li, J. Y., Li, Z., Zhu, R. F., Zhang, L., et al. (2015a). Hydrocarbon and Crude Oil Adsorption Abilities of Minerals and Kerogens in Lacustrine Shales. *Pet. Geol. Exp.* 37 (06), 776–780. doi:10.11781/sysydz201506776

Zhang, S., Chen, S. J., Yan, J. H., Tan, M. Y., Zhang, Y. Y., Gong, W. L., et al. (2015b). Characteristics of Shale Lithofacies and Reservoir Space in the 3rd and 4th Members of Shahejie Formation, the West of Dongying Sag. *Nat. Gas Geosci.* 26 (02), 320–332. doi:10.11764/j.issn.1672-1926.2015.02.0320

Zhao, Y. Z., Zhou, L. H., Pu, X. G., Jin, F. M., Shi, Z. N., Xiao, D. Q., et al. (2019). Favorable Formation Conditions and Enrichment Characteristics of Lacustrine Facies Shale Oil in Faulted lake basin: a Case Study of Member 2 of Kongdian Formation in Cangdong Sag, Bohai Bay Basin. *Acta Petrolei Sinica* 40 (09), 1013–1029. doi:10.7623/syxb201909001

Zhi, D. M., Tang, Y., Yang, Z. F., Guo, X. G., Zheng, M. L., Wan, M., et al. (2019). Geological Characteristics and Accumulation Mechanism of continental Shale Oil in Jimusaer Sag, Junggar Basin. *Oil Gas Geol.* 40 (03), 524–534. doi:10.11743/ogg20190308

Zhou, S. W., Liu, L. H., Yan, G., Xue, H. Q., and Guo, W. (2016). NMR Research of Movable Fluid and T_2 Cutoff of marine Shale in South China. *Oil Gas Geol.* 37 (04), 612–616. doi:10.11743/ogg20160420

Zhu, R. F., Zhang, L. Y., Li, J. Y., Liu, Q., Li, Z., Wang, R., et al. (2015). Quantitative Evaluation of Residual Liquid Hydrocarbons in Shale. *Acta Petrolei Sinica* 36 (1), 13–18. doi:10.7623/syxb201501002

Zhu, R. F., Zhang, L. Y., Li, Z., Wang, R., and Zhang, S. L. (2019). Evaluation of Shale Oil Resource Potential in continental Rift basin A Case Study of Lower Es3Member in Dongying Sag. *Pet. Geol. Recovery Efficiency* 26 (01), 129–136. doi:10.13673/j.cnki.cn37-1359/te.2019.01.014

Zou, C. N., Pan, S. Q., Jing, Z. H., Gao, J. L., Yang, Z., Wu, S. T., et al. (2020). Shale Oil and Gas Revolution and its Impact. *Acta Petrolei Sinica* 41 (01), 1–12. doi:10.7623/syxb202001001

Zou, C. N., Yang, Z., Cui, J. W., Zhu, R. K., Hou, L. H., Tao, S. Z., et al. (2013). Formation Mechanism, Geological Characteristics and Development Strategy of Nonmarine Shale Oil in China. *Pet. Exploration Dev.* 40 (01), 14–26. doi:10.1016/s1876-3804(13)60002-6

Conflict of Interest: ZL, RZ, and HL were employed by the company Shengli Oilfield Company, SInopec.

The remaining authors declare that the research was conducted in the absence of any commercial or financial relationships that could be construed as a potential conflict of interest.

frontiers in Earth Science

ORIGINAL RESEARCH
published: 30 June 2021
doi: 10.3389/feart.2021.703070

The Sedimentary Facies and Evolution Characteristics of the Middle and Deep Strata in the Nanpu No. 3 Structural Area

Hui Zhang, Zhiqin Lan, Xiaoyan Li and Xinglong Huang*

Shandong Institute of Coal Geology Planning and Exploration, Jinan, China

In this study, due to the inconsistencies in the understanding of the sedimentary types in the second section of the Dongying Formation (Ed_2) and the third section of the Shahejie Formation (Es_3) in the middle and deep strata of Nanpu No. 3 structural area, the depositional characteristics of the deep braided river delta, fan delta, deep-water slump turbidite fan, and coastal and shallow lake in the Nanpu No. 3 structural area were examined in-depth. The investigations were begun based on the descriptions and observations of core samples obtained from eight cored wells in the study area, in combination with seismic, well logging, and rock ore data. The results revealed that the sources of the material in the study area originated from the Shaleitian salient in the southwest direction. It was determined that the fan deltas and the shallow lake sedimentary system had developed during the SQ1 sequence and SQ2 sequence periods. The braided river deltas and the shallow lake and turbidite sedimentary system with multi-stage superposition had developed during the SQ3 to SQ7 sequence periods, and their distribution range had been controlled by the structural background of the gentle slope zone of the lake basin. On that basis, a sequence deposition filling model controlled by a slope break zone in the middle and deep strata of the Nanpu No. 3 structural area was established in this study starting from the typical seismic profile, in which such factors as the tectonic activity characteristics, lake basin boundary shape, water depths, and so on, were comprehensively considered. The goal of this research investigation was to provide beneficial information for oil and gas explorations in similar areas.

Keywords: Nanpu No 3 structural area, sedimentary facies, sedimentary evolution, slope break zone, Braided river delta

OPEN ACCESS

Edited by:
Dawei Lv,
Shandong University of Science and Technology, China

Reviewed by:
Xianfeng Tan,
Chongqing University of Science and Technology, China
Pengwei Wang,
SINOPEC Petroleum Exploration and Production Research Institute, China

****Correspondence:***
Hui Zhang
22207536@qq.com

Specialty section:
This article was submitted to Sedimentology, Stratigraphy and Diagenesis, a section of the journal Frontiers in Earth Science

Received: *30 April 2021*
Accepted: *16 June 2021*
Published: *30 June 2021*

Citation:
Zhang H, Lan Z, Li X and Huang X (2021) The Sedimentary Facies and Evolution Characteristics of the Middle and Deep Strata in the Nanpu No. 3 Structural Area. Front. Earth Sci. 9:703070. doi: 10.3389/feart.2021.703070

INTRODUCTION

The Nanpu Sag is a type of Mesozoic-Cenozoic superimposed compound sag located in the northern section of the Huanghua Depression in the Bohai Bay Basin. The Nanpu Sag displays the active rift characteristics of polyphase extensions and inheritance development which occurred during the Mesozoic and Cenozoic Periods (Qi et al., 2010; Ran et al., 2010). Since oil and gas explorations in the Nanpu No. 3 structural area began, industrial oil flow has been found in the Paleogene Shahejie Formation. In August of 2014, a breakthrough discovery was made in the Dongying Formation. The

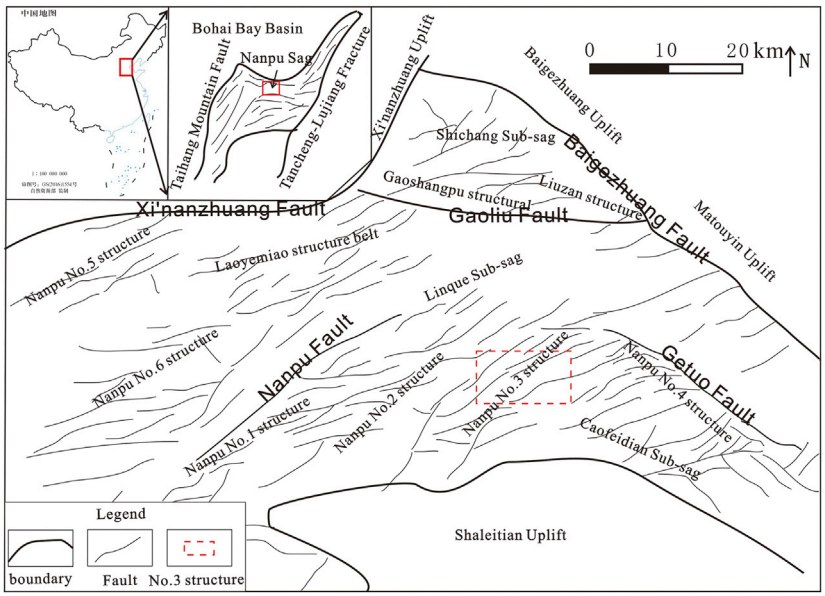

FIGURE 1 | Structural location diagram of the Nanpu No. 3 structural area.

daily oil production of the Nanpu 306 × 9 well was 7.679 m^3 during the oil production tests. A series of new discoveries showed that the No. 3 structural area was an important oil and gas exploration target and replacement position in the Nanpu Sag. In recent years, some researchers have studied the middle and deep strata of the Nanpu No. 3 structural area. The previous studies mainly focused on the characterization analyses of sedimentary sand bodies and the reservoir characteristics in the first section of the Shahejie Formation and the third section of the Dongying Formation (Xu, 2006; Feng et al., 2010; Huang et al., 2012; Jiang et al., 2013; Dong et al., 2014; Jiang et al., 2018; Wang et al., 2019; Wu et al., 2019). Previous research on the source direction of the Nanpu No. 3 structure has not been unified, and it is believed that it may have originated from the uplift plate of the Bogezhuang fault, the uplift plate of the Gaoliu fault, the Shalietian uplift, and the Shiyutuo uplift (Xian et al., 2012; Liu et al., 2017). Most scholars agree that in the Nanpu Sag the fan delta is developed in the steep slope zone, braided river delta in gentle slope zone and slump turbidite fan (Li et al., 2018; Wang et al., 2020; Sun et al., 2021). The slope break zone is an important concept formed on the basis of studying the sedimentology and sequence stratigraphy of marine sedimentary basins. This term refers to the zone where the topographic slope changes. More and more examples of oil and gas exploration show that there are slope break zones present in both of the continental basins, which clearly control the distribution of the overlying strata, lithology and lithofacies and the distribution of oil and gas reservoirs (Lin et al., 2000; Wang et al., 2002; Li et al., 2008). However, at the present time, there is a lack of in-depth research regarding the sedimentary facies and sedimentary filling processes of the middle and deep strata. In the current investigation, the main sedimentary facies and sedimentary evolution characteristics of the Nanpu No. 3 structural area were systematically examined in accordance with the observations and descriptions of 168 m cores taken from 14 cored wells in Nanpu No. 3 structural area, in combination with the seismic data, logging data, and testing data. In addition, such factors as the tectonic activity characteristics, boundary fault morphology, climate conditions, water depth, and so on, were comprehensively considered. Then, taking the Nanpu No. 3 structural area as a prototype, a sedimentary filling model controlled by a slope break zone was established in order to provide a basis for searching for favorable reservoir sand bodies with potential for further evaluations.

GEOLOGIC SETTING

The Nanpu No. 3 structure is located in the southeastern section of the Nanpu Sag, which is situated in the northern region of the Huanghua Depression in the Bohai Bay Basin. The Nanpu No. 3 structure is adjacent to the Nanpu No. 4 structure in the east; Nanpu No. 2 structure in the west; Shaleitian Salient and Caofeidian Sub Sag in the south; and the Linque Sub Sag in the north (Zhou et al., 2000; Jiang et al., 2009; Fan et al., 2010; Li et al., 2011) (**Figure 1**). It is essentially an uplift area between the two sub sags, with a structural area of approximately 240 km^2. Its overall structural pattern is that of an east-west spreading, and the secondary faults mainly trend in a NE direction. The Nanpu No. 3 structural area is a fault anticline structure developed on a Cambrian buried hill, which is characterized by the Paleogene Shahejie formation, Dongying Formation, Neogene Guantao Formation, Minghuazhen Formation, and a quaternary plain formation in turn above it. This is also a lack of Paleozoic to Mesozoic strata in the area. According to the characteristics of sequence boundaries, the Paleogene in the Nanpu No. 3 structural area can be divided into three second-order sequences and eight

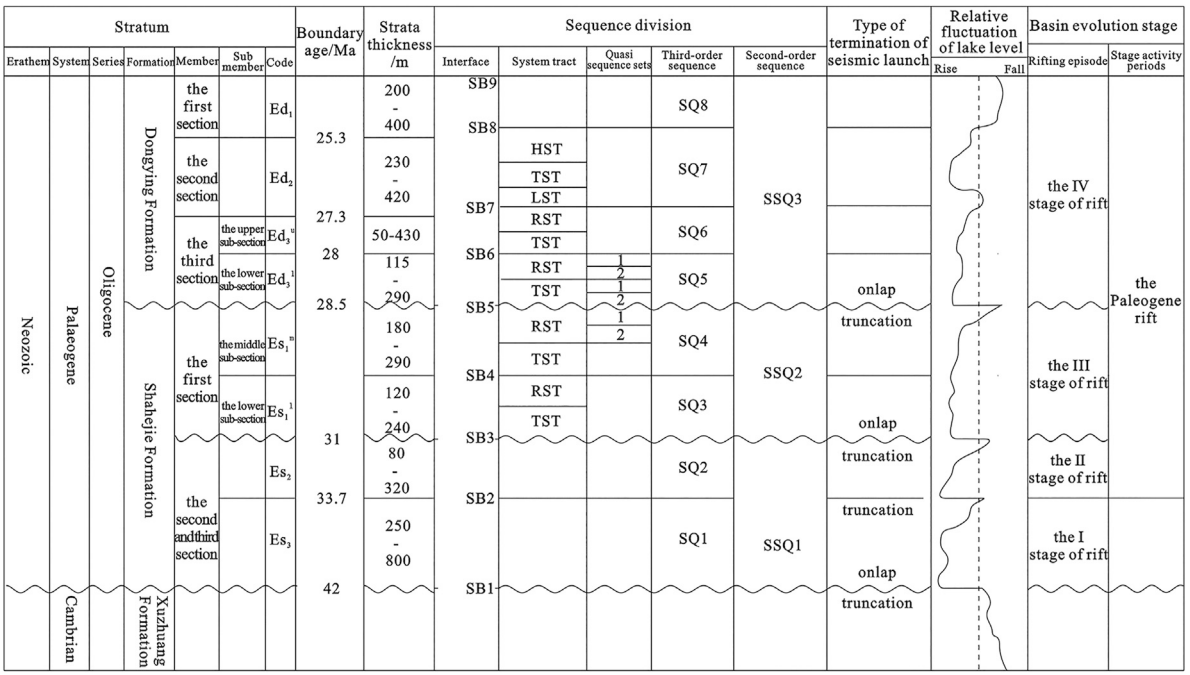

FIGURE 2 | Division and correlation of the Paleogene sequence stratigraphy and lithostratigraphy in the Nanpu No. 3 structural area.

third-order sequences using the stratigraphic division scheme of strata (for example, SQ1 to SQ8). The system tracts of each sequence can also be subdivided, as shown in **Figure 2**. The middle and deep strata in the study area include the second section of the Dongying Formation (Ed_2) and the third section of the Shahejie Formation (Es_3), referred to in this study as SQ1 to SQ7.

SAMPLES AND METHODS

The observations and descriptions of 168 m cores in 14 coring Wells in the Nanpu No. 3 structural area were carried out, and 10 rock ore analyses were completed. At the same time, the data of drilling, logging, testing and seismic data of 32 wells in the middle and deep depths of the study area were collected from oil field companies for reprocessing, interpretation and research analysis. In this study, the middle and deep layers of the Nanpu No. 3 structure were taken as the research object, and the second member of Dongying Formation to the first member of Shahejie Formation was taken as the key research section. Next, the sequence stratigraphy and sedimentology were studied, the provenance direction was clarified, and the sedimentary characteristics and filling mode of the gentle slope zone in the study area were analyzed.

RESULTS

Source Directions

The southern margin of the Nanpu No. 3 structural area is located close to the Shaleitian Salient area, and structurally belongs to the northern slope of the Shaleitian Salient. The rock composition characteristics of the first section of the Shahejie Formation in the study area include light mineral quartz content (<50%) and feldspar (content of 25–50%), which belong to arkose and lithic arkose (**Figure 3A**). The heavy minerals in the area mainly include zircon, pyrite, and anatase (**Figure 3B**). According to the plane distribution trend of the light mineral content, the relative quartz content generally increases from the southwest to the northeast. It is believed that the material sources of the Nanpu No. 3 structural area mainly originate from the Shaleitian Salient area in the southwestern direction (**Figure 3C**), and the material source openings are distributed in the developmental parts of the main fault in the north-eastern direction. The material sources were injected along the trough fault formed by the NE-trending faults. During the advancement processes from the edges of the gentle slope to the lake basin along the material source direction, the grain sizes of the sediment became finer; degrees of sorting and grinding became higher; composition maturity increased; and the argillaceous content levels in the lake basin area increased significantly, while the relative sand content significantly decreased.

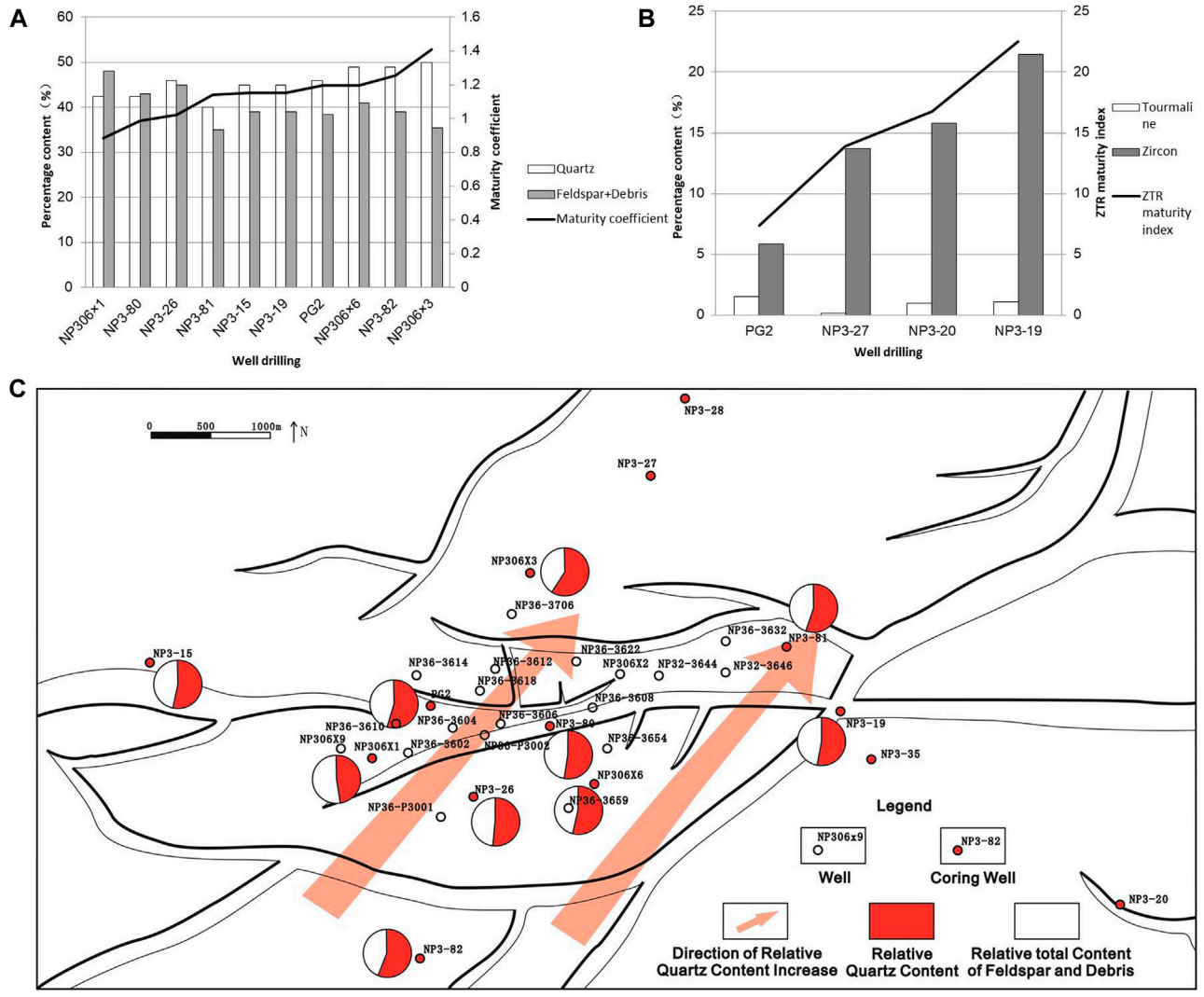

FIGURE 3 | Analysis results of material source directions in the middle and deep strata of the Nanpu No. 3 structural area. **(A)** Histogram of light mineral content of rock in different well areas; **(B)** Histogram of heavy mineral content of rock in different well areas; **(C)** Distribution trend of light mineral content in rocks of Nanpu No. 3 structural area.

Types and Characteristics of the Sedimentary Facies

Braided River Delta

When the braided river carried large amounts of terrigenous sediment into the lake after long-term transportation processes, the sediment carried by the braided river rapidly accumulated at the mouth of the lake due to the decreases in the braided river's velocity. As a result, tongue-shaped, fan-shaped, or lobate sedimentary complexes were formed on the plane and wedge-shaped sedimentary complexes were formed on the section (e.g. the braided river delta deposits) (Liu et al., 2015). The braided river delta deposits in the Nanpu No. 3 structural area were developed in each system tract of the SQ3 to SQ8 sequence. There were observed to be mainly located in the lacustrine regression tract, and the high-stand tract and low-stand tract of each sequence and were apparent in the central and southern plane sections of the study area. In addition, there were deposits of dark gray mudstone, argillaceous siltstone, and sandstone interbedding mixed with small amounts of fine sandstone and glutenite. In term of the sedimentary tectonics, these were found to be dominated by parallel bedding, oblique bedding, and plate cross-bedding, and with scour filling structures located at the bottom. The Nanpu No. 3 structural area was observed to be dominated by braided delta front sub-facies with limited sedimentary range, which further identified in the underwater distributary bay, main body of the underwater distributary channel, estuary dam, and the lateral edges of the underwater distributary channel.

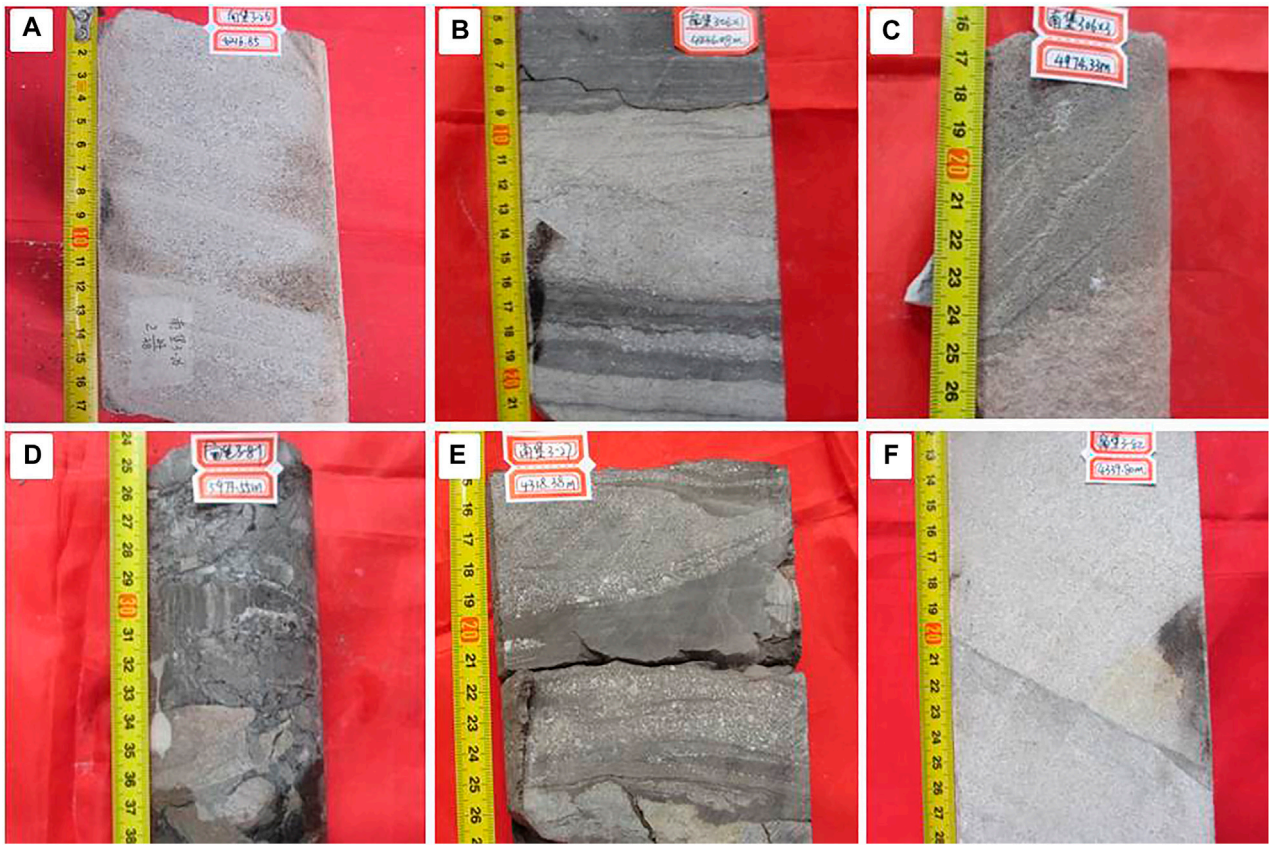

FIGURE 4 | Lithofacies marks of the middle and deep layers in the Nanpu No. 3 structural area: **(A)** NP3-26 (4,216.85 m), positive rhythm coarse sandstone gravel in the main body of underwater distributary channel in the braided river delta front; **(B)** NP306 × 1 (4,236.08 m), greyish black gravelly mudstone and grayish white sandstone in the underwater distributary bay of the braided river delta front; **(C)** NP306 × 3 (4974.33 m), grey medium sandstone of estuary dam in the braided river delta front; **(D)** NP3-81 (5,973.55 m), grey black mudstone interbedded with gravel in the braided river delta front; **(E)** NP3-27 (4,318.94 m) deep-water slump turbidite fan with mudstone bands in the grey pebbled sandstone of the agitated structure; **(F)** NP3-82 (4,339.8 m), grayish white medium sandstone of the beach bar.

Main Body of the Underwater Distributary Channel

The lithology of the study was mainly composed of gravelly sandstone and fine sandstone, and presented multiple sets of vertically positive rhythm with typical structures, such as bottom scouring and oblique bedding (**Figure 4A**) and significant progradational reflection characteristics. These features were widely developed and distributed in each sequence of the study area, displaying good physical properties associated with reservoirs and oil-bearing reservoirs. The grain sizes were observed to be coarse in the lower parts and fine in the upper parts. In addition, the logging curve amplitude was determined to be medium to high, and characterized by thick layer bell shapes, box shapes, and bell-box combined shapes. The natural gamma ray curves revealed toothed box shapes (**Figure 5A**). In the vertical direction, the area transitioned from multi-stage pebbled gray stone and sandstone to fine sandstone and siltstone, and the bottom scouring structure was considered to be common.

Side Edge of the Underwater Distributary Channels

The underwater distributary channel in front of the braided river was further subdivided and generally located at the edges or lateral edges of the distributary channels. These were found to have similar sedimentary characteristics as the subaqueous distributary channels but were characterized with finer rock granularity.

Underwater Distributary Bays

The underwater distributary bays were located in relatively low-lying areas between the underwater distributary channels and had small distribution areas within the study area. Therefore, they were considered to not have the conditions suitable for oil storage. The cores were dominated by mudstone and silty mudstone (**Figure 4B**). In terms of the logging responses, the natural gamma logging curves and resistivity logging curves displayed low amplitude tooth shapes (**Figure 5B**).

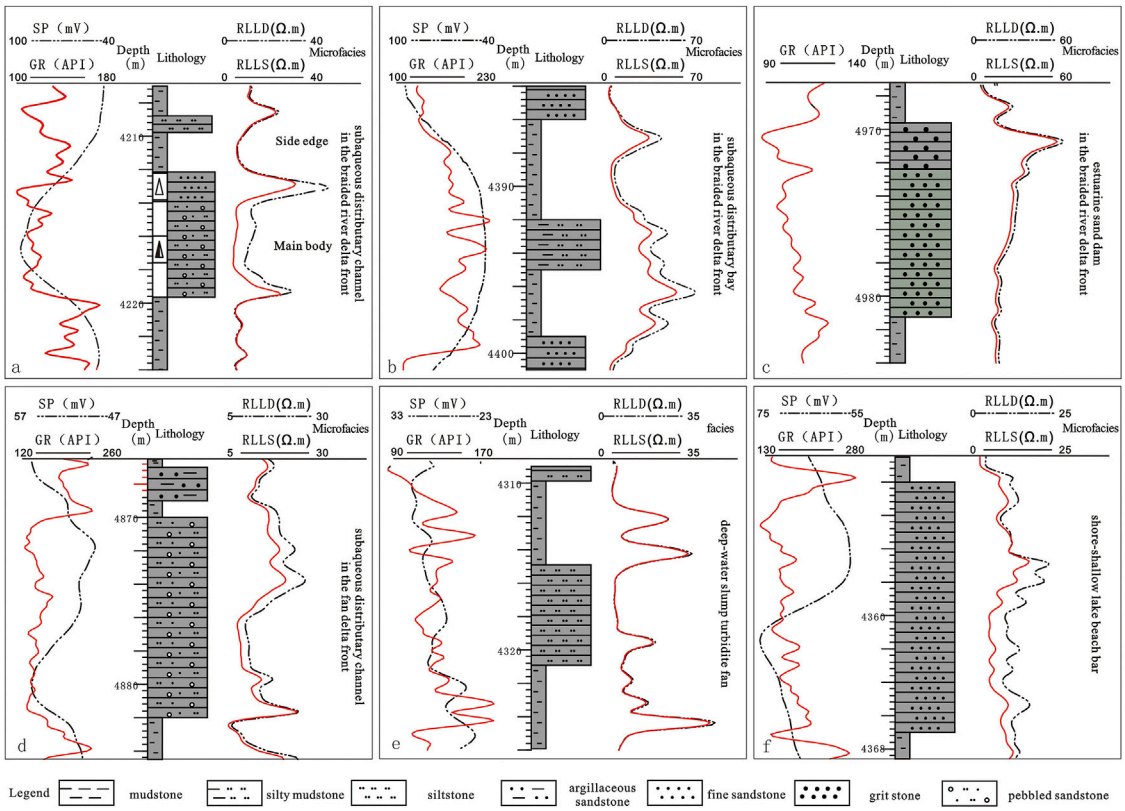

FIGURE 5 | Lithologic assemblage and logging response characteristics of the different sedimentary facies in the middle and deep layers of the Nanpu No. 3 structural area. **(A)** NP3-26, SQ4; **(B)** PG2, SQ4; **(C)** NP306 × 3, SQ4; **(D)** NP3-82, SQ2; **(E)** NP3-27, SQ5; **(F)** NP3-82, SQ4.

Estuarine Sand Dams

In the front section of the underwater distributary channels, estuarine sand dams were observed to have formed at the entrances of the estuaries emptying into the lakes. These were generally oval in shape, with long axis advances along the river direction to the lake basin. The lithology was determined to be composed of medium and fine-grained sandstone (**Figure 4C**), with high maturity in composition and structure. In addition, in the vertical direction, the lithology was characterized by inverse grain sequences, and the logging curves were funnel-shaped (**Figure 5C**). These features were only developed on a small scale in the NP306 × 3 section. However, in other well areas in the northern part of the study area, they were found to be mainly developed as massive bedding, small cross-bedding, and parallel bedding formations.

Fan Deltas

Fan deltas are fan-shaped or cone-shaped sedimentary bodies (Jiao et al., 1998; Liu et al., 2008; Zhang et al., 2015) which are formed by the rapid accumulation of alluvial fans when they enter a lake or sea. These are one of the important genetic types of reservoirs in the Shahejie Formation within the Nanpu No. 3 structural area. The fan deltas are mainly distributed in the southern section of the study area. In the southwestern and northeastern sections, the fan deltas are mainly wedge-shaped, and in the northwestern and southeastern sections, they are mainly mound-shaped. The development of fan deltas is affected by the backgrounds of the lake basins, material source supplies, and tectonic activities. Steep slope zones are considered to be more favorable to fan delta formation. In the study area, fan-delta front sub-facies were observed to be developed. These were mainly composed of coarse-grained clastic deposits characterized by coarse granularity and small distributions.

The fan delta fronts were mainly developed during the sedimentary periods of the SQ1 and SQ2, and the lithology is mainly conglomerate, glutenite, and massive mudstone deposits (**Figure 4D**). The content of conglomerate has been found to be relatively high, and the gravel composition is primarily calcareous and argillaceous, showing obvious contrast with the braided river delta fronts. The logging curves indicate a combination of toothed bell types and toothed box types (**Figure 5D**), and the seismic event axis display the characteristics of high frequency progradation or random reflection.

Deep-Water Slump Turbidite Fans

In the current study, sedimentary sand bodies of different scales and limited distributions were found to be developed in the lacustrine sedimentary area of the Nanpu No. 3 structural area. These were observed to be rich in sedimentary structure types, such as scour surfaces, oblique bedding, undulated bedding, and the directional alignment of grains. They were found in the

NP306 × 1 well, NP306 × 6 well, NP3-81 well, and so on, which reflected the dynamic characteristics of traction water. Some cored intervals (such as the PG2 well (3,632.7 m) and the NP3-27 well (4,137.75 m) displayed the phenomena of agitation deformations and trough membrane, which represented the characteristics of gravity flow deposition. In addition, from a lithological perspective, mainly mudstone intercalated with siltstone was observed, with obvious agitation deformation structures (**Figure 4E**). The logging curves were bell-shaped with low amplitude teeth (**Figure 5E**), and the seismic reflection events mainly showed wavy or random reflection characteristics.

The deep-water slump turbidite fan sand bodies in the Nanpu No. 3 structural area were determined to be distributed in each system tract of the SQ3 to SQ8 period, and were commonly found in the low-stand tract and the lake regression areas. They were considered to have been formed by the slumping effects of the fan deltas and braided river delta front sand bodies toward the center of the lake basin. These types of sand bodies are known to easily form into lithologic reservoirs. However, they can also develop into self-generating and self-preserving reservoirs with source rock.

Shore-Shallow Lakes

When compared with other sedimentary microfacies, shore-shallow lakes are characterized by finer grain sizes, darker coloration, and higher organic matter content. The rock types are mainly composed of claystone and siltstone with well-developed horizontal bedding, and belong to the categories of weak reducing or reducing environments. The lithology is generally stable horizontally, and mainly composed of dark grey mudstone with horizontal bedding, which is controlled by the structural slope break zone. There may also occasionally be mixtures of massive fine sand and siltstone of slump turbidite origin.

The beach bars of shore-shallow lakes could be seen locally in the study area, and were particularly developed in the NP3-82 well at the edge of the lake basin. The lithology was observed to be composed of pure medium-fine sandstone with gray coloration (**Figure 4F**). The composition maturity and structural maturity were found to be high, and the logging curves were smooth funnel-shaped or symmetrical (**Figure 5F**).

Sedimentary Evolution Characteristics

The sand-bodies located in the middle and deep strata of the Nanpu No. 3 structural area were found to have the characteristics of inheritability and variability during each period. Overall, the distribution characteristics of the sand bodies (from old to new) in the study area from the SQ1 sedimentary period to the SQ7 sedimentary period were as follows: The channel sand bodies were controlled by the sedimentary conditions, and were mainly distributed in strips and sheets on the plane; the estuary sand dams and shore-shallow lake beach dams were distributed in elliptical shapes, potato shapes, or irregular shapes sat the ends of the underwater distributary channels; the lateral edges of the underwater distributary channels were distributed in strips and sheet shapes along the sides of the main channel body; the slump turbidite bodies were mainly distributed irregularly at the boundaries of or outside the channel sand bodies, and the distribution ranges had differed during the different periods; the study area presented the characteristics of a sedimentary assemblage composed of fan deltas, shore-shallow lakes or braided river delta fronts, and shore-shallow lakes and turbidite, with the sand bodies displaying good connectivity.

Sedimentary Evolution Characteristics of the SQ1 and SQ2 Sequences

SQ1 and SQ2 sequences are the initial development stages of the second-order sequence of the Shahejie Formation, which correspond to the third and second section of the Shahejie Formation, respectively. The gentle slope zone in the Nanpu No. 3 structural area developed thick proximal fan delta deposits due to the intense activities of the northern Shahejie Fault in the southwest. In addition, fan delta front deposits can be seen in the western well area of the region, but the distribution is relatively limited. Those deposits are mainly composed of the main body of the underwater distributary channels, side edges of the underwater distributary channels, and the inter-distributary bays in the fan delta fronts. In the plane areas, two lobes have developed in the fan delta fronts which advance toward the lake basin. The first lobe includes the main underwater distributary channel which is distributed along the NP3-82, NP32-3646, and NP3-81 wells in a strip shape. The other lobe is the advancing direction of the fan delta front close to the eastern section of the study area. Its scale is smaller than that of the delta front in the west, and its underwater distributary channel advances toward the NP3-20 well (**Figure 6A**). During the periods of sequences SQ1 and SQ2, the lacustrine sediment in the study area were widely distributed. SQ1 and SQ2 are considered to be the two complete water transgression-regression cyclic sedimentation sequences which correspond to the Stage I and Stage II activity periods of the Paleogene rifts in the Nanpu No. 3 structural area.

SQ3 Sedimentary Evolution Characteristics

The SQ3 sequence was formed during Stage III of the rifts in the Nanpu Sag, which roughly corresponds to the lower subsection of the Shahejie Formation 1. The lake water in the Nanpu No. 3 structural area began to regress during that period, and could be divided into a transgressive system tract and a regressive system tract. The rock characteristics of the study area from the SQ3 sequence period were observed to be obviously different from those of the SQ1 and SQ2 sequence periods. For example, they were mainly composed of fine-grained sandstone and sand mudstone, with small amounts of magmatic rock observed in local areas. It has been considered that braided river deltas and lacustrine facies were probably dominant during the period. It has been determined that braided river delta front-shore shallow lake depositional systems were developed during the lake transgression tract period, evidenced by the two braided river delta fans in the eastern and western sections of the study area. The \distribution ranges of the braided river delta fronts were small (**Figure 6B**), and the water bodies experienced temporary expansions within a small range. In the vertical direction, the area was mainly composed of retrograding para-sequence formations, in which the lower single sand layers

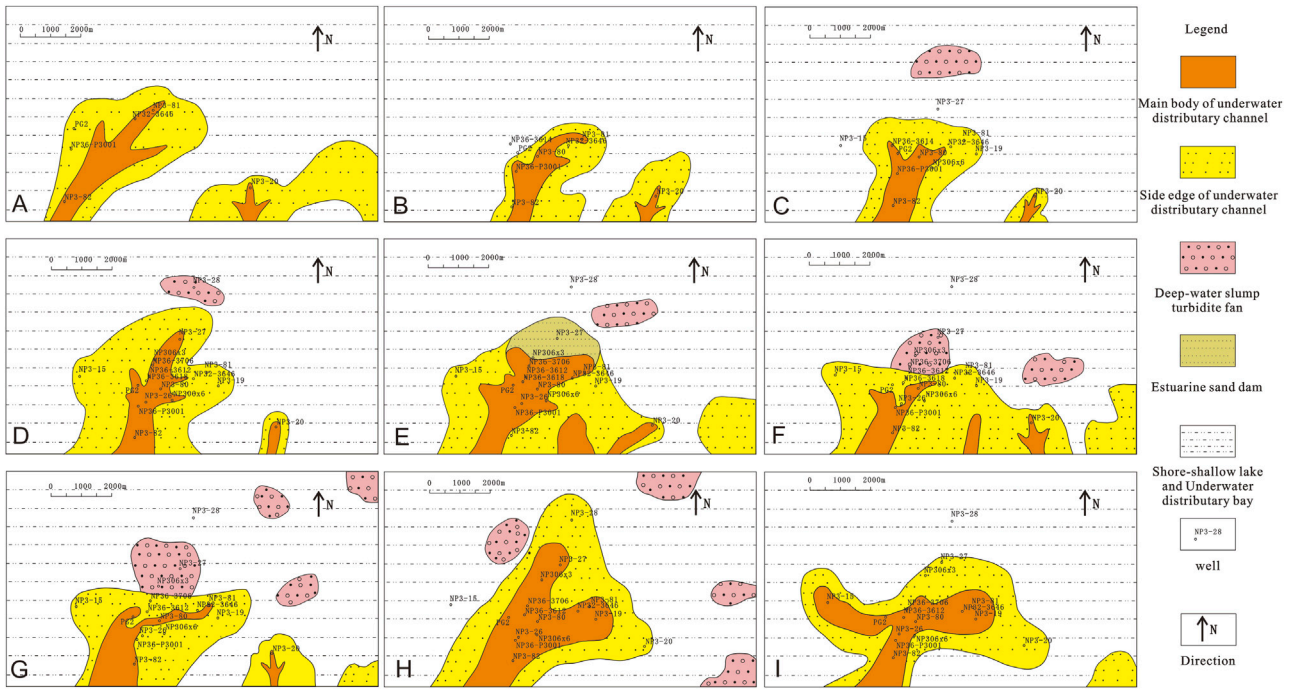

FIGURE 6 | Sedimentary microfacies of SQ1 to SQ7 system tracts in the Nanpu No. 3 structural area. **(A)** Sedimentary microfacies of SQ1 and SQ2; **(B)** Sedimentary microfacies of SQ3 transgressive system tract; **(C)** Sedimentary microfacies of SQ3 regressive system tract; **(D)** Sedimentary microfacies of SQ4 transgressive system tract; **(E)** Sedimentary microfacies of SQ4 regressive system tract; **(F)** Sedimentary microfacies of SQ5 transgressive system tract; **(G)** Sedimentary microfacies of SQ5 regressive system tract; **(H)** Sedimentary microfacies of SQ7 lowstand system tract; **(I)** Sedimentary microfacies of SQ7 highstand system tract.

were thick; upward sand bodies were relatively thin; and the amount of upper mudstone had increased, particularly in the well area. Generally speaking, the lake regression tract indicated that the braided river deltas continued to advance into the lake basin, and a depositional system of braided river delta fronts with shallow-shore lake and turbidite was dominant. In addition, when compared with the lacustrine transgression stage, the lobe bodies of the braided river deltas had gradually become larger and the underwater distributary channels became wider during the lacustrine retrogression stage. As a result, along the advancing direction of the braided river deltas, potato-shaped deep-water slump turbidite sand bodies had developed (**Figure 6C**). This study found that the majority of the wells in the study area (for example, the PG2 well, NP3-80 well, and so on) exhibited progradation para-sequence formations in the vertical direction. It could be observed that the content levels of sandstone increased upward, while the content levels of mudstone were lower with reduced thicknesses, indicating that there had been a temporary water regression in the lacustrine regressive system tract.

SQ4 Sedimentary Evolution Characteristics

The SQ4 roughly corresponded to the middle subsection of the Shahejie Formation 1, which had formed during the late period of the Stage III rifts in the Nanpu Sag. The water areas in the study area showed continuous water regression had occurred. After the SQ4 period, the study area was uplifted as a whole. Meanwhile, the entire upper subsection of the Shahejie Formation 1 was denudated. The SQ4 sequence can be divided into a lacustrine transgressive system tract and a lacustrine regressive system tract where the braided river delta fronts and deep-water slump turbidite deposits can be seen to have developed. Its plane distribution range was obviously larger than that of the SQ3 sequence system tract. During the SQ4 sequence period, the braided river deltas advanced forward to the lake basin, and the braided river delta front deposition was the most developed. However, the main channel was also very prominent. This study observed that, along the southwestern direction of the material sources, delta fronts had formed and been distributed toward the lake basin (**Figures 6D,E**). The underwater distributary channels were the main part of the deposition during that period, and estuary dam deposits had become well developed in the channel fronts. The drilling data revealed that a large set of argillaceous deposits in the underwater distributary bays were also developed in the lateral margin, and potato-shaped beach dam sand bodies were scattered in parts of para-sequence 1. The deep-water slump turbidites were found to have been mainly distributed in the northeastern section. Underwater channel deposits with large sand thicknesses were encountered during the drilling processes of well NP36-3618, well NP3-26, well NP36-3612, and well NP36-3706. In addition, estuary dam microfacies were encountered during the drilling of wells NP306 × 3 and NP3-27 in the northeastern margin, and beach dam microfacies were

encountered during the drilling of well NP3-82 near the central and southern margins. As the study area was relatively small, the lobate shapes of the braided river delta fronts were the only local shape observed.

SQ5 Sedimentary Evolution Characteristics

Following the tectonic uplifts which occurred in the late sedimentary period of the Shahejie Formation, the Nanpu No. 3 structural area was denuded as a whole and entered Stage IV of the rift activity period. During the early stage, SQ5 was formed by sedimentary filling action, which roughly corresponds to the third eastern subsection. During that period, the lake basin had strongly expanded and presented a trend of transgression, which could be divided into a lacustrine transgressive system tract and a lacustrine regressive system tract. Each system tract could then be subdivided into two para-sequence formations. The braided river delta front-shallow shore lake-deep-water slump turbidite deposits had mainly accumulated during the period of the SQ5 lacustrine transgressive system tract. During that time period, the sedimentary sand bodies in the underwater distributary channels of the braided river delta fronts were reduced, and the water channels became narrower and smaller. Those channels were mainly distributed in the area of the NP306 × 1 and NP3-80 wells. The argillaceous sediment in shallow shore lakes increased, indicating that the depths of the water bodies had increased to a certain extent. In the northern section, deep-water slump turbidite deposits of semi-deep and deep lakes were evident, with the number of turbidite sand bodies continuously increasing from the bottom to the top. In addition, from the middle section to the northeastern section, it was observed that the turbidite sand bodies were mainly potato-shaped and irregular due to the smaller range of the turbidite sand bodies in the direction of the material sources (**Figure 6F**). During the lacustrine regression system tract period of the SQ5, the sedimentary system and lacustrine transgressive system tracts displayed the characteristics of inheritance. On the whole, the braided river deltas were still in the form of retrogradation, and the deep-water slump turbidite sand bodies were smaller (**Figure 6G**). In summary, the lake basin area had strongly expanded during the early stage of the Dongying Formation, and the delta lobes regressed as a whole during the SQ5 period. Moreover, the scale of the lobes was small, and the channels had become narrower with poor continuity. A large number of slump turbidite deposits were formed in front of the deltas under the influencing effects of the tectonic activities.

Sedimentary Evolution Characteristics of SQ6 and SQ7

A lacustrine transgressive system tract and a lacustrine regressive system tract were developed during the SQ6 sequence period, and that period was a period of structural transformation. The strata in the Nanpu No. 3 structural area were seriously faulted, especially in the middle fault block area. The braided river delta front and shallow shore lake depositional systems were mainly developed during the SQ6 sequence period. However, when compared with the SQ5 sequence period, the depositional range of the braided river delta fronts was reduced, while the lake basin range was enlarged.

The low stand tract, lacustrine transgressive system tract and high stand tract were developed during the SQ7 sequence period. During that period, the tectonic activities were generally stable and the material sources were sufficient. In addition, the braided river delta areas also had larger scales overall. The underwater distributary channels were significantly larger in scale than during the SQ5 and SQ6 sequence periods and had migrated to the northeast. The lake areas had also regressed to the northeast, and the scope was smaller than during the SQ5 and SQ6 sequence periods, as illustrated in **Figures 6H,I**.

Sedimentary Filling Mode

The sequence stratigraphic characteristics, system tract composition and sedimentary system were analyzed in detail, and the control factors of the Nanpu No. 3 structural sequence development were taken as the starting points in the present study. Then, based on the comprehensive study of the types and characteristics of the sequence boundaries; division of the sequence boundaries at all levels; determination of the sequence division scheme; and the establishment of the isochronal sequence stratigraphic framework suitable for the study area, such factors as the tectonic activities, lake basin form, and so on were highlighted. Subsequently, in accordance with the interpretations of the typical seismic sections and some three-dimensional seismic sections in the Nanpu No. 3 structural area, this study's sequence stratigraphic models of the area could be summarized as the following two types: (1) A sequence sedimentary filling model without a slope break zone; and (2) A sequence sedimentary filling model with a slope break zone (Ren et al., 2004; Xu et al., 2006; Li et al., 2010; Lv et al., 2019; Lv et al., 2020).

Sequence Sedimentary Filling Model Without a Slope Break Zone

The SQ1 to SQ6 developmental periods in the Nanpu No. 3 structural area were characterized by asymmetric faulted lacustrine basin deposits. Therefore, it was considered that that type of sequence filling model was the most important sedimentary filling model in the study area. The model lacked a slope break zone in its structural design style. It was divided into a lacustrine transgression system tract and a lacustrine regressive system tract due to the difficulty in determining the initial flood surfaces in the system tract composition. During the development of that particular sequence model, the subsidence and sedimentary centers of the lake basin were located in the northeastern section of the study area, and multiple faults were developed in the gentle slope areas, which were considered to be basically normal faults. The most important fault was the No. 3 fault (Zhang and Liu, 2012; Zhou et al., 2016). In the gentle slope zone of the Nanpu No. 3 structural area, the material sources originated from the Shalietian Salient in the southwestern direction. On the seismic profile, each sequence showed wedge-shaped bodies overlapping to the shore, with small overall thicknesses but long extension distances. The sedimentary system was mainly composed of alluvial fans, braided river deltas, shallow-shore

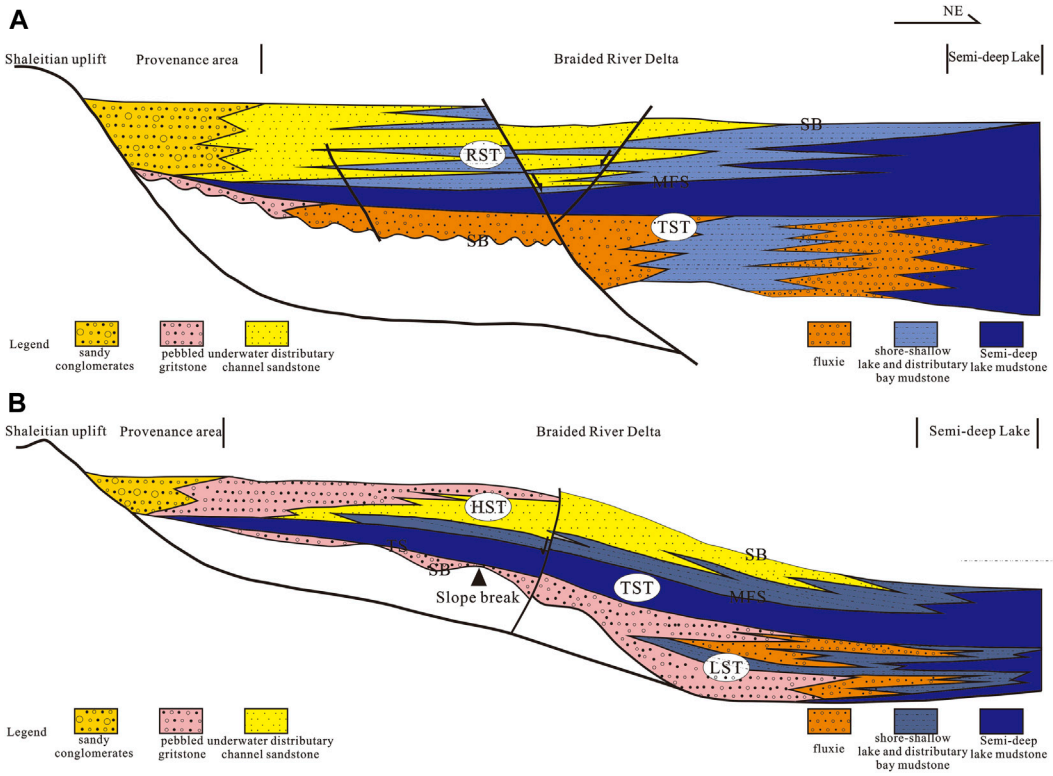

FIGURE 7 | Sedimentary filling model of the middle and deep strata in the Nanpu No. 3 structural area. **(A)** Sequence sedimentary filling model without slope break zone (SW to NE); **(B)** Sequence sedimentary filling model with slope break zone (SW to NE).

lakes, and semi-deep lakes. Some of the sequences (for example, SQ1 and SQ2) had developed fan deltas instead of braided river deltas.

In the present research investigation, the SQ4 sequence period was taken as the object in order to establish the sequence of the gentle slope zones without slope break zones. Its system tract development model is detailed in **Figure 7A**. This model sequence was internally divided into a lacustrine transgressive system tract and a lacustrine regressive system tract, and the sedimentary characteristics of each system tract were significantly different. For example, at the bottom of the lacustrine transgressive system tract (TST), small braided-river delta front sand bodies were developed. At the lower part, there were mudstone deposits of shallow shore lakes. In addition, slump turbidite deposits with mixed particles in a limited distribution range appeared and a transition to semi-deep lacustrine facies occurred. After that, the lake level began to rise, and the scope of the lake basin expanded, resulting in the beginning of a large-scaled lake transgression. At that time, the growth rate of the accommodation spaces was greater than the sediment supply rate. In the Nanpu No. 3 structural area, the large-scale deposition of the lacustrine facies had been dominated by dark mudstone. Then, after the lake basin reached its maximum range, the lake level began to decline, which indicated that the area had entered into a lacustrine regressive system tract (RST) period. During the early stages of the lacustrine regressive system tract, the main body was stable. The supply of deposits was small during that period and shallow-shore lake deposits had developed. Subsequently, the accommodation spaces became decreased. However, with the increases of the sediment supplies, a series of large-scaled braided river deltas were gradually formed, which advanced toward the lacustrine basin displaying a series of progradation characteristics.

Sequence Sedimentary Filling Model With a Slope Break Zone

This type of sequence filling pattern mainly appeared during the SQ7 sequence period when a tectonic slope break zone had appeared due to tectonic actions. The occurrence of this structural slope break zone had a controlling effect on the formations of the low water level system tract and the sequence boundaries. For example, when the lake level had not exceeded the slope break zone, the area above the slope break zone entered a state of weathering and denudation, and unconformity surfaces and cut valleys had easily formed. The area under the slope break zone normally received sedimentation, and usually formed basin fans and slope fans dominated by coarse clasts. Those types of formations generally correspond to the sedimentary characteristics of low water level system tracts. Under such conditions, the identification of the initial lake flood surfaces can be determined using the interfaces corresponding to the overlapping points under the in-phase axis caused by rising lake levels, as well as the overland migration of the lake shore, which tends to connect the

relatively independent water bodies together. Therefore, the low stand system tract, transgressive system tract and high stand system tract can be identified within the sequence. This sequence filling model was limited to the SQ7 sequence period in the current study. The sedimentation during that period was mainly composed of alluvial fan, braided river delta, shallow-shore lake, and semi-deep lake sedimentary systems.

The SQ7 sequence period was selected as the object in order to establish a development model of the sequence system tract of gentle slope zones with a slope break zone (**Figure 7B**). During the development stage of the lake basin, the boundary of the abrupt changes from shallow water facies to deep water was represented by a slope break zone. During the period of the low water level system tract, the fan body-turbidite fans of the alluvial system dominated by coarse clastic had developed in the slope break zone, and both disorganized reflection and mound reflection were dominant in the seismic profile. The characteristics of the denudation zone appeared above the slope break zone, and the main features below the slope break zone were cut valleys and denudation surfaces. Furthermore, during the lacustrine transgression system tract period, a large set of dark pure mudstone was deposited under the action of rapid transgression, which was a lacustrine deposit. During the period of the high-water system tract, large-scaled braided river delta deposits had developed, and the slope break zone had major influencing effects on the distributions of the braided river delta front zones and depositional centers.

This study found that from the SQ1 sequence period to the SQ7 sequence period, the Nanpu No. 3 structure had undergone long-term uplifts and denudation since the Cambrian Period. The study area received proximal sediment deposits from the Shaleitian Salient in the southwestern direction during the 3rd and 2nd stages of the Shahejie Formation, forming the SQ1 and SQ2 sequences. These were mainly fan deltaic and lacustrine sedimentary systems, which were characterized with large thicknesses and secondary stratification sequences of a lacustrine regressive system tract and a transgressive system tract. Subsequently, local tectonic uplifts occurred in the Nanpu No. 3 structural area. In the first section of Shahejie Formation, the grain sizes of the sediment from the Shaleitian Salient became finer, and the sorting and grinding became better. Then, according to the large-scaled water transgression and regression periods, the SQ3 and SQ4 sequences were formed. These sequences mainly included braided river delta-lacustrine facies with small thicknesses, as well as a secondary stratification sequence of a lacustrine regressive system tract and a transgressive system tract. Following the formation of the Shahejie Formation, the study area suffered strong tectonic activities and large-scaled denudation. During the eastern third section period, the study area showed retrogradation overall and the scope of the lake basin expanded. Then, according to the transgression and regression periods, as well as the distributions of the sediment, the SQ5 and SQ6 sequences were formed, which mainly included braided river delta-lacustrine facies with medium thicknesses, and secondary stratification sequences of a lacustrine regressive system tract and a transgressive system tract. In the second section of the Dongying Formation, a structural slope break zone was formed in the area of the NP3-27 well due to local uplifts in the structure. Then, after the sediment from the southwest had crossed the slope break zone, the SQ7 deposits were formed. These consisted of a low stand system tract dominated by fan bodies and turbidite; a lacustrine transgressive system tract dominated by shallow-shore lakes and fairly deep lakes; and a high-stand system tract dominated by braided river delta fronts.

CONCLUSION

1) The material sources of the Nanpu No. 3 structural area were determined to have originated from the southwest Shaleitian Salient. In the middle and deep strata, fan delta deposits, braided river delta deposits, shallow-shore lake deposits, and deep-water slump turbidite fan deposits were mainly developed. In the SQ1 and SQ2 sequences, a fan delta and shallow-shore lake depositional system was mainly developed. Then, from the SQ3 sequence to SQ7 sequence, a braided river delta-shallow-shore lake/turbidite depositional system with multi-stage superimposition was developed. The distribution range was obviously controlled by the tectonic setting of the gentle slope zones within the lake basin. There was also a set of braided river delta deposits formed by the braided river system directly entering the lake basin in the shallow-shore lake areas.
2) Two types of sequence filling models were established in this study by taking the Nanpu No. 3 structural area as the prototype. These included a sequence filling model without a slope break zone and a sequence filling model with a slope break zone. The sequence depositional model without a slope break zone was the main sequence filling model for the study area. It included the development of a lacustrine transgressive system tract and a lacustrine regressive system tract. The sequence depositional model with a slope break zone appeared only in the SQ7 sequence, with the development of a low-stand system tract, lacustrine transgressive system tract, and a high-stand system tract. During the Paleogene Period, three tectonic uplifting activities occurred in the Nanpu No. 3 structural area, and three large-scaled water transgression and regression periods occurred. The area had continuously received sediment from the southwestern direction, forming the present day SQ1 to SQ7 sedimentary patterns.

DATA AVAILABILITY STATEMENT

The original contributions presented in the study are included in the article/supplementary material, further inquiries can be directed to the corresponding author.

AUTHOR CONTRIBUTIONS

HZ, ZL was mainly responsible for the conception of the article. They put forward a good idea and completed the research content related to sedimentary facies and evolution characteristics in the article. XL, XH wrote sections of the

manuscript. All authors contributed to manuscript revision, read, and approved the submitted version.

ACKNOWLEDGMENTS

We greatly thank China University of Petroleum (East China) and Exploration and Development Research Institute of PetroChina Jidong Oilfield Branch for providing all the related core samples, geological data and permission to publish these data. This study supported by the state key scientific project "The central government guided local science and technology development special project (Shandong Unconventional Hydrocarbon Resources technology innovation platform)". We thank our scientific research team for their help and guidance in the field investigation.

REFERENCES

Dong, Y. X., Yang, S., Chen, L., Wang, Q., and Cao, Z. H. (2014). Braided River Delta Deposition and Deep Reservoirs in the Bohai Bay Basin: A Case Study of the Paleogene Sha 1 Member in the Southern Area of Nanpu Sag. *Pet. Exploration Dev.* 41 (4), 429–436 [in Chinese with English Abstract]. doi:10.1016/s1876-3804(14)60049-5

Fan, B. J., Liu, C. L., Liu, G. D., and Zhu, J. (2010). Forming Mechanism of the Fault System and Structural Evolution History of Nanpu Sag. *J. Xi'an Shi you University (Natural Sci. Edition)* 25 (2), 13–17 [in Chinese with English Abstract]. doi:10.3969/j.issn.1673-064X.2010.02.003

Feng, Y. L., Zhou, H. M., Ren, J. Y., Zheng, H. R., and Miao, S. D. (2010). Paleogene Sequence Stratigraphy in the East of the Bohai Bay Basin and its Response to Structural Movement. *Sci. Sin Terrae* 40 (10), 1356–1376 [in Chinese with English Abstract]. doi:10.3724/SP.J.1011.2010.01081

Huang, M. N., Dong, Y. X., Pang, X. Q., Hao, H. J., and Guo, J. G. (2012). Controlling Factors of Structural Reservoir Distribution and its Prediction Method in Nanpu depressionBohai Bay Basin. *Oil Gas Geol.* 33 (05), 695–704 [in Chinese with English Abstract]. doi:10.11743/ogg20120505

Jiang, F. J., Dong, Y. X., Pang, X. Q., Wang, Y. X., Guo, J. G., and Fan, B. J. (2013). Hydrocarbon Distribution Features and Main Controlling Factors in the Nanpu Sag. *Geoscience* 27 (05), 1258–1264 [in Chinese with English Abstract]. doi:10.3969/j.issn.1000-8527.2013.05.031

Jiang, F. J., Pang, X. Q., Li, L., Wang, Q. C., Dong, Y. X., et al. (2018). Petroleum Resources in the Nanpu Sag, Bohai Bay Basin, Eastern China. *AAPG Bulletin* 102 (7), 1213–1237. doi:10.1306/0906171608017148

Jiang, H., Wang, H., Lin, Z. L., Fang, X. X., Zhao, S. E., and Ren, G. Y. (2009). Periodic Rifting Activity and its Controlling on Sedimentary Filling of Paleogene Periodin Nanpu Sag. *Acta sedimentologica Sinica* 27 (05), 976–982 [in Chinese with English Abstract]. doi:10.14027/j.cnki.cjxb.2009.05.022

Jiao, Y. Q., Zhou, H. M., Zhuang, X. G., Liu, S. F., Yang, S. K., and Ma, M. Y. (1998). Fan Deltaic Depositional Systems and Their Relationship to Oil and Gas Accumulation. *Acta sedimentologica Sinica* 16 (01), 70–75 [in Chinese with English Abstract]. doi:10.14027/j.cnki.cjxb.1998.01.012

Li, H., Zhang, H. Y., Xu, Y. X., Wang, Y. L., Zhao, Q., and Wang, K. (2018). Sedimentary Characteristics and Genetic of the Lower Ed3 Formation Fluxoturbidite in the East of Nanpu Structure 5. *Oil Geophys. Prospecting* 53 (S2), 321–328 [in Chinese with English Abstract]. doi:10.13810/j.cnki.issn.1000-7210.2018.s2.050

Li, S. T., Wang, D. Y., Wang, B., Tao, H. F., and Liu, Z. W. (2008). Identification of Sedimentary Slope Breaks in the Margin of a Down Warped Lake Basin's Ramp Belt: A Case from Triassic Yanchang Formation'Ordos Basin. *Nat. Gas Geosci.* 19 (1), 83–88 [in Chinese with English Abstract].

Li, S. Z., Suo, Y. H., Zhou, L. H., Dai, L. M., Zhou, J. T., Zhao, F. M., et al. (2011). Pull-Apart Basins within the North China Craton: Structural Pattern and Evolution of Huanghua Depression in Bohai Bay Basin. *J. Jilin U University(Earth Sci. Edition)* 41 (05), 1362–1379 [in Chinese with English Abstract]. doi:10.13278/j.cnki.jjuese.2011.05.041

Li, X. B., Liu, H. Q., Chen, Q. L., Wan, Y. R., Wei, L. H., Feng, M., et al. (2010). Characteristics of Slope Break Belt in Large Depression Lacustrine Basin and its Controlling Effect on Sandbody and Petroleum. *Acta sedimentologica Sinica* 28 (04), 717–729 [in Chinese with English Abstract]. doi:10.14027/j.cnki.cjxb.2010.04.016

Lin, C. S., Pan, Y. L., Xiao, J. X., Kong, F. X., and Liu, J. Y. (2000). Structural Slope-Break Zone: Key Concept for Stratigraphic Sequence Analysis and Petroleum Forecasting in Fault Subsidence Basins. *Earth Sci.* 25 (30), 260–265 [in Chinese with English Abstract]. doi:10.3969/j.issn.1671-5888.2011.05.010

Liu, L., Zhong, Y. J., Chen, D. H., and Wang, J. (2015). Contrastive Research of Fan Deltas and Braided River Deltas in Half-Graben Rift Lake Basin in East China. *Acta sedimentologica Sinica* 33 (06), 1170–1181 [in Chinese with English Abstract]. doi:10.14027/j.cnki.cjxb.2015.06.010

Liu, X., Liu, Z., Lu, C. J., Ren, M. Y., Li, L., Wang, S. L., et al. (2017). Evolution of Sedimentary Source and Controlling Factors of sandstone Body Distribution in the Middle-Upper Part of the Third Member of Shahejie Formation in Liuzan area, Nanpu Depression. *Acta Petrolei Sinica* 38 (8), 888–901 [in Chinese with English Abstract]. doi:10.7623/syxb201708004

Liu, Y. L., Qiu, C. G., Deng, H. W., and Li, M. (2008). Control of the Structure of the Paleogene Dongying Formation upon Fan-Deltadeposition in the Nanpu Depression Jidong Oilfield. *Oil & Gasgeology* 29 (01), 95–101 [in Chinese with English Abstract]. doi:10.11743/ogg20080115

Lv, D. W., Song, Y., Shi, L. Q., Wang, Z. L., Cong, P. Z., and T van Loon, A. J. (2020). The Complex Transgression and Regression History of the Northern Margin of the Palaeogene Tarim Sea (NW China), and Implications for Potential Hydrocarbon Occurrences. *Mar. Pet. Geology.* 112. doi:10.1016/j.marpetgeo.2019.104041

Lv, D., Li, Z. X., Wang, D. D., Li, Y., Liu, H. Y., Liu, Y., et al. (2019). Sedimentary Model of Coal and Shale in the Paleogene Lijiaya Formation of the Huangxian Basin: Insight from Petrological and Geochemical Characteristics of Coal and Shale. *Energy Fuels* 33 (11), 10442–10456. doi:10.1021/acs.energyfuels.9b01299

Qi, P., Ren, J. Y., Lu, G. C., Shi, S. S., Tong, D. J., and Zhang, J. X. (2010). Cenozoic Episodic Subsidence in the Middle and North Part of Huanghua Depression , Bohai Bay Basin. *Earth Sci. — J. China Univ. o f Geosciences* 35 (6), 1041–1052 [in Chinese with English Abstract]. doi:10.3799/dqkx.2010.118

Ren, J. Y., Liao, Q. J., Lu, G. C., Fu, L. X., Zhou, J. Y., Qi, P., et al. (2010). Deformation Framework and Evolution of the Huanghua Depression, Bohai Gulf. *Geotecton. Metallog.* 34 (4), 461–472. doi:10.16539/j.ddgzyckx.2010.04.006

Ren, J. Y., Lu, Y. C., and Zhang, Q. L. (2004). Forming Mechanism of Structural Slope-Break and its Control on Sequence Style in Faulted Basin. *Earth Sci. — J. China Univ. Geosciences* 29 (5), 596–602 [in Chinese with English Abstract]. doi:10.3799/dqkx.2010.118

Sun, P. K., Jia, L. B., Zhu, H. Z., Zhang, L., He, T. H., Xu, Z. H., et al. (2021). Sequence Architecture and Sedimentary Filling Characteristics of the Middle-Upper Part of the Es3 Formation in the Liuzan Area, Nanpu Depression. *Pet. Sci. Bull.* 01, 16–30 [in Chinese with English Abstract]. doi:10.3969/j.issn.2096-1693.2021.01.002

Wang, E. Z., Liu, G. Y., Pang, X. Q., Wu, Z. Y., Li, C. R., Bai, H., et al. (2020). Sedimentology, Diagenetic Evolution, and Sweet Spot Prediction of Tight sandstone Reservoirs: A Case Study of the Third Member of the Upper Paleogene Shahejie Formation, Nanpu Sag, Bohai Bay Basin, China. *J. Pet. Sci. Eng.* 186, 1–10. doi:10.1016/j.petrol.2019.106718

Wang, J. W., Du, J. X., Zhang, Y. C., Wang, Q. L., and Zhao, S. E. (2019). The Geological Conditions, Resource Potential and Exploration Direction in Nanpu Sag of Jidong Depression. *Bohai Bay Basin* 24 (3), 21–28 [in Chinese with English Abstract]. doi:10.3969/j.issn.1672-9854.2019.03.003

Wang, Y. M., Liu, H., Li, L. C., Qi, X. F., and Wang, Y. (2002). Types and Distribution Characteristics of Slope Breaks of Large-type Down-Warped Lake Basins. *Earth Sci.* 27 (6), 683–687 [in Chinese with English Abstract]. doi:10.1007/s11769-002-0045-5

Wu, H., Ji, Y. L., Zhou, Y., Meng, L. J., Zhang, Y. Z., Wu, H., et al. (2019). Origin of the Paleogene Deep Burial High-Quality Reservoirs in the Southern Nanpu Sag.

J. China Univ. Mining Technolog 48 (3), 553–569 [in Chinese with English Abstract]. doi:10.13247/j.cnki.jcumt.000952

Xian, B. Z., Wan, J. F., Jiang, Z. X., Zhang, J. G., Li, Z. P., and She, Y. Q. (2012). Sedimentary Characteristics and Model of Gravity Flow Deposition in the Depressed belt of Rift Lacustrine basin: A Case Study from Dongying Formation in Nanpu Depression. *Earth Sci. Front.* 19 (1), 121–135 [in Chinese with English Abstract].

Xu, A. N., Zheng, H. J., Dong, Y. X., Wang, Z. C., Yin, J. F., and Yan, W. P. (2006). Sequence Stratigraphic Framework and Sedimentary Facies Preiction in Dongying Formation of Nanpu Sag. *Pet. Exploration Dev.* 33 (4), 437–443 [in Chinese with English Abstract].

Xu, C. G. (2006). Genetic Types of Paleogene Slope-Break Zones and Their Controls on Depositional System in Bohai Offshore. *China Offshore Oil and Gas* 18 (06), 365–371 [in Chinese with English Abstract]. doi:10.3969/j.issn.1673-1506.2006.06.002

Zhang, C. M., and Liu, X. F. (2012). The Boundary Faults and basin Formation Mechanism of Nanpu Sag. *Acta Petrolel Sinica* 33 (4), 581–587 [in Chinese with English Abstract]. doi:10.7623/syxb201204006

Zhang, C. M., Zhu, R., Yin, T. J., and Yin, Y. S. (2015). Advances in Fan Deltaic Sedimentology, *Xinjiang Pet. Geology*. 36(03), 362–368 [in Chinese with English Abstract]. doi:10.7657/XJPG20150323

Zhou, Y. H., Yang, S. C., Feng, J. W., Lan, Z. Q., and Zhang, B. M. (2016). Characteristics of fault activities and the controlling on sand bodies during Es1 period in Nanpu No.3 unit. Journal of Northeast Petroleum University. 40 (02), 27–35 (in Chinese with English Abstract). doi:10.3969/j.issn.2095-4107.2016.02.004

Zhou, H. M., Wang, Z. C., and Guo, Y. H. (2000). Tectonic Controls on Sequence Stratigraphy in Tertiary Period in Nanbao Depression. *J. China Univ. Mining Tech nology* 29 (03), 104–108 [in Chinese with English Abstract]. doi:10.3321/j.issn:1000-1964.2000.03.025

Conflict of Interest: The authors declare that the research was conducted in the absence of any commercial or financial relationships that could be construed as a potential conflict of interest.

frontiers in Earth Science

ORIGINAL RESEARCH
published: 19 August 2021
doi: 10.3389/feart.2021.733397

The Fluid Evolution of Ancient Carbonate Reservoirs in Sichuan Basin and Its Implication for Shale Gas Exploration

Zhenzhu Zhou[1,2]*, *Xiaolan Chen*[1]* and *Haiyang Xia*[1]

[1]Shandong Key Laboratory of Depositional Mineralization and Sedimentary Mineral, Shandong University of Science and Technology, Qingdao, China, [2]Department of Earth and Atmospheric Sciences, University of Alberta, Edmonton, AB, Canada

Sichuan Basin is the only successful basin for shale gas exploration in China. In addition to the main shale in the Lower Silurian Longmaxi formation, the lower Cambrian Qiongzhusi shale is an important potential formation. However, it was once considered that shale gas is difficult to enrich because of its poor sealing conditions and hydrocarbon migration to adjacent reservoirs. With the increasing research on hydrocarbon generation and reservoir in shale of Qiongzhusi Formation in recent years, it has become an important exploration target in Sichuan Basin. The enrichment of oil and gas is closely related to fluid activities. Limited by the degree of exploration, there is little analysis of fluid activities in Qiongzhusi Formation, and there is little analysis of shale gas enrichment potential from the perspective of fluid. The hydrocarbon generated from Qiongzhusi shale in the rift could migrate laterally to the uplift area and form a reservoir in Dengying Formation. The fluid activities from source rock to reservoir are basically the same. Therefore, this paper reconstructed the history of hydrocarbon activities in Dengying reservoirs based on fluid inclusion analysis. Then the fluid activity process in Qiongzhusi shale was studied, and its enrichment conditions of shale gas was discussed. The results show that the hydrocarbon activities of Dengying Formation can be divided into three stages: 1) oil charging stage, 2) oil cracking gas generation stage and 3) gas reservoir adjustment stage. The first stage is under normal pressure, and the second and third stages developed overpressure with pressure coefficients of 1.3 and 1.2, respectively. High pressure coefficient is an important indicator of shale gas enrichment. Because the source rock of Qiongzhusi Formation has always been the main source rock of Dengying Formation, it can supply hydrocarbon to Dengying Formation only with overpressure in gas generation stage. Therefore, overpressure in the last two stages of gas generation indeed existed. As long as the sealing condition of shale itself is not particularly poor, shale gas “sweet points” would be formed. Therefore, the thick shale in Deyang-Anyue rift is the focus of shale gas exploration in Qiongzhusi Formation.

Keywords: fluid inclusion, fluid activity, shale gas, Sichuan Basin, Qiongzhusi Formation

OPEN ACCESS

Edited by:
Jon Jincai Zhang,
Sinopec Tech Houston Center (STHC), United States

Reviewed by:
Yongqiang Yang,
China University of Petroleum, China
Cui Mao,
Northeast Petroleum University, China

***Correspondence:**
Zhenzhu Zhou
zhouzhenzhu1983@163.com
Xiaolan Chen
157573053@qq.com

Specialty section:
This article was submitted to Sedimentology, Stratigraphy and Diagenesis, a section of the journal Frontiers in Earth Science

Received: *01 July 2021*
Accepted: *09 August 2021*
Published: *19 August 2021*

Citation:
Zhou Z, Chen X and Xia H (2021) The Fluid Evolution of Ancient Carbonate Reservoirs in Sichuan Basin and Its Implication for Shale Gas Exploration. Front. Earth Sci. 9:733397. doi: 10.3389/feart.2021.733397

INTRODUCTION

Shale gas is a kind of unconventional natural gas and has been successfully developed commercially abroad. It has become an important new energy (Han, et al., 2016). However, China started late and made a breakthrough in Sichuan Basin until 2010, when shale gas was drilled in Wufeng Formation of Upper Ordovician and Longmaxi formation of Lower Silurian (Huang et al., 2012; Jin et al., 2016). After more than a decade of exploration, China has made important progress in Yongchuan, Fuling, Weiyuan, Changning and other places, developing the shale gas fields (Zou et al., 2020). Sichuan Basin has become the second largest shale gas production area after the United States (Yang et al., 2021). So far, China has started to exploit the shale gas in marine strata with the depth shallower than 3500 m in the southern Sichuan Basin (Yang et al., 2021). In addition, some petroleum companies has begun to focus on the deeper layers of the basin, including the deeper buried Wufeng and Longmaxi shale, the third member of the Sinian Dengying Formation and the lower Cambrian Qiongzhusi shale. In particular, the Qiongzhusi shale is adequately thick, mature and has great potential for shale gas (Huang et al., 2012; Potter, 2018). Although only a few wells were designed to explore the Qiongzhusi shale at present, it was really successful because some of them successfully produced natural gas after fracturing. However, because of low degree of exploration, the research on Qiongzhusi shale gas is not enough. Previous studies mainly focused on the source rock qualities (Huang et al., 2012; Zheng et al., 2014; Wei et al., 2015; Yang et al., 2020), and some of them preliminarily analyzed the reservoir characteristics (Gao et al., 2020; Wang et al., 2016). The history of hydrocarbon evolution is still not clear, which restricts the further exploration.

The Sinian Dengying Formation is dominated by dolomite in Sichuan Basin. There is an unconformity between it and the overlying Qiongzhusi Formation. This unconformity provided a good pathway for oil migration from Qiongzhusi shale to the top of Dengying Formation (Zhou et al., 2016). In the Anyue gas field discovered in Gaoshiti-Moxi area, the Sinian Dengying Formation and Lower Cambrian formed the petroleum system, and the natural gas in the Dengying Formation was mainly generated from the Qiongzhusi Formation (Han et al., 2013; Zheng et al., 2014; Wei et al., 2015). Consequently, if lacking of data and being unable to directly study Qiongzhusi shale, the hydrocarbon evolution of Qiongzhusi shale could be interpreted by analyzing the hydrocarbon activities of the Dengying reservoirs. Therefore, using the fluid inclusions bearing in Dengying reservoirs, this paper studied the history of fluid activities, and then analyzed the hydrocarbon evolution of Qiongzhusi shale. The results can provide reference for further shale gas exploration of Qiongzhusi shale in Sichuan Basin and surrounding areas.

GEOLOGICAL SETTING

Sichuan Basin is located in Southwest China. It is the most important natural gas producing area and the only shale gas producing area in China. Gaoshiti-Moxi area, where the Aanyue gas field was discovered, is located in the middle of Sichuan Basin. It is the core of a successively developing uplift (**Figure 1A**). The Dengying Formation included four members numbered 1–4 respectively from bottom to top. The second and fourth members were relatively rich in cyanobacteria and formed algal mounds and granular beaches on carbonate platform (Li et al., 2013; Zhou et al., 2014). They were also the main reservoirs of Dengying Formation. At the end of Sinian, the basement of Sichuan Basin was uplifted due to Tongwan movement, and the top of Dengying Formation was extensively eroded. Two regional unconformities were formed at the top of the second member (Deng 2) and the fourth member (Deng 4) respectively. Meanwhile, two paleogeomorphic highlands, Gaoshiti-Moxi and Weiyuan-Ziyang, were formed in the same process (Du et al., 2014). Between the Highlands was Deyang-Anyue rift. The Cambrian system deposited over the erosion surface (Zou et al., 2010). The stratigraphic column of the paleouplift area is shown in **Figure 1B**. The Sinian Dengying formation (member 2 and 4) and the lower Cambrian Longwangmiao Formation are the main reservoirs, while the lower Cambrian Qiongzhusi Formation is the main source rock. The thickness of Qiongzhusi Formation is generally 120–150 m, while it is up to 350 m in the rift (Zou et al., 2020). The lower part of the Qiongzhusi Formation is dark gray carbonaceous shale and silty shale, and the color gradually becomes lighter upward. Some gray calcareous fine sandstone or siltstone are stuck in the middle, and the top part is yellow green shale. Its petrologic characteristics show that the Qiongzhusi Formation was formed in shallow or deep sea shelf (Yang et al., 2020). Previous studies suggested that the rift was the sedimentary center of high-quality source rocks in the lower Cambrian (Han et al., 2013; Wei et al., 2015; Zheng et al., 2014), the generated hydrocarbon could migrate laterally to the reservoirs on both sides of the rift (**Figure 1C**). Now, the Weiyuan and Anyue gas fields have been found on both sides of the rift, and shale gas is also under exploration (Zou et al., 2014, 2020; Wei et al., 2017; Chen, et al., 2021).

Qiongzhusi Formation is one of the main source rocks in Sichuan Basin. In the uplift area, its TOC ranges from 0.5 to 8.49%, with an average of 1.95% (Wei et al., 2015, 2017). Within the rift, the TOC ranges from 0.5 to 25.7% (Zhu et al., 2006; Zou et al., 2010; Huang et al., 2012), organic rich carbonaceous shales were mainly developed in the lower part of the Qiongzhusi Formation, with TOC generally greater than 2%, and TOC decreases upward. The carbon isotopic of kerogen is generally light, ranging from −36.0‰ to −31.0‰, with an average of 33.3‰ (Wei et al., 2017). The black shale of Qiongzhusi Formation is mainly composed of sapropel macerals (more than 95%) and a small amount of humic macerals, which has great hydrocarbon generation potential. In addition, the mature degree of Qiongzhusi shale is very high. In the uplift area, the equivalent vitrinite reflectance is 1.84–2.42% (Wei et al., 2017), reaching the high or/and over mature stage. In the rift area, the equivalent vitrinite reflectance is generally greater than 2.5%, with an average of 3.5%, which is in the over mature stage (Zou et al., 2006; Wang et al., 2010; Huang et al., 2012). The pore structure and type of shale in Qiongzhusi Formation are similar to those in the

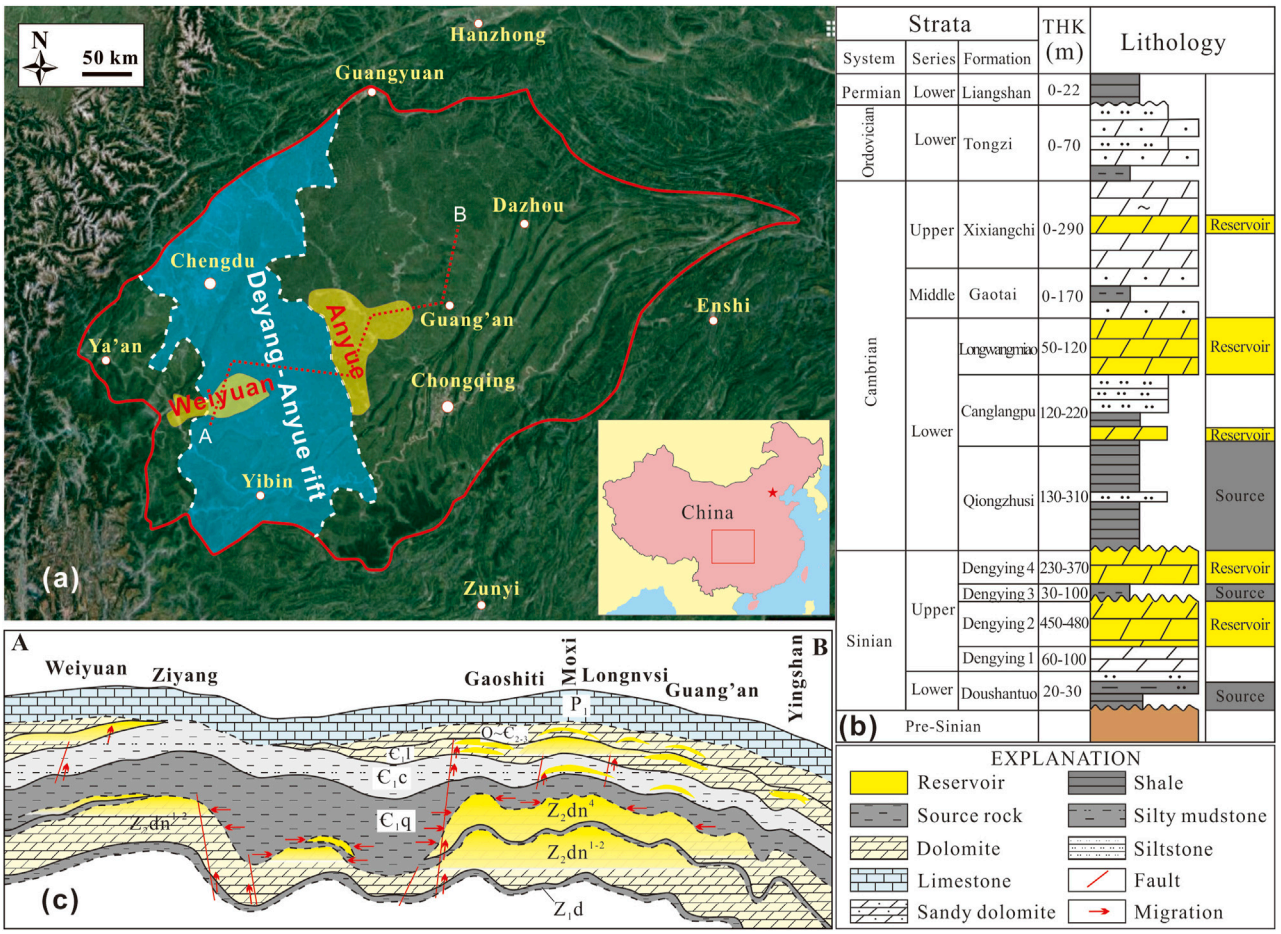

FIGURE 1 | Geographical location **(A)**, stratigraphic column **(B)** and a representative profile of the paleouplift **(C)** in Sichuan Basin.

Longmaxi Formation, the main shale gas procucing formation in Sichuan Basin (Wang et al., 2013). According to the analysis of drilling samples, the porosity of Qiongzhusi shale is 0.82–4.86%, with an average of 2.44%, and the permeability is 0.006 × 10^{-3}~0.158 × 10^{-3} μm^2, with an average of 0.046 × 10^{-3}μm^2 (Huang et al., 2012). This indicates that the Qiongzhusi shale in the study area can be good reservoir for shale gas. Therefore, the hydrocarbon generation capacity of the Qiongzhusi shale was very strong, and part of the hydrocarbon was kept in the shale, and the other migrated from the source rock to the lateral Sinian Dengying reservoirs. The hydrocarbon activities related the source rock and reservoirs, which provides a theoretical basis for studying the hydrocarbon evolution of the Qiongzhusi Formation by analyzing the fluid activities of the Dengying reservoirs.

SAMPLES AND METHODS

Fluid inclusions directly record the paleofluid, and is the main method to study paleofluid activities (Wang et al., 2020). In this paper, fluid inclusion analysis was used to describe the fluid evolution of reservoir, and then to analyze the fluid activities in source rocks. 12 samples were collected from 9 exploration wells such as GS21 in Gaoshiti-Moxi area, Sichuan Basin. The depth of the selected samples ranged from 5,010 m to 5,450 m. They were all from the fourth member of Dengying Formation. All samples were made into doubly-polished thick sections in order to observe and analyze fluid inclusions in transparent minerals. Bitumen often exists in the samples, filling in the intergranular pores and dissolution cavities. The dolomite crystals in the cavities is generally clean and bright, maybe resulting from recrystallization. Some cavities contain authigenic quartz, which are mostly wrapped by bitumen.

In order to clarify the characteristics of fluid activities and evolution of ancient oil reservoirs, we conducted a series of experiments of fluid inclusions based on microscope observation. Petrographic observation, microthermometric measurement and Raman spectroscopy were combined to study the fluid activities. All the experiments were conducted in the Lab of Fluid Inclusions in China University of Petroleum (East China). A polarizing/fluorescence microscope (Leica DM 2700p) was used for petrographic observation.

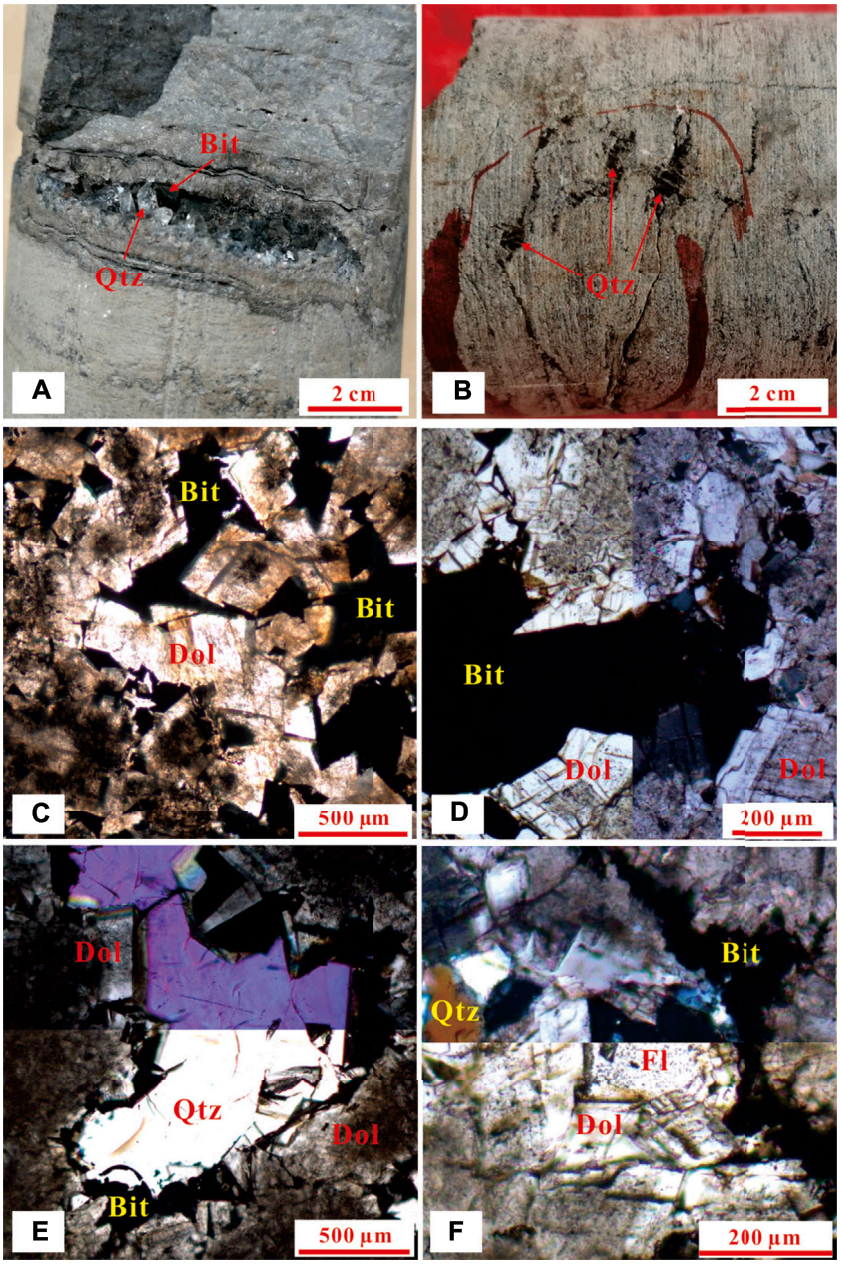

FIGURE 2 | Photograps of filled pores in dolomite of Dengying formation in Sichuan basin. **(A)** The photo shows a big cavity filled with bitumen and quartz; **(B)** The photo shows three small cavities filled with bitumen; **(C)** shows the bitumen filled in the intergranular pores; **(D)** A cavity filled with recrystallized dolomite along the wall and bitumen in the center; **(E)** A cavity filled with recrystallized dolomite along the wall, quartz in the center and bitumen sandwiched between the two minerals; **(F)** A cavity filled with recrystallized dolomite, bitumen, quartz and fluorite. Bit = Bitumen; Qtz = Quartz; Dol = Dolomite; Fl = Fluorite.

Microthermometric measurements of fluid inclusions (FIs) were done on a heating/freezing stage (Linkam THMSG600) with an estimated uncertainty of ±0.1°C. Raman analyses were conducted with a laser Raman spectrometer (Horiba LabRam-010). Excitation was achieved using a laser tuned to 532 nm. The diameter of the confocal hole was 400 μm and the slit-width was 100 μm. The accumulation time was 10 s and each measurement was made twice. Raman shift was calibrated using a silicon wafer before collection.

RESULTS

Petrography

Pores, cavities and fractures commonly occur in the dolomite of Dengying Formation. They are the main reservoir space of hydrocarbon. The cavities in the second member are generally larger (**Figure 2A**), while the ones in the fourth member are smaller (**Figure 2B**). The cavities are usually filled with bitumen and minerals, such as recrystallized dolomite,

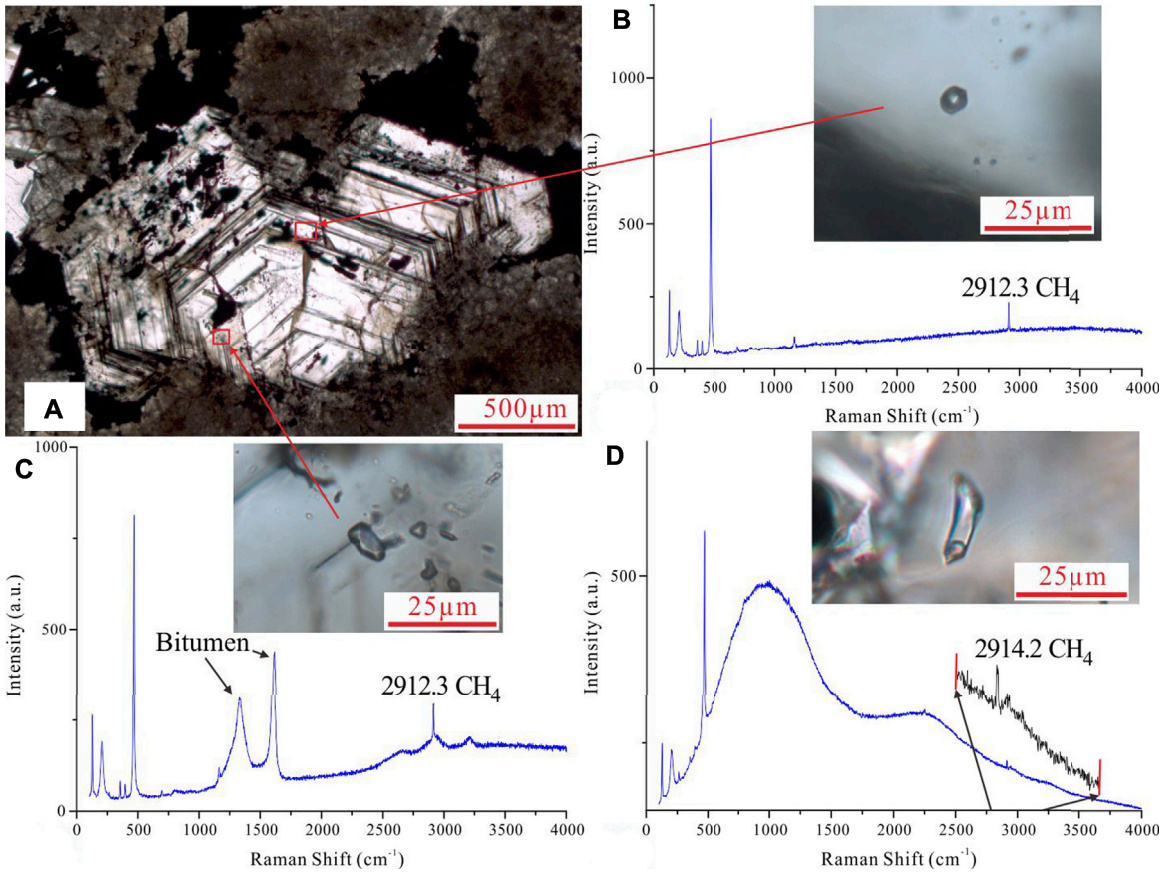

FIGURE 3 | Different kinds of fluid inclusions in quartz filled in the cavity of dolomite in Dengying formation. **(A)** A perfect crystal of quartz; Raman spectra respectively show **(B)** methane gas inclusion, **(C)** methane gas inclusion with bitumen, and **(D)** methane-bearing two-phase aqueous inclusion.

quartz and a little of fluorite. Microscopic photos show that bitumen is also widely developed among dolomite grains (**Figure 2C**), but the degree of filling is different, indicating that the carbonate reservoir has been filled with oil to varying degrees, and the oil has been fully cracked in a high degree of thermal evolution process. In the dissolution cavity, bright dolomite always occur along the wall. Some smaller pores can be completely filled with dolomite, but most of them are also filled with bitumen (**Figure 2D**), which is the residue of paleo-oil cracking. Some larger cavities also precipitate quartz (**Figure 2E**) or fluorite (**Figure 2F**), which are generally located in the center of the cavities and surrounded by bitumen. This phenomenon shows that the quartz or fluorite were formed after paleo-oil filling, and can record the evolution process after paleo-oil filling.

In order to interpret the relationship between the fillings in the cavities better, the occurrences of fluid inclusions hosted in different minerals were observed. In the recrystallized dolomite, fluid inclusions are very abundant, mainly gas-liquid two-phase inclusions, and only a few methane bearing aqueous inclusions are found. There is no bitumen in the grain, but the bitumen is only located among the crystals, which indicates that it may be formed earlier than the oil injection. Quartz is generally located in the center of the cavity and surrounded by bitumen (**Figure 3A**). Fluid inclusions hosted in quartz are also very abundant. There are various types of inclusions, including aqueous inclusions, pure methane gas inclusions (**Figure 3B**), bitumen and methane bearing gas inclusions (**Figure 3C**) and methane bearing aqueous inclusions (**Figure 3D**). A few fluorite grains are found in the cavities, but they contain a lot of fluid inclusions. The type is the same as that in quartz, which may precipitate in the same period as quartz.

Microthermometry

The microthermonetric results are summarized in **Table 1**. The fluid inclusions in recrystallized dolomite are almost all aqueous inclusions. Only one methane bearing inclusion was found, and its bubble didn't change when the temperature was above 250°C, indicating that it is inhomogeneous and may be formed by mixing methane into the original fluid inclusion. The distribution of homogenization temperature is very wide, ranging from 71.9 to 186.6°C. Dolomite is carbonate rock with perfect cleavage and low hardness, which make it easy to be re-equilibrated under over heat and pressure. Therefore, the information recorded by fluid inclusions in dolomite may be changed due to the change of temperature and pressure

TABLE 1 | Microthermometric data and calculations based on fluid inclusions from Sinian Dengyingzu formation in Sichuan basin.

Group no	Host mineral	Type	Number	Th (Ave.)/°C	Salinity (Ave.)/%	Tt/°C	Pt (MPa)
1	Dolomite	Aq	6	71.9–98.6 (82.4)	12.7–20.7 (16.6)	--	--
2			9	104.9–134.8 (117.8)	3.2–8.7 (6.0)	--	--
3			6	138.6–150.8 (143.4)	9.6–16.8 (11.9)	--	--
4			31	151.4–186.6 (165.7)	11.7–20.7 (16.8)	--	--
5	Dolomite	CH_4-Aq	1	>250 inhomogeneous		--	--
6	Quartz	Aq	2	104.3–106.7 (105.5)	18.9–19.3 (19.1)	--	--
7a	Quartz	Aq	18	121.1–139.7 (131.0)	6.2–20.0 (13.7)	148.0	36.9
7b	Quartz	CH_4-Bit-Aq	5	144.1–152.3 (148.0)	12.4–16.4 (14.8)		
8a	Quartz	Aq	22	140.3–161.8 (148.1)	5.4–19.2 (10.1)	178.8	62.7
8b	Quartz	CH_4-Aq	16	163.2–187.6 (178.8)	2.9–17.7 (11.4)		
9a	Quartz	Aq	15	162.6–189.2 (171.4)	2.9–18.2 (9.2)	211.2	76.2
9b	Quartz	CH_4-Aq	12	197.3–227.5 (211.2)	2.9–18.9 (8.6)		
10	Fluorite	CH_4-Aq	16	188.8–208.5 (194.7)	7.9–13.9 (9.9)		

Notes: Aq = Aqueous inclusion; CH_4-(Bit)-Aq = Methane-(Bitumen)-bearing aqueous inclusions; Th = Homogenization temperature; Tt = Trapping temperature; Pt = Trapping pressure.

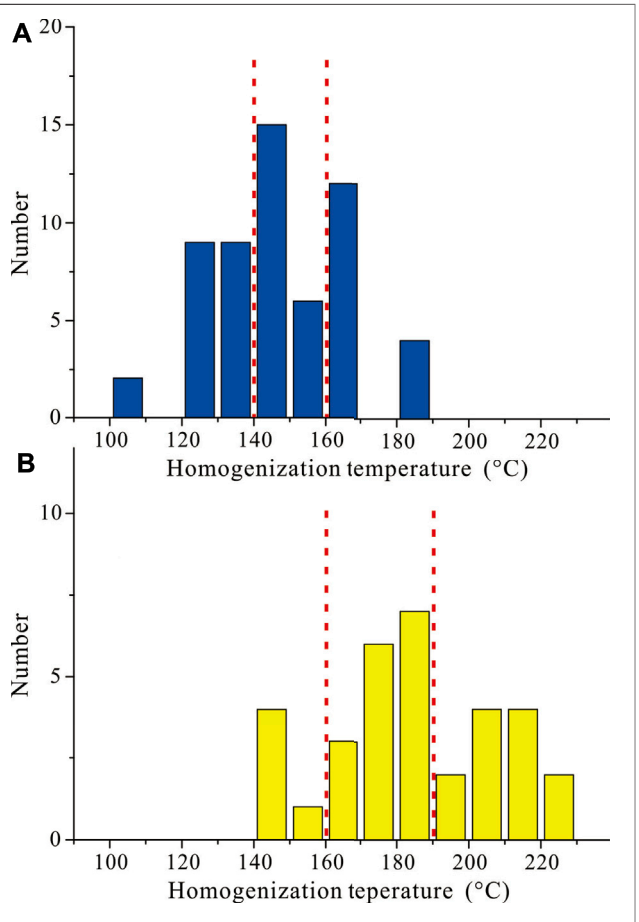

FIGURE 4 | Histograms of the homogenization temperatures of **(A)** aqueous inclusions and **(B)** methane-bearing inclusions in quartz filled in cavities of dolomite in Sinian Dengying Formation.

in the later periods. This restricts its application. In particular, the homogenization temperature of fluid inclusions in quartz indicates that the reservoir has indeed experienced high temperature. However, quartz is relatively more stable than dolomite and not easy to be re-equilibrated. In addition, there are many methane bearing aqueous inclusions in fluorite. Due to their regular shape and pulsating bubbles without restriction, the bubbles run away when they are irradiated by laser under Raman spectroscope. It is not easy to completely identify their types. Their homogenization temperatures are very high and similar (**Table 1**), so it is difficult to quantitatively analyze them. Therefore, this paper only used the microthermometric data of fluid inclusions in quartz for paleofluid analysis.

According to the above description, quartz crystallized after the earliest hydrocarbon charging. The coexistence of fluid inclusions in quartz, such as methane gas inclusions, methane-bearing aqueous inclusions, aqueous inclusions and even some bitumen inclusions, indicates that the precipitation of quartz is consistent with the process of early oil-gas transformation and the later natural gas activities. The cavities developed in some core samples deposited some bitumen and quartz, but are not filled completely. Growth striation can be found in some quartz crystals, and this can be interpreted that the precipitation of quartz is a continuous process. So the fluid activities after the early oil charging can be fully expressed through multi particle comprehensive measurements.

The homogenization temperature histogram of fluid inclusions in quartz is shown in **Figure 4**. **Figure 4A** shows the homogenization temperature histogram of aqueous inclusions in quartz, and **Figure 4B** shows the homogenization temperature histogram of methane-bearing inclusions. According to the distribution and occurrence of fluid inclusions in minerals, combined with their homogenization temperature and salinity, the fluid inclusions in quartz can be divided into three stages. The three stages of aqueous inclusions and methane-bearing aqueous inclusions correspond one by one. The data of homogenization temperatures and salinities are shown in **Table 1**. The methane-bearing aqueous inclusions are immiscible inclusions. We can assume that the methane is saturated during trapping, so the homogenization temperature equals to the trapping temperature. Combined with the homogenization temperatures and salinities data of aqueous inclusions, the trapping temperatures and pressures of fluid inclusions in different

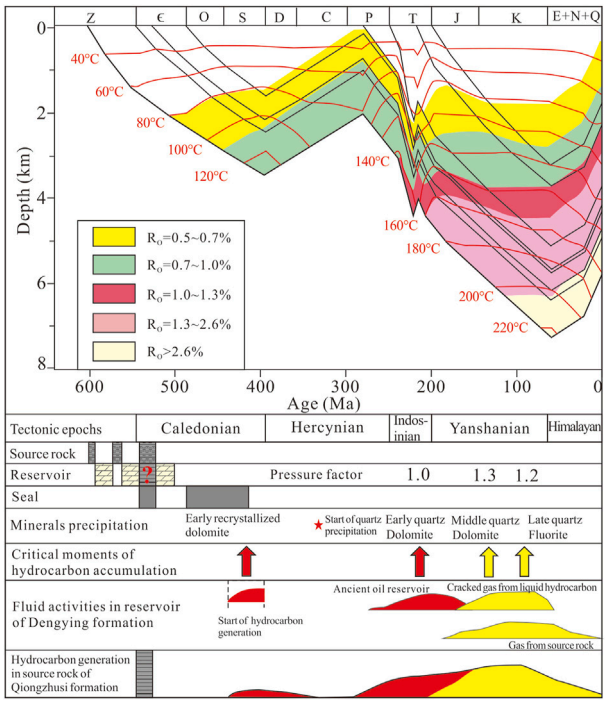

FIGURE 5 | The fluid evolution mode of the Sinian Dengying reservoirs in the Gaoshiti-Moxi area, Sichuan basin (modified from Wei et al., 2017 and Shuai et al., 2021).

periods can be calculated. Microthermometric data were interpreted using the equations given by Bodnar and Vityk (1994) as implemented in the program "HokieFlincs" (Steele-MacInnis et al., 2012). The calculation results are also listed in **Table 1**. In addition, a small number of inclusions with low homogenization temperature hosted in some quartz and located near the wall, might be trapped at the beginning of early quartz precipitation.

DISCUSSION

The Evolution of Fluid in Reservoir

From the above analysis, it can be seen that quartz precipitation should be later than the earliest oil charging. Therefore, the lowest homogenization temperature of fluid inclusions in quartz can limit the latest time for the ancient reservoir to start charging. According to the burial history and thermal history of Gaoshiti-Moxi area (Wei et al., 2017; Shuai et al., 2021), the activity history of fluid can be obtained by projecting the calculated trapping temperature onto the burial history map (**Figure 5**). The burial depth of the formation bearing fluid inclusions at the trapping period can be obtained easily, and then the pressure coefficient can be calculated by dividing the trapping pressure by hydrostatic pressure.

According to the maturity of source rocks simulated in the burial history map, it can be deduced that the earliest generation and migration of hydrocarbon occurred in Ordovician. The lowest homogenization temperature of fluid inclusions in quartz indicates that the period of quartz precipitation may be Permian, when some hydrocarbon has been injected into the reservoirs.

Fluid inclusions in quartz mainly record three stages of fluid activities. The first stage occurred in the Late Permian or early Triassic, in the late Hercynian movement and early Indosinian movement. After a long period of uplift and erosion from Devonian to Carboniferous, the basin subsided again, burial deepened rapidly and temperature increased rapidly at the same time. The organic matter in the source rocks continued to mature and generate a large amount of hydrocarbon, which migrated and formed an ancient reservoir. All the methane-bearing inclusions in this period also contained bitumen in them, indicating that when the inclusions were trapped, they did not directly capture natural gas, but captured oil, and methane was the result of later transformation. The calculated pressure coefficient at this period was 1.0, indicating that it was normal pressure in the reservoir at this period. Fluid activity in this period was mainly oil generation, migration and accumulation, which was the largest oil activity and the last prosperity of oil activity, because with the rapid rise of temperature, oil was facing cracking.

The second stage of fluid activities recorded in quartz occurred in Jurassic, which belongs to the early Yanshanian movement. With the continuous increase of burial depth, the temperature increased rapidly, and it was close to 180°C. The early formed ancient oil reservoirs had begun to crack, release methane and remain bitumen, and the oil reservoirs had transformed into gas reservoirs. The oil in the cavities gradually changed into bitumen, and quartz precipitated in some cavities, which squeezed the space and made bitumen distributed at the edge of the cavities. The fluid activity in this period was the largest ancient reservoir transformation from oil to gas. The calculated reservoir pressure coefficient reached 1.3, indicating that the reservoir generally develops over pressure and the oil and gas activities had reached the peak.

The third stage of fluid activities occurred in the Cretaceous, which is the late Yanshanian. At this time, the buried depth reached the deepest, and the temperature exceeded 200°C. The oil in the reservoir had already been cracked. The pressure coefficient in the reservoir decreased to less than 1.2, indicating the leakage of natural gas in the reservoir. In addition to quartz, some pores were filled with a small amount of fluorite, which indicated that there were external hydrothermal fluids entering the reservoir. All these phenomena indicated that the gas reservoirs were reformed and adjusted again, which was closely related to the basin stopping subsidence and turning to uplift.

To sum up, fluid inclusions in quartz record the fluid activities of reservoir after initial hydrocarbon injection. We described the fluid evolution process of the formation, cracking and destruction of the ancient oil reservoirs and the reconstruction of the gas reservoirs in Dengying Formation.

The Significance to Shale Gas Exploration

Sichuan Basin is the only basin with successful shale gas exploration in China. The main stratum is upper Ordovician

Wufeng Formation and Lower Silurian Longmaxi Formation, mainly distributed in the northeast of Sichuan Basin. In addition to this layer of shale, the most likely breakthrough stratum is the lower Cambrian Qiongzhusi Formation shale. The Qiongzhusi Formation is above the Sinian Dengying Formation with an unconformity, and its thickness greatly increases in the Deyang-Anyue rift. It is in lateral contact with the Dengying Formation and is basically at the same depth in the rift. The above description illustrates the evolution process of hydrocarbon fluid in the Sinian Dengying Formation, which also has a good indication for shale gas exploration in the Qiongzhusi Formation with the same buried depth, because the oil in the Dengying Formation is mainly from the mature hydrocarbon generation of the shale in the Qiongzhusi Formation. The thermal history evolution of Dengying Formation is the same as that of Qiongzhusi Formation.

Figure 5 shows the hydrocarbon generation history of the source rocks. It mainly generated oil at the beginning. With the increase of burial depth and temperature, the source rocks reached the peak of oil generation, which corresponded to the fluid activity in the first stage of Dengying Formation. After that, the temperature exceeded 150°C and the oil began to crack. The kerogen and oil in the source rocks also began to crack, and the rapid transition from oil generation to gas generation corresponds to the second stage of fluid activity. Since then, the gas reservoir transformation and adjustment also occurred in the source rocks of the Qiongzhusi Formation. Because its lower part was in unconformity contact with the Dengying Formation, forming a good carrier layer, the natural gas generated in the shale was easy to escape along the unconformity surface. This may be an important factor that it is difficult to break through in the previous shale gas exploration of the Qiongzhusi Formation. However, the Qiongzhusi formation in the rift had large thickness, high TOC content and high maturity, so there is a great possibility of exploring "sweet point".

According to the carbon isotope characteristics of natural gas and bitumen, it is considered that the natural gas in Dengying Formation mainly is generated from kerogen rather than oil cracking (Shuai et al., 2021). This indicates that during the second and third stage of fluid activities, the Qiongzhusi Formation has been generating natural gas and providing gas to the lower Dengying Formation and the upper Longwangmiao Formation. High pressure coefficient is an important indicator of shale gas enrichment. The pressure coefficient of Dengying Formation was 1.3 in the second stage, and 1.2 in the third stage of fluid activities. The Qiongzhusi Formation was still the main gas source of Dengying Formation, which indicates that the pressure coefficient of the Qiongzhusi Formation in some areas was more than 1.2, or even more than 1.3. Only in this way could it provide gas to Dengying Formation reservoirs. For example, the pressure coefficient of shale gas reservoirs in Longmaxi Formation, the main shale gas production layer in Sichuan Basin, is about 1.2. Hence the Qiongzhusi Formation has a well potential of shale gas exploration, especially in the rift area, where the upper and lower sealing ability is good enough, it is easier to form shale gas "sweet points" because of larger thickness. Therefore, the fluid evolution process of Dengying Formation reservoir shows that the Qiongzhusi shale in the rift has the conditions to form shale gas "sweet points", and strengthening exploration is helpful to find them. In recent years, some petroleum companies have strengthened exploration efforts in the rift area. In the Weiyuan area, some industrial wells have been successfully drilled and gradually been put into production. It is believed that more shale gas "sweet points" will be found in the future.

CONCLUSION

1) Dolomite, bitumen, quartz and fluorite are filled in the pores or cavities of dolomite reservoir of Sinian Dengying Formation in Gaoshiti Moxi structure of Sichuan Basin. Fluid inclusions in quartz record the evolution process of fluid after the earliest oil injection. This process can be divided into three stages: 1) oil charging stage. Charging occurred with normal pressure. It is dominated by oil migration and accumulation, and also the peak of oil activities. 2) Stage of gas generation through oil cracking. The temperature had exceeded 150°C. Oil began to crack with the residual bitumen. The pressure coefficient were 1.3. 3) Adjustment stage of gas reservoir. The maximum temperature had exceeded 200°C. The basin subsided first and then uplifted, and the original gas reservoirs were destroyed, and began to transform and adjust to new conditions. The pressure coefficient was 1.2.

2) The lower Cambrian Qiongzhusi Formation is the main source rock of Dengying Formation. In the second and third stage of fluid activities, Dengying reservoirs developed over pressure, and the gas source were mainly kerogen cracking gas from Qiongzhusi shale. This indicates the higher hydrocarbon generation pressure in Qiongzhusi Formation. Together with its thickness, high TOC content and over mature, it has good shale gas exploration potential.

DATA AVAILABILITY STATEMENT

The original contributions presented in the study are included in the article/Supplementary Material, further inquiries can be directed to the corresponding author.

AUTHOR CONTRIBUTIONS

ZZ carried out conceptualization, methodology, writing original draft, and validation and software. XC conducted the microthermometric measurements and Raman spectroscopy. HX also conducted the microthermometric measurements and Raman spectroscopy.

FUNDING

This work was supported by the National Natural Science Foundation of China (Grant No. 41703060).

REFERENCES

Bodnar, R. J., and Vityk, M. O. (1994). "Interpretation of Microthermometric Data for H_2O-NaCl Fluid Inclusions," in *Fluid Inclusions in Minerals, Methods and Applications*. Editors B. De Vivo and M. L. Frezzotti (Blacksburg, VA: Virginia Tech), 117–130.

Chen, S., Gong, Z., Li, X., Wang, H., Wang, Y., and Zhang, Y. (2021). Pore Structure and Heterogeneity of Shale Gas Reservoirs and its Effect on Gas Storage Capacity in the Qiongzhusi Formation. *Geosci. Front.* 12, 101244. doi:10.1016/j.gsf.2021.101244

Du, J. H., Zou, C. N., and Xu, C. C. (2014). Theoretical and Technical Innovations in Strategic Discovery of a Giant Gas Field in Cambrian Longwangmiao Formation of central Sichuan Paleo-Uplift, Sichuan Basin. *Pet. Exploration Dev.* 41 (3), 268–277. doi:10.1016/s1876-3804(14)60035-5

Gao, B., Liu, Z. B., Shu, Z. G., Liu, H. T., Wang, R. Y., Jin, Z. G., et al. (2020). Reservoir Characteristics and Exploration of the Lower Cambrian Shale Gas in the Middle-Upper Yangtze Area. *Oil Gas Geology.* 41 (2), 284–294. doi:10.11743/ogg20200205

Han, C., Jiang, Z., Han, M., Wu, M., and Lin, W. (2016). The Lithofacies and Reservoir Characteristics of the Upper Ordovician and Lower Silurian Black Shale in the Southern Sichuan Basin and its Periphery, China. *Mar. Pet. Geology.* 75, 181–191. doi:10.1016/j.marpetgeo.2016.04.014

Han, H., Li, D., Ma, Y., Cheng, L., Qi, L., Wang, Q., et al. (2013). The Origin of marine Shale Gas in the Northeastern Sichuan Basin, China: Implications from Chemical Composition and Stable Carbon Isotope of Desorbed Gas. *Shiyou Xuebao/Acta Petrolei Sinica* 34, 453–459. doi:10.7623/syxb201303005

Huang, J. L., Zou, C. N., Li, J. Z., Dong, D. Z., Wang, S. J., Wang, S. Q., et al. (2012). Shale Gas Generation and Potential of the Lower Cambrian Qiongzhusi Formation in Southern Sichuan Basin, China. *Pet. Exploration Dev.* 39, 69–75. doi:10.1016/s1876-3804(12)60017-2

Jin, Z. J., Hu, Z. Q., Gao, B., and Zhao, J. H. (2016). Controlling Factors on the Enrichment and High Productivity of Shale Gas in the Wufeng-Longmaxi Formation, southeastern Sichuan Basin. *Earth Sci. Front.* 23 (1), 1–10.

Li, L., Tan, X. C., and Zeng, W. (2013). Development Characteristics and Reservoir Significance of Mortar mounds in the Sinian Dengying Formation in Sichuan Basin. *Pet. Exploration Dev.* 40, 666–673. doi:10.1016/s1876-3804(13)60096-8

Potter, C. J. (2018). Paleozoic Shale Gas Resources in the Sichuan Basin, China. *AAPG Bull.* 102 (6), 987–1009. doi:10.1306/0828171607817072

Shuai, Y. H., Liu, K. Y., Hu, G. Y., Wang, T. S., Tian, X. W., Zhang, B., et al. (2021). Gas Accumulation Mechanisms of the Sinian Reservoir in the Sichuan basin and Their Significance for Deep Gas Exploration. *Acta Geologica Sinica* 95. doi:10.19762/j.cnki.dizhixuebao.2021141

Steele-MacInnis, M., Lecumberri-Sanchez, P., and Bodnar, R. J. (2012). HokieFlincs_H2O-NaCl : A Microsoft Excel Spreadsheet for Interpreting Microthermometric Data from Fluid Inclusions Based on the PVTX Properties of H 2 O-NaCl. *Comput. Geosciences* 49, 334–337. doi:10.1016/j.cageo.2012.01.022

Wang, D. F., Wang, Y. M., Dong, D. Z., Wang, S. Q., Huang, J. L., Huang, Y. B., et al. (2013). Quantitative Characterization of Reservoir Space in the Lower Cambrian Qiongzhusi Shale, Southern Sichuan Basin. *Nat. Gas Industry* 33 (7), 1–10.

Wang, F. Y., Chen, J. Y., and Gao, G. (2010). Reflectance of Macroalgae-Derived Vitrinite-like Macerals: An Organic Maturity Indicator for Pre-devonian marine Strata. *Pet. Exploration Dev.* 37 (2), 250–256.

Wang, M., Chen, Y., Bain, W. M., Song, G., Liu, K., Zhou, Z., et al. (2020). Direct Evidence for Fluid Overpressure during Hydrocarbon Generation and Expulsion from Organic-Rich Shales. *Geology* 48, 374–378. doi:10.1130/g46650.1

Wang, T., Xiong, L., Xu, M., Dong, X. X., Zhou, R. Q., and Fu, X. N. (2016). Shale Reservoir Characteristics of the Lower Cambrian Qiongzhusi Formation in the Southern Sichuan Basin. *Peroleum Geology. Exp.* 38 (2), 197–203. doi:10.11781/sysydz201602197210

Wei, G. Q., Wang, Z. H., and Li, J. (2017). Characteristics of Source Rocks, Resource Potential and Exploration Direction of Sinian and Cambrian in Sichuan Basin. *Nat. Gas Geosci.* 28 (1), 1–13.

Wei, G. Q., Xie, Z. Y., Song, J. R., Yang, W., Wang, Z. H., Li, J., et al. (2015). Features and Origin of Natural Gas in the Sinian-Cambrian of central Sichuan Paleo-Uplift, Sichuan Basin, SW China. *Pet. Exploration Dev.* 42 (6), 702–711. doi:10.1016/s1876-3804(15)30073-2

Yang, S. J., Wang, W. F., Zhang, D. L., Fu, X. D., and Zhang&Li, J. Y. W. Z. (2020). Distribution Characteristics and Formation Environment of High Quality Source Rocks of Qiangzhusi Formation in Northeastern Sichuan Basin. *Nat. Gas Geosci.* 31, 507–517.

Yang, Y. M., Chen, Y. L., Liu, S. Y., Deng, B., Xu, H., Chen, L. Q., et al. (2021). Status, Potential and prospect of Shale Gas Exploration and Development in the Sichuan Basin and its Periphery. *NATURAL GAS INDUSTRY* 41, 42–58. doi:10.3787/j.issn.1000-0976.2021.01.004

Zheng, P., Shi, Y., Zou, C., Kong, L., and Liu, J. (2014). Natural Gas Sources in the Dengying and Longwangmiao Fms in the Gaoshiti-Maoxi Area, Sichuan basin. *Nat. Gas Industry* 34 (3), 50–54.

Zhou, W., Xu, H., Yu, Q., Xie, R. C., and Deng, K. (2016). Shale Gas-Bearing Property Differences and Their Genesis between Wufeng-Longmaxi Formation and Qiongzhusi Formation in Sichuan Basin and Surrounding Areas. *Lithologic Reservoirs* 28 (5), 18–25.

Zhou, Z., Wang, X. Z., and Xie, L. (2014). Reservoir Characteristics and Physical Property Influencing Factors of Sinian Dengying Formation in central Sichuan Basin. *Nat. Gas Earth Sci.* 25, 701–708.

Zhu, G. Y., Zhang, S. C., and Liang, Y. B. (2006). The Characteristics of Natural Gas in Sichuan basin and its Sources. *Earth Sci. Front.* 13 (2), 234–248.

Zou, C. N., Du, J. T., Xu, C. C., Wang, Z. C., Zhang, B. M., Wei, G. Q., et al. (2014). Formation, Distribution, Resource Potential and Discovery of the Sinian-Cambrian Giant Gas Field, Sichuan Basin, SW China. *Pet. Exploration Dev.* 41 (3), 278–293. doi:10.1016/s1876-3804(14)60036-7

Zou, C. N., Zhang, G. Y., and Tao, S. Z. (2010). Geological Features, Major Discoveries and Unconventional Petroleum Geology in the Global Petroleum Exploration. *Pet. Exploration Dev.* 37 (2), 129–145.

Zou, C., Yang, Z., Sun, S., Zhao, Q., Bai, W., Liu, H., et al. (2020). "Exploring Petroleum inside Source Kitchen": Shale Oil and Gas in Sichuan Basin. *Sci. China Earth Sci.* 63, 934–953. doi:10.1007/s11430-019-9591-5

Conflict of Interest: The authors declare that the research was conducted in the absence of any commercial or financial relationships that could be construed as a potential conflict of interest.

frontiers in Earth Science

ORIGINAL RESEARCH
published: 26 August 2021
doi: 10.3389/feart.2021.702902

Shale Gas Exploration Potential in Southwestern Shandong Province of Eastern China

Li Cuifang, Huang Xinglong, Shao Yubao and Dou Fengke*

Shandong Institute of Coal Geology Planning and Exploration, Jinan, China

The shale layers of the Permian Shanxi Formation and Taiyuan Formation in the southwestern part of Shandong Province are marine-continental transitional sedimentary facies. When compared with the Ordos Basin, which was a typical breakthrough in marine-continental transitional shale gas exploration, the geological characteristics, exploration, and development prospects of marine-continental transitional shale gas in the southwestern section of Shandong Province are more defined. The shale gas deposits of the Shanxi and Taiyuan Formations in southwestern Shandong Province have the following geological characteristics. The sedimentary environments of Shanxi and Taiyuan Formations are considered to be stable and characterized with widely distributed organic-rich shale, which can be used as composite evaluation layers. The total thickness of the shale range is between 140 and 350 m, with an average of 230 m. The main types of organic matter in the Shanxi Formation are Type III and Type II_2 kerogen, while the main types of organic matter in the Taiyuan Formation are rock types. The abundance and maturity of the organic matter are high, and the gas generating capacity is strong. The reservoir rock mineral composition is complex in the region. The clay mineral content is relatively high and the brittle mineral content is rich. Also, the shale fracturing ability is good. The region has the characteristics of a low porosity and low permeability reservoir, with relatively good reservoir capacity. Three primary points of interest have stably been developed within the region, which are located in the upper high water level system, near the initial flood surface, and the majority of flood surface, including a transgressive system tract and high level system tract. The total gas content is estimated to range between 0.03 and 4.47 m^3/t, with an average of 0.30 m^3/t. The shale gas resources are rich, including one favorable Class I location with an area of 819.06 km^2 and a resource amount of 985.84 × 108 m^3; four favorable Class II locations with an area of 1,979.68 km^2 and a resource amount of 2,278.14 × 108 m^3; and five prospective locations with an area of 8,385.52 km^2 and a resource amount of 7,299.48 × 10^8 m^3. Therefore, the region was considered to have major exploration potential.

Keywords: Shanxi formation-Taiyuan formation composite evaluation layer, shale gas, mud shale, exploration potential, Type III, total organic carbon content

OPEN ACCESS

Edited by:
Dawei Lv,
Shandong University of Science and Technology, China

Reviewed by:
Peng Li,
SINOPEC Petroleum Exploration and Production Research Institute, China
Ziqi Feng,
China University of Petroleum (East China), China

****Correspondence:***
Li Cuifang
76901802@qq.com

Specialty section:
This article was submitted to Sedimentology, Stratigraphy and Diagenesis, a section of the journal Frontiers in Earth Science

Received: *30 April 2021*
Accepted: *23 July 2021*
Published: *26 August 2021*

Citation:
Cuifang L, Xinglong H, Yubao S and Fengke D (2021) Shale Gas Exploration Potential in Southwestern Shandong Province of Eastern China. Front. Earth Sci. 9:702902. doi: 10.3389/feart.2021.702902

INTRODUCTION

Outside of North America, China is currently the largest shale gas producer in the world. It is expected that with the continuing breakthroughs which are being made in domestic shale gas exploration and development, the development potential and prospects of shale gas will attract significant attention from researchers (Zou et al., 2021). Shale gas is a type of unconventional natural gas which exists mainly in either an adsorbed or free state. Shale gas is self-generating and self-storing and continually accumulates in shale deposits. Adsorbed gas occurs on the surfaces of organic matter or clay minerals, and free gas occurs in matrix pores and cracks (Zhang et al., 2004; Zou et al., 2010). Therefore, shale gas reservoirs' storage and fluid permeability characteristics are highly valued.

In recent years, in the region of the Ordos Basin Permian Taiyuan-Shanxi Group; Qinshui Basin of the Hunan Permian Dalong-Longtan Group; and the Permian Longtan Group of the eastern Sichuan Basin, well-drilling test results have revealed a sea-land transition phase of shale gas exploration and development potential. The Ordos Basin, which is a transitional facies shale gas resource, is one of the main exploration sites. The single well of the Shanxi Formation has attained stable gas production, highly controlled reserves, and good formation recoverability and fracturing ability. It is expected that a breakthrough will soon be made in the eastern margin of the basin and large-scaled production will be achieved (Kuang et al., 2020). According to the national shale gas survey and evaluation carried out by the Ministry of Land and Resources in 2012, it is believed that massive thick shale gas reservoirs have developed in the Carboniferous Permian of the southern section of northern China and other North China regions (2012). It has been found that although the shallow areas of Shandong Province lack oil and gas resources, the deeper areas have become research hotspots for the exploration of unconventional oil and gas resources. The Late Paleozoic mixed marine-terrestrial deposits in the North China region are rich in mud shale. There are relatively high degrees of evolution not only the shale-rich Carboniferous Permian shale preserved intact but the source rock in the coal measures in the deep areas of western Shandong. These findings have resulted in the deeper areas of western Shandong becoming the focus of shale gas research in recent years. Zhang et al. (2012a) comprehensively evaluated the shale occurrence layers, gas generation potential, and development feasibility and proposed that the areas with the highest potential for shale gas in Shandong Province include the Jiyang Concavity, Linqing Concavity, Jiaolai Concavity, Huang County Depression, and the southwestern Shandong buried uplift area. Zhang et al. (2019) believed that the Type II and III Kerogen of the Shanxi-Taiyuan Formation mixed marine-terrestrial shale, as well as the Type II and III Cenozoic Kong 2 lacustrine shale and the Type I and II lacustrine shale between the Cenozoic Sha 4 and Sha 3 strata of the Shahejie Formation, were also favorable exploration strata for shale gas in Shandong. It has been estimated to be $1.42 \times 1012\,m^3$ of the resource present in Shandong's favorable shale gas exploration areas. Han et al. (2015) proposed that the Taiyuan Formation in western Shandong has excellent shale gas potential due to its characteristics of high thickness; moderate burial depths; high organic matter content levels; Types II and III kerogen; high gas adsorption capacity; high maturity; high brittle mineral content; and well-developed pores and fissures. Wang (2016) believed that the dark shale of the Shanxi-Taiyuan and Heishan Formations in western Shandong has favorable conditions for shale gas formation and predicted the Cao County Coalfield, Yutai Depression, Huanghebei Coalfield, and Yanggu-Chiping Coalfield as four prospective areas. Gong et al. (2018) considered that the Upper Paleozoic dark shale in western Shandong had high thickness; high abundance of organic matter (primarily Type III); moderate thermal evolution; well-developed micropores and nanopores; high brittle mineral content; and good sealing conditions, making it conducive to shale gas accumulation. Huang (2018) and Li (2020a) (Li, 2020b) pointed out that the shale of the Shanxi-Taiyuan Formation in the coal-bearing area of southwestern Shandong is part of the low-porosity and low-permeability reservoirs of the region, which are known to have high brittle mineral content and high organic matter abundance, as well as both low-maturity strata and mature strata. The Jining Depression was the area with the highest hydrocarbon generation potential.

The above-mentioned studies indicated that as a potential shale gas area, the southwestern section of Shandong Province is characterized by the complete development of Carboniferous and Permian systems and organic-rich shale. However, there remains a lack of understanding of the distribution patterns of favorable intervals, and the prospects of exploration and development have yet to be clarified. These factors have restricted large-scaled development projects in the region. It was assumed in this study that by systematically combing the geological characteristics of marine-continental transitional shale gas in the Shanxi and Taiyuan Formations in the southwestern Shandong Province and then comparing the findings with the typical marine-continental transitional shale gas characteristics of the Ordos Basin, the geological conditions and exploration and development prospects of the shale gas in the Shanxi and Taiyuan Formations could be successfully clarified. The goal of this study was to clearly point out the most effective directions for the pursuit of unconventional oil and gas explorations in western Shandong Province.

GEOLOGICAL BACKGROUND

The study area was located within the eastern portion of the North China Plate (Level I structural unit). The study area was a buried uplift area of the southwestern Shandong Uplift (Zhang et al., 2014), which could be further divided into the Heze-Yanzhou Buried Uplift Level IV structural unit, and thirteen Level 5 structural units (Heze Buried Bulge, Chengwu Buried Depression, Wenshang-Ningyang Buried Depression, Jiaxing Buried Bulge, Jining Buried Depression, Yanzhou Buried Bulge, Jinxiang Buried Depression, Shilou Buried Depression, Qingkuji Buried Bulge, Huanggang Buried Depression, Longwangmiao Buried Bulge, Yutai Depression, and Tengzhou

Buried Depression). There were observed to be many geotectonic units across the study area, with obvious differences in the structural characteristics and structural evolutions found among the various structural units. These differences made the overall structural characteristics of the region more complex. In the study area, brittle fractures were determined to be the primary structural deformations. These deformations had occurred since the Mesozoic Period and were widely developed.

The regional stratigraphy was determined to fall under the western Shandong stratigraphic division of the Hebei-Shandong-Henan (Jin-Ji-Lu-Yu) stratigraphic area within the North China stratigraphic region (Zhang et al., 2014). The generational strata in each section of the study area were observed to be relatively complete, ranging from the Neoarchean to the Quaternary. Among those, the Taiyuan Carboniferous Formation and the Shanxi Permian Formation were the target intervals for this study's shale gas survey in western Shandong. The stratum thickness, lithology, and number of coal seams of the Shanxi Formation varied by location. However, thicknesses tended to decrease from NE to SW. In terms of lithology, the proportion of sandstone in Jining and Zaozhuang is known to be high and becomes thicker and coarser from SW to NE. There were obvious differences observed between the coal seams located in the northern and southern sections. For example, proceeding north from the Ningwen area, there were found to be relatively more coal seams. However, they were thinner, with generally only two layers of coal which could be potentially mined. The Jining-Linyi area generally contained two to three layers of coal, with each single layer being relatively thick and stable. Changes in the coal seams occurred horizontally, making them primary coal mining seams and highly valuable for industrial use.

EXPERIMENTAL TESTING EQUIPMENT AND DATA ACQUISITION

This study's sample testing content included the shale organic geochemical characteristics (kerogen microscopic composition, organic carbon content, rock pyrolysis, and vitrinite reflectance); reservoir characteristics (mineral composition, porosity, and permeability); and the gas-bearing characteristics (on-site desorption and gas composition analysis results). The kerogen microscopic compositions (SY/T 5125–2014) and vitrinite reflectance (SY/T 5124–2012) were measured using an Axio Scope.A1 microphotometer. The organic carbon content levels (GB/T19145-2003) were measured using a US LECO-CS230 carbon and sulfur analyzer. The rock pyrolysis (GB/T 18602–2012) was conducted using a ROCK-EVAL VI rock pyrolysis analyzer (France). The X-ray diffraction analyses of the clay minerals and common nonclay minerals in the sedimentary rocks (SY/T 5163–2010) were conducted using a Dutch PANalytial brand X'Pert Pro X-ray diffractometer. A Poro PDP-200 overburden porosity and permeability measuring instrument was used to measure the porosity and permeability (SY/T 6385–1999) of the samples. The shale gas content levels (GB/T 19559–2008) were determined using a SH-CBM8 fully automatic high-precision coalbed methane/shale gas content multichannel detector and HT-4 residual gas detector Hengtai Shanghe Energy Technology (Beijing) Co., Ltd. Finally, this study's gas composition analysis (GB/T 13610–2014) was conducted using an Agilent 7,890 gas chromatograph.

CHARACTERISTICS OF THE SHALE BASE SOURCE ROCK

Sedimentary Environmental and Distributions

Sedimentary environmental conditions play key roles in the formation of organic-rich mud shale (Zou et al., 2014; Lv et al., 2019; Lv et al., 2020). The Carboniferous-Permian shale in southwestern Shandong is known to have evolved from the surface sea deposits in cratonic basins to offshore river-delta-lake deposits (Chen, 2000). In the present research investigation, the field geological profiles, macrosedimentary facies analysis of borehole cores, and the types of lithofacies in the study area were utilized to determine that, based on the vertical combination relationships of the various lithofacies and the characteristics of their distributions across the plane, the Taiyuan Formation and the Shanxi Formation in the southwestern Shandong area were previously a large surface sea basin. The area's sedimentary systems were identified as being primarily tidal flat sedimentary systems, barrier-lagoon sedimentary systems, and large river-dominated shallow-water delta sedimentary systems. During the Early to Late Permian Period, the study area was mainly a set of epicontinental sea barrier coastal sedimentation deposits. The sea water gradually withdrew from north to south, and the climate changed to an arid climate. In addition, the coastal river-deltaic lacustrine sedimentation system transitioned to the west of Shandong, which was a sedimentation sequence of sea level fall and basin progression. In previous laboratory tests, the Heishan Member of the Shihezi Formation was proven to be characterized with low brittle mineral content, TOC, porosity, permeability, and gas content (<0.2 m^3/t), which had been removed from the evaluation layer. The Shanxi Formation and Taiyuan Formation were found to have similar sedimentary environments, stable stratigraphic development, and small effective thicknesses after the limestone was removed, with coal seams and sandstone layers larger than 3 m observed. The expert group of Provincial Department of Natural Resources confirmed that Shanxi Formation and Taiyuan Formation had been combined as a composite evaluation layer. The extent of Carboniferous-Permian erosion has been observed to vary greatly in each fault block in southwestern Shandong. The effective thicknesses of the shale of the Shanxi and Taiyuan Formations in the study area range between 140 and 350 m, with an average thickness of 230 m. Those thicknesses are greater than that of marine-continental shale located in the Ordos Basin (30–40 m in Shanxi and 30–60 m in Taiyuan) (Zhai et al., 2020). The two thickest centers were determined to be the south side of Well CY1 and the west side of Well Beibu2, as detailed in **Figure 1**. The west side of Well Beibu2 was the thickest at up to 350 m, and the thinnest shale layers were approximately 140 m, which were

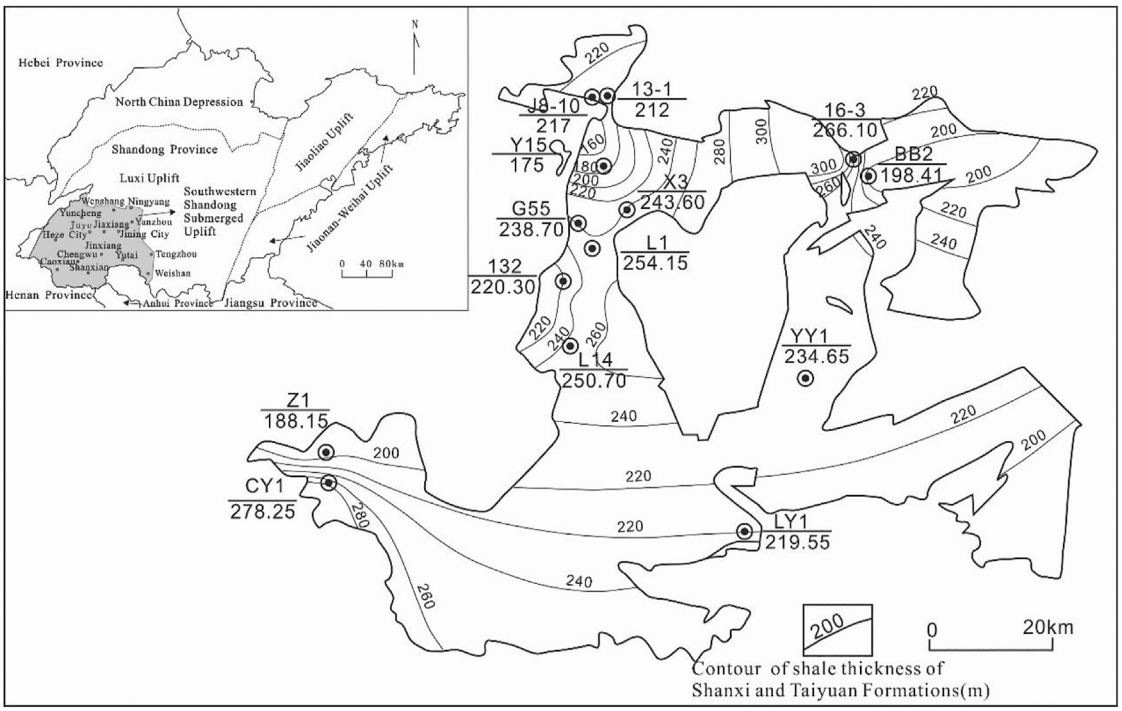

FIGURE 1 | Contour map of the shale thicknesses of Shanxi and Taiyuan Formations.

located on the north side of Well Y15 (175 m). According to the comprehensive analysis of the drilling exposures combined with seismic interpretations, the effective burial depths of the shale in the Shanxi and Taiyuan Formations ranged from 0 to 5,000 m. Those depths were controlled by the structural characteristics and observed to vary greatly.

Characteristics and Evolution of the Sequence Stratigraphy

According to regional unconformity surfaces and regional tectonic stress transformation surfaces, the Benxi Formation, Taiyuan Formation, and Shanxi Formation in the study area were divided into three third-order sequence structural sequences SIII1-S **section 3** and eight fourth-order sequences SIV2-SIV8, as shown in **Figure 2**. The Benxi Formation corresponded to the transgressive system tract of Sequence SIII1. The Taiyuan Formation corresponded to the high system tract of Sequence S square 1 and the entirety of Sequence S square 2. The Shanxi Formation corresponded to the entirety of Sequence S square 3. Sequence SIII1 mainly included a developed transgressive system tract and high system tract. The bottom of the sequence was a regional unconformity surface, an interface between Ordovician and Carboniferous. The majority of the oceanic flood surfaces were located at the bottom of the L2 limestone, where coal seams 17 and 18 were developed. Sequence SIII2 mainly included a developed transgressive system tract and high system tract. The bottom boundary of the sequence was mainly a 16_2 coal seam which had formed in a lagoon and swamp environment. The majority of the oceanic flood surfaces were located at the bottom of the L9 limestone. This study observed that Seams 6, 8, 9, 10_2, 12_1, 12_2, 14, 15_1, 15_2, 16_1, and 16_2 were all developed. In addition, Sequence SIII3 corresponded to the Shanxi Formation, which included a low-level system tract, transgressive system tract, and high-level system tract. The initial sea flood surfaces were located on the floor of No. 3 coal seam, and the maximum sea flood surfaces were located on No. 2 coal seam or the top of No. 3 coal seam. The sequence bottom interfaces were mainly the cut valley of the distributary channel in the lower delta plain, along with the interfaces of the Shanxi Formation and Taiyuan Component. No. 2 and No. 3 coal seams were developed, among which No. 3 coal seam was thicker and was the main mined coal seam in the area. To explain the evolution of the sedimentary environment in the Carboniferous and Permian coal measure sequence framework of the study area, a comparison map of the three-level sequence sedimentary environment was compiled along the east-west direction. The evolution of the sedimentary environment under the sequence framework is detailed in **Figure 3**. The sedimentary environment evolved under the sequence framework of the study area. With the decline in the sea level, the basin evolved from the epicontinental sea of the craton basin to the offshore fluvial-deltaic lacustrine deposits. The Carboniferous Benxi Formation mainly developed from the offshore shelf system, followed by the barrier-tidal flat-lagoon systems. The Late Carboniferous to Early Permian Taiyuan Formation mainly developed from the barrier-tidal flat-lagoon

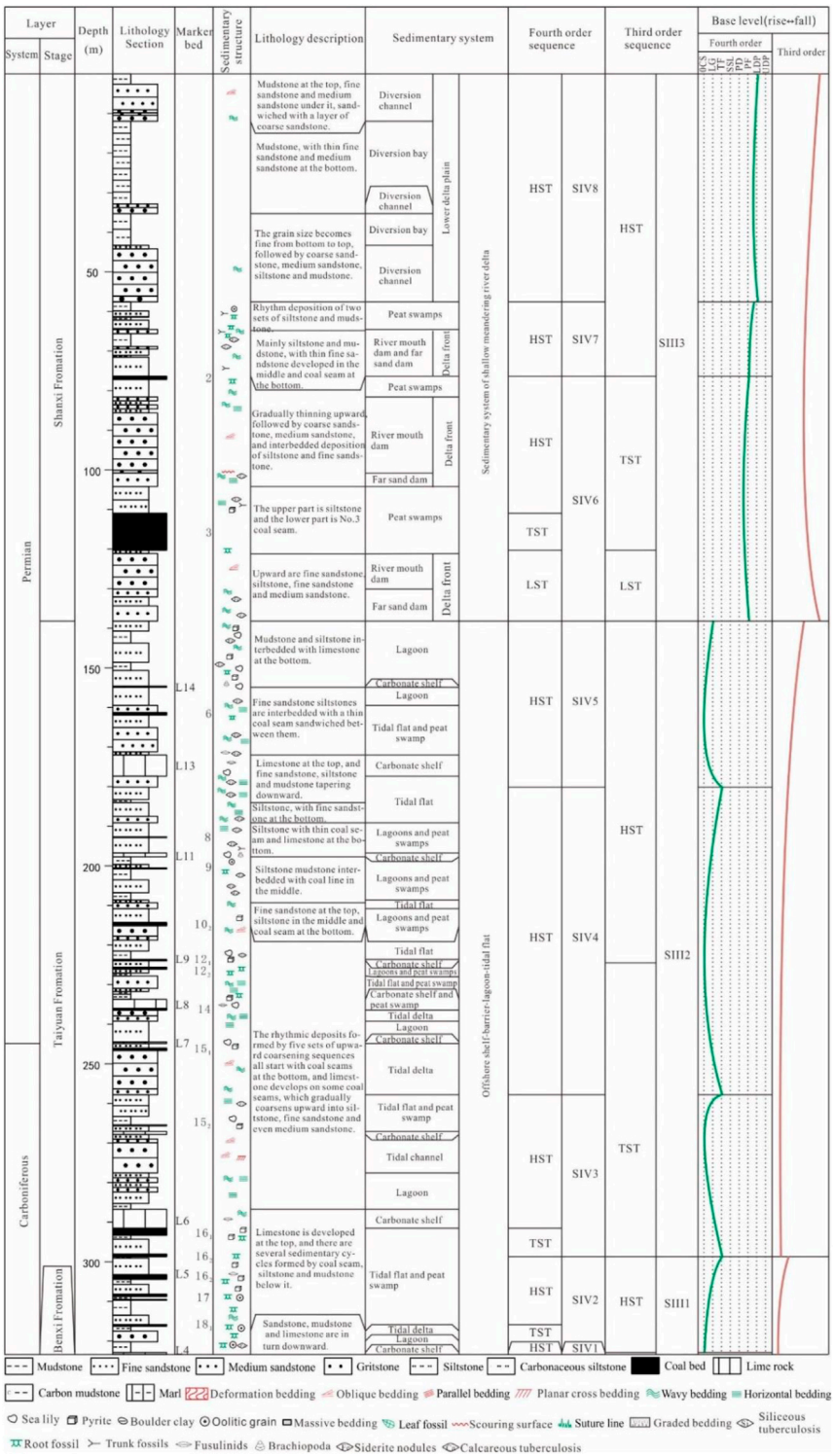

FIGURE 2 | Well XLZ-47: Comprehensive histogram of the sedimentary facies and sequence stratigraphy of the Carboniferous-Permian coal-bearing series.

depositional systems, followed by the offshore shelf depositional system. The lower part of the Shanxi Formation was determined to be mainly composed of a set of shallow water deltaic lower delta plains. Meanwhile, the upper part of the Shanxi Formation was observed to be composed of shallow water deltaic upper delta plains and meandering river deposits.

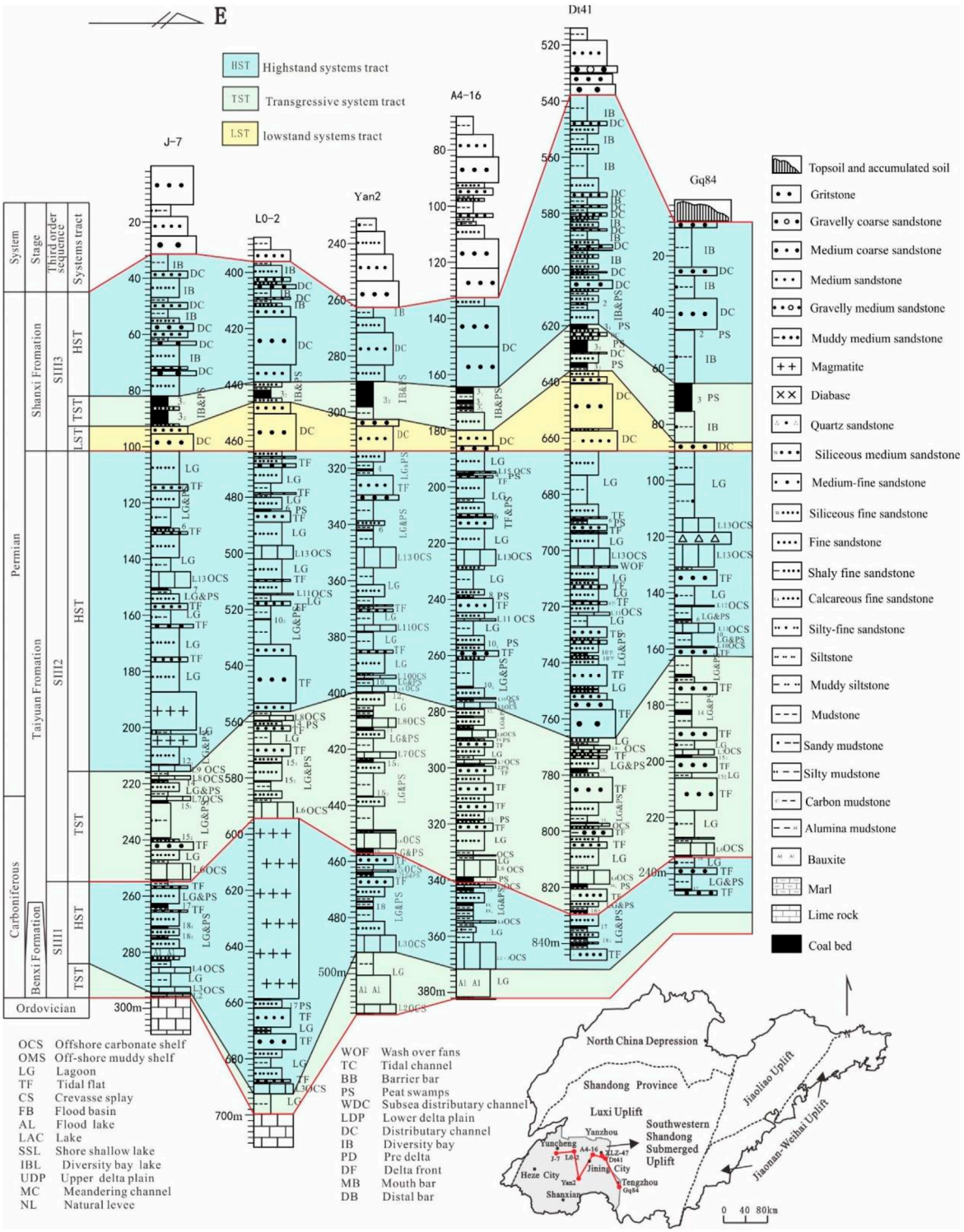

FIGURE 3 | Sedimentary facies and sequence stratigraphic correlation map (West to East).

TABLE 1 | Evaluation criteria for the abundance of organic matter in coal-measure source rock of sea and land interactions (Chen et al., 1997).

Oil source rock type	Evaluation parameters	Source rock grade				
		Very good	Good	Medium	Poor	Non
Mudstone	TOC (%)	>6	3-6	1.5-3	0.75-1.5	<0.75
	Chloroform pitch "A"/%	>0.12	0.06-0.12	0.03-0.06	0.015-0.03	<0.015
	S_1+S_2 (mg/g)	>20	6-20	2-6	0.5-2	<0.50
	Total hydrocarbons/$\times10^{-6}$	>700	300-700	120-300	50-120	<50
Organic matter type			I_1	I_2	II	III_1

Types of Organic Matter in the Mud Shale of the Study Area

The content levels of the seven shale sapropelic formations in the Shanxi Formation ranged from 0 to 2%, with an average of 0.57%. The exinite content ranged from 15 to 66%, with an average of 48.57%. The vitrinite content ranged from 24 to 62%, with an average of 37.57%. The average composition of inertinite ranged between 6 and 15%, with an average of 10.14%, and the Ti index type ranged from −58 to 5, with an average of −14.69. According to the results, the organic matter types of the Shanxi Formation were mainly type III and type II_2.

The sapropelic content levels of 59 samples from the Taiyuan Formation were found to range from 0 to 50%, with an average of 4.51%. In addition, the content levels of exinite ranged between 0 and 81%, with an average of 38.97%. The vitrinite content levels were between 12 and 81%, with the average determined to be 42.53%. The inertinite content ranged from 1 to 23%, with an average value of 9.76%. The Ti index type ranged from −79 to 75, with an average value of −13.99. Therefore, the organic matter types of the Taiyuan Formation were mainly type III, followed by type II_2.

In summary, the shale of the Shanxi and Taiyuan Formations was dominated by exinite and vitrinite. The content of exinite in the Shanxi Formation was greater than that of the vitrinite, while the content of vitrinite in the Taiyuan Formation was the opposite. It was determined that the main organic matter types of the Shanxi Formation in the study area were type III and type II_2, and the main organic matter types of the Taiyuan Formation were mainly of Algebrine types. However, the marine and continental transition facies of the Shanxi and Taiyuan Formations in the Ordos Basin were both found to be suitable types for gas generation (Xue et al., 2019; Zhai et al., 2020). The results indicated that the source rock of the Taiyuan Formation in the study area had better hydrocarbon generation ability.

Abundance of Organic Matter in the Mud Shale of the Study Area

The parent material of shale gas is organic matter. The relative content of organic matter is expressed by the abundance of organic matter. Therefore, the abundance of organic matter is an important indicator for determining the hydrocarbon generation potential of shale gas. Total organic carbon content (TOC), chloroform bitumen "A," and the hydrocarbon generation potential (S_1+S_2) are all common indicators which are utilized in evaluations of the abundance of organic matter in source rock (Chen et al., 1997) (**Table 1**). In the current study, based on the results of the measured analysis of the organic matter abundance index of the shale in the Shanxi and Taiyuan Formations of the study area, it was concluded that the source rock was mainly medium coal-measure source rock and had good hydrocarbon generation potential.

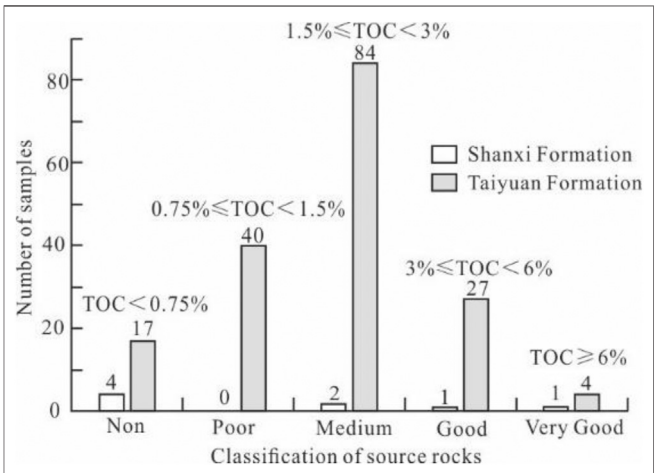

FIGURE 4 | TOC evaluation statistics for typical boreholes.

Organic Carbon Content

According to the test results of shale samples from the parameter wells in the study area and the logging inversion results of the coal exploration holes, it was considered that most of the source rocks were medium coal-measure source rocks. The results of this study's TOC content analysis of 181 samples from Wells YY1, CY1, XY601, and DY3-2 revealed that the organic carbon content levels of the Shanxi and Taiyuan Formations were slightly different. The nine samples from the Shanxi Formation showed that they were mainly nonsource rock and medium source rock (**Figure 4**), with TOC ranging from 0.21 to 6.26% and an average of 2.15%. The overall source rock level was determined to be medium. The 172 samples obtained from the Taiyuan Formation were mainly medium source rock, followed by poor source rock, and good source rock, respectively, as shown

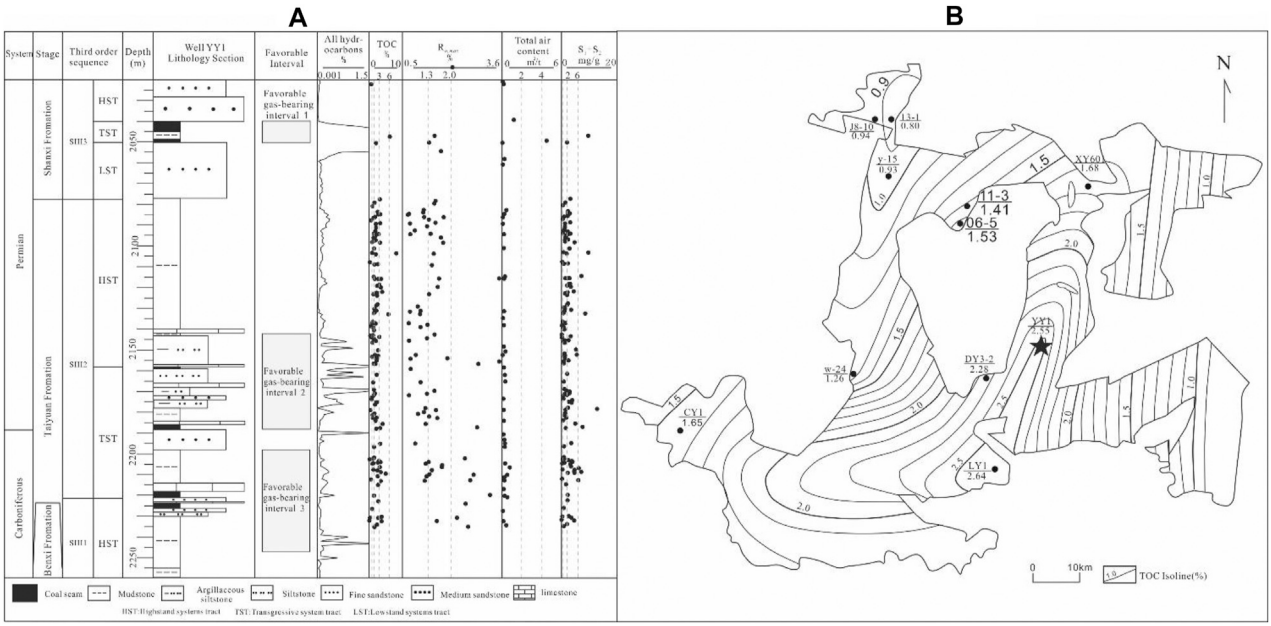

FIGURE 5 | TOC features of the Shanxi and Taiyuan Formations shale.

in **Figure 4**. The TOC ranged from 0.23 to 10.62%, with an average of 2.15%. The overall source rock level was also determined to be medium. The TOC of Well YY1 was tested 145 times. The results revealed that the TOC ranged from 0.23 to 8.11%, with an average of 2.03%. The high value areas with TOC > of 3.0% were mainly concentrated in the middle and lower parts of the Taiyuan Formation. The YY1 area of the Taiyuan Group's sandstone and the shale depositional environment in the marina outer shelf-barrier-lagoon and tidal flat environments were given priority. This was due to the regional stability of the coal seams, dark mudstone, carbonaceous mudstone, siltstone, fine sandstone and limestone layers, and sandstone sections containing high amounts of organic matter. The Taiyuan Group sandstone and shale displayed no obvious differences in total organic carbon content, as shown in **Figure 5A**.

At the same time, coal exploration drilling holes in Kaihe, Liangbaosi, Wanfu, Yuncheng, and Heihumiao were selected for this study's logging inversions. The TOC content of the Shanxi Formation was found to range between 0.17 and 1.65% and that of the Taiyuan Formation ranged between 0.48 and 2.93%.

In the current investigation, the above-mentioned data were combined, and it was determined that the minimum TOC value of the Shanxi Formation and Taiyuan Formation was 0.17%; maximum TOC value was 10.62%; and the majority ranged between 1.0 and 2.5%. In addition, it was observed that when compared with the Ordos Basin, the study area of the Shanxi Formation was found to have better potential than the Ordos Basin, and the organic matter development of Taiyuan Formation was like that of the Ordos Basin (Xue et al., 2019; Kuang et al., 2020; Zhai et al., 2020). On the plains, the Yutai Sag and the first line of the Shanxian coalfield displayed a distribution trend of "high in the middle and low on both sides," as detailed in **Figure 5B**. The abundance of organic matter was medium, which met the conditions for shale gas generation.

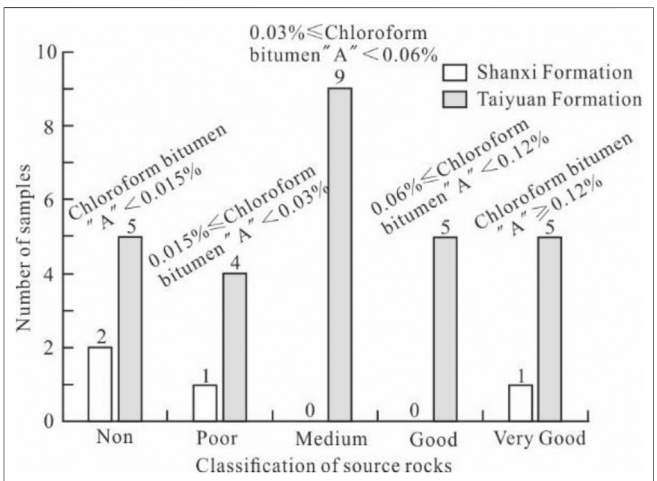

FIGURE 6 | Evaluation statistics of the chloroform bitumen "A" content in typical boreholes.

Chloroform Bitumen "A"

In this study, 32 samples of chloroform bitumen "A" obtained from Well XY601, Well DY3-2, and Well CY1 were analyzed. It was found that the chloroform bitumen "A" of the four shale samples from the Shanxi Formation ranged between 0.003 and 0.14%, with an average of 0.04%. Those results indicated that they

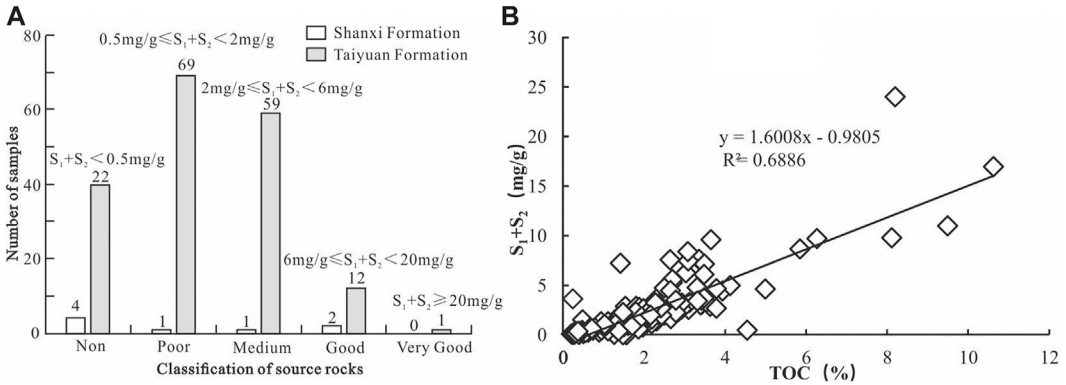

FIGURE 7 | Hydrocarbon generation potential evaluation statistics of mudshale and the relationship between them and TOC.

were medium source rock. The chloroform bitumen "A" of 28 shale samples from the Taiyuan Formation was found to range from 0.005 to 0.42%, with an average value of 0.08%, which indicated that the source rock is good and superior to that of the Shanxi Formation (**Figure 6**).

Potential for Hydrocarbon Generation

According to the analysis results of 171 pyrolysis samples from Wells YY-1, CY-1, XY601, and DY3-2 (**Figure 7A**), the S_1+S_2 content of eight shale samples from the Shanxi Formation ranged from 0.09 mg/g to 9.73 mg/g, with an average of 2.63 mg/g. The grade of the source rock was nonsource rock to medium source rock. The content of S_1+S_2 in 163 shale samples from the Taiyuan Formation ranged from 0.01 mg/g to 24.00 mg/g, with an average of 2.43 mg/g, and the grade of source rock was medium. The potential hydrocarbon generation capacity of the Taiyuan Formation and the Shanxi Formation was found to be slightly different. The potential hydrocarbon generation of each sample (S_1+S_2) had a significant positive correlation with the TOC (**Figure 7B**). The potential hydrocarbon generation capacities of the shale of the Shanxi and Taiyuan Formations were not significantly different from that of the Ordos Basin (Xue et al., 2019), which was related to the fact that the Yanshanian volcanic activities in the study area had occurred during the accumulation period of the regional source rock, and those activities had promoted the regional hydrocarbon generation.

Organic Matter Maturity

The degrees of organic matter maturity reflect the degrees of maturity and evolution of source rock organic matter and can be used to determine whether or not organic matter has reached or exceeded the maturity range for hydrocarbon generation (Zhang et al., 2011). In the vertical direction, the maximum reflectance ($R_{o,max}$) of three shale samples from well YY1 was found to range between 1.33 and 1.70%, with an average value of 1.51%. In addition, the $R_{o,max}$ of 68 shale samples from the Taiyuan Formation ranged between 0.68 and 3.51%, with an average value of 1.49%. Therefore, it was determined that they were all in a stage of low maturity-maturity. There were no obvious differences observed in the organic matter maturity between the Shanxi Formation and the coal-bearing source rock of the transitional facies in the Ordos Basin. However, the Taiyuan Formation was determined to be lower than the Ordos Basin [4, 17 to 19, 21], and the degree of thermal evolution increased with depth, as shown in **Figure 5A**. The values of the $R_{o,max}$ in the Taiyuan Formation were found to be relatively large. Some sections of the study area were found to have been affected by the late Yan Mountains magmatic intrusion, which had accelerated the maturation of the source rock around the intrusive rock. In the current study, based on previous data, it was determined that the $R_{o,max}$ in southwestern Shandong ranged between 0.68 and 3.51%, with an average of 1.51%. In addition, from the $R_{o,max}$ contour maps of the Shanxi and Taiyuan Formations in southwestern Shandong (**Figure 8**), it could be seen that the $R_{o,max}$ plane gradually increased from north to south, which was considered to be closely related to the burial depths of the shale. Most of the study area was in a low-maturity state, with mature resources concentrated near the Chengwu Depression.

CHARACTERISTICS OF SHALE GAS RESERVOIRS

Petrology Characteristics and Mineral Content Levels

This study's X-ray diffraction analysis results of the shale in Well YY1 (twenty-nine samples) indicated that the siliceous mineral content was relatively high. The brittle minerals accounted for 18.27–84.23%, with an average of 47.21%, which was mainly quartz, followed by feldspar, and with small amounts of calcite, dolomite, pyrite, and clay minerals mainly mixed in the kaolinite, illite, and imonite layers. The kaolinite, imonite mixed layers, quartz, feldspar, dolomite, and Pyrite successively accounted for 5–68%, 0–81%, 13.96–53.91%, 0–24.83%, 0–10.09%, and 0–8.2%, with an average of 30, 27.04, 41.25, 8.19, 0.90, and 1.88% accounted for 0–81%, with an average of 27.04%. Quartz accounted for 0–81%, with an average of 27.04%. The Brittleness Index II represented the fracturing ability of the shale (Zhang et al., 2015; Brittleness Index II = (quartz + feldspar + calcite + dolomite)/(quartz +

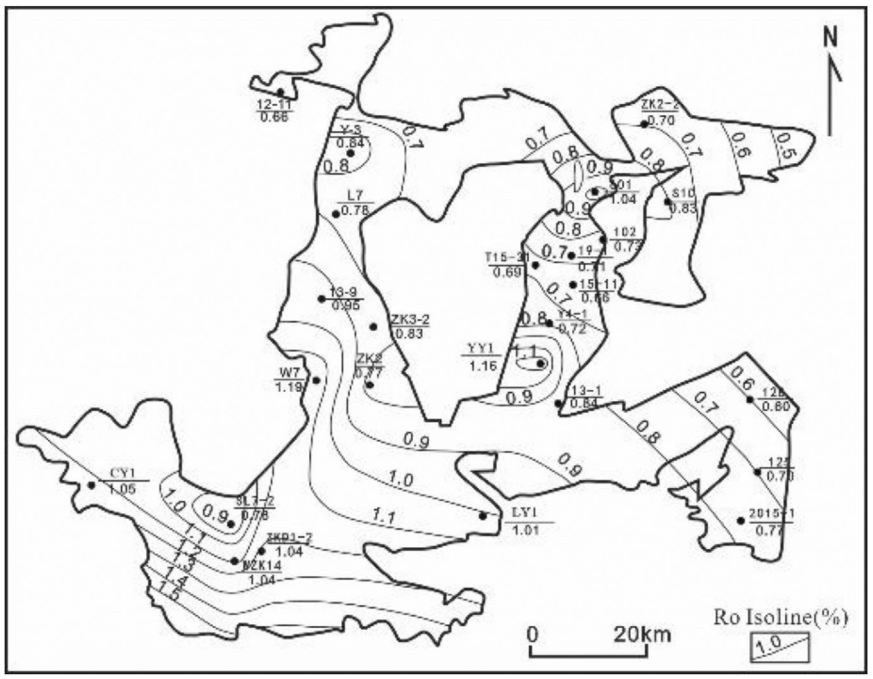

FIGURE 8 | Organic matter maturity distribution in the Shanxi and Taiyuan Formations.

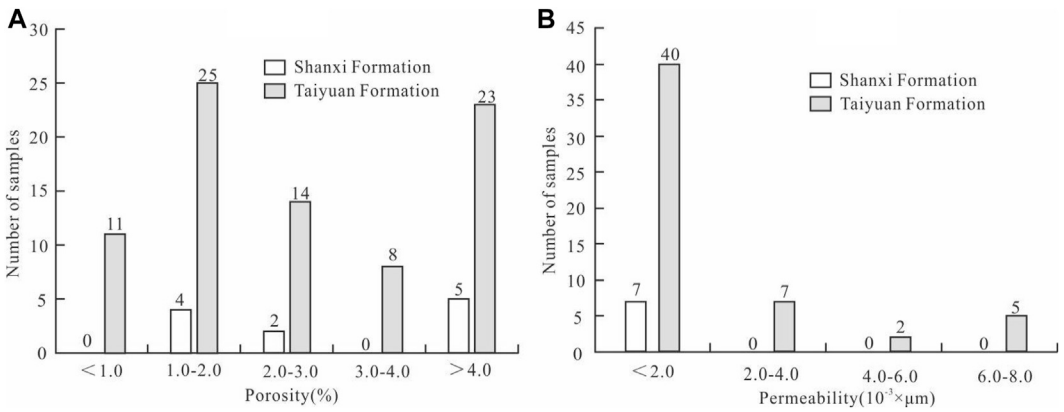

FIGURE 9 | Porosity distribution and permeability distribution of the mudshale.

feldspar + calcite + dolomite + clay minerals) × 100%). It was found that the Taiyuan Formation was rich in brittle minerals with a higher fraction of brittleness index (Brittleness Index II was 14.22–81.73, with an average of 51.61), which was slightly better than that of the Ordos Basin (Xue et al., 2019; Kuang et al., 2020; Zhai et al., 2020). Therefore, it was considered to have conditions which would be suitable for future industrial development.

Physical Characteristics of the Study Area

Permeability levels are highly significant for determining the economic development values of shale gas reservoirs. The permeability of shale tends to be very low and increases with the development of rock fractures (Fu et al., 2018). The porosity of the shale in Shanxi Formation was determined to range from 1.0 to 9.43%, with an average of 4.33% for a total of eleven samples. Also, the permeability was 0.02×10^{-3} to 1.40×10^{-3} μm^2, with an average of 0.22×10^{-3} μm^2 for eight samples. The porosity of the shale in the Taiyuan Formation ranged between 0.33 and 11.96%, with an average of 3.26% for a total of 81 samples. The permeability was determined to range from 0.01×10^{-3} to 7.98×10^{-3} μm^2, with an average of 1.36×10^{-3} μm^2 for 54 samples. The porosity and permeability conditions of the Shanxi and Taiyuan Formations were found

TABLE 2 | Statistics of the gas logging anomalies, mudshale gas content tests, and gas composition analysis results for Well YY1.

Strata	Number of anomaly segments	Thickness of the anomaly segments/m	Maximum total hydrocarbon value/%	Maximum C_1/%	Desorption gas/m^3/t	Total gas content/m^3/t	Gaseous composition/%			
							CH_4	CO_2	N_2	C_2-C_8
Shanxi Formation	7	17.83	3.5979	2.7679	0.01–2.02 0.28 (12)	0.03–4.47 0.58 (12)	0–81.93 53.96 (8)	2.24–25.68 8.42 (8)	8.51–75.54 31.36 (8)	0–11.44 6.27 (8)
Taiyuan Formation	19	13.56	2.1099	1.1278	0.01–5.17 0.43 (33)	0.05–9.15 0.84 (33)	9.58–81.23 60.10 (27)	1.55–6.5 3.35 (27)	2.56–76.31 22.28 (27)	7.61–20.41 14.27 (27)

to be similar, as shown in **Figures 9A,B**. They were determined to belong to low porosity and low permeability reservoirs overall and were not significantly different from the Ordos Basin (Xue et al., 2019; Kuang et al., 2020; Zhai et al., 2020). These findings indicated that the shale in the study area had relatively good reservoir capacity.

Gaseous Characteristics of the Study Area

Taking Well YY1 as an example, this study determined that, based on the previous data analysis results, the gas logging processes (using the SK-2000G gas logging tool) had revealed 32 layers of gas logging anomalies at different levels in the Shanxi and Taiyuan Formations (**Table 2**). The cumulative thickness of the abnormal intervals was 38.84 m, of which the Taiyuan Formation had the most gas measurement anomaly segments. However, the cumulative thickness of the anomaly segments was lower than that of the Shanxi Formation. The highest maximum total hydrocarbon value (3.5979%) was found in the Shanxi Formation.

This study's field gas content desorption test results showed that the desorption volume of Shanxi Formation was between 0.01 and 2.02 m^3/t, with an average of 0.28 m^3/t. The total gas content ranged between 0.03 and 4.47 m^3/t, with an average of 0.58 m^3/t. The desorption volume of the Taiyuan Group ranged from 0.01 to 0.29 m^3/t, with an average of 0.08 m^3/t, and the total gas content ranged from 0.05 to 0.69 m^3/t, with an average of 0.22 m^3/t. This study's wet tests of the shale samples from the Shanxi and Taiyuan Formations showed obvious bubbles. It was observed in the ignition test of the desorption sample that the flame was light blue, could not burn smoothly in the air, and was accompanied with a boom sound. The analytical gas-gas composition analysis results (**Table 2**) indicated that the gas compositions of the Shanxi and Taiyuan Formations were dominated by CH_4, followed by N_2 and CO_2 and C_2-C_8 in lower amounts. The content levels of CH_4 in the Shanxi Group ranged up to 81.93%, with an average of 53.96%. Meanwhile, that in Taiyuan Group ranged up to 74.47%, with an average of 57.77%. The direct data from the gas logging and field analysis results showed that the Taiyuan and Shanxi Formations in the Jining Depression had certain hydrocarbon generation abilities and gas storage capacities. The shale gas and CH_4 content levels of the Shanxi and Taiyuan Formations in the study area were found to be obviously lower than those of the Ordos Basin (Xue et al., 2019; Kuang et al., 2020; Zhai et al., 2020).

Characteristics of the Shale Gas "Sweet Spots" (Points of Interest)

The concept of sweet spots (points of interest) was first proposed by Shurr and Ridgley, (2002) and was later used in the evaluations of unconventional oil and gas resources (Pollastro, 2007). Chinese researchers have expanded the use range of sweet spots (Yang et al., 2015; Zou et al., 2015; Ma et al., 2018) to the most concentrated oil and gas enriched intervals, which are defined as "sweet-spot intervals" and serve as the target intervals for exploration and development. The Lower Shihezi Formation was excluded from the evaluation layers due to its low brittleness

TABLE 3 | Breakdown of the shale gas "sweet spots" (points of interest) in southwestern Shandong Province.

Well number	Points of interest (sweet spot intervals)	Layer	Depth/m	Thickness/m	Total hydrocarbon net added value/%	Total hydrocarbon average value/%	Average TOC content/%	Average desorbed gas volume/m^3/t	Ro average value/%	Average carbonate content/%	Chloroform bitumen "A"/%	Average SiO_2 content/%	Porosity/%	Permeability/$\times10^{-3}$ μm^2
Well YY1	1	Shanxi Formation	2039.80-2050.30	10.50	3.56	1.91	5.72	2.81	1.41	2.95	—	33.76	1.00	1.40
	2	Taiyuan Formation	2,142.35-2,187.05	44.70	2.10	0.44	2.00	1.24	1.45	31.10	—	44.88	1.85	2.62
			2,197.40-2,247.45	50.05	1.72	0.22	2.21	1.04	1.93	18.76	—	46.06	4.47	7.58
Well CY1	1	Shanxi Formation	1845.00-1860.78	15.78	1.38	0.43	4.54	0.72	0.98	3.24	0.0032	46.60	6.25	0.03
	2	Taiyuan Formation	1908.70-1937.15	28.45	0.52	0.17	2.89	0.26	1.09	1.52	0.0439	35.34	1.67	0.53
			2040.64-2059.40	18.76	0.51	0.27	—	—	—	—	—	—	—	—

index, TOC, S_1+S_2, porosity, and gas content. The Xiazhihezi Formation was also excluded from the evaluation layers.

In the present research investigation, the mud shale reservoir evaluation system (Zhang et al., 2011; Fu et al., 2018; Qiu et al., 2020) was referenced and the data obtained from wells CY1, YY1, LAY1, and LY1 were comprehensively analyzed. Therefore, it was believed that the composite evaluation layers of the Shanxi and Taiyuan Formation had three developed "sweet spots," as shown in **Figure 5A**. This study's division basis is detailed in **Table 3**. For example, for the YY1 Well, the desert section was in the initial flooding surfaces, as well as in the flooding surfaces near the sea. Therefore, those areas were given priority due to the observed sea development in the transgressive system tracts and high system domain; lithology combination of coal-mudstone-silty mudstone; presence of argillaceous siltstone (mainly limestone); and the sedimentary environmental conditions in the lagoon, tidal flat, peat bog, carbonate shelf, and lower delta plain areas. The specific characteristics were as follows.

"Sweet Spot" Interval 1

Interval 1 was located within the Shanxi Formation at well sections situated between 2,039.80 and 2050.30 m. The apparent thickness was 10.50 m, and the primary lithology was black coal and gray-black carbonaceous mudstone. The measured total hydrocarbons in the gas ranged between 0.04 and 3.60%. The total hydrocarbon net value was 3.56%; total hydrocarbon average value was 1.91%; measured methane in the gas was between 0.03 and 2.35%; methane net value was 2.32%; methane average value was 1.24%; average desorption gas volume was 2.81 m^3/t; TOC average value was 5.72%; $R_{o,max}$ average value was 1.41%; average SiO_2 content was 33.76%; carbonate content was 2.95%; porosity was 1.00%; and permeability was 1.40×10^{-3} μm^2.

"Sweet Spot" Interval 2

The second interval with the Taiyuan Formation was located at the well sections situated between 2,142.35 m and 2,187.05 m. The apparent thickness was 44.70 m, and the primary lithology included gray-dark gray mudstone, silty mudstone, argillaceous siltstone, gray siltstone, and coal-bearing lines. The measured total hydrocarbons in the gas ranged between 0.01 and 2.11%; total hydrocarbon net value was 2.10%; total hydrocarbon average value was 0.44%; measured methane in the gas ranged between 0.02 and 1.60%; methane net value was 1.57%; methane average value was 0.30%; average desorbed gas volume was 1.24 m^3/t; TOC average value was 2.00%; $R_{o,max}$ average value was 1.45%; average SiO_2 content was 44.88%; carbonate content was 31.10%; average porosity was 1.85%; and average permeability was 2.62×10^{-3} μm^2.

"Sweet Spot" Interval 3

Interval 3 was in the Taiyuan Formation at the well sections situated between 2,197.40 m and 2,247.45 m. The apparent thickness was 50.05 m, and the primary lithology included gray-dark gray mudstone intercalated with thin layers of sandstone and limestone and coal-bearing lines. The measured total hydrocarbons in the gas ranged from 0.03 to 1.75%; total hydrocarbon net value was 1.72%; total hydrocarbon average

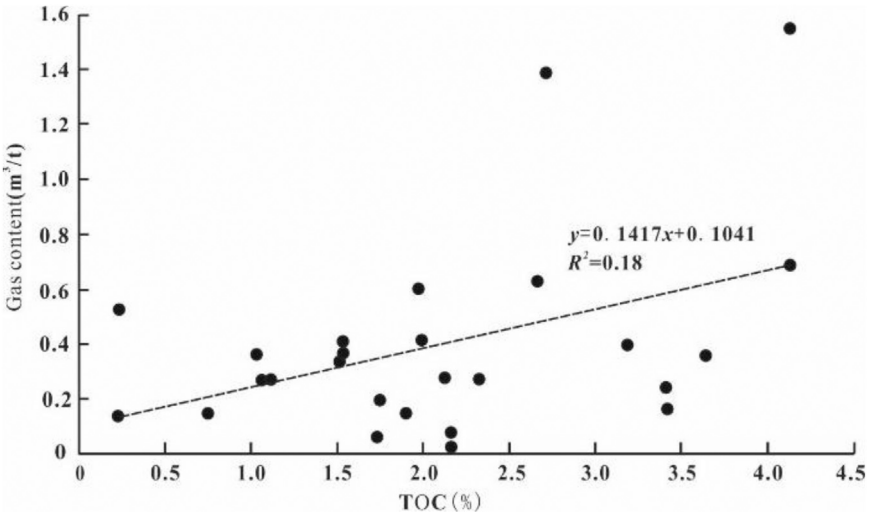

FIGURE 10 | Linear relationship model between the gas content and the TOC in the coal-bearing areas of southwestern Shandong Province.

value was 0.22%; measured methane in the gas ranged between 0.01 and 1.43%; methane net value was 1.42%; methane average value was 0.17%; average desorbed gas volume was 1.04 m^3/t; TOC average value was 2.21%; $R_{o,max}$ average value was 1.93%; average SiO_2 content was 46.06%; carbonate content was 18.76%; average porosity was 4.47%; and the average permeability was 7.58×10^{-3} μm^2.

Characteristics of the Distribution Planes

There was observed to be little measured gas content data for the shale in the Shanxi and Taiyuan Formations area. The gas content of the organic-rich mud shale in the Shanxi and Taiyuan Formations, which had been measured from Wells YY1 and CY1, was determined to be between 0.03 m^3/t and 4.47 m^3/t, with an average of 0.30 m^3/t. Since gas content is known to be positively correlated with TOC (Zou et al., 2014; Qiu et al., 2020), the gas content of the shale in the study area was estimated based on the results. Then, using the completed gas content and TOC test data from Wells CY1, YY1, LY1, along with the surrounding Well LAY1, a linear relationship model between the gas content and TOC in the southwestern Shandong area was established, as illustrated in **Figure 10**. Subsequently, by calculating the corresponding gas content according to the TOC values of the shale throughout the entire study area, it was determined that the Jining-Yutai Depression and the Chengwu Depression were potentially high gas-bearing areas. The potential gradually decreased to the northwest and southeast wings, with the Yutai Depression displaying the highest overall potential (above 0.5 m^3/t).

PREDICTED SHALE GAS RESOURCE FORECASTS

Forecasting Standards

This study consulted the evaluations of the shale gas resources survey sampling test results of the Tribune of Land and Resources, as well as the "regulations of technology of shale gas resource evaluations (draft)" data from the Geological Survey Institute of Shandong Province, and the requirements for determining shale gas resources were compiled. Then, by combining the characteristics of China's shale gas, the shale gas distribution divisions were divided into vision areas and core areas which were favorable for Level 3 resources.

Recently, a breakthrough in marine-continental transitional shale gas exploration was achieved in the eastern margin of the Ordos Basin. This study found that when compared with the Ordos Basin, the shale of the Shanxi and Taiyuan Formations in the study area had displayed similar geological characteristics which could potentially indicate rich shale gas resources and major development potential. The favorable geological characteristics of the study area were as follows:

a) The sedimentary environmental conditions were stable and the sedimentary thicknesses were larger than those of the Ordos Basin. The vertical sedimentary sequence was interbedded with shale, coal seams, and densifying siltstone, and organic-rich shale was found to be distributed in a large area.
b) The main types of organic matter in the Shanxi Formation were Type III and Type Quan 2 kerogen. The main types of organic matter in the Taiyuan Formation were lacustrine types. The abundance and maturity of the organic matter were observed to be high and the gas generating capacity was strong.
c) The reservoir rock mineral composition was complex. The clay mineral content was relatively high. Also, the content of brittle minerals was rich and found to be slightly better than that of the Ordos Basin, with good shale fracturing ability observed.
d) The study area was categorized as containing low porosity and low permeability reservoirs, with relatively good reservoir capacities observed.

TABLE 4 | Reference standards for shale gas selection in the coal-bearing areas of Shandong Province.

Type classification	TOC/%	Ro/%	Buried depth/m	Surface conditions	Preservation condition	Average interval gas content	Effective coverage thickness	Degree of control
Class I Favorable Area	Average not less than 2.0%	Not less than 0.5%	300-4,500	Good	Medium structure, continuing strata development, traceable correlation	Not less than 0.5 m^3/t	Pre-Cenozoic stratum thickness >300 m	Drilling shows good results
Class II Favorable Area	Average not less than 2.0%	Not less than 0.5%	300-4,500	Good	Medium structure, continuing strata development, traceable correlation	Not less than 0.5 m^3/t	Pre-Cenozoic stratum thickness >300 m	
Prospective Areas	Average not less than o.5%	Not less than 0.4%	100-4,500	Good	Extant regional development and distribution of shale strata, moderate preservation conditions	No requirement	No requirements	

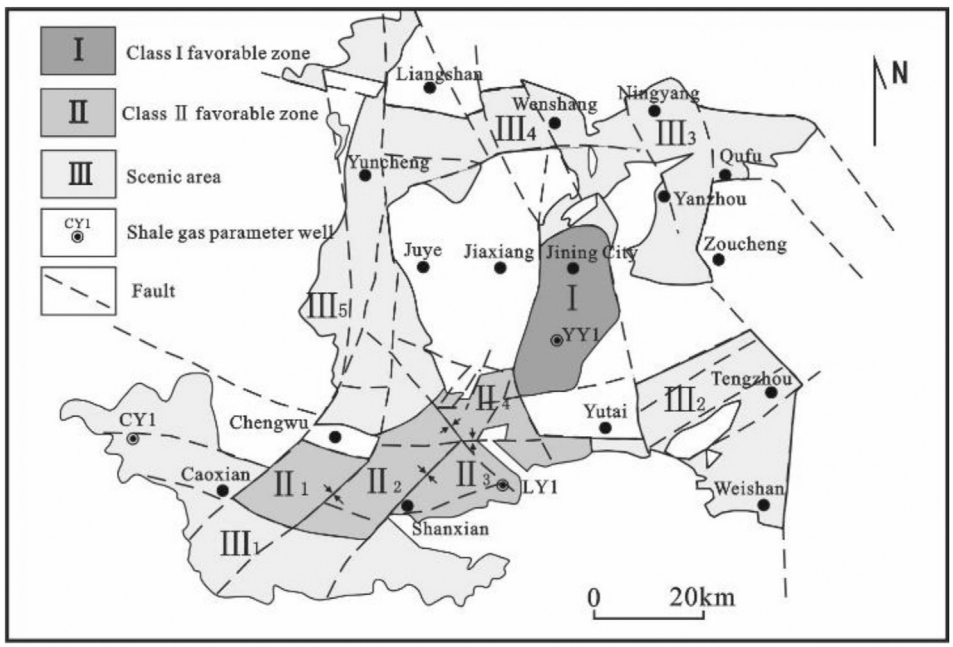

FIGURE 11 | Distribution map of the prospective and favorable shale gas areas in the western Shandong region.

e) The total gas content was general and lower than the Ordos Basin. However, the resources were rich.
f) The "sweet spot intervals" were generally located in the upper high water level system, near the initial and maximum sea flooding surfaces, and had developed in the transgressive system tract and the high-level system tract.

Although the study area was large, there are significant differences observed in the degrees of drilling, geophysical prospecting controls, and the work carried out in wells after the shale gas layers were exposed. Therefore, in order to more accurately reflect the current state of the shale gas resource explorations in the coal-bearing areas of Shandong Province, the optimal conditions for favorable shale gas areas and

prospective areas across China were prioritized. Zhang et al. (2012b) further divided the favorable areas into Type I and Type II favorable areas according to the degrees of control in the shale gas surveys. The specific selection criteria are outlined in **Table 4**. In this study's survey, based on the Shanxi and Taiyuan Formation composite evaluation layers, the Class I and Class II favorable areas, as well as potential prospective areas, were identified in the study region, as detailed in **Figure 11**.

Forecasting Results

The Upper Paleozoic Carboniferous-Permian strata in southwestern Shandong Province represented a major sedimentation transgression period. The strata experienced the entire process of an epicontinental basin's formation, development, flourishing, shrinkage, and transformation. It also experienced the evolutionary process of a tidal flat-lagoon sedimentary system → platform-lagoon sedimentary system → delta sedimentary system → meandering river sedimentary system. As a result, the strata are characterized by multiple developed layers of stable integrated limestone in contact with the underlying strata, all of which being conducive to the preservation of shale gas.

During the Early and Middle Triassic Periods, due to the remote effects of plate collision, a compressional continental basin was formed in the northern margin of the West Shandong Block and fluviolacustrine detrital assemblages were deposited. Then, during the Late Triassic Period, the basin was uplifted due to the influencing effects of the reentry and uplift of the rock at the root of the orogenic belt. The sediments during the Early and Middle Triassic Period were mainly denuded, forming an important unconformable interface between the Mesozoic and Paleozoic strata. During the Jurassic Period, local subsidence occurred. The Early Cretaceous magmatic activities were extensive and intense, making it the most intense magmatic activity period in Shandong. The Cenozoic tectonic framework exhibited obvious characteristics of inheritance and neogenesis, and the tectonic characteristics and dynamic evolution inherit the Mesozoic tectonic characteristics, which form the present tectonic framework of the study area. It was observed that when compared with the surrounding area, the central part of the study area had experienced relatively weak tectonic activities and faults were not developed. The preservation conditions of shale gas in the study area were destroyed to some extent, which led to a general decrease in the total gas content of the formation. Therefore, to identify favorable blocks for shale gas in southwestern Shandong, in addition to the development of dark shale strata, it was also necessary to select areas with relatively weak tectonic activity and underdeveloped faults. Those areas were the most conducive to the preservation of the Late Paleozoic strata, which could potentially provide favorable conditions for the occurrence of shale gas.

This study collected and then integrated, sorting through the relevant geological and mineral data for southwestern Shandong, the actual conditions in western Shandong Province. Subsequently, five advantageous areas and five prospective areas were identified, including one Class I favorable area and four Class II advantageous areas. Among the identified areas, the favorable area of Category I was 819.06 km^2 with 985.84 × 108 m^3 of resources; the favorable area of Category II was 1,979.68 km^2 with 2,278.14 × 108 m^3 of resources; and the prospective area measured 8,385.52 km^2 with 7,299.48 × 108 m^3 of resources, as detailed in **Figure 11**.

Class I Favorable Area

The drilling revealed good results, with points of interest mainly located within the Jining-Yutai Depression, in the southeastern section of the coal-bearing area in southwestern Shandong (**Figure 11**). This favorable area had relatively abundant seismic, drilling, and geochemical data. The organic-rich mud shale of the Shanxi Formation and the Taiyuan Formation displayed thicknesses of 103–110 m; effective buried depths from 300 m to 2,500 m; and organic carbon content levels of generally 2.0–3.0%. The colonic type (III) was observed to be the most common, and the second was the sapropel humus type (II_2). The Ro generally ranged between 0.7 and 1.3%. Overall, the area could be described as a monoclinic structure inclined toward the northwest.

Class II Favorable Areas

The Class II areas were comprised of four favorable areas, including Chengwu (II_1), Chengwu-Danxian (II_2), Shanxian (II_3), and Jinxiang (II_4), as shown in **Figure 11**. These areas were fault-block structures with two high-angle normal faults in the north-south direction and east-west direction. The stratum remained intact, and the overall structure was that of a monoclinic structure inclined to the west or southwest. The degrees of drilling control were relatively low. The shale of the Shanxi Formation and Taiyuan Formation had thicknesses ranging between 95 and 112 m, with effective buried depths of 300 m to 3,500 m. The organic carbon content levels were generally between 1.90 and 2.65%. The most common organic matter type was humus (III), with the second most common being the sapropel humus type (II2). The Ro generally ranged between 0.8 and 1.2%.

Other Prospective Areas (Class III)

A total of five prospective spots were also identified in the study region, as shown in **Figure 11**. The Cao County (III_1) prospective area was in the Cao County coal field region situated in the southwestern section of the study area and was distributed in a strip. The Tengzhou (III_2) prospective area was in and near the Tengxian coal field in the southeastern section of the study area. The Yang-Yanzhou (III_3) prospective area was in the Ningyang-Yanzhou coal field in the northeastern section of the study area. The Wenshang (III_4) prospective area was in Wenshang County, which was situated in the northwestern section of the coal-bearing area in southwestern Shandong. The Liangshan-Yuncheng (III_5) prospective area was identified in the Liangshan-Yuncheng-Northern Chengwu area, located in the central west and northwest portions of the study area, along a north-south strip.

CONCLUSION

This study found that when compared with the Ordos Basin, the shale of the Shanxi and Taiyuan Formations in the southwestern section of Shandong Province had similar geological characteristics, abundant shale gas resources, and major development potential. The sedimentary environmental conditions were stable, and the sedimentary thicknesses were larger than those of the Ordos Basin. The vertical sedimentary sequence was observed to be interbedded with shale, coal seams, and densifying siltstone, and organic-rich shale was distributed in a large area. The main types of organic matter in Shanxi Formation are Type III and Type II_2 kerogen. The main types of organic matter in Taiyuan Formation were lacustrine type. The abundance and maturity of the organic matter were high and the gas generating capacity was strong. The reservoir rock mineral composition was found to be complex, with relatively high clay mineral content levels. In addition, the content of brittle minerals was rich and slightly better than that of the Ordos Basin, with good shale fracturing observed. The reservoirs of the study area belonged to low porosity and low permeability reservoirs and were characterized with relatively good reservoir capacity. The total gas content was general and lower than that of the Ordos Basin. However, the resources were determined to be rich. There are three points of interest ("sweet spot intervals") identified in the vertical direction, all of which were located in the upper high water level system near the initial flood surface and the most flood surface and developed in the transgressive system tract and high-level system tract.

According to the basic geological characteristics of the shale strata of the Shanxi and Taiyuan Formations, combined with the selection evaluation index of the marine-continental transitional shale gas, Class I favorable areas and favorable areas of stratum and potential prospecting were identified in the southwestern area of Shandong. The favorable areas of Class I stratum covered an area of 819.06 km^2, with a resource amount of 985.84 × 108 m^3. The favorable areas of the Dahe type covered an area of 1,979.68 km^2. The resource amount was 2,278.14 × 108 m^3; the prospect area was 8,385.52 km^2; the resource amount was 7,299.48 × 108 m^3, and the exploration potential was very high.

DATA AVAILABILITY STATEMENT

The original contributions presented in the study are included in the article/supplementary materials, further inquiries can be directed to the corresponding author

AUTHOR CONTRIBUTIONS

All authors listed have made a substantial, direct, and intellectual contribution to the work and approved it for publication.

FUNDING

This study is supported by the special fund project of geological exploration in Shandong Province "Exploration Prospect of Shale Gas from Shanxi Formation to Taiyuan Formation in Coal-Bearing Area of Southwestern Shandong Province of Eastern China." We thank our scientific research team for their help and guidance in the field investigation.

REFERENCES

Chen, J. P., Zhao, C. Y., and He, Z. H. (1997). Criteria for Evaluating the Hydrocarbon Generating Potential of Organic Matter in Coal Measures. *Pet. Exploration Development.* 24 (1), 1–5. (in Chinese with English Abstract)

Chen, S. Y. (2000). *Sequence Stratigraphy and Coal Accumulation Regularity of Late Paleozoic in North China*. Beijing: Petroleum Industry Press. (in Chinese with English Abstract).

Fu, X. H., Zhang, M., Zhang, Q. H., Zhu, Y. M., and Guo, Y. H. (2018). Evaluation Index System for the Permo-Carboniferous Mud Shale Reservoirs of Coal Measures in Shanxi Province. *J. China Coal Soc.* 43 (6), 1644–1660. (in Chinese with English Abstract). doi:10.13225/j.cnki.jccs.2018.4029

Gong, G., Zhang, C. C., Gao, B. Y., Peng, W. Q., Huang, X. L., Zhang, H., et al. (2018). Study on Reservoir-Forming Conditions of Shale Gas in the Upper Paleozoic in the West of Shandong Province. *China Coal Geology* 30 (10), 34–38. (in Chinese with English Abstract).

Han, Z. Z., Li, Y., Gao, L. H., Qin, Z., Meng, Y., Han, M., et al. (2015). Shale Gas Potential of Carboniferous - Permian Taiyuan Formation in Western Shandon. *J. Shandong Univ. Sci. Technology (Natural Sci. Edition).* 34 (2), 51–57. (in Chinese with English Abstract). doi:10.3969/j.issn.1672-3767.2015.02.009

Huang, X. L. (2018). Shale Gas Exploration prospect of Shanxi and Taiyuan Formations in Coal-Bearing Area, Southwest Shandong Province. *Coal Technology* 37 (8), 82–85. (in Chinese with English Abstract).

Kuang, L. C., Dong, D. Z., He, W. Y., Wen, S. M., Sun, S. S., Li, S. X., et al. (2020). Geological Characteristics and Exploration and Development Prospects of Marine and Continental Transitional Shale Gas in the Eastern Marginal of Ordos Basin. *Pet. Exploration Development.* 47 (03), 435–446. (in Chinese with English Abstract. doi:10.11698/PED.2020.03.01

Li, C. F. (2020a). Shale Gas Resource Potential Analysis of Carboniferous-Permian Coal Measures in Southwestern Shandong Province. *Coal Geology China* 32 (10), 15–21. (in Chinese with English Abstract). doi:10.3969/j.issn.1674-1803.2020.10.04

Li, C. F. (2020b). Unconventional Hydrocarbon Potential of Carboniferous Permian in Jining Sag. *Coal Technology* 39 (08), 63–66. (in Chinese with English Abstract). doi:10.13301/j.cnki.ct.2020.08.018

Lv, D., Li, Z., Wang, D., Li, Y., Liu, H., Liu, Y., et al. (2019). Sedimentary Model of Coal and Shale in the Paleogene Lijiaya Formation of the Huangxian Basin: Insight from Petrological and Geochemical Characteristics of Coal and Shale. *Energy Fuels* 33 (11), 10442–10456. doi:10.1021/acs.energyfuels.9b01299

Lv, D., Song, Y., Shi, L., Wang, Z., Cong, P., Van Loon, A. J., et al. (2020). The Complex Transgression and Regression History of the Northern Margin of the Palaeogene Tarim Sea (NW China), and Implications for Potential Hydrocarbon Occurrences. *Mar. Pet. Geology* 112, 104041. doi:10.1016/j.marpetgeo.2019.104041

Ma, Y. S., Cai, X. Y., and Zhao, P. R. (2018). Theoretical Understanding and Practice of Shale Gas Exploration and Development in China. *Pet. Exploration Development.* 45 (4), 1–14. (in Chinese with English Abstract). doi:10.1016/s1876-3804(18)30065-x

Pollastro, R. M. (2007). Total Petroleum System Assessment of Undiscovered Resources in the Giant Barnett Shale Continuous (Unconventional) Gas Accumulation, Fort Worth Basin, Texas. *Bulletin.* 91, 551–578. doi:10.1306/06200606007

Qiu, Z., Zou, C. N., Wang, H. Y., Dong, D. Z., Lu, B., Chen, Z. H., et al. (2020). Discussion on Characteristics and Controlling Factors of Differential

Enrichment of Wufeng-Longmaxi Formations Shale Gas in South China. *Nat. Gas Geosci.* 31 (2), 163–175. (in Chinese with English Abstract). doi:10.11764/j.issn.1672-1926.2019.11.003

Shurr, G. W., and Ridgley, J. L. (2002). Unconventional Shallow Biogenic Gas System. *AAPG Bull.* 86 (11), 1939–1969. doi:10.1306/61EEDDC8-173E-11D7-8645000102C1865D

Wang, L. J. (2016). Characteristics of Upper Paleozoic Mud Shale and Prediction of Shale Gas Prospects in Luxi Area, Shandong Province. *Shandong Land Resour.* 32 (1), 21–25. (in Chinese with English Abstract). doi:10.3969/j.issn.1672-6979.2016.01.004

Xue, C. Q., Wu, J. G., Zhong, J. H., Zhang, S. L., Zhang, B., Hao, B., et al. (2019). Study on the Development Characteristics of marine-continental Sedimentary Shales —— Taking Taiyuan Formation in Linxing Area of Ordos Basin as an Example. *J. China Univ. Mining Technol.* 48 (04), 870–881. (in Chinese with English Abstract). doi:10.13247/j.cnki.jcumt.000974

Yang, Z., Hou, L. H., Tao, S. Z., Cui, J. W., Wu, S. T., Lin, S. H., et al. (2015). Formation Conditions and "Sweet Spot" Evaluation of Tight Oil and Shale Oil. *Pet. Exploration Development.* 42 (5), 555–565. (in Chinese with English Abstract). doi:10.13247/j.cnki.jcumt.000974

Zhai, G. Y., Wang, Y. F., Liu, G. H., Zhou, Z., Zhang, C., and Liu, X. C. (2020). Enrichment and Accumulation Characteristics and Prospect Analysis of the Permian Marine Conticental Multiphase Shale Gas in China. *Sediment. Geology. Tethyan Geology* 40 (03), 102–117. (in Chinese with English Abstract). doi:10.19826/j.cnki.1009-3850.2020.07003

Zhang, C. C., Peng, W. Q., Gao, B. Y., Yu, D. M., and Yang, C. J. (2019). Favorable Exploration Strata and Resource Evaluation of Shale Gas in Shandong Province. *Pet. Geology. Recovery Efficiency.* 26 (2), 7–13. (in Chinese with English Abstract). doi:10.13673/j.cnki.cn37-1359/te.2019.02.002

Zhang, J. C., Jin, Z. J., and Yuan, M. S. (2004). Formation Mechanism and Distribution of Shale Gas Reservoirs. *Nat. Gas Industry.* 24 (7), 15–18. (in Chinese with English Abstract). doi:10.3321/j.issn:1000-0976.2004.07.005

Zhang, M. Y., Li, X. Q., Dong, Z. L., Guo, M., Sun, M. M., and Fan, J. P. (2015). Analyses on Mineral Compositions and Brittleness of the Lower Cambrian Hetang Formation Shale in South Anhui Province. *J. Mineralogy, Petrology Geochem.* 34 (1), 177–183. (in Chinese with English Abstract). doi:10.3969/j.issn.1007-2802.2015.01.020

Zhang, W. D., Guo, M., and Jiang, Z. X. (2011). Parameters and Method for Shale Gas Reservoir Evaluation. *Nat. Gas Geosci.* 22 (6), 1093–1099. (in Chinese with English Abstract).

Zhang, D. W., Li, Y. X., Zhang, J. C., Qiao, D. W., Jiang, W. L., Zhang, J. F., et al. (2012a). *Shale Gas Resource Potential Investigation and Evaluation in China*. Beijing: Geological Publishing House. (in Chinese with English Abstract).

Zhang, Z. Q., Tian, J. X., Zhang, C. C., Cheng, G. S., Sun, W. Q., Sun, B., et al. (2012b). Shale Gas Research Progress at Home and Abroad and Shale Gas Resource Potential in Shandong Province. *Shandong Land Resour.* 28 (10), 1–6. (in Chinese with English Abstract).

Zhang, Z. Q., Zhang, C. J., Wang, S. J., Liu, S. C., Wang, L. M., Du, S. X., et al. (2014). Views on Classification and Contrast of Tectonic Units in Strata in Shandong Province. *Shandong Land Resour.* 30 (03), 1–23. (in Chinese with English Abstract). doi:10.3969/j.issn.1672-6979.2014.03.001

Zou, C. N., Dong, D. Z., Wang, S. J., Li, J. Z., Li, X. J., Wang, Y. M., et al. (2010). Formation Mechanism, Geological Characteristics and Resource Potential of Shale Gas in China. *Pet. Exploration Development.* 37 (6), 6–18. (in Chinese with English Abstract). doi:10.1016/s1876-3804(11)60001-3

Zou, C. N., Dong, D. Z., Wang, Y. M., Li, X. J., Huang, J. L., Wang, S. F., et al. (2015). Shale Gas in China: Characteristics, Challenges and Prospects (I). *Pet. Exploration Development.* 42 (6), 689–701. (in Chinese with English Abstract). doi:10.1016/s1876-3804(15)30072-0

Zou, C. N., Tao, S. Z., Hou, L. H., Zhu, R. K., Yuan, L. X., Zhang, G. S., et al. (2014). *Unconventional Petroleum Geology*. Beijing: Geological Publishing House. (in Chinese with English Abstract).

Zou, C. N., Zhao, Q., Cong, L. Z., Wang, H. Y., Shi, Z. S., Wu, J., et al. (2021). Progress, Potential and prospect of Shale Gas Development in China. *Nat. Gas Industry.* 41 (01), 1–14. (in Chinese with English Abstract)

Conflict of Interest: The authors declare that the research was conducted in the absence of any commercial or financial relationships that could be construed as a potential conflict of interest.

Publisher's Note: All claims expressed in this article are solely those of the authors and do not necessarily represent those of their affiliated organizations, or those of the publisher, the editors and the reviewers. Any product that may be evaluated in this article, or claim that may be made by its manufacturer, is not guaranteed or endorsed by the publisher.

frontiers in Earth Science

ORIGINAL RESEARCH
published: 22 November 2021
doi: 10.3389/feart.2021.695978

Effects of Carbonate Minerals on Shale-Hydraulic Fracturing Fluid Interactions in the Marcellus Shale

Brennan Ferguson[1], Vikas Agrawal[1], Shikha Sharma[1], J. Alexandra Hakala[2] and Wei Xiong[2,3]*

[1]Department of Geology and Geography, West Virginia University, Morgantown, WV, United States, [2]National Energy Technology Laboratory, U.S. Department of Energy, Pittsburgh, PA, United States, [3]Leidos Research Support Team, Pittsburgh, PA, United States

Natural gas extracted from tight shale formations, such as the Marcellus Shale, represents a significant and developing front in energy exploration. By fracturing these formations using pressurized fracturing fluid, previously unobtainable hydrocarbon reserves may be tapped. While pursuing this resource, hydraulic fracturing operations leave chemically complex fluids in the shale formation for at least two weeks. This provides a substantial opportunity for the hydraulic fracturing fluid (HFF) to react with the shale formation at reservoir temperature and pressure. In this study, we investigated the effects of the carbonates on shale-HFF reactions with a focus on the Marcellus Shale. We performed autoclave experiments at high temperature and pressure reservoir conditions using a carbonate-rich and a decarbonated or carbonate-free version of the same shale sample. We observed that carbonate minerals buffer the pH of the solution, which in turn prevents clay dissolution. Carbonate and bicarbonate ions also scavenge reactive oxidizing species (ROS), which prevents oxidation of shale organic matter and volatile organic compounds (VOCs). Carbonate-free samples also show higher pyrite dissolution compared to the carbonate-rich sample due to chelation reactions. This study demonstrates how carbonate minerals (keeping all other variables constant) affect shale-HFF reactions that can potentially impact porosity, microfracture integrity, and the release of heavy metals and volatile organic contaminants in the produced water.

Keywords: marcellus shale, hydraulic fracturing, carbonate minerals, chemical additives, hydrocarbons, dissolution, precipitation, oxidation

OPEN ACCESS

Edited by:
Dongdong Wang,
Shandong University of Science and Technology, China

Reviewed by:
Cheng Shen,
Petrochina South Oil and Gas Field Company, China
Jihua Cai,
China University of Geosciences Wuhan, China

****Correspondence:***
Vikas Agrawal
vikas.agrawal@mail.wvu.edu
va0012@mix.wvu.edu

Specialty section:
This article was submitted to Economic Geology, a section of the journal Frontiers in Earth Science

Received: *15 April 2021*
Accepted: *26 October 2021*
Published: *22 November 2021*

Citation:
Ferguson B, Agrawal V, Sharma S, Hakala JA and Xiong W (2021) Effects of Carbonate Minerals on Shale-Hydraulic Fracturing Fluid Interactions in the Marcellus Shale. Front. Earth Sci. 9:695978. doi: 10.3389/feart.2021.695978

1 INTRODUCTION

The use of hydraulic fracturing to extract natural gas from shale reservoirs has become a widespread practice of considerable importance to America's energy portfolio (U.S. EIA, 2017). The Marcellus Shale is one of the major shale reservoirs that has been utilized in this boom, making hydraulic fracturing an enormously important industry to West Virginia and the Appalachian region. Hydraulic fracturing, often referred to as fracturing or fracking, is generically the fracturing of rocks around a wellbore in order to increase the permeability of the rock and therefore enable gas flow from the reservoir. Many wells are drilled in close proximity on a well pad and, after reaching a specific depth, the drill pivots to go horizontally into the target formation (e.g., the Marcellus Shale). This multitude of wells creates a wheel-spoke pattern in the gas-bearing shale formation and

dramatically increases the yield of hydrocarbons from shale compared to what is available through conventional means (Arthur et al., 2008). Approximately 4.25 million gallons of water per well are used to hydraulically fracture the Marcellus Shale (Kondash and Vengosh, 2015), and is mixed with a variety of chemicals to create fractures and maintain the well integrity. To prop open these fractures, silica proppant is injected along with gelling agents to help push the proppant into place (PA DEP, 2010). This is followed by oxidative breakers, such as persulfates, which break down the gel in order to recover it following a shut-in period of several days to weeks (Marcon et al., 2017). After this shut-in period, a portion of this water and the natural brine in the formation, totaling approximately 1.37 million gallons per well in the Marcellus Shale (Kondash and Vengosh, 2015), are produced in order to recover the natural gas.

The Marcellus Shale is the most productive shale formation for dry gas in the United States (EIA, 2016) and is economically vital to the Appalachian region. However, within the Marcellus shale Formation, there can be significant variations in total organic carbon, organic matter type, thermal maturity, and mineralogy (U.S. EIA, 2017; Agrawal and Sharma, 2018a, 2018b, 2018c, 2020; Pilewski et al., 2019; Sharma et al., 2020a; Sharma et al., 2020b). Due to these variations in physicochemical properties, the chemical reactions that occur within hydraulically fractured unconventional formations can vary significantly, and influence the selection of hydraulic fracturing fluid (HFF) components used at any given well site (Abualfaraj et al., 2014).

During hydraulic fracturing operations, the mixture of water and chemical additives that comprise HFF is in contact with the target shale formation for weeks and reacts with the brine and shale in the formation at high temperature and pressure. During this time, numerous interactions can take place that significantly alter HFF fluid chemistry, the mineral composition and petrophysical properties of shale, and the release of organic and inorganic contaminants (Hoelzer et al., 2016; Harrison et al., 2017; Paukert Vankeuren et al., 2017; Sumner and Plata, 2018a, 2018b, 2019; Pilewski et al., 2019; Hakala et al., 2021). Studies conducted using benchtop reactors showed that multiple shale-HFF reactions could occur, such as mineral precipitation and dissolution, organo-metallic complex formation, ion adsorption onto shale organic matter and clay minerals, and organic matter degradation (Jew et al., 2017; Sumner and Plata, 2018a; Pilewski et al., 2019; Hakala et al., 2021). Among these, mineral dissolution and precipitation reactions impact the porosity and permeability of shale the most. Changes in flow dynamics from precipitation reactions have been implicated as a potential cause for discrepancies between modeled and actual late-stage hydrocarbon production in hydraulically fractured wells (Jew et al., 2017). Dissolution of shale minerals and organic matter degradation can increase the porosity and permeability of shale but increases the toxicity of produced waters (Harrison et al., 2017; Armstrong et al., 2019; Sharma et al., 2020; Donmoyer et al., 2021) and the risks posed by produced water spills.

Carbonate mineral reactions are one of the critical variables controlling reservoir geochemistry (Jew et al., 2017; Pilewski et al., 2019). Carbonate minerals play a dominant role by buffering the pH of shale-HFF interactions, which significantly impacts most reactions taking place in the reservoir and affects the stability of all other reactive components. The Marcellus Shale has a variable composition of carbonate minerals with calcite ($CaCO_3$) ranging from 3 to 48% and dolomite ($CaMg(CO_3)_2$) ranging from 0 to 10%, as well as trace amounts of other carbonates such as siderite (Morsy et al., 2013; U.S. EIA, 2017). Carbonates react with acids in HFF, such as HCl, and release Ca^{2+}, Mg^{2+} (in the case of dolomite), HCO_3^-, and trace metals such as Sr^{2+} via dissolution or ion exchange. The reaction neutralizes acid through the formation of HCO_3^-, which further buffers the chemical system and controls the pH (Wang et al., 2015; Pilewski et al., 2019). The extent of the reaction between HFF and carbonate minerals depends on the carbonate content of the shale formation and acid added in the HFF (Wang et al., 2015, 2016). Previous work on shale-HFF interactions demonstrated a strong relationship between increases in pH, Ca, Mg, and dissolved inorganic carbon (DIC) proportionate to the amount of carbonate in the system (Wang et al., 2015; Pilewski et al., 2019). X-ray diffraction analysis demonstrated commensurate losses of the primary carbonate minerals in reservoir shales, calcite and dolomite, to the fluid chemistry changes (Pilewski et al., 2019). Carbonate mineral dissolution can have either a desirable effect for gas extraction by increasing pore size (Paukert Vankeuren et al., 2017) or cause instability and collapse in microfractures depending on the particular physical dynamics of the well (Harrison et al., 2017; Jew et al., 2017; Pilewski et al., 2019).

Although numerous studies have investigated shale-HFF reactions to understand the influence of these reactions on shale permeability and fluid flow (Wang et al., 2015; Harrison et al., 2017; Jew et al., 2017; Pilewski et al., 2019), the influence of other variables such as mineralogy (e.g., varied clay and pyrite content), organic matter type and amount, and different fracturing fluid composition affected the ability to isolate the specific impact of carbonate minerals on shale-HFF interactions. Evaluating the impact of carbonate content on shale-HFF reactions requires keeping other experimental variables constant. Further, most prior studies were conducted at ambient pressure conditions and may not best represent *in situ* reservoir conditions. The aim of this study is to isolate the effects of carbonate mineral content on the shale-HFF reactions, keeping all the other variables constant, and to represent reservoir conditions using high pressure temperature reactors. Developing a refined understanding of how carbonates affect the geochemistry of hydraulic fracturing operations will allow operators to create targeted strategies for unconventional reservoir design and management.

2 MATERIALS AND METHODS

2.1 Sample Preparation

A series of experiments were conducted to isolate the effects of calcium carbonate on shale-HFF interactions. We utilized a leftover sample of Marcellus Shale that was fully characterized in our laboratory (Pilewski et al., 2019). Sample LM-2 is a

TABLE 1 | LM-2 shale depth, thermal maturity, organic content and mineral composition. Error is ±1% (Pilewski et al., 2019).

Shale sample	LM-2
Depth (ft)	5,825.7
%Ro	0.8
Tmax (°C)	443
TOC(wt%)	15.4
Quartz (wt%)	28
Calcite (wt%)	21
Dolomite (wt%)	5
Pyrite (wt%)	5
Mixed Clays (wt%)	42

relatively immature Marcellus shale sample (VRo = 0.8) with high total organic carbon (15.4 wt%), high carbonate content (21 wt% calcite, 5 wt% dolomite), moderate mixed clay content (42 wt%), and moderate pyrite content (5 wt%) (Pilewski et al., 2019) (**Table 1**). The minerals wt% were calculated to the nearest unit, and the total sum of the minerals was within 100 ± 1 wt%. This Marcellus Shale sample was chosen because it had the highest carbonate content in our sample collection.

Sample exteriors were removed using a cleaned Dremel tool before grinding to prevent any contaminating drill mud. Shale samples were ground to 100 mesh to maximize surface area for reaction, with a small amount of shale cores broken into ~0.25 cm^2 chips for SEM-EDS analysis. The ground shale and shale chips were divided into two samples: SH-HFF, which was not altered, and SH-HFF ($-CO_3$), which had carbonate minerals removed. Carbonate removal in SH-HFF ($-CO_3$) was accomplished by selective digestion using trace metal grade hydrochloric acid, following the procedure outlined in (Riley et al., 2012). Hydraulic fracturing fluid, in the absence of shale, was also reacted for 14 days which acted as a control to determine chemical changes caused by elevated temperature and pressure reactor conditions and was named HFF.

All pH measurements were taken with a calibrated YSI Pro Series Instrument equipped with a YSI Pro Series 1,001 pH sensor. A separate portion of the rock chips was also acid digested to collect pre-reaction SEM-EDS for comparison with the post-reaction carbonate-free experiment. This allows for comparison of pre-and post-experimental samples without changing the remaining mass of the primary acid digested sample for the reactor experiment.

The mixture of synthetic brine and HFF was prepared using the methods reported in (Paukert Vankeuren et al., 2017) (**Table 2**). Some proprietary chemicals that were used as part of the mixture in previous studies were no longer available. These included a gelling agent WGA-15L, a clay stabilizer WCS-631LC, a friction reducer WFR-61LA, and a corrosion inhibitor WAI-251LC. Substitutes for these were based upon MSDS sheet data and common chemicals used in the same region for the same purposes per FracFocus. Petroleum distillates were used in place of the proprietary gelling agent and friction reducer, choline chloride replaced the proprietary clay stabilizer, and cinnamaldehyde replaced the proprietary corrosion inhibitor.

2.2 Experimental Set-Up and Analysis

The shale-HFF reactions were conducted in 600 ml Parr 4768 static reactors to simulate high pressure temperature conditions in the reservoir. The reactions were conducted at 100°C and ~2,500 psi for 14 days to mimic shut-in phase duration and conditions (Marcon et al., 2017; Paukert Vankeuren et al., 2017; Pilewski et al., 2019). Inert N_2 (100% pure) was used to pressurize the reactors. A borosilicate glass sleeve containing 420 ml of HFF, 20 g of 100 mesh shale powder, and 1 gram of shale chips at a

TABLE 2 | Fracturing fluid additives and brine salts used to make the synthetic fracturing fluid mixture used in reactions.

Ingredient	Amount per liter	Purpose
Hydrochloric acid	0.634 ml	Perforation Cleaner
Ammonium Persulfate	0.200 g	Oxidative Breaker
Petroleum distillates	1.149 ml	Gelling agent, Friction Reducer
Choline Chloride	1.060 g	Clay Stabilizer
Glutaraldehyde	0.343 ml	Biocide
Potassium hydroxide	0.0357 ml	pH adjuster
Potassium Carbonate	0.240 g	pH adjuster
Ethylene Glycol	0.0222 ml	Scale Inhibitor
Citric Acid	0.0336 g	Iron Control
Boric Acid	0.0200 g	Cross Linker
Ethanolamine	0.0138 ml	Cross Linker
Cinnamaldehyde	0.0012 ml	Corrosion Inhibitor
Barium Chloride Dehydrate	0.464 g	Brine
Potassium Chloride	0.416 g	Brine
Strontium Chloride Hexahydrate	1.360 g	Brine
Ammonium Chloride	0.160 g	Brine
Sodium Bromide	0.180 g	Brine
Calcium Chloride Dehydrate	7.400 g	Brine
Magnesium Chloride Sesquihydrate	1.900 g	Brine
Sodium Chloride	16.700 g	Brine
Sodium Sulfate	0.00029 g	Brine
Sodium Bicarbonate	0.150 g	Brine

fixed mass ratio of 20:1 solid: liquid were placed inside the reactors, with the shale and HFF mixed immediately before the pressurization and heating of the reactors, following the methods of Macron et al., 2017. The control experiment was conducted with 420 ml of synthetic HFF mixture with no shale.

Upon completion of the reactions at 14 days, samples were collected and analyzed by ion chromatography (IC), Total Organic Carbon/Total Inorganic Carbon (TOC/TIC) analyzer, gas chromatography-mass spectrometry (GC-MS), and inductively coupled plasma mass spectrometry (ICP-MS). The IC samples were filtered to 0.22 microns using a syringe filter and collected in 10 ml plastic vials with zero headspace. DIC samples were also collected in 10 ml plastic vials with zero headspace. GC-MS samples were collected with zero headspace in 60 ml amber volatile organics analysis (VOA) vials acidified with HCl. Samples for ICP-MS were collected with zero headspace 10 ml plastic vials after being filtered to 0.45 μm and acidified with nitric acid. The reacted shale was vacuum filtered and oven-dried at 50°C. All collected samples were refrigerated immediately after collection.

Ion chromatography (IC), inductively coupled plasma mass spectrometry (ICP-MS), and total dissolved organic and inorganic carbon (TOC/TIC) analyses were performed at the NETL Pittsburgh campus. IC was measured on a ThermoFisher ICS-5000+ with AS11-HC column for anion and CS16 column for cation quantification. This method provided sulfate data with an error of less than 4% in each of the four standards run with the samples. The lower and upper limits of detection for sulfate were 0.2 and 25 mg/L, respectively. At the 1:10 dilution factor, all of the samples were within the calibrated range. Citrate data gathered with this method had 4%, and 3% errors in the two standards. The lower and upper calibration limits for citrate were 0.1–0.5 mg/L. Trace metals present in fluids were measured using a Perkin Elmer Nexion 300D ICPMS instrument. Samples were run at 1:100 dilution. The duplicate analysis of samples showed a relative percent difference of less than 4%. TOC/TIC analysis was conducted using a Shimadzu Total Organic Carbon/Total Inorganic Carbon (TOC/TIC) analyzer. The highest error in TIC/TOC analysis was 14.0%, and the average error was 11.76%.

GC-MS analysis was conducted by Pace Analytical Services following EPA method SW8260B. Samples were put on ice immediately after collection and were brought to Pace Analytical Services' Morgantown Branch immediately after sampling and were analyzed within 24 h of sampling. In accordance with method SW8260B, samples were purged from the aqueous sample with helium gas flowing at 40 ml/min for 11 min onto a Supelco Trap A, Tenax 24 cm sorbent trap. Volatile organics were liberated from the trap by heating it to 180°C and flushed into the GC-MS.

Qualitative analysis of spatial elemental distribution performed on the shale samples was performed using the Oxford INCA EDS capabilities of the JEOL JSM-7600F SEM at the West Virginia University's Shared Research Facility. The chip portion of the dried reacted shales was separated and mounted on aluminum pin mounts with carbon tape. Each mounted chip was sputter-coated with a gold-palladium source to prevent charging during SEM analysis.

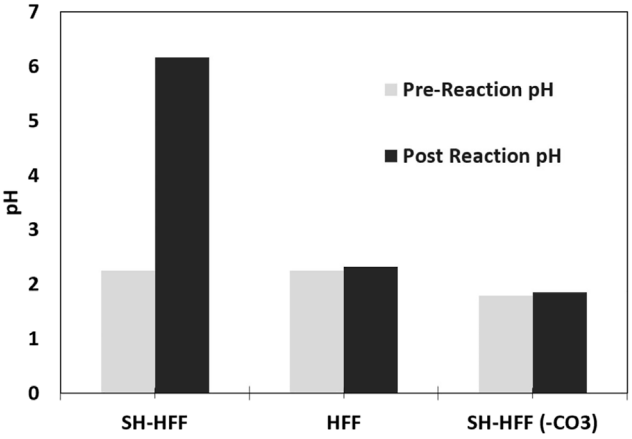

FIGURE 1 | pH measured immediately before reaction vs post-reaction pH for each sample.

Mineral saturation indices were calculated using Geochemists' Workbench with Pitzer and Minteq databases based on measured species concentrations and pH. Geochemical modeling of clay mineral solubility at different pH and reservoir temperatures was performed using the Visual MINTEQ 3.1 modeling program. The SIT method of correction was used for ionic strength, which was set at 0.5 to avoid overloading the program with a higher value. The model was run for kaolinite to determine the mole percent dissolved under the pH conditions of each shale reaction.

3 RESULTS

3.1 pH of the Solution

A contrasting difference was observed in pH of the carbonate-rich and carbonate-free experiments. The pH of the SH-HFF experiment rose from 2.2 to 6.2 after the reaction, whereas in the SH-HFF (-CO_3), pH was similar (1.79 before and 1.85 after) as shown in **Figure 1**. The pH of the control sample (HFF) also remained similar before and after the reaction (2.25 before and 2.32 after).

3.2 Ions in Solution

Post reaction aluminum, iron, arsenic, cadmium, and uranium concentrations were all higher in SH-HFF (-CO_3) than in either SH-HFF or HFF (**Table 3**). Iron in solution was over 800 times higher in SH-HFF (-CO_3) than in SH-HFF. Cadmium and arsenic were 8.7 and 10.5 times more concentrated in SH-HFF (-CO_3) than in SH-HFF, respectively, as shown in **Figure 2**. Iron was also detected in the HFF sample at 36.42 mg/L though no shale was added, nor was any iron included in the HFF. This likely indicates some corrosion of the stainless-steel temperature probe in the reactor by the acidic conditions. We also observed aluminum concentrations in SH-HFF (-CO_3) with two orders of magnitude higher than the other samples. Based on XRD results, the primary sources of aluminum in our shale samples are aluminosilicate

TABLE 3 | pH, IC and ICP-MS fluid chemistry results for each reaction and control fracturing fluid (with no shale).

Sample ID	pH	SO4 (mg/L)	Ba (mg/L)	Fe (mg/L)	Ca (mg/L)	Al (mg/L)	As (µg/L)	Cd (µg/L)	U (µg/L)	Citrate (mg/L)	DIC (mg/L)
SH-HFF	6.2	162.45	3.2	0.2	3,224.181	<0.025	23.2	9.15	<0.155	1.97	12.59
HFF	2.3	6.27	52.29	36.42	3,299.880	0.12	5.06	6.43	0.155	1.1	1.463
SH-HFF (-CO_3)	1.8	137.63	3.36	162.4	3,292.053	29.84	243.3	79.7	95.9	20.44	5.749

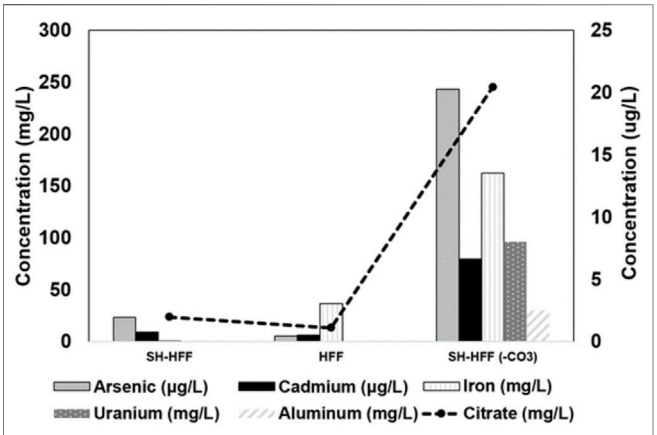

FIGURE 2 | Metals in solution released from reactions with shale. HFF serves as a control for contaminants in additives, reactor corrosion (Fe), and instrument error.

clays which comprised 42% of the mineral content (Pilewski et al., 2019).

Both SH-HFF and SH-HFF (-CO_3) had similarly low barium concentrations at 3.20 mg/L and 3.36 mg/L, respectively. HFF had comparatively more barium at 52.29 mg/L but was still well below the 306 mg/L initial concentration (**Tables 2** and **3**). Sulfate displayed an opposite trend with SH-HFF and SH-HFF (-CO_3) at 162.45 mg/L and 137.63 mg/L, respectively, and much lower in HFF at 6.27 mg/L.

Citrate ion concentration was 10 times higher in SH-HFF (-CO_3) than in SH-HFF or HFF though still lower than the amount originally added as citric acid (**Tables 2** and **3**). The IC used to detect organic anions reports total citrate ion concentration as it does not distinguish between citric acid and citrate ion. In the unreacted fluid 33.6 mg/L of citrate ion were initially included, while 20.44 mg/L were detected in SH-HFF (-CO_3), and only 1.97 and 1.10 mg/L were detected in SH-HFF and HFF, respectively.

Dissolved inorganic carbon was highest in SH-HFF, followed by SH-HFF (-CO_3) and then HFF with 12.59, 5.749, and 1.463 mg/L, respectively (**Tables 2** and **3**). This indicates that DIC in SH-HFF was 2.19 times higher than SH-HFF (-CO_3) and 8.60 times higher than HFF, while SH-HFF (-CO_3) was 3.92 times higher than HFF. Based on the pH dependent speciation of carbonate species, SH-HFF (-CO_3) and HFF will have predominantly $CO_{2\ (aq)}$ and SH-HFF will contain a mixture of $CO_{2\ (aq)}$ and HCO_3^- (Stefansson et al., 2014).

3.3 SEM-EDS of Shale Chips Post-reaction

Characteristic morphologies of pyrite crystals for SH-HFF and SH-HFF (-CO_3) are shown in **Figure 3**. EDS spectra in both samples revealed areas predominantly composed of iron and sulfur, indicating pyrite. In SH-HFF, pyrite areas were mostly found as clusters of tiny crystals, as shown in **Figure 3**. SH-HFF (-CO_3) exclusively displayed pyrite areas in the form of larger single crystals with much lower volume-to-surface area ratios. The crystalline precipitate collected from the HFF reaction primarily gave EDS spectra that indicated barium and sulfur composition, indicating barite precipitation; however, barium was diffused in both shale reactions and insufficiently concentrated to give useful EDS results from the shale.

3.4 Volatile Organic Compounds (VOCs)

SH-HFF had significantly higher concentrations of VOCs: benzene, toluene, ethylbenzene, and xylene, relative to the other experiments (**Figure 4**). It was the only reaction in which ethylbenzene or toluene was detected and had 288% higher benzene, 960% higher m,p-xylene, and 792% higher o-xylene than SH-HFF (-CO_3). Only m,p-xylene was above detection in HFF, and there was 1,300% more in SH-HFF. All BTEX compounds detected in SH-HFF (-CO_3), and HFF are qualitative concentrations as they were above the method detection limit but below the practical quantification limit for the GC-MS method. Amounts detected in each reaction and limits of detection for each analyte are listed in **Table 4**.

3.5 Saturation Index (SI) Calculation

The geochemical modeling performed to determine SI of minerals is shown in **Table 5** and **Figure 5**. In this study, we discuss the relative SI compared to other groups instead of the absolute value because the geochemical modeling databases do not account for organic-complexation/chelation reactions, sorption reactions, cationic exchange reactions, and organic ions (in Pitzer database). SH-HFF fluid has the highest SI for barite, followed by SH-HFF (-CO_3) and HFF. Ca-oxalate hydrates were most saturated in SH-HFF fluid, followed by HFF and SH-HFF (-CO_3). Celestite and anhydrite SI values were highest in SH-HFF fluid, followed by SH-HFF (-CO_3) fluid and HFF fluid. Fe-related minerals (oxides and hydroxides) and calcite also have the highest SI in SH-HFF fluid, but SI in the SH-HFF (-CO_3) fluid and HFF fluid was similar.

4 DISCUSSION

4.1 Carbonate Dissolution

SH-HFF experiment demonstrates a significant increase in pH post-reaction (**Figure 1**). On the other hand, the SH-HFF (-CO_3)

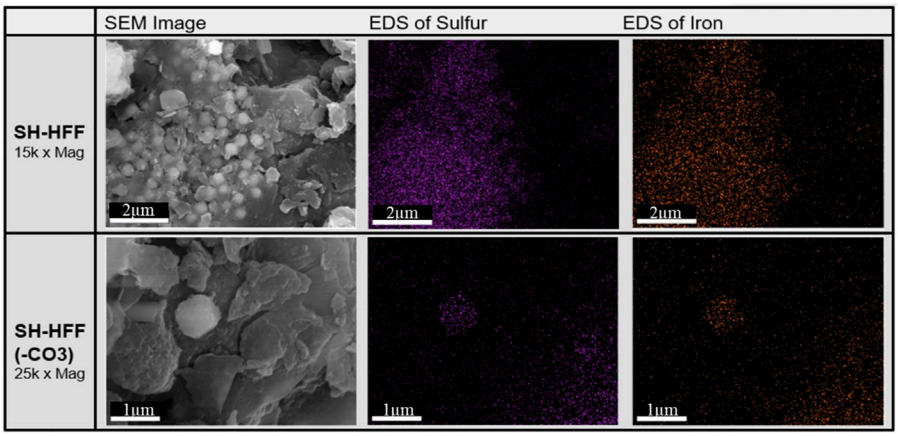

FIGURE 3 | SEM and SEM-EDS images of reacted SH-HFF and SH-HFF (-CO3) shale chips. The sulfur and iron dense areas detected by EDS are presumed to be pyrite.

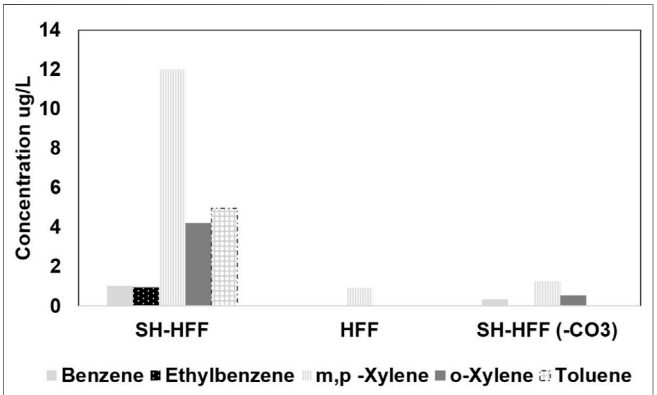

FIGURE 4 | BTEX in solution for each reaction by GC-MS.

sample maintained a stable acidic pH before and after the reaction (**Figure 1**). Since the only difference between the SH-HFF and SH-HFF ($-CO_3$) sample was the lack of carbonate in the latter, and we can conclude that the carbonate minerals are the primary factor controlling the pH of shale-HFF solutions. These results are in agreement with previous studies that reacted shale samples of varying mineral composition with HFF and reported that pH in the post-reaction solution is strongly correlated with the carbonate content of the shale (Harrison et al., 2017; Jew et al., 2017; Pilewski et al., 2019). For example, prior experimental studies show that carbonate-rich Eagle Ford shale samples had a consistently higher pH than the lower carbonate Marcellus Shale following reaction with acidic solutions (Jew et al., 2017). Our results also strongly support that the pH of the SH-HFF reaction increased due to the dissolution of carbonate minerals, while the SH-HFF ($-CO_3$) maintained the lower pH due to lack of buffering by carbonates.

Carbonate dissolution should also increase the Ca ion concentration in the solution (as observed by Harrison et al., 2017). However, in our experiment, the calcium in the solution does not show any trend. We hypothesize that the high amount of calcium added to the brine component of our fracturing fluid mixture as calcium chloride probably swamped out any increasing calcium trend due to $CaCO_3$ dissolution (**Table 2** and **3**).

4.2 Dissolution of Clay Minerals

In the SH-HFF ($-CO_3$) reaction, the aluminium concentration was 29,835 µg/L, while it was below the detection limit (25.1 µg/L) in SH-HFF (**Figure 6**). The sources of aluminum in these reactions are the aluminosilicate mixed clay minerals and possibly minor amounts of feldspar present in the shale, indicating that clay dissolution occurred in the SH-HFF ($-CO_3$) reaction. Several clays are most soluble at very low pH values when exposed to longer durations (days to weeks) and least

TABLE 4 | BTEX in solution from GC-MS analysis with detection and quantification limits.

Compound	Benzene (µg/L)	Ethylbenzene (µg/L)	m,p -xylene (µg/L)	o-Xylene (µg/L)	Toluene (µg/L)
SH-HFF	1.01	0.95	12	4.2	4.97
HFF	Non-detect	Non-Detect	0.92	Non-Detect	Non-Detect
SH-HFF ($-CO_3$)	0.35	Non-Detect	1.25	0.53	Non-Detect
Limit of Detection	0.0790	0.2080	0.3700	0.1120	0.1020
Quantification Limit	0.5000	2.0000	1.0000	1.0000	0.5000

TABLE 5 | Saturation indices (SI) of selected minerals. Ca-oxalates and calcite SI were calculated using MINTEQ database and other minerals were calculated using Pitzer database. The temperature of experimental groups is 100°C. *-UR-HFF values are determined using data from (Pilewski et al., 2019).

Mineral		SH-HFF	HFF	SH-HFF-CO_3	UR-HFF 100C*	UR-HFF 25C*
Barite	log Q/K	0.24	0.02	0.14	0.56	1.24
Celestite	log Q/K	−0.03	−1.36	−0.10	−1.09	−1.37
Anhydrite	log Q/K	−0.36	−1.78	−0.46	−1.72	−2.56
FeO(c)	log Q/K	−2.14	−7.57	−7.88		
$Fe(OH)_{2(ppd)}$	log Q/K	−3.82	−9.25	−9.56		
Ca-Oxalate:H_2O	log Q/K	0.97	0.00	−1.02		
Ca-Oxalate:$3H_2O$	log Q/K	0.53	−0.44	−1.46		
Calcite	log Q/K	−0.09	−8.33	−8.68		

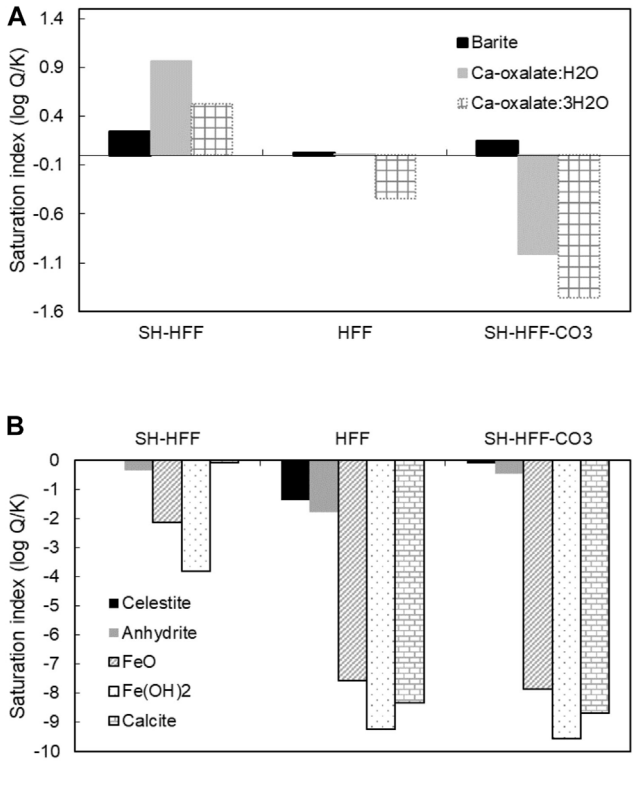

FIGURE 5 | Saturation indices (SI) of selected minerals. Ca-oxalates and calcite SI were calculated using MINTEQ database and other minerals were calculated using Pitzer database. The temperature of experimental groups is 100°C.

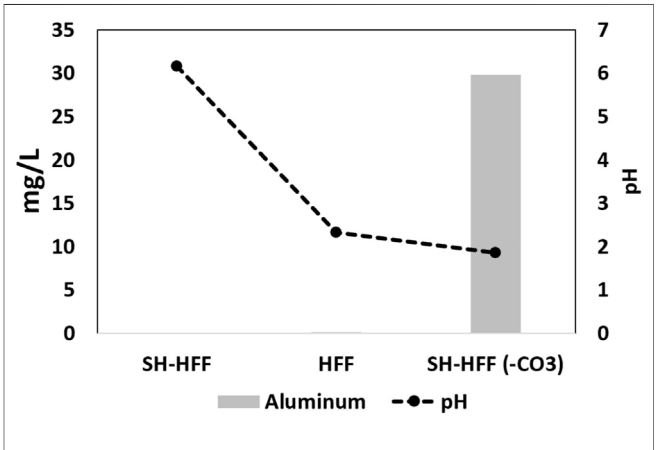

FIGURE 6 | Aluminum in solution plotted against pH to highlight the role of pH in aluminum dissolution from clay minerals.

soluble near pH 6 (Oelkers et al., 1994; Takahashi et al., 1995). The Visual MINTEQ 3.1 program shows that kaolinite was slightly soluble at 100°C and pH 1.89 as in SH-HFF (-CO_3) and was not soluble when the pH was raised to 6.2 similar to SH-HFF reaction. In this simplified model, kaolinite was added as a finite solid and it dissolved over 1800 times more at pH 1.89 compared to 6.2 pH when the model reached equilibrium. Based on this simple modeling, it seems likely that the absence of carbonates buffers the pH and results in some clay mineral dissolution. Since clay generally constitutes the major fraction of shale, in real field situations dissolution of clays (especially in low carbonate shales) can substantially increase the porosity and permeability of shale. However, large scale clay dissolution could also result in instability and collapse of microfractures decreasing permeability.

Using stoichiometric calculations, we determined the amount of clay minerals that dissolved in SH-HFF (-CO_3) reaction (**Supplementary Material**). We determined clay dissolution by considering two end-member models: one with 100% kaolinite and other with 100% illite mineral. Based on our calculations, if we assume 100% of clay minerals are comprised of kaolinite, ~57.02 mg of kaolinite can be dissolved. On the other hand, if 100% of clay is illite, ~28.66 mg of illite can be dissolved. Since clay minerals in Marcellus shale are primarily composed of illite and kaolinite clay minerals (Hupp and Donovan, 2018), the total amount of clay mineral dissolution should range between 28.66 and 57.02 mg. Such low percent of clay mineral dissolution is likely to increase the porosity/permeability and flow of HFF in shale instead of collapsing microfractures.

4.3 Pyrite Dissolution

Previous studies on shale-HFF reactions have shown that pyrite dissolution is mainly controlled by Eh and pH conditions. Several bench-scale experiments demonstrated that pyrite becomes unstable under oxidizing conditions, leading to oxidative dissolution that releases iron and sulfur into solution

(Harrison et al., 2017; Jew et al., 2017; Marcon et al., 2017; Paukert Vankeuren et al., 2017). In this system, numerous reactions are proposed to occur due to diverse oxidizing species in solution. For example, oxidizing breakers, including ammonium persulfate, have been observed to produce a range of oxidizing species such as the sulfate and hydroxide anions in the injected HFF that can oxidize pyrite, in addition to dissolved molecular oxygen (Sumner and Plata, 2019). Several previous studies have also observed that pyrite dissolution is higher under conditions of higher pH and carbonate contents (Harrison et al., 2017; Jew et al., 2017; Paukert Vankeuren et al., 2017). However, the actual impact of pH and carbonate content could not be determined as other factors affecting pyrite dissolution such as Eh and ionic strength were not kept constant.

Although many previous studies have shown increased pyrite dissolution with higher carbonate content, higher pH, and higher Eh conditions, no such trends are observed in this study. Interestingly, an opposite trend was observed in carbonate-rich and carbonate-free reactions. Our SEM-EDS results indicate more significant pyrite dissolution in SH-HFF (-CO3) than in SH-HFF by depicting different morphologies of pyrite crystals on the surface of shale chips after reactions (**Figure 3**). Under the SEM in the SH-HFF chips, most pyrite crystals were found as framboids of many small crystals with large surface area to volume ratios, while in the SH-HFF (-CO3) chips, the pyrite was found exclusively as larger single crystals. This suggests that the greater extent of pyrite dissolution in the SH-HFF (-CO3) dissolved the smaller framboidal crystals (seen in SH-HFF) due to their greater surface area to volume ratio, leaving only the most robust pyrite crystals intact. We postulate the pyrite dissolution in this study was mainly controlled by chelation reactions by citrate (and possibly by bitumen) instead of pH and Eh conditions.

The pH buffering by carbonate minerals can influence the ability of dissolved organic compounds to chelate and oxidize dissolved iron. Organic iron chelation can accelerate pyrite dissolution by 2 to 3 orders of magnitude depending on conditions (Jones et al., 2015). This has been demonstrated both for citric acid, which is added to HFF to control iron, and bitumen mobilized from the shale formation (Jones et al., 2015; Jew et al., 2017). Citric acid's level of protonation varies with pH, which affects its reactivity. When carbonates raise the solution pH, the citric acid molecule loses hydrogen and becomes a more reactive anion. Bitumen has an indeterminate chemical composition as it is a blend of soluble organic components found in shales. However, the organic acids present in bitumen are affected by pH similar to citric acid. The citrate ion concentration was an order of magnitude greater in SH-HFF ($-CO_3$) than in SH-HFF (**Figure 2**). Therefore, the higher citrate in SH-HFF ($-CO_3$) promoted higher pyrite dissolution through iron chelation and oxidation. During this process, citric acid chelates iron, increasing the iron II rate to iron III oxidation. Additionally, iron III in solution could promote further oxidation of sulfide in pyrite to sulfate, resulting in a cyclical breakdown of pyrite catalyzed by citric acid (Bonnissel-Gissinger et al., 1998). Another factor that can influence iron II oxidation in SH-HFF ($-CO_3$) could be the presence of bitumen mobilized from the shale by acid treatment (Jew et al., 2017). However, this possibility needs to be further investigated.

Heavy metals such as arsenic and cadmium are commonly associated with pyrite in organic-rich shales (Wang et al., 2016; Armstrong et al., 2019) and are released when pyrite is dissolved. This indicates that pyrite dissolution can pose a challenge for produced water treatment. The LM-2 shale sample was comprised of 5% pyrite by weight (Pilewski et al., 2019), and pyrite is the presumptive primary source of heavy metals in the shale (Salomons, 1995; Rimstidt and Vaughan, 2003; Jew et al., 2017; Mehta and D. Kocar, 2019). Our data also demonstrate this trend and show that under acidic conditions (sample SH-HFF($-CO_3^{2-}$)), a higher concentration of metals such as As, Cd, and Fe are released due to pyrite dissolution (as shown in **Figure 2** and **Table 3**).

Another possibility is that pyrite dissolution occurred in both SH-HFF ($-CO_3$) and SH-HFF, but the precipitation reactions (e.g. iron oxyhydroxides precipitation) did not occur in SH-HFF ($-CO_3$) experiment (e.g., Jew et al., 2017; Hakala et al., 2021). The secondary precipitation reactions are also expected to scavenge trace metals from the solution. This observation is consistent with the calculated low saturation indices of iron (oxy) hydroxides in SH-HFF ($-CO_3$) as compared to the SH-HFF sample (**Figure 5B**). However, since no evidence of such precipitation of iron (oxy) hydroxides was observed in SEM-EDS analysis of SH-HFF sample, iron mineral precipitation most likely played a minor role in controlling fluid chemistry in these experiments.

Our results reveal the importance of understanding organic complexation/chelation reactions in pyrite dissolution and heavy metals release. Further, our geochemical modeling calculations failed to predict such chelation-based reactions and demonstrate the limitations of geochemical software in modeling complex shale-HFF interactions. Therefore, results from geochemical modeling should be used with caution as several of the thermodynamics-based software packages do not incorporate extensive organic complexation/chelation reactions.

4.4 Carbonate Effect on Fracturing Fluid Chemistry

IC analysis of fluids post-reaction indicates that the citric acid added to the HFF was retained at 61% of the initial concentration in SH-HFF ($-CO_3$) and 10 times less in SH-HFF and HFF (**Figure 7**). The disparity in citric acid left in the solution could have been controlled by 1) different reactivity of citrate ions at different pH and 2) calcium citrate precipitation. Citric acid has a pKa1 of 2.79, indicating it remains protonated at pH below 2.79 and deprotonated above it (Al-Khaldi et al., 2007). In the presence of calcite, the deprotonated citrate anions attach to positive sites on the calcite surface, resulting in a decrease in citrate concentrations in solution. Additionally, calcium citrate precipitation has been previously reported to increase further when the pH of the solution is greater than 6 (Al-Khaldi et al., 2007). Since the SH-HFF had a final pH of 6.2, calcium citrate precipitation seems to be the most likely scenario that controlled total citrate concentration. On the other hand, the SH-HFF ($-CO_3$) sample had a pH of 1.8, which would not allow for calcium citrate precipitation (**Figure 7**). Additionally, SH-HFF ($-CO_3$) had a pH below citric acid's pKa_1 of 2.79 (Al-Khaldi et al., 2007), and citric acid was less likely to react with other chemical species while protonated.

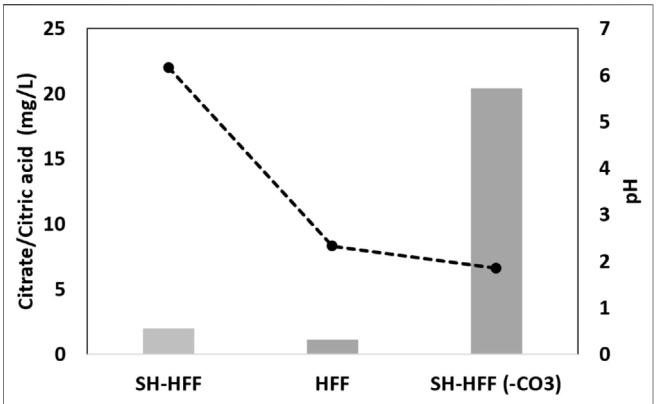

FIGURE 7 | Citrate plotted against pH demonstrating the pH dependency of calcium citrate.

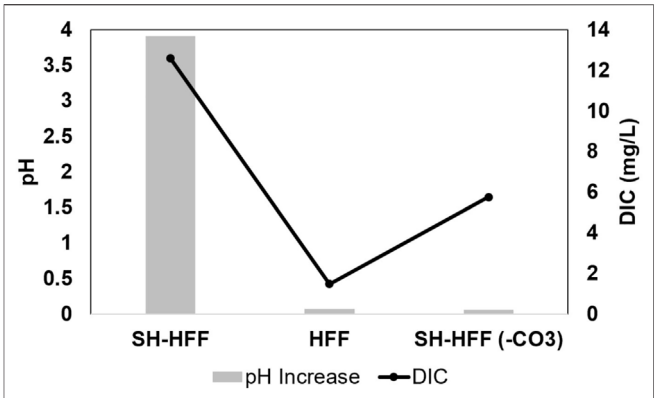

FIGURE 8 | The change in pH due to carbonate dissolution plotted with DIC.

Although calcium citrate precipitation is not predicted by geochemical modeling, this is probably due to the unaccountability of chelation reactions by citrate ions in the Pitzer and Minteq databases. However, Ca-oxalate hydrates were predicted to be supersaturated in the SH-HFF (**Figure 5A**; **Table 5**), supporting the hypothesis of Ca -organic ions precipitation. The oxalate ions are potentially derived from shale organic matter or from petroleum distillate added in the fracturing fluid (Pilewski et al., 2019; Donmoyer et al., 2021).

In the control reaction, although HFF had a similar pH and lacked any carbonate minerals, the detected citrate was similar to SH-HFF rather than SH-HFF (-CO_3). This is likely a result of the ammonium persulfate breaker reacting with citric acid added in the fracturing fluid in the absence of minerals and organic matter. Al-Khaldi et al., 2007 found that oxidizing breakers in fracturing fluid predominantly reacted with pyrite when oxidizer concentrations were low and more aggressively oxidized shale organic matter when the amount of oxidizer needed to dissolve pyrite was exceeded. It is likely that ammonium persulfate preferentially reacted with shale mineral and organic phases in the reactions containing shale; however, in the HFF-only experiment, ammonium persulfate reacted with citric acid and decreased their net concentration.

Carbonate minerals in the shale-HFF experiment also seem to affect oxidation strength of the fluid by impacting the oxidizing ability of the ammonium persulfate in the fracturing fluid. Ammonium persulfate is a highly soluble salt ($(NH_4)_2S_2O_8$) and dissociates into separate ions in solution. The persulfate ion ($S_2O_8^{-2}$) is strongly oxidizing and reduces to two sulfate ions which are also strongly oxidizing. This step requires activation energy and can be limiting in ambient conditions (Liang et al., 2008). However, at 100°C for 14 days, the persulfate is exposed to conditions that enhance its oxidation kinetics; for example, persulfate was found to fully decompose in 2 h at 90°C and decompose more quickly at higher temperatures (Babu et al., 2002). The sulfate ions react with water to produce HSO_4^- and OH, the latter of which is a reactive oxidizing species (ROS) (Deng and Ezyske, 2011). Carbonate dissolution produces bicarbonate ions (HCO_3^-), which are ROS scavengers and react with oxidizing hydroxide ions to produce water and carbonate ions, which are not oxidizing. Because of this, alkalinity from carbonate minerals probably reduced ammonium persulfate's overall ability to oxidize (Deng and Ezyske, 2011).

4.5 BTEX Oxidation

All BTEX compounds were present at higher concentrations in SH-HFF compared to SH-HFF (-CO_3) or HFF (**Figure 4**). A major reason for the discrepancy between the shale reactions is the oxidizing strengths of the solutions. In environmental remediation, ammonium persulfate is used as a remediation strategy (Deng and Ezyske, 2011; Hilles et al., 2016) to oxidize BTEX compounds; we expect it is performing the same function in our experiments. The greater efficacy of ammonium persulfate as an oxidizer in SH-HFF (-CO_3), due to the absence of ROS scavenging bicarbonate, resulted in higher oxidation of BTEX compounds in solution.

Concurrent oxidation of BTEX and shale organic matter in the SH-HFF (-CO_3) experiment is supported by evidence of increased shale organic matter oxidation. Uranium in shale is associated with organic matter and is released into solution under oxidizing conditions when organic matter is broken down (Armstrong et al., 2019). Elevated concentration of uranium in the SH-HFF (-CO_3) fluids relative to the other samples suggests that it is released from the shale (**Figure 2**). Enhanced organic matter oxidation in the SH-HFF (-CO_3) experiment is also supported by the increased level of TIC in the SH-HFF (-CO_3) experiment compared to the HFF experiment (5.749 mg/L and 1.463 mg/L, respectively: **Figure 8**). Since the SH-HFF (-CO_3) experiment contained shale with carbonate phases removed, the only source of DIC would have been CO_2 released by the oxidation of organic matter. The oxidative decomposition of BTEX has also been shown to produce carbon dioxide, which could have also increased DIC (Lovley, 1997). HFF had a similar pH of 2.3 to SH-HFF (-CO_3) at 1.8 and experienced the same pressure and temperature effects on CO_2 solubility; however, since it did not have the shale organic matter to oxidize, it had a lower DIC in solution. The uranium and dissolved inorganic carbon in solution both

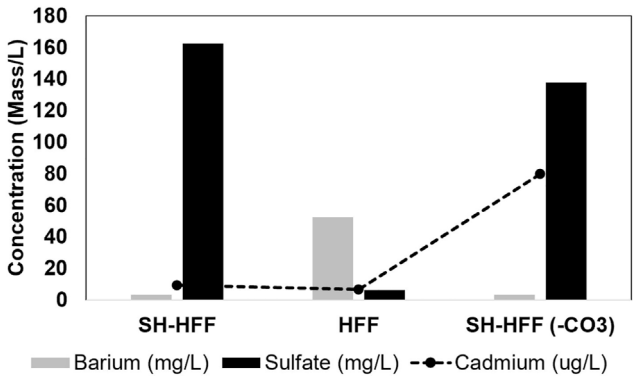

FIGURE 9 | Barium and sulfate ions in solution indicating limiting reagent or barite precipitation. Cadmium is plotted as a proxy for pyrite dissolution vs sulfate in solution.

indicate that SH-HFF ($-CO_3$) experienced organic matter oxidation, which would also explain the low BTEX in the solution.

4.6 Barium and Sulfate

Evidence for barite precipitation is found in all three experiments, as barium concentration is much lower in all three post-reaction solutions than the initial concentration added to the fracturing fluid (**Figure 9**). The geochemical modeling results also show the SI values > 0 for all three reactions indicating barite precipitation (**Figure 5**; **Table 5**). This matches with observations from previous workers as barite is typically found oversaturated under well conditions (Paukert Vankeuren et al., 2017; Pilewski et al., 2019).

Using geochemical data from Pilewski et al., 2019, we determined that barite SI values were much higher in unreacted HFF (**Table 5**). The higher SI value of unreacted HFF indicates the HFF was not thermodynamically stable, and it led to the precipitation of barite even before the high T-P reaction started. Similar evidence of barite precipitation was observed in field-collected HFF (Xiong et al., 2020b) and similar synthetic HFF (Xiong et al., 2020a). Interestingly, in the three high T-P reactions, the barite SI and sulfate concentrations were generally higher in both shale-containing batches as compared to reacted HFF (**Figure 5**; **Table 5**). Moreover, the sulfate and SI trends in these three reactions were opposite to the Ba trend. This is probably due to the addition of sulfate released from pyrite dissolution compared to the HFF batch. In HFF, sulfate was the limiting factor as its only source was the breakdown of persulfates, and there was more barium added to the fracturing fluid stoichiometrically. In the shale reactions, sulfate was released from pyrite dissolution, but there was relatively less barium released, which was likely the limiting reagent (Xiong et al., 2020a). Similar to barite, celestite and anhydrite SI were higher in the two batches with shale than the HFF batch due to sulfate released from the shale (**Figure 5A**; **Table 5**).

It is noteworthy that despite showing other evidence of higher pyrite oxidation, SH-HFF ($-CO_3$) had lower sulfate than SH-HFF, though it is a product of pyrite oxidation. It is likely that the oxidation reactions with organics led to the binding of the sulfur species with shale organic matter. Evidence of sulfur uptake by organic matter in shale-HFF reactions has been reported previously, particularly during kerogen oxidation (Yan et al., 2013; Hull et al., 2019). It is also possible that some of the sulfur reacted with BTEX compounds or the oxidized products of BTEX compounds. However, these proposed reaction mechanisms need to be further investigated.

5 CONCLUSION

The results of our study demonstrate that carbonate mineral content controls several critical shale-HFF reactions in the reservoir and need to be accounted for in designing the chemical make-up of HFF. The key observations of our study are:

1) The presence of carbonate minerals in shale increased the pH of the solution dramatically. The pH increase is accompanied by a lack of aluminum released to the solution, indicating that carbonates prevented clay mineral dissolution. Carbonate free experiments had lower pH which led to the dissolution of clay minerals.
2) Lower citrate concentration in carbonate rich shale (SH-HFF experiment) indicated that citric acid included in the HFF was removed via precipitation of calcium citrate.
3) Pyrite dissolution is mainly controlled via chelation by citrate ions. The lower concentration of citrate in the carbonate rich shale limited the pyrite dissolution and vice versa in the carbonate free sample. Pyrite dissolution in carbonate free sample led to release of inorganic contaminants such as As and Cd.
4) The oxidizing breaker ammonium persulfate was less effective at dissolving pyrite in carbonate rich shale due to higher ROS scavenging by carbonate and bicarbonate anions.
5) ROS scavenging by carbonate and bicarbonate anions led to lower uranium and higher BTEX in solution in the carbonate rich shale experiment, indicating that less organic matter is impacted by ROS.
6) A higher DIC in the carbonate free shale experiments indicate that shale organic matter was possibly oxidized in the presence of a greater abundance of ROS.

The key limitations of this study were that 1) due to limited sample size, duplicate experiments could not be performed and, 2) there could be minor artifacts related to the carbonate dissolution, such as increased specific surface area and release of carbonate bound metals/organics.

6 IMPLICATIONS

The combination of the amount and type of carbonate minerals in the shale formation and the acid added to the HFF controls the pH, Eh, and ionic strength of downhole conditions. In high

carbonate shale formations, carbonate dissolution by HCl is the dominant dissolution process that can significantly increase the porosity/permeability while there is little or no effect on the clay minerals. However, in low carbonate shale, HCl can dissolve substantial amount of clay. Clays are generally hard to fracture due to their ductile nature, so dissolving clay minerals could improve permeability and stimulate fracture propagation. Generally during drilling in lower carbonate shales, HCl is either not added or added in lower amounts to the HFF. Our study shows that HCl could be added to HFF even for low carbonate high clay shales to improve permeability of the formation.

Another important implication of the study is that dissolution/precipitation of minerals such as pyrite, calcium citrate/oxalate, barite is controlled directly or indirectly by carbonate content. The dissolution/precipitation of these minerals could also significantly impact hydrocarbon recovery. For example, we found that pyrite dissolution increases in absence of carbonates due to "chelation" by citrate ions. Pyrite accounts for 5% by weight in our sample and its dissolution could result in significant increase of porosity/permeability in the formation. This study therefore reflects light on the role of "chelation" in fluid chemistry and dissolution precipitation reactions that has been generally overlooked in previous studies. Understanding these dissolution mechanisms are also critical for reservoir stimulation.

This study also developed an understanding of the role of carbonate minerals and HFF interactions with shale organic matter on the release of heavy metals and volatile organic compounds in produced water. High carbonate sample generated higher organic contaminants, but lower inorganic contaminants as compared to low carbonate content sample. Using this information, fracturing fluids could be engineered to reduce/remediate contaminants in different types of shales.

Our study demonstrates that a better understanding of how carbonate minerals affect shale-HFF interactions will enable shale-gas operators to improve long-term yield and reduce environmental risks posed by the operation.

DATA AVAILABILITY STATEMENT

The original contributions presented in the study are included in the article/**Supplementary Material** further inquiries can be directed to the corresponding author.

AUTHOR CONTRIBUTIONS

BF, VA and SS designed, conducted the experiments and wrote the initial draft of the manuscript. VA, SS, JAH, and WX reviewed and edited the manuscript. WX and VA performed geochemical modeling.

FUNDING

The research was supported by two Department of Energy's National Energy Technology Laboratory grants (DE#FE0024297; DE#FE0004000) awarded to Sharma, and the Onshore Unconventional Resources Portfolio through the NETL Research and Innovation Center (Field Work Proposal 1022415, Task 3).

ACKNOWLEDGMENTS

We thank the NETL Pittsburgh Analytical Laboratory for performing ICP-MS analyses and Dr. Mengling Stuckman and Mr. Joshua Miller for performing IC and TOC/TIC analyses. We also thank West Virginia University's Shared Research Facility and Dr. Marcela Redigolo for helping in the SEM-EDS analysis. SWN Energy are acknowledged for providing sample for the study.

SUPPLEMENTARY MATERIAL

The Supplementary Material for this article can be found online at: https://www.frontiersin.org/articles/10.3389/feart.2021.695978/full#supplementary-material

REFERENCES

Abualfaraj, N., Gurian, P. L., and Olson, M. S. (2014). Characterization of Marcellus Shale Flowback Water. *Environ. Eng. Sci.* 31, 514–524. doi:10.1089/ees.2014.0001

Agrawal, V., and Sharma, S. (2020). Are We Modeling the Properties of Unconventional Shales Correctly? *Fuel* 267, 117316. doi:10.1016/j.fuel.2020.117316

Agrawal, V., and Sharma, S. (2018a). Improved Kerogen Models for Determining Thermal Maturity and Hydrocarbon Potential of Shale. *Sci. Rep.* 8, 17465. doi:10.1038/s41598-018-35560-8

Agrawal, V., and Sharma, S. (2018b). Molecular Characterization of Kerogen and its Implications for Determining Hydrocarbon Potential, Organic Matter Sources and Thermal Maturity in Marcellus Shale. *Fuel* 228, 429–437. doi:10.1016/j.fuel.2018.04.053

Agrawal, V., and Sharma, S. (2018c). Testing Utility of Organogeochemical Proxies to Assess Sources of Organic Matter, Paleoredox Conditions, and Thermal Maturity in Mature Marcellus Shale. *Front. Energ. Res.* 6, 42. doi:10.3389/fenrg.2018.00042

Al-Khaldi, M. H., Nasr-El-Din, H. A., Mehta, S., and Al-Aamri, A. D. (2007). Reaction of Citric Acid with Calcite. *Chem. Eng. Sci.* 62, 5880–5896. doi:10.1016/j.ces.2007.06.021

Armstrong, J. G. T., Parnell, J., Bullock, L. A., Boyce, A. J., Perez, M., and Feldmann, J. (2019). Mobilisation of Arsenic, Selenium and Uranium from Carboniferous Black Shales in West Ireland. *Appl. Geochem.* 109, 104401. doi:10.1016/j.apgeochem.2019.104401

Arthur, J. D., Bohmand, B., and Layne, M. (2008). Hydraulic fracturing considerations for natural gas wells of the Marcellus shale. in Proceedings of ground water protection council 2008 annual forum, Cincinnati; 21-24 September 2008.

Babu, M. N., Sahu, K. K., and Pandey, B. D. (2002). Zinc Recovery from Sphalerite Concentrate by Direct Oxidative Leaching with Ammonium, Sodium and Potassium Persulphates. *Hydrometallurgy* 64, 119–129. doi:10.1016/S0304-386X(02)00030-0

Bonnissel-Gissinger, P., Alnot, M., Ehrhardt, J.-J., and Behra, P. (1998). Surface Oxidation of Pyrite as a Function of pH. *Environ. Sci. Technol.* 32, 2839–2845. doi:10.1021/es980213c

Deng, Y., and Ezyske, C. M. (2011). Sulfate Radical-Advanced Oxidation Process (SR-AOP) for Simultaneous Removal of Refractory Organic Contaminants and Ammonia in Landfill Leachate. *Water Res.* 45, 6189–6194. doi:10.1016/j.watres.2011.09.015

Dep, P. A. (2010). Hydraulic Fracturing Overview. Available at: http://files.dep.state.pa.us/OilGas/BOGM/BOGMPortalFiles/MarcellusShale/DEP%20Fracing%20overview.pdf.

Donmoyer, S., Agrawal, V., Sharma, S., and Hakala, J. A. (2021). Effect of Oxidative Breakers on Organic Matter Degradation and Metals Release during Shale-Fracturing Fluid Interactions in the Marcellus Shale. Manuscript in preparation.

EIA (2016). Hydraulically Fractured wells Provide Two-Thirds of U.S. Natural Gas Production - Today in Energy - U.S. Energy Information Administration (EIA). Available at: https://www.eia.gov/todayinenergy/detail.php?id=26112 (Accessed November 4, 2018).

Hakala, J. A., Paukert Vankeuren, A. N., Scheuermann, P. P., Lopano, C., and Guthrie, G. D. (2021). Predicting the Potential for mineral Scale Precipitation in Unconventional Reservoirs Due to Fluid-Rock and Fluid Mixing Geochemical Reactions. *Fuel* 284, 118883. doi:10.1016/j.fuel.2020.118883

Harrison, A. L., Jew, A. D., Dustin, M. K., Thomas, D. L., Joe-Wong, C. M., Bargar, J. R., et al. (2017). Element Release and Reaction-Induced Porosity Alteration during Shale-Hydraulic Fracturing Fluid Interactions. *Appl. Geochem.* 82, 47–62. doi:10.1016/j.apgeochem.2017.05.001

Hilles, A. H., Abu Amr, S. S., Hussein, R. A., El-Sebaie, O. D., and Arafa, A. I. (2016). Performance of Combined Sodium persulfate/H2O2 Based Advanced Oxidation Process in Stabilized Landfill Leachate Treatment. *J. Environ. Manage.* 166, 493–498. doi:10.1016/j.jenvman.2015.10.051

Hoelzer, K., Sumner, A. J., Karatum, O., Nelson, R. K., Drollette, B. D., O'Connor, M. P., et al. (2016). Indications of Transformation Products from Hydraulic Fracturing Additives in Shale-Gas Wastewater. *Environ. Sci. Technol.* 50, 8036–8048. doi:10.1021/acs.est.6b00430

Hull, K. L., Jacobi, D., and Abousleiman, Y. N. (2019). Oxidative Kerogen Degradation: A Potential Approach to Hydraulic Fracturing in Unconventionals. *Energy Fuels* 33, 4758–4766. doi:10.1021/acs.energyfuels.9b00104

Hupp, B. N., and Donovan, J. J. (2018). Quantitative Mineralogy for Facies Definition in the Marcellus Shale (Appalachian Basin, USA) Using XRD-XRF Integration. *Sediment. Geology.* 371, 16–31. doi:10.1016/j.sedgeo.2018.04.007

Jew, A. D., Dustin, M. K., Harrison, A. L., Joe-Wong, C. M., Thomas, D. L., Maher, K., et al. (2017). Impact of Organics and Carbonates on the Oxidation and Precipitation of Iron during Hydraulic Fracturing of Shale. *Energy Fuels* 31, 3643–3658. doi:10.1021/acs.energyfuels.6b03220

Jones, A. M., Griffin, P. J., and Waite, T. D. (2015). Ferrous Iron Oxidation by Molecular Oxygen under Acidic Conditions: The Effect of Citrate, EDTA and Fulvic Acid. *Geochimica et Cosmochimica Acta* 160, 117–131. doi:10.1016/j.gca.2015.03.026

Kondash, A., and Vengosh, A. (2015). Water Footprint of Hydraulic Fracturing. *Environ. Sci. Technol. Lett.* 2, 276–280. doi:10.1021/acs.estlett.5b00211

Liang, C., Huang, C.-F., and Chen, Y.-J. (2008). Potential for Activated Persulfate Degradation of BTEX Contamination. *Water Res.* 42, 4091–4100. doi:10.1016/j.watres.2008.06.022

Lovley, D. R. (1997). Potential for Anaerobic Bioremediation of BTEX in Petroleum-Contaminated Aquifers. *J. Ind. Microbiol. Biotechnol.* 18, 75–81. doi:10.1038/sj.jim.2900246

Marcon, V., Joseph, C., Carter, K. E., Hedges, S. W., Lopano, C. L., Guthrie, G. D., et al. (2017). Experimental Insights into Geochemical Changes in Hydraulically Fractured Marcellus Shale. *Appl. Geochem.* 76, 36–50. doi:10.1016/j.apgeochem.2016.11.005

Mehta, N., and Kocar, B. D. (2019). Geochemical Conditions Conducive for Retention of Trace Elements and Radionuclides during Shale-Fluid Interactions. *Environ. Sci. Process. Impacts* 21, 1764–1776. doi:10.1039/C9EM00244H

Morsy, S., Sheng, J. J., Hetherington, C. J., Soliman, M. Y., and Ezewu, R. O. (2013). "Impact of Matrix Acidizing on Shale Formations," in *SPE Nigeria Annual International Conference And Exhibition* (Lagos, Nigeria: Society of Petroleum Engineers). doi:10.2118/167568-MS

Oelkers, E. H., Schott, J., and Devidal, J.-L. (1994). The Effect of Aluminum, pH, and Chemical Affinity on the Rates of Aluminosilicate Dissolution Reactions. *Geochimica et Cosmochimica Acta* 58, 2011–2024. doi:10.1016/0016-7037(94)90281-X

Paukert Vankeuren, A. N., Hakala, J. A., Jarvis, K., and Moore, J. E. (2017). Mineral Reactions in Shale Gas Reservoirs: Barite Scale Formation from Reusing Produced Water as Hydraulic Fracturing Fluid. *Environ. Sci. Technol.* 51, 9391–9402. doi:10.1021/acs.est.7b01979

Pilewski, J., Sharma, S., Agrawal, V., Hakala, J. A., and Stuckman, M. Y. (2019). Effect of Maturity and Mineralogy on Fluid-Rock Reactions in the Marcellus Shale. *Environ. Sci. Process. Impacts* 21, 845–855. doi:10.1039/C8EM00452H

Riley, K. W., French, D. H., Farrell, O. P., Wood, R. A., and Huggins, F. E. (2012). Modes of Occurrence of Trace and Minor Elements in Some Australian Coals. *Int. J. Coal Geology.* 94, 214–224. doi:10.1016/j.coal.2011.06.011

Rimstidt, J. D., and Vaughan, D. J. (2003). Pyrite Oxidation: a State-Of-The-Art Assessment of the Reaction Mechanism. *Geochimica et Cosmochimica Acta* 67, 873–880. doi:10.1016/S0016-7037(02)01165-1

Salomons, W. (1995). Environmental Impact of Metals Derived from Mining Activities: Processes, Predictions, Prevention. *J. Geochemical Exploration* 52, 5–23. doi:10.1016/0375-6742(94)00039-E

Sharma, S., Agrawal, V., and Akondi, R. N. (2020a). Role of biogeochemistry in efficient shale oil and gas production. *Fuel* 259, 116207–47. doi:10.1016/j.fuel.2019.116207

Sharma, S., Agrawal, V., Akondi, R. N., Wang, Y., and Hakala, A. (2020b). Understanding Controls on the Geochemistry of Hydrocarbon Produced Waters from Different Basins across the US. *Environ. Sci. Process. Impacts* 23, 28–47. doi:10.1039/D0EM00388C

Stefansson, A., Benezeth, P., and Schott, J. (2014). Potentiometric and spectrophotometric study of the stability of magnesium carbonate and bicarbonate ion pairs to 150°C and aqueous inorganic carbon speciation and magnesite solubility. *Geochimica et Cosmochimica Acta* 138, 21–31. doi:10.1016/j.gca.2014.04.008

Sumner, A. J., and Plata, D. L. (2018a). Exploring the Hydraulic Fracturing Parameter Space: a Novel High-Pressure, High-Throughput Reactor System for Investigating Subsurface Chemical Transformations. *Environ. Sci. Process. Impacts* 20, 318–331. doi:10.1039/C7EM00470B

Sumner, A. J., and Plata, D. L. (2018b). Halogenation Chemistry of Hydraulic Fracturing Additives under Highly Saline Simulated Subsurface Conditions. *Environ. Sci. Technol.* 52, 9097–9107. doi:10.1021/acs.est.8b01591

Sumner, A. J., and Plata, D. L. (2019). Oxidative Breakers Can Stimulate Halogenation and Competitive Oxidation in Guar-Gelled Hydraulic Fracturing Fluids. *Environ. Sci. Technol.* 53, 8216–8226. doi:10.1021/acs.est.9b01896

U.S. EIA (2017). *Updates to the Marcellus Shale Play Maps*. Washington, DC: U.S. Department of Energy, 14.

Wang, L., Burns, S., Giammar, D. E., and Fortner, J. D. (2016). Element Mobilization from Bakken Shales as a Function of Water Chemistry. *Chemosphere* 149, 286–293. doi:10.1016/j.chemosphere.2016.01.107

Wang, L., Fortner, J. D., and Giammar, D. E. (2015). Impact of Water Chemistry on Element Mobilization from Eagle Ford Shale. *Environ. Eng. Sci.* 32, 310–320. doi:10.1089/ees.2014.0342

Xiong, W., Gill, M., Moore, J., Crandall, D., Hakala, J. A., and Lopano, C. (2020a). Influence of Reactive Flow Conditions on Barite Scaling in Marcellus Shale during Stimulation and Shut-In Periods of Hydraulic Fracturing. *Energy Fuels* 34, 13625–13635. doi:10.1021/acs.energyfuels.0c02156

Xiong, W., Lopano, C., Hakala, A., and Carney, B. (2020b). "Investigation of Barite Scaling during Reaction between Pre-treated Hydraulic Fracturing Fluid from the Field and Marcellus Shale," in Proceedings of the Unconventional Resources Technology Conference July 20–22, 2020(URTeC), 2275–2284. doi:10.15530/urtec-2020-2734

Yan, J., Jiang, X., Han, X., and Liu, J. (2013). A TG-FTIR Investigation to the Catalytic Effect of mineral Matrix in Oil Shale on the Pyrolysis and Combustion of Kerogen. *Fuel* 104, 307–317. doi:10.1016/j.fuel.2012.10.024

Conflict of Interest: The authors declare that the research was conducted in the absence of any commercial or financial relationships that could be construed as a potential conflict of interest.

Publisher's Note: All claims expressed in this article are solely those of the authors and do not necessarily represent those of their affiliated organizations, or those of the publisher, the editors and the reviewers. Any product that may be evaluated in this article, or claim that may be made by its manufacturer, is not guaranteed or endorsed by the publisher.

Advantages of publishing in Frontiers

OPEN ACCESS
Articles are free to read for greatest visibility and readership

FAST PUBLICATION
Around 90 days from submission to decision

HIGH QUALITY PEER-REVIEW
Rigorous, collaborative, and constructive peer-review

TRANSPARENT PEER-REVIEW
Editors and reviewers acknowledged by name on published articles

Frontiers
Avenue du Tribunal-Fédéral 34
1005 Lausanne | Switzerland

Visit us: www.frontiersin.org
Contact us: frontiersin.org/about/contact

REPRODUCIBILITY OF RESEARCH
Support open data and methods to enhance research reproducibility

DIGITAL PUBLISHING
Articles designed for optimal readership across devices

FOLLOW US
@frontiersin

IMPACT METRICS
Advanced article metrics track visibility across digital media

EXTENSIVE PROMOTION
Marketing and promotion of impactful research

LOOP RESEARCH NETWORK
Our network increases your article's readership